OPTICAL SCIENCES

M. Yamashita
H. Shigekawa
R. Morita (Eds.)

Mono-Cycle Photonics and Optical Scanning Tunneling Microscopy

Route to Femtosecond Ångstrom Technology

Springer

Springer Series in
OPTICAL SCIENCES 99

founded by H.K.V. Lotsch

Springer Series in

OPTICAL SCIENCES

The Springer Series in Optical Sciences, under the leadership of Editor-in-Chief *William T. Rhodes*, Georgia Institute of Technology, USA, provides an expanding selection of research monographs in all major areas of optics: lasers and quantum optics, ultrafast phenomena, optical spectroscopy techniques, optoelectronics, quantum information, information optics, applied laser technology, industrial applications, and other topics of contemporary interest.
With this broad coverage of topics, the series is of use to all research scientists and engineers who need up-to-date reference books.

The editors encourage prospective authors to correspond with them in advance of submitting a manuscript. Submission of manuscripts should be made to the Editor-in-Chief or one of the Editors.

M. Yamashita H. Shigekawa R. Morita
(Eds.)

Mono-Cycle Photonics and Optical Scanning Tunneling Microscopy

Route to Femtosecond Ångstrom Technology

With 241 Figures

Springer

Professor Mikio Yamashita
Hokkaido University
Department of Applied Physics
Kita-12, Nishi-8, Kita-ku
Sapporo 060-8628, Japan
E-mail: mikio@eng.hokudai.ac.jp

Professor Ryuji Morita
Hokkaido University
Department of Applied Physics
Kita-13, Nishi-8, Kita-ku
Sapporo 060-8628, Japan
E-mail: morita@eng.hokudai.ac.jp

Professor Hidemi Shigekawa
University of Tsukuba
Institute of Applied Physics
1-1-1 Tennodai, Tsukuba, 305-8573 Japan
E-mail: hidemi@ims.tsukuba.ac.jp

ISSN 0342-4111

ISBN 3-540-21446-1 Springer Berlin Heidelberg New York

Library of Congress Control Number: 2004111705

Springer is a part of Springer Science+Business Media

springeronline.com

Printed in Germany

Typesetting and production: PTP-Berlin, Protago-TEX-Production GmbH, Germany
Cover concept by eStudio Calamar Steinen using a background picture from The Optics Project. Courtesy of John T. Foley, Professor, Department of Physics and Astronomy, Mississippi State University, USA.
Cover production: *design & production* GmbH, Heidelberg

Printed on acid-free paper 10948460 57/3141/YU 5 4 3 2 1 0

To our families, our mentors, our colleagues and our students.

Preface

Extreme technology has always opened new exciting fields in science and technology. This book is mainly concerned with extreme technologies in the ultrashort time scale (around sub-ten femtoseconds ; 10^{-14}–10^{-15} s) and in the ultrasmall space scale (around sub-nanometers ; $\sim 10^{-10}$ m). Unfortunately, until recent years both technologies developed separately. This book is the first attempt to describe recent advances in femtosecond technology and the fusion of this to nanometer technology. That is, the purpose of this book is to review contributions we have made to the fields of ultrafast optics as well as optical scanning tunneling microscopy (STM) in recent years (1996-2004). Also, in the introductions of several chapters, historical progresses from various sights in this interdisciplinary field are summarized briefly with tables.

Ultrashort optical pulse technology in the near-infrared, the visible and the ultraviolet region is now in a time scale into the few femtosecond range in the optical-mono-cycle region. The full-width at half-maximum (FWHM; T_{du}) of the temporal intensity profile in the mono-cycle pulse equals the single cycle period T_{per} of the electric field, $T_{\mathrm{du}} = T_{\mathrm{per}}$ (Fig. 1). For example, the mono-cycle pulse of a Gaussian profile with a 580 nm center wavelength has a $T_{\mathrm{du}} = 1.9$ fs duration and a $\Delta\nu_{\mathrm{B}} = 228$ THz FWHM bandwidth (the corresponding wavelength bandwidth of $\Delta\lambda_{\mathrm{B}} = 269$ nm) with a spectral broadening from 370 to 1342 nm, according to a relationship of $T_{\mathrm{du}} \times \Delta\nu_{\mathrm{B}} = k$. Here, k is a constant depending on the temporal intensity profile. This equation suggests that with the decrease in pulse duration the spectral bandwidth rapidly increases.

"Few-to-Mono Cycle Photonics" means technology and science are necessary for the realization and application of the few-to-mono cycle pulse in the optical frequency region. In this book, among these widely and rapidly developing fields, four basic technologies of the ultrabroadband pulse generation, the ultrabroadband chirp or phase compensation, the phase and amplitude characterization of the ultrashort pulse, and the feedback field control of the ultrabroadband, ultrashort pulse are dealt with. In addition, the theory of the ultrashort pulse nonlinear prorogation beyond the slowly-varying-envelope approximation is developed. In particular, the generation of the shortest pulse with a 2.8 fs duration, a 1.5 cycle and a 460–1060 nm spectral broadening in the near-infrared and visible region, and the computer-controlled feedback

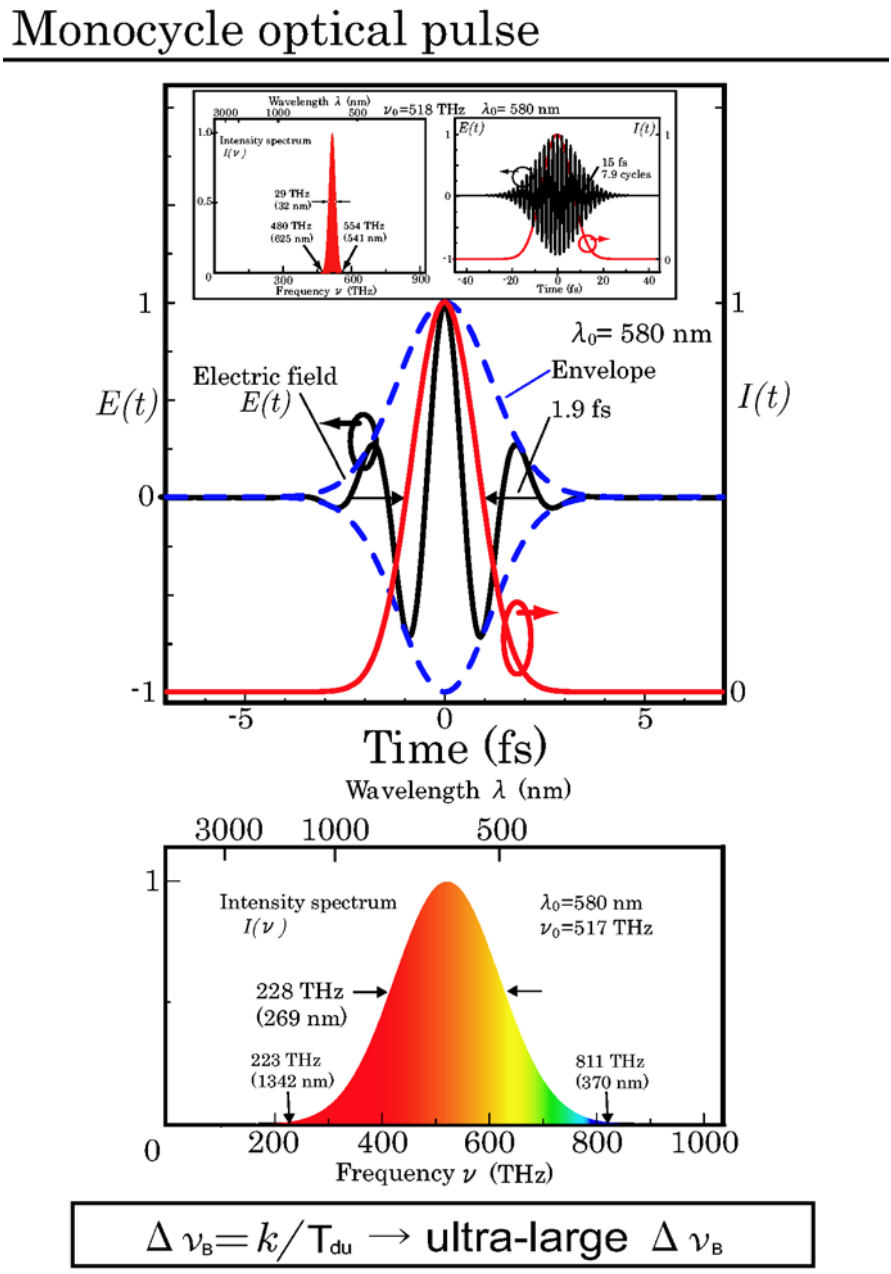

Fig. 1. Monocycle Gaussian pulse with a center wavelength of 580 nm and a duration of 1.9 fs. The inset shows a 15-fs Gaussian pulse with the same center wavelength, for the comparison

manipulation that combines spectral-phase characterization and compensation should be noted. However, the carrier-envelope phase technology, which is currently developing rapidly, is hardly described.

Ultrashort optical pulse technology, which is based on sophisticated laser technology, has the following significant, unique capabilities: to clarify ultrafast phenomena in all fields of natural science and engineering at the highest time resolution; to control ultrafast time-sequential phenomena; to produce an ultra-high peak electric field; and to generate, transmit and process an ultra-high density information signal. In addition, since time is one of essential parameters to describe temporal dynamic phenomena in any disciplines, this fastest technology (among the human-developed ones) is called for across all the fields and disciplines in natural science and engineering. However, this optical technology has the drawback of relatively low spatial resolution ($\gtrsim \mu$m) because of the electro-magnetic wave with a finite wavelength.

On the other hand, STM has the highest spatial resolution of sub-nm, which enables us to observe spatial dynamics at single-atomic and single-molecular levels in real space. There have been a lot of studies using STM, which is related to various phenomena that occur on conductive surfaces, such as thin film growth, molecular adsorption, chemical reaction, electron standing wave, charge density wave, Kondo effect, thermo-dynamics of voltex at surface of high-T_c superconductors. For current researchers, nanoscale science and technology is one of the most attractive and important fields, and realizing new functional devices with nanoscale elements is one of their main goals. In these cases, interactions between optical and electronic systems play essential roles. When the scale of specimens was larger, photo-assisted spectroscopy provided a very helpful way to investigate such structures in materials. For example, photoelectron spectroscopy, photo-scattering spectroscopies and reflection methods have revealed various physical properties of materials until now. However, since the device size is already as small as a few tens of nanometers, these conventional optical methods are not applicable because of the spatial resolutions limited by light source wavelengths, which are generally more than 100 nm as mentioned before. At this moment, only STM related technology is a promising candidate for the investigation of the characteristics of nanoscale structures. Since tunneling current is used as the probe, electronic structures are picked up. Therefore, when STM is combined with the optical system, the analysis of the transient response of photo-induced electronic structures is expected at the ultimate spatial resolution. Therefore, the combination of optical systems with STM is considered to be a very promising technique. However, STM has the inevitable disadvantage of very low time resolution ($\sim$ sub ms) because of the slow response time of the highly sensitive, integrated detector for the very low tunneling current.

To overcome the problems of both technologies and to utilize both features, a new technology and science is required. That is "optical STM". Optical STM means technology and science of the femtosecond-time resolved

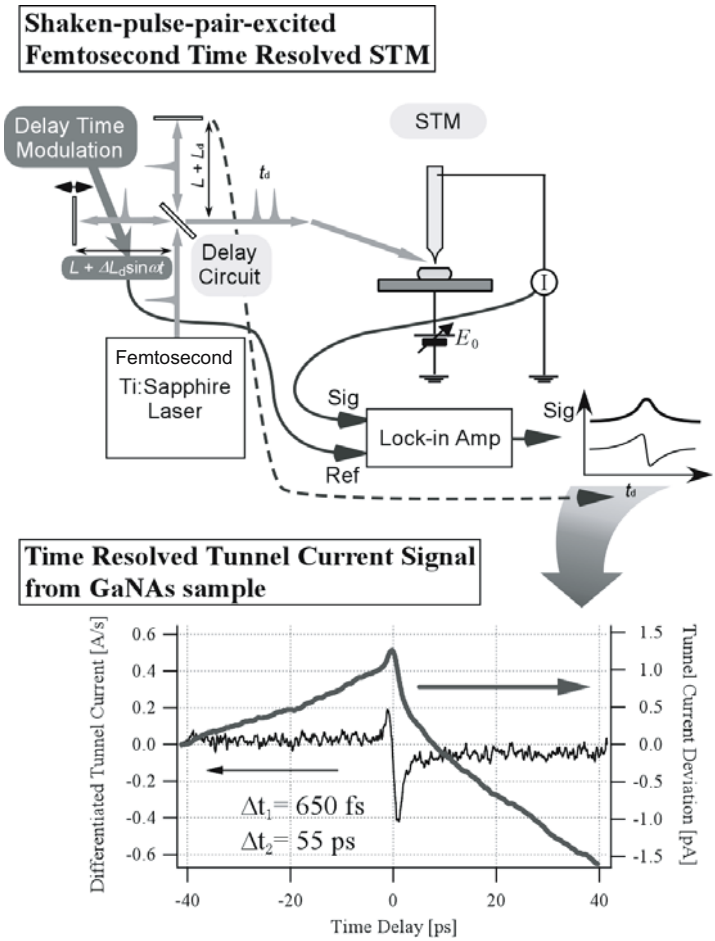

Fig. 2. Femtosecond-time-resolved STM and its application

STM (FTR-STM) and the STM-level phenomena controlled by femtosecond optical pulses, tunable laser excitation and laser excitation power including nonlinear optical phenomena at the atomic level. One example of the principles for FTR-STM is shown in Fig. 2. Its upper part is the schematic of the FTR-STM system, and the lower part is an example result measured for a GaAs sample. Relaxation of the photoinduced current in the band structure is picked up as the two components in the picosecond range. The vales are close to those obtained by the conventional optical pump probe technique, however, since the probe is the tunneling current, the spatial resolution is atomic scale in this case. That is, the controlled delay time between two femtosecond optical pulses for excitation is employed to get highly temporal resolution. The integrated tunneling current of a tip at a fixed position for

each pulse-delay time is employed to get highly spatial resolution, This principle is similar to the conventional pump (a pulse pair) and probe techniques in ultrafast optics. That is, two sequential photon energies of two optical pulses with delay time play the role of the pump to induce or change the tunneling current. And, the observed signal of the integrated tunneling current plays the role of the probe to get information on the temporal surface phenomena at the atomic level. As a result, the probe signal as a function of the delay time provides nonlinear-optically induced dynamics at the spatiotemporal extreme level. Thus, this spatiotemporal-extreme frontier technology has a possibility to open a new field by clarifying and manipulating ultrafast dynamic phenomena at the atomic level, which have not been revealed so far by conventional techniques because of measurements of the temporally coarsened and spatially averaged information in addition to the statisical treatment of a single element.

Accordingly, this book consists of two parts. The first part of few-cycle photonics is organized into six chapters. The second part of optical STM is organized into four chapters.

In Chap. 1, Karasawa, Mizuta and Fang discuss theoretically nonlinear propagation of ultrashort, ultrabroadband optical pulses exceeding the conventional approximation of the slowly-varying envelope in an electric field by various methods of numerical computer analysis.

In Chap. 2, Yamashita, Karasawa, Adachi and Fang review the experiments leading to the generation of ultrabroadband optical pulses with a near or over one-octave bandwidth and a well-behaved spectral phase by unconventional methods including an induced phase modulation technique.

In Chap. 3, Yamashita, Morita and Karasawa focus experimentally and theoretically on the active chirp compensation for ultrabroadband pulses using a spatial light modulator (SLM) technique.

In Chap. 4, Morita, Yamane and Zhang cover the phase and amplitude characterization of the electric field in few-cycle pulses with some techniques.

In Chap. 5, Yamashita, Yamane, Zhang, Adachi and Morita detail experimentally and theoretically the feedback control that combines spectral-phase characterization and compensation for optical pulse generation in the few-to-mono cycle region in the case of various kinds of fiber outputs.

In Chap. 6, Morita and Toda discuss experimentally and theoretically wavelength-multiplex electric-field manipulation of ultrabroadband pulses and its application to the vibration motion control of molecules.

In Chap. 7, Shigekawa and Takeuchi introduce the fundamentals of laser combined STM after brief explanation of the STM bases.

In Chap. 8, Shigekawa and Takeuchi review light-modulated scanning tunneling spectroscopy for visualization of nano-scale band structure in semiconductors.

In Chap. 9, Futaba focuses on the control experiment of semiconductor surface phenomena by femtosecond optical pulse-pair excitation at the atomic level.

In Chap. 10, Shigekawa and Takeuchi discuss the development of FTR-STM using a method of two optical pulse excitation and its application.

In Chap. 11, Yamashita, Shigekawa and Morita describe briefly near-future subjects and directions in few-cycle photonics and optical STM.

Many works introduced here have been carried out by many Hokkaido University and Tsukuba University postdoctoral fellows, visiting associates, graduate (and undergraduate) students. And, most of those works were done under the support of Japan Science and Technology Corporation (JST) as a project of "Optical-wave technology in the cycle-time region and its application to single-atomic and single-molecular dynamic phenomena" for 1997 to 2002.

Finally, the editors wish to thank all of the authors who have contributed to the excellent individual chapters and sections of this book. One of the editors (M. Yamashita) greatly acknowledges Mr. Naoya Nakagawa and Ms. Noriko Yoshida for their secretarial assistance.

Sapporo,
October 2004

Mikio Yamashita
Hidemi Shigekawa
Ryuji Morita

Contents

List of Contributors

Mikio Yamashita
Department of Applied Physics
Hokkaido University
Kita-13, Nishi-8
Kita-ku, Sapporo 060-8628, Japan
mikio@eng.hokudai.ac.jp

Hidemi Shigekawa
Institute of Applied Physics
University of Tsukuba
1-1-1 Tennodai, Tsukuba, 305-8573,
Japan
hidemi@ims.tsukuba.ac.jp

Ryuji Morita
Department of Applied Physics
Hokkaido University
Kita-13, Nishi-8
Kita-ku, Sapporo 060-8628
Japan
morita@eng.hokudai.ac.jp

Naoki Karasawa
Department of Applied Physics
Hokkaido University
Kita-13, Nishi-8
Kita-ku, Sapporo 060-8628, Japan
Current Address:
Chitose Institute of Science
and Technology
758-65, Bibi, Chitose, 066-8655
Japan
n-karasa@photon.chitose.ac.jp

Keisaku Yamane
Department of Applied Physics
Hokkaido University
Kita-13, Nishi-8
Kita-ku, Sapporo 060-8628, Japan
k-yamane@eng.hokudai.ac.jp

Osamu Takeuchi
Institute of Applied Physics
University of Tsukuba
1-1-1 Tennodai, Tsukuba, 305-8573
Japan
osamu@big.or.jp

Zhigang Zhang
Department of Applied Physics
Hokkaido University
Kita-13, Nishi-8
Kita-ku, Sapporo 060-8628, Japan
Current Address:
School of Precision Instruments
and Optoelectronics Engineering
University of Tianjin
92 Weijin Road, Tianjin 300072
People's Republic of China
zhgzhang@tju.edu.cn

Muneyuki Adachi
Department of Applied Physics
Hokkaido University
Kita-13, Nishi-8
Kita-ku, Sapporo 060-8628, Japan
muneyuki@eng.hokudai.ac.jp

Don Futaba
Department of Applied Physics
Hokkaido University
Kita-13, Nishi-8
Kita-ku, Sapporo 060-8628, Japan
dfutaba@eng.hokudai.ac.jp

Yo Mizuta
Department of Applied Physics
Hokkaido University
Kita-13, Nishi-8
Kita-ku, Sapporo 060-8628, Japan
yomizuta@eng.hokudai.ac.jp

Yasunori Toda
Department of Applied Physics
Hokkaido University
Kita-13, Nishi-8
Kita-ku, Sapporo 060-8628, Japan
toda@eng.hokudai.ac.jp

Xiaojun Fang
Department of Applied Physics
Hokkaido University
Kita-13, Nishi-8
Kita-ku, Sapporo 060-8628, Japan

1 Nonlinear Propagation Theory for Few-to-Mono Optical-Cycle Pulses beyond the Slowly-Varying-Envelope Approximation (SVEA)

N. Karasawa, Y. Mizuta, and X. Fang

The recent development of ultrashort pulse lasers as well as spectral-broadening and pulse-compression techniques permit us to use optical pulses which have a duration as short as few-to-mono optical cycles and a bandwidth of several hundred terahertz. To describe propagation of these pulses in a nonlinear optical medium, care must be taken to select what approximations may be used. The slowly-varying-envelope approximation (SVEA) has been used widely to describe nonlinear pulse propagation in an optical fiber [1]. However, it is applicable only to pulses whose temporal envelope changes more slowly compared with optical cycles. The other issue is how to describe correctly linear dispersion relations of the medium when the bandwidths of these pulses become large such that the conventional Taylor expansion at the center frequency and the use of only first several terms may not be applicable. Here we show methods to include the linear dispersion relations rigorously.

Section 1 shows the fundamental equations of the slowly-evolving wave approximation (SEWA) method. Section 2 introduces different numerical methods that do not use an envelope function to describe the electric field of a pulse. Section 3 compares between numerical results and experimental results. Section 4 concludes the chapter.

1.1 Wave Equations for Nonlinear Pulse Propagation

1.1.1 Introduction

We start from Maxwell's equations without source terms:

$$\nabla \times \boldsymbol{E}(x,y,z,t) = -\mu_0 \frac{\partial \boldsymbol{H}(x,y,z,t)}{\partial t}, \tag{1.1}$$

$$\nabla \times \boldsymbol{H}(x,y,z,t) = \frac{\partial \boldsymbol{D}(x,y,z,t)}{\partial t}, \tag{1.2}$$

$$\boldsymbol{D}(x,y,z,t) = \varepsilon_0 \varepsilon_\infty \boldsymbol{E}(x,y,z,t) + \boldsymbol{P}(x,y,z,t), \tag{1.3}$$

where $\boldsymbol{E}$, $\boldsymbol{H}$, $\boldsymbol{D}$, and $\boldsymbol{P}$ are electric field, magnetic field, electric displacement, and polarization respectively. ε_0 and μ_0 are permittivity and permeability constants of a vacuum and ε_∞ is the relative permittivity at infinite

frequency. Numerical methods that do not use an envelope function to describe the electric field of an optical pulse are derived from these equations. The polarization $\boldsymbol{P}$ consists of a linear part $\boldsymbol{P}_{\mathbf{L}}$ and a nonlinear part $\boldsymbol{P}_{\mathbf{NL}}$. By combining (1.1)–(1.3), we have

$$\nabla^2 \boldsymbol{E}(x,y,z,t) - \frac{1}{c^2}\partial_t^2 \boldsymbol{D}_{\mathrm{L}}(x,y,z,t) = \mu_0 \partial_t^2 \boldsymbol{P}_{\mathrm{NL}}(x,y,z,t), \tag{1.4}$$

where c is the speed of light and $\boldsymbol{D}_{\mathbf{L}} = \varepsilon_0 \varepsilon_\infty \boldsymbol{E} + \boldsymbol{P}_{\mathbf{L}}$. Here, the linear polarization and its Fourier transform are given by

$$\boldsymbol{P}_{\mathrm{L}}(x,y,z,t) = \varepsilon_0 \int_{-\infty}^{\infty} \chi^{(1)}(t-t')\boldsymbol{E}(x,y,z,t')\mathrm{d}t', \tag{1.5}$$

$$\tilde{\boldsymbol{P}}_{\mathbf{L}}(x,y,z,\omega) = \varepsilon_0 \tilde{\chi}^{(1)}(\omega)\tilde{\boldsymbol{E}}(x,y,z,\omega), \tag{1.6}$$

where $\chi^{(1)}(t)$ is the linear susceptibility, ω is the angular frequency, and the Fourier transform is defined as $\tilde{\boldsymbol{P}}_{\mathbf{L}}(x,y,z,\omega) = \int_{-\infty}^{\infty} \boldsymbol{P}_{\mathrm{L}}(x,y,z,t)\exp(\mathrm{i}\omega t)\mathrm{d}t$. In these equations, the medium is assumed to be isotropic. Using (1.6), we have the Fourier transform of (1.4) as follows:

$$\left(\nabla_\perp^2 + \partial_z^2 + \frac{\varepsilon(\omega)\omega^2}{c^2}\right)\tilde{\boldsymbol{E}}(x,y,z,\omega) = -\mu_0\omega^2 \tilde{\boldsymbol{P}}_{\mathbf{NL}}(x,y,z,\omega), \tag{1.7}$$

where $\nabla_\perp^2 = \partial_x^2 + \partial_y^2$ and $\varepsilon(\omega) = \varepsilon_\infty + \tilde{\chi}^{(1)}(\omega)$ is the linear dielectric constant. This equation is a starting point for deriving pulse propagation equations using an envelope function. The following derivation is based on [1] and [2].

From now on, we consider propagation of a pulse in the z direction and assume that all fields are linearly polarized in the x direction and hence consider only that component. Then we write $\boldsymbol{E}(x,y,z,t) = \hat{\boldsymbol{x}}[E(x,y,z,t)\exp(-\mathrm{i}\omega_0 t) + \mathrm{c.c.}]/2$ where $\hat{\boldsymbol{x}}$ is the unit vector in the x direction, ω_0 is the center angular frequency, $E(x,y,z,t)$ is the envelope function and c.c. specifies the complex conjugate. We introduce the Fourier transform of the electric field $E(x,y,z,t)$ in the following form:

$$\tilde{E}(x,y,z,\omega) = F(x,y,\omega)\tilde{A}(z,\omega-\omega_0)\exp(\mathrm{i}\beta_0 z), \tag{1.8}$$

where $\beta_0 \equiv \beta(\omega_0)$ is the real part of the propagation constant at ω_0. In this equation, the unperturbed cross-section field $F(x,y,\omega)$ is determined by (1.7) without the nonlinear polarization,

$$\left(\nabla_\perp^2 + \frac{\varepsilon(\omega)\omega^2}{c^2}\right)F(x,y,\omega) = \gamma^2(\omega)F(x,y,\omega), \tag{1.9}$$

where $\gamma(\omega) \equiv \beta(\omega) + \mathrm{i}\alpha(\omega)/2$ is the propagation constant with $\alpha(\omega)$ to be the attenuation constant. For one dimensional propagation, $\gamma(\omega)$ is given by $\gamma(\omega) = \sqrt{\varepsilon(\omega)}\omega/c$, because in this case, $\nabla_\perp F(x,y,\omega) = 0$. When $\gamma(\omega)$ is determined by (1.9), both material dispersion and waveguide dispersion are

included. $\gamma(\omega)$ can have an imaginary part even if the material does not have a loss or gain as in the case of pulse propagation in a gas-filled hollow fiber [3]. For the nonlinear polarization, we consider only the third-order nonlinear optical effect with a coefficient $\chi^{(3)}$ and assume that the medium is isotropic. In the most general form, $\boldsymbol{P}_{\mathrm{NL}}(x,y,z,t)$ is given by

$$\boldsymbol{P}_{\mathrm{NL}}(x,y,z,t) = \varepsilon_0 \iiint_{-\infty}^{\infty} \chi^{(3)}(t-t_1, t-t_2, t-t_3) \times \boldsymbol{E}(x,y,z,t_1)\boldsymbol{E}(x,y,z,t_2)\boldsymbol{E}(x,y,z,t_3)\mathrm{d}t_1\mathrm{d}t_2\mathrm{d}t_3. \quad (1.10)$$

In this section, we only consider the form

$$\boldsymbol{P}_{\mathrm{NL}}(x,y,z,t) = \varepsilon_0\chi^{(3)}\boldsymbol{E}(x,y,z,t) \times \int_{-\infty}^{\infty} R(t-t')|\boldsymbol{E}(x,y,z,t-t')|^2\mathrm{d}t', \quad (1.11)$$

where $R(t)$ is a response function. By using this form, we can treat the instantaneous electronic response (with $R(t) = \delta(t)$) and the delayed vibrational response (the Raman response) of the nonlinear medium. We assume that the nonlinear polarization envelope function can be written in the following form:

$$\tilde{P}_{\mathrm{NL}}(x,y,z,\omega) = \varepsilon_0\chi^{(3)}(\omega)F^3(x,y,\omega)\tilde{p}_{\mathrm{NL}}(z,\omega-\omega_0)\exp(\mathrm{i}\beta_0 z), \quad (1.12)$$

By writing in this form, it is assumed that the frequency dependence of the cross-section field $F(x,y,\omega)$ is small (in the sense that the convolution integral is replaced by the product in the frequency domain). We further assume that we can separate the forward propagating wave and the backward propagating wave and consider only the forward propagating one. We consider that the nonlinear term is small and that the perturbation theory can be used, i.e., the unperturbed operator $H_0 = \nabla_\perp^2 + \varepsilon(\omega)\omega^2/c^2$ in (1.9) is added by the small perturbation operator

$$\Delta H = \frac{\omega^2}{c^2}\chi^{(3)}(\omega)\frac{\tilde{p}_{\mathrm{NL}}(z,\omega-\omega_0)}{\tilde{A}(z,\omega-\omega_0)}F^2(x,y,\omega), \quad (1.13)$$

which is obtained by (1.7), (1.8) and (1.12). Using the first-order perturbation theory, the change of the propagation constant $\Delta\gamma^2$ is calculated to be

$$\Delta\gamma^2 = \frac{\int F(x,y,\omega)\Delta H F(x,y,\omega)\mathrm{d}x\mathrm{d}y}{\int F(x,y,\omega)F(x,y,\omega)\mathrm{d}x\mathrm{d}y} = \frac{\omega^2}{c^2}\chi^{(3)}(\omega)\frac{\tilde{p}_{\mathrm{NL}}(z,\omega-\omega_0)}{\tilde{A}(z,\omega-\omega_0)}N(\omega), \quad (1.14)$$

where $N(\omega) = \int F^4(x,y,\omega)\mathrm{d}x\mathrm{d}y / \int F^2(x,y,\omega)\mathrm{d}x\mathrm{d}y$. By using the first-order perturbation theory, we assume that the pulse propagates in a single spatial eigenmode. Using this result in an equation for $\tilde{A}(z,\omega-\omega_0)$, we obtain

$$(\partial_z^2+\gamma^2)(\tilde{A}(z,\omega-\omega_0)\exp(\mathrm{i}\beta_0 z))=-\Delta\gamma^2\tilde{A}(z,\omega-\omega_0)\exp(\mathrm{i}\beta_0 z). \quad (1.15)$$

Thus we have

$$(\partial_z^2+2\mathrm{i}\beta_0\partial_z-\beta_0^2+\gamma^2(\omega))\tilde{A}(z,\omega-\omega_0)= -\frac{\omega^2 N(\omega)\chi^{(3)}(\omega)}{c^2}\tilde{p}_{\mathrm{NL}}(z,\omega-\omega_0). \quad (1.16)$$

Converting the unit of A to [watt$^{1/2}$] by multiplying $(\int F^2(x,y,\omega)\mathrm{d}x\mathrm{d}y)^{1/2}/(2/\varepsilon_0 cn(\omega))^{1/2}$ and using the relation $\chi^{(3)}(\omega)=4\varepsilon_0 cn^2(\omega)n_2^{\mathrm{I}}(\omega)/4$, where $n_2^{\mathrm{I}}(\omega)$ (in [m^2/W]) is the nonlinear index of refraction of the medium, we have

$$(\partial_z^2+2\mathrm{i}\beta_0\partial_z-\beta_0^2+\gamma^2(\omega))\tilde{A}(z,\omega-\omega_0)= -\frac{8n(\omega)n_2^{\mathrm{I}}(\omega)\omega^2}{3c^2A_{\mathrm{eff}}(\omega)}\tilde{p}_{\mathrm{NL}}(z,\omega-\omega_0), \quad (1.17)$$

where the effective mode area A_{eff} is given by

$$A_{\mathrm{eff}}(\omega)=\frac{(\int F^2(x,y,\omega)\mathrm{d}x\mathrm{d}y)^2}{\int F^4(x,y,\omega)\mathrm{d}x\mathrm{d}y}. \quad (1.18)$$

By inverse Fourier transforming (1.17), we have

$$(\partial_z^2+2\mathrm{i}\beta_0\partial_z-\beta_0^2+\widehat{D}^2)A(z,t)= -\frac{8g(\omega_0)\omega_0^2}{3c^2}\left(1+\frac{\mathrm{i}}{\omega_0}\partial_t\right)^2(1+\mathrm{i}(\partial_\omega(\ln g(\omega))|_{\omega_0})\partial_t)p_{\mathrm{NL}}(z,t), \quad (1.19)$$

where $g(\omega)=n(\omega)n_2^{\mathrm{I}}(\omega)/A_{\mathrm{eff}}(\omega)$ and we include the dispersion of $g(\omega)$ up to the first order terms in the Taylor expansion at ω_0. $\widehat{D}$ is given by the Taylor expansion of the propagation constant as

$$\widehat{D}=\sum_{n=0}^{\infty}\frac{\mathrm{i}^n}{n!}\left(\partial_\omega^n\left(\beta(\omega)+\frac{\mathrm{i}\alpha(\omega)}{2}\right)|_{\omega_0}\right)\partial_t^n. \quad (1.20)$$

At this point, we convert time coordinate such that the center of the pulse is always at time origin as $T=t-\dot{\beta}_0 z$ ($\dot{\beta}_0=\partial_\omega(\beta(\omega))|_{\omega_0}$) and $\xi=z$ ($\partial_t=\partial_T, \partial_z=\partial_\xi-\dot{\beta}_0\partial_T$). Then we have

$$\left[\partial_\xi^2+2\mathrm{i}\beta_0\left(1+\mathrm{i}\frac{\dot{\beta}_0}{\beta_0}\partial_T\right)(\partial_\xi-\mathrm{i}\widehat{D}')+\widehat{D}'^2\right]A(\xi,T)= -\frac{8g(\omega_0)\omega_0^2}{3c^2}\left(1+\frac{\mathrm{i}}{\omega_0}\partial_T\right)^2(1+\mathrm{i}(\partial_\omega(\ln g(\omega))|_{\omega_0})\partial_T)p_{\mathrm{NL}}(\xi,T), \quad (1.21)$$

where $\widehat{D}'=\widehat{D}-\beta_0-\mathrm{i}\dot{\beta}_0\partial_T$. Applying the operator $(2i\beta_0(1+\mathrm{i}\dot{\beta}_0\partial_T/\beta_0))^{-1}$ to both sides of this equation, we have

$$\left[\frac{1}{2\mathrm{i}\beta_0}\left(1+\mathrm{i}\frac{\dot{\beta}_0}{\beta_0}\partial_T\right)^{-1}(\partial_\xi^2+\widehat{D}'^2)+\partial_\xi-\mathrm{i}\widehat{D}'\right]A(\xi,T)$$
$$=\mathrm{i}\frac{4g(\omega_0)\omega_0^2}{3c^2\beta_0}\left(1+\mathrm{i}\frac{\dot{\beta}_0}{\beta_0}\partial_T\right)^{-1}\left(1+\frac{\mathrm{i}}{\omega_0}\partial_T\right)^2$$
$$\times(1+\mathrm{i}(\partial_\omega(\ln g(\omega))|_{\omega_0})\partial_T)p_{\mathrm{NL}}(\xi,T). \tag{1.22}$$

Up to this point, no approximations concerning the slowness of the change of the pulse envelope function with respect to time nor position have been introduced. Now we introduce the approximation with respect to position in (1.22). The first term of the left hand side of this equation can be ignored if $|\partial_\xi A| \ll \beta_0|A|$, which physically means that the spatial variation of the envelope is negligible in the scale of the wavelength of the pulse. Also, we can show that

$$\left(1+\mathrm{i}\frac{\dot{\beta}_0}{\beta_0}\partial_T\right)^{-1}\left(1+\frac{\mathrm{i}}{\omega_0}\partial_T\right)^2$$
$$=1+\mathrm{i}\left(\frac{2}{\omega_0}-\frac{\dot{\beta}_0}{\beta_0}\right)\partial_T-\left(\frac{\dot{\beta}_0}{\beta_0}-\frac{1}{\omega_0}\right)^2\partial_T^2\left(1+\mathrm{i}\frac{\dot{\beta}_0}{\beta_0}\partial_T\right)^{-1}.$$

The third term of the right hand side of the above equation can be neglected if the difference between the group velocity ($v_{\mathrm{g}}=1/\dot{\beta}_0$) and the phase velocity ($v_{\mathrm{p}}=\omega_0/\beta_0$) of the pulse is small. These two approximations are the same as SEWA [4] but unlike SVEA, and in the former approximations there are no conditions specifying the slowness of the temporal change of the envelope compared with the optical cycle time. Thus this equation can be used for the pulse as short as single optical cycle. By using these approximations, (1.22) becomes

$$\partial_\xi A(\xi,T)=\mathrm{i}(\widehat{D}'+\widehat{D}_{\mathrm{corr}})A(\xi,T)$$
$$+\mathrm{i}\frac{4g(\omega_0)\omega_0^2}{3c^2\beta_0}(1+\mathrm{i}s\partial_T)p_{\mathrm{NL}}(\xi,T), \tag{1.23}$$

where $\widehat{D}_{\mathrm{corr}}=(1+\mathrm{i}\dot{\beta}_0\partial_T/\beta_0)^{-1}\widehat{D}'^2/(2\beta_0)$ is a small correction term and $s=2/\omega_0-\dot{\beta}_0/\beta_0+\partial_\omega(\ln g(\omega))|_{\omega_0}$ is a coefficient for a steepening term.

1.1.2 Dispersion Terms

When the nonlinear polarization is not present ($p_{\mathrm{NL}}=0$) and the correction term $\widehat{D}_{\mathrm{corr}}$ is neglected, we have

$$\partial_\xi A(\xi,T)=\mathrm{i}\widehat{D}'A(\xi,T)$$
$$=\left(-\frac{\alpha_0}{2}-\mathrm{i}\frac{\dot{\alpha}_0}{2}\partial_T-\frac{\mathrm{i}}{2}\gamma_0^{(2)}\partial_T^2+\frac{1}{6}\gamma_0^{(3)}\partial_T^3+\ldots\right)A(\xi,T), \tag{1.24}$$

where $\alpha_0 = \alpha(\omega_0)$, $\dot{\alpha}_0 = \partial_\omega \alpha(\omega)|_{\omega_0}$, and $\gamma_0^{(n)} = \partial_\omega^n \gamma(\omega)|_{\omega_0}$. If the loss or the gain of the medium is not present ($\alpha = 0$), we have the following equation in the lowest order

$$\partial_\xi A(\xi, T) = -\frac{\mathrm{i}}{2}\beta_0^{(2)} \partial_T^2 A(\xi, T), \tag{1.25}$$

where $\beta_0^{(2)}$ is a group velocity dispersion (GVD) parameter. Due to this parameter, a linear chirp is introduced to the pulse during propagation.

1.1.3 Nonlinear Terms

The nonlinear term p_{NL} for the single pulse propagation is obtained by inserting the relation $\boldsymbol{E}(x, y, z, t) = \hat{\boldsymbol{x}}[E(x, y, z, t)\exp(-\mathrm{i}\omega_0 t) + \mathrm{c.c.}]/2$ in (1.11) and keeping only terms that contain $\exp(-\mathrm{i}\omega_0 t)$. The term that contains $\exp(-3\mathrm{i}\omega_0 t)$ (third-harmonic generation term) is ignored because the phase-matching condition is not usually satisfied. Using (1.8) and (1.12) and considering only the forward propagating wave, we have

$$\begin{aligned} p_{\mathrm{NL}}(\xi, T) = \frac{1}{4}\int_0^\infty R(T')[2|A(\xi, T - T')|^2 A(\xi, T) \\ + A^2(\xi, T - T')A^*(\xi, T)\exp(2\mathrm{i}\omega_0 T')]\mathrm{d}T', \end{aligned} \tag{1.26}$$

where the response function $R(t)$ is given by

$$R(T) = (1 - f_{\mathrm{R}})\delta(T) + f_{\mathrm{R}} h_{\mathrm{R}}(T). \tag{1.27}$$

This $R(t)$ contains both the instantaneous Kerr nonlinearity ($\delta(T)$) and the delayed Raman response ($h_{\mathrm{R}}(T)$). For gas-filled hollow fiber experiments, noble gas is used as the nonlinear medium. In this case, only the electronic instantaneous term is present ($f_{\mathrm{R}} = 0$) and (1.26) becomes

$$p_{\mathrm{NL}}(\xi, T) = \frac{3}{4}|A(\xi, T)|^2 A(\xi, T). \tag{1.28}$$

When an optical pulse propagates in the medium with this type of nonlinear polarization, the phase of the pulse is modulated. This phase modulation is called self-phase modulation (SPM). During the propagation of the pulse, the refractive index of the medium is increased by the time-dependent intensity of the pulse by the nonlinear polarization. This phase modulation results the time-dependent nonlinear chirp and new frequency components are created during propagation. This is a very important mechanism for the generation of the ultrabroadband pulse. In (1.23), the term $s\partial_T$ is called the steepening term since it modifies the shape of the pulse such that it is steepened at the trailing edge during propagation.

For a medium like fused-silica, the Raman response term $h_{\mathrm{R}}(T)$ that arises from the molecular vibration must also be considered. This Raman term was determined experimentally and for the fused-silica, $f_{\mathrm{R}} = 0.3$ and

$$h_{\mathrm{R}}(T) = \frac{\tau_1^2 + \tau_2^2}{\tau_1 \tau_2^2} \exp(-T/\tau_2) \sin(T/\tau_1), \tag{1.29}$$

where $\tau_1 = 12.2\,\mathrm{fs}$ and $\tau_2 = 32\,\mathrm{fs}$ [5]. Since the change of h_{R} is much slower than the optical cycles of $2\omega_0$, (1.26) can be written as

$$\begin{aligned} p_{\mathrm{NL}}(\xi, T) = \frac{3}{4}[&(1 - f_{\mathrm{R}})|A(\xi, T)|^2 \\ &+ \frac{2}{3} f_{\mathrm{R}} \int_0^\infty h_{\mathrm{R}}(T')|A(\xi, T - T')|^2 \mathrm{d}T']A(\xi, T). \end{aligned} \tag{1.30}$$

1.1.4 Induced Phase Modulation

If two pulses are co-propagating in the same medium, we have additional nonlinear terms due to the interaction between these pulses. In this case, we insert the electric field of the form

$$\begin{aligned} \boldsymbol{E}(x, y, z, t) = \hat{\boldsymbol{x}}[&E_1(x, y, z, t) \exp(-\mathrm{i}\omega_{01} t) \\ &+ E_2(x, y, z, t) \exp(-\mathrm{i}\omega_{02} t) + \mathrm{c.c.}]/2, \end{aligned} \tag{1.31}$$

where ω_{01} and ω_{02} are the center angular frequencies of the pulses 1 and 2, in (1.11) and keeping only terms that contain $\exp(-\mathrm{i}\omega_{01} t)$ and $\exp(-\mathrm{i}\omega_{02} t)$. Terms that contain $\exp(-\mathrm{i}3\omega_{01} t)$ or $\exp(-\mathrm{i}3\omega_{02} t)$ (third-harmonic terms) and terms that contain $\exp(-\mathrm{i}(2\omega_{01} - \omega_{02})t)$ or $\exp(-\mathrm{i}(2\omega_{02} - \omega_{01})t)$ (four-wave mixing terms) are ignored because the phase-matching conditions are not usually satisfied. We obtain the following equation for each pulse j ($j =$ 1 or 2):

$$\begin{aligned} \partial_{\xi_j} A_j(\xi_j, T_j) = \mathrm{i}(&\widehat{D}_j' + \widehat{D}_{\mathrm{corr},j}) A_j(\xi_j, T_j) \\ &+ \mathrm{i}\eta_j \left[(1 + \mathrm{i}s_j \partial_{T_j}) S_j + \frac{h_j(\omega_{0j})}{g(\omega_{0j})} (1 + \mathrm{i}u_j \partial_{T_j}) I_j \right], \end{aligned} \tag{1.32}$$

where

$$\begin{aligned} S_j = \Bigg[&(1 - f_{\mathrm{R}})|A_j(\xi_j, T_j)|^2 \\ &+ \frac{2}{3} f_{\mathrm{R}} \int_0^\infty h_{\mathrm{R}}(T')|A_j(\xi_j, T_j - T')|^2 \mathrm{d}T' \Bigg] A_j(\xi_j, T_j), \end{aligned} \tag{1.33}$$

$$\begin{aligned} I_j = \Bigg[&2(1 - f_{\mathrm{R}})|A_{3-j}(\xi_{3-j}, T_{3-j})|^2 \\ &+ \frac{2}{3} f_{\mathrm{R}} \int_0^\infty h_{\mathrm{R}}(T')|A_{3-j}(\xi_{3-j}, T_{3-j} - T')|^2 \mathrm{d}T' \Bigg] A_j(\xi_j, T_j). \end{aligned} \tag{1.34}$$

In this equation, $\eta_j = \omega_{0j}^2 g(\omega_{0j})/c^2 \beta_{0j}$, $\xi_j = z$ and $T_j = t - \dot{\beta}_{0j} z$. $\widehat{D}_j'$, $\widehat{D}_{\mathrm{corr},j}$ and s_j are obtained from $\widehat{D}'$, $\widehat{D}_{\mathrm{corr}}$ and s by replacing ω_0 and

$\partial_\omega^n(\gamma(\omega))|_{\omega_0}$ with ω_{0j} and $\partial_\omega^n(\gamma(\omega))|_{\omega_{0j}}$ respectively. Also, $h_j(\omega) = n(\omega)n_2^{\mathrm{I}}(\omega)/O(\omega,\omega_{03-j})$, $u_j = 2/\omega_{0j} - \dot{\beta_{0j}}/\beta_{0j} + \partial_\omega \ln(h_j(\omega))|_{\omega_{0j}}$, and the mode overlap integral is given by

$$O(\omega,\omega_{03-j}) = \frac{\int F^2(x,y,\omega)\mathrm{d}x\mathrm{d}y \int F^2(x,y,\omega_{03-j})\mathrm{d}x\mathrm{d}y}{\int F^2(x,y,\omega)F^2(x,y,\omega_{03-j})\mathrm{d}x\mathrm{d}y}. \tag{1.35}$$

In (1.32), S_j is the nonlinear term that arises from the intensity of the same pulse, while I_j is the nonlinear term the arises from the intensity of the other pulse. The phase modulation that arises from the latter term is called the induced-phase modulation (IPM) or the cross-phase modulation (XPM). Equation (1.34) shows that the instantaneous part of the IPM term is twice as large as the SPM term if the mode overlap is the same. Due to the IPM term, the phase of each pulse is modulated by the intensity of the other pulse and the nonlinear chirp is created. Due to this nonlinear chirp, new frequency components are created. The use of IPM for the generation of the ultrabroadband optical pulse has been proposed [6–8].

1.1.5 Comparison with the Previous Derivation

SVEA Equation

In the SVEA, we neglect ∂_z^2 term in (1.17). Also it is assumed that $\gamma^2(\omega) - \beta_0^2 = (\gamma(\omega)+\beta_0)(\gamma(\omega)-\beta_0) \simeq 2\beta_0(\gamma(\omega)-\beta_0)$ in (1.17). This implies that $|\gamma(\omega)-\beta_0| \ll |\beta_0|$. After these operations and dividing both sides of this equation by $2\mathrm{i}\beta_0$, we obtain

$$\begin{aligned}(\partial_z - \mathrm{i}(\gamma(\omega)-\beta_0))\tilde{A}(z,\omega-\omega_0) = \\ \mathrm{i}\frac{4n(\omega)n_2^{\mathrm{I}}(\omega)\omega^2}{3c^2A_{\mathrm{eff}}(\omega)\beta_0}\tilde{p}_{\mathrm{NL}}(z,\omega-\omega_0).\end{aligned} \tag{1.36}$$

By inverse Fourier transforming this equation, neglecting terms containing powers of ∂_t/ω_0 from the assumption $|\partial_t A/\omega_0| \ll |A|$, converting to the moving time coordinate ($T = t - \dot{\beta}_0 z$), and approximating $\widehat{D}' \simeq -\beta_0^{(2)}\partial_T^2/2 - \mathrm{i}\beta_0^{(3)}\partial_T^3/6$ for the fused-silica fiber ($\beta_0^{(j)} = \partial_\omega^j(\beta(\omega))|_{\omega_0}$), we have

$$\begin{aligned}\partial_\xi A(\xi,T) = (-\frac{\mathrm{i}}{2}\beta_0^{(2)}\partial_T^2 + \frac{1}{6}\beta_0^{(3)}\partial_T^3)A(\xi,T) \\ +\mathrm{i}\frac{4g(\omega_0)\omega_0^2}{3c^2\beta_0}p_{\mathrm{NL}}(\xi,T).\end{aligned} \tag{1.37}$$

In addition to the assumptions $|\partial_\xi A| \ll \beta_0|A|$ and $|\partial_T A| \ll \omega_0|A|$, $|\gamma(\omega)-\beta_0| \ll |\beta_0|$ is conventionally assumed in the SVEA. The latter condition implies that $|\omega-\omega_0| \ll |\omega_0|$ and this condition is clearly not satisfied for the ultrabroadband pulse propagation. Also in the conventional SVEA, the

Raman term is not considered in $\mathbf{P}_{\mathrm{NL}}$ ($f_{\mathrm{R}} = 0$ in (1.27)). If only the GVD term is considered for dispersion and does not consider the Raman term, we have

$$\partial_\xi A(\xi,T) = -\frac{\mathrm{i}}{2}\beta_0^{(2)}\partial_T^2 A(\xi,T) + \mathrm{i}\frac{g(\omega_0)\omega_0^2}{c^2\beta_0}|A(\xi,T)|^2 A(\xi,T). \quad (1.38)$$

This equation is known as the nonlinear Schrödinger equation (NLSE). It is well known that the optical soliton solutions can be obtained from this equation when $\beta_0^{(2)} < 0$ [1].

The Equation by Blow and Wood

In the paper by Blow and Wood [5], the right hand side of (1.17) is formally defined as $-\widehat{\Pi}\tilde{A}$ using the operator $\widehat{\Pi}$ and it is written as

$$(\mathrm{i}\partial_z - \beta_0 + \sqrt{\gamma^2(\omega) + \widehat{\Pi}}) \times (\mathrm{i}\partial_z - \beta_0 - \sqrt{\gamma^2(\omega) + \widehat{\Pi}})\tilde{A} = 0. \quad (1.39)$$

It is identified that the first term corresponds to the forward propagating wave and only the following equation is considered:

$$(\mathrm{i}\partial_z - \beta_0 + \sqrt{\gamma^2(\omega) + \widehat{\Pi}})\tilde{A} = 0. \quad (1.40)$$

By approximating $\sqrt{\gamma^2(\omega) + \widehat{\Pi}} \simeq \gamma(\omega) + \widehat{\Pi}/(2\gamma(\omega))$, we have

$$(\partial_z - \mathrm{i}(\gamma(\omega) - \beta_0))\tilde{A} = \frac{\mathrm{i}\widehat{\Pi}\tilde{A}}{2\gamma(\omega)} = \frac{\mathrm{i}4n(\omega)n_2^{\mathrm{I}}(\omega)\omega^2}{3\gamma(\omega)c^2 A_{\mathrm{eff}}}\tilde{p}_{\mathrm{NL}}. \quad (1.41)$$

For the fused-silica fiber case, we can set $\gamma(\omega) = \omega n(\omega)/c$. The inverse Fourier transformation and the conversion of the time coordinate yield

$$\partial_\xi A(\xi,T) = \mathrm{i}\widehat{D}'\,A(\xi,T) + \mathrm{i}\frac{4g'(\omega_0)\omega_0}{3c}(1 + \mathrm{i}s'\partial_T)p_{\mathrm{NL}}(\xi,T), \quad (1.42)$$

where $g'(\omega_0) = n_2^{\mathrm{I}}(\omega_0)/A_{\mathrm{eff}}(\omega_0)$ and $s' = 1/\omega_0 + \partial_\omega(\ln g'(\omega))|_{\omega_0}$. This equation does not assume neither $|\partial_z A| \ll \beta_0|A|$ nor $|\partial_T A| \ll \omega_0|A|$. However the nonlinear term must be small to satisfy $\sqrt{\gamma^2(\omega) + \widehat{\Pi}} \simeq \gamma(\omega) + \widehat{\Pi}/(2\gamma(\omega))$. In fact, for the most experimental situations covered in this section, the condition $|\widehat{\Pi}/\gamma^2(\omega)| \ll 1$ does not hold. However, its form is almost identical to the equation derived using the SEWA method.

1.2 Different Numerical Methods

In this section, various numerical methods to simulate the nonlinear propagation of the ultrabroadband and/or few-optical-cycle pulse are shown. In

the SEWA method derived in Sect. 1.1.1, an envelope function is used to represent the electric field of an optical pulse as in the conventional SVEA method. It makes numerical calculations more efficient than methods that don't use the envelope function. This is because the optical field of the pulse is calculated only at discrete points and the number of points required to represent the pulse is much lower in the method with the envelope function than in the method without it. The step sizes for time and position must be much smaller than the period and the wavelength of the carrier optical wave in the method without the envelope function. In spite of this disadvantage, it is desirable to use the method without the envelope function in some situations. For example, if the dispersion and/or the nonlinearity of the medium is very strong, the condition $|\partial_\xi A| \ll \beta_0|A|$ or $v_\mathrm{g} \simeq v_\mathrm{p}$ may not be satisfied. Also, for a few-optical-cycle pulse, the influence of the carrier-envelope offset phase on the pulse waveform during propagation can become significant and this effect cannot be included in the method with the envelope function. Moreover, nonlinear polarization terms neglected due to the phase-mismatch can become significant in some situations. In these cases, the direct integrations of Maxwell's equations may become necessary. The Fourier direct method (FDM), the finite-difference frequency-domain (FDFD) method, and the finite-difference time-domain (FDTD) method have been developed to integrate Maxwell's equations directly.

In Table 1.1, selected accomplishments in numerical methods to simulate ultrashort optical pulses are summarized.

1.2.1 Split-Step Fourier Method

To simulate the nonlinear propagation of an optical pulse using an envelope function by SEWA and SVEA methods, the split-step Fourier method [1] is commonly used. In this method, we formally rewrite (1.23) with p_NL given in (1.30) in the following form:

$$\partial_\xi A(\xi, T) = \widehat{D} A(\xi, T) + \widehat{N} A(\xi, T), \tag{1.43}$$

where $\widehat{D} = \mathrm{i}(\widehat{D}' + \widehat{D}_\mathrm{corr})$ is the dispersion operator and $\widehat{N}$ is the nonlinear operator that depends on $A(\xi, T)$ and its time derivative. Given the initial field $A(\xi, T)$, we calculate the field $A(\xi + \Delta\xi, T)$ in the following three steps, where $\Delta\xi$ is a step size for position. In the first operation, we ignore the nonlinear term and integrate (1.43) for a half step $\Delta\xi/2$ as follows,

$$A(\xi + \Delta\xi/2, T) = \exp(\widehat{D}\Delta\xi/2) A(\xi, T). \tag{1.44}$$

In the frequency domain, this equation becomes

$$\tilde{A}(\xi + \Delta\xi/2, \omega) = \exp(D(\omega)\Delta\xi/2)\tilde{A}(\xi, \omega). \tag{1.45}$$

Table 1.1. Progress in numerical methods to simulate ultrashort laser pulses

Year	Accomplishment	Researcher	References
1966	Finite-difference time-domain method for the linear medium	Yee	[9]
1973	Slowly-varying envelope approximation for the nonlinear Schrödinger equation to describe a fiber soliton	Hasegawa, Tappert	[10]
1973	Split-step Fourier method	Hardin, Tappert, Fisher, Bischel	[11, 12]
1989	The extension of the slowly-varying wave approximation to include the analytic Raman function and steepening	Blow, Wood	[5]
1992	Finite-difference time-domain method for the nonlinear medium	Goorjian, Taflove, Joseph, Hagness	[13, 14]
1997	Slowly-evolving wave approximation	Brabec, Krausz	[4]
2002	Fourier direct method	Mizuta, Nagasawa, Ohtani, Morita, Yamashita	[15]
2002	Finite-difference frequency-domain method	Karasawa	[16]

In this equation, the dispersion operator becomes a function of angular frequency and can be calculated easily. Also, the Fourier transform can be calculated very efficiently using the fast Fourier transform (FFT) routine. Thus we have

$$A(\xi + \Delta\xi/2, T) = FT^{-1}[\exp(D(\omega)\Delta\xi/2)\tilde{A}(\xi, \omega)], \tag{1.46}$$

where FT^{-1} is the inverse Fourier transform. In the second operation, the nonlinear operator is evaluated for the entire step at this point as

$$A'(\xi + \Delta\xi/2, T) = \exp(\widehat{N}\Delta\xi)A(\xi + \Delta\xi/2, T), \tag{1.47}$$

where the nonlinear operator $\widehat{N}$ is calculated using $A(\xi + \Delta\xi/2, T)$ in (1.46). In the third operation, only the dispersion operator is applied for the half step as in the first operation as follows:

$$A(\xi + \Delta\xi, T) = FT^{-1}[\exp(D(\omega)\Delta\xi/2)\tilde{A}'(\xi + \Delta\xi/2, \omega)]. \tag{1.48}$$

By repeating these operations, optical fields at any distance can be calculated. The dispersion terms in (1.23) can be evaluated in the frequency domain as:

$$\widehat{D}'(\omega) = \beta(\omega) + \frac{\mathrm{i}\alpha(\omega)}{2} - \beta_0 - \dot{\beta}_0(\omega - \omega_0), \tag{1.49}$$

$$\widehat{D}_{\mathrm{corr}}(\omega) = \frac{\widehat{D}'^2(\omega)}{2(\beta_0 + \dot{\beta}_0(\omega - \omega_0))}. \tag{1.50}$$

These functions can be obtained from the dispersion relation of the medium and the waveguide using (1.9). The material dispersion of the fused-silica can be obtained by the Sellmeier equation [17], where the refractive index $n(\lambda)$ of the fused-silica a as function of wavelength $\lambda = 2\pi c/\omega$ in μm ($0.21\,\mu\mathrm{m} < \lambda < 3.71\,\mu\mathrm{m}$) is given as

$$n^2(\lambda) - 1 = \frac{0.6961663\lambda^2}{\lambda^2 - (0.0684043)^2} + \frac{0.4079426\lambda^2}{\lambda^2 - (0.1162414)^2} + \frac{0.8974794\lambda^2}{\lambda^2 - (9.896161)^2}. \tag{1.51}$$

In practice, only the limited number of frequency points used in the fast Fourier transform routine are necessary in calculations and (1.49) and (1.50) are evaluated once and stored in the memory, thus the calculation of this method is very efficient.

1.2.2 Finite-Difference in the Frequency Domain Method

In the finite-difference frequency-domain (FDFD) method [16], an envelope function is not used and the fields of the pulse are directly calculated with Maxwell's equations. Thus no assumptions regarding the slowness of the variation of the envelope function with respect to time or position are introduced. Also, it is possible to investigate effects that cannot be treated in the method with the envelope function, e.g., the effect of the carrier-envelope offset phase or the effect of the four-wave mixing terms in the case of co-propagation of multiple pulses. Compared with the FDTD method, the FDFD method has an advantage that arbitrary linear dispersion relations can be incorporated easily since all calculations are done in the frequency domain. On the other hand, only simple Lorentz dispersion relations have been simulated in the FDTD method.

To derive the FDFD equations, we start from Maxwell's equations ((1.1) to (1.3)) in one dimension:

$$\frac{\partial \mu_0 H_y(x,t)}{\partial t} = \frac{\partial E_z(x,t)}{\partial x}, \tag{1.52}$$

$$\frac{\partial D_z(x,t)}{\partial t} = \frac{\partial H_y(x,t)}{\partial x}, \tag{1.53}$$

$$D_z(x,t) = \varepsilon_0 \varepsilon_\infty E_z(x,t) + P_z(x,t), \tag{1.54}$$

where E_z, H_y, D_z, and P_z are electric field, magnetic field, electric displacement, and polarization, respectively, and fields are assumed to be propagating

in the x direction. Introducing a new time variable $T = t - \beta_1 x$ and Fourier transforming, we have

$$-\mathrm{i}\omega\mu_0\widetilde{H}_y(x,\omega) = \mathrm{i}\omega\beta_1\widetilde{E}_z(x,\omega) + \frac{\partial\widetilde{E}_z(x,\omega)}{\partial x}, \tag{1.55}$$

$$-\mathrm{i}\omega\widetilde{D}_z(x,\omega) = \mathrm{i}\omega\beta_1\widetilde{H}_y(x,\omega) + \frac{\partial\widetilde{H}_y(x,\omega)}{\partial x}. \tag{1.56}$$

To solve (1.55) and (1.56) using a finite-difference scheme, we use a small position increment Δx and write using a leap-frog scheme,

$$\begin{aligned}\widetilde{E}_z(x+\Delta x,\omega) &= \widetilde{E}_z(x,\omega) - \mathrm{i}\omega\Delta x\mu_0\widetilde{H}_y(x+\frac{\Delta x}{2},\omega)\\ &\quad - \mathrm{i}\omega\Delta x\frac{\beta_1}{2}(\widetilde{E}_z(x+\Delta x,\omega)+\widetilde{E}_z(x,\omega)),\end{aligned} \tag{1.57}$$

$$\begin{aligned}\widetilde{H}_y(x+\frac{3\Delta x}{2},\omega) &= \widetilde{H}_y(x+\frac{\Delta x}{2},\omega) - \mathrm{i}\omega\Delta x\widetilde{D}_z(x+\Delta x,\omega)\\ &\quad - \mathrm{i}\omega\Delta x\frac{\beta_1}{2}(\widetilde{H}_y(x+\frac{3\Delta x}{2},\omega)+\widetilde{H}_y(x+\frac{\Delta x}{2},\omega)).\end{aligned} \tag{1.58}$$

These equations are solved for the fields at new position from the fields at previous position with the equation for $\widetilde{D}_z(x+\Delta x,\omega)$ as follows,

$$\begin{aligned}\widetilde{D}_z(x+\Delta x,\omega) &= \varepsilon_0(\varepsilon_\infty + \widetilde{\chi}^{(1)}(\omega))\widetilde{E}_z(x+\Delta x,\omega)\\ &\quad + (1-f_\mathrm{R})\varepsilon_0\chi^{(3)}FT[E_z^3(x+\Delta x,t)]\\ &\quad + f_\mathrm{R}\chi^{(3)}FT[E_z(x+\Delta x,t)G(x+\Delta x,t)],\end{aligned} \tag{1.59}$$

where the nonlinear polarization of (1.11) and the response function of (1.29) are used and $G(x,t)$ is given by

$$G(x,t) = \varepsilon_0\int_0^\infty h_\mathrm{R}(t-t')E_z^2(x,t')\mathrm{d}t'. \tag{1.60}$$

Starting with initial fields $\widetilde{E}_z(x,\omega)$ and $\widetilde{H}_y(x+\Delta x/2,\omega)$, we obtain $\widetilde{E}_z(x+\Delta x,\omega)$ using (1.57). Then we calculate $\widetilde{D}_z(x+\Delta x,\omega)$ using (1.59). Finally, we obtain $\widetilde{H}_y(x+3\Delta x/2,\omega)$ using (1.58). By repeating these operations, fields at an arbitrary position can be calculated.

1.2.3 Finite-Difference Time-Domain Method

In the finite-difference time-domain (FDTD) method, the electric field and the magnetic field of a pulse are directly calculated in the time domain [13, 14, 18]. For a one-dimensional case, equations to be solved are (1.52)–(1.54). The finite-difference equations for optical fields are given as

$$\frac{\mu_0}{\Delta t}(H_y(x+\Delta x/2, t+\Delta t/2) - H_y(x+\Delta x/2, t-\Delta t/2)) = \frac{1}{\Delta x}(E_z(x+\Delta x, t) - E_z(x,t)), \tag{1.61}$$

$$\frac{1}{\Delta t}(D_z(x, t+\Delta t) - D_z(x,t)) = \frac{1}{\Delta x}(H_y(x+\Delta x/2, t+\Delta t/2) - H_y(x-\Delta x/2, t+\Delta t/2)), \tag{1.62}$$

where Δt is a step size for time. Starting from the initial fields $E_z(x,t)$ and $H_y(x, t-\Delta t/2)$, we calculate $H_y(x, t+\Delta t/2)$ from (1.61). Then we calculate $D_x(x, t+\Delta t)$ from (1.62). Next, we obtain $E_z(x, t+\Delta t)$ from $D_x(x, t+\Delta t)$ using (1.54). If we assume the nonlinear polarization given by (1.11), we have

$$E_z = \frac{D_z - F - f_{\mathrm{R}}\chi^{(3)}E_z G}{\varepsilon_0(\varepsilon_\infty + (1-f_{\mathrm{R}})\chi^{(3)}E_z^2)}, \tag{1.63}$$

where F is the linear polarization given by

$$F(x,t) = \varepsilon_0 \int_0^t \chi^{(1)}(t-t')E_z(x,t')\mathrm{d}t' \tag{1.64}$$

and G is given by (1.60). To calculate $E_z(x, t+\Delta x)$ by (1.63), we need to know $F(x, t+\Delta t)$ and $G(x, t+\Delta t)$ in addition to $D_z(x, t+\Delta t)$. For the Lorentz linear dispersion and the Raman response function given in (1.29), second-order differential equations for both F and G can be obtained and these equations are solved using the finite difference scheme. In the original FDTD method, only the Lorentz linear dispersion with a single resonance term was solved. Modified equations were derived for the linear dispersion terms with three resonance terms. By using these modified FDTD equations, nonlinear pulse propagation in the fused-silica material with the accurate linear dispersion relation have been simulated [19] (See Sect. 1.3.3).

1.2.4 Fourier Direct Method

Preliminary Remarks

The Fourier Direct Method (FDM) was extended from the split-step Fourier method that is generally employed for solving the nonlinear Schrödinger equation (NLSE). In the NLSE, the envelope of the electric field is the only variable to be solved, and its solution is easily obtained by the exponential integral. On the other hand, methods that directly solve Maxwell's equations without assumptions or approximations incorporate several linear and nonlinear effects. In addition, even if Maxwell's equations are one-dimensionalized, they are still multi-dimensional evolution equations to be solved for both the electric field and the magnetic field, and some terms are described by differentials or integrals.

In the FDM, Maxwell's equations are re-composed into the "bi-directional propagation equations" for the right-traveling forward wave and the left-traveling backward wave. Since they are coupled through a nonlinear term and solved simultaneously, the solution procedure must be multi-dimensional, and the nonlinear term should be integrated by general methods other than the exponential integral. In the FDM, the bi-directional propagation equations suggest proper initial conditions, and clarify how the slowly varying envelope approximation (SVEA) is discarded.

Polarization-preserving fibers maintain the linear polarization of the light launched with the polarization along one of the principal axes of the fiber. We choose here the z-direction parallel to the fiber, the x-direction along the axis of the polarization, and the y-direction normal to both the x- and z-directions. Since the electric field $\boldsymbol{E}$ and the magnetic field $\boldsymbol{H}$ have, in this case, only the components E_x and H_y, we derive averaged Maxwell's equations (notations in this section are consistently used also in Sect. 1.3.4):

$$\begin{cases} \dfrac{\partial E}{\partial z} = -\dfrac{\partial B}{\partial t}, \\ -\dfrac{\partial H}{\partial z} = \dfrac{\partial D}{\partial t}. \end{cases} \tag{1.65}$$

These are a set of evolution equations for

$$E(z,t) \equiv \{E_x(x,y,z,t)\}_{\mathrm{AV}}\,, \tag{1.66a}$$

$$H(z,t) \equiv \{H_y(x,y,z,t)\}_{\mathrm{AV}}\,, \tag{1.66b}$$

where $\{\cdots\}_{\mathrm{AV}}$ means the average over a cross section normal to the fiber, $B(z,t) = \mu_0 H(z,t)$ is an averaged component of the magnetic flux density, and an averaged component of the electric flux density $D(z,t)$ is related with the linear and nonlinear parts of the induced polarization $P_{\mathrm{L}}(z,t)$ and $P_{\mathrm{N}}(z,t)$ as

$$D(z,t) = \varepsilon_0 E(z,t) + P_{\mathrm{L}}(z,t) + P_{\mathrm{N}}(z,t).$$

Usually, the three-dimensional wave propagation equation is derived from the full three-dimensional Maxwell's equations, which are solved by the method of separation of variables as

$$E_x(x,y,z,t) = \frac{1}{2\pi}\int_{-\infty}^{\infty} \mathrm{d}\omega e^{-\mathrm{i}\omega t} F(x,y,\omega)\tilde{E}(z,\omega).$$

We stress here the importance of the core dispersion, the frequency-dependence of the intensity distribution in the cross section $F(x,y,\omega)$, showing the change of the effective core area according to the frequency of the field. The form of $F(x,y,\omega)$ is determined from one of the equations separated from the three-dimensional wave propagation equation. Thus, instead of $E_x(x,y,z,t)$ or $E(z,t)$, we use

$$\begin{aligned}\tilde{E}(z,\omega) &\equiv \mathsf{F}E(z,t) = \mathsf{F}\left\{E_x(x,y,z,t)\right\}_{\mathrm{AV}} \\ &= \left\{F(x,y,\omega)\tilde{E}(z,\omega)\right\}_{\mathrm{AV}} \\ &= \frac{1}{A^{(2)}(\omega)}\iint \mathrm{d}x\mathrm{d}y\left|F(x,y,\omega)\right|^2\tilde{E}(z,\omega),\end{aligned} \tag{1.67}$$

and $\tilde{H}(z,\omega) = -c\mu_0\mathsf{F}H(z,t)$ as the proper dependent variables hereafter. The operator F denotes the Fourier transform in time, and

$$\{\cdots\}_{\mathrm{AV}} \equiv \frac{1}{A^{(2)}(\omega)}\iint \mathrm{d}x\mathrm{d}y F(x,y,\omega)\cdots, \tag{1.68a}$$

$$A^{(n)}(\omega) \equiv \iint \mathrm{d}x\mathrm{d}y\left|F(x,y,\omega)\right|^n \tag{1.68b}$$

defines the average over a cross section normal to the fiber. As with the basic equations, we derive

$$\begin{cases}\dfrac{\partial\tilde{E}}{\partial z} = -\dfrac{\mathrm{i}\omega}{c}\tilde{H}, \\ \dfrac{\partial\tilde{H}}{\partial z} = -\dfrac{\mathrm{i}\omega}{c}\left(n_{\mathrm{L}}^2\tilde{E} + \mathsf{F}\dfrac{P_{\mathrm{N}}}{\varepsilon_0}\right),\end{cases} \tag{1.69}$$

from the Fourier transform of (1.65), where the term including the frequency-dependent complex linear refractive index $n_{\mathrm{L}}(\omega) = n_{\mathrm{L}}^{\mathrm{R}}(\omega) + in_{\mathrm{L}}^{\mathrm{I}}(\omega)$ coming from $P_{\mathrm{L}}(z,t)$ in (1.65) includes the effects of absorption and finite-time response. Furthermore, for the nonlinear induced polarization, we use the following expression, third-order in $E_x(x,y,z,t)$ or $E(z,t)$ and including the delayed Raman response represented by $\chi^{(3)}R(t)$:

$$\mathsf{F}\frac{P_{\mathrm{N}}(z,t)}{\varepsilon_0} = \mathsf{F}\left\{\chi^{(3)}E_x(x,y,z,t)\int_{-\infty}^{t}\mathrm{d}t_1 R(t-t_1)E_x^2(x,y,z,t_1)\right\}_{\mathrm{AV}}. \tag{1.70}$$

Bi-directional Propagation Equation

Orthodoxly, a set of equations with a constant n_0

$$\begin{cases}\dfrac{\partial E}{\partial z} = \dfrac{1}{c}\dfrac{\partial H}{\partial t}, \\ \dfrac{\partial H}{\partial z} = \dfrac{n_0^2}{c}\dfrac{\partial E}{\partial t}\end{cases} \tag{1.71}$$

are solved as the general solution

$$E(t,z) = g_+\left(t - n_0 z/c\right) + g_-\left(t + n_0 z/c\right) \tag{1.72}$$

of the second-order partial differential equation $\partial^2 E/\partial z^2 = \left(n_0/c\right)^2\partial^2 E/\partial t^2$, which is derived by eliminating H between the equations in (1.71). Each term

in (1.72) means the forward wave and the backward wave, and is determined from the initial $E(t, z = 0)$ with its derivative in z. An alternative way is to combine both equations in (1.71) as

$$\begin{cases} \dfrac{\partial(E - H/n_0)}{\partial z} = -\dfrac{n_0}{c}\dfrac{\partial(E - H/n_0)}{\partial t}, \\ \dfrac{\partial(E + H/n_0)}{\partial z} = \quad \dfrac{n_0}{c}\dfrac{\partial(E + H/n_0)}{\partial t}. \end{cases} \tag{1.73}$$

They are equations for a_1 and a_2 defined as below, and solved independent of each other:

$$\begin{cases} a_1 \equiv \dfrac{1}{2}\left(E - \dfrac{H}{n_0}\right) = g_+\left(t - \dfrac{n_0}{c}z\right), \\ a_2 \equiv \dfrac{1}{2}\left(E + \dfrac{H}{n_0}\right) = g_-\left(t + \dfrac{n_0}{c}z\right). \end{cases} \tag{1.74}$$

Of course, a_1 and a_2 mean the forward wave and the backward wave, respectively, and we can reproduce (1.72) by summing them up. (1.71) is the simplification of (1.65) and (1.69). Hereafter, this approach is extended so that the linear refractive index depends on the frequency, the nonlinear interaction between the forward wave and the backward wave is included as well within each of them, and so on.

For a high-power, ultrashort optical pulse to be propagated in a fiber, we need to scale the spatial coordinate, the time, the frequency and the fields in (1.69) by the characteristic length Z, the characteristic time T and the peak power of the pulse P as follows:

$$\xi = z/Z, \tag{1.75a}$$

$$\tau = (t - z/v)/T, \tag{1.75b}$$

$$\omega_{\mathrm{C}} = T\omega, \tag{1.75c}$$

$$\begin{pmatrix} \tilde{E}(z,\omega) \\ \tilde{H}(z,\omega) \end{pmatrix} = E_{\mathrm{p}}(\omega)\begin{pmatrix} B_1(\xi,\omega_{\mathrm{C}}) \\ B_2(\xi,\omega_{\mathrm{C}}) \end{pmatrix}, \tag{1.75d}$$

where v is the velocity of the coordinate system moving together with the pulse. As T, Z and v, at present, the half-width of the envelope of the temporal electric field profile ($t_1/1.665$ for the Gaussian profile where t_1 is its full-width at half-maximum, FWHM), the dispersion length L_{D} (see (1.92a)) and the group velocity are properly chosen, respectively. We scale the electric and the magnetic fields by $E_{\mathrm{p}}(\omega) \equiv \sqrt{P/[c\varepsilon_0 n_{\mathrm{L}}^{\mathrm{R}}(\omega)A^{(2)}(\omega)]}$ referring to

$$P = \max_t\left\{c\varepsilon_0 n_0 \iint \mathrm{d}x\mathrm{d}y|E(x,y,z,t)|^2\right\} \simeq c\varepsilon_0 n_0 A^{(2)} E_{\mathrm{p}}^2 \max_\tau\left\{|b_1(\xi,\tau)|^2\right\},$$

where $\max_{t,\tau}\{\cdots\}$ means the maximum in time, n_0 is $n_{\mathrm{L}}^{\mathrm{R}}(\omega)$ at the central angular frequency ω_0, and $b_1(\xi,\tau) \equiv \mathsf{F}^{-1}B_1(\xi,\omega_{\mathrm{C}})$ is the scaled electric field. Then, $\max_\tau\left\{|b_1(\xi,\tau)|^2\right\}$ is the order of one, and (1.69) reduces to

$$\begin{cases} \dfrac{\partial B_1}{\partial \xi} = -\mathrm{i}\omega Z \left(\dfrac{B_1}{v} + \dfrac{B_2}{c} \right), \\ \dfrac{\partial B_2}{\partial \xi} = -\mathrm{i}\omega Z \left(\dfrac{B_2}{v} + \dfrac{n_\mathrm{L}^2 B_1}{c} \right) + G_\mathrm{N}, \end{cases} \tag{1.76a}$$

$$G_\mathrm{N} \equiv \frac{Z}{E_\mathrm{p}(\omega)} \left(-\frac{i\omega}{c} \mathsf{F} \frac{P_\mathrm{N}}{\varepsilon_0} \right). \tag{1.76b}$$

Here we define $A_{1,2}$ from $B_{1,2}$, and express $B_{1,2}$ by $A_{1,2}$ inversely as follows:

$$\boldsymbol{A} = \begin{pmatrix} A_1 \\ A_2 \end{pmatrix} = \frac{1}{n_\mathrm{L} + n_\mathrm{L}^*} \begin{pmatrix} n_\mathrm{L}^* B_1 - B_2 \\ n_\mathrm{L} B_1 + B_2 \end{pmatrix}, \tag{1.77a}$$

$$\boldsymbol{B} = \begin{pmatrix} B_1 \\ B_2 \end{pmatrix} = \begin{pmatrix} A_1 + A_2 \\ n_\mathrm{L}^* A_2 - n_\mathrm{L} A_1 \end{pmatrix}. \tag{1.77b}$$

Using these $A_{1,2}$, we diagonalize the linear terms in the right side of (1.76a) as

$$\begin{cases} \dfrac{\partial A_1}{\partial \xi} = F_\mathrm{L1} - F_\mathrm{N}, \quad F_\mathrm{L1} \equiv \mathrm{i}Z \left(\quad \beta - \dfrac{\omega}{v} \right) A_1, \\ \dfrac{\partial A_2}{\partial \xi} = F_\mathrm{L2} + F_\mathrm{N}, \quad F_\mathrm{L2} \equiv \mathrm{i}Z \left(-\beta^* - \dfrac{\omega}{v} \right) A_2, \end{cases} \tag{1.78a}$$

where

$$\beta(\omega) \equiv \frac{\omega n_\mathrm{L}(\omega)}{c}, \tag{1.79a}$$

$$F_\mathrm{N} \equiv \frac{G_\mathrm{N}}{n_\mathrm{L} + n_\mathrm{L}^*} \equiv \frac{Z}{2 n_\mathrm{L}^\mathrm{R}(\omega) E_\mathrm{p}(\omega)} \left(-\frac{\mathrm{i}\omega}{c} \mathsf{F} \frac{P_\mathrm{N}}{\varepsilon_0} \right) \tag{1.79b}$$

$$= -\mathrm{i}\gamma_\mathrm{FDM}(\omega) \mathsf{F} b_1(\xi, \tau) \mathsf{F}^{-1} \tilde{R}(\omega) \mathsf{F} [b_1(\xi, \tau)]^2, \tag{1.79c}$$

$$\gamma_\mathrm{FDM}(\omega) \equiv \frac{\omega Z}{c} \frac{\chi^{(3)}}{2 n_\mathrm{L}^\mathrm{R}(\omega)} [\tilde{E}_\mathrm{p}(\omega)]^2, \tag{1.79d}$$

$$[\tilde{E}_\mathrm{p}(\omega)]^2 \equiv \frac{P}{c\varepsilon_0 n_\mathrm{L}^\mathrm{R}(\omega) A_\mathrm{eff}(\omega)}, \tag{1.79e}$$

$$A_\mathrm{eff}(\omega) \equiv \frac{[A^{(2)}(\omega)]^2}{A^{(4)}(\omega) \{1 + \Delta(\omega)\}}. \tag{1.79f}$$

For the linear refractive index, we adopt here the following modified Sellmeier equation with the attenuation [20]

$$[n_\mathrm{L}(\omega)]^2 = 1 + \sum_{j=1}^{N} S_j \left(\frac{1}{\omega_j - \mathrm{i}\Gamma_j - \omega} + \frac{1}{\omega_j + \mathrm{i}\Gamma_j + \omega} \right), \tag{1.80}$$

where $N = 2$, $\omega_1 = 0.21\,\mathrm{rad/fs}$, $S_1 = 0.06\ \mathrm{fs}^{-1}$, $\Gamma_1 = 3.77 \times 10^{-3}\,\mathrm{rad/fs}$, $\omega_2 = 18.9\,\mathrm{rad/fs}$, $S_2 = 10.2\ \mathrm{fs}^{-1}$, and $\Gamma_2 = 0.00\,\mathrm{rad/fs}$. At the wavelength

$\lambda_0 = 800\,\mathrm{nm}$ (the frequency $\omega_0 = 2.356\,\mathrm{rad/fs}$), (1.80) gives $n_{\mathrm{L}}^{\mathrm{R}}(\omega_0) = 1.446$. The propagation constant $\beta(\omega)$ is extended to complex numbers together with $n_{\mathrm{L}}(\omega)$. Both A_1 and A_2 attenuate with z, since $\mathrm{Im}\,\beta(\omega) > 0$.

Furthermore, the nonlinear response function, composed of the instantaneous part and the delayed Raman part, and its Fourier-transform are [5]:

$$R(t) = (1 - f_{\mathrm{R}})\delta(t) + f_{\mathrm{R}} h_{\mathrm{R}}(t), \tag{1.81a}$$

$$\tilde{R}(\omega) = \mathsf{F}R(t) = (1 - f_{\mathrm{R}}) + f_{\mathrm{R}}\mathsf{F}h_{\mathrm{R}}(t), \tag{1.81b}$$

$$\mathsf{F}h_{\mathrm{R}}(t) = \tilde{H}(\omega - \omega_0) + \tilde{H}^*(-\omega - \omega_0), \tag{1.81c}$$

$$\tilde{H}(\omega) = \mathsf{F}\frac{\tau_1^2 + \tau_2^2}{\tau_1\tau_2^2} e^{-t/\tau_2} \sin\left(\frac{t}{\tau_1}\right) = \frac{\tau_1^2 + \tau_2^2}{\tau_1^2(1 - \mathrm{i}\omega\tau_2)^2 + \tau_2^2}. \tag{1.81d}$$

The value of the nonlinear susceptibility was obtained from

$$n_2 = (3\chi^{(3)})/(8n_{\mathrm{L}}^{\mathrm{R}}(\omega_0)) = 1.220 \times 10^{-22}\ (\mathrm{V/m})^{-2}$$

$$(= 40\pi\varepsilon_0 n_2(\mathrm{esu}), \quad n_2(\mathrm{esu}) = 1.097 \times 10^{-13}\ \mathrm{esu})$$

for the fused-silica fiber [21], and $\tau_1 = 12.2\,\mathrm{fs}$, $\tau_2 = 32.0\,\mathrm{fs}$ and $f_{\mathrm{R}} = 0.30$ in the nonlinear response function $R(t)$ were used referring to [5].

In the expression for F_{N} by the electric field as

$$E_x(x, y, z, t) = \mathsf{F}^{-1}F(x, y, \omega)E_{\mathrm{p}}(\omega)\mathsf{F}b_1(\xi, \tau), \tag{1.82}$$

the following $S_{\mathrm{B}}(\omega)$ needs to be approximated by $S_{\mathrm{A}}(\omega)$. Their relative difference $\Delta(\omega)$ in (1.83c) is neglected even for the pulses with a wide spectrum when $F(x, y, \omega)E_{\mathrm{p}}(\omega)$ depends on ω weakly compared with $B_1(\xi, \omega_{\mathrm{C}})$:

$$\begin{aligned} S_{\mathrm{B}}(\omega) &\equiv \left\{\mathsf{F}E_x(x, y, z, t)\int_{-\infty}^{t} \mathrm{d}t_1 R(t - t_1)[E_x(x, y, z, t_1)]^2\right\}_{\mathrm{AV}} \\ &= \left\{\mathsf{F}E_x(x, y, z, t)\mathsf{F}^{-1}\tilde{R}(\omega)\mathsf{F}[E_x(x, y, z, t)]^2\right\}_{\mathrm{AV}}, \end{aligned} \tag{1.83a}$$

$$\begin{aligned} S_{\mathrm{A}}(\omega) &\equiv \left\{[F(x, y, \omega)E_{\mathrm{p}}(\omega)]^3\mathsf{F}b_1(\xi, \tau)\mathsf{F}^{-1}\tilde{R}(\omega)\mathsf{F}[b_1(\xi, \tau)]^2\right\}_{\mathrm{AV}} \\ &= \frac{A^{(4)}(\omega)}{A^{(2)}(\omega)}[E_{\mathrm{p}}(\omega)]^3\mathsf{F}b_1(\xi, \tau)\mathsf{F}^{-1}\tilde{R}(\omega)\mathsf{F}[b_1(\xi, \tau)]^2, \end{aligned} \tag{1.83b}$$

$$\Delta(\omega) \equiv S_{\mathrm{B}}(\omega)/S_{\mathrm{A}}(\omega) - 1. \tag{1.83c}$$

Equation (1.79d) allows us to consider the frequency dependence of the coefficient of the nonlinear term $\gamma_{\mathrm{FDM}}(\omega)$, which causes "nonlinear dispersion", leading to such effects as self-steepening or the core dispersion. Instead of using (1.79d), we can evaluate $\gamma_{\mathrm{FDM}}(\omega)$ as

$$\gamma_{\mathrm{FDM}}(\omega) = \gamma_{\mathrm{FDM}}(\omega_0)\frac{\omega}{\omega_0}\left[\frac{n_{\mathrm{L}}^{\mathrm{R}}(\omega)}{n_{\mathrm{L}}^{\mathrm{R}}(\omega_0)}\right]^{-2}\left[\frac{A_{\mathrm{eff}}(\omega)}{A_{\mathrm{eff}}(\omega_0)}\right]^{-1} \tag{1.84}$$

from the value of $\gamma_{\mathrm{FDM}}(\omega)$ at the central frequency ω_0 and the behavior of $n_{\mathrm{L}}^{\mathrm{R}}(\omega)$ and $A_{\mathrm{eff}}(\omega)$ in that region.

A_1 and A_2 in (1.78) are the forward wave and the backward wave, respectively. Thus, when we intend to set only the forward wave as the initial condition, $\tilde{H}(z,\omega) = -n_{\mathrm{L}}(\omega)\tilde{E}(z,\omega)$ at $z = 0$ is appropriately used, which is derived from (1.77a) with $A_2 = 0$. Equation (1.78) can even describe a situation in which two extremely short pulses propagating in opposite directions collide with a strong interaction, and leave a long distance from each other. Even if this occurs, the term F_{N} describes not only the nonlinear self-interaction but also the nonlinear interaction between the pulses during the collision. Therefore, we call (1.78a) "bi-directional propagation equations". This approach is more natural and general for analyzing the optical pulses in fibers, compared with [5] where the formal decomposition and the Taylor expansion were employed.

Direct Derivation of Nonlinear Schrödinger Equation

When the pulse spectrum localizes around the central frequency, we can distinguish the envelope wave from the carrier wave clearly. The forward wave and the backward wave in (1.74) are $a_1(\xi,\tau) = \mathsf{F}^{-1}A_1$ and $a_2(\xi,\tau) = \mathsf{F}^{-1}A_2$. We decompose each of them into the carrier wave and the envelope wave $a_\pm(\xi,\tau)$ as

$$\begin{cases} a_1(\xi,\tau) = \left[a_+(\xi,\tau)\mathrm{e}^{\mathrm{i}(\beta_{0\mathrm{C}}\xi-\omega_{0\mathrm{C}}\tau)} + a_+^*(\xi,\tau)\mathrm{e}^{\mathrm{i}(-\beta_{0\mathrm{C}}\xi+\omega_{0\mathrm{C}}\tau)}\right]/2, \\ a_2(\xi,\tau) = \left[a_-(\xi,\tau)\mathrm{e}^{\mathrm{i}(\beta_{0\mathrm{C}}\xi+\omega_{0\mathrm{C}}\tau)} + a_-^*(\xi,\tau)\mathrm{e}^{\mathrm{i}(-\beta_{0\mathrm{C}}\xi-\omega_{0\mathrm{C}}\tau)}\right]/2, \end{cases} \tag{1.85}$$

where $\omega_{0\mathrm{C}} = T\omega_0$ and $\beta_{0\mathrm{C}} = Z\beta(\omega_0) \equiv Z\beta_0$. They are Fourier-transformed as

$$\begin{cases} A_1(\xi,\omega_{\mathrm{C}}) = \left[A_+(\xi,\omega_{\mathrm{C}}-\omega_{0\mathrm{C}})\mathrm{e}^{\mathrm{i}\beta_{0\mathrm{C}}\xi} + A_+^*(\xi,-\omega_{\mathrm{C}}-\omega_{0\mathrm{C}})\mathrm{e}^{-\mathrm{i}\beta_{0\mathrm{C}}\xi}\right]/2, \\ A_2(\xi,\omega_{\mathrm{C}}) = \left[A_-(\xi,\omega_{\mathrm{C}}+\omega_{0\mathrm{C}})\mathrm{e}^{\mathrm{i}\beta_{0\mathrm{C}}\xi} + A_-^*(\xi,-\omega_{\mathrm{C}}+\omega_{0\mathrm{C}})\mathrm{e}^{-\mathrm{i}\beta_{0\mathrm{C}}\xi}\right]/2, \end{cases} \tag{1.86}$$

where

$$\begin{cases} A_\pm(\xi,\omega_{\mathrm{C}}\mp\omega_{0\mathrm{C}}) &= \mathsf{F}a_\pm(\xi,\tau)\mathrm{e}^{\mp\mathrm{i}\omega_{0\mathrm{C}}\tau}, \\ A_\pm^*(\xi,-\omega_{\mathrm{C}}\mp\omega_{0\mathrm{C}}) &= \mathsf{F}a_\pm^*(\xi,\tau)\mathrm{e}^{\pm\mathrm{i}\omega_{0\mathrm{C}}\tau}. \end{cases} \tag{1.87}$$

For simplicity, we define here the "envelope-wave transform operator" E to take out the envelope wave from the forward wave as $\mathsf{E}a_1(\xi,\tau) = a_+(\xi,\tau)$, $\mathsf{E}A_1(\xi,\omega_{\mathrm{C}}) = A_+(\xi,\omega_{\mathrm{C}})$ and $\mathsf{E}(\partial A_1/\partial\xi) = \partial A_+/\partial\xi + \mathrm{i}\beta_{0\mathrm{C}}A_+$.

Hereafter, we summarize the derivation of the nonlinear Schrödinger equation (NLSE) for $a_+(\xi,\tau)$, composed of the lowest order linear-dispersion and nonlinearity, under the following assumptions or approximations:

1. Quadratic linear dispersion: $\beta(\omega)$ is expanded into the Taylor series around ω_0, and $\beta(\omega) - \beta(\omega_0) \simeq \beta_1(\omega-\omega_0) + \beta_2(\omega-\omega_0)^2/2$ where $\beta_n \equiv \beta^{(n)}(\omega_0)$. This expansion is valid only when the spectrum of the pulse is localized around ω_0 (Condition 1).

2. Restricted frequency region: The terms proportional to $\mathrm{e}^{\pm 3\mathrm{i}\omega_0 t}$ are dropped. This restriction is effective as far as the spectrum of the pulse is confined sufficiently within the region $-2\omega_0 < \omega < 2\omega_0$ (Condition 2).
3. Nearly instantaneous nonlinear response: Only the terms up to the first-order in the Taylor series in $\omega - \omega_0$ of the Fourier-transform of the nonlinear response function in (1.81b) are left as $\tilde{R}(\omega) \simeq 1 + \tilde{R}^{(1)}(\omega - \omega_0)$ (Condition 3).
4. Weak nonlinear dispersion such as the self-steepening or the core dispersion: Only the terms up to the first-order in the Taylor series in $\omega - \omega_0$ of the coefficient of the nonlinear term are left as $\gamma_{\mathrm{SPM}}(\omega) \equiv (3/4)\gamma_{\mathrm{FDM}}(\omega) \simeq \gamma^{(0)}_{\mathrm{SPM}} + \gamma^{(1)}_{\mathrm{SPM}}(\omega - \omega_0)$ (Condition 4).

In addition,

5. Unidirectional propagation approximation: Only a forward wave A_1 is considered throughout the propagation, and $B_1 \simeq A_1$, $b_1 \simeq a_1$ (Condition 5).

As seen from the second equation of (1.78a), the backward wave A_2 can be generated from A_1 through F_{N} even if A_2 is initially absent. However, we can derive the NLSE only from the first equation of (1.78a) for the forward wave:

$$\begin{aligned} &\frac{\partial A_1}{\partial \xi} = F_{\mathrm{L}1} - F_{\mathrm{N}}, \quad F_{\mathrm{L}1} = \mathrm{i}Z\left(\beta - \frac{\omega}{v}\right)A_1, \\ &F_{\mathrm{N}} = -\mathrm{i}\gamma_{\mathrm{FDM}}(\omega)\mathsf{F}b_1(\xi,\tau)\mathsf{F}^{-1}\tilde{R}(\omega)\mathsf{F}[b_1(\xi,\tau)]^2. \end{aligned} \tag{1.88}$$

We operate EF^{-1} on both sides of (1.88), and use Conditions 1–5 (Condition 5 is used only in F_{N}). Then, each term becomes:

$$\mathsf{EF}^{-1}\frac{\partial A_1}{\partial \xi} = \mathsf{F}^{-1}Z\left(\frac{\partial A_+}{\partial z} + \mathrm{i}\beta_0 A_+\right) = \frac{\partial a_+}{\partial \xi} + \mathrm{i}\beta_{0\mathrm{C}}a_+, \tag{1.89a}$$

$$\begin{aligned} \mathsf{EF}^{-1}F_{\mathrm{L}1} &= \mathsf{F}^{-1}Z\left(\mathrm{i}\beta - \frac{\mathrm{i}\omega}{v}\right)A_+ = \mathsf{F}^{-1}Z\left[\mathrm{i}\sum_{n=0}^{\infty}\frac{\beta_n}{n!}(\omega-\omega_0)^n - \frac{\mathrm{i}\omega}{v}\right]A_+ \\ &\simeq \mathrm{i}\beta_{0\mathrm{C}}a_+ - \beta_{1\mathrm{C}}\frac{\partial a_+}{\partial \tau} - \frac{\mathrm{i}\beta_{2\mathrm{C}}}{2}\frac{\partial^2 a_+}{\partial \tau^2} + \frac{Z/T}{v}\left(\frac{\partial a_+}{\partial \tau} - \mathrm{i}\omega_{0\mathrm{C}}a_+\right), \end{aligned} \tag{1.89b}$$

$$\mathsf{EF}^{-1}(-F_{\mathrm{N}}) \simeq \mathrm{i}\left(\gamma^{(0)}_{\mathrm{SPM}} + \frac{\mathrm{i}\gamma^{(1)}_{\mathrm{SPM}}}{T}\frac{\partial}{\partial \tau}\right)a_+\left(1 - \frac{T_{\mathrm{R}}}{T}\frac{\partial}{\partial \tau}\right)|a_+|^2. \tag{1.89c}$$

The following relation is used conveniently in these transformations:

$$\mathsf{EF}^{-1}(\omega - \omega_0)^n A_1 = \left(\frac{\mathrm{i}}{T}\frac{\partial}{\partial \tau}\right)^n a_+. \tag{1.90}$$

As the result, the following extended NLSE with the effects of the nonlinear dispersion and the Raman frequency shift is derived:

$$\frac{\partial a_+}{\partial \xi} = -\left(\beta_{1\mathrm{C}} - \frac{Z/T}{v}\right)\frac{\partial a_+}{\partial \tau} - \frac{\mathrm{i}\beta_{2\mathrm{C}}}{2}\frac{\partial^2 a_+}{\partial \tau^2} - \frac{\mathrm{i}(Z/T)\omega_{0\mathrm{C}}}{v}a_+ + \mathrm{i}\left(\gamma^{(0)}_{\mathrm{SPM}} + \frac{\mathrm{i}\gamma^{(1)}_{\mathrm{SPM}}}{T}\frac{\partial}{\partial \tau}\right)a_+\left(1 - \frac{T_\mathrm{R}}{T}\frac{\partial}{\partial \tau}\right)|a_+|^2, \tag{1.91}$$

where

$$\beta_{1\mathrm{C}} \equiv Z\beta_1/T, \quad \beta_{2\mathrm{C}} \equiv Z\beta_2/T^2 = Z/L_\mathrm{D}, \quad L_\mathrm{D} \equiv T^2/\beta_2, \tag{1.92a}$$

$$\gamma^{(0)}_{\mathrm{SPM}} \equiv \gamma_{\mathrm{SPM}}(\omega_0) = Z\frac{\omega_0}{c}\frac{3\chi^{(3)}}{8n_0}[\tilde{E}_\mathrm{p}(\omega_0)]^2 = Z/L_\mathrm{N}, \tag{1.92b}$$

$$L_\mathrm{N} \equiv \left\{\frac{\omega_0}{c}\frac{3\chi^{(3)}}{8n_0}\frac{P}{c\varepsilon_0 n_0 A_\mathrm{eff}(\omega_0)}\right\}^{-1}, \tag{1.92c}$$

$$\gamma^{(1)}_{\mathrm{SPM}} \equiv \left[\frac{\mathrm{d}\gamma_{\mathrm{SPM}}(\omega)}{\mathrm{d}\omega}\right]_{\omega=\omega_0}, \tag{1.92d}$$

$$T_\mathrm{R} \equiv \frac{1}{\mathrm{i}}\tilde{R}^{(1)} = \frac{1}{\mathrm{i}}\left[\frac{\mathrm{d}\tilde{R}(\omega)}{\mathrm{d}\omega}\right]_{\omega=\omega_0} = \int_0^\infty R(t)t\mathrm{d}t = \frac{2f_\mathrm{R}\tau_1^2\tau_2}{\tau_1^2+\tau_2^2}. \tag{1.92e}$$

L_D and L_N are the dispersion length and the nonlinear length, respectively. When Z is chosen as L_D, $\gamma^{(0)}_{\mathrm{SPM}} = L_\mathrm{D}/L_\mathrm{N} = N^2$ with the soliton order N.

Under the conditions that (1) v is adjusted to the group velocity $1/\beta_1$, (2) the phase factor $\mathrm{e}^{-\mathrm{i}\omega_0\beta_1 z}$ independent of t is separated from a_+, and (3) the terms with $\gamma^{(1)}_{\mathrm{SPM}}$ or T_R are dropped, (1.91) reduces to the usual NLSE:

$$\frac{\partial a_+}{\partial \xi} = -\frac{\mathrm{i}\beta_{2\mathrm{C}}}{2}\frac{\partial^2 a_+}{\partial \tau^2} + \mathrm{i}\gamma^{(0)}_{\mathrm{SPM}}|a_+|^2 a_+. \tag{1.93}$$

Unidirectional Propagation Instead of Slowly Varying Envelope Approximation

In the conventional derivation of the extended NLSE (1.91) or the usual NLSE (1.93) the following approximation is always employed:

6. Slowly-varying-envelop approximation (SVEA) [1, 22]: The second derivative of the envelop function is neglected by $\left|\partial^2 A_+/\partial\xi^2\right| \ll |2\beta_{0\mathrm{C}}\partial A_+/\partial\xi|$ (Condition 6).

In contrast, the present derivation from the first partial differential equation (1.88) as shown above does not call for the SVEA.

The conventional derivation usually begins with the wave propagation equation

$$\frac{\partial^2 \tilde{E}}{\partial z^2} + \beta^2\tilde{E} = -\frac{\omega^2}{c^2}\mathsf{F}\frac{P_\mathrm{N}}{\varepsilon_0} = -\frac{2i\beta E_\mathrm{p}}{Z}F_\mathrm{N} \tag{1.94}$$

with the nonlinear term expressed by (1.79b), which is derived by eliminating $\tilde{H}(z,\omega)$ between the equations in (1.69). The Fourier-transform of the electric field $\tilde{E}(z,\omega)$ in the left side of (1.94) is expressed as

$$\begin{aligned}\tilde{E}(z,\omega) &= E_{\rm p}(\omega)B_1(\xi,\omega_{\rm C}) = E_{\rm p}(\omega)\left\{A_1(\xi,\omega_{\rm C}) + A_2(\xi,\omega_{\rm C})\right\}\\ &= \frac{E_{\rm p}(\omega)}{2}\Big\{\left[A_+(\xi,\omega_{\rm C}-\omega_{0\rm C}) + A_-(\xi,\omega_{\rm C}+\omega_{0\rm C})\right]{\rm e}^{{\rm i}\beta_{0\rm C}\xi}\\ &\qquad + \left[A_+^*(\xi,-\omega_{\rm C}-\omega_{0\rm C}) + A_-^*(\xi,-\omega_{\rm C}+\omega_{0\rm C})\right]{\rm e}^{-{\rm i}\beta_{0\rm C}\xi}\Big\}\\ &\equiv \frac{E_{\rm p}(\omega)}{2}\left[B_+(z,\omega){\rm e}^{{\rm i}\beta_0 z} + B_-(z,\omega){\rm e}^{-{\rm i}\beta_0 z}\right] \qquad (1.95)\end{aligned}$$

by (1.75d), (1.77b) and (1.86). Furthermore,

$$\begin{aligned}&\frac{\partial B_+}{\partial z} - {\rm i}\left(\beta-\beta_0\right)B_+ = \mathsf{E}\left(\frac{\partial B_1}{\partial z} - {\rm i}\beta B_1\right)\\ &= -{\rm i}(\beta+\beta^*)\mathsf{E}A_2 = -{\rm i}(\beta+\beta^*)A_- \qquad (1.96)\end{aligned}$$

by $\partial B_1/\partial z = -{\rm i}\omega B_2/c$, $A_2 = (n_{\rm L}B_1 + B_2)/(n_{\rm L}+n_{\rm L}^*)$ and $\mathsf{E}A_2 = A_-$ ((1.76a), (1.77a) and (1.86)).

We operate $\mathsf{EF}^{-1}Z/(2{\rm i}\beta E_{\rm p})$ on both sides of (1.94), which leads the right side of (1.94) to $\mathsf{EF}^{-1}(-F_{\rm N})$ of (1.89c). On the other hand, the left side of (1.94) becomes rigorously as follows:

$$\begin{aligned}&\mathsf{EF}^{-1}\frac{Z}{2{\rm i}\beta E_{\rm p}}\left(\frac{\partial^2\tilde{E}}{\partial z^2} + \beta^2\tilde{E}\right)\\ =&\mathsf{F}^{-1}\frac{Z}{2{\rm i}\beta}\left[\frac{\partial^2 B_+}{\partial z^2} + 2{\rm i}\beta_0\frac{\partial B_+}{\partial z} + (\beta^2-\beta_0^2)B_+\right] \qquad (1.97a)\\ =&\mathsf{F}^{-1}\frac{Z}{2{\rm i}\beta}\left[2i\beta\left(\frac{\partial B_+}{\partial z} - {\rm i}(\beta-\beta_0)B_+\right) + Res\right], \qquad (1.97b)\end{aligned}$$

where the residual term *Res* is defined and transformed as:

$$\begin{aligned}Res &\equiv \frac{\partial^2 B_+}{\partial z^2} - 2{\rm i}(\beta-\beta_0)\frac{\partial B_+}{\partial z} - (\beta-\beta_0)^2 B_+\\ &= {\rm e}^{{\rm i}(\beta-\beta_0)z}\frac{\partial^2}{\partial z^2}{\rm e}^{-{\rm i}(\beta-\beta_0)z}B_+\\ &= \left(e^{{\rm i}(\beta-\beta_0)z}\frac{\partial}{\partial z}{\rm e}^{-{\rm i}(\beta-\beta_0)z}\right)^2 B_+\\ &= {\rm e}^{{\rm i}(\beta-\beta_0)z}\frac{\partial}{\partial z}{\rm e}^{-{\rm i}(\beta-\beta_0)z}\left(\frac{\partial B_+}{\partial z} - {\rm i}\left(\beta-\beta_0\right)B_+\right)\\ &= -{\rm i}(\beta+\beta^*){\rm e}^{{\rm i}(\beta-\beta_0)z}\frac{\partial}{\partial z}{\rm e}^{-{\rm i}(\beta-\beta_0)z}A_-. \qquad (1.98)\end{aligned}$$

Equation (1.96) is used in the last line of (1.98). The NLSE is derived again if *Res* can be neglected and $B_+ \simeq A_+$ (from Condition 5) is used, since (1.97b)

is equal to the difference between (1.89a) and (1.89b). The SVEA is nothing but neglecting *Res* in comparison with the first term in (1.97b), since *Res* approximately agrees with $\partial^2 A_+/\partial z^2$ for

7. Infinitesimal $\beta(\omega) - \beta(\omega_0)$ (Condition 7).

In the above, we derived the NLSE in two ways: from the first-differential equation for the forward wave in (1.88); and from the second-differential wave propagation equation (1.94) by the use of the SVEA. Though the derived equations agreed with each other, the latter used the unidirectional propagation approximation (Condition 5) and Condition 7 in addition to the SVEA (Condition 6). Therefore, the former derivation from the forward wave equation is much more straightforward than the latter, which supposes more restrictions in the range of validity.

1.3 Comparison between Theoretical and Experimental Results

1.3.1 Split-Step Fourier Analysis beyond SVEA

Calculations for Fused-Silica Fiber

4.5-Cycle Pulse SPM Case

Calculations for 4.5-cycle pulses in a single-mode fused-silica fiber were performed and compared with experimental results [2]. In the experiments, an optical pulse from a Ti:Sapphire oscillator was introduced in a 2.5 mm-long single-mode fiber (Newport F-SPV, the core radius a =1.32 μm). The pulse width measured by an autocorrelator was 12 fs and the input-pulse peak power calculated from the measured pulse energy at fiber output was 175 kW. The input pulse was obtained by inverse Fourier transforming the spectrum of the input pulse. However, the transform-limited pulse width (8.6 fs) was smaller than the experimentally measured pulse width (12 fs) obtained by a fringe-resolved autocorrelator. To use the pulse with the correct spectrum and the pulse width in the calculation, the temporal duration was adjusted by adding the quadratic spectral phase of the form $\phi(\omega) = c_1(\omega - \omega_0)^2$ to the experimental spectrum to make the inverse Fourier transformed pulse width same as that of the measured one. It gave the value $c_1 = \pm 9.9\,\mathrm{fs}^2/\mathrm{rad}$. Both values were used in initial calculations. However, it was found that the difference of spectra was negligible. Thus in the following, only the results with the negative value are shown.

We consider the material dispersion of fused-silica using the Sellmeier equation for the linear dispersion terms with zero loss. For a single-mode fused-silica fiber, it is well known that the effective core area of the fiber depends on the wavelength and it becomes larger as the wavelength becomes

longer compared with the cut-off wavelength of the fiber [1]. For the fiber used in this experiment, the cut-off wavelength and the numerical aperture are 550 nm and 1.6 respectively which give the core radius a =1.32 μm. It is evaluated that at the long wavelength, the effective core area becomes quite large. For example, the effective core area A_{eff}, calculated from the approximate fundamental mode distribution in [1] ($F = J_0(\kappa r)$ $(r < a)$, and $F = (a/r)^{1/2} J_0(\kappa a) e^{-\eta(r-a)}$ $(r > a)$, where J_0 is the zeroth order Bessel function, $r = (x^2 + y^2)^{1/2}$, $\kappa^2 = n_1^2 k_0^2 - \beta^2$ and $\eta^2 = \beta^2 - n_2^2 k_0^2$, n_1 and n_2 are refractive indices of the core and the clad, respectively) are $2.01\pi a^2$ at wavelength 790 nm and $3.68\pi a^2$ at 1000 nm, respectively. Thus it is expected that at longer wavelength, the nonlinear effect becomes smaller since the effective core area becomes larger. To include this effect in the calculation, the term $\partial_\omega(\ln g(\omega))|_{\omega_0}$ in (1.23) was calculated at the center wavelength and added for the steepening parameter. From the mode equation of the single-mode fiber, the derivative of the effective core area was numerically calculated as a function of wavelength and the value at center wavelength (798 nm) was obtained as $-\omega_0 \partial_\omega(\ln A_{\text{eff}}(\omega))|_{\omega_0} = 2.06$. We used the value of the nonlinear refractive coefficient $n_2^{\text{I}} = 2.48 \times 10^{-20}\,\text{m}^2/\text{W}$ from [23].

Calculations with different levels of approximations were performed. For case (a), the Raman term as well as rigorous linear dispersion terms were used in calculations (1.30). For case (b), to examine the effect of the Raman term on the spectrum broadening, the Raman term was omitted ($f_{\text{R}} = 0$ in (1.30)). For case (c), in addition, dispersion of the effective core area was omitted ($\partial_\omega(\ln g(\omega))|_{\omega_0} = 0$ in (1.30)), and for case (d), the SVEA was used ((1.37) and (1.30) with $f_{\text{R}} = 0$).

In Fig. 1.1, experimental spectra as well as calculated spectra are shown. It is seen that the agreement between the calculation with the equation including all the terms (a) and the experiment is good. When the Raman term is omitted (b), the spectrum broadening at the short wavelength is larger in calculation than experiment. This is because the optical energy is transferred to that at the longer wavelength by exciting the molecular vibrations when the Raman effect is present [1]. When the dispersion of the effective core area is omitted (c), the spectrum broadening at the long wavelength is larger in calculation than experiment. This is because this effect is included as the additional steepening term in the calculation. When the steepening term is present, the trailing edge of the pulse becomes steep because group velocity of the pulse depends on its intensity [1]. And this steep trailing edge generates large positive chirp from SPM. In this way, energy is transferred to the shorter wavelength when the steepening term is present. For the SVEA (d), the spectrum broadening at the long wavelength is larger in calculation than in experiment. This is because no steepening term is included in the SVEA. Also in this case, it was found that the spectrum including rigorous dispersion terms and the spectrum including only up to third order terms are almost identical. Thus, in this case, the approximation using up to third order terms is sufficient.

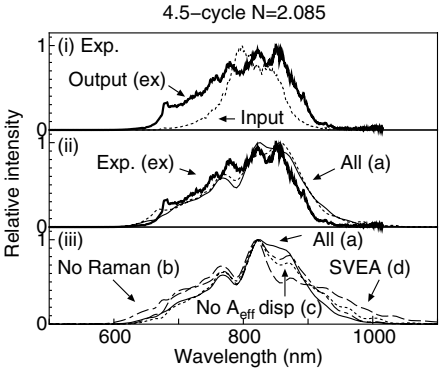

Fig. 1.1. The experimental and calculated spectra for 4.5-cycle pulse propagation in a 2.5 mm-long fused-silica fiber. The input power is 175 kW (soliton number $N = 2.085$). (**i**) The experimental input (*thick solid line*) and output (*dotted line*) spectra. (**ii**) The experimental spectrum (*thick solid line*) is compared with the calculated spectrum including all terms (*solid line*). (**iii**) The calculated spectra: (a) including all terms (*solid line*), (b) without the Raman term (*dot-dashed line*), (c) without the effective core area dispersion (*dotted line*), and (d) the SVEA (*dashed line*) [2]

Calculations of 2-Cycle and Monocycle Pulse SPM Cases

Calculations of spectra were performed for 2-cycle pulse and monocycle pulse propagations [2]. The fiber parameters were the same as in the previous subsection. Gaussian input pulses were used and the same soliton number of 1 for both cases was used in the calculations ($N = 1$). The input pulse width and peak power were 5.32 fs and 204 kW for 2-cycle pulses and 2.66 fs and 815 kW for monocycle pulses, respectively.

Calculated spectra are shown in Fig. 1.2(i) for 2-cycle pulses. When the Raman term is not included (b), the spectrum intensity at the short wavelength is larger than that with all terms (a). On the other hand, when dispersion of the effective core area is not included (c), the spectrum intensity at the long wavelength is larger than that with all terms.

The calculated spectra for the monocycle case are shown in Fig. 1.2(ii). Similar but more pronounced tendencies are observed when the Raman term is omitted (b) and dispersion of the effective core area is omitted (c) compared with the calculations with all terms (a), like as the 2-cycle pulse calculations. In this case, the additional calculation with the same terms as in (a) except that only up to third order dispersion terms are included ($\widehat{D}' = -\beta_0^{(2)}\partial_T^2/2 - i\beta_0^{(3)}\partial_T^3/6, \widehat{D}_{\rm corr} = 0$ in (1.23)) is shown (d). There is a difference in spectra between this (d) and the one with all terms (a). Thus for this monocycle case, the inclusion of the dispersion terms only up to third order terms is not enough. For the 2-cycle calculation, the same calculation was performed and

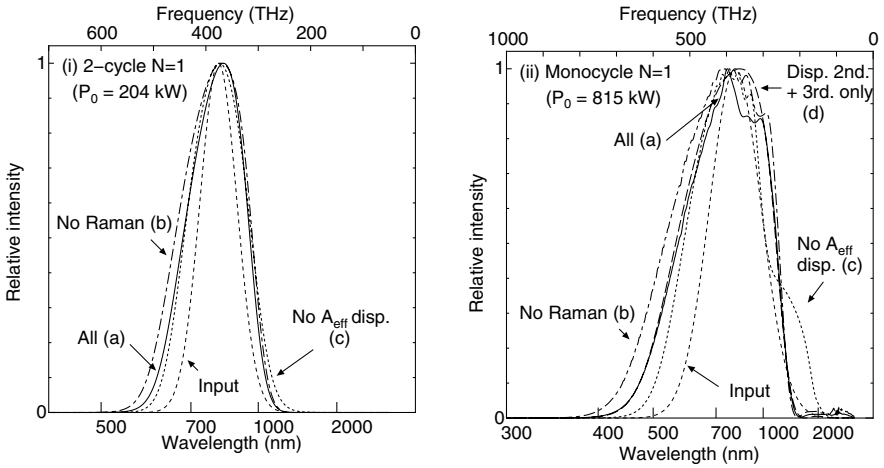

Fig. 1.2. The calculated spectra for 2-cycle (**i**) and monocycle (**ii**) pulses after propagating 2.5 mm-long fused-silica fiber. The soliton number N is 1 for both cases corresponding to 204 kW and 815 kW input powers for 2-cycle and monocycle cases, respectively. In this figure, (a) all terms are included (*solid line*), (b) without the Raman term (*dot-dashed line*), (c) without the effective core area dispersion (*dotted line*), and (d) only up to third order dispersion terms in (a) are included (*dashed line*). Input spectra are shown by short dashed lines [2]

no difference was found between these two spectra. Thus for the calculation of the monocycle pulse, it is important to include more than third order terms.

IPM+SPM Case

For the IPM experiments, the fundamental pulse (center wavelength 797 nm) and the idler pulse (center wavelength 1087 nm) from the Ti:sapphire amplifier system with the optical parametric amplifier (OPA) were co-propagated in a 3.5 mm-long single-mode fiber (Newport F-SPV) [2]. The reflective objective was used to couple these pulses in the fiber and the relative delay time between these pulses were adjusted by an optical delay line with a micrometer and a position sensor. This delay was calibrated by observing the sum-frequency signal generated by both pulses using a 10 µm-thick β-barium borate (BBO) crystal. In this experiment, both input pulses were evaluated by a second-harmonic generation frequency-resolved optical gating (SHG FROG) apparatus [24]. The measured pulse widths were 75 and 79 fs for the fundamental pulse and the idler pulse, respectively. The spectra when each pulse was propagated separately (i) and when both pulses were co-propagated with the three different delay times of the fundamental pulse with respect to the idler pulse (0 fs (ii), −27 fs (iii) and −67 fs (iv)) are shown in Fig. 1.3(a). The effective core area A_{eff} and its dispersion $-\omega_0 \partial_\omega (\ln A_{\text{eff}}(\omega))|_{\omega_0}$ are included as like in the SPM case, which are $2.05(4.92)\pi a^2$ and 2.06(3.80) for the

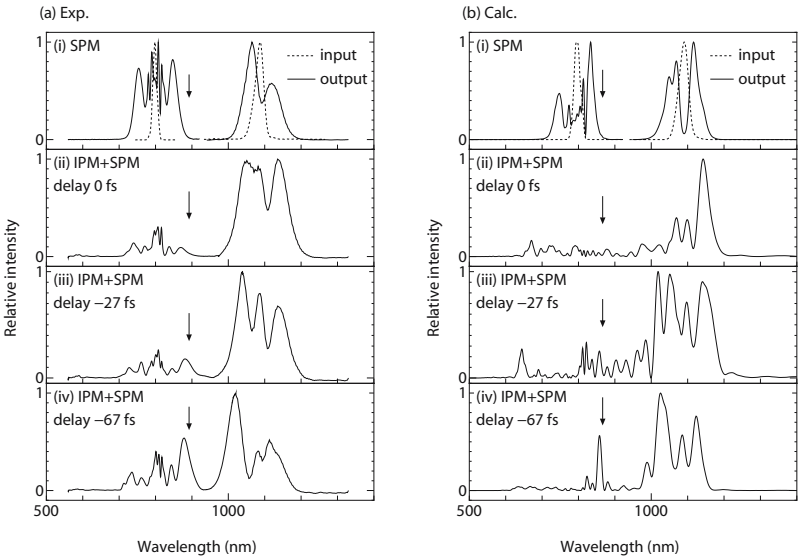

Fig. 1.3. The experimental (**a**) and calculated (**b**) spectra after the fundamental pulse (center wavelength 797 nm, pulse width 79 fs, peak power 225 kW) and the idler pulse (center wavelength 1087 nm, pulse width 75 fs, peak power 480 kW) from the Ti:sapphire laser amplifier OPA system are propagated in a 3.5 mm-long fused-silica fiber. In this figure: (**i**) pulses propagated separately, with input spectra, are shown by dotted lines, (**ii**) co-propagation of both pulses where the delay time of the fundamental pulse with respect to the idler pulse is set to be 0 fs, (**iii**) co-propagation with delay time of −27 fs, and (**iv**) co-propagation with delay time of −67 fs [2]

fundamental (idler) pulse, respectively. The mode overlap integral is given as $O(\omega_{01}, \omega_{02}) = 3.30\pi a^2$ and its derivatives $-\omega_{0j}\partial_\omega(\ln O(\omega, \omega_{03-j}))|_{\omega_{0j}}$ are calculated to be 0.837 and 2.19 for the fundamental pulse ($j = 1$) and the idler ($j = 2$) pulse, respectively. Due to the difficulty of separating the propagated output pulse energy from the pulse energy propagating in the clad, the input power for each pulse was estimated by the fitting of the self-phase modulation measurements and determined to be 225 (480) kW for the fundamental (idler) pulse. The calculated spectra from (1.32) are compared with the experimental ones in Fig. 1.3(b). It is shown in the both cases of the experiment and the calculation that when these pulses are propagated separately (i), there is no intensity between 880–970 nm. When both pulses are co-propagated (ii)–(iv), the spectra for the fundamental wave and the idler wave are connected by induced-phase modulation. The intensity of the middle position (indicated by arrows in Fig. 1.3) is the largest when the delay time is −67 fs compared with that when the delay time is 0 fs. The propagation time difference between these two pulses for a 3.5 mm-long fiber is 58.6 fs. Thus when the delay time is −67 fs, both pulses overlap near the fiber exit end. For the capillary fiber

IPM using the fundamental and the second-harmonic pulses, we have analytically [25] and experimentally shown [26] that the spectrum overlapping becomes largest when both pulses meet near the fiber exit end (see Sect. 2.3). The fact that the intensity of the middle position is the largest when the delay time is −67 fs indicates that the similar tendency holds for the fused-silica fiber. It is observed that the delay time dependence of the spectra between the experiment and theory agree qualitatively.

Calculations for the Argon-Filled Single-Mode Hollow Waveguide

Single-mode capillary fibers filled with noble gases have been used to broaden the spectrum of optical pulses through dispersive SPM [27]. Because of the chemical stability of the noble gases, the damage threshold of the capillary fiber is relatively high compared with the glass fiber. Also, the large walk-off length is advantageous for spectral broadening using IPM (see Sect. 2.3).

In the experiment [26], the output beam of a Ti:sapphire laser-amplifier system (center wavelength ∼ 790 nm, pulse width 24 fs, repetition rate 1 kHz and pulse energy 1 mJ) was passed through a 0.5-mm-thick β-barium borate (BBO) crystal and the second-harmonic pulse was generated. The second-harmonic pulse was combined with the fundamental pulse after a proper delay time was added. Then, these pulses were co-propagated in a capillary fiber with 34-cm length and 0.1-mm inner diameter filled with argon gas with a pressure of 3.3 atm. For details of the experiment, see Sect. 2.3. The fundamental pulse of 40.8 μJ energy and the second-harmonic pulse of 37.8 μJ energy were focused at the fiber entrance. Figures 1.4(a)–(c) show experimental spectra at the output of a fiber and compare them with calculations. In Fig. 1.4a, two spectra when both pulses were propagated separately are shown. In this case, the spectral broadening is due to only SPM. When the delay time between two co-propagated pulses was adjusted such that these pulses overlapped inside the fiber, we observed the larger spectral broadening due to IPM and SPM (Figs. 1.4(b)–(c)). In Fig. 1.4(b), the spectrum is shown when both pulses met near the fiber entrance ($T_\mathrm{d} = 13$ fs) and in Fig. 1.4(c), it is shown when both pulses met near the fiber exit ($T_\mathrm{d} = -80$ fs).

In the calculations, the following parameters are used: $\lambda_\mathrm{c} = 767.95$ nm, $T_\mathrm{p} = 24$ fs, $P_0 = 1.03$ GW and $n_2 = 2.99 \times 10^{-23}\,\mathrm{m^2/W}$ for the fundamental pulse, and $\lambda_c = 404.84$ nm, $T_\mathrm{p} = 58$ fs, $P_0 = 0.46$ GW and $n_2 = 4.78 \times 10^{-23}\,\mathrm{m^2/W}$ for the second-harmonic pulse, where λ_c is the center wavelength, T_p is the pulse width, P_0 is the peak power and n_2 is the nonlinear refractive index [28]. The effective core area of the EH_{11} mode is calculated to be $0.477\pi a^2$ where a is the radius of the capillary fiber. Here, the spatial profile of the electric field is assumed to be $J_0(2.405r/a)$ [3], where J_0 is the zeroth-order Bessel function. The theoretical propagation loss due to the waveguide itself [3] is 52% for the fundamental wave and 17% for the second-harmonic wave. If we consider only this loss, the net input energy evaluated from the output energy (11.9 μJ) for the fundamental

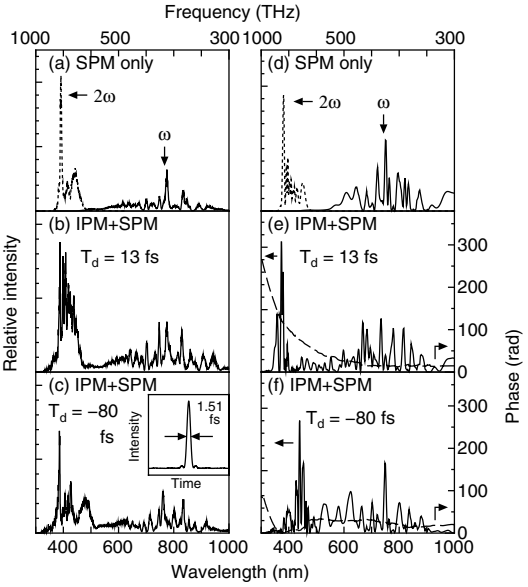

Fig. 1.4. Experimental (**a**)–(**c**) and calculated (**d**)–(**f**) spectra when the fundamental pulse and the second-harmonic pulse were propagated separately and were co-propagated in a fiber: (**a**) and (**d**) SPM only, (**b**) and (**e**) IPM+SPM, $T_{\mathrm{d}} = 13\,\mathrm{fs}$, (**c**) and (**f**) IPM+SPM, $T_{\mathrm{d}} = -80\,\mathrm{fs}$ [26]

wave is 24.8 μJ (11.9 μJ/0.48). The calculated spectral broadening by SPM using this value (24.8 μJ) agrees with the experimental broadening. For the second-harmonic wave, the net input energy evaluated from the output energy by considering the theoretical waveguide loss is 13.4 μJ (11.1 μJ/0.83). However, it was necessary to set 26.7 μJ as the practical input-pulse energy to obtain the similar broadening by SPM experiments. In Figs. 1.4(d)–(f), the numerically-calculated spectra using parameters thus determined are shown. In Fig. 1.4(d), calculated spectra for SPM for fundamental and second-harmonic waves are shown. In Figs. 1.4(e)–(f), calculated spectra for IPM + SPM at two different delay times are shown. It is seen that the relative spectral intensity around the central part between 400 and 800 nm is larger for (f) compared with (e). In addition, the more homogeneous spectrum broadens from 300 to 1000 nm for (f) than (e). These behaviors agree with the experimental spectra. In Figs. 1.4(e)–(f), calculated wavelength-dependent phases are shown. It is seen that the phase-variations are relatively smooth, which is important for phase-compensation for pulse-compression and synchronous multi-color shaping.

Calculations for the Photonic Crystal Fiber

Photonic crystal fibers have attracted significant research interest in recent years for their zero-dispersion wavelength shifted into the visible range and hence efficient supercontinuum generation [29, 30]. To clarify both experimentally and theoretically the mechanism of supercontinuum generation for propagation of a-few-cycle pulses in a photonic crystal fiber, systematic information regarding spectral and temporal evolutions of the pulses at different propagation distances was obtained [31].

In the experiment, the photonic crystal fiber consisted of a 1.7-μm-diameter undoped silica core surrounded by an array of 1.3-μm-diameter air holes in a hexagonal close-packed arrangement [29]. 12-fs-duration pulses with 800-mW average power centered at 795 nm were generated from a mode-locked Ti:sapphire laser at the repetition rate of 75 MHz. Photonic crystal fibers with four different lengths (4, 8, 15, and 61 mm) were prepared. Pulses were coupled into these fibers by a reflective objective. The polarization axis of the linearly-polarized pulses coincided with one of the principal axes of the fibers. The spectra of the pulses before and after propagation are shown in Fig. 1.5(a). In the insets of Fig. 1.6(a), the autocorrelation traces are shown.

In the calculations, the SEWA method of (1.23) was used with the rigorous dispersion relations of the photonic crystal fiber. Calculated spectral intensities and temporal profiles are shown in Fig. 1.5(b) and Fig. 1.6(a). The agreement between the experiment and the calculation is excellent. In addition, calculations with the SVEA method with the inclusion of the self-steepening term and the delayed-nonlinear Raman term were performed. In this method, only up to the third-order linear dispersion was included and the $\widehat{D}_{\rm corr}$ term was not included. Also, the self-steepening coefficient was set to be $s' = 1/\omega_0$ (ω_0 : center angular frequency of the input pulse). The calculated result indicated that spectral broadening at a shorter wavelength was much larger in this case than in the experimental result, especially at the longest propagation distance, as shown by dotted lines of Fig. 1.6(b)(1)–(5). Furthermore, even if the rigorous dispersion terms were used, the spectral broadening at the short wavelength was still too large as shown by a dashed line for the longest distance. The difference was mainly due to the neglect of $\widehat{D}_{\rm corr}$ term rather than the approximate self-steepening coefficient.

The mechanism of the superconinuum generation for propagation of a-few-cycle pulses with peak power on the order of tens of kilowatts (67 kW: soliton number $N = 5.7$) and a central wavelength (795 nm) slightly longer than the zero dispersion wavelength (767 nm) is found out as follows. At first (up to several millimeters), most of the pulse energy in the spectral band forms a higher order soliton due to the SPM and the negative group velocity dispersion. Since the third-order dispersion (TOD) of the fiber is considerably large (critical parameter $\delta_3 = 0.24$ [1]), asymmetric multifold splitting of the temporal-intensity profile occurs. In addition, the spectrum is blue shifted due to the self-steepening effect (Fig. 1.5(2)

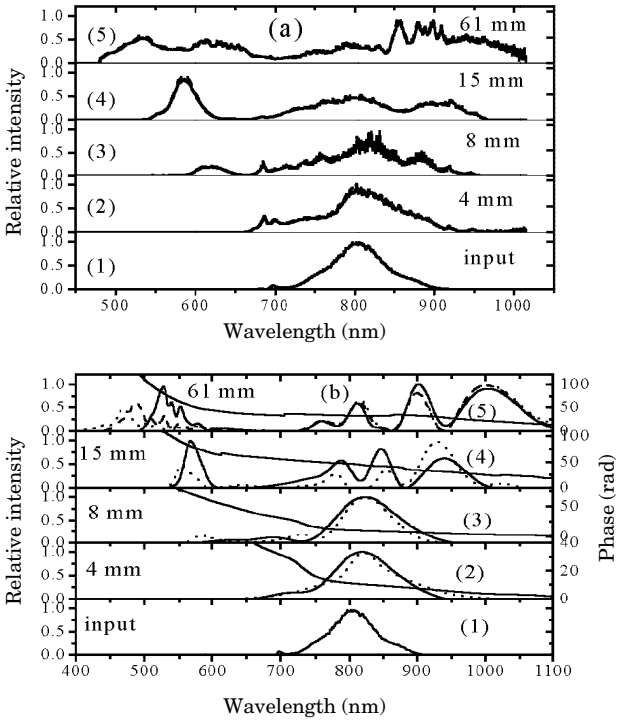

Fig. 1.5. (**a**) Experimental spectra generated from 4.5-cycle optical pulses in different-length PCFs. (**b**) Numerically simulated intensity and phase spectra with SEWA (*solid lines*), SVEA (*dotted lines*), and SVEA plus all-order dispersion for only 61-mm case (*dashed lines*) [31]

and Fig. 1.6(a)). Around the 8-mm propagation distance (Fig. 1.5(3)), the short-wavelength component in the positive group-velocity dispersion region ($< 767\,\mathrm{nm}$) efficiently causes the intrapulse four-wave mixing. Here, the wavelength component slightly shorter than the zero dispersion wavelength plays the role of the pump (ω_p) for the four-wave mixing processes (for example, $\omega_\mathrm{p}(766\,\mathrm{nm}) + \omega_\mathrm{p}(766\,\mathrm{nm}) = \omega_\mathrm{s}(930\,\mathrm{nm}) + \omega_\mathrm{as}(610\,\mathrm{nm})$). These processes are phase-matched and nearly group-velocity matched. As a result, the anti-Stokes (ω_as) and Stokes (ω_s) wavelength components appear and the spectral gap is yielded. The further propagation (Fig. 1.5(4)) extends their wavelength regions. However, the group-velocity matching worsens and the wavelength-dependent parametric gain is reduced. The result of spectral broadening gives rise to the temporal pulse broadening to form the wings because of the large dispersion in their regions. In addition, large TOD causes the oscillatory structure near the trailing edge of the pulse. Finally (Fig. 1.5(5)), the intensified anti-Stokes and Stokes waves are spectrally modulated due to the wavelength-dependent group-velocity matching and parametric gain. Conse-

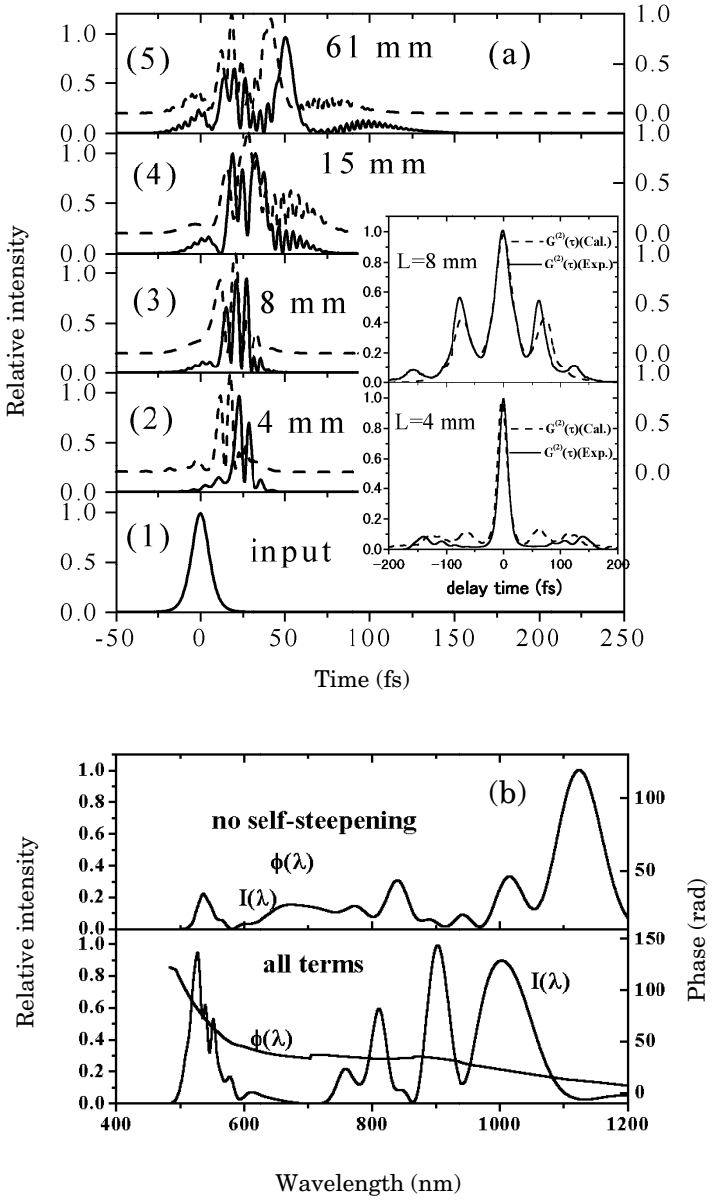

Fig. 1.6. (**a**) Numerically simulated temporal-intensity profiles with SEWA (*solid lines*) and with SVEA (*dashed lines*). The insets are the experimental intensity autocorrelation traces (*solid lines*) with the corresponding calculated results (*dashed lines*) with increasing propagation distance. (**b**) Effect of self-steepening in spectral broadening [31]

quently, the ultrabroad-band pulse from 480 to 1020 nm is generated. These findings suggest that the self-steepening effect is essential for the existance of the spectral gap. Figure 1.6(b), indicating the comparison between the calculated results without and with the self-steepening term, gives the evidence for this point. The evolution of the supercontinuum generated by propagating a-few-cycle pulses in the photonic crystal fiber has been well explained by a numerical analysis based on the extended nonlinear envelope equation beyond the SVEA method.

1.3.2 Finite-Difference Frequency-Domain Analysis

Comparison with FDTD

By using the FDFD method derived in Sect. 1.2.2, propagation of an optical pulse in the negative group velocity dispersion region in a dielectric medium was simulated [16]. The parameters used in the simulation were taken from [13, 14] where the FDTD method was used. In the calculations, the linear permittivity in the frequency domain was given by

$$\varepsilon(\omega) = \varepsilon_\infty + \widetilde{\chi}^{(1)}(\omega) = \varepsilon_\infty + \frac{\omega_0^2(\varepsilon_\mathrm{s} - \varepsilon_\infty)}{\omega_0^2 - \mathrm{i}\delta\omega - \omega^2}, \tag{1.99}$$

where $\varepsilon_\mathrm{s} = 5.25$, $\varepsilon_\infty = 2.25$, $\omega_0 = 4.0 \times 10^{14}\,\mathrm{rad/s}$, $\delta = 2.0 \times 10^9\,1/\mathrm{s}$ and $\chi^{(3)} = 7 \times 10^{-2}\,(\mathrm{V/m})^{-2}$. An initial pulse had a sinusoidal carrier electric field frequency $f_\mathrm{c} = 1.37 \times 10^{14}\,\mathrm{Hz}$ ($\lambda_\mathrm{c} = 2.19\,\mu\mathrm{m}$) with a unity amplitude and a hyperbolic secant envelope function with a characteristic pulse width of 14.6 fs (full width at half maximum divided by 1.763). β_1 was calculated to be $6.924 \times 10^{-9}\,\mathrm{s/m}$ at the carrier frequency. In the initial pulse, the phase was chosen such that the maximum of the envelope function coincided with the maximum of the sinusoidal function. At the end of calculations, waveforms at position $x = 126\,\mu\mathrm{m}$ were obtained in both time and frequency domains using (inverse) Fourier transforms.

In Fig. 1.7(a), spectral intensities and phases from both FDFD and FDTD calculations are shown. In these calculations, increment parameters selected were $\Delta t = 0.02\,\mathrm{fs}$ and $\Delta x = 5\,\mathrm{nm}$, by which correct results from the FDTD calculations were obtained [13, 14]. As shown in the figure, both spectral intensities and phases from these calculations are almost identical for these small increment parameters. In Fig. 1.7(b), spectral intensities and phases are shown when Δt and Δx were increased and compared with the FDTD calculation in Fig. 1.7(a) (FDTD (0)). All calculations gave similar intensities. However, phases calculated using $\Delta t = 0.2\,\mathrm{fs}$ and $\Delta x = 40\,\mathrm{nm}$ by the FDTD method (FDTD (i)) were shifted by about 1.5 radian from FDTD (0) and had an extra negative slope compared with FDTD (0). Phases calculated from FDFD using these parameters (FDFD (i)) were almost identical to FDFD (0) except that it was shifted by about 0.7 radian from FDTD (0). Calculations

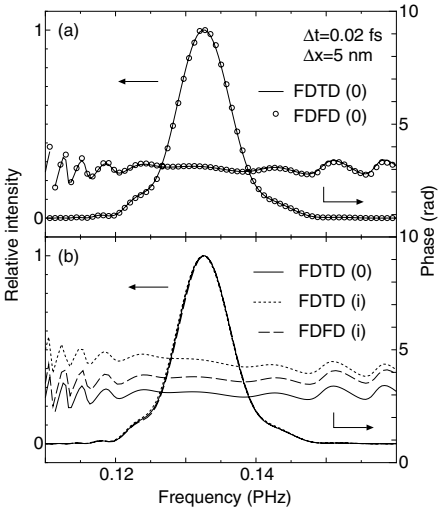

Fig. 1.7. Calculated spectral intensities and phases by FDTD and FDFD methods at $x = 126\ \mu$m. (**a**) Comparison between FDTD and FDFD, where $\Delta t = 0.02$ fs and $\Delta x = 5$ nm were used (FDTD (0) and FDFD (0)). (**b**) Comparison between FDTD and FDFD, where $\Delta t = 0.2$ fs, $\Delta x = 40$ nm (FDTD (i) and FDFD (i)) were used [16]

using $\Delta t = 0.4$ fs and $\Delta x = 80$ nm were tried and for the FDFD calculation, results with almost identical spectral intensities were obtained. The FDTD calculation for these parameters could not be performed due to the numerical instabilities. For this model, the phase velocity of the pulse in the entire pulse spectrum is larger than group velocity of the pulse, thus FDFD should be stable independent of Δx if we can consider pulse propagation to be almost linear. This may be the reason why FDFD is more stable than FDTD in this case. In Fig. 1.8, temporal waveforms of FDTD (0), FDTD (i) and FDFD (i) are shown for different time scales. As shown in this figure, the results from FDTD (0) and FDFD (i) calculations gave almost identical waveforms in the middle part of the pulse, except that FDFD (i) was shifted by about 1 fs from FDTD (0). The shape of the envelope function by FDTD (i) calculation was different from that of FDTD (0) and there were larger phase shifts inside the envelope function compared with FDFD (i). Calculation times for FDTD (i) and FDFD (i) were 162 and 80 seconds, respectively, using a personal computer with an Athlon 900 MHz processor.

IPM Calculations

In Sect. 1.3.1, the SEWA calculations of the co-propagation of two pulses in a fused-silica fiber were shown. In these calculations, (1.32) was used for the idler pulse (pulse 1, center angular frequency ω_{01}) and the fundamental pulse

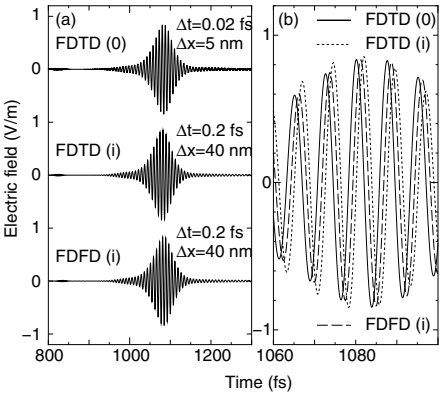

Fig. 1.8. Calculated electric fields by FDTD and FDFD methods at $x = 126$ μm. Parameters used were the same as in Fig. 1.7: (**a**) Long-range view, (**b**) Expanded view near the pulse-center [16]

(pulse 2, center angular frequency ω_{02}). This equation includes both SPM and IPM terms. However, it neglects the four-wave mixing terms based on the assumption that the phase-matching conditions are not satisfied. If these terms were taken into account, optical waves with center angular frequencies of $\omega_{03} = 2\omega_{01} - \omega_{02}$ and $\omega_{04} = 2\omega_{02} - \omega_{01}$ could be generated. It is possible to include these four-wave mixing waves in the SEWA method by including two extra electric-field-envelope functions whose center angular frequencies are ω_{03} and ω_{04}. However, if these four-wave mixing waves are generated, other four-wave mixing waves will also be generated (e.g., combinations of ω_{01} and ω_{03}, etc.). Thus it becomes difficult to include all these successively-generated four-wave mixing waves by this method. On the other hand, whole four-wave mixing interactions are automatically included in the methods that do not use the envelope functions and integrate the Maxwell's equations directly. To evaluate the magnitude of these four-wave mixing terms, the results between FDFD and SEWA calculations have been compared.

In calculations, center wavelength (λ_{0j}), full width at half maximum pulse width ($T_{\mathrm{p}j}$), and peak power (P_j) of input pulse 1 (2) were set to be 1087 (797) nm, 75 (79) fs, and 480 (225) kW respectively. Initial pulse shapes were assumed to be hyperbolic secant functions. For the FDFD calculations, the initial electric field was given as follows,

$$E(0,t) = E_1 \mathrm{sech}(t/T_{01}) \cos(-\omega_{01} t + \phi_{01}) + E_2 \mathrm{sech}((t-t_d)/T_{02}) \cos(-\omega_{02}(t-t_{\mathrm{d}}) + \phi_{02}),$$

where $E_j = \sqrt{2P_j/(\varepsilon_0 cn(\omega_{0j})A_{\mathrm{eff}})}$ was the amplitude of the pulse j. T_{0j} was related to $T_{\mathrm{p}j}$ by $T_{0j} = T_{\mathrm{p}j}/1.763$, and t_{d} was the delay time between these two pulses. The initial phase of each pulse ϕ_{0j} was set to be zero. For the SEWA calculations, initial envelope functions were set to be $A_1(0, T_1) =$

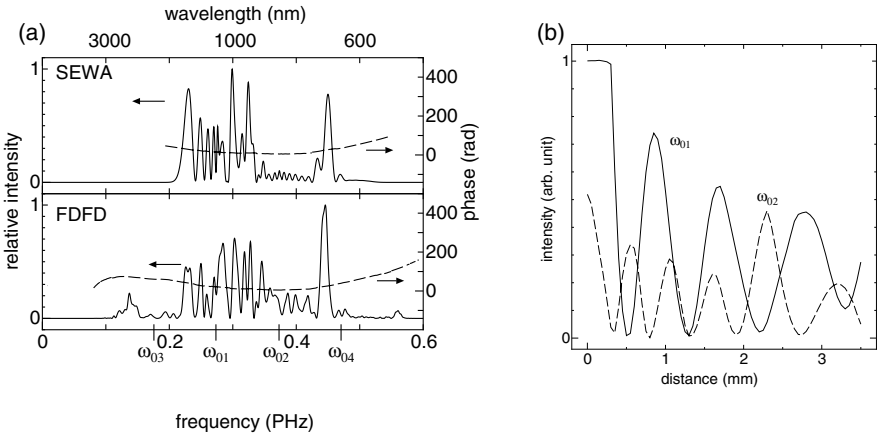

Fig. 1.9. (**a**) Comparison of spectral intensities and phases between the SEWA method and the FDFD method after pulses were propagated 3.5 mm in a fused-silica fiber. The center angular frequencies of the input pulses (ω_{01} and ω_{02}) and the four-wave mixing pulses (ω_{03} and ω_{04}) are indicated. (**b**) Plots of intensities at ω_{01} and ω_{02} as a function of propagation distance calculated by the FDFD method

$\sqrt{P_1}\mathrm{sech}(T_1/T_{01})$ and $A_2(0,T_2) = \sqrt{P_2}\mathrm{sech}((T_2 - t_\mathrm{d})/T_{02})$. The fiber used in these calculations was made of fused-silica and its core radius and length were 1.89 μm and 3.5 mm. (A_eff was set to be π (1.89 μm)^2). The dispersion of this fiber was calculated by the Sellmeier equation for fused-silica (1.51). The linear susceptibility was given by $1 + \widetilde{\chi}^{(1)}(\omega) = n^2(\omega)$. Also $\chi^{(3)}$ was given by $4\varepsilon_0 c n^2 n_2^\mathrm{I}/3$ with $n = 1.45$ and $n_2^\mathrm{I} = 2.48 \times 10^{-20}$ m^2/W [23]. The increment of distance and time were set to be 0.1 μm and 0.2 fs respectively for the FDFD method, and these were set to be 1.0 μm and 0.5 fs for the SEWA method.

The results of calculations are shown in Fig. 1.9(a), where the delay time τ_d was set to be 0. As shown in the figure, the spectral components below ω_{01} and above ω_{02} are observed when the FDFD method was used and not observed when the SEWA method was used. These components are considered to be generated by the four-wave mixing. The frequency of the low frequency component corresponds to $\omega_{03} = 2\omega_{01} - \omega_{02}$ and that of the high frequency component corresponds to $\omega_{04} = 2\omega_{02} - \omega_{01}$. The phase-mismatches Δk_3 and Δk_4 that correspond to waves for ω_{03} and ω_{04}, are given by $\Delta k_3 = \beta_{02} + \beta_{03} - 2\beta_{01} + \Delta k_\mathrm{NL}$ and $\Delta k_4 = \beta_{01} + \beta_{04} - 2\beta_{02} + \Delta k_\mathrm{NL}$, where $\Delta k_\mathrm{NL} = \eta_1 P_1 + \eta_2 P_2$ is the phase-mismatch due to the nonlinear polarization and η_j is defined in (1.32). The coherence lengths are calculated to be $L_{\mathrm{coh},3} = 2\pi/\Delta k_3 = 0.427$ mm and $L_{\mathrm{coh},4} = 2\pi/\Delta k_4 = 0.246$ mm. Since these lengths are much shorter than the fiber length of 3.5 mm, the phase-matching conditions are not satisfied for both waves. To analyze the reason of the generation of these four-wave mixing waves under the non-phase-matched

conditions, the spectral intensities at ω_{01} and ω_{02} are calculated as the function of a propagation distance and are shown in Fig. 1.9(b). From this figure, it is observed that the spectral intensity at ω_{01} oscillates with a period of about 0.5 mm, which is about the same length as the coherence length for four-wave mixing. Because of this oscillation, cancellation of the waves due to the phase-mismatch is incomplete and relatively intense waves due to the four-wave mixing are generated. Similar oscillation is observed for the intensity at ω_{02}. Thus it is found that the strong modulation of spectral intensity due to SPM is responsible for the generation of these non-phase-matched four-wave mixing optical waves. The length scale of this oscillation due to SPM is given by $L_{\mathrm{SPM},j} = \pi/(\eta_j \alpha P_{0,j}) = \pi L_{\mathrm{NL},j}$, where $L_{\mathrm{NL},j} = 1/(\eta_j \alpha P_{0,j})$ is the nonlinear length. The generation of four-wave mixing waves can occur if these lengths are about the same order as the coherence lengths for the four-wave mixing. In the simulations shown above, $L_{\mathrm{SPM},1} = 0.732$ mm and $L_{\mathrm{SPM},2} = 1.15$ mm and these conditions are indeed satisfied.

1.3.3 Finite-Difference Time-Domain Analysis

In this subsection, comparison between calculation using the FDTD method and experiment for nonlinear propagation of a 12 fs pulse in a fused-silica fiber is shown [19]. To accurately describe the linear dispersion relation of the fused-silica fiber, the conventional FDTD method is extended such that it is possible to use the Sellmeier equation (1.51) for the linear susceptibility. In the FDTD method, the propagation of a pulse in a medium is described by (1.61) and (1.62) as shown in Sect. 1.2.3. These equations are used to obtain the fields $H_y(x, t + \Delta t/2)$ and $D_z(x, t + \Delta t)$ from $E_z(x, t)$, $H_y(x, t - \Delta t/2)$ and $D_z(x, t)$. To calculate $E_z(x, t + \Delta t)$ from $D_z(x, t + \Delta t)$, Eq. (1.63) is used with the linear polarization $F(x, t + \Delta t)$ and the nonlinear polarization $G(x, t + \Delta t)$. If the Lorentz linear susceptibility (1.99) is considered as in the previous FDTD method [13, 14], we obtain the equation,

$$\partial_t^2 F + \delta \partial_t F + \omega_0^2 F = \varepsilon_0 \omega_0^2 (\varepsilon_\mathrm{s} - \varepsilon_\infty) E_z, \tag{1.100}$$

from the definition of $F(x, t)$ in (1.64). Similarly, from (1.29) and (1.60), we obtain the equation for the nonlinear polarization $G(x, t)$,

$$\partial_t^2 G + \bar{\delta} \partial_t G + \bar{\omega}_0^2 G = \varepsilon_0 \bar{\omega}_0^2 E_z^2, \tag{1.101}$$

where $\bar{\delta} = 2/\tau_2$ and $\bar{\omega}_0^2 = (1/\tau_1)^2 + (1/\tau_2)^2$. To include the accurate linear dispersion relations for the fused-silica fiber in the FDTD calculations, the linear dielectric constant $\varepsilon(\omega) = \varepsilon_\infty + \tilde{\chi}^{(1)}(\omega)$ should be given by the Sellmeier equation (1.51) as follows,

$$\varepsilon(\omega) = n^2(\omega) = 1 + \sum_{j=1}^{3} \frac{b_i \omega_i^2}{\omega_i^2 - \omega^2} = 1 + \sum_{j=1}^{3} \tilde{\chi}_j^{(1)}(\omega). \tag{1.102}$$

From this equation, we can set $\varepsilon_\infty = 1$. Also, by defining

$$F_j(x,t) = \varepsilon_0 \int_0^t \chi_j^{(1)}(t-t')E_z(x,t')\mathrm{d}t', \tag{1.103}$$

we have

$$\partial_t^2 F_j + \omega_j^2 F_j = \varepsilon_0 \omega_j^2 E_z, \tag{1.104}$$

and $F(x,t)$ in (1.64) is given by $F(x,t) = F_1(x,t) + F_2(x,t) + F_3(x,t)$. Using E_z in (1.63) in the right hand side of (1.104), we have the equation for F_1 as follows,

$$\frac{1}{\omega_1^2}\partial_t^2 F_1 + (1 + \frac{b_1}{1+(1-f_\mathrm{R})\chi^{(3)}E_z^2})F_1 + \frac{b_1 f_\mathrm{R}\chi^{(3)}E_z}{1+(1-f_\mathrm{R})\chi^{(3)}E_z^2}G = \frac{b_1(D_z - F_2 - F_3)}{1+(1-f_\mathrm{R})\chi^{(3)}E_z^2}. \tag{1.105}$$

Similar equations can be obtained for F_2 and F_3. Also, we have the following equation for G from (1.63) and (1.101),

$$\frac{1}{\bar{\omega}_0^2}\partial_t^2 G + \frac{\bar{\delta}}{\bar{\omega}_0}\partial_t G + (1 + \frac{f_\mathrm{R}\chi^{(3)}E_z^2}{1+(1-f_\mathrm{R})\chi^{(3)}E_z^2})G + \frac{E_z}{1+(1-f_\mathrm{R})\chi^{(3)}E_z^2}(F_1+F_2+F_3) = \frac{E_z}{1+(1-f_\mathrm{R})\chi^{(3)}E_z^2}D_z. \tag{1.106}$$

The finite-difference forms of the second-order coupled equations (1.105) and (1.106) are written and $F_j(x,t+\Delta t)$ and $G(x,t+\Delta t)$ are solved in terms of $F_j(x,t-\Delta t)$, $F_j(x,t)$, $G(x,t-\Delta t)$, $G(x,t)$, $E_z(x,t)$ and $D_z(x,t-\Delta t)$ [14]. Finally, $E_z(x,t+\Delta t)$ is obtained by using (1.63), where in the right hand side, all fields are at time $t+\Delta t$ except for E_z. This equation is used iteratively until the value of $E_z(z,t+\Delta t)$ converges [14].

In the FDTD calculations, the time step is set as $\Delta t = 4.4475215$ fs, and the spatial step is set as $\Delta x = 0.018315\,\mu$m. b_j and ω_j are determined by the Sellmeier equation of the fused-silica (1.51). $\chi^{(3)}$ is determined from the relation $\chi^{(3)} = (4/3)\varepsilon_0 c n^2(\omega_0) n_2^\mathrm{I}$, where ω_0 is the center angular frequency of the optical pulse. This gives $\chi^{(3)} = 1.85 \times 10^{-22}\,\mathrm{m}^2/\mathrm{V}^2$ at 800 nm. The parameters f_R, τ_1, and τ_2 are set to be $f_\mathrm{R} = 0.3$, $\tau_1 = 12.2$ fs, and $\tau_2 = 32$ fs. The total fiber length is $L = 2.5$ mm and 293000 time steps are required to measure the electric field until the pulse tail passes completely. The peak power of an input pulse is set to be 175 kW (soliton number $N = 2.09$). The effective core area A_eff is set to be $5.47\,\mu\mathrm{m}^2$. Figure 1.10(a) shows the results calculated by the FDTD method (A), the solution of the SVEA equation obtained by the split-step Fourier method (B) (up to the third-order dispersion terms with the Raman term using the Raman time constant of $T_\mathrm{R} = 5$ fs [1] which is related to the slope of the Raman gain), and experimental result

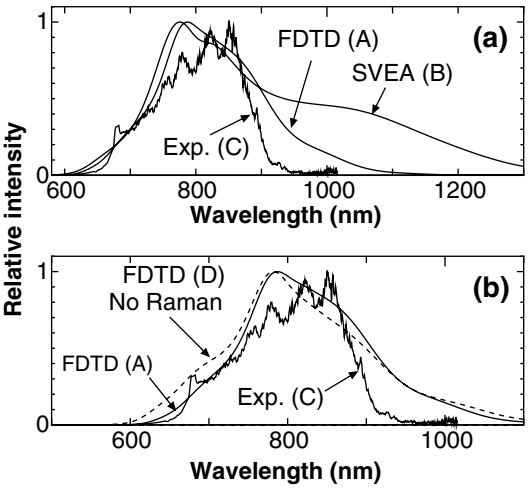

Fig. 1.10. (**a**) Spectra of a 12-fs laser transmission through a 2.5-mm silica fiber, calculated by (A) the FDTD method considering all orders of dispersions and the Raman response ($f_{\mathrm{R}} = 0.3$), (B) the solution of SVEA (considering up to the third-order dispersion terms and the Raman term using the parameter $T_{\mathrm{R}} = 5$ fs), and (C) experiment result. (**b**) Comparison between spectra calculated by (D) the FDTD method without the Raman response ($f_{\mathrm{R}} = 0$) and (A) with the Raman response. (A) and (C) are the same data as those in (**a**) [19]

(C). It is seen that with SVEA (B) the spectrum intensity at long wavelength is much higher than those for FDTD (A) and the experimental result (C). This indicates that the FDTD is superior to SVEA. The Raman gain is approximated as a linear function in SVEA. Also, only up to the third-order dispersion terms are included in SVEA (B). Furthermore, in SVEA, the second derivative of the electric field with respect to position is neglected, which corresponds to neglecting the backward propagation wave. In contrast to this, the extended FDTD method (A) accurately includes the delayed Raman response and all orders of the dispersion of silica using the Sellmeier equation. Thus the difference between (A) and (B) is considered to be due to the Raman effect, the higher order dispersion effect, or the backward propagation wave. In order to clarify this, we performed a calculation using the FDTD method without the Raman response ($f_{\mathrm{R}} = 0$) (D) in Fig. 1.10(b), where (A) and (C) show the same data as those in Fig. 1.10(a). In Fig. 1.10(b), the spectrum for case (A) is closer to the experimental result (C) than that of the case of FDTD which does not consider the Raman effect (D). It is evident that by including the Raman term (A), the spectral intensity at a shorter wavelength is smaller and the agreement between the experimental and calculated results becomes better than that in the case of (D). For example, the spectral intensity at 700 nm in (D) is 48% higher than that in (A), which is almost same as that in the experimental result (C). On the other hand, at a

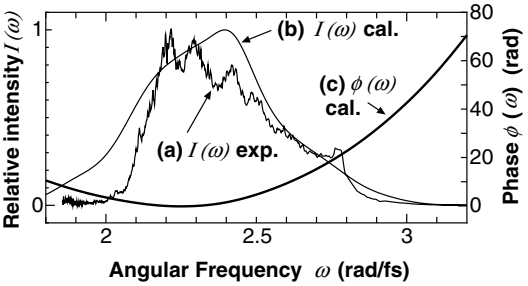

Fig. 1.11. Spectral intensity obtained experimentally (a) and numerically (b), and spectral phase obtained numerically (c) as a function of angular frequency for a 12-fs laser transmission through a 2.5-mm silica fiber [19]

longer wavelength, for example, 850 nm, the spectral intensity of (A) is 15% higher than that of (D). This feature of (A) shows a tendency analogous to (C) because there is a larger peak at 850 nm than at the center wavelength of 800 nm in (C). These tendencies of the spectral characteristics indicate that it is important to include the Raman term.

Figure 1.11 shows spectral intensities obtained experimentally (a) and numerically (b), and the spectral phase obtained numerically (c) as a function of angular frequency for 12-fs laser transmission through a 2.5-mm silica fiber. From the calculation corresponding to Fig. 1.11(c), the group-delay dispersion (GDD), the TOD, and the fourth-order dispersion (FOD) values are determined to be 136.5 fs^2, 80.65 fs^3, and -35.59 fs^4, respectively. These values are very important for single-cycle pulse generation via phase compensation of the nonlinear-chirped supercontinuum generated in a silica fiber.

1.3.4 Analysis by Fourier Direct Method

Before showing the results concerning few-cycle pulse propagation in a fused-silica fiber by the Fourier direct method (FDM: see Sect. 1.2.4), we first investigate the effects of several following assumptions or approximations used up to now: the unidirectional propagation approximation instead of the bidirectional propagation, the instantaneous response instead of the delayed Raman response, as well as the assumptions concerning the nonlinear dispersions such as the neglected self-steepening or core dispersion.

The notations in Sect. 1.2.4 are consistently used in this section. The conditions and parameter values for each figure in this section are tabulated in Table 1.2 and the sub-table accompanying the figure. Throughout the figures and tables in this section, (a), (b), (c), etc., (without parentheses in the tables) denote case numbers executed under the respective conditions, instead of (A), (B), (C), (D), etc., just indicating parts of the figure, as in for example Fig. 1.12.

Table 1.2. List of all conditions and parameter values. Fig.: figure number, Cs.: case number (Sld: solid curve/ Dsh: dashed curve/ Dot: dotted curve), Mtd.: method (FD: Fourier direct method/ SG: nonlinear Schrödinger (SPM-GVD) equation), Pro.: propagation (1: unidirectional/ 2: bi-directional), Rng.: frequency range (B: basic/ A: all), Nres.: nonlinear response (I: instantaneous/ D: delayed Raman), Ndis.: nonlinear dispersion (S: self-steepening/ F: flat core dispersion/ T: theoretical core dispersion/ E: experimental core dispersion), Ldis.: linear dispersion (N: no dispersion/ 2: second order/ 3: third order/ 4: fourth order/ 5: fifth order/ S: Sellmeier/ S_m: modified Sellmeier with absorption), Ini.: envelope of initial temporal electric field profile (G: Gaussian/ S: sech/ E: experimental, 0.0: all of B/F, C_0 and ϕ_I are zero), B/F: ratio of initial backward wave to forward wave, C_0: initial coefficient related to chirp, ϕ_I: initial phase of envelope wave relative to carrier wave, λ_0: central wavelength, P: initial peak power of pulse, N_{sol}: soliton order, t_1: initial FWHM pulse width, t_{max}: maximum time-domain size, M_{sam}: number of temporal division, L_D: dispersion length, L_N: nonlinear length, L_S: shock length, z_{max}: maximum fiber length, M_{stp}: maximum step number. The values replaced with "—" are tabulated separately hereafter

Fig.	Cs.	Mtd.	Pro.	Rng.	Nres.	Ndis.	Ldis.	Ini.:
1.12	—	FD	2	A	D	SE	S_m	G: —
1.12	—	FD	1	A	D	SE	S_m	G: —
1.14	—	FD	2	A	D	—	S_m	E: —
1.15	—	FD	2	A	—	—	S_m	S:0.0
1.16	—	FD	2	A	D	—	S_m	G:0.0
1.17–1.19	Sld	FD	2	A	D	SE	S_m	G:0.0
1.17–1.19	Dsh	SG	1	B	I	SF	2	G:0.0
1.17–1.19	Dot	SG	1	B	I	F	2	G:0.0
1.21	—	—	—	—	—	—	—	S:0.0
1.23–1.24	—	FD	2	A	D	SE	S_m	G: —

Fig.	Cs.	λ_0 (nm)	P (kW)	N_{sol}	t_1 (fs)	t_{max} (fs)	M_{sam}	L_D (mm)	L_N (mm)	L_S (mm)	z_{max} (mm)	M_{stp}
1.12	—	800	2290	4.99	5.00	500	2048	0.249	0.010	0.028	1.000	80000
1.14	—	798	175	3.30	12.00	400	2048	1.427	0.131	0.868	2.500	30000
1.15	—	830	2290	4.78	5.00	500	2048	0.238	0.010	0.029	1.000	80000
1.16	—	800	2290	4.99	5.00	500	2048	0.249	0.010	0.028	1.000	80000
1.17–1.19	Sld	800	—	—	—	500	2048	—	—	—	1.000	80000
1.17–1.19	Dsh	800	—	—	—	500	2048	—	—	—	1.000	80000
1.17–1.19	Dot	800	—	—	—	500	2048	—	—	—	1.000	80000
1.21	—	830	2290	4.78	5.00	500	2048	0.238	0.010	0.029	1.000	80000
1.23–1.24	—	800	6870	5.87	3.40	500	2048	0.115	0.003	0.006	0.006	800

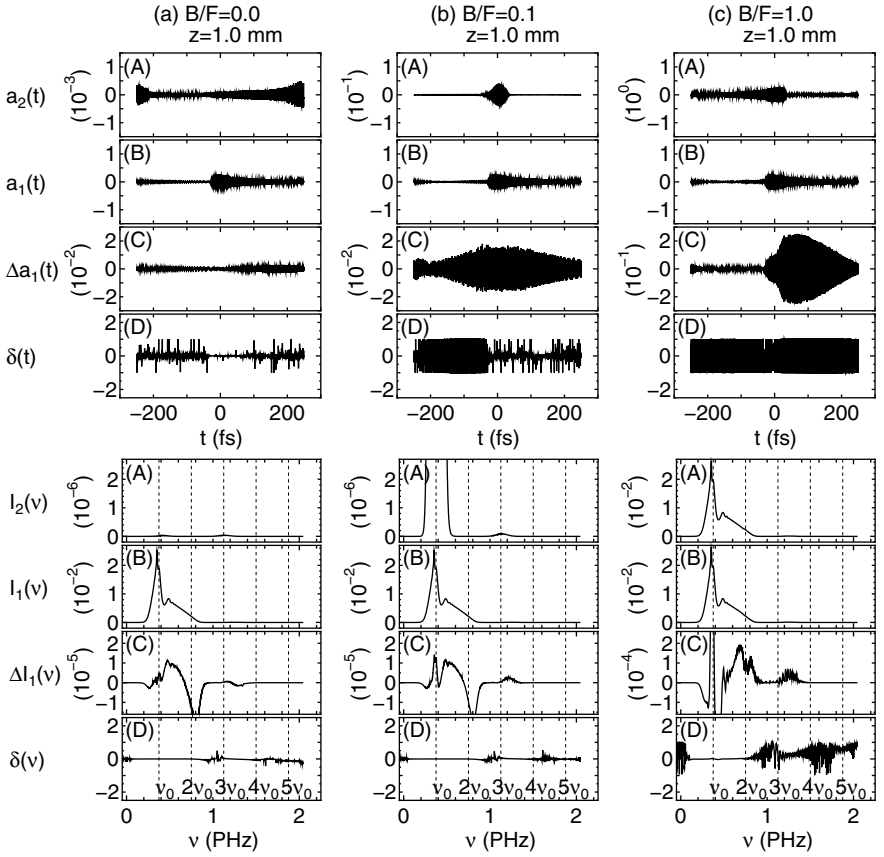

Fig. Cs.		B/F	C_0 (rad fs^2)	$\phi_{\rm I}$ (rad/π)
1.12	a	0.0	0.0	0.0
1.12	b	0.1	0.0	0.0
1.12	c	1.0	0.0	0.0

Fig. 1.12. Effect of bi-directional propagation for initial amplitude ratio $B/F = 0.0\,/\,0.1\,/\,1.0$ ((a) / (b) / (c)) at $z = 1.0\,mm$. Upper row: **(A)** temporal profile of backward wave $a_2(t)$; **(B)** temporal profile of forward wave $a_1(t)$; **(C)** $\Delta a_1(t) \equiv a_1(t) - a_1^{\rm U}(t)$ where $a_1^{\rm U}(t)$ is forward wave calculated without action of backward wave; **(D)** $\delta(t) \equiv \{a_1(t) - a_1^{\rm U}(t)\}/\{|a_1(t)| + |a_1^{\rm U}(t)|\}$. Lower row: **(A)** intensity spectrum of backward wave $I_2(\nu) \equiv |A_2(\nu)|^2$; **(B)** intensity spectrum of forward wave $I_1(\nu) \equiv |A_1(\nu)|^2$; **(C)** $\Delta I_1(\nu) \equiv |A_1(\nu)|^2 - |A_1^{\rm U}(\nu)|^2$ where $A_1^{\rm U}(\nu)$ is Fourier transform of $a_1^{\rm U}(t)$; **(D)** $\delta(\nu) \equiv \{I_1(\nu) - I_1^{\rm U}(\nu)\}/\{I_1(\nu) + I_1^{\rm U}(\nu)\}$

The central wavelength is limited around $\lambda_0 = 800\,\mathrm{nm}$, the initial FWHM pulse width is $t_1 = 2.67$–$12.00\,\mathrm{fs}$, and the initial peak power of pulse ranges widely as $P = 175$–$6870\,\mathrm{kW}$, which is below the damage threshold 6 MW [32]. We chose these values considering our current and future experimental conditions. The initial temporal electric field profile is Gaussian in most cases, and sech (hyperbolic secant) or experimental profiles are sometimes used for comparison.

Effect of Bi-Directional Propagation

The present analysis allows bi-directional propagation, that is, components of the wave propagating both in the right direction and the left direction. Then, we can consider the effect of the unidirectional propagation approximation starting with the arbitrary-changed ratio of the right-traveling forward wave and the left-traveling backward wave as the initial pulse.

In Fig. 1.12(A) and (B), we show the temporal electric field profile of the forward wave $a_1(t)$, the backward wave $a_2(t)$ and their intensity spectra $I_1(\nu) \equiv |A_1(\nu)|^2$, $I_2(\nu) \equiv |A_2(\nu)|^2$, propagated in the fiber with the initial amplitude ratio $B/F = 0.0\,/\,0.1\,/\,1.0$ of the backward wave to the forward wave. In Fig. 1.12(C) and (D), we compare $a_1(t)$, $A_1(\nu)$ with the temporal amplitude $a_1^{\mathrm{U}}(t)$ and the spectral amplitude $A_1^{\mathrm{U}}(\nu)$ of the forward wave calculated under F_{N} with $b_1(\xi,\tau)$ which was approximated by $a_1(\xi,\tau)$ in (1.79c). This means we neglect the action of the backward wave on the forward wave. The compared results are represented by the following absolute differences $\Delta a_1(t)$, $\Delta I_1(\nu)$ and the relative differences $\delta(t)$, $\delta(\nu)$:

$$\begin{cases} \Delta a_1(t) \equiv a_1(t) - a_1^{\mathrm{U}}(t), \\ \quad \delta(t) \equiv \{a_1(t) - a_1^{\mathrm{U}}(t)\}/\{|a_1(t)| + |a_1^{\mathrm{U}}(t)|\}, \\ \Delta I_1(\nu) \equiv |A_1(\nu)|^2 - |A_1^{\mathrm{U}}(\nu)|^2, \\ \quad \delta(\nu) \equiv \{|A_1(\nu)|^2 - |A_1^{\mathrm{U}}(\nu)|^2\}/\{|A_1(\nu)|^2 + |A_1^{\mathrm{U}}(\nu)|^2\}. \end{cases}$$

In the case of only the initial forward wave $B/F = 0.0$, the amplitude of $a_2(t)$ generated after propagation is less than 10^{-4} of $a_1(t)$, and $I_2(\nu)$ rises slightly around $3.0\nu_0$ (ν_0: the central frequency of the input pulse). In the region $1.3\nu_0 < \nu < 2.2\nu_0$ in $\Delta I_1(\nu)$, we find that the lower spectral component in the forward wave increases slightly and the higher component decreases slightly in the bi-directional propagation. This tendency is the same for $B/F = 0.1$ but is reversed for $B/F = 1.0$. We also find that $\delta(\nu)$ almost vanishes in $1.3\nu_0 < \nu < 2.2\nu_0$ as well as close to the main peak and around $3.4\nu_0$ where the higher harmonics are generated by the self-interaction of each wave.

In spite of their many periodic overlaps due to the periodic boundary condition in the time-domain, it is concluded that the backward wave absent initially and generated naturally is quite weak, and the forward wave and the backward wave propagate as if independent of the other. For the interaction

between these waves to be observed more effectively, the relative group velocity should be controlled to come closer. Anyhow, the unidirectional propagation approximation can be used, if desired, when the backward wave leaves far away from the forward wave fast enough, as now.

Effects of Delayed Raman Response and Nonlinear Dispersion

Figure 1.13 shows the Fourier-transform of the delayed Raman nonlinear response function $\tilde{R}(\omega)$. It is unity at the central frequency ω_0, but approaches $1 - f_R$ outside of the Stokes frequency ω_S or the anti-Stokes frequency ω_A, reducing the nonlinear effect. According to (1.92e), the gradient of its imaginary part at ω_0 is $T_R = 2.44\,\text{fs}$, which gives rise to the infinite Raman self-frequency shift in the extended NLSE (1.91).

To determine the core dispersion, we consulted the experimental input spectrum $I_{in}(\nu)$ and the experimental output spectrum $I_{out}(\nu)$, as shown by (d) and (c) in Fig. 1.14(B). They were generated by introducing an optical pulse with $(P, t_1) = (175\,\text{kW}, 12.00\,\text{fs})$ and $\lambda_0 = 798\,\text{nm}$ into a polarization-preserving single-mode fused-silica fiber (Newport, F-SP-V, the length $z = 2.5\,\text{mm}$, the core radius $a = 1.35\,\mu\text{m}$, the numerical aperture $(NA) = 0.16$) [2, 33]. Figure 1.14(A) shows the experimental and theoretical scaled effective core radius $w(\omega)/a$ as a function of the normalized frequency $V(\omega) \equiv (NA)a\omega/c$. We modified the theoretical core dispersion (dotted

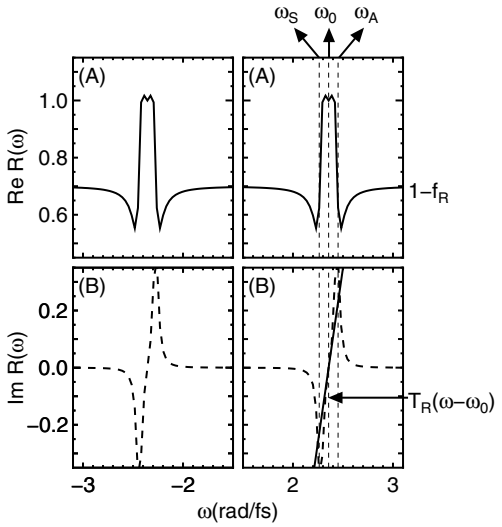

Fig. 1.13. (A) Real part and **(B)** imaginary part of Fourier-transformed nonlinear Raman response function. Region $-1.5\,\text{rad/fs} < \omega < 1.5\,\text{rad/fs}$ is omitted. Linear approximation to its imaginary part around ω_0 is also shown. $\omega_S = 2.262\,\text{rad/fs}$, $\omega_0 = 2.356\,\text{rad/fs}$, $\omega_A = 2.450\,\text{rad/fs}$ and $T_R = 2.44\,\text{fs}$, respectively

(A)

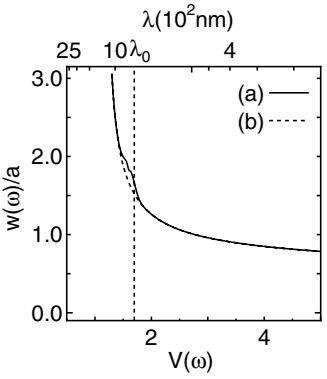

(B)

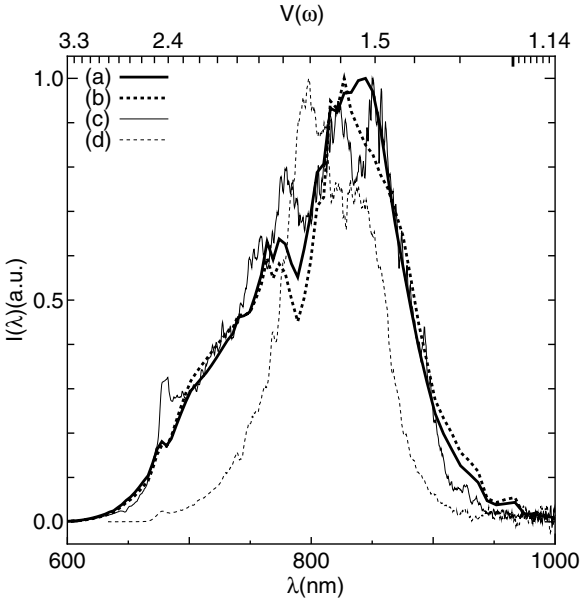

(C)

Fig.	Cs.	Ndis.	B/F	C_0 (rad fs^2)	ϕ_I (rad/π)
1.14	a(Sld)	SE	0.0	-12.0	0.0
1.14	b(Dot)	ST	0.0	-12.0	0.0

Fig. 1.14. Effect of core dispersion. **(A)** (a) Experimental / (b) theoretical effective core radius $w(\omega)/a$ as function of normalized frequency $V(\omega) \equiv (NA)a\omega/c$. **(B)** (a) / (b) Intensity spectra after propagation of $z = 2.5$ mm calculated from experimental / theoretical core dispersion ((a) / (b) of (A)) and (d) experimental input spectrum. They are compared with (c) experimental output spectrum

curve, [34]) mainly in the region $1.5 < V(\omega) < 2.0$ ($900\,\mathrm{nm} > \lambda > 680\,\mathrm{nm}$). With each core dispersion, we calculated the output spectrum $I(\nu)$ as far as $z = 2.5\,\mathrm{mm}$, starting with the initial temporal electric field profile $\tilde{E}(z = 0, \omega) \propto \sqrt{I_{\mathrm{in}}(\nu)}\exp[\mathrm{i}C_0(\nu - \nu_0)^2]$ where $C_0 = -12.0\,\mathrm{rad\,fs^2}$ is the coefficient related to the linear down-chirp. Then, we chose the one which fits best to $I_{\mathrm{out}}(\nu)$. As (a) in Fig. 1.14(B) shows, $I(\nu)$ obtained in this way fits better than (b) $I(\nu)$ obtained by the theoretical core dispersion. The experimental core dispersion used then is shown in Fig. 1.14(A) (solid curve). In the region shorter than the central wavelength of $I(\nu)$, sub-peaks grow or shrink rather sensitively to the effective core radius $w(\omega)$. In this region, $w(\omega)$ should be neither too large nor too small. When it is large and hence the nonlinearity is reduced, the spectrum is hard to change. When it is small, the spectral components pass through this region too fast toward the higher frequency and no sub-peaks remain. The further difference between $I(\nu)$ and $I_{\mathrm{out}}(\nu)$ may be attributed to the axial asymmetry of the polarization-maintaining and absorption reducing (PANDA) fiber used for this experiment. In the long wavelength-region, however, the spectrum is rather insensitive to $w(\omega)$.

The combined effect of the delayed Raman response and the core dispersion is investigated in Fig. 1.15, under the same quantitative conditions as Kalosha–Herrmann (hereafter K–H) [20], $(P, t_1) = (2290\,\mathrm{kW}, 5.00\,\mathrm{fs})$, $\lambda_0 = 830\,\mathrm{nm}$ and $z = 1.0\,\mathrm{mm}$. The spectrum $I(\nu)$ of (d) corresponds to that obtained in [20] with the instantaneous response and the flat core dispersion. The comparison between the delayed Raman response and the instantaneous response — (a) and (b) or (c) and (d) in Fig. 1.15 — shows that the effect of the delayed Raman response is small whether with the experimental core dispersion or without the core dispersion. It is limited between ω_{S} and ω_{A} of Fig. 1.13, and the imaginary part of $\tilde{R}(\omega)$ vanishes outside of this region. Under the present condition of the broad initial spectrum and the short propagation distance, only the slight deformation of the spectrum is observed instead of the self-frequency shift. On the other hand, after the core dispersion is introduced ((a),(b)), the satellite in the lower frequency disappears, the main peak sharpens, the sub-peak in the higher frequency appears and the wing stretches. They are caused by the nonlinear effects decreased in the low frequency region and increased in the high frequency region by the core dispersion. On the other hand, the spectral phase in the right of Fig. 1.15 is rather insensitive to these effects.

Figure 1.16 compares $I(\nu)$ for different nonlinear dispersions (the self-steepening and the core dispersion). The delayed Raman response is considered in all of them. In (d) with no nonlinear dispersion, there are three peaks around $0.12\,/\,0.43\,/\,0.54\,\mathrm{PHz}$ ($\mathrm{D_1}\,/\,\mathrm{D_2}\,/\,\mathrm{D_3}$), among which $\mathrm{D_2}$ and $\mathrm{D_3}$ are above ν_0. From (d) to (c), only the self-steepening increasing proportionally to the frequency is added. Then, $\mathrm{D_1}$ becomes a broad satellite around $0.19\,\mathrm{PHz}$ ($\mathrm{C_1}$), and $\mathrm{D_2}$ and $\mathrm{D_3}$ merge into one peak around $0.35\,\mathrm{PHz}$ ($\mathrm{C_2}$) with the broad wing in the high frequency region. From (c) to (b), the theoretical core dispersion is introduced, which weakens the nonlinearity in the lower fre-

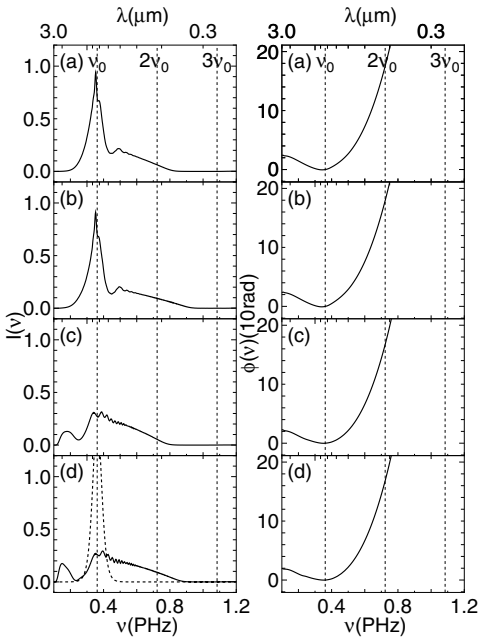

Fig.	Cs.	Nres.	Ndis.
1.15	a	D	SE
1.15	b	I	SE
1.15	c	D	SF
1.15	d	I	SF

Fig. 1.15. Combined effect of (D) delayed Raman response, (I) instantaneous response, (SE) core dispersion and (SF) no core dispersion, shown by intensity spectrum (left) and spectral phase (right) at $z = 1.0\,\mathrm{mm}$ under condition of [20]. **(a)** D-SE; **(b)** I-SE; **(c)** D-SF; and **(d)** I-SF. Initial spectrum is shown by dotted curve together with (d)

quency region and strengthens it in the higher frequency region more. Owing to this, C_1 vanishes, C_2 sharpens into the main peak (B_1) without the shift of the position, and a slight shoulder appears around 0.43 PHz (B_2). From (b) to (a), the core dispersion is replaced with the experimental one, where the core radius above ν_0 is slightly larger (below λ_0 in Fig. 1.14(A)). Then, B_2 is recognized as a sub-peak because the flow of the spectral components from ν_0 toward the higher frequency is relaxed. In the nonlinear dispersions, the self-steepening forms the basic structure of $I(\nu)$, and the core dispersion reforms it.

Analysis at Different Initial Peak Powers and Pulse Widths

In Figs. 1.17–1.19, we show the intensity spectra $I(\nu)$ (upper-left), the spectral phases $\phi(\nu)$ (lower-left), the temporal electric field profiles $E(t)$ (upper-right) as well as the pulses compressed after the complete phase compensation $E_c(t)$ (lower-right) at different propagation distances $z = 0.1$ / 0.5 / 1.0 mm, which were calculated under the initial peak power $P = 763$ / 2290 / 5725 kW and the initial pulse width $t_1 = 10.00$ / 5.00 /2.67 fs.

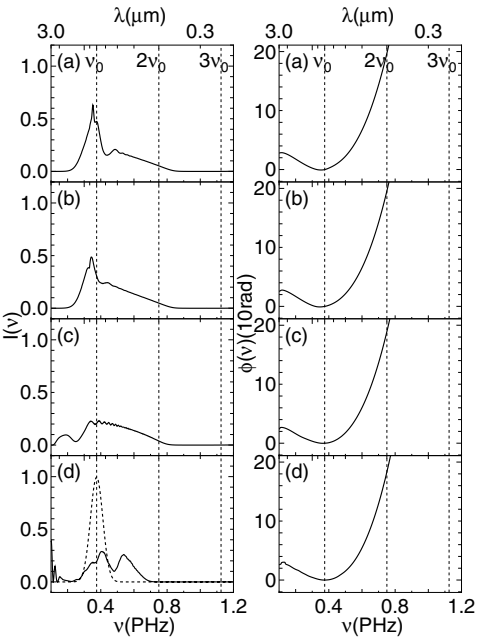

Fig.	Cs.	Ndis.
1.16	a	SE
1.16	b	ST
1.16	c	SF
1.16	d	F

Fig. 1.16. Effect of nonlinear dispersion shown by intensity spectrum (left) and spectral phase (right) at $z = 1.0\,\mathrm{mm}$. **(a)** Experimental core dispersion and self-steepening. **(b)** Theoretical core dispersion and self-steepening. **(c)** No core dispersion and only self-steepening. **(d)** Neither core dispersion nor self-steepening. Initial spectrum is shown by dotted curve in (d)

We compare here the results by the FDM (solid curve, (1.78)) with those by the NLSE with self-steepening (dashed curve, (1.91), without term of T_R) and the NLSE without self-steepening (dotted curve, (1.93)). In some cases of large P, the results by the NLSE with self-steepening are not shown due to the breakdown of calculation. As for $E(t)$, only the results by the FDM are shown for simplicity. Part of $\phi(\nu)$ is sometimes omitted in the region where $I(\nu)$ is weak.

The nonlinear length L_N, the shock length $L_\mathrm{S} = 0.39 L_\mathrm{N}\omega_0 t_1$ (the case of the Gaussian temporal profile for the envelope of $E(t)$) and the dispersion length L_D, are the measures for the nonlinear effects (SPM and self-steepening) and the linear dispersion. They are directly calculated from the initial peak power P and the initial FWHM pulse width t_1, and are tabulated in Fig. 1.20(B). For the case of $t_1 = 10.0\,\mathrm{fs}$ ($L_\mathrm{D} = 0.995\,\mathrm{mm}$), these L_N, L_S and L_D are plotted in Fig. 1.20(A) for different P, together with those for $P = 25$ / 100 / 350 / 500 kW ($L_\mathrm{N} = 0.917$ / 0.229 / 0.065 / 0.046 mm). At the propagation distance z below the lowest of them, which is L_N in all the cases shown, the results by the NLSE agree with those by the FDM. At the propagation distance of $z = 0.1\,\mathrm{mm}$, it was confirmed that $I(\nu)$ obtained by

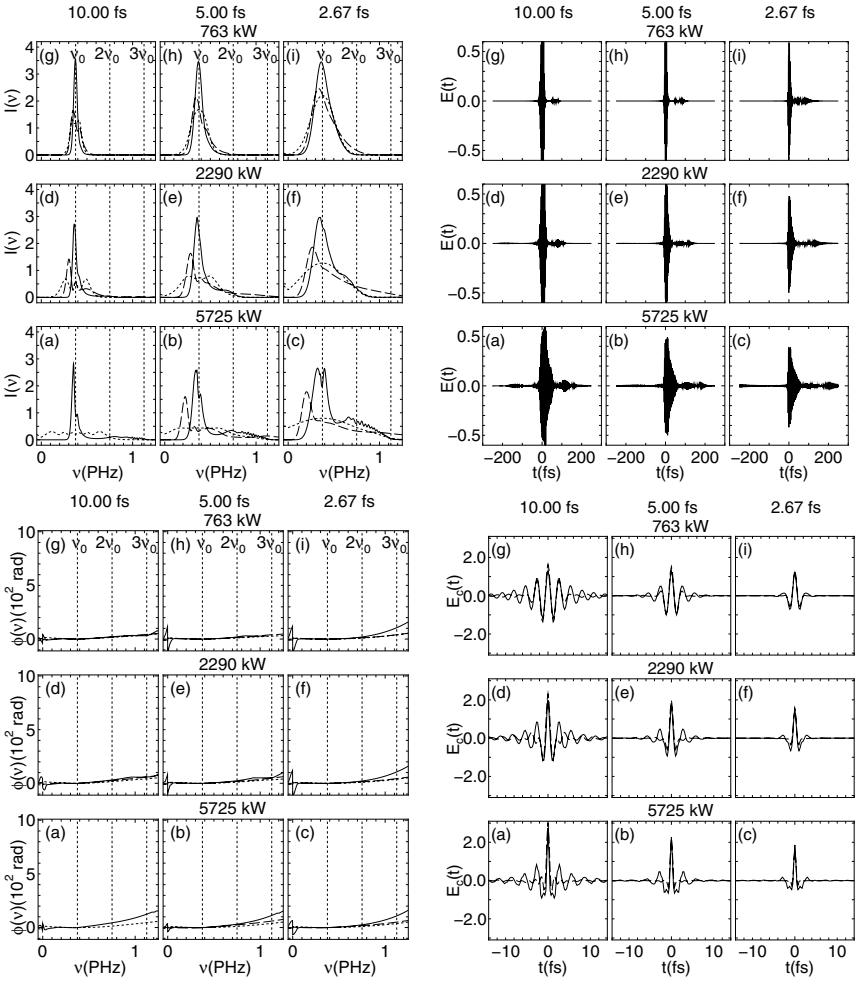

Fig. 1.17. Effect of initial peak power and pulse width at $z = 0.1\,\mathrm{mm}$. Intensity spectrum (upper-left). Spectral phase (lower-left). Temporal electric field profile (upper-right). Temporal electric field profile of compressed pulse after complete phase compensation (lower-right). Those calculated by FDM / NLSE with self-steepening / NLSE without self-steepening are shown by solid / dashed / dotted curves

the NLSE and the FDM agree well for $P = 25$ / $100\,\mathrm{kW}$ since $z < L_\mathrm{N}$, and differ slightly for $P = 350$ / $500\,\mathrm{kW}$ since $z \geq L_\mathrm{N}$.

In Figs. 1.17–1.19 or in Fig. 1.20(B) for P larger than 500 kW, $z > L_\mathrm{N}$ even at $z = 0.1\,\mathrm{mm}$ since $L_\mathrm{N} = 0.004$–$0.030\,\mathrm{mm}$, and the nonlinear effects must appear in all the cases shown there. As for the dispersion length $L_\mathrm{D} = 0.071$–$0.995\,\mathrm{mm}$ and $z = 1.0\,\mathrm{mm}$, $z \simeq L_\mathrm{D}$ only for $t_1 = 10.00\,\mathrm{fs}$

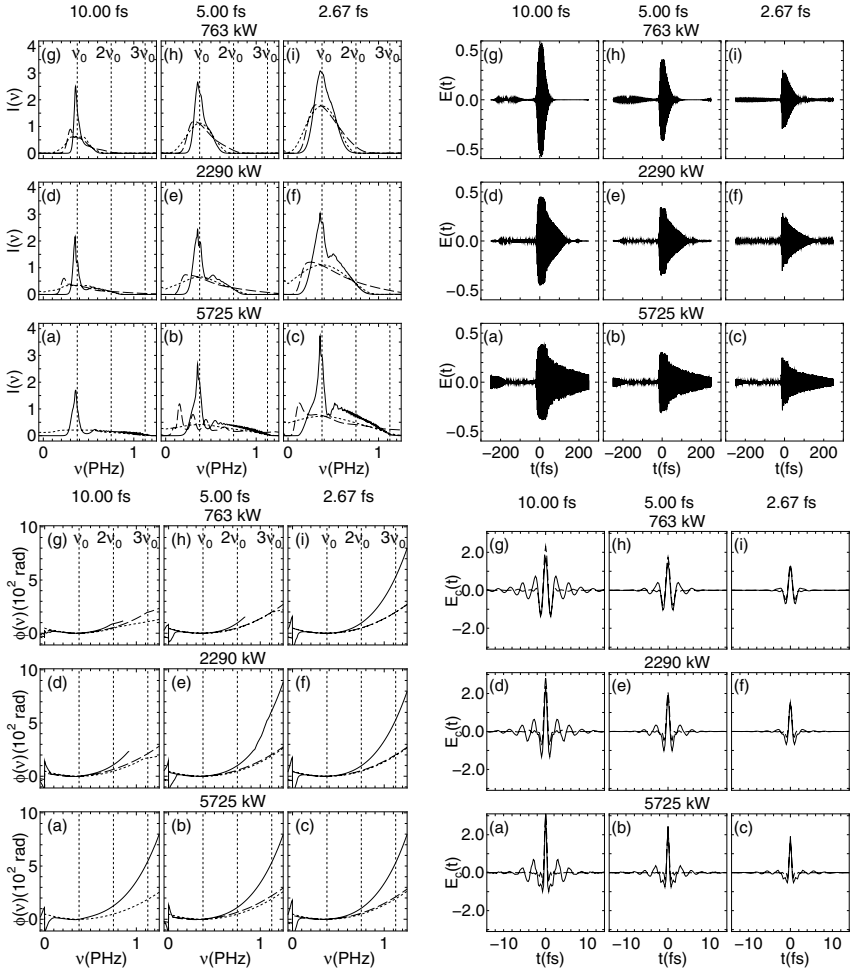

Fig. 1.18. Same as Fig. 1.17 at $z = 0.5\,\mathrm{mm}$

and any P ((a),(d),(g)), and the linear dispersion cannot be dominant. For $t_1 = 2.67\,\mathrm{fs}$ ((c),(f),(i)), on the other hand, even $z = 0.1\,\mathrm{mm}$ exceeds L_D and the linear dispersion can appear. The distance $z = 1.0\,\mathrm{mm}$ exceeds $L_\mathrm{S} = 0.006$–$0.166\,\mathrm{mm}$ in all the cases, but $z = 0.1\,\mathrm{mm}$ exceeds L_S only for (g), $(P, t_1) = (763\,\mathrm{kW}, 10.00\,\mathrm{fs})$. Thus, the SPM, the self-steepening and the linear dispersion appear as the dominant, middle and slight effects for the parameter values of P and t_1 chosen here, respectively.

In all the cases in Fig. 1.17 at the propagation distance $z = 0.1\,\mathrm{mm}$, we observe the difference of the intensity spectrum $I(\nu)$ by the FDM from that by the NLSE, as expected from $z > L_\mathrm{N}$. It is asymmetric with respect to

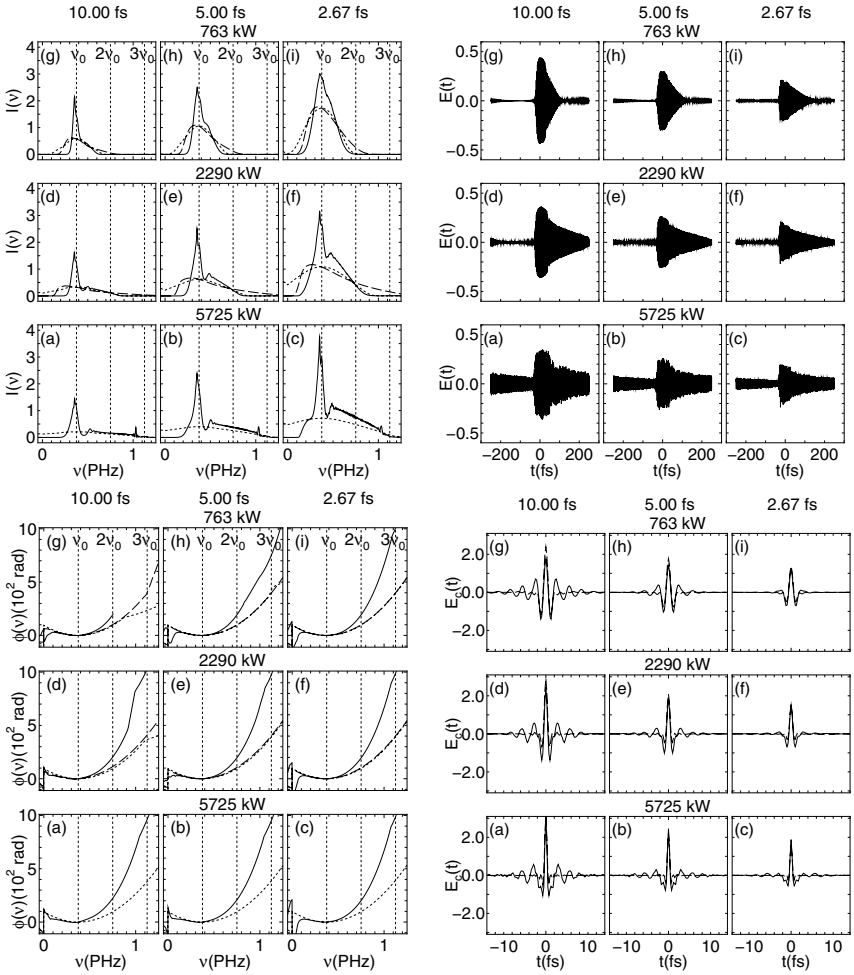

Fig. 1.19. Same as Fig. 1.17 at $z = 1.0\,\mathrm{mm}$

the central frequency ν_0, and diminishes in the lower frequency, in contrast to the NLSE results without self-steepening. It has a sharp main peak just below ν_0 and a broad wing in the high frequency region. For larger P, this structure is clearer, but the shift of the main peak and the broadening of the wing are reduced by the delayed Raman response and the core dispersion, compared with $I(\nu)$ by the NLSE with self-steepening. The main peak splits in the frequency region corresponding to the transitional region of the core dispersion (below λ_0 in Fig. 1.14(A)). When t_1 is shorter, $I(\nu)$ looks magnified similarly toward the higher frequency.

(A)

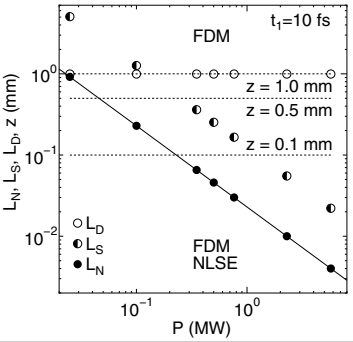

(B)

Fig.	Cs.	P (kW)	$N_{\rm sol}$	t_1 (fs)	$L_{\rm D}$ (mm)	$L_{\rm N}$ (mm)	$L_{\rm S}$ (mm)
1.17–1.19	a	5725	15.76	10.00	0.995	0.004	0.022
1.17–1.19	b	5725	7.88	5.00	0.249	0.004	0.011
1.17–1.19	c	5725	4.21	2.67	0.071	0.004	0.006
1.17–1.19	d	2290	9.97	10.00	0.995	0.010	0.055
1.17–1.19	e	2290	4.99	5.00	0.249	0.010	0.028
1.17–1.19	f	2290	2.66	2.67	0.071	0.010	0.015
1.17–1.19	g	763	5.76	10.00	0.995	0.030	0.166
1.17–1.19	h	763	2.88	5.00	0.249	0.030	0.083
1.17–1.19	i	763	1.54	2.67	0.071	0.030	0.044

Fig. 1.20. Nonlinear length $L_{\rm N}$, shock length $L_{\rm S}$, and dispersion length $L_{\rm D}$ (full / half-full / empty circle) as functions of initial peak power P for $t_1 = 10.0\,$fs. Above $L_{\rm N}$, only FDM is applicable instead of NLSE

The spectral phase $\phi(\nu)$ apart from ν_0 rises. Among the numerical methods used in this monograph, $\phi(\nu)$ by the FDM is the steepest in the high frequency region.

As for the temporal electric field profile $E(t)$, we find a main pulse with the front steeper than the rear and following wave packets with a small amplitude. In $I(\nu)$, we observe a sharp peak around ν_0 and a broad wing in the higher frequency region. Due to this spectral structure and the central wavelength in the normal dispersion, nearly-coherent long-waves come around the steep front, and the rear and the following wave packets are composed of random short-waves.

As we proceed farther to $z = 0.5\,$mm and $1.0\,$mm (Figs. 1.18 and 1.19), the main peak of $I(\nu)$ broadens, and a hollow and a sub-peak develop between the main peak and the wing due to the core dispersion. In addition, the split main peak merges. These changes with propagation by the FDM are the slowest compared with $I(\nu)$ by the other methods because of the nonlinearity reduced by the delayed Raman response and the core dispersion. We attributed the small sharp peak around $2.6\nu_0$ in (a),(b),(c) of Fig. 1.19 to the numerical origin because it diminished when we extended the maximum time-domain size $t_{\rm max}$. In the frequency region higher than this, we found also a third

harmonics generated by the interaction of the main peak and the sub-peak. However, in the real single-mode fiber with the delayed Raman response and the core dispersion, its amplitude was much smaller than that of the third harmonic wave predicted by Kalosha–Herrmann [20]. In the high frequency region apart from ν_0, the spectral phase $\phi(\nu)$ rises with propagation, and that obtained by the FDM is the highest in all the cases.

The temporal electric field profile $E(t)$ spreads wide even before z reaches L_D because the spectrum broadened by the nonlinearity induces the dispersion combined with the fiber dispersion.

Pulse Compression by Complete Phase Compensation

Optical pulses are compressed below the initial width by the complete phase compensation in addition to the spectral broadening by the SPM. When the electric field profile at the exit of a fiber is expressed as

$$\tilde{E}(z_\mathrm{max}, \omega) = |\tilde{E}(z_\mathrm{max}, \omega)| \exp\left\{\mathrm{i}\phi(z_\mathrm{max}, \omega)\right\},$$

the field after the compressor is

$$\tilde{E}_\mathrm{c}(\omega) = |\tilde{E}(z_\mathrm{max}, \omega)| \exp\left\{\mathrm{i}\phi(z_\mathrm{max}, \omega) + \mathrm{i}\phi_\mathrm{c}(\omega)\right\},$$

with the phase compensated as $\phi(z_\mathrm{max}, \omega) + \phi_\mathrm{c}(\omega) = 0$. The temporal profile of the compressed pulse $E_\mathrm{c}(t)$ is the inverse Fourier-transform of $\tilde{E}_\mathrm{c}(\omega)$ and the temporal intensity is $I_\mathrm{c}(t)$ which is proportional to $|E_\mathrm{c}(t)|^2$.

In Fig. 1.21(A), we compare the temporal electric field profiles obtained by the FDM with those by Kalosha–Herrmann (K–H) [20] and the NLSE at $z_\mathrm{max} = 0.1$ / 0.5 / 1.0 mm, under the common condition of $P = 2290$ kW and $t_1 = 5.00$ fs. Figure 1.21(C) shows their FWHM t_c measured from $I_\mathrm{c}(t)$ as a function of the propagation distance.

In addition to the FWHM t_c of $I_\mathrm{c}(t)$, we observe the breadth $t_\mathrm{c}^{(\mathrm{e})}$ of the pulse concerned with the envelope wave. In contrast to $t_\mathrm{c}^{(\mathrm{e})}$ which is short when $I(\nu)$ broadens, t_c is short when the mean frequency of $I(\nu)$ shifts toward the higher frequency.

As far as $t_\mathrm{c}^{(\mathrm{e})}$ is concerned, the pulse by the NLSE is shorter than that by the FDM, because $I(\nu)$ by the NLSE broadens wider than that by the FDM, as shown in Figs. 1.17–1.19. However, t_c by the NLSE is longer, and t_c by K–H is shorter than $t_\mathrm{c} = 0.476$ fs by the FDM which is almost independent of z_max. In the NLSE without self-steepening, $I(\nu)$ broadens symmetrically toward the lower frequency across $\nu = 0$ as well as the higher frequency. Then, the central frequency of its $I(\nu)$ lowers, and t_c is longer than those obtained by the other numerical methods. Contrarily, in K–H's results with the nonlinearity reduced by neither the delayed Raman response nor the core dispersion, the central frequency of $I(\nu)$ is kept higher, and t_c is shorter than that by the FDM.

(A)

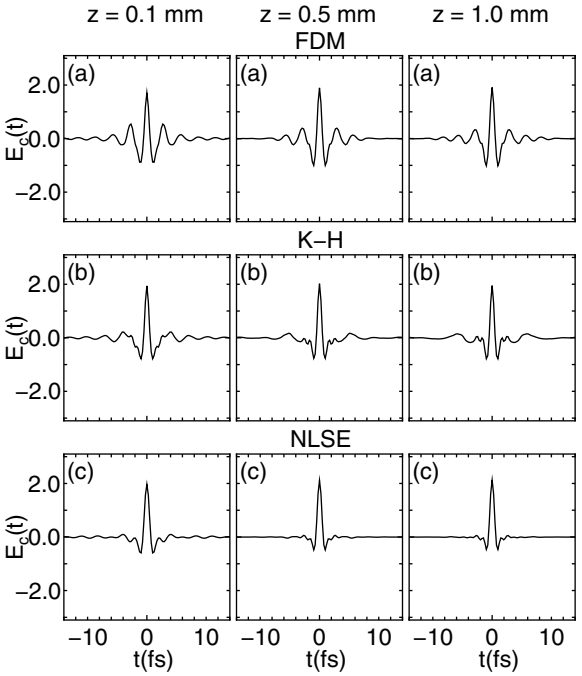

(B)

Fig.	Cs.	Mtd.	Pro.	Rng.	Nres.	Ndis.	Ldis.
1.21	a	FD	2	A	D	SE	S_m
1.21	b	FD	2	A	I	SF	S_m
1.21	c	SG	1	B	I	F	2

(C)

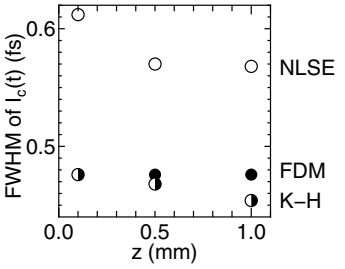

Fig. 1.21. Compressed pulses calculated by different methods for $P = 2290\,\mathrm{kW}$ and $t_1 = 5.00\,\mathrm{fs}$. **(A)** Temporal intensity $I_c(t)$ by FDM / K–H / NLSE ((a) / (b) / (c)) at $z_{max} = 0.100$ / 0.500 / $1.0\,\mathrm{mm}$ (left / center / right). **(C)** Distance dependence of FWHM t_c according to (A) by FDM / K–H / NLSE (full / half-full / empty circle)

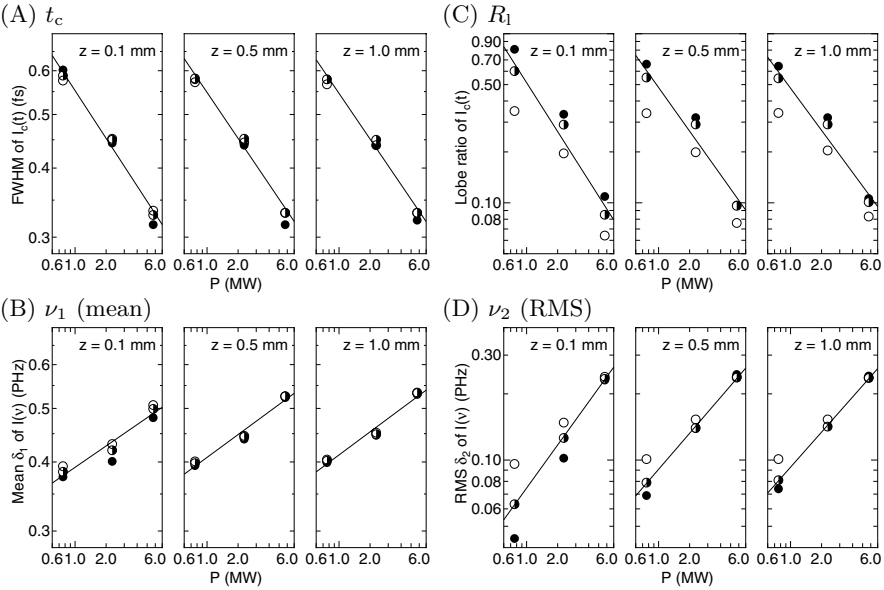

(E)

z (mm)	α_w	β_w	α_1	β_1	α_r	β_r	α_2	β_2
0.100	-0.594	-0.287	-0.938	0.128	-0.667	-0.960	-2.60	0.650
0.500	-0.601	-0.276	-0.897	0.137	-0.733	-0.858	-2.40	0.544
1.000	-0.605	-0.274	-0.887	0.139	-0.743	-0.828	-2.38	0.530

Fig. 1.22. Dependence on initial peak power P (MW) of parameters in compressed pulses and intensity spectra according to Figs. 1.17-1.19. **(A)** FWHM t_c (fs) of temporal intensity of compressed pulse $I_c(t)$. **(B)** Mean ν_1 (PHz) of $I(\nu)$. **(C)** Height of first lobe R_l relative to main peak in $I_c(t)$. **(D)** RMS ν_2 (PHz) of $I(\nu)$. Those for initial pulse width t_1 = 10.00 / 5.00 / 2.67 fs are shown by full / half-full / empty circles. They are fitted against P as $t_c = e^{\alpha_w} P^{\beta_w}$, $\nu_1 = e^{\alpha_1} P^{\beta_1}$, $R_l = e^{\alpha_r} P^{\beta_r}$ and $\nu_2 = e^{\alpha_2} P^{\beta_2}$ for t_1 = 5.00 fs and z_{max} = 0.100 / 0.500 / 1.0 mm. Fit parameters are tabulated in **(E)**

In the lower-right part of Figs. 1.17–1.19, the compressed temporal electric-field profiles for different P and t_1 are shown. Their t_c measured from $I_c(t)$ for P = 763 / 2290 / 5725 kW, t_1 = 10.00 / 5.00 / 2.67 fs and z_{max} = 0.1 / 0.5 / 1.0 mm are shown in Fig. 1.22(A). The dependence of t_c on P is remarkably large compared with t_1 and z_{max}. Its decrease with P is fitted well as $t_c = e^{\alpha_w} P^{\beta_w}$ with $\beta_w \simeq -2.8$. The mean frequency

$$\nu_1 \equiv \int_0^\infty d\nu I(\nu)\nu \Big/ \int_0^\infty d\nu I(\nu)$$

of $I(\nu)$ in Fig. 1.22(B), changing as $\nu_1 = e^{\alpha_1} P^{\beta_1}$ with $\beta_1 \simeq 0.13$, is related with t_c. The height of the first lobe R_l relative to the main peak in $I_c(t)$ is shown in Fig. 1.22(C). It also depends on P most remarkably, on t_1 but more than t_c, and hardly on z_{max}. The root mean square

$$\nu_2 \equiv \sqrt{\int_0^\infty \mathrm{d}\nu I(\nu)(\nu-\nu_1)^2 \Big/ \int_0^\infty \mathrm{d}\nu I(\nu)}$$

as the measure for the breadth of $I(\nu)$ is shown in Fig. 1.22(D).

Short t_1 diminishes R_l and refine the quality of the optical pulse. But it contributes little to the compression of the pulse. Both t_c and R_l are almost independent of z_max after 0.1 mm much longer than L_N. As we observe in Figs. 1.17–1.19, $\phi(\nu)$ to be compensated increases with z_max. Then, a short z_max is preferable if we consider the limited range of the phase to be compensated by the compressor. A large P refines the profile and the pulse quality of the compressed pulse most effectively. The pulse is compressed to as short as 0.3 fs at $P = 6\,\mathrm{MW}$.

Carrier-Envelope Phase

It is expected that the carrier-envelope phase (CEP), the initial phase of the carrier wave relative to the envelope of the electric field, influences the propagation behavior of few-optical-cycle pulses. We compare here the propagation of pulses with different initial conditions as

$$E^j(z=0,t) = \mathrm{Re}\, E_+(z=0,t)\mathrm{e}^{-\mathrm{i}(\omega_0 t+\phi_\mathrm{I}^j)}$$

composed of only the right-traveling wave $a_1(\xi,\tau)$ in (1.85), where the CEP ϕ_I^j is $0\,/\,\pi/2\,/\,\pi$ for the cases $j =$(a) / (b) / (c). Instead of the direct difference after propagation of a distance z, we use the function

$$D^j(z,\omega) \equiv \mathrm{e}^{\mathrm{i}\phi_\mathrm{F}^j}\tilde{E}^j(z,\omega) - \mathrm{e}^{\mathrm{i}\phi_\mathrm{F}^{(\mathrm{a})}}\tilde{E}^{(\mathrm{a})}(z,\omega),$$

which extracts the essential differences caused by the CEP from the results apparently different owing to the initial conditions. In this equation, $\tilde{E}^j(z,\omega) = \mathsf{F}E^j(z,t)$ from (1.67) and the value of the restoration phase ϕ_F^j is ϕ_I^j $(\omega > 0)$ or $-\phi_\mathrm{I}^j$ $(\omega < 0)$. We observe the difference between the two cases $j = (a)$ and $j \neq (a)$ by the temporal profile $\Delta E(t) = \mathsf{F}^{-1}D^j(z,\omega)$ and the spectrum $\Delta I(\nu) = |D^j(z,\omega)|^2$.

In (B), (C) and (D) of Fig. 1.23, we compare $E(t)$, $\phi(\nu)$ and $I(\nu)$ of pulses with different ϕ_I^j, where initial $E(t)$ are shown in (A). $\Delta E(t)$ and $\Delta I(\nu)$ are shown in (B') and (D'), respectively. The condition $(P, t_1) = (6870\,\mathrm{kW},\ 3.40\,\mathrm{fs})$ and the propagation distance $z = 10.0\lambda$ are common where $\lambda = \lambda_0/n_\mathrm{L}^\mathrm{R}(\omega_0)$ is the wavelength in the fiber. The pulse duration was chosen on the basis of the recent result of pulses generated experimentally by us (see Sect. 5.2.3) [37]. We observe the generation of the third harmonics by the wave packet in the rear of $E(t)$ and also by $\phi(\nu)$ flattened around ν_0 and its harmonics though slight in $I(\nu)$. However, the differences by the CEP are hard to observe. By contrast, $\Delta E(t)$ and $\Delta I(\nu)$ clearly show the differences between (a) and (b) or (a) and (c). We find no differences between (a) and (c)

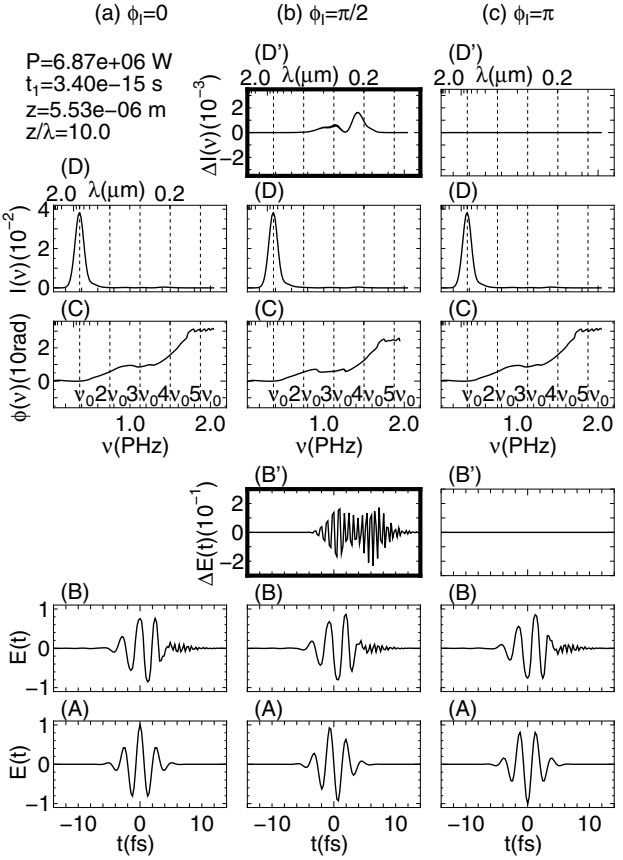

Fig.	Cs.	B/F	C_0 (rad fs^2)	ϕ_I (rad/π)
1.23–1.24	a	0.0	0.0	0.0
1.23–1.24	b	0.0	0.0	0.5
1.23–1.24	c	0.0	0.0	1.0

Fig. 1.23. Effect of carrier-envelope phase (CEP) at $P = 6870\,\mathrm{kW}$ and $z = 10\lambda$ for **(a)** $\phi_\mathrm{I} = 0$, **(b)** $\phi_\mathrm{I} = \pi/2$ and **(c)** $\phi_\mathrm{I} = \pi$. **(A)** Initial temporal electric field profile. **(B)** Temporal electric field profile after propagation. **(C)** Spectral phase. **(D)** Intensity spectrum at $z = 10\lambda$. Temporal electric field profile differences $\Delta E(t)$ and spectral differences $\Delta I(\nu)$ are shown in **(B')** and **(D')**, respectively

because they are just the sign inversion of the other concerning the electric field in the envelope. Then, we concentrate on the differences between (a) and (b).

Figure 1.24 shows the evolution of $\Delta E(t)$ and $\Delta I(\nu)$ between $\phi_\mathrm{I} = 0$ and $\phi_\mathrm{I} = \pi/2$ ((a) and (b)) as functions of the propagation distance from $z/\lambda = 0.0$ to 10.0. This result was confirmed to be independent of the an-

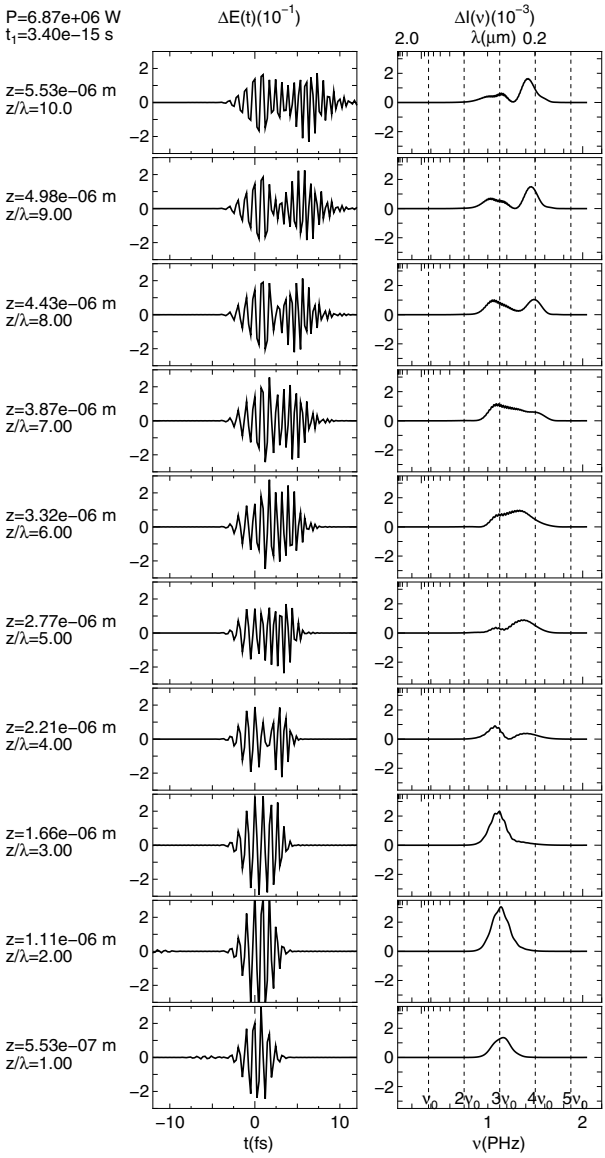

Fig. 1.24. Effect of CEP difference between $\phi_{\mathrm{I}} = 0$ and $\phi_{\mathrm{I}} = \pi/2$ for the respective propagation distances z: Temporal electric field profile differences $\Delta E(t)$ (left). Spectral intensity differences $\Delta(\nu)$ (right)

alytic conditions such as the change from $(t_{\max}, M_{\mathrm{sam}}) = (500\,\mathrm{fs}, 2048)$ to $(t_{\max}, M_{\mathrm{sam}}) = (1000\,\mathrm{fs}, 4096)$. Before $z/\lambda = 3.0$, a single wave packet in $\Delta E(t)$ and a peak around $3.0\nu_0$ in $\Delta I(\nu)$ grow gradually with the propa-

gation. We can attribute them to the third harmonics, because they do not appear when ϕ_{F}^{j} is modified as $3\phi_{\mathrm{I}}^{j}$ $(2\omega_0 < \omega < 4\omega_0)$ or $-3\phi_{\mathrm{I}}^{j}$ $(-4\omega_0 < \omega < -2\omega_0)$ to remove the differences in the region of the third harmonics furthermore. After $z/\lambda = 3.0$, $\Delta E(t)$ tends to split into two wave packets, the faster of which has the longer period than the slower. In $\Delta I(\nu)$, the components higher than the third harmonics appear, and the two peaks around $3.0\nu_0$ and $3.8\nu_0$ change their height alternately distance by distance. Above $z/\lambda = 10.0$, $\Delta E(t)$ disperses, and the peak around $3.0\nu_0$ splits into many low peaks though the one at $3.8\nu_0$ remains un-spread as far as $z/\lambda = 1000.0$. These results clearly show that the CEP can be used as the marker to monitor the evolution of the nonlinear process.

Though the present analysis considers the broad spectrum as well as the delayed-Raman response and the core dispersion, we try to consider newly observed results of Fig. 1.24 here simply on the basis of the coherence length $l_{\mathrm{c}} = \pi/\{\beta(3\omega_0) - 3\beta(\omega_0)\}$, derived for the third-order nonlinear interaction of coherent waves. By use of the modified Sellmeier equation, $l_{\mathrm{c}}/\lambda = n(\omega_0)/6\,\{n(3\omega_0) - n(\omega_0)\}$ is evaluated as 4.3711. Though the wave, due to the nonlinear process under consideration, is clearly defined at the propagation distance below l_{c}, it diminishes above l_{c} by the phase mixing. Figure 1.24 shows the generation of the third harmonics from the initial wave around ν_0 below $z/\lambda = 3.0$. Above this distance, the wave around $3.8\nu_0$ considered to be generated from the initial wave and the third harmonics begins to grow. Thus, the coherence length can be a measure of the distance for the generation of the higher harmonics also in the present accurate analysis, though its estimation is rough due to the presence of the spectral components distributed continuously around ν_0 in the initial $I(\nu)$.

To verify the above-found CEP effect, the following experimental setup will be proposed. The beam from the few-cycle optical source [37] is split into two, and the CEP and the temporal delay is given to one of them. They are propagated in the extremely short fiber with the time difference to avoid the interaction between them in the fiber. After the propagation, the CEP and the temporal delay of that beam are restored, and interference by these beams is observed. The broad spectral range up to the higher harmonics requires some attention to avoid dispersion of the air and resonance of the fiber material, and to calibrate the frequency-dependent characteristics of the optical detectors. The fiber with a length as short as some times of the wavelength is also necessary. This new simple technique to observe and control the CEP will be valuable for upgrading the few-optical-cycle wave-packet source used for experiments.

1.4 Conclusion

To simulate the nonlinear propagation of a few-to-mono optical-cycle and/or ultrabroadband pulse, several novel numerical methods were developed. Con-

ventionally, the electric field of an optical pulse was described by an envelope function and an equation for the envelope function was derived using various approximations. In the SVEA method, the variation of the envelope function in both the temporal scale of an optical period and the spatial scale of a wavelength of a carrier wave was assumed to be negligible. From this assumption, the second derivatives of the envelope function with respect to time and position were neglected. Also, the spectral bandwidth of the pulse was assumed to be much smaller than the carrier frequency. These assumptions break down for the few-to-mono optical-cycle and/or ultrabroadband optical pulse. A novel equation for the envelope function was derived to simulate the propagation of the few-to-mono optical-cycle and/or ultrabroadband pulse based on SEWA. This equation includes the rigorous linear dispersion, the Raman effect and the dispersion of the effective core area. For the propagation of a 4.5-cycle pulse in a fused-silica fiber, the calculation using the newly-derived equation gave a spectrum that agreed well with the experimental spectrum. The effects of omitting the Raman term and the dispersion of the effective core area in the calculation were investigated and it was found that when the Raman term was omitted, the relative intensity at the shorter wavelength became larger and when the dispersion of the effective core area was omitted, the relative intensity at the longer wavelength became larger. The calculations for propagation of 2-cycle and monocycle pulses were performed and it was shown that the inclusion of up to third-order dispersion terms was enough for the 2-cycle pulse but not enough for the monocycle pulse. Also, the co-propagation of the fundamental and the idler pulses from the Ti:sapphire optical parametric amplifier (OPA) system was experimentally performed and the spectra from IPM as well as SPM as a function of delay time were measured and compared with calculated spectra. The delay time dependence of the calculated spectra agreed qualitatively with the experimental spectra. Similarly, calculations for the SPM and IPM spectral broadening in the argon-filled capillary fiber were compared with the experimental spectra using the newly-derived equation. In this case, the fundamental pulse and its second-harmonic pulse from a femtosecond Ti:sapphire amplifier system were co-propagated inside the capillary fiber, and the ultrabroadband (300–1000 nm) optical pulses were generated. The IPM + SPM spectral broadening behavior as a function of the delay time was experimentally clarified and the agreement with the calculated behavior was confirmed. This method was also used for the calculations of the spectral broadening of a-few-cycle pulses propagated in the photonic crystal fiber. Comparison between the calculated spectrum and the experimental ultrabroadband spectra (480–1020 nm) showed excellent agreement. From this comparison, the mechanism of the supercontinuum generation was clarified.

In some situations, it is desirable to use a numerical method to integrate Maxwell's equations without introducing the envelope function. The conventional method to solve Maxwell's equations directly is the FDTD method. Previously, this method was only applied to the medium which is modeled by

a collection of harmonic-oscillators with one resonance frequency (the Lorentz model). To calculate the propagation of a pulse accurately in the fused-silica material, the medium must be modeled by a collection of harmonic-oscillators with three different resonance frequencies, and these resonance frequencies are determined by the Sellmeier equation. The FDTD method was extended to handle this case. The spectral intensity after propagation for a 12-fs optical pulse, input in a 2.5-mm fused-silica fiber, was calculated and compared with the experimentally-obtained spectral intensity. The spectrum obtained in the experiment agreed very well with the spectrum calculated by the extended FDTD method.

In the FDFD method, Maxwell's equations are integrated without introducing the envelope functions as in the FDTD method. But in this method, all fields are calculated in the frequency domain, rather than time domain. The advantage of this method is that any linear dispersion relations can be incorporated in a simple manner if its functional form is known in the frequency domain. It was shown that this method indeed gave the equivalent results with the FDTD method for the nonlinear pulse propagation. Also, it was shown that significant four-wave mixing waves could be generated under non-phase-matched conditions when two pulses with different center frequencies were co-propagated in a fiber.

The split-step Fourier method for solving the NLSE originally was extended to the Fourier Direct Method (FDM). Instead of the wave propagation equation of the second differential order, the one-dimensional Maxwell's equations were re-composed into the bi-directional propagation equations for the forward and the backward wave, which are independent of each other on the linear stage. They are easily solved by the straightforward extension of the split-step Fourier method, though the nonlinear force $\boldsymbol{F}_{\mathrm{N}}$ including differentials or integrals must be integrated by more general methods than the exponential integral. In the FDM, the initial condition is easily prepared. Furthermore, it was clarified that the SVEA restricting the range of validity of the NLSE is replaced with the unidirectional propagation approximation. The delayed Raman response and the nonlinear dispersion (self-steepening, core dispersion) are naturally incorporated as well as arbitrary linear dispersions like the FDFD.

Since equations are solved as evolved in space, we obtain directly the temporal electric field profile or the intensity spectrum at each spatial step, favorable for comparing with experimental results. Calculations in the time or frequency domain are accelerated by the fast Fourier transform (FFT). The FDM shows the robustness even for long propagation distances with many evolution steps, and facilitates tracing the cause of numerical troubles.

By this FDM, we can investigate the influence caused by several assumptions or approximations used conventionally for deriving the NLSE in fused-silica-fiber propagation. Instead of bi-directional propagation, unidirectional propagation approximation can be used, if desired, when the backward wave leaves a distance from the forward wave. As already stated, it is unneces-

sary to consider the SVEA with infinitesimal $\beta(\omega) - \beta(\omega_0)$ further in this case. Among the effects on the nonlinearity, the self-steepening determines the rough structure of the spectrum with the sharp peak and the broad wing. The delayed Raman response reduces the nonlinear effects and just modifies the spectrum. The core dispersion affects the spectrum most sensitively, especially in the frequency region higher than the main peak. In some cases, the intensity spectrum or the temporal profile of the electric field spread wide. The maximum size of the frequency domain must be much broader than the basic frequency region $-2\omega_0 < \omega < 2\omega_0$ to avoid the numerical breakdown. The maximum size of the time domain with the periodic boundary condition must cover the optical pulse wholly to avoid overlap with itself. The maximum time-domain size $t_{\max}$ and the number of temporal division M_{sam} must be chosen carefully to satisfy these contradictory requirements. In addition to nonlinear dispersion, the results are sensitive to linear dispersion under the wide-spread intensity spectrum. A realistic refractive index by the modified Sellmeier equation is preferable rather than the quadratic dispersion modified by the higher order terms.

For the pulses with initial peak power of 763 / 2290 / 5725 kW and initial pulse width of 10.00 / 5.00 / 2.67 fs, the intensity spectrum by the FDM is clearly different from the NLSE. The reduction of the nonlinearity by the delayed Raman response and the core dispersion slows down the changes by the FDM during the propagation. The dispersion induced by the nonlinear spread of the spectra disperses the temporal electric field profiles even before the linear dispersion length. In spite of that, they are compressed under the initial width by the complete phase compensation. It was shown that methods other than the FDM estimate the FWHM of the compressed pulse t_{c} too short. The dependence of t_{c} on the initial peak power P is remarkable compared with the initial width t_1 and the propagation distance $z_{\max}$. Large P_1 refines the compression and the quality of the pulse most effectively, and the pulse is compressed as short as 0.3 fs at $P_1 = 6\,\text{MW}$. Both t_{c} and the quality hardly change even if the pulse is compressed after being propagated in the fiber longer than $z_{\max} = 0.100\,\text{mm}$. Then, a short $z_{\max}$ is preferable if we consider the limited range of the compressor phase.

The difference of the temporal profile and the spectrum after propagation were investigated with the different initial phases of the carrier wave relative to the envelope wave (CEP). After extracting the essential difference hidden behind the initial conditions, we confirmed that the difference is generated in the higher harmonics region of the spectra, which grows from the third harmonics to more components with the propagation. Then, the CEP is considered to be used as the marker to monitor the progress of the nonlinear process. Experimentally, this phenomena will be observed by mixing two beams with the interference after different CEPs and propagation in a fiber, and its control serves for upgrading the pulse train.

In this chapter, we have only considered the numerical methods for one-dimensional propagation of an optical pulse (or optical pulses) inside a waveg-

uide under the non-resonant condition. As the temporal width of the pulse becomes shorter, the peak power becomes larger and the spectral bandwidth becomes broader. For the high peak power pulse propagation, the nonlinearity becomes so large that the change of the spatial profile of the pulse should be considered due to self-focusing [4, 35]. Also, for the broadband pulse, the resonant interactions between the pulse and the medium can become important [36]. These suggest that the numerical methods to integrate Maxwell's equations directly will become more important in the future.

Acknowledgment

Some of the calculational results presented in this chapter were obtained in collaboration with S. Nakamura, whose input is gratefully acknowledged.

References

1. G.P. Agrawal: *Nonlinear Fiber Optics, 3rd edn.* (Academic, San Diego, CA 2001)
2. N. Karasawa, S. Nakamura, N. Nakagawa, M. Shibata, R. Morita, H. Shigekawa, M. Yamashita:
3. E.A.J. Marcatili, R.A. Schmeltzer: Bell Sys. Tech. J. **43**, 1783 (1960)
4. T. Brabec, F. Krausz: Phys. Rev. Lett. **78**, 3282 (1997)
5. K.J. Blow, D. Wood: IEEE J. Quantum Electron. **25**, 2665 (1989)
6. M. Yamashita, H. Sone, R. Morita: Jpn. J. Appl. Phys. **35**, L1194 (1996)
7. M. Yamashita, H. Sone, R. Morita, H. Shigekawa: IEEE J. Quantum Electron. **34**, 2145 (1998)
8. L. Xu, N. Karasawa, N. Nakagawa, R. Morita, H. Shigekawa, M. Yamashita: Opt. Commun. **162**, 256 (1999)
9. K.S. Yee: IEEE Trans. Antennas Propag. **14**, 302 (1966)
10. A. Hasegawa, F. Tappert: Appl. Phys. Lett. **23**, 142 (1973)
11. R.H. Hardin, F.D. Tappert: SIAM Rev. Chronicle **15**, 423 (1973)
12. R.A. Fisher, W.K. Bischel: Appl. Phys. Lett. **23**, 661 (1973)
13. P.M. Goorjian, A. Taflove: Opt. Lett. **17**, 180 (1992)
14. P.M. Goorjian, A. Taflove, R.M. Joseph, S.C. Hagness: IEEE J. Quantum Electron. **28**, 2416 (1992)
15. Y. Mizuta, M. Nagasawa, M. Ohtani, R. Morita, M. Yamashita: Rev. of Laser Eng. **30**, 435 (2002) (in Japanese)
16. N. Karasawa: IEEE J. Quantum Electron. **38**, 626 (2002)
17. I.H. Malitson: J. Opt. Soc. Am. **35**, 1205 (1965)
18. R.M. Joseph, S.C. Hagness, A. Taflove: Opt. Lett. **16**, 1412 (1991)
19. S. Nakamura, Y. Koyamada, N. Yoshida, N. Karasawa, H. Sone, M. Ohtani, Y. Mizuta, R. Morita, H. Shigekawa, M. Yamashita: IEEE Photon. Technol. Lett. **14**, 480 (2002)
20. V.P. Kalosha, J. Herrmann: Phys. Rev. A **62**, 011804(R) (2000)
21. R.H. Stolen, C. Lin: Phys. Rev. A **17**, 1448 (1978)
22. D.N. Christodoulides, R.I. Joseph: Appl. Phys. Lett. **47**, 76 (1985)

23. A.J. Taylor, G. Rodriguez, T.S. Clement: Opt. Lett. **21**, 1812 (1996)
24. D.J. Kane, R. Trebino: IEEE J. Quantum Electron. **29**, 571 (1993)
25. N. Karasawa, R. Morita, L. Xu, H. Shigekawa, M. Yamashita: J. Opt. Soc. Am. B **16**, 662 (1999)
26. N. Karasawa, R. Morita, H. Shigekawa, M. Yamashita: Opt. Lett. **25**, 183 (2000)
27. M. Nisoli, S. De Silvestri, O. Svelto: Appl. Phys. Lett. **68**, 2793 (1996)
28. H.J. Lehmeier, W. Leupacher, A. Penzkofer: Opt. Commun. **56**, 67 (1985)
29. J. Ranka, R. S. Windeler, A. J. Stentz: Opt. Lett. **25**, 25 (2000)
30. S. Coen, A. Hing, L. Chau, R. Leonhardt, J.D. Harvey, J.C. Knight, W.J. Wadsworth, P.S.J. Russell: Opt. Lett. **26**, 1356 (2001)
31. X. Fang, N. Karasawa, R. Morita, R.S. Windeler, M. Yamashita: IEEE Photon. Technol. Lett. **15**, 233 (2003)
32. A. Baltuska, Z. Wei, M.S. Pshenichnikov, D.A. Wiersma: Opt. Lett. **22**, 102 (1997)
33. S. Nakamura, L. Li, N. Karasawa, R. Morita, H. Shigekawa, M. Yamashita: Jpn. J. Appl. Phys. **41**, 1369 (2002)
34. D. Marcuse: J. Opt. Soc. Am. **68**, 103 (1978)
35. J.K. Ranka, A.L. Gaeta: Opt. Lett. **23**, 534 (1998)
36. R.W. Ziolkowski, J.M. Arnold, D.M. Gogny: Phys. Rev. A **52**, 3082 (1995)
37. K. Yamane, Z. Zhang, K. Oka, R. Morita, M. Yamashita, A. Suguro: Opt. Lett. **28**, 2258 (2003)

2 Generation of Ultrabroadband Optical Pulses

M. Yamashita, N. Karasawa, M. Adachi, and X. Fang

2.1 Introduction

Since the first study of white-light-continuum generation in the field of picosecond nonlinear optics (1970) [1], extensive research for experimental and theoretical development of mechanisms for the generation of coherent optical pulses with an ultrabroad bandwidth and their technical applications have been carried out in solids (including optical fibers), liquids and gases. Most of those works until 1989 were reviewed in an excellent book edited by R. R. Alfano [2]. It was found that such nonlinear optical phenomena are mainly based on self-phase modulation (SPM) where an intense optical pulse propagating in a medium with a refractive index interacts with the medium and imposes a phase modulation on itself through a change in reflective index by its light intensity [3]. That is, there are two important physical quantities for understanding of such ultrafast phenomena. One is a time-dependent phase $\varphi(t)$ (or the corresponding spectral phase $\phi(\omega)$) of the electric field in the ultrashort pulses and another is a temporal pulse-intensity profile $I(t)$. But, until the early 1990s those optical quantities could not be measured directly.

After that, however, the development of a high-powered femtosecond-pulse Ti:sapphire laser in the period from 1991 to 1998 [4, 5] led the development of sophisticated ultrashort-pulse measurement technology which enables us to accurately evaluate the temporal phase $\varphi(t)$ and intensity profiles $I(t)$ (or the corresponding spectral phase $\phi(\omega)$ with the intensity spectrum $I_F(\omega)$) [6–8]. Those two advanced technologies are opening a new field of "few-to-mono cycle photonics" which requires coherent optical pulses having a several-hundred THz bandwidth $\Delta\nu_T = \Delta\omega_T/2\pi$ and a well-defined spectral phase $\phi(\omega)$ over the entire bandwidth.

To produce extremely broadband pulses with a well-defined spectral phase, their pulses must have no spatial chirp in which the spectral phase and the intensity spectrum do not change along the radial direction of the pulse beam cross-section. For this reason, single-mode optical fibers are conveniently employed as nonlinear media [9] (except for combined employment of an SPM glass and nonlinear crystals for noncollinear parametetric amplification [10]). Moreover, to avoid the optical damages of fibers and to efficiently produce such well-defined ultrabroadband pulses, two new approaches of in-

duced phase modulation (IPM:1996–1999) [11–15] and structure-controlled fibers (1996–2000) [16–18] have been recently proposed and demonstrated. The former is related to mutual phase interaction between two-color co-propagated pulses with carrier phase locking [33] instead of SPM. The latter is related to a gas-contained hollow fiber providing a high damage threshold [18,19], and a photonic crystal glass fiber [16] and a tapered glass fiber [17] significantly controlling a wavelength of zero group-delay dispersion (GDD). Table 2.1 summarizes significant achievements in this field after 1990 (see [2] for works before this year).

In this chapter we are concerned with the efficient generation of well-defined ultrabroadband pulses with a near- or over-one-octave bandwidth in the near-infrared to visible, ultraviolet region, which is based on IPM in a conventional fused-silica fiber, IPM in a hollow fiber, SPM in a photonic crystal fiber (PCF) or SPM in a tapered fiber (TF).

2.2 Conventional Glass Fiber Technique Using IPM

2.2.1 Theoretical Prediction

When 13-fs, 3-MW (40 nJ) pulses with a spectral width from 720 to 890 nm (a center wavelength of 790 nm) at a 1-MHz repetition rate were injected into a 3–4-mm-length fused-silica fiber with a single mode, the output pulse spectrum was broadened from 630 to 1020 nm by the effect of dispersive SPM (1997) [20]. However, further spectral broadening is greatly difficult because the higher input-peak power to be required causes optical damage and the optimum fiber length becomes shorter due to the dispersion effect. In addition, the input optical source generating shorter pulses with a higher peak power, which is also required, is not easily obtainable. To overcome those problems, the IPM technique, which was proposed in 1996 for the generation of pulses ultrabroadened from near-infrared to near-ultraviolet [11, 12], is useful, as shown later. That is, the IPM technique has some advantages compared to the SPM technique as follows: the efficiency in phase modulation is double, and the fiber-output electric fields with different central wavelengths are constructively synthesized in the spectral region to efficiently broaden the spectral width. Those permit us to use the lower input power and the longer input-pulse duration, and hence to avoid optical damage to a glass fiber.

Let us introduce the principle of the IPM technique in a single-mode fused-silica fiber. In Fig. 2.1, a schematic of a system concept for the efficient generation of well-defined ultrabroadband pulses by the IPM technique is illustrated [12]. IPM between two femtosecond pulses with a constant carrier-phase difference is utilized. Those pulses are generated by the fundamental wave (ω_{01}: the carrier angular frequency of the I_1 pulse) and its second-harmonic (SH) wave ($\omega_{02} = 2\omega_{01}$: the carrier angular frequency of the I_2 pulse) from one common femtosecond pulse of a commercially available

Table 2.1. Progress in ultrabroadband pulse generation and its related works after 1990

Year	Accomplishment	Researcher	References
1991	The discovery of self-mode-locking in a Ti:sapphire laser	Spence, Kean, Sibbett	[4]
1993	Ultrashort pulse phase and amplitude characterization by FROG	Trebino, Kane	[6]
1995	Ultrabroadband pulse generation ranging from near-infrared, visible to ultraviolet from multi-mode gas-filled hollow fiber by TW optical pulses	Nishioka, Odajima, Ueda, Takuma	[19]
1996-2000	Proposal and demonstration of efficient ultrabroadband pulse generation from near-infrared, visible to near-ultraviolet with well-behaved phase by IPM technique	Yamashita, Sone, Morita, Xu, Karasawa	[11–15]
1996	High powered ultrabroadband pulse generation with well-behaved phase from single-mode gas-filled hollow fiber	Nisoli, Silvestri, Svelto	[18]
1997	Ultrabroadband pulse generation from single-mode fused silica fiber	Baltuska, Wei, Pshenichnikov, Wiersma	[20]
1999	Ultrabroadband pulse generation with well-behaved phase by noncollinear OPA	Shirakawa, Sakane, Takasaka, Kobayashi	[10]
2000	Efficient ultrabroadband pulse generation (over one-octave bandwidth) from photonic crystal fiber	Ranka, Windeler, Stentz	[25]
2000	Efficient ultrabroadband pulse generation (over one-octave bandwidth) from tapered fiber	Birks, Wadsworth, Russel	[17]
2001	Octave-scanning Ti:sapphire laser	Morgner, Kärtner, Fujimoto, Ippen, Scheuer et al	[31]
2003	Optical wave synthesis of two different femtosecond lasers	Schibli Kim, Kuzucu, Gopinath, Tandon, Petrich, Kolodziejski, Fujimoto, Ippen, Kärtner	[32]

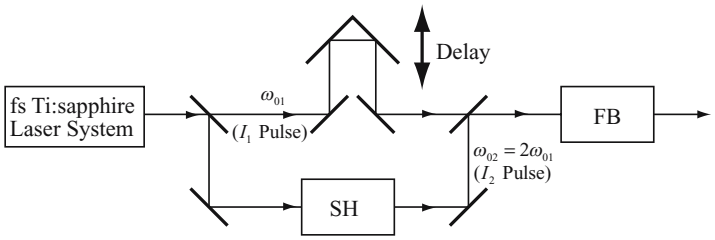

Fig. 2.1. An experimental system concept for the efficient generation of ultrabroadband pulses with a well-behaved spectral phase by the IPM technique. SH and FB denote second-harmonic generation and a single-mode fiber, respectively [12]

Ti:sapphire laser system. In this technique, the following points are essential. First, the carrier–phase difference between two waves is kept constant according to an equation $\phi_{02} - \phi_{01} = (2n + 1)\pi/2 + \phi_{01}$ where ϕ_{0i} denotes the carrier phase of the I_i pulse ($i = 1, 2$; n is an integer) [21–24]. This is because the conditions of phase matching and frequency conservation are satisfied to ensure cumulative in-phase addition of the radiation power in the second-order nonlinear processes. This enables us to synthesize constructively two spectrally broadband waves at the fiber output after dispersive IPM and SPM in a short fiber. Second, the relative values of input pulse durations between the two pulses and the propagation distance are chosen under the condition of equal input-peak powers between them so that at the fiber output the broadened frequency bandwidth of the deduced spectrum of each pulse becomes almost equal to the other and each pulse spectrum slightly overlaps and interferes with the other at each spectral edge. For this estimation of equal broadening, the ratio of the dispersion length for the I_2 pulse to that for the I_1 pulse is a useful parameter.

Let us describe the numerical analysis for nonlinear propagation of two color pulses in a single-mode fused-silica fiber. We adapted a slowly-varying-envelope approximation to the coupled-mode theory of nonlinear propagation of the I_1 and I_2 pulses with the same linear polarization [11, 12]. The normalized envelopes $u^{(i)}(\xi_1, \tau_1) = (\gamma_i (T_{0i})^2/|\ddot{k}_{0i}|)^{1/2} \times A_i(z, t - t_{i0})$ $(= (N_{\mathrm{sol}.i}/\sqrt{P_{0i}})A_i(z, t - t_{i0}))$ of the electric fields $E_i(z, t) = 2^{-1}A_i(z, t)$ $\exp[\mathrm{i}(k_{0i}z - \omega_{0i}t + \phi_{0i})]$+c.c. ($i = 1, 2$) in the group-velocity coordinate (ξ_1, τ_1) of the I_1 pulse satisfy the following set of modified nonlinear Schrödinger equations with the normalized parameter T_{oi} of the initial pulse duration $t_{p,i}$:

$$\frac{\partial u^{(1)}(\xi_1, \tau_1)}{\partial \xi_1} = -\frac{\mathrm{i}}{2} sgn(\ddot{k}_{01}) \frac{\partial^2 u^{(1)}(\xi_1, \tau_1)}{\partial \tau_1^2} + \beta_{01} \frac{\partial^3 u^{(1)}(\xi_1, \tau_1)}{\partial \tau_1^3} + \mathrm{i}[|u^{(1)}(\xi_1, \tau_1)|^2 + 2g_{12}|u^{(2)}(\xi_1, \tau_1)|^2] u^{(1)}(\xi_1, \tau_1), \quad (2.1)$$

$$\frac{\partial u^{(2)}(\xi_1,\tau_1)}{\partial \xi_1} = -\frac{\mathrm{i}}{2} sgn(\ddot{k}_{02}) S_{12} \frac{\partial^2 u^{(2)}(\xi_1,\tau_1)}{\partial \tau_1^2} + S_{22} \frac{\partial^3 u^{(2)}(\xi_1,\tau_1)}{\partial \tau_1^3} + S_{32} \frac{\partial u^{(2)}(\xi_1,\tau_1)}{\partial \tau_1} + \mathrm{i} S_{42} [|u^{(2)}(\xi_1,\tau_1)|^2 + 2 g_{21} |u^{(1)}(\xi_1,\tau_1)|^2] u^{(2)}(\xi_1,\tau_1). \quad (2.2)$$

Here the normalized variables are $\xi_i = (|\ddot{k}_{0i}|z)/(T_{0i})^2$ and $\tau_i = (t - t_{i0} - \dot{k}_{0i} z)/T_{0i}$ ($t_{i0} = 0$ if $i = 1$), z is the longitudinal coordinate of the fiber, and t is time. For the I_i pulse, k_{0i} is the propagation constant, λ_{0i} is the center wavelength, $\dot{k}_{0i}$ is the inverse of the group velocity $v_{g,i}$, $\ddot{k}_{0i}$ is the group velocity dispersion (GVD), $\beta_{0i} = \dddot{k}_{0i}/(6|\ddot{k}_{0i}|T_{0i})$ is the normalized third-order dispersion ($\dddot{k}_{0i}$ is the third-order dispersion (TOD)), $T_{0i} = t_{p,i}/1.763$ is the parameter of the initial pulse duration $t_{p,i}$, P_{0i} is the input peak power, $N_{\mathrm{sol},i} = [\gamma_i P_{0i} (T_{0i})^2/|\ddot{k}_{0i}|]^{1/2}$ is the soliton number, $\gamma_i = \omega_{0i} n_2/(2c^2 \varepsilon_0 n_{0i} A_{\mathrm{eff}})$ is the nonlinear parameter, n_2 is the nonlinear refractive index and n_{0i} is the linear refractive index. t_{i0} is the initial delay time of the I_i pulse ($i \neq 1$) relative to the I_1 pulse, and A_{eff} is the effective core area of the fiber. c and ε_0 are the vacuum light velocity and dielectric constant, respectively. $u^{(2)}(\xi_1,\tau_1) \equiv u^{(2)}(a_2\xi_1, b_2\tau_1 + c_2 + d_2\xi_1)$, $b_2 = T_{01}/T_{02}$, $c_2 = -t_{20}/T_{02}$, $d_2 = (\dot{k}_{01} - \dot{k}_{02}) T_{01}^2/(T_{02}|\ddot{k}_{01}|)$, $g_{mn} = |\ddot{k}_{0n}|\omega_{0m}(T_{0m})^2/[|\ddot{k}_{0m}|\omega_{0n}(T_{0n})^2]$ and $a_2 (= S_{42}) = |\ddot{k}_{02}|(T_{01})^2/|\ddot{k}_{01}|(T_{02})^2$ is the ratio of the dispersion lengths for the I_1, and I_2 pulses. For the S coefficients, $S_{12} = |\ddot{k}_{02}|/|\ddot{k}_{01}|$ is the ratio of the GVD for the pulses I_2 and I_1, $S_{22} = \beta_{02}|\ddot{k}_{02}|T_{02}/(|\ddot{k}_{01}T_{01}|)$ is proportional to the TOD for the I_2 pulse, $S_{32} = (\dot{k}_{01} - \dot{k}_{02})T_{01}/|\ddot{k}_{01}|$ is proportional to the group-velocity mismatch between the pulses I_1 and I_2.

The first and second terms in the right-hand sides of (2.1) and (2.2) represent the GVD and the TOD due to the fiber, respectively. The third term in (2.1) and fourth term in (2.2) represent SPM and the fourth term in (2.1) and fifth term in (2.2) represent IPM, both of which originate from the effect of the nonlinear refractive index in the third-order nonlinear polarization. Accordingly, IPM is always accompanied by SPM. The third term in (2.2) explicitly represents the effect of the group velocity mismatch between the I_1 and I_2 pulses. In deriving (2.1) and (2.2) the following assumptions have been made: (1) the nonlinear polarization terms other than the nonlinear-refractive-index ones are neglected because their polarizations do not generally contribute significantly under the condition of non-phase-matching in the four-wave-mixing processes in the fiber, [25]. (2) n_2 is frequency-independent in the non-resonant region, and (3) two different values for n_{0i}, k_{0i}, $\dot{k}_{0i}$, $\ddot{k}_{0i}$, and $\dddot{k}_{0i}$ at each carrier frequency are applied as representative ones in the ultrabroadband frequency region and $g_{mn} \fallingdotseq 1$.

The above coupled equations were solved numerically for a fused-silica fiber with a core diameter of 2 μm and a nonlinear refractive index $n_2 = 1.22 \times 10^{-22}$ $(\mathrm{m/V})^2$ [26] using the split-step Fourier method [25], under the assumption that the initial pulse shapes $I_i(\tau_i)$ are sech^2 at $\xi_i = 0$. Typical

Table 2.2. Input pulse and fiber parameters [12]

	1st pulse I_1	2nd pulse I_2		
		ω_{01}	$\omega_{0c} = 3\omega_{01}/2$	$\omega_{02} = 2\omega_{01}$
Input pulse				
	λ_{0i} (nm)	750	500	375
	$t_{\mathrm{p}.i}$ (fs)	50		70.7
	P_{0i} (kW)	900		900
	t_{i0} (fs)	0		-53.7
fiber				
	n_2 ($\mathrm{m}^2/\mathrm{V}^2$)		1.22×10^{-22}	
	d (μm)		2	
	z_0 (mm)		0.5	
	$\ddot{k}$ (s^2/m)	4.036×10^{-26}		10.741×10^{-26}
	$\dddot{k}$ (s^3/m)	2.605×10^{-41}		3.248×10^{-41}

input pulse parameters employed for the calculations are shown in Table 2.2. They are chosen by taking into account the output pulse characteristic obtained from a commercially available Ti:sapphire laser system.

At the fiber output, z_0 ($= (T_{01})^2\xi_{10}/|\ddot{k}_{01}|$), the amplitude $A_T(z_0, t)$ of the total electric field $E_T(z_0, t) = 2^{-1}A_T(z_0, t)\exp[-\mathrm{i}3\omega_{01}t/2] + \mathrm{c.c.}$ of the composite wave is described as follows by regarding $\omega_{0c} = (\omega_{02} - \omega_{01})/2 + \omega_{01} = 3\omega_{01}/2$ as a carrier angular frequency:

$$\begin{aligned} A_T(z_0, t) = {} & (n_{01}/n_{0c})^{1/2}A_1(z_0, t)\exp[\mathrm{i}(\omega_{01}t/2 + \phi_{T1})] \\ & + (n_{02}/n_{0c})^{1/2}A_2(z_0, t - t_{20}) \\ & \exp[\mathrm{i}(-\omega_{01}t/2 + \phi_{T2})], \end{aligned} \tag{2.3}$$

where $A_i(z_0, t - t_{i0}) \equiv (\sqrt{P_{0i}}/N_{\mathrm{sol},i})u^{(i)}(\xi_i, \tau_i)$ is the electric field envelope of the I_i pulse at the fiber output z_0 and n_{0c} is the linear refractive index at ω_{0c}. $\phi_{T1} = k_{01}z_0 + \phi_{01}$ and $\phi_{T2} = k_{02}z_0 + \phi_{02} + 2\omega_{01}t_{20}$ which represent the phase constants. The Fourier transform $A_T(\xi_{10}, \Omega) \equiv |A_T(\xi_{10}, \Omega)|\exp[\mathrm{i}\phi_T(\xi_{10}, \Omega)]$ of the total envelope $A_T(\xi_{10}, \tau_1)$ at the normalized fiber output distance ξ in the ξ_1, τ_1 coordinate is obtained from the linear combination of the shifted Fourier transform $U^{(i)}(\xi_{10}, \Omega + \delta_i\omega_{01}T_{01}/2)$ ($\delta_i = -1, 1$ for $i = 1, 2$) of $u^{(i)}(\xi_{10}, \tau_1)$. Consequently, the intensity spectrum $I_T(\Omega)$ and the frequency-dependent phase $\phi_T(\Omega)$ ($\equiv \phi_T(\xi_{10}, \Omega)$) of the fiber output pulse are calculated from $\epsilon_0 c n_{0c}|A_T(\xi_{10}, \Omega)|^2/2$ and $\tan^{-1}(\mathrm{Im}(A_T(\xi_{10}, \Omega))/\mathrm{Re}(A_T(\xi_{10}, \Omega)))$, respectively. Figure 2.2 shows the evolution of the intensity spectrum during propagation along the fiber. In addition, Fig. 2.3 shows the intensity spectrum and the frequency-dependent phase at the fiber output $z_0 = 0.5\,\mathrm{mm}$, where $\omega_{01} = 2.513 \times 10^{15}\,\mathrm{rad/s}$ ($\lambda_{01} = 750\,\mathrm{nm}$), $\omega_{02} = 5.027 \times 10^{15}\,\mathrm{rad/s}$ ($\lambda_{02} = 375\,\mathrm{nm}$), $\phi_{01} = 0$, and

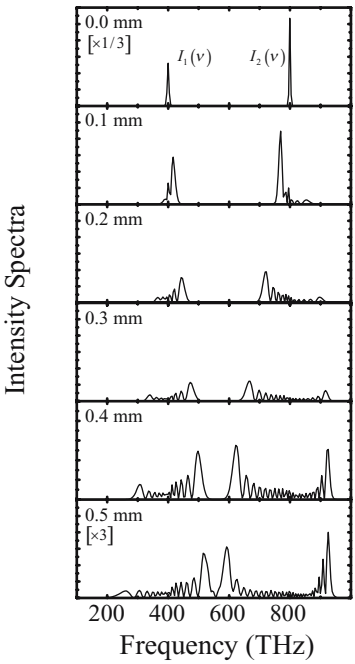

Fig. 2.2. An evolution of the entire pulse-intensity spectrum $I_T(\nu)$ during fiber propagation under IPM (see the text concerning the values of the parameters) [12]

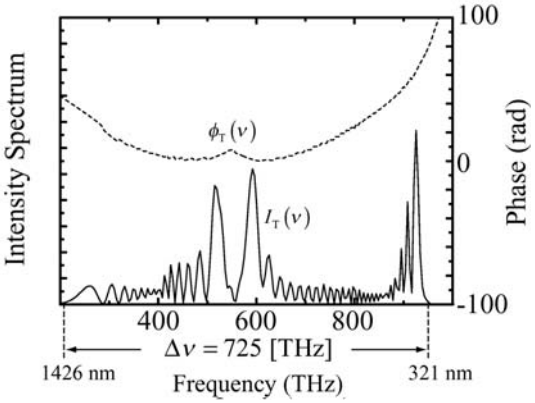

Fig. 2.3. The entire pulse-intensity spectrum $I_T(\nu)$ (*solid line*), and the frequency-dependent phase $\phi_T(\nu)$ (*dotted line*) generated by the IPM technique [12]

$\phi_{02} = -\pi/2$ (see Table 2.2). From this figure, it is seen that the spectrum is extremely broad over the near-infrared, the visible, and the near-ultraviolet wavelengths from 320.6 to 1426.4 nm which corresponds to the spectral full width of $\Delta\nu_T = 725$ THz. Also, the chirp is moderately nonlinear and is

composed of two linear chirps having different slopes. This transform-limited pulse has a duration of 1.28 fs.

It should be pointed out that the group velocity difference between the two pulses plays an important role in IPM because it limits the IPM interaction length. For two pulses of width $T_0' = T_{01}' = T_{02}'$ (where the intensity becomes 1/e), the walk-off length is defined as:

$$L_w = \frac{T_0'}{|v_{g1}^{-1} - v_{g2}^{-1}|}. \tag{2.4}$$

It is easy to understand that IPM occurs only over distances $\sim L_w$ irrespective of the actual fiber length L. The L_w depends on the relative center-wavelengths, and decreases as the center-wavelength difference $\delta\lambda_0$ increases. If the fiber length L satisfies the condition of $L \leq L_w$, the IPM terms on the right-hand sides of (2.1) and (2.2) show that the IPM effect is two times as large as SPM and a broader spectrum with both IPM and SPM effects than that with SPM alone could be generated. Furthermore, it was found that the initial phase difference $\phi_{02} - \phi_{01}$ between the I_2 and I_1 pulses does not influence the output-pulse intensity and spectral phase ($I_T(\Omega)$ and $\Phi_T(\Omega)$), except for the small interference part where the highest frequency edge of the I_1 spectrum and the lowest frequency edge of the I_2 spectrum slightly overlap.

In [11], similar numerical simulations were reported for the case of three-color input pulses.

2.2.2 Experiment

Experimental Setup

The first experimental generation of ultrabroadband optical pulses by the IPM technique was demonstrated in 1999 [13]. A schematic of the experimental setup is shown in Fig. 2.4. The first pulse I_1 was generated from a Ti:sapphire regenerative amplifier at 1 kHz repetition rate. The pulse duration was about 120 fs (full width at half maximum, FWHM) with a bandwidth of 12 nm (FWHM) centered at 795 nm and the output energy was 750 μJ (henceforth called fundamental pulse). The main output energy from the regenerative amplifier was used to generate a continuum wave and pump an optical parametric amplifier (OPA). The signal-pulse tuning range in OPA was from 480 to 740 nm with output energy beyond 10 μJ at 1 kHz. The wavelength of the second pulse I_2 was chosen to be 640 nm from OPA and the pulse duration was measured to be about 120 fs (FWHM) with a spectral bandwidth of 12 nm (FWHM) (henceforth called signal pulse). Since the continuum wave was generated by SPM of the fundamental pulse under the single-filament condition and was selectively amplified using its second harmonic pulse by optical parametric process with the phase matching condition [27], the phase

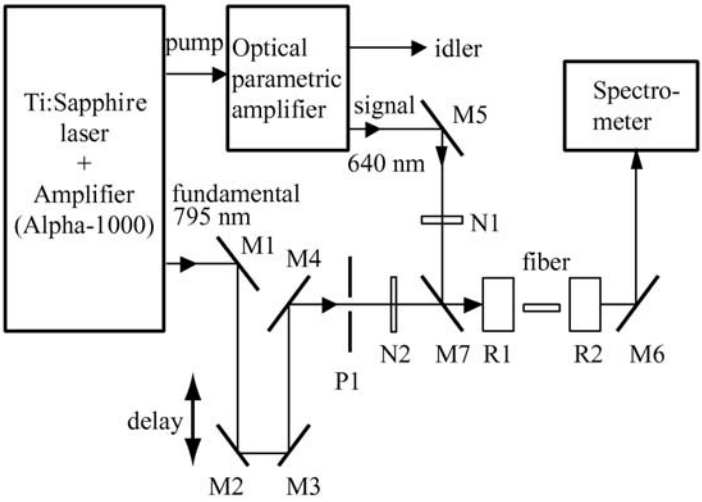

Fig. 2.4. Schematic of the experimental setup. Alpha 1000 is a 1 kHz regenerative amplifier, and an optical parametric amplifier (OPA) is pumped by Alpha 1000. M1–M6 are aluminum plane mirrors, M7 is a dichroic plane mirror highly transmitting at 795 nm and highly reflecting at 640 nm; P1 is an aperture, N1, N2 are neutral filters, R1, R2 are reflective objectives [13]

of the signal wave should have a relation to the phase of the fundamental wave. This condition is critical for generating a stable combined spectrum with IPM in a single-mode glass fiber, which will be confirmed later. From (2.4) the calculated walk-off length between the signal pulse and the fundamental pulse is about 2.7 mm. The reason why the second pulse wavelength is selected to be 640 nm lies in the fact that that the walk-off length of these two pulses in a fused silica fiber ($L_w = 2.7$ mm) is around the length that we are to cut well (∼3 mm) and then the IPM effect between the two pulses could be observed clearly. The two pulses were combined by a dichroic mirror, M7, which had high transmission for the fundamental pulse and high reflection for the signal pulse. The optical path of the fundamental pulse was varied by an optical delay stage formed by M2, M3, so that the delay of the two pulses in the fiber was adjusted. N_1 and N_2 were variable neutral-density filters and energies of the two pulses were controlled independently. The beam size of the signal pulse was about 1.5 mm with a perfect Gaussian distribution and an aperture P1 with a diameter of around 2.0 mm was added in the fundamental pulse beam to improve beam quality. The combined two pulses which had the same linear polarizations were coupled into a 3-mm single-mode polarization-preserving fused-silica fiber (2.7 μm core diameter) by a ×36 reflective objective R_1. The advantage of this kind of reflective objective is that no additional GVD is introduced to both pulses because of its reflective components. The coupling efficiency was measured to be around

35% and 40% for the fundamental and signal pulses, respectively. The output from the fiber was collimated by the same type of reflective objective R_2 to a wavelength-calibrated spectrometer to monitor the output spectrum.

Observation of IPM Spectrum

Figure 2.5(a) shows the spectra of the input fundamental (solid line) and signal (dashed line) pulses. Figure 2.5(b) depicts the spectra of the two pulses with SPM alone at the energy of 20 nJ in the fiber for each pulse. The solid line represents the SPM-induced spectrum of the fundamental pulse and the dashed line represents the SPM-induced spectrum of the signal pulse. From Fig. 2.5(b) we observe the separated spectra for the two pulses with only the SPM effect at 20 nJ energy levels. When the two pulses are launched simultaneously into the same fiber with an optimum initial delay between the two pulses (two pulses meet at the center of the fiber, to be discussed later), because of the IPM effect of the two pulses, the two spectra meet each other. It was observed that the output spectrum is significantly stable including the overlapping part. This means that the phase of the spectral-broadband fundamental wave and the phase of the spectral-broadband signal wave have some relation. Accordingly, the output spectrum is constructively synthesized. The optimized spectrum all over the range from 480 to 900 nm was measured (Fig. 2.5(c)). The pulse energy measured after fiber propagation was about 40 nJ. The shortest pulse attainable by phase correction of this ultra-broad spectrum is obtained by the Fourier transform of the spectrum of Fig. 2.5(c) assuming a constant spectral phase (see Sects. 3.3.1 and 5.2.1). This yields the pulse duration of ∼4 fs (Fig. 2.5(c) inset). It should be noted that a well-behaved spectral phase of the generated broad spectrum is significantly important for the bandwidth-limited-pulse generation.

Delay Effect Between Two Pulses

Because of the group velocity difference between the two optical pulses propagating in the fiber, they travel at different speeds and after some distance propagation they are separated. The IPM-induced spectra were measured for different initial time delays between the two pulses. The results are shown in Fig. 2.6. The initial time delay between the two pulses $t_{20} = 0$ fs represents that the two pulses coincide at the fiber entrance (dashed line), and the delays $t_{20} = -40$ fs and $t_{20} = -80$ fs represent that the two pulses meet at the center (thicker solid line) and the end of the fiber (thinner solid line), respectively. When the two pulses meet at the entrance of the fiber ($t_{20} = 0$ fs), because the fundamental pulse travels faster than the signal pulse in the fused-silica fiber, the leading edge of the signal pulse interacts with the trailing edge of the fundamental pulse. As a result, the signal pulse has IPM-induced positive chirp and the fundamental pulse has IPM-induced negative chirp. This leads to larger modulation of the signal pulse spectrum at shorter wavelengths and

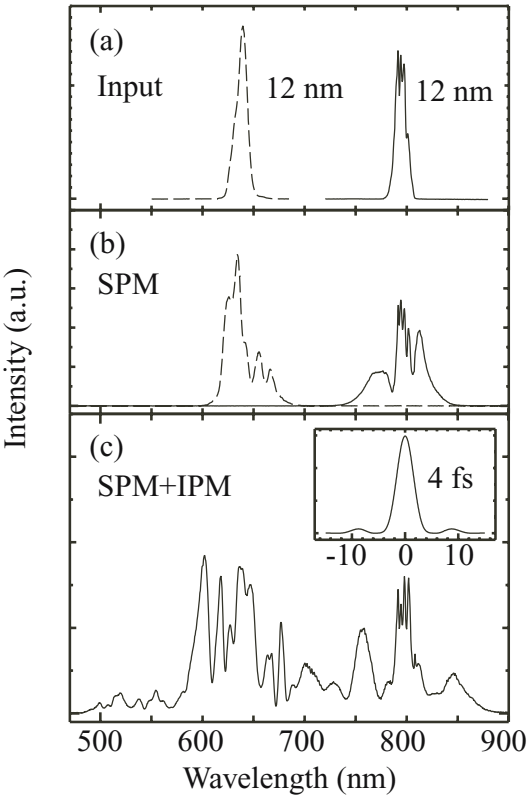

Fig. 2.5. (**a**) The spectra of the input fundamental (*solid line*) and signal (*dashed line*) pulses; (**b**) The measured spectra induced by SPM in a 3-mm single-mode fused-silica fiber. The solid line represents the fundamental pulse spectrum by SPM and the dashed line represents the signal pulse spectrum by SPM at the pulse duration of 120 fs, energy of 20 nJ in the fiber for each pulse; (**c**) The measured spectrum induced by IPM of the two pulses, the same parameters as in (b), the initial time delay between the two pulses is chosen so the two pulses meet at the center of the fiber. The Fourier transformed pulse intensity is shown in the inset [13]

larger spectral modulation of the fundamental pulse at longer wavelengths. A larger gap between the two spectra is observed in this case (Fig. 2.6, dashed line). On the contrary, when the two pulses meet at the end of the fiber ($t_{20} = -80$ fs), the trailing edge of the signal pulse mainly interacts with the leading edge of the fundamental pulse. As a result, the IPM-induced spectrum of the signal pulse shifts towards its longer wavelengths and the IPM-induced fundamental pulse spectrum shifts to shorter wavelengths and larger overlap of the two pulse spectra is observed (thinner solid line in Fig. 2.6). It is found that when the two pulses meet at the center of the fiber, the fundamental pulse passes through the signal pulse in a symmetric manner. As a result,

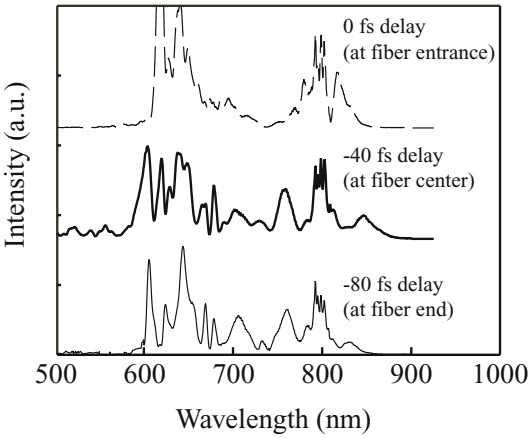

Fig. 2.6. The measured spectra induced by IPM for the two pulses with different initial time delays under the same parameters as in Fig. 2.5. The thicker solid line represents the spectrum when the two pulses meet at the center of the fiber, the dashed line represents the spectrum when the two pulses meet at the entrance of the fiber and the thinner solid line represents the spectrum when the two pulses meet at the end of the fiber [13]

the spectra are broadened by the IPM effect to shorter and longer wavelengths simultaneously for both pulses and the broadest combined spectrum is generated (thicker solid line in Fig. 2.6). This case is referred to as the optimum initial time delay which was mentioned above. Note that an even broader spectrum could be expected by tuning the second pulse to shorter wavelength, and utilizing a shorter optical fiber owing to the walk-off length L_w decreasing as the center wavelength difference $\delta\lambda_0$ increases.

Spectral Phase Characterization

The similar experiment in the infrared region for obtaining information on the spectral phase behavior of the fiber-output pulse was carried out using a combination of two input pulses with center-wavelengths of 800 nm (the fundamental pulse: the first pulse I_1) and 1070 nm (the idler pulse: the second pulse I_2) [28, 30, 42]. The fundamental pulse had a 80-fs pulse duration and 15-nJ energy per pulse, and the idler pulse had a 80-fs duration and 45-nJ energy, both at 1-kHz repetition rate. The output pulse from a 3-mm-length fused-silica fiber was directed to a chirp compensator consisting of a pair of fused-silica, 60-degree prisms with double paths. The distance between prisms was 61 cm. A width- and position-controllable slit was set between the second prism and a roof mirror for spectrally-resolved intensity-autocorrelation (AC) measurements. The compensated pulse was guided to a non-collinear intensity autocorrelator with a 10-μm-thick BBO crystal. The

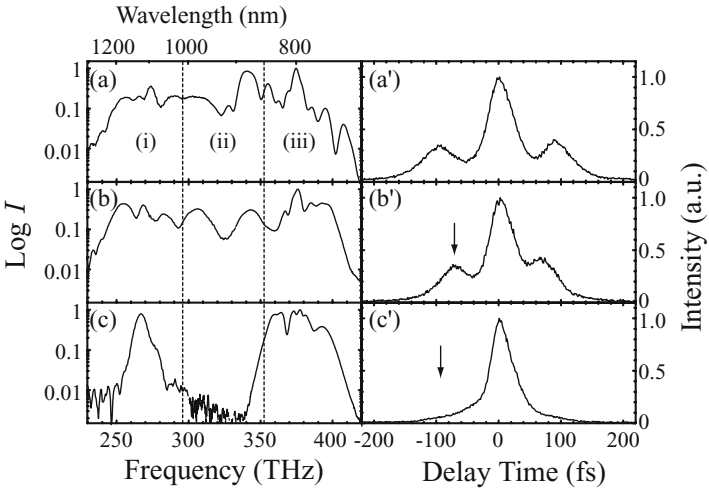

Fig. 2.7. The spectra (the vertical axis is a logarithmic scale) of output pulses broadened by the SPM + IPM effects from a fused-silica fiber (the left column). Each curves corresponds to different input timings between two-pulses; (**a**) $t_{20} =$ 67 fs, two pulses meet at the output face of the fiber. (**b**) 0 fs, they are injected simultaneously at the entrance of the fiber; (**c**) −67 fs, the idler pulse passes the fiber without overlapping with the fundamental pulse. The curves in the right column, corresponding to the left spectra, are traces of intensity autocorrelation for the whole pulse spectrum after chirp compensation by a pair of prisms. The notations (**i**), (**ii**), and (**iii**) correspond to the spectral region of 1100–1250 nm, 850–1010 nm and 730–850 nm respectively.

61-cm distance of the prism pair was chosen to compensate for chirp due to the dispersive SPM effect for only the fundamental pulse propagation. That is, the 130-fs fundamental pulse at the fiber output was compensated for to have a 35-fs duration of transform limitation. For chirp compensation of only the idler pulse at this prism distance, the comparable pulse duration was observed. The whole pulse spectrum was measured by two-forked-fiber-coupled spectrometers with a Si-photodiode array for the spectral part of the short wavelength and an InGaAs array for the spectral part of the long wavelength.

Figure 2.7 shows fiber-output spectra as a function of the delay-time t_{20} and their corresponding AC traces after chirp compensation. Spectra (a), (b) and (c) (hence traces (a′), (b′) and (c′)) correspond to $t_{20} = 67$, 0 and −67 fs, respectively. The fiber-propagation-time difference between the 80-fs idler pulse and the 80-fs fundamental pulse due to the group-velocity difference was 48 fs. In case (a), where two pulses meet almost at the fiber output end, IPM as well as SPM occurs strongly and hence a stable continuous spectrum from 710 to 1250 nm is observed. In case (b), where two pulse co-propagate simultaneously at the fiber entrance, IPM also occurs. However, the peaks around the center of the continuous spectrum from 710 to 1250 nm

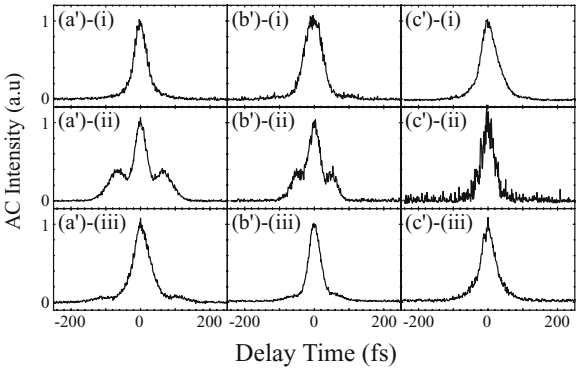

Fig. 2.8. Spectrally-resolved autocorrelation traces after chirp compensation by a pair of prisms for the output from a fused-silica fiber. The spectrum of the output pulses was divided into three spectral regions shown as (**i**) 1010–1250 nm, (**ii**) 850–1010 nm, and (**iii**) 730–850 nm. The curves in the each column (**a**′), (**b**′), and (**c**′) correspond to different input timings between two pulses; $t_{20} = 67$, 0, and -67 fs, respectively

have different structures and become slightly weak compared with case (a). In case (c), where the idler pulse propagates through the fiber in advance of the fundamental pulse without overlapping, the spectra of two pulses are broadened independently from 730 to 900 nm for the fundamental and from 1040 to 1220 nm for the idler by the dispersive SPM effect alone. The AC traces of (a′) and (b′) in Fig. 2.7 have a three-peak shape and the separation between sub-peaks decreases with decreasing the delay time. At the -67 fs delay time (c′), the trace becomes a single-peak shape with a small pedestal. The further decrease in delay time ($t_{20} < -67$ fs) indicated again an AC trace of a three-peak shape. The former AC traces, (a′) and (b′), imply temporal intensity profiles with two peaks, and the latter AC trace (c′) implies a single-peak intensity profile with a small pedestal. Figure 2.8 shows the AC traces after spectrally-resolved chirp compensation when keeping the same prism distance, for the three delay-times corresponding (a), (b) and (c) in Fig. 2.7. The fiber output spectra from 730 to 1250 nm were divided into three equal bandwidths ($\Delta\nu \cong 50$ THz) : The spectral regions of (i) 1010 to 1250 nm, (ii) 850 to 1010 nm and (iii) 730 to 850 nm (Fig. 2.7). In the two strong-IPM cases ((a′) and (b′) in Fig. 2.8), the AC traces in the spectral regions (i) and (iii) have a single peak with different widths between them, while that in the region (ii) has three peaks. On the other hand, in the SPM-dominant case ((c′) in Fig. 2.8), the AC trace even in the region (ii) has a relatively weak signal peak as well as those in the regions (i) and (iii) with the almost same width.

To understand these results, a numerical analysis for two-pulse nonlinear copropagation in a fused-silica fiber using a theory based on the slowly-

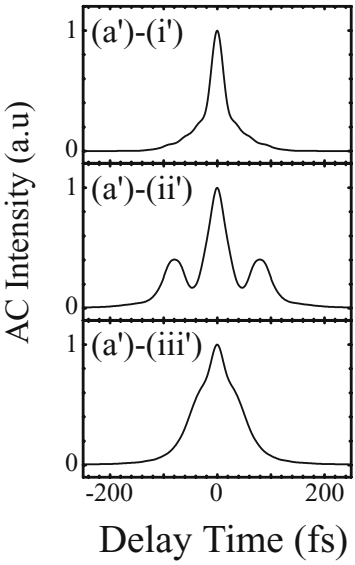

Fig. 2.9. Calculated autocorrelation traces in the three spectral region corresponding to the delay-time $t_{20} = 67\,\text{fs}$ of (a′) in Fig. 2.8 (left)

varying-envelope approximation ((2.1), (2.2)) was performed. The IPM analysis includes all orders of linear dispersion effects, the delayed-nonlinear Raman response and the dispersion effect of the effective core area (see Sect. 1.3) [42]. In addition, the obtained spectral phase was compensated for using the theoretically calculated dispersion applied by the double-pass prism pair [62] with experimental parameters. Fig. 2.9 shows the results of calculated AC traces after chirp compensation for cases of (a′)-(i′), (a′)-(ii′) and (a′)-(iii′). Comparison between the calculation (Fig. 2.9) and the experiment (in Fig. 2.8(a′)) indicates the good agreement between them. This implies for the IPM spectral phase that the group delay has a discontinuity around the central wavelength of 930 nm, and the group delay dispersion in the low frequency region is different from that in the high frequency region. This funding will be confirmed in Sect. 3.3 [29] and 5.2 [28, 30].

2.3 Gas-Filled Hollow Fiber Technique using IPM

In the original proposals of the generation of ultrabroadband optical pulses using induced phase modulation (IPM) [11, 12], fused silica fibers were considered as nonlinear media. Fused silica fibers have been conventionally used to broaden the spectrum of optical pulses through dispersive SPM and one of the shortest pulses up to date was generated by this method [34]. Optical propagation loss of a fused silica fiber is negligibly small for small distance.

However, its damage threshold is relatively small, making applications requiring large energy difficult. The maximum energy that can be allowed by this method is about 40 nJ for a 13-fs input pulse [20].

In 1996, single-mode hollow fibers filled with noble gases have been used to broaden the spectrum of optical pulses through dispersive SPM in single-channel propagation [18, 35] and sub-5 fs, high powered pulses have been generated using this technique [35]. Because of the chemical stability of the noble gases, the damage threshold is relatively high and the maximum energy that can be allowed is about 10 μJ. However, since the linear refractive index of the noble gas ($\simeq$1.0) is smaller than that of the glass used in the wall of the hollow fiber, the optical field is not completely confined in the fiber during propagation. Hence, a loss always occurs in this method. In addition, the nonlinear refractive index and second-order dispersion of the noble gas are smaller than those of fused silica by a factor of thousands.

2.3.1 Theoretical Prediction

We consider a case where two optical pulses with different center frequencies and widths are co-propagating in a hollow fiber with a length z_l whose axis is parallel to the z-direction. For each pulse j (j = 1,2), the electric field (linearly polarized in the x-direction) can be written as $\mathbf{E}_j(\mathbf{r}_j, t) = (1/2)\hat{\mathbf{x}}\{F_j(x,y)A_j(z,t)\exp[\mathrm{i}(\beta_{0j}z - \omega_j t + \phi_{0j})] + \text{c.c.}\}$, where β_{0j}, ω_j and ϕ_{0j} are a wave number of the propagation mode, a center angular frequency and a constant phase for a pulse j and c.c. represents the complex conjugate. All notations defined here apply only within Sect. 2.3. $F_j(x,y)$ represents the transverse distribution of the mode and $A_j(z,t)$ represents the slowly-varying-envelope part of the field. For convenience, two time-coordinates that move with the speed of a group velocity for each pulse are defined as $T_j = t - \beta_{1j}z$, where β_{1j} is the inverse of the group velocity of the pulse j. By using a slowly-varying-envelope approximation (SVEA), and if dispersion terms are neglected, $A_j(z, T_j)$ satisfies the following equations: [36, 37]

$$\frac{\partial A_1}{\partial z} = -\frac{\alpha_1}{2}A_1 + \mathrm{i}\frac{n_2\omega_1}{c}[f_{11}|A_1|^2 + 2f_{12}|A_2|^2]A_1, \tag{2.5}$$

$$\frac{\partial A_2}{\partial z} = -\frac{\alpha_2}{2}A_2 + \mathrm{i}\frac{n_2\omega_2}{c}[f_{22}|A_2|^2 + 2f_{12}|A_1|^2]A_2, \tag{2.6}$$

where α_j represents a loss, n_2 is a nonlinear refractive index. f_{jk} is a mode overlap integral between transverse modes of the pulses j and k. Writing $A_j = \sqrt{P_j}\exp(-\alpha_j z/2)U_j(z, T_j)$, where P_j is the peak power of the pulse j, the solutions of (2.5) and (2.6) are given by $U_j(z, T_j) = \exp[\mathrm{i}\phi_j(z, T_j)]U_j(0, T_j)$, where $\phi_j(z, T_j)$ is the time-dependent nonlinear phase [14].

From the nonlinear phase, the nonlinear chirp, which represents the instantaneous frequency shift from the carrier frequency, is calculated by the equation $\delta\omega_j = -\partial_{T_j}\phi_j$. By assuming the Gaussian input-pulses of the

form $A_1(0,T_1) = \sqrt{P_1}\exp[-T_1^2/(2T_{01}^2)]$ and $A_2(0,T_2) = \sqrt{P_2}\exp[-(T_2 - T_{d2})^2/(2T_{02}^2)]$, where T_{0j} is a pulse width where its intensity becomes 1/e and T_{d2} is a delay time of the pulse 2 with respect to the pulse 1, the chirps are calculated to be

$$\begin{aligned}\delta\omega_1(z_l,T_1) = \frac{2n_2\omega_1}{c}\frac{z_l}{T_{01}}\Bigg[&\frac{z_{1\mathrm{eff}}}{z_l}f_{11}\tau_1\exp(-\tau_1^2)P_1\\ &+\frac{f_{12}}{\delta_1}\exp[-2\eta_2(\tau_2-\tau_{d2})+\eta_2^2]P_2\sqrt{\pi}\eta_2\\ &\times\{\mathrm{erf}(\tau_2-\tau_{d2}-\eta_2)-\mathrm{erf}(\tau_2-\tau_{d2}-\eta_2-\delta_2)\}\\ &+\frac{f_{12}}{\delta_1}\exp[-2\eta_2(\tau_2-\tau_{d2})+\eta_2^2]P_2\\ &\times\{\exp[-(\tau_2-\tau_{d2}-\eta_2-\delta_2)^2]-\exp[-(\tau_2-\tau_{d2}-\eta_2)^2]\}\Bigg], \quad (2.7)\end{aligned}$$

$$\begin{aligned}\delta\omega_2(z_l,T_2) = \frac{2n_2\omega_2}{c}\frac{z_l}{T_{02}}\Bigg[&\frac{z_{2\mathrm{eff}}}{z_l}f_{22}(\tau_2'-\tau_{d2})\exp[-(\tau_2'-\tau_{d2})^2]P_2\\ &-\frac{f_{12}}{\delta_2}\exp(2\eta_1\tau_1'+\eta_1^2)P_1\sqrt{\pi}\eta_1\\ &\times\{\mathrm{erf}(\tau_1'+\eta_1+\delta_1)-\mathrm{erf}(\tau_1'+\eta_1)\}\\ &-\frac{f_{12}}{\delta_2}\exp(2\eta_1\tau_1'+\eta_1^2)P_1\\ &\times\{\exp[-(\tau_1'+\eta_1+\delta_1)^2]-\exp[-(\tau_1'+\eta_1)^2]\}\Bigg]. \quad (2.8)\end{aligned}$$

Here, $\mathrm{erf}(x) = \frac{2}{\sqrt{\pi}}\int_0^x \exp(-t^2)dt$ is an error function and the following quantities are defined by $\tau_j = T_1/T_{0j}$, $\tau_j' = T_2/T_{0j}$, $\tau_{d2} = T_{d2}/T_{02}$, $\delta_j = z_l d/T_{0j}$, and $\eta_j = \alpha_j T_{0j}/(2d)$. Also, $d = \beta_{12} - \beta_{11}$ is the difference between the inverses of the group velocities and $z_{j\mathrm{eff}} = (1-\exp(-\alpha_j z_l))/\alpha_j$ is the effective fiber length for the pulse j. In (2.7) and (2.8), the first terms are due to SPM and the second and the third terms are due to IPM. Especially, the second term appears because of the loss during propagation. In Fig. 2.10, the chirps are shown as functions of normalized time.

We set ω_1 as the fundamental wave and $\omega_2 = 2\omega_1$ as the second-harmonic wave. To cover fully the spectrum between ω_1 and ω_2, we wish to maximize $\delta\omega_1$ and $-\delta\omega_2$ ($\delta\omega_2 < 0$). From (2.7) and Fig. 2.10, the second term (IPM 1 in Fig. 2.10) is small if the loss is small, thus we ignore the second term. From the conditions that the first term and the third term become maxima, the optimum delay to maximize $\delta\omega_1$ is given by

$$T_{d2} = T_{01}/\sqrt{2} - T_{02}\eta_2 - z_l d. \quad (2.9)$$

Similarly, the condition of maximizing $-\delta\omega_2$ is given by

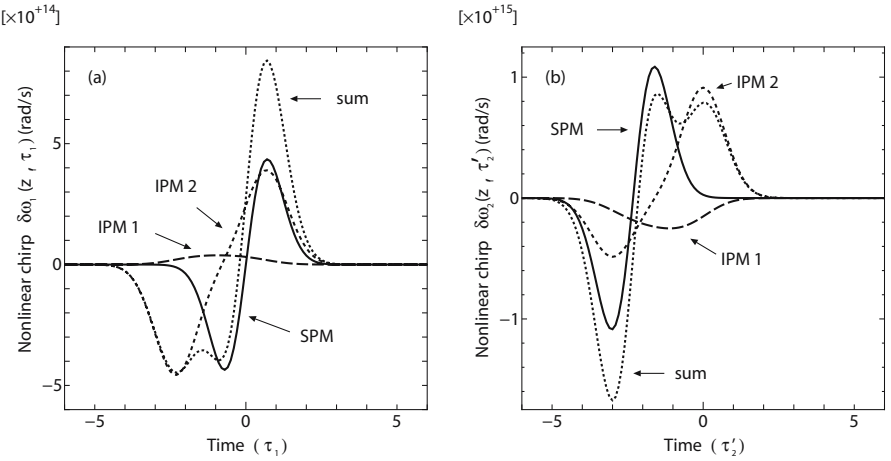

Fig. 2.10. Calculated chirps versus normalized time for (**a**) $\delta\omega_1$ and (**b**) $\delta\omega_2$ when dispersion terms are neglected. Solid lines show chirps from SPM, long and short dashed lines show chirps from IPM, and dotted lines show the total chirps. Pulse centers are at 0 for (**a**) and -2.32 for (**b**). In these calculations, ω_1 is the fundamental wave and ω_2 is the second-harmonic wave of a Ti:sapphire laser system (λ_1 = 790 nm). These waves are co-propagated in an argon-filled (300 K, 3.3 atm) hollow fiber with a radius of 50 μm and a length of 29.2 cm. Also, $P_1 = P_2 = 1.29$ GW, $T_{01} = T_{02} = 30/(2\sqrt{\ln 2})$ fs ($\tau_1 = \tau_2$, $\tau_1' = \tau_2'$), $n_2 = 3.234 \times 10^{-23}$ m^2/W and $T_{d2} = -41.8$ fs ($T_{d2} \simeq -z_l d$) are used [14]

$$T_{d2} = T_{02}/\sqrt{2} - T_{01}\eta_1 - z_l d. \tag{2.10}$$

Comparison of (2.9) and (2.10) shows that for small η_1 and η_2, two conditions above can be satisfied if both pulses have the same widths ($T_{01} = T_{02}$). In particular, if there are no loss ($\eta_1 = \eta_2 = 0$), these conditions can be satisfied exactly. This condition $T_{d2} = T_{02}/\sqrt{2} - z_l d$ specifies that both pulses meet almost at the fiber exit end.

To fully cover the spectrum between ω_1 and ω_2, we set the condition: $(\delta\omega_1)_{\max} + (-\delta\omega_2)_{\max} = \omega_2 - \omega_1 = \omega_1$, where $(\delta\omega_1)_{\max}$ and $(-\delta\omega_2)_{\max}$ are obtained at the optimal delay time (2.9). Using this condition, the minimum required powers of pulses were calculated for the propagation of the fundamental (center wavelength 790 nm) and the second-harmonic (center wavelength 395 nm) pulses in a hollow fiber (radius 50 μm, length 29.2 cm) filled with 3.3-atm-argon [14]. When the width of each pulse was set to be $T_{0j} = 30/(2\sqrt{\ln 2})$ fs, the required power of each pulse was calculated to be 1.29 GW with the optimal delay time $T_{d2} = -41.8$ fs. In Fig. 2.11, the spectral intensity obtained by a numerical simulation for the above condition is shown. As shown in the figure, the spectrum between ω_1 and ω_2 is indeed fully covered.

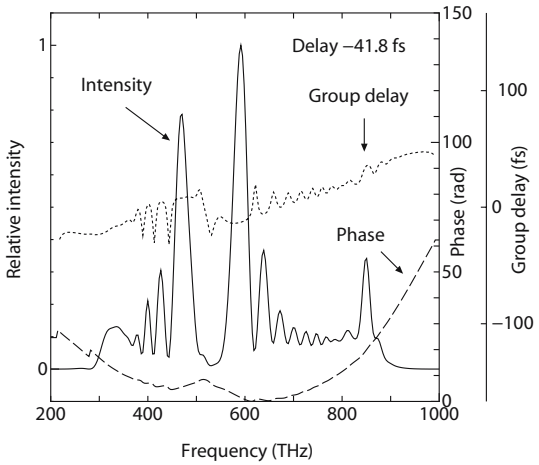

Fig. 2.11. Calculated intensity, phase and group delay versus frequency of the fundamental wave and the second-harmonic wave after propagating an argon-filled hollow fiber under the condition $P_1 = P_2 = 1.29\,\mathrm{GW}$, $T_{d2} = -41.8\,\mathrm{fs}$ [14]

2.3.2 Experiment

The generation of ultrabroadband optical pulses by the use of induced phase modulation in an argon-filled hollow fiber was experimentally demonstrated [15]. The experimental setup is shown in Fig. 2.12. The output beam of a Ti:sapphire laser-amplifier system (center wavelength ∼790 nm, pulse width 24 fs, repetition rate 1 kHz and pulse energy 1 mJ) was passed through a 0.5-mm-thick β-barium borate (BBO) crystal (C_1). The second-harmonic pulse generated by the type-I phase-matching was separated from the fundamental pulse by two harmonic separators (HS). The polarization direction of the fundamental pulse was rotated by 90 degrees by two periscopes (PS) to match it with that of the second-harmonic pulse. The fundamental pulse and the second-harmonic pulse were combined using a dichroic mirror (DM) and collimated by a spherical mirror with a 20-cm focal length. In a chamber, a hollow fiber with 34-cm length and 0.1-mm inner diameter was positioned and argon gas with a pressure of 3.3 atm was filled. The chamber had two 1 mm-thick sapphire windows (S_1 and S_2). A retro-reflector (RR) was used to adjust the delay time of the second-harmonic pulse with respect to the fundamental pulse. Input energies of these pulses were adjusted by variable neutral-density filters (VND).

Both input pulses were redirected by flip mirrors (F_1 and F_2) and were evaluated using a transient-grating frequency-resolved optical gating (TG-FROG) apparatus [38]. To include the influence of the sapphire window S_1, the sizes of these beams were adjusted and the beams were passed through the equivalent sapphire plate S_3 before entering the TG-FROG apparatus. The measured time-dependent intensities and phases were used for numeri-

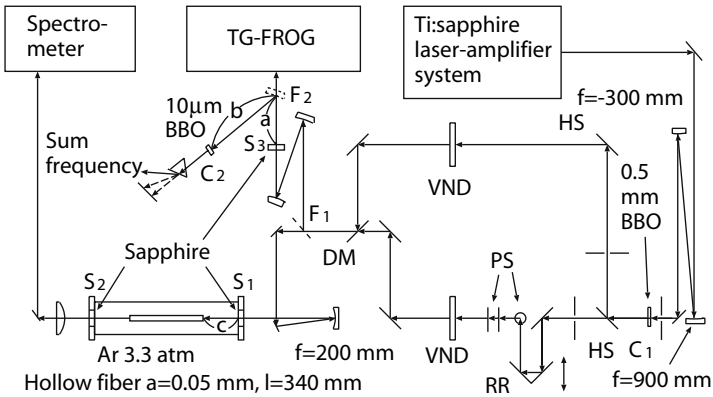

Fig. 2.12. Experimental set-up for the ultrabroadband optical pulse generation. Here, BBO (C_1 and C_2) is β-barium borate crystal, HS is harmonic separator, RR is retroreflector, PR is periscope, VND is variable neutral-density filter, DM is dichroic mirror, and TG-FROG is transient-grating frequency-resolved optical gating equipment. Flip mirrors (F_1 and F_2) are shown by dashed lines [15]

cal calculations. To calibrate the delay time between the fundamental pulse and the second-harmonic pulse, a 10 μm-thick BBO crystal (C_2) was used to generate a sum-frequency pulse from these pulses. To avoid the necessity of positioning the crystal inside the chamber, the pulse beams were redirected by a flip mirror F_2 and were focused at the crystal. The crystal was positioned such that the product of the path length and $d = 1/v_{g2} - 1/v_{g1}$, where v_{gj} was the group velocity of the pulse j (1 for fundamental and 2 for second-harmonic), was equivalent to the original path to the fiber entrance, i.e., $(a + b) \times d_{\text{air}} = c \times d_{\text{Ar},3.3\,\text{atm}}$ in Fig. 2.12. Also, S_3 was positioned such that the path length from F_1 to S_1 was equal to that from F_1 to S_3. The delay position that gave the largest sum-frequency signal was determined as the delay time 0 ($T_d = 0$), which corresponded to the situation where the fundamental pulse and the second-harmonic pulse coincided at the fiber input end. The negative T_d corresponded to the case where the second-harmonic pulse entered the fiber before the fundamental pulse. The fundamental pulse of 40.8 μJ energy and the second-harmonic pulse of 37.8 μJ energy were focused at the fiber entrance.

Figures 2.13(a)–(c) show the spectra at the output of the hollow fiber. In Fig. 2.13(a), two spectra when both pulses were propagated separately are shown. In this case, the spectral broadening was due to only SPM. When the delay time between two co-propagated pulses was adjusted such that these pulses overlapped inside the fiber, we observed the larger spectral broadening due to IPM and SPM (Fig. 2.13(b) and (c)). Inside the fiber, $d = 185$ fs/m, thus the propagation-time difference between the fundamental pulse and the second-harmonic pulse for the entire fiber length of 34 cm was 63 fs (185 fs/m

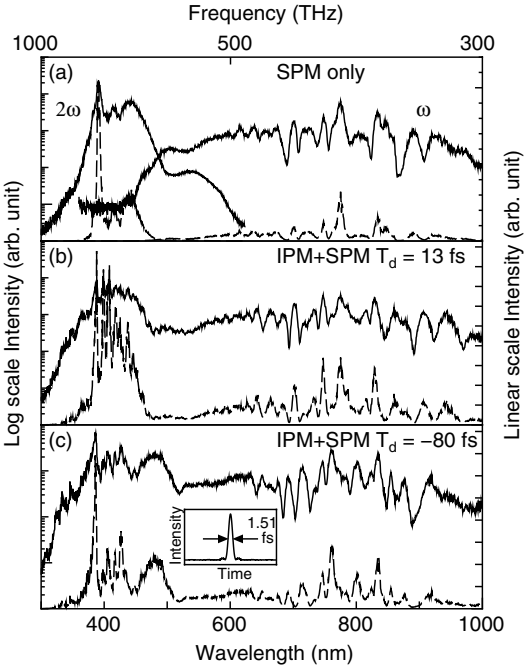

Fig. 2.13. Experimental spectral intensities in logarithmic scales (*solid line*) and in linear scales (*dashed line*) when the fundamental pulse and the second-harmonic pulse were propagated separately and were co-propagated in a fiber: (**a**) SPM only, (**b**) IPM+SPM, $T_d = 13\,\text{fs}$, and (**c**) IPM+SPM, $T_d = -80\,\text{fs}$. In the inset in (**c**), the temporal intensity of the inverse Fourier transform of the spectrum assuming the constant phase is shown [15]

$\times\ 0.34\,\text{m}$). In Fig. 2.13(b), the spectrum is shown when both pulses met near the fiber entrance ($T_d = 13\,\text{fs}$). It was observed that the spectral intensity near both edges increased (the intensity of the shorter wavelength than the second-harmonic and the longer wavelength than the fundamental), but it did not increase much at the middle. In Fig. 2.13(c), the spectrum is shown when both pulses met near the fiber exit ($T_d = -80\,\text{fs}$). In this case, in contrast to the previous case, the intensity increase of the spectrum was observed at the middle section (450–550 nm), especially a new peak was observed at around 480 nm. The best overlapping of the spectrum between two pulses with the more homogeneous broadening from 300 to 1000 nm (700-THz bandwidth) was observed at this delay time. This delay-time dependence of the spectral broadening agreed well with the theoretical prediction (see Sect. 1.3). Also, the peak powers required to obtain the spectrum-overlapping of both pulses were consistent with those obtained from the theoretical analysis. The total output pulse energy was 23.0 μJ (29.3% efficiency) corresponding to 11.9 μJ for the fundamental pulse and 11.1 μJ for the second-harmonic pulse, respec-

tively. These each gave throughput of 29.2% (11.9 μJ/40.8 μJ) for the fundamental pulse and 29.4% (11.1 μJ/37.8 μJ) for the second-harmonic pulse. The output spectra were compared with the calculated spectra and the coupling loss was estimated to be 39% for the fundamental wave and 29% for the second-harmonic wave.

In the inset of Fig. 2.13(c), the inverse Fourier transform of the experimental spectrum of Fig. 2.13(c) when its spectral-phase was set to be constant is shown. The evaluated pulse duration was 1.51 fs. Since this spectrum was generated by the interaction between two pulses, the chirp was not expected to be linear. To compress the ultrabroadband pulse, it is necessary to use a method that can compensate for the nonlinear chirp. One such method is the use of an adaptive spatial light modulator (see Chaps. 3 and 5), which has a potential of generating a monocycle-like pulse.

2.3.3 The Oscillatory Spectrum Due to Only IPM

When the intense fundamental pulse from the Ti:sapphire laser amplifier system and its second-harmonic pulse were co-propagated in an argon-filled hollow fiber, the periodic oscillatory structure in the second-harmonic spectrum was observed [46].

The experimental setup was similar to the one shown in Fig. 2.12 (except that the argon pressure was 2.8 atm in this experiment). Input pulse energies were 40.8 μJ for the fundamental pulse and 27.0 μJ for the second-harmonic pulse and output pulse energies were 15.5 μJ for the fundamental pulse and 10.5 μJ for the second-harmonic pulse, respectively. The temporal widths of these input pulses were measured by the TG-FROG apparatus [38] and were found to be 32 fs and 72 fs for the fundamental pulse and the second-harmonic pulse, respectively.

Observed spectra for the second-harmonic pulse are shown in Fig. 2.14(a)–(e). In Fig. 2.14(a), the delay time ($T_{d2} = -207$ fs) was selected such that both pulses did not overlap inside a fiber. In this case, the IPM spectrum (solid curve) was almost identical to the SPM spectrum (dotted curve, measured for the propagation of only the second-harmonic pulse). The oscillatory structure with a period of ∼20 THz was shown in the high frequency region. When the delay time T_{d2} was increased (Fig. 2.14(b)–(d)), pulses began to overlap inside a fiber, and a new oscillatory structure with the shorter period of ∼10 THz in the low frequency region was observed as indicated by arrows. As the overlap increased, this new structure became more pronounced. For the even larger delay time T_{d2} (Fig. 2.14(e)), the overlap between the fundamental pulse and the second-harmonic pulse became large such that the original SPM spectrum shape was modified considerably. Although the oscillatory structure was still present in this case, the strong modification of the main spectrum by the SPM made the identification of the IPM oscillation difficult.

The instantaneous frequencies were calculated by (2.8) and were plotted in Fig. 2.15 with the temporal pulse shapes at different delay times. As shown

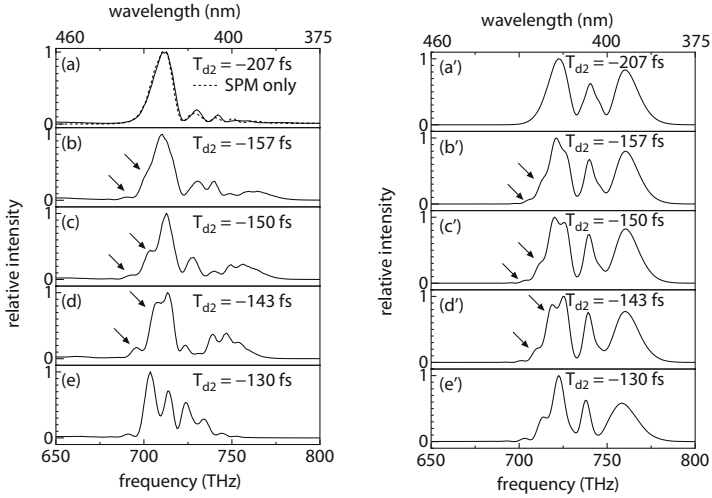

Fig. 2.14. (**(a)**–**(e)**) Experimental spectra where both fundamental pulse and its second-harmonic pulse were co-propagated in an argon-filled hollow fiber with different delay times. The oscillatory structure due to only IPM is indicated by arrows. In (**a**), the spectrum where only the second-harmonic pulse was propagated (SPM alone) is shown by a dotted line. (**a′-e′**) Numerically calculated spectra at the same delay time. In calculations, the dispersion of the gas medium and the waveguide and the steepening effect were taken into account [46]

in Fig. 2.15, the spectral components for the second-harmonic pulse whose frequency is lower than the center frequency (740 THz) are created by both SPM and IPM. However, it is found that the spectral components less than the minimum frequency created by the SPM (∼720 THz, indicated by thin horizontal lines in Fig. 2.15) are created only by the IPM from the intense fundamental pulse (which is described by the third term of (2.8)) and these frequencies are created twice at different times (hatched by thin lines in Fig. 2.15). The novel oscillatory structure in the spectrum appears because of the interference between these two electric field components with the identical instantaneous frequencies by the IPM. When the delay is sufficiently negative (Fig. 2.15(a)), the intensity of the second-harmonic pulse $I_{2\omega}(t)$ in this region is essentially zero, so that the interference is not observed. When the delay times become less negative (Fig. 2.15(b)–(d)), the intensity in this region (hatched by thick lines) becomes stronger and the interference patterns can be observed. When the delay becomes even less negative (Fig. 2.15(e)), the chirps due to SPM and IPM in the region from 675 to 775 THz are becoming similar in magnitude because of the large intensity of the pulse and the interference pattern shown here becomes difficult to identify.

In Fig. 2.14(a′)–(e′), the spectra calculated by numerically solving the nonlinear fiber propagation equation at the same delay times as in the exper-

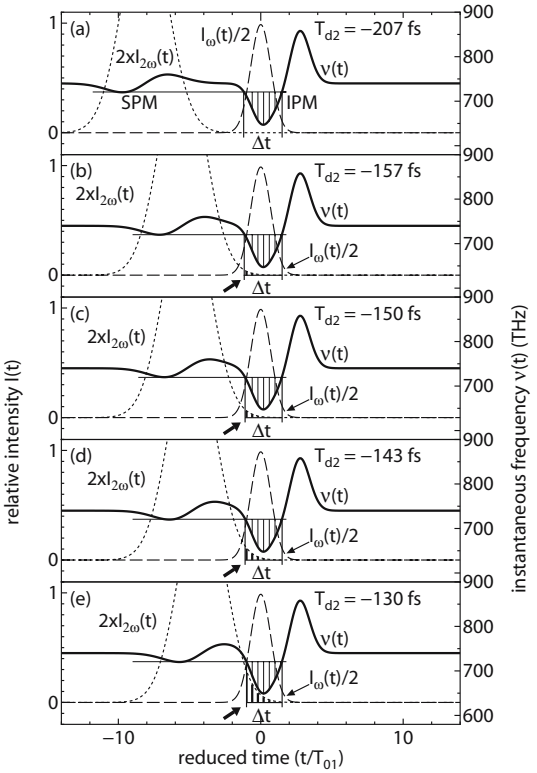

Fig. 2.15. Calculated instantaneous frequencies $\nu(t)$ (*solid line*) and the intensities $I_{2\omega}(t)$ (*dotted line*) of the second-harmonic pulse and the intensities I_ω of the fundamental pulse at the fiber output at different delay times. Thin horizontal lines show the minimum instantaneous frequency created by SPM. The instantaneous frequencies and the intensities of second-harmonic pulses in the temporal region where the instantaneous frequencies are created twice due to only IPM are hatched by thin lines and thick lines, respectively. Gaussian input pulses are assumed and the dispersion and the steepening effects are neglected. See text for input parameters [46]

iment are shown. In these calculations, the dispersion of the gas medium and the waveguide (including loss dispersion) was rigorously included, and the steepening effect was taken into account [42]. As shown in Fig. 2.14, the clear oscillatory structure in the low frequency region, as observed in the experiment for cases (b′)–(d′)), was obtained. The spectral feature, the oscillatory period (∼10 THz) and the delay-time range show excellent agreement with the experimental results.

2.4 Unconventional Glass Fiber Technique Using SPM

2.4.1 Photonic Crystal Fiber

By periodically structuring a material in two or three dimensions with a pitch of the order of the optical wavelength, one can fabricate new optical materials with unusual properties [61]. The monomode waveguide based on the use of a two-dimensional photonic crystal material is called photonic crystal fiber (PCF) (Fig. 2.16) [16], which has a hexagonal array of air holes running down its length. The pitch of the hexagonal crystal pattern is in the range of 1–10 μm. By leaving a single lattice site without an air hole, we can form a localized region that effectively has a higher refractive index than the rest of the structure. The microstructure fiber was measured to have net anomalous dispersion over this entire spectral range, owing to a large anomalous waveguide dispersion, with the dependence of dispersion on the PCF geometry (Fig. 2.17). This unusual dispersion property enabled us to efficiently generate the supercontinuum (SC) light [16].

The behavior of SC generation in PCFs is qualitatively different from SPM-induced broadening, and soliton dynamics plays a crucial role in the propagation. However, the mechanisms in SC generation are extremely complicated due to the interactions among many nonlinear optical processes such as self-phase modulation (SPM), stimulated Raman Scattering (SRS), parametric four-ware mixing (FWM), soliton formation and self-steepening (SST) as well as the unusual dispersion profile. Furthermore, the roles of these nonlinear effects strongly depend on the parameters of initial optical pulse, such as peak power, pulse duration and central wavelength.

In 2000, the authors of [16] first demonstrated that the combined effects of SPM and SRS in the long length of the fiber (75 cm) produced SC from 390 to 1600 nm, where 100-fs input pulses with 8-kW peak power and a center wavelength (790 nm) slightly longer than zero-dispersion wavelength (ZDW:

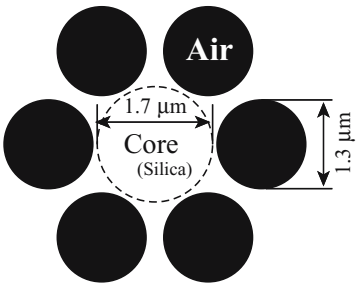

Fig. 2.16. Photonic crystal fiber consists of a 1.7-μm-diameter silica core surrounded by an array of 1.3-μm-diameter air holes in a hexagonal close packed arrangement. A small ellipticity in the fiber core results in a polarization-maintaining birefringence [16]

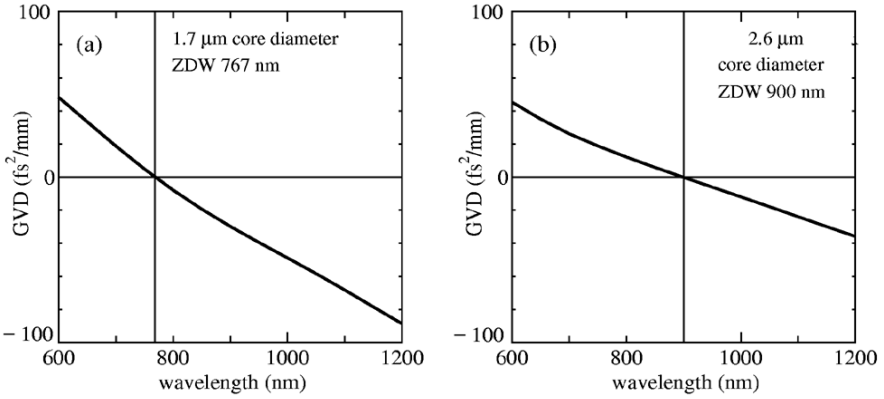

Fig. 2.17. Example for dispersion profiles of PCFs. (a) and (b) correspond to 1.7 and 2.6 μm core diameters, respectively [16]. GVD denotes group velocity dispersion

767 nm) were propagated. In 2001 another group [39] reported that the experimentally generated SC from 400 to 1000 nm with two spectrally sharp peaks near the center wavelength was due to the combined effects of SRS and conventional FWM with a negligible contribution from SPM in the longer length of the fiber (10 m), where 60-ps pulses with 675-W peak power and a center wavelength (647 nm) slightly-shorter than ZDW (675 nm) were propagated. More recently, by a theoretical analysis for optical pulse propagation in the short-length PCF (7.5 cm), it has been shown that the SC generation from 400 to 1000 nm is due to the fission of high-order solitons into red-shifted fundamental solitons and blue-shifted nonsolitonic radiation, where 100-fs input pulses with several-kilowatt peak power and a center wavelength (830 nm) longer than ZDW (710 nm) are propagated [44]. Furthermore, numerical analysis has indicated that 17.5-fs short-pulse propagation does not cause dramatic spectral broadening. In its analysis, however, the employed equation does not consider the effect of the delayed Raman response, which has characteristic constants of several-ten femtoseconds [40].

In this subsection, let us describe the spectral evolution of a-few-cycle pulses at different propagation distances in a PCF, which we have clarified in [55] (see Sect. 1.3.1 for theoretical understanding). With ZDW at 767 nm and negative group delay dispersion (GDD) at its longer wavelength, high-delta PCFs used in our experiment consisted of a 1.7-μm-diameter undoped silica core surrounded by an array of 1.3-μm-diameter air holes in a hexagonal close-packed arrangement (the pitch of $\Lambda = 1.65\,\mu$m, the radius of the omitted hole of $\alpha = 0.65\,\mu$m), same as that used in [16]. The 12-fs-duration pulses with 800-mW average power centered at 795 nm were generated from a mode-locked Ti:sapphire laser at the repetition rate of 75 MHz. The corresponding spectrum ranged from 700 to 910 nm with 69-nm width (FWHM), as shown in Fig. 2.18(a)–(1). PCFs with different lengths (4, 8, 15, 61 mm) were carefully

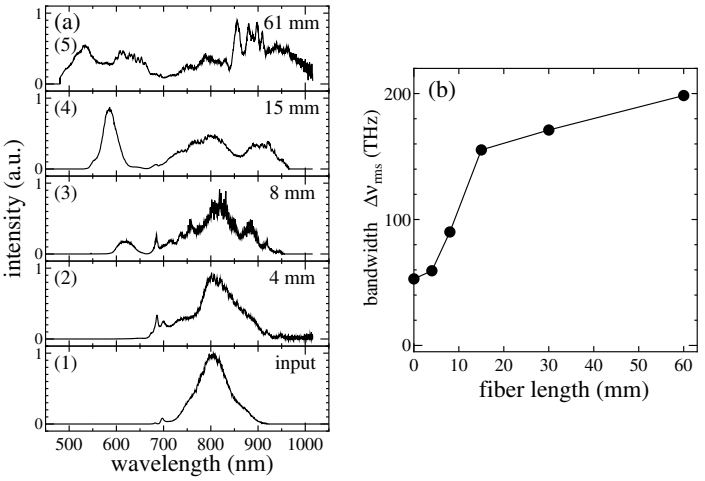

Fig. 2.18. (**a**) Experimental spectra generated from 4.5-cycle optical pulses in different-length PCFs. (**b**) Dependence of full spectral width $\Delta\nu_{\rm rms}$ on fiber length [55]

cleaved to produce both pristine and undamaged surface. Pulses were then coupled into those PCFs by a reflective objective of $\times 36$ magnification to avoid additional dispersion from transmission in a dielectric medium. The fibers were rotated to make the polarization axis of the linearly polarized pulses coincide with one of the principal axes in the fibers. Outputs from the fibers were collimated by another identical reflective objective. The spectra of the pulses before and after propagation (Fig. 2.18(a)) were measured by a calibrated spectrometer. The typical input and output average powers were 400 and 60 mW, respectively.

From Fig. 2.18(a) we find that the evolution of the intensity spectra during propagation has the following notable features. At first (4 mm), the spectrum broadens asymmetrically (625 to 915 nm) to form a shoulder on the blue side. With an increase in propagation distance (8 mm), the asymmetric spectrum continues to broaden (590 to 950 nm) with small peaks at the blue (625 nm) and red (915 nm) edges and the spectral gap appears near 660 nm. After the 15-mm distance, with the further asymmetric broadening the peak at the blue edge (580 nm) grows in size and the red edge extends to 965 nm. In addition, the spectral gap (650 nm) becomes more clear. Finally (the 61 mm distance), the spectrum broadens the most (480 to 1020 nm) with two peaks on the blue side (530 and 610 nm) and several peaks on the red side. For details of the spectral broadening mechanism, see Sect. 1.3.1.

Finally, let us show briefly the core-diameter dependence of the output spectrum from 3-mm long fibers (Fig. 2.19). The upper (a) and lower (b) figures correspond to 2.6 (900 nm ZDW) and 1.7-μm (767 nm ZDW) core

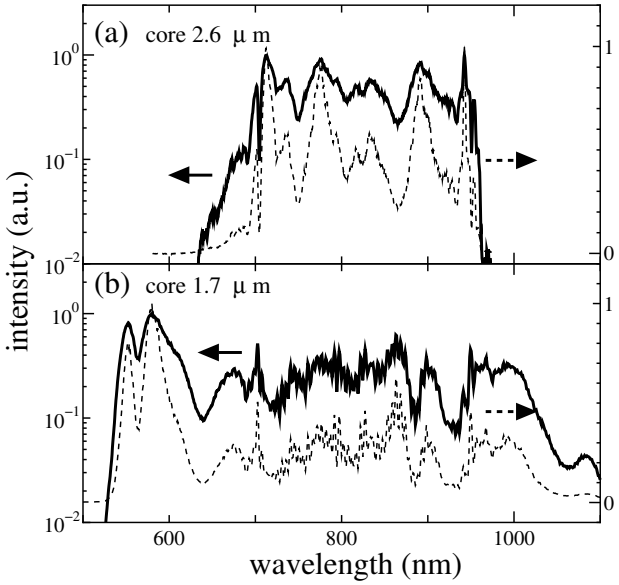

Fig. 2.19. Dependence of the output spectrum on the core diameter. (**a**) and (**b**) are for 2.6 and 1.7 μm core diameters, respectively

diameters, respectively, for the same input-pulse condition of a 12-fs duration, a 450-mW average power (including the objective reflective lens for focusing), and a 800-nm center wavelength at a 75-MHz repetition rate. The output average power (including the objective reflective lens for collimating) is 60 and 40 mW for 2.6- and 1.7-μm core diameter fibers, respectively. The difference of the spectral broadening (630 to 970 nm and 520 to 1100 nm) is mainly due to the ZDW and the power density in the fiber. The drawback of the PCF SC generation for optical pulse compression is the point that the intensity spectrum is greatly inhomogeneous with structures.

2.4.2 Tapered Fiber

A tapered silica fiber (TF), as well as a photonic crystal silica fiber (PCF), has attracted much attention because of its unusual dispersion profile and hence its efficient generation of ultrabroadband pulses [16,17,47–49,61]. Since the first experimental demonstration of these fibers in 2000 [16, 17], a variety of applications such as pulse compression [16, 17], ultrabroadband and frequency-conversion optical sources for spectroscopy and biomedicine [48], optical frequency metrology [49], and telecommunication technologies have been pointed out and investigated. Among them, it is expected that further pulse compression of ultrashort laser pulses may open the way for monocycle fiber optics.

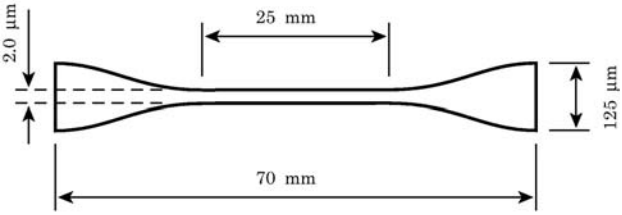

Fig. 2.20. Structure of the tapered fiber

A TF has the following advantages over a PCF: easier manufacturing, more efficient coupling of the fiber input pulse, easier connection with the conventional fiber (hence higher output power), a more stable continuum generating source and wider potential availability. However, it is difficult to use for a reproducible experiment because the quality of TFs varies significantly depending on the present fabrication technique. Therefore, it sometimes can be difficult to have a quantitative discussion regarding spectral broadening for TFs. In addition, TFs are mechanically quite weak at the waist, which makes their handling relatively difficult.

A TF is made from a conventional single-mode fused-silica fiber (125 μm outer diameter, 9 μm core diameter). Through precise heating with a gas torch, a 10 mm segment of this optical fiber is slowly stretched to roughly 7 times its length. The typical structure is shown in Fig. 2.20. A fiber has a total length of 74 mm and a 25 mm waist where it has a uniform 2 μm diameter. At each end the diameters are the original outer and core diameters.

In the waist region, the residual fiber core is so small that the waist is effectively a simple thread of silica suspended in air, which guides light from the open ends. The original 125-μm cladding diameter now acts as the core and the air surrounding it effectively acts as a new cladding. Hence, the TF has the large difference in the refractive index between the silica and air. The typical zero-dispersion wavelength (ZDW) of the TF obtained from the material dispersion and waveguide dispersion is approximately 778 nm. The measured dispersion profile of the TF (2 μm waist diameter) is shown in Fig. 2.21 [60]. The ZDW is almost same as the Ti:sapphire laser wavelength. The ultrabroad spectrum is efficiently generated by self-phase modulation (SPM), because the pulses can propagate in the TF without temporal pulse broadening due to the dispersion. (For the relation between waist diameter and dispersion, see [17, 61].)

The experimental setup for ultrabroadband spectrum generation by TF is shown in Fig. 2.22. The pulses from a mode-locked Ti:sapphire laser (100-MHz repetition rate, 150-fs pulse width, 295-mW average power, and 790-nm center wavelength with up-chirp) were focused into the fiber (24% output efficiency). The output pulses were measured by a spectrometer. We characterized the input power dependence of spectral broadening by changing the input average power. Figure 2.23 shows the dependence of the output spec-

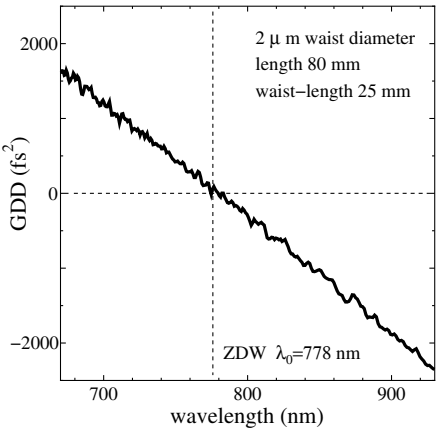

Fig. 2.21. Typical measured group delay dispersion (GDD) of tapered fiber [60]

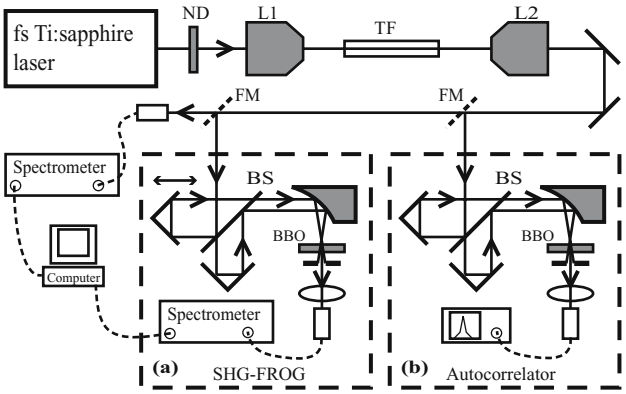

Fig. 2.22. Experimental setup for TF output pulse measurement. FM, flipper mirror; ND, neutral density filter; L1, L2, reflective objective lenses (×36). (**a**) SHG-FROG; BS, beam splitter; BBO, type I thickness 50 μm. (**b**) Autocorrelator; BBO, type I thickness 45 μm

trum on the average input power. Spectral broadening due to dispersive SPM in the fiber was found to occur when the average input power was greater than 90 mW. In addition, increased input power resulted in rapidly increased output spectral widths. The maximum spectral width was measured to range from 425 to 945 nm, with an input power of 295 mW.

Next, the output pulses were characterized by a second-harmonic generation frequency-resolved optical gating (SHG-FROG) apparatus [6,38,52] that was equipped with a spectrometer. The optical configuration of SHG-FROG apparatus are shown in Fig. 2.22. A delay was introduced with a Michelson interferometer arm for the fiber output pulses. After that, the pulses were

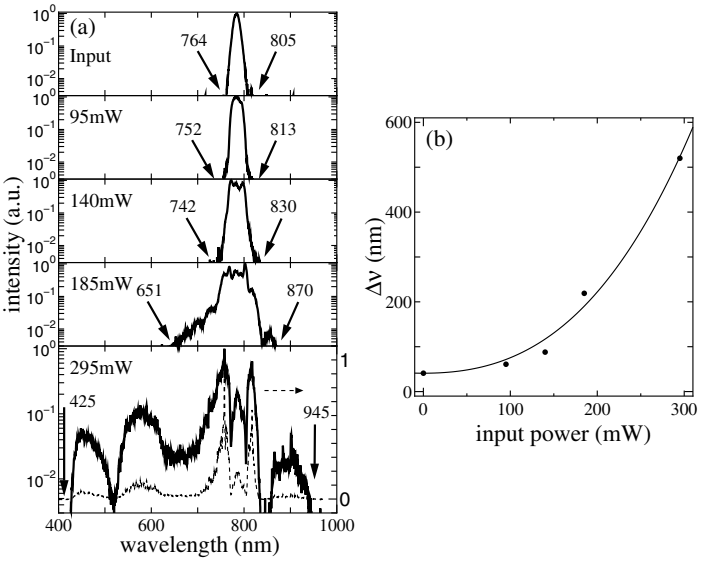

Fig. 2.23. (a) Dependence of the output spectrum on the input average power. (b) Input average power dependence of the full width in output spectrum

then focused onto a BBO crystal (type I; thickness 50 μm) by a parabolic mirror (f =50 mm) for second harmonic generation. The second harmonic wave was separated from the fundamental wave with a band pass-filter and measured with a spectrometer. The temporal profile was reconstructed by the analysis [6, 38, 52] based on these spectra as a function of the delay time. Additionally, we measured output pulses by an autocorrelator in order to compare autocorrelation traces with the SHG-FROG results.

The output power dependence (accordingly, input power dependence) of the spectral phase and the temporal profile is shown in Fig. 2.24. We approximated these spectral phases by a third order polynomial and calculated the group delay time $\dot{\phi}$, the group delay dispersion (GDD) $\ddot{\phi}$, and the third order dispersion $\dddot{\phi}$ including the up-chirp effect of the input pulses. When $\ddot{\phi}_{\mathrm{IN}}$ denotes the corresponding effective GDD at 785 nm (center wavelength) of the input up-chirped pulses and $\ddot{\phi} = \ddot{\phi}_{\mathrm{IN}} + \ddot{\phi}_{\mathrm{W+M}} + \Delta_{\mathrm{SPM}}$ at 785 nm, it was confirmed that $\ddot{\phi}_{IN} > \ddot{\phi} > 0$. Here, $\ddot{\phi}_{\mathrm{W+M}}$ and Δ_{SPM} denote the effective GDD due to the waveguide and material dispersions and SPM in TF, respectively. This result suggests that the effective GDD of $\ddot{\phi}_{\mathrm{W+M}} + \Delta_{\mathrm{SPM}}$ for the TF at the central wavelength of the input pulse was negative, which is consistent with the calculated GDD of $\ddot{\phi}_{\mathrm{W+M}} < 0$ in [17] because of $\Delta_{\mathrm{SPM}} > 0$. As the output power from the fiber increases, the $\ddot{\phi}$ and $\dddot{\phi}$ decrease slowly (+2500 to +1800 fs^2 for $\ddot{\phi}$ at 785 nm; +3000 to +1000 fs^3 for $\dddot{\phi}$ at 78 nm).

When the output power from the fiber was large, the output pulse was divided into three pulses, as shown in Fig. 2.24(b). Moreover, the larger the

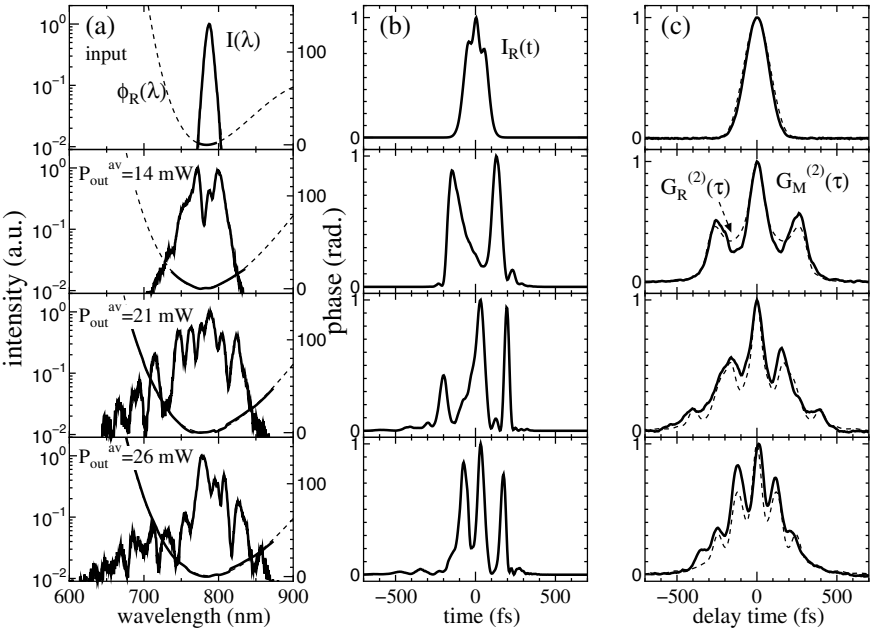

Fig. 2.24. Fiber output average-power dependences. (**a**) Measured spectrum $I(\lambda)$ and spectral phase $\phi_{\mathrm{R}}(\lambda)$. (**b**) Reconstructed pulse $I_{\mathrm{R}}(t)$. (**c**) Reconstructed $G_{\mathrm{R}}^{(2)}(\tau)$ (*solid line*) and measured $G_{\mathrm{M}}^{(2)}(\tau)$ (*dotted line*) autocorrelation traces

output power, the shorter the trailing pulse tended to be. The shortest trailing pulse was a result of a soliton effect near the ZDW region at the minimum group velocity.

The autocorrelation traces are shown in Fig. 2.24(c). Measured autocorrelation traces are also in agreement with the reconstructed autocorrelation traces, particularly in regards to the widths and the positions of the small internal structure within the traces. For quantitative clarification of mechanisms, an analysis of the nonlinear propagation equation such as Chap. 1 will be needed.

2.5 Concluding Remarks

This chapter reviewed our recent studies (1996–2003) on the efficient generation of ultrashort optical pulses having a near or over one-octave bandwidth with a well-behaved spectral phase by new methods (not by the conventional method using SPM glass fibers). That is, for the pulse generation with a several-hundred THz bandwidth in the near-infrared to the visible, ultraviolet region, the IPM technique for glass fibers (480–900 nm; 710–1250 nm) and

gas-filled hollow fibers (300–1000 nm) and the SPM technique for structure-controlled glass fibers (480–1020 nm; 425–955 nm) with a shorter zero-GDD wavelength were described in detail. Both of them enable us to more efficiently broaden the bandwidth than the general SPM technique for conventional glass fibers and hollow fibers. Moreover, comparison between both methods shows that the former (IPM technique) has the advantage of the capability to generate the continuum with an arbitrary center wavelength regardless of fiber dispersion, by selective combinations of different wavelength signal and idler pulses from an OPA, the fundamental pulse and its harmonic pulses as different-color fiber-input pulses. On the other hand, the latter (structure-controlled glass fiber technique) has the advantage of providing more efficient generation at a high pulse-repetition rate under the limited center wavelength of the input pulse. Therefore, the application of the IPM technique with high-harmonic waves as input pulses for the structure-controlled fibers with unusual dispersion characteristics may lead to interesting possibilities as optical sources of electric-field manipulation (see Chap. 6) for applications to optical information technology and quantum state control.

Many interesting works concerning photonic crystal fibers (for example: pulse generation with an over-two-octave bandwidth [59, 61]), tapered fibers [16, 17] and conventional SPM spectral broadening have been reported recently, a very few of which have been mentioned in this chapter.

One of the authors (M. Yamashita) thanks L. Xu and M. Hirasawa for their experimental works on IPM glass fiber.

References

1. R.R. Alfano, S.L. Shapiro: Phys. Rev. Lett. **24**, 584 (1970)
2. R.R. Alfano ed.: *The Supercontinuun Laser Source* (Springer-Verlag, Berlin, 1989)
3. F. Shimizu: Phys. Rev. Lett. **19**, 1097 (1967)
4. D.E. Spence, P.N. Kean, W. Sibbett: Opt. Lett. **16**, 42 (1991)
5. T. Brabec, F. Krausz: Rev. Mod. Phys. **72**, 545 (2000)
6. R. Trebino, D.J. Kane: J. Opt. Soc. Am. A **10**, 1101 (1993)
7. J.-C. Diels, W. Rudolph: *Ultrashort Laser Pulse Phenomena* (Academic Press, San Diego, 1996)
8. C. Iaconis, I.A. Walmsley: Opt. Lett. **23**, 792 (1998)
9. D. Grischkowsky, A.C. Balant: Appl. Phys. Lett. **41**, 1 (1981)
10. A. Shirakawa, I. Sakane, M. Takasaka, T. Kobayashi: Appl. Phys. Lett. **74**, 2268 (1999)
11. M. Yamashita, H. Sone, R. Morita: Jpn. J. Appl. Phys. **35**, L1194 (1996)
12. M. Yamashita, H. Sone, R. Morita, H. Shigekawa: IEEE J. Quantum Electron. **34**, 2145 (1998)
13. L. Xu, N. Karasawa, N. Nakagawa, R. Morita, H. Shigekawa, M. Yamashita: Opt. Commun. **162**, 256 (1999)
14. N. Karasawa, R. Morita, L. Xu, H. Shigekawa, M. Yamashita: J. Opt. Soc. Am. B **16**, 662 (1999)

15. N. Karasawa, R. Morita, H. Shigekawa, M. Yamashita: Opt. Lett. **25**, 183 (2000)
16. J.K. Ranka, R.S. Windeler, A.J. Stentz: Opt. Lett. **25**, 25 (2000)
17. T.A. Birks, W.J. Wadsworth, P.S.J. Russel: Opt. Lett. **25**, 1415 (2000)
18. M. Nisoli, S. De Silvestri, O. Svelto: Appl. Phys. Lett. **68**, 2793 (1996)
19. H. Nishioka, W. Odajima, K. Ueda, H. Takuma: Opt. Lett. **20**, 2505 (1995)
20. A. Baltuska, Z. Wei, M.S. Pshenichnikov, D.A. Wiersma: Opt. Lett. **22**, 102 (1997)
21. J.A. Armstrong, N. Bloembergen, J. Ducuing, P.S. Pershan: Phys. Rev. **127**, 1918 (1962)
22. G.D. Boyd, D.A. Kleinman: J. Appl. Phys. **39**, 3597 (1968)
23. A. Yariv : *Optical Electronics* (Saunders, Philadelphia, PA, 1991) pp.285-308
24. R. Wynands, O. Coste, C. Renbe, D. Maschede: Opt. Lett. **20**, 1095 (1995)
25. G.P. Agrawal : *Nonlinear Fiber Optics* (Academic Press, San Diego, CA, 1995) pp.44-48, 172-179
26. W.J. Tomlinson, R.H. Stolen, C.V. Shank: J. Opt. Soc. Am. B **1**, 139 (1984)
27. A. Shirakawa, I. Sakane, T. Kobayashi: Opt. Lett. **23**, 1292 (1998)
28. M. Hirasawa, N. Nakagawa, M. Shibata, R. Morita, H. Shigekawa, M. Yamashita: *Tech. Digest of Conf. Lasers and Electro-Opt. 2001* (Opt. Soc. Ame. Washington DC 2001)
29. M. Shibata, M. Hirasawa, N. Nakagawa, R. Morita, A. Suguro, H. Shigekawa, M. Yamashita: Appl. Phys. B **74**, S291 (2002)
30. M. Yamashita, M. Hirasawa, N. Nakagawa, K. Yamamoto, K. Oka, R. Morita: J. Opt. Soc. Ame. B **21**, 458 (2004)
31. R.E.U. Morgner, F.X. Kärtner, J.G. Fujimoto, E.P. Ippen, V. Scheuer, G. Angelow, T. Tschudi, M.J. Lederer, A. Boiko, B. Luther-Davies: Opt. Lett. **26**, 373 (2001)
32. T.R. Schibli, J. Kim, O. Kuzucu, J.T. Gopinath, S.N. Tandon, G.S. Petrich, L.A. Kolodziejski, J.G. Fujimoto, E.P. Ippen, F.X. Käertner: Opt. Lett. **28**, 947 (2003)
33. R.R. Alfano, P.P. Ho: IEEE J. Quantum Electron. **24**, 351 (1988)
34. Z. Wei, M.S. Pshenichnikov, D.A. Wiersma, R. Szipőcs: Appl. Phys. B **65**, 175 (1997)
35. Nisoli, S. Stagira, S. De Silvestri, O. Svelto, S. Sartania, Z. Cheng, M. Lenzner, C. Spielmann, F. Krausz: Appl. Phys. B **65**, 189 (1997)
36. G.P. Agrawal: *Nonlinear Fiber Optics*, 3rd ed. (Academic, San Diego, CA 2001), Chaps. 2, 5 and 10.
37. G.P. Agrawal, P.L. Baldeck, R.R. Alfano: Phys. Rev. A **40**, 5063 (1989)
38. J.N. Sweetser, D.N. Fittinghoff, R. Trebino: Opt. Lett. **22**, 519 (1997)
39. S. Coen, A. Hing, L. Chau, R. Leonhardt, J.D. Harvey, J.C. Knight, W.J. Wadsworth, P.S.J. Russell: Opt. Lett. **26**, 1356 (2001)
40. K.J. Blow, D. Wood: IEEE J. Quantum Electron. **25**, 2665 (1989)
41. T. Brabec, F. Krausz: Phys. Rev. Lett. **78**, 3282 (1997)
42. N. Karasawa, S. Nakamura, N. Nakagawa, M. Shibata, R. Morita, H. Shigekawa, M. Yamashita: IEEE J. Quantum Electron. **37**, 398 (2001)
43. J.M. Dudley, S. Coen: Opt. Lett. **27**, 1180 (2002)
44. A.V. Husakou, J. Herrmann: Phys. Rev. Lett. **87**, 203901-1 (2001)
45. J. Herrmann, U. Griebner, N. Zhavoronkov, A. Husakou, D. Nickel, J.C. Knight, W.J. Wadsworth, P.S.J. Russell, G. Korn: Phys. Rev. Lett. **88**, 173901-1 (2002)

46. N. Karasawa, R. Morita, H. Shigekawa, M. Yamashita: Opt. Commun. **197**, 475 (2001)
47. D.A. Akimov, A.A. Ivanov, M.V. Alfimov, S.N. Bagayev, T.A. Birks, W.J. Wadsworth, P.S.J. Russell, A.B. Fedotov, V.S. Pivtsov, A.A. Podshivalov, A.M. Zheltikov: Appl. Phys. B **74**, 307 (2002)
48. I. Hartl, X.D. Li, C. Chuclaba, R. Ghanta, T. Ko, J.G. Fujimoto, J.K. Ranka, R.S. Windeler, A.J. Stentz: Opt. Lett. **26**, 608 (2001)
49. R. Holzwarth, T. Udem, T.W. Hansch, J.C. Knight, W.J. Wadsworth, P.S.J. Russell: Phys. Rev. Lett. **85**, 2264 (2000)
50. M. Hirasawa, N. Nakagawa, K. Yamamoto, R. Morita, H. Shigekawa, M. Yamashita: Appl. Phys. B **74**, S225 (2002)
51. M. Zavelani-Rossi, G. Cerullo and S. Silvestri, L. Gallmann, N. Matuschek, G. Steinmeyer, U. Keller, G. Angelow, V. Scheuer, T. Tschudi: Opt. Lett. **26**, 1155 (2001)
52. N. Karasawa, L. Li, A. Suguro, H. Shigekawa, R. Morita, M. Yamashita: J. Opt. Soc. Am. B **18**, 1742 (2001)
53. A.M. Weiner, D.E. Leaird, J.S. Patel, J.R. Wullert: Opt. Lett. **15**, 326 (1990)
54. S. Coen, A.H.L. Chau, R. Leonhardt, J.D. Harvey, J.C. Knight, W.J. Wadsworth, P.S.J. Russell: Opt. Lett. **26**, 1356 (2001)
55. X. Fang, N. Karasawa, R. Morita, R.S. Windeler, M. Yamashita: IEEE Photonics. Technol. Lett. **15**, 233 (2003)
56. C. Dorrer, P. Londero, I.A. Walmsley: Opt. Lett. **26**, 1510 (2001)
57. K. Yamane, N. Karasawa, S. Kusaka, M. Hirasawa, A. Suguro, H. Shigekawa, R. Morita, M. Yamashita: *Tech. Digest of Conf. Lasers and Electro-Opt 2002* (Optical Society of America, Washington DC, 2002) pp. 457
58. L. Li, S. Kusaka, N. Karasawa, R. Morita, H. Shigekawa, M. Yamashita: Jpn. J. Appl. Phys. **40**, L684 (2001)
59. D.A. Akimov, A.A. Ivanov, M.V. Alfimov, S.N. Bagayev, T.A. Birks, W.J. Wadsworth, P.S. Russell, A.B. Fedotov, V.S. Pivisov, A.A. Podshivalov, A.M. Zheltikov: Appl. Phys. B **74**, 307 (2002)
60. K. Naganuma: *Extendea Abstracts of the 49th Spring Annual Meeting of Japanese Applied Physics* (Japan Society of Applied Physics, Tokyo, 2002, March), No. 3, p. 1067
61. A. Bjarklev, J. Broeng, A.S. Bjarklev: *Photonic Crystal Fibers* (Kluwer Academic Publishers, Dordrecht, 2003)
62. R.L. Fork, O.E. Martinez, G.P. Gordon: Opt. Lett. **9**, 150 (1984)

3 Active Chirp Compensation for Ultrabroadband Optical Pulses

M. Yamashita, R. Morita, and N. Karasawa

3.1 Introduction

Frequency chirp refers to the physical phenomenon in which the electric-field frequency $\nu(t)$ of an optical pulse is swept instantaneously during its pulse dilation t_p as a function of time t [1]. When the time-dependent frequency is done constantly by techniques, the pulse has its shortest duration which is limited by its spectral bandwidth $\Delta\nu_T$ (Fig. 3.1) [2,3]. This process is called chirp compensation, and its chirp-free pulse is said to be Fourier transform-limited. Accordingly, for the generation of ultrashort optical pulses (from picoseconds (ps) to femtoseconds (fs) :$10^{-12} - 10^{-15}$ s) having an ultrabroadband width (from sub terahertz (THz) to sub petahertz (PHz) :$10^{11} - 10^{15}$ Hz) with strong chirp, techniques for chirp compensation are needed.

Figure 3.2 shows an illustrated scheme of techniques developed for chirp compensation. In the most simple case, linear up- or down-chirp occurs corresponding to the linearly increasing or decreasing frequencies with the increase of time, respectively. Among them, linear up-chirp is often observed owing to pulse propagation through a medium with second-order positive phase dispersion and/or a positive nonlinear refractive index causing self-phase modulation (SPM). Then, the first optical chirp compensation was carried out by a pair of gratings providing second-order negative phase dispersion to generate shorter pulses in 1969 [4]. After that (in 1980 to 1990), for intracavity chirp compensation of a dye laser, two pairs of Brewster-angled prisms [5], or a pair of Gires-Tournois interferometers [6], or double-stacked dielectric mirrors [7] were employed. In addition, for external optical pulse compression, nonlinear chirp yielded by dispersive SPM in a fused-silica fiber was compensated for by a combination of double pairs of prisms and double pairs of gratings [8]. Moreover, in 1995 chirped-layer dielectric mirrors were demonstrated to be useful for compensation of intracavity chirp in a Ti:sapphire laser for the generation of sub-10 fs pulses [9]. Furthermore, improved double-chirped mirrors were reported [10]. As pulses (to be compensated) become shorter and shorter, however, it was found that those chirp compensators (which we call passive elements) have problems as follows: a bandwidth limitation, an inter-relation among different orders ($\phi^{(n)}(\omega_0) \equiv \mathrm{d}^n\phi(\omega)/\mathrm{d}\omega^n|_{\omega=\omega_0}$) of phase dispersion $\phi(\omega)$, and the requirement of physical realignment for the adjustment of compensation. That is, it is significantly difficult for pulses

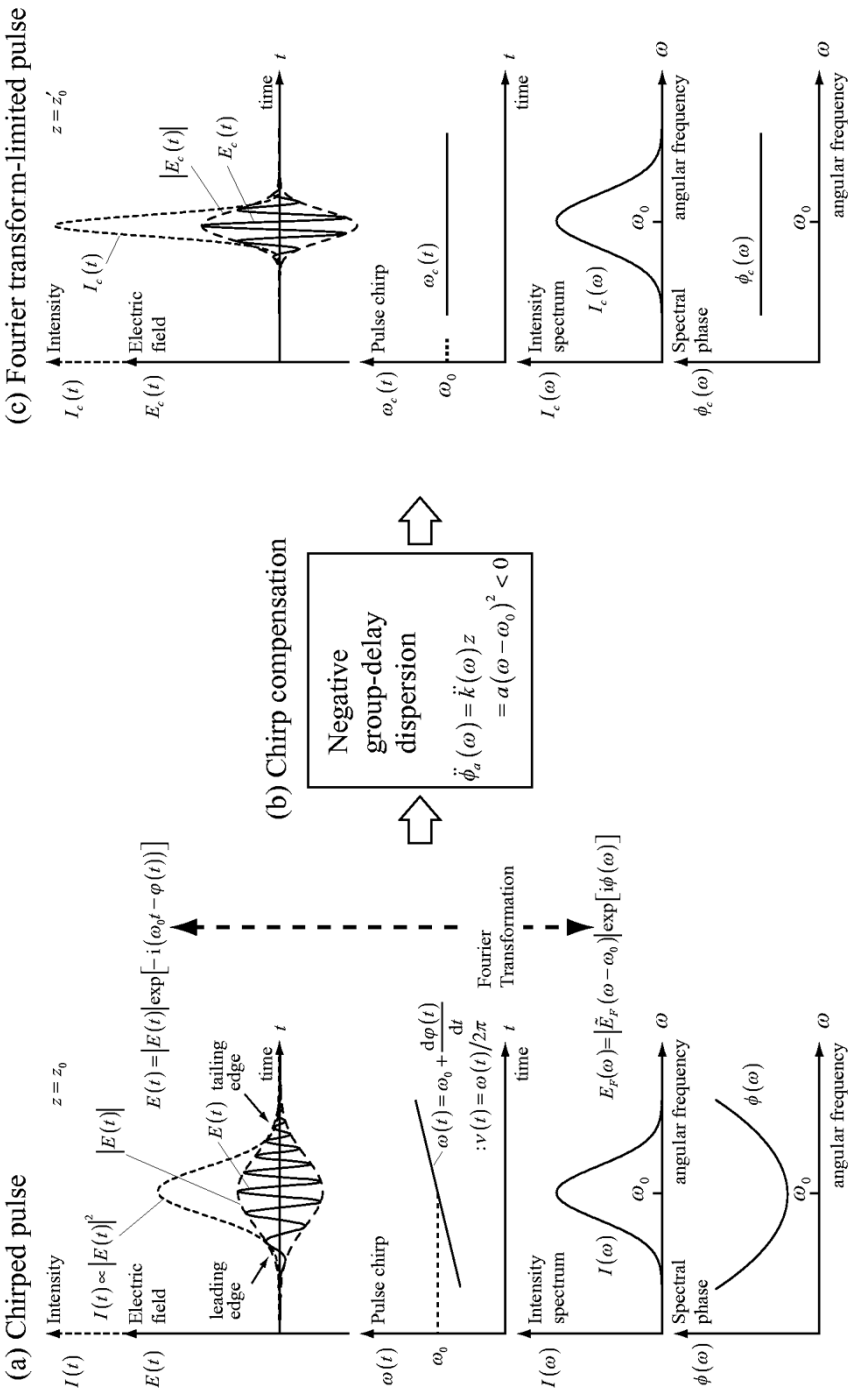

Fig. 3.1. Linearly up-chirped pulse and its chirp compensation

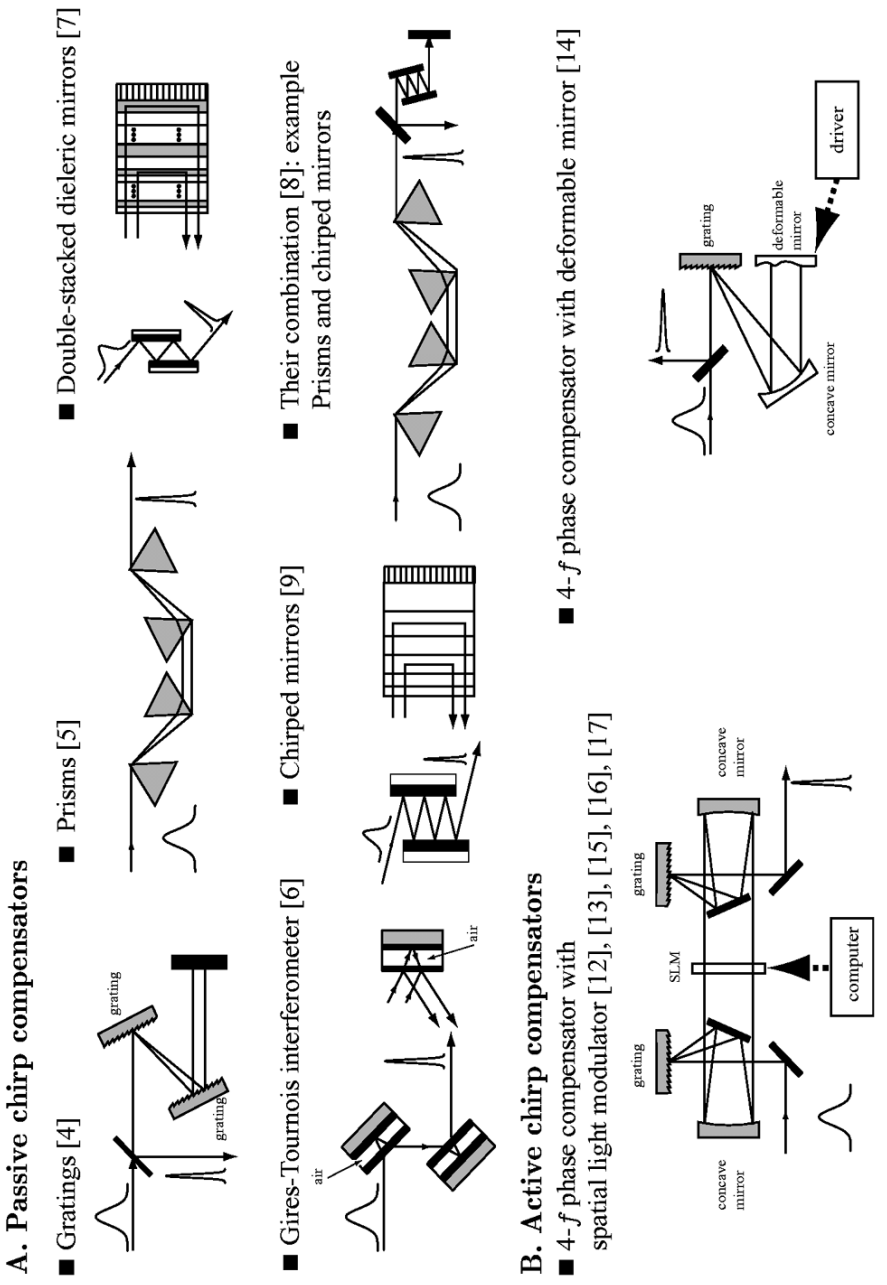

Fig. 3.2. Various passive and active chirp compensators. SLM: spatial light modulator

with an ultrabroadband width of near or over one-octave to compensate for their nonlinear chirps using those passive elements.

To overcome those problems, in 1996 it was pointed out [11] that a 4-f pulse shaper [12] with a spatial light modulator (SLM) (which consists of one-dimensional liquid-crystal-cell array with many pixels) can be applied for chirp compensation of one-octave-exceeding pulses corresponding to few or one optical-cycle pulses after its compensation. This SLM technique has many advantages, including over one-octave bandwidth, compensation ability for arbitrary, complicated phase dispersion $\phi(\omega)$, computer-programmable phase control, quasi-real-time phase adjustment by applied DC electric fields without any realignment and automatic-feedback control. We call this device an active compensator. In 1997, it was demonstrated that the SLM technique is available for a compensator of 80-fs chirped pulses (to 11 fs) directly from a Ti:sapphire laser [13]. In 1999, another active compensator was reported, which consists of membrane deformable mirrors controlled by a mechanical activator [14]. However, this technique is inferior to the SLM one concerning the following points: a low spatial and phase resolution, cumbersome and imperfect phase calibration due to complex membrane deflection and high deflection losses. Recently, the SLM technique was applied for a programmable pulse compression to the sub-6 fs regime [15] and the 4-fs regime [16]. This is the first demonstration of few-cycle pulse generation by an SLM compensator. More recently, the feedback phase compensation that combines the SLM technique and a spectral-phase measurement technique has enabled us to generate optical pulses in the monocycle region, which is the shortest one in the near infrared to visible region [17] (see Chap. 5). Table 3.1 summarizes the major accomplishments in this field over past 30 years.

In this chapter we focus on the practical SLM technique as an active chirp compensator for the generation of few-cycle optical pulses (bandwidths of up-to several hundred THz) including the description of its principle and theory.

3.2 Principle and Theory: Chirp Compensator with Spatial Light Modulator (SLM)

In order to obtain monocycle or few-cycle optical pulses, a nonlinear chirp compensation technique for ultrabroadband femtosecond optical pulses is essential. Conventionally, chirp compensation was performed by passive techniques using prism-pairs, grating-pairs, chirped mirrors or the combination of some of these. However, these passive techniques have some disadvantages such as inter-dependence of different orders of dispersion compensation, inability to fine-tune the phase in experimental setup and bandwidth limitation. Thus, to overcome these disadvantages, a nonlinear chirp compensation technique using a 4-f optical pulse shaper with a spatial light phase modulator (SLM), which gives, inter-independent of different orders of dispersion,

Table 3.1. Progress in chirp compensation and optical pulse compression

Year	Accomplishment	Researcher	References
1969	Picosecond optical pulse compression based on chirp compensation by a grating pair	Treacy	[4]
1981	Optical pulse compression using single-mode fused silica fiber	Grischkowsky, Balant	[50]
1984	Dye laser chirp compensation by Brewster-angled prism pairs for pulse generation shorter than 100 fs	Fork, Martinez, Gordon	[5]
1986	Dye laser chirp compensation by Gires–Tournois interferometers	J. Kuhl, J. Heppner	[6]
1986	Dye laser chirp compensation by double-stacked laser-cavity mirrors by themselves	Yamashita, Ishikawa, Torizuka, Sato	[7]
1987	6-fs pulse compression consisting of fused silica fiber and combination of prism-pairs and grating-pairs chirp compensators	Fork, Brito Cruz, Becker, Shank	[8]
1988	Intracavity pulse compression using nonlinear organic material	Yamashita, Torizuka, Sato	[51]
1991	Efficient external pulse compression using nonlinear organic-crystal fiber	Yamashita, Torizuka, Umemiya, Shimada	[52]
1992	Chirp compensation by SLM phase compensator	Weiner, Leaird, Patel, Wullert	[12]
1994-1995	Ti:sapphire laser chirp compensation by chirped mirrors	Szipőcs, Ferencz, Spielmann, Krausz, Stingl, Lenzner	[9], [53]
1996	High powered pulse compression using gas-filled hollow fiber	Nisoli, Silvestri, Svelto	[54]
1996-2003	4-6 fs pulse compression using SPM and/or IPM techniques and SLM phase compensation	Yamashita, Sone, Morita, Xu, Karasawa, Suguro	[11], [15], [16], [21] [42], [43]
1997	Chirp compensation by doubled-chirped mirrors	Jung, Kärtner, Matuschek, Sutter, Grenoud, Zhang, Keller, Scheuer, Tilsch, Tschudi	[10]

Table 3.1. (cont.)

Year	Accomplishment	Researcher	References
1997	sub-5 fs compression of cavity-dumped laser pulse using fused silica fiber	Baltuska, Wei, Szipőcs, Pshenichnikov, Wielsma	[55]
1997	Feedback chirp compensation of Ti:sapphire laser pulse (80 fs to 11 fs) by combination of SLM phase compensator and SHG output	Yelin, Meshulach, Silberberg	[13]
1998-1999	High powered 5-fs pulse compression using gas-filled hollow fiber	Cheng, Fürbach, Sartania, Lenzner, Spielmann, Krausz	[24], [25]
1999	Chirp compensation for laser output pulse by deformable mirror	Zeek, Maginnis, Backus, Russek, Murmane, Mourou, Kapteyn	[14]
1999	Sub 5-fs compression for non-collinear optical-parametric amplified pulse	Shirakawa, Sakane, Takasaka, Kobayashi	[36]
2001	5-fs pulse generation from octave-scanning Ti:sapphire laser	Morgner, Kärtner, Fujimoto, Ippen, Scheuer, Angelow, Tschudi, et al	[56]
2002	4-fs pulse generation based on chirp compensation for OPA pulse by combination of prisms, chirped mirrors and deformable mirror	Baltuska, Fuji, Kobayashi	[57]
2003	Direct feedback 3.3-fs-pulse compression using gas-filled hollow fiber by combination of SLM phase compensator and M-SPIDER	Yamane, Zhang, Oka, Morita, Yamashita, Suguro	[17]
2003	Feedback pulse compression of tapered fiber pulse by combination of SLM phase compensator and M-SPIDER	Adachi, Hirasawa, Suguro, Karasawa, Kobayashi, Morita, Yamashita	[58]
2003	Feedback pulse compression of photonic crystal fiber by combination of SLM phase compensator and M-SPIDER	Adachi, Yamane, Morita, Yamashita	[59]
2004	Generation of 2.8-fs, 1.5 cycle, single, clean TL pulse using direct feedback compression technique	Yamane, Kito, Morita, Yamashita	[60]

(quasi-arbitrary dispersion), *in-situ* adaptive phase control and has a broader bandwidth, was proposed and demonstrated [11,15,16]. However, this active method using an SLM has some restrictions such as (i) a frequency-dependent time window due to finite beam size, (ii) the existence of pixel gaps, (iii) the discreteness of the modulated phase in an SLM due to its finite pixel size, and (iv) the maximum phase applied by SLM is limited and thus the phase is applied in the wrapped form. The effects of these restrictions on the nonlinear chirp compensation have not been studied so far.

First, we describe the principle and theory of the nonlinear chirp compensation with an SLM in this section.

Second, to investigate the effects of above-mentioned restrictions on pulse compression, we numerically analyze chirp compensation for ultrabroadband femtosecond optical pulses using an SLM, especially taking these restrictions into account.

Projection of Ultrabroadband Pulses on the Fourier Plane

First, we analyze the phase modulation using a 4-f pulse shaper [12,13] with an SLM. The nonlinear chip compensation system composed of a 4-f pulse shaper with an SLM is schematically shown in Fig. 3.3.

The real electric field $E(t)$ can be decomposed into its complex electric fields $E^{(+)}(t)$ and $E^{(-)}(t)$ using the following relations:

$$\tilde{E}(\omega) = \int_{-\infty}^{\infty} \mathrm{d}t \; \mathrm{e}^{\mathrm{i}\omega t} E(t), \tag{3.1}$$

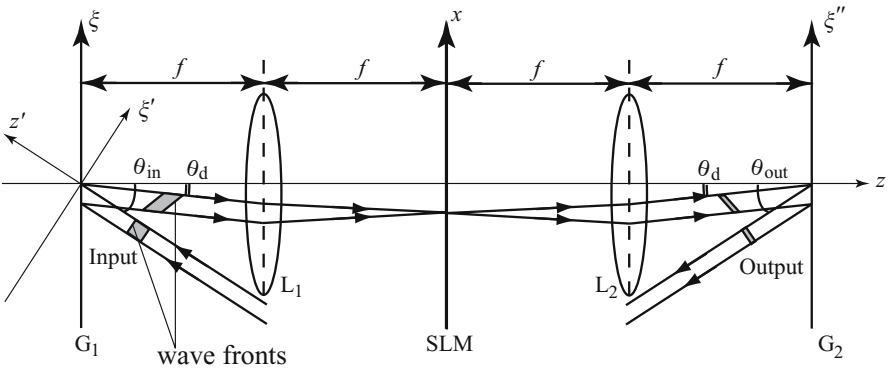

Fig. 3.3. 4-f chirp compensator. G_1, G_2: gratings, L_1, L_2: lenses, SLM: spatial light modulator. Since the diffraction angle θ_d on G_1 differs from the incident angle θ_{in}, the wave front of the input beam is tilted after diffraction, resulting in the temporal-to-spatial conversion

$$E^{(+)}(t) = \frac{1}{2\pi}\int_0^\infty \mathrm{d}\omega\ \mathrm{e}^{-\mathrm{i}\omega t}\tilde{E}(\omega), \tag{3.2}$$

$$E^{(-)}(t) = \frac{1}{2\pi}\int_{-\infty}^0 \mathrm{d}\omega\ \mathrm{e}^{-\mathrm{i}\omega t}\tilde{E}(\omega), \tag{3.3}$$

$$E(t) = E^{(+)}(t) + E^{(-)}(t) = 2\mathrm{Re}[E^{(+)}(t)]. \tag{3.4}$$

Here, $E^{(+)}(t)$ and $E^{(-)}(t)$ are complex-conjugate with each other. This temporal representation is related to a frequency representation by a Fourier transform,

$$\tilde{E}^{(+)}(\omega) = \int_{-\infty}^\infty \mathrm{d}t\ \mathrm{e}^{\mathrm{i}\omega t}E^{(+)}(t), \tag{3.5}$$

and vice versa (inverse Fourier transform),

$$E^{(+)}(t) = \frac{1}{2\pi}\int_{-\infty}^\infty \mathrm{d}\omega \mathrm{e}^{-\mathrm{i}\omega t}\tilde{E}^{(+)}(\omega). \tag{3.6}$$

Let us now consider an input complex electric field $E_0^{(+)}(\xi', z', t)$ expressed by

$$\begin{aligned} E_0^{(+)}(\xi', z', t) &= R(\xi')U(t - z'/c)\exp[-\mathrm{i}\omega_0(t - z'/c)] \\ &= R(\xi')\int_{-\infty}^\infty \frac{\mathrm{d}\omega}{2\pi}\tilde{U}(\omega - \omega_0)\exp[-\mathrm{i}\omega(t - z'/c)]. \end{aligned} \tag{3.7}$$

including the spatial coordinates explicitly. Here $U(t)$ is the temporal shape of the envelope and $R(\xi')$ is the spatial pattern of the input field, where ξ' is the spatial coordinate perpendicular both to the propagation direction z' of the input pulse and to the groove direction of the first grating G_1 (Fig. 3.3). The variable t is time, c is the velocity of light in a vacuum and ω_0 is the carrier angular frequency. $\tilde{U}(\omega)$ is the Fourier transform of $U(t)$ as defined by

$$\tilde{U}(\omega) = \int_{-\infty}^\infty \mathrm{d}t\, U(t)\exp(\mathrm{i}\omega t) \tag{3.8}$$

where ω is the optical angular frequency.

After diffraction by the grating G_1, the diffracted complex field $E_1^{(+)}(\xi, z = 0, t)$ on the grating (at $z = 0$) is expressed by

$$\begin{aligned} &E_1^{(+)}(\xi, z = 0, t) \\ &= g(\xi)R(\xi\cos\theta_{\mathrm{in}})U(t - \xi\sin\theta_{\mathrm{in}}/c)\exp[-\mathrm{i}\omega_0(t - \xi\sin\theta_{\mathrm{in}}/c)] \\ &= g(\xi)R(\xi\cos\theta_{\mathrm{in}})\int_{-\infty}^\infty \frac{\mathrm{d}\omega}{2\pi}\,\tilde{U}(\omega - \omega_0)\exp[-\mathrm{i}\omega(t - \xi\sin\theta_{\mathrm{in}}/c)] \\ &= \exp(-\mathrm{i}\omega_0 t)g(\xi)R(\xi\cos\theta_{\mathrm{in}})\int_{-\infty}^\infty \frac{\mathrm{d}\omega}{2\pi}\,\tilde{U}(\omega) \\ &\quad\times\exp[-\mathrm{i}\omega(t - \xi\sin\theta_{\mathrm{in}}/c)], \end{aligned} \tag{3.9}$$

where ξ is the spatial coordinate perpendicular both to the propagation direction z of the diffracted pulse and to the groove direction of the first grating G_1, θ_{in} is the incident angle to the grating G_1 and $g(\xi)$ is the reflectivity of the grating G_1 at ξ. It should be noted that, since the diffraction angle θ_d on G_1 differs from the incident angle θ_{in}, the wave front of the input beam is tilted (not normal to the propagation direction) after diffraction. This results in the temporal-to-spatial conversion, which is seen as the replacement of the argument t of the function U before diffraction in (3.7) with $t - \xi \sin\theta_{in}/c$ after diffraction in (3.9).

After passing through a lens L_1 with a focal length f located at a distance of f from the grating G_1, the field of the pulse is spatially Fourier transformed. The complex electric field $E_2^{(+)}(x, z = 2f, t)$ on the focal plane of $z = 2f$ is written by

$$\begin{aligned} &E_2^{(+)}(x, z = 2f, t) \\ &\propto \exp(-\mathrm{i}\omega_0 t) \int_{-\infty}^{\infty} \mathrm{d}\xi \int_{-\infty}^{\infty} \frac{\mathrm{d}\omega}{2\pi}\, g(\xi) R(\xi \cos\theta_{in}) \omega \tilde{U}(\omega) \\ &\quad \times \exp[-\mathrm{i}\omega(t - \xi \sin\theta_{in}/c)] \exp(-\mathrm{i}\omega x \xi / cf) \\ &= \mathrm{i} \exp(-\mathrm{i}\omega_0 t) \frac{\partial}{\partial t} \int_{-\infty}^{\infty} \mathrm{d}\xi\; g(\xi) R(\xi \cos\theta_{in}) U\left(t - \frac{\xi}{c}(\sin\theta_{in} - x/f)\right) \end{aligned} \tag{3.10}$$

on the basis of the Fourier optics [18], where x is the spatial coordinate in the intersection of $z = 2f$ and ξz-planes. In the diffraction theory of monochromatic light for a specific frequency ω, the factor ω is sometimes omitted [19,20]. However, it should be noted that, for ultrabroadband pulses, it cannot be omitted and the integration with respect to ω is necessary.

Hereafter, we consider only the first-order diffraction by G_1 and we put the reflectivity function of the grating as $g(\xi) \propto \exp(-\mathrm{i}2\pi\xi/d)$. Hence,

$$\begin{aligned} &E_2^{(+)}(x, z = 2f, t) \\ &\propto \mathrm{i} \frac{c}{\sin\theta_{in} - x/f} \frac{\partial}{\partial t} \int_{-\infty}^{\infty} \frac{\mathrm{d}k}{2\pi}\; \tilde{R}(k) \tilde{U}\left(\frac{c}{\sin\theta_{in} - x/f}\left(\frac{2\pi}{d} - k\cos\theta_{in}\right) - \omega_0\right) \\ &\times \exp\left\{-\mathrm{i}\left[\frac{c}{\sin\theta_{in} - x/f}\left(\frac{2\pi}{d} - k\cos\theta_{in}\right)\right] t\right\}. \end{aligned} \tag{3.11}$$

Here, the function $\tilde{R}(k)$ is defined as a spatial Fourier transform by

$$\tilde{R}(k) = \int_{-\infty}^{\infty} \mathrm{d}\xi\, R(\xi) \exp(-\mathrm{i}k\xi), \tag{3.12}$$

where k is the spatial frequency.

Under the condition that $t_p \ll w_0/c$ with the beam radius w_0 and pulse duration t_p, the function $\tilde{U}$ varies more gently than the function $\tilde{R}$ does.

This condition is satisfied, for the beam width $w_0 \simeq 1$ mm and $\cos\theta_{\rm in} \simeq 1$, when the pulse duration less is less than $\sim$3 ps. Hence, $E_2^{(+)}(x, z = 2f, t)$ is approximated by

$$\begin{aligned} & E_2^{(+)}(x, z = 2f, t) \\ \propto & \frac{2\pi}{d}\left(\frac{c}{\sin\theta_{\rm in} - x/f}\right)^2 \tilde{U}\left(\frac{2\pi}{d}\frac{c}{\sin\theta_{\rm in} - x/f} - \omega_0\right) \\ & \times \exp\left[-{\rm i}\left(\frac{2\pi}{d}\frac{c}{\sin\theta_{\rm in} - x/f}\right)t\right]. \end{aligned} \tag{3.13}$$

Here we suppose that the function $\tilde{R}(k)$ has its maximum value at $k = 0$. The function $\tilde{U}(\omega)$ is the spectrum of the temporal shape of the input electric field $U(t)$, thus we consider a specific frequency $\bar{\omega}$ that satisfies

$$\bar{\omega} = \frac{2\pi}{d}\frac{c}{\sin\theta_{\rm in} - x/f} \tag{3.14}$$

and the corresponding wavelength $\bar{\lambda} \equiv 2\pi c/\bar{\omega}$. From (3.14),

$$x = f\left(\sin\theta_{\rm in} - \frac{\bar{\lambda}}{d}\right). \tag{3.15}$$

It shows that wavelength components, not frequency components, are projected linearly on the x-coordinate on the Fourier plane at $z = 2f$ unlike the conventional analysis for narrow band pulses [19, 20].

In addition, when $x \ll f$, x/f can be approximated by

$$\frac{x}{f} \simeq -\tan\theta_{\rm d} \simeq -\sin\theta_{\rm d}, \tag{3.16}$$

where $\theta_{\rm d}$ is the diffraction angle at the grating G_1. Hence, from (3.13), we obtain the well-known first-order diffraction formula

$$d(\sin\theta_{\rm in} + \sin\theta_{\rm d}) = \lambda. \tag{3.17}$$

Principle of Chirp Compensation Using an SLM

To obtain the shortest pulse or the Fourier-transform-limited pulse for a given spectrum, phase compensation is necessary. This phase compensation makes the spectral phase $\phi(\omega)$ of the pulse satisfy the condition that

$$\frac{{\rm d}\phi(\omega)}{{\rm d}\omega} = {\rm const.} \tag{3.18}$$

or

$$\phi(\omega) = a^{(1)}\omega + a^{(0)}, \tag{3.19}$$

where the coefficients $a^{(1)}$ and $a^{(0)}$ are constant numbers. In the latter case, the pulse after modulation is delayed by the constant group delay $a^{(1)}$. However, since it is not important the for pulse compression result, the perfect phase compensation condition here is considered as (3.18). For the spectral phase $\phi_{\rm in}(\omega)$ of the input pulse into the 4-f pulse shaper, we can apply the arbitrary phase $\phi^{\rm SLM}(\omega)$ by SLM located on the Fourier plane ($z = 2f$) in principle. When we apply the phase $\phi^{\rm SLM}(\omega)$ such that

$$\frac{\rm d}{{\rm d}\omega}[\phi_{\rm in}(\omega) + \phi^{\rm SLM}(\omega)] = 0, \tag{3.20}$$

we achieve the phase compensation and obtain the Fourier-transform-limited pulse. The principle of this phase compensation is schematically shown in Fig. 3.4.

On the Fourier plane ($z = 2f$), the input complex electric field $E_{\rm in}^{(+)}(t)$ is approximately decomposed into the sum of plane waves $\exp(-{\rm i}\omega_k t)$ where ω_k is the center angular frequency projected on the kth pixel of the SLM. That is,

$$E_{\rm in}^{(+)}(t) \simeq \sum_{k=\pm 1}^{\pm N} \frac{\Delta\omega_k}{2\pi} \tilde{E}^{(+)}(\omega_k) \exp(-{\rm i}\omega_k t) W_k(t), \tag{3.21}$$

where ω_{-k} is defined as $-\omega_k$, $\Delta\omega_k$ is the bandwidth projected on the kth pixel, and $W_k(t)$ is the time-window function for the ω_k frequency component written by

$$W_k(t) = W_{-k}(t) = \begin{cases} 1, & \text{if } |t| \le T_{\rm w}(|\omega_k|)/2, \\ 0, & \text{if } |t| > T_{\rm w}(|\omega_k|)/2. \end{cases} \tag{3.22}$$

Here, $T_{\rm w}(\omega)$ is the frequency-dependent time window expressed by

$$T_{\rm w}(\omega) = \frac{2\pi w_0}{\omega d \cos\theta_{\rm in}}, \tag{3.23}$$

where w_0 is the beam size and $\theta_{\rm d}(\omega)$ is the frequency-dependent diffraction angle. The frequency-dependent time window $T_{\rm w}(\omega)$ is attributed to the tilted wave front after diffraction by the grating $\rm G_1$.

For the chirped pulse, the maximum points of frequency-resolved waves do not generally meet together at any specific time, as shown in Fig. 3.4(a). Hence, to perform the chirp compensation, the frequency-dependent spectral phase $\phi^{\rm SLM}(\omega_k)$ satisfying (3.20) is applied at each pixel using SLM and the electric field after this phase modulation is expressed by

$$\begin{aligned} E_{\rm mod}^{(+)}(t) \simeq & \sum_{k=\pm 1}^{\pm N} \frac{\Delta\omega_k}{2\pi} \tilde{E}^{(+)}(\omega_k) \exp\left\{-{\rm i}[\omega_k(t - \phi^{\rm SLM}(\omega_k)/\omega_k)]\right\} \\ & \times W_k(t - \phi^{\rm SLM}(\omega_k)/\omega_k). \end{aligned} \tag{3.24}$$

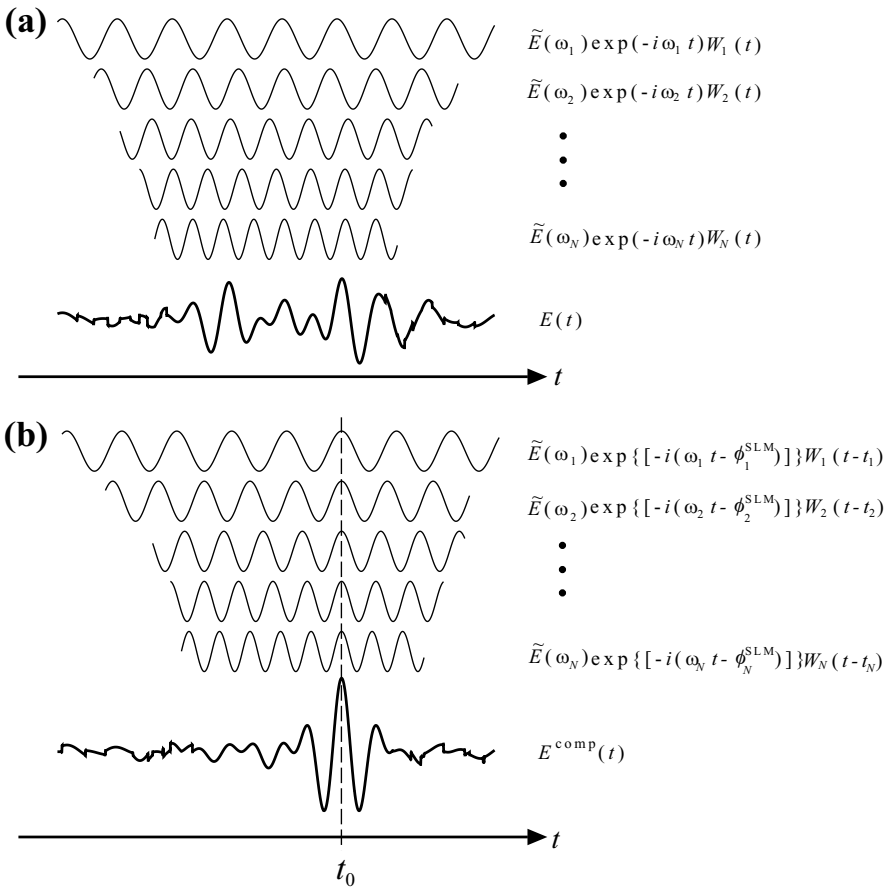

Fig. 3.4. Principle of phase compensation by 4-f pulse shaper. The phase $\phi^{\mathrm{SLM}}(\omega_k)$ and the delay $\phi^{\mathrm{SLM}}(\omega_k)/\omega_k$ are abbreviated to ϕ_k^{SLM} and t_k, respectively

Thus, by adjusting the delays of frequency-resolved waves, the maximum points of frequency-resolved waves meet at a specific time t_0. After passing through the right-half of the 4-f system, as a sum, the chirp-compensated pulse which peaks at t_0 is obtained as shown in Fig. 3.4(b). This implies that the maximum points of frequency-resolved waves do not necessarily coincide at the center temporal point ($t = 0$). That is, the phase variance at least 2π at the pixel of each frequency, which can make maximum points coincide at least at a certain time, is sufficient in principle. This is quite different from the conventional techniques using prism-pairs, grating pairs or chirped mirrors.

Thus, after the phase modulation by the SLM, passing through the second-half of the $4f$-system, the second lens L_2 and the second grating G_2,

the pulses are inverse-Fourier transformed and the compressed pulses in the time domain are obtained.

Model for Calculation

Let us consider the following 4-f chirp compensator for femtosecond ultrabroadband optical pulses (see Fig. 3.15). The 4-f system consists of a pair of diffraction gratings with grating constant d =1/150 mm, a pair of concave mirrors with focal length f =200 mm and an SLM with 150 pixels (pixel width is 95 μm and gap width is 5 μm). These parameters are the same as in a previously-reported study [16]. As an example of an optical pulse to be chirp-compensated, we treat optical pulses with the spectrum shown in Fig. 3.5, which was generated using an Ar-filled hollow optical fiber [15–17,21]. The spectrum was broadened from 509 to 891 nm owing to self-phase modulation. The duration of its Fourier-transform-limited pulse is evaluated to be 4.37 fs with ideal chirp compensation. In addition, we use a beam size of 5 mm, which is a typical value for our experiment.

Results

The phase $\phi^{\mathrm{SLM}}(\omega)$ modulated by the SLM in our calculation is an up-to fourth-order function of the angular frequency ω, and can be expressed by

$$\phi^{\mathrm{SLM}}(\omega) = \mathsf{W}\left\{\frac{C_2}{2}(\omega-\omega_0)^2 + \frac{C_3}{6}(\omega-\omega_0)^3 + \frac{C_4}{24}(\omega-\omega_0)^4\right\}, \qquad (3.25)$$

where $\omega_0(\equiv 2\pi c/\lambda_0)$ is the center angular frequency of the Taylor expansion (c is the velocity of light in a vacuum). The phase $\phi^{\mathrm{SLM}}(\omega)$ is assumed to be

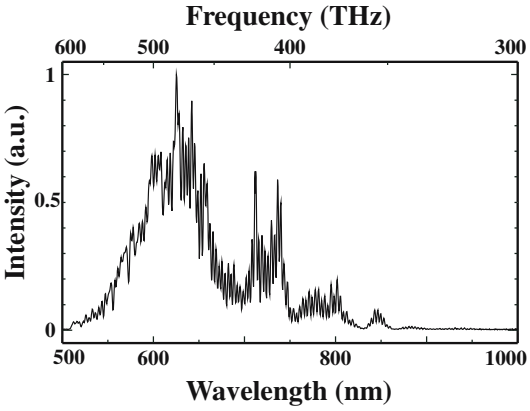

Fig. 3.5. The spectrum of generated ultrabroadband femtosecond optical pulses using an Ar-filled hollow optical fiber. Duration of the corresponding Fourier-transform-limited pulse is 4.37 fs [16]

in the wrapped form, that is, in the range of 0 to 2π, where the Wrapping operator W is expressed by

$$\mathsf{W}\phi = \phi - 2\pi \times [\phi/2\pi], \tag{3.26}$$

where [ ] is the Gauss' notation and $[x]$ represents the maximum integer that does not exceed a real number x. With this operator W, the absolute phase is wrapped into the interval $[0, 2\pi)$. Thus, the restriction (iv) that the maximum phase applied by the SLM is limited is taken into account hereafter. The group delay dispersion C_2, third-order dispersion C_3 and fourth-order dispersion C_4 values are put to be $-217\,\mathrm{fs}^2$, $-240\,\mathrm{fs}^3$ and $0\,\mathrm{fs}^4$, respectively, at the expansion center wavelength $\lambda_0 = 800\,\mathrm{nm}$, based on our best chirp-compensated experiment [16] with the spectrum shown in Fig. 3.5.

We first investigate only (i) the frequency-dependent time window effect on nonlinear chirp compensation for ultrabroadband femtosecond optical pulses with the expansion center wavelength $\lambda_0 = 800\,\mathrm{nm}$. The frequency-dependent time window $T_\mathrm{w}(\omega)$ is expressed by (3.23). Our calculations show that this effect gives very small side lobes of 0.019% in intensity that can be neglected. The duration of the compensated pulse is 4.37 fs, almost equal to that of the Fourier-transform-limited pulse. This result is reasonable because the frequency-dependent time windows for all Fourier components of the input pulse are easily wide enough compared with the duration of the pulse before chirp compensation or the largest group-delay difference among the all frequency components. While the pulse duration before chirp compensation is few hundred femtoseconds, the width of the time window for $\lambda = 509$ and 891 nm is 1.27 and 2.24 ps, respectively. Namely, for pulse compression using the 4-f system, the time window for the short-wavelength component should be much longer than the duration before compensation. Inversely, we can say that chirped pulses whose duration is less than the shortest time window of its frequency components can be compressed using this 4-f system configuration with the SLM.

Second, we investigate (ii) the pixel gap effect, as well as effect (i), for the expansion center wavelength $\lambda_0 = 800\,\mathrm{nm}$. The pixel gap effect is assumed to give no modulation and to be transparent. Our calculations show that this effect, giving very small side pulses of 0.059% in intensity, is not significant. The duration of the compensated pulse is 4.37 fs, being almost equal to that of the Fourier-transform-limited pulse. In our case, the duty of unmodulated and modulated area is $5/95 = 0.053$. This low duty value does not affect the performance of the pulse compression.

Third, we investigate (iii) the effect of discreteness of the modulated phase in the spatial light phase modulator, as well as effects (i) and (ii), for the expansion center wavelength $\lambda_0 = 800\,\mathrm{nm}$. In this case, $\phi^\mathrm{SLM}(\omega)$ is discretized in each wavelength-interval corresponding to each pixel size, as schematically shown in Fig. 3.6. The calculated result is shown in Fig. 3.7. It is found that this effect is the most significant because it gives a side pulse of 7.55% in

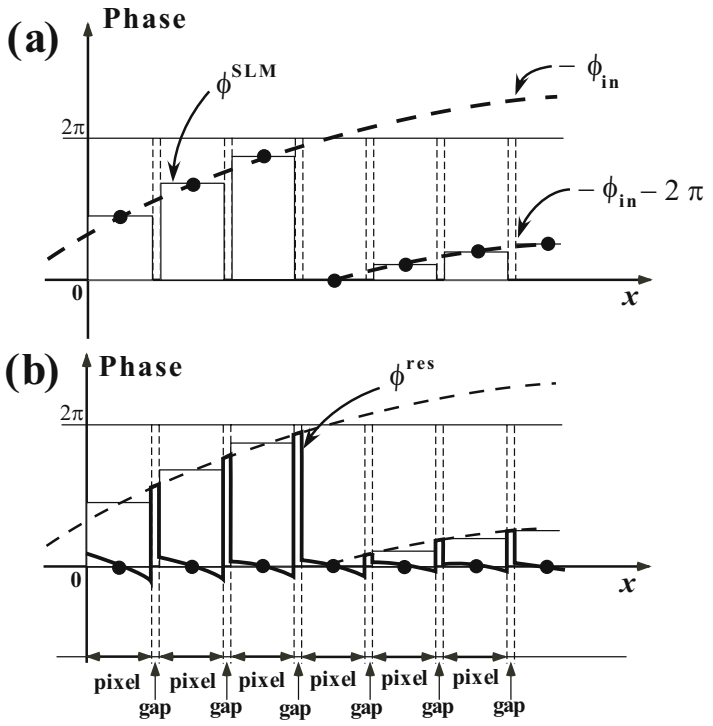

Fig. 3.6. (a) $\phi_{\rm in}$ and $\phi^{\rm SLM}$ are the phases of the input pulse and applied by the SLM, respectively, both projected on the spatial coordinate x on the SLM. Although $\phi^{\rm SLM}$ is discretized, $\phi^{\rm SLM}$ is applied the best to cancel the wrapped phase $\mathsf{W}\phi_{\rm in}$ of the input pulse. **(b)** the actual residual phase $\phi^{\rm res} \equiv \mathsf{W}\phi_{\rm in} + \phi^{\rm SLM}$ is depicted by the *thick solid line*. The phases in the gap region of the SLM are not assumed to be compensated for

intensity. In addition, the duration of the main pulse is 5.82 fs, which is larger by 33% than that of the Fourier-transform-limited pulse.

This imperfection in nonlinear chirp compensation is due to the flat phase modulation in each pixel, which leads to a step-like phase modulation in the whole wavelength region of interest. The modulated phase $\phi^{\rm SLM}(\omega)$, as expressed by (3.25), is a nonlinear function of ω, but the projection of wavelength components (as opposed to frequency) on the SLM (in the Fourier plane) is almost linear. Thus the error height of the phase step due to the discreteness at each pixel is higher in the short-wavelength region with respect to the center expansion wavelength than in the long-wavelength region. That causes worse chirp-compensation in the short-wavelength region than in the long-wavelength region. To avoid this imbalance of chirp compensation and to obtain a better chirp compensation in the short-wavelength region, we perform the phase modulation by shifting the center expansion wavelength λ_0

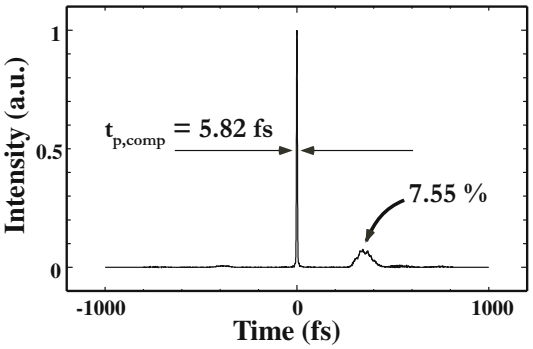

Fig. 3.7. Numerically-calculated chirp-compensated optical pulse using the 4-f system with an SLM. The effects (i)–(iii) are taken into consideration. The expansion center wavelength is λ_0 =800 nm. C_2 =217 fs^2, C_3 =240 fs^3 and C_4 =0 fs^4

to 600 nm and putting C_2, C_3 and C_4 to be $-405\,\mathrm{fs}^2$, $-240\,\mathrm{fs}^3$ and $-0.45\,\mathrm{fs}^4$, respectively. Thus we obtain a better chirp-compensated pulse with a much smaller side pulse of 0.522% in intensity, as shown in Fig. 3.8. The duration of the main pulse is 4.82 fs, which is very close to that of the Fourier-transform-limited pulse. An appropriate blue shift of the expansion center wavelength λ_0 thus enables us to perform better effective nonlinear chirp compensation for ultrabroadband femtosecond optical pulses, which has been in fact confirmed by our experiment [16] (see Sect. 3.3.1).

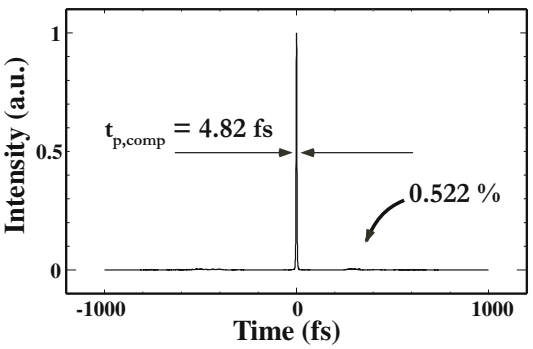

Fig. 3.8. Numerically-calculated chirp-compensated optical pulse using the 4-f system with an SLM. The effects (i)–(iii) are taken into consideration. The expansion center wavelength λ_0 is blue-shifted to 600 nm. C_2 =405 fs^2, C_3 =240 fs^3 and C_4 =0.45 fs^4

3.3 Programmable Chirp Compensator for Generation of Few-Optical Cycle Pulses

For the generation of extremely short optical pulses exceeding the laser gain bandwidth such as a Ti:sapphire laser, the technique of extracavity pulse compression is needed (Fig. 3.9). The technique is required to broaden the spectrum of laser output pulses and subsequently to completely compensate for the chirp of their pulses. The former can be realized by SPM or induced phase modulation (IPM) ($\phi(\omega)$: the spectral phase after modulation) using a single-mode fiber (see Chap. 2), while the latter can be realized by adjustable dispersive devices providing the opposite spectral phase $-\phi(\omega)$ such as negative group-delay dispersion (GDD) and higher-order phase dispersion (after a Taylor expansion series of $-\phi(\omega)$). Since the spectral phases become complicated rapidly with the increase of the spectral width, the latter phase compensator should be adaptive with an ultrabroadband width, For this purpose, a 4-f pulse shaper with a programmable SLM (we call this the SLM compensator), whose principle was described in the previous section, is the most suitable. In this section, we introduce two types of SLM compensator, a grating-pair-formed one and a prism-pair-formed one. The former is a dispersion-free system, and has a higher wavelength resolution, a better linear wavelength distribution as a function of the spatial position at the SLM phase mask and a higher flexibility by suitable selection of the grating groove, the blaze wavelength and the grating coating. But, it has drawbacks of diffraction losses and second-order diffraction (which can be avoided by suitable selection of the blaze wavelength, as shown in Chap. 5). On the other hand, the latter has a broader bandwidth of the transmission, smaller losses, a better linear frequency distribution as a function of the spatial position and no requirement of for a large-size SLM. But, it also has drawbacks of non-dispersion free system and a lower frequency resolution. Accordingly, we can choose these two types depending on the application purpose.

3.3.1 Grating-Pair-Formed Compensator with SLM

Gas-Filled Hollow Fiber Experiment

Liquid Crystal Spatial Light Modulator

In our experiments, a liquid crystal device, where several hundred pixels were positioned in one dimension, was used as the SLM [15–17]. The phase of each frequency component of the pulse can be modified by changing the refractive index of the liquid crystal. The liquid crystal device consists of rod-like liquid crystal molecules and the average orientation of the liquid crystal molecules is changed by the electric field between electrodes. The direction of the average molecular alignment is determined by the strength of the electric field and the refractive index of the liquid crystal is modified according to this direction.

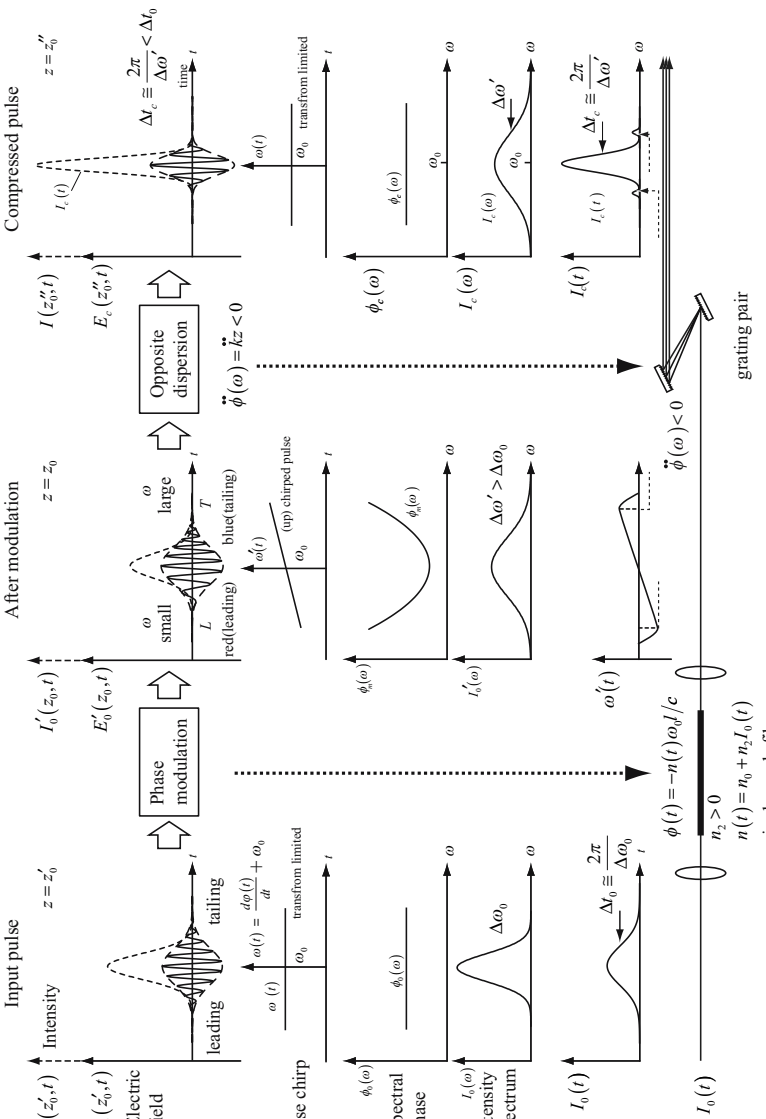

Fig. 3.9. Principle of optical pulse compression

The electric field applied to the liquid crystal device can be a static field or a field in the form of the electric pulse train. The phase change of the pixel is controlled either by changing the amplitude (amplitude modulation) or the pulse width (pulse-width modulation) of the electric field applied to the pixel. To accurately control the phase, we measured the phase change as a function of wavelengths and the strength of the electric field. Thus the SLM was calibrated.

In experiments, three different liquid crystal SLMs with different pixel numbers (128, 256, and 648) were used. The one with 648 pixels (made by Citizen Co.) was used for the generation of a few-optical-cycle pulse by compressing an ultrabroadband pulse from a gas-filled hollow fiber. The phase change of this SLM was controlled by a pulse-width modulation and its magnitude was specified by a number called a gray scale (GS) by a computer. The gray scale ranged from 0 to 191, so 192 different phase changes were possible. Initially, this scale was determined by an electronic circuit such that the phase change was approximately proportional to it. The size of each pixel was $97\,\mu\text{m} \times 8\,\text{mm}$ and a gap between the pixel was $5\,\mu\text{m}$. The liquid crystal was birefringent and the phase change was observed only for a light whose linear polarization direction was in the short axis ($97\,\mu\text{m}$).

To measure the phase change as a function of wavelengths and gray scales, a method based on a spectral interferometry was used (this method was similar to one described in [22]). In this method, light beams with two linear polarizations from a broadband light source (Xe-arc lamp) were obtained and were interfered after these passed the SLM with an analyzer. And, the spectral intensity of the interfered beams was measured by a spectrometer. During one measurement, the gray scale of the liquid crystal was kept constant. By analyzing the interference pattern in the spectral intensity, the phase change dependence on wavelengths for the given gray scale was obtained. The measured phase changes for different gray scales are shown in Fig. 3.10. In the same figure, the transmission of the SLM is shown. By repeating the measurements for all gray scales and using a least-square fitting, the phase change dependence on wavelengths and gray scales was obtained. The phase change dependence on gray scales is shown in Fig. 3.11 for different wavelengths. As shown in this figure, the phase change is not a simple linear function for this particular SLM. Also, it can be seen that it is not possible to change the phase more than 2π if the wavelength is longer than about 1200 nm. It is possible to change the phase up to 5π for a short-wavelength light. However, the phase change of the pixel when its gray scale is changed by one becomes larger as the wavelength becomes shorter (i.e., the resolution becomes worse as the wavelength becomes shorter).

Important points for selecting a liquid crystal SLM for a pulse compression are the pixel number, the pixel size, the maximum phase change, the resolution, the gap size, and the transmission of the SLM. For a given pulse bandwidth, the pixel number and the pixel size determine the frequency width assigned for each pixel. To select this value, it is necessary to evaluate the

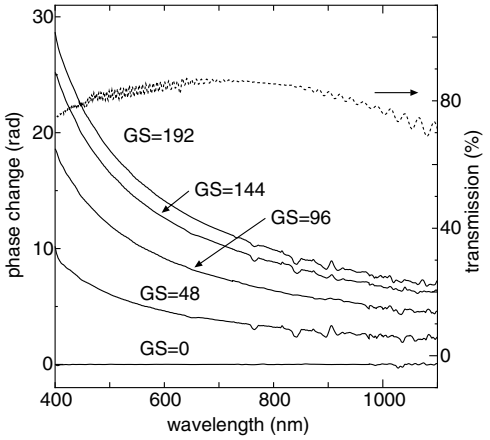

Fig. 3.10. Phase change as a function of wavelengths for different gray scales (GS's). The transmission of an SLM is also shown

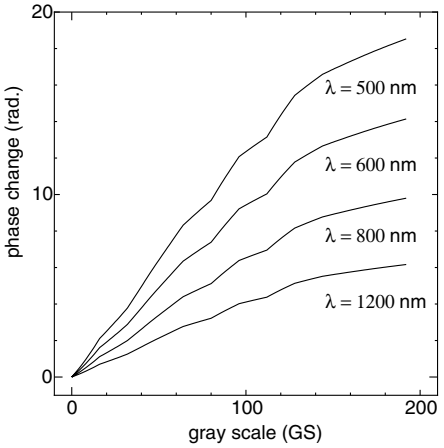

Fig. 3.11. Phase change as a function of gray scales for different wavelengths

value of a phase change per pixel for the pulse to be compressed. If the phase change per pixel exceeds π, it becomes difficult to perform effective pulse compression. The maximum phase change of the SLM should be more than 2π for the entire wavelengths of the pulse to compress it perfectly. The resolution, the gap size, and the transmission of the SLM influence the quality of the compressed pulse waveform. Especially, as the gap size of the SLM becomes larger, more pronounced side pulses tend to be generated.

Combination of a Prism-Pair and a Spatial Light Modulator Compensator

Optical pulses of ∼5 fs have been generated using the external compression of ultrabroadband pulses from a hollow fiber filled with a noble gas [23–25]. In these references, chirped mirrors have been utilized for chirp compensation. Chirped mirrors have the advantage of high throughput. However, the difficulty of obtaining the large bandwidth, the interdependence of different phase-dispersion orders $\phi^{(n)}(\omega_0)$, and the inability to fine-tune the phase in the experimental setup are disadvantages. A pulse-shaping technique [12] that uses a liquid crystal SLM for pulse compression has the advantage of large bandwidth and *in situ* adaptive phase control.

An experimental setup for the pulse compression of an ultrabroadband pulse from a hollow fiber filled with argon using a prism-pair and an SLM is shown in Fig. 3.12 [15]. A prism-pair and a 4-*f* pulse shaper were used as phase compensators in this experiment. In the pulse shaper, two plane mirrors, M7 and M8, were used to fold beams to make the folding angles away from two spherical mirrors M10 and M11 as small as possible. The SLM used (Meadowlark Optics, SLM 2256) had 128 pixels with each pixel width of 97 μm and each interpixel gap of 3 μm. The transmittance of the unbiased SLM was about 90%. Gratings, G1 and G2, were Al-coated with the braze wavelength at 800 nm and the groove of 1/150 mm. The measured diffraction efficiency was over 70% within the 550–900 nm range. We used a multipass 1-kHz Ti:sapphire amplifier, which produced pulses with a duration of 30 fs centered at 780 nm. A pulse of energy 300 μJ was focused by a 300-mm focal lens L1 into an argon-filled glass hollow fiber with an inner diameter of 140 μm and a length of 60 cm. At the gas pressure of 2.0 bar, due to dispersive

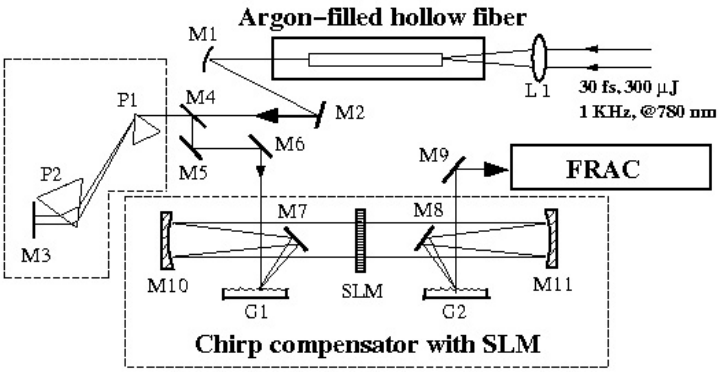

Fig. 3.12. Layout of experimental setup. M2-M9, silver-coated plane mirrors; M1, M10, and M11, Al-coated spherical mirrors, R = −400 mm; L1, f = 300 mm; P1 and P2, Brewster-angle cut BK7 prisms; G1 and G2, diffraction gratings with d = 150 lines/mm; SLM, a one-dimensional 128-pixel spatial light modulator. The SLM chirp compensator is shown within the dashed frames [15]

Table 3.2. Dispersion of an SLM and a prism-pair at 780 nm [15]

Optical components	GDD (fs^2)	TOD (fs^3)	FOD (fs^4)
SLM substrate (2 mm silica)	+75	+54	−22
BK7 glass (24 mm in a prism-pair)	+1116	+754	−235
BK7 prism-pair (50 cm)	−1546	−2084	−3550
Total	−355	−1276	−3807

SPM, an almost continuum broadbanded from 570 to 970 nm was produced. The output mode was circular (fundamental mode) and the pulse energy was around 38 μJ. The output pulse was measured to be of longer than 300-fs full width at half-maximum (FWHM) with a strong chirp.

The chirped pulse was launched to a precompressor which consisted of a pair of BK7 prisms cut at the Brewster angle at 780 nm. Since the maximum phase shift that could be applied on the SLM was $\phi_{\max} = \pi N$ ($N = 128$ is the pixel number) [12], the precompressor was explored to remove the major linear chirp of the self-phase modulated pulse with a separation length of 50 cm. The dispersion of the SLM and the prism-pair at 780 nm is shown in Table 3.2. However, the prism-pair also lead in large negative third-order dispersion (TOD) and fourth-order dispersion (FOD) resulting in the observation of big structures on the wings of the measured fringe-resolved autocorrelation (FRAC) trace at its output (see Fig. 3.13(a)). These wing-shapes of the FRAC could be reduced by launching the nonlinear-chirped pulse in the pulse shaper for its nonlinear chirp compensation.

In order to realize the programmable phase control on the SLM, we wrote the nonlinear phase dispersion applied on the SLM as

$$\phi_{\mathrm{SLM}}(\omega_j) = \frac{1}{2}\frac{\mathrm{d}^2\phi}{\mathrm{d}\omega^2}(\omega-\omega_0)^2 + \frac{1}{6}\frac{\mathrm{d}^3\phi}{\mathrm{d}\omega^3}(\omega-\omega_0)^3 + \frac{1}{24}\frac{\mathrm{d}^4\phi}{\mathrm{d}\omega^4}(\omega-\omega_0)^4 + \cdots$$

where ω_j ($j = 1, 2, \ldots, 128$) represented the angular-frequency spatially distributed on the SLM, and $(\mathrm{d}^2\phi/\mathrm{d}\omega^2)|_{\omega_0}$, $(\mathrm{d}^3\phi/\mathrm{d}\omega^3)|_{\omega_0}$, and $(\mathrm{d}^4\phi/\mathrm{d}\omega^4)|_{\omega_0}$ represented the GDD $\phi^{(2)}(\omega_0)$, TOD $\phi^{(3)}(\omega_0)$, and FOD $\phi^{(4)}(\omega_0)$ at the center angular-frequency, respectively. In practice, the center angular-frequency ω_0 (corresponding to $\lambda_0 = 780$ nm) was set to $\omega_0 = \omega_{60}$. The imparted phase shifts were folded back into the range $-\pi \le \Delta\phi \le \pi$. The SLM phase response as a function of the applied voltage was calibrated by using a He–Ne laser, and the maximum phase shift in excess of 6π was obtained. The output beam from the SLM phase compensator had a good circular mode with the pulse energy around 4–5 μJ. The output pulse was directed to the fringe-resolved autocorrelator to monitor the pulse duration. Initially, the negative quadratic phase of $-400\,\mathrm{fs}^2$ at the center frequency was applied to the SLM and the

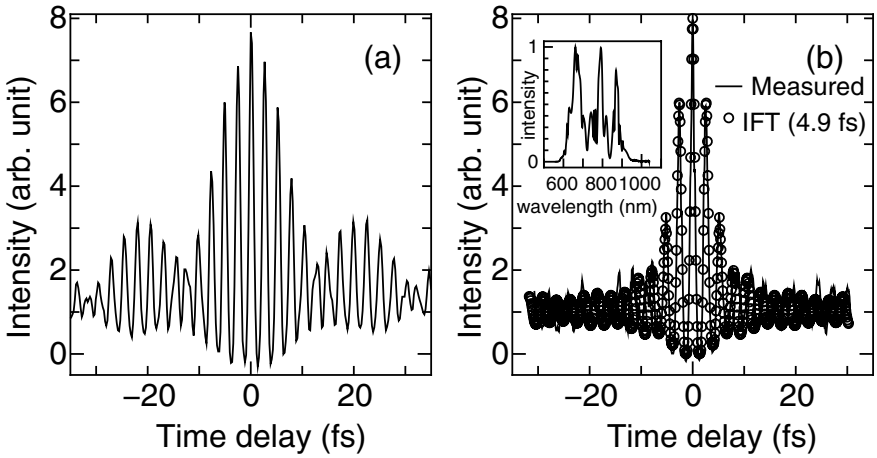

Fig. 3.13. (**a**) Measured FRAC trace of the procompensated pulse using a pair of BK7 prisms alone. (**b**) Measured FRAC trace of the shortest pulse (*solid line*). The calculation from direct inverse Fourier-transform (IFT) of the measured pulse spectrum presents 4.9 fs (FWHM) (*circles*). The measured spectrum of the shortest compressed pulse is shown in the inset [15]

material path of the second BK7 prism was increased to recompensate for the negative GVD. To compensate for the negative TOD and FOD of the prism-pair (see Table 3.2), the positive cubic phase and the positive quartic phase were applied on the SLM. As a result, better and shorter FRAC traces were observed. When the cubic phase and the quartic phase were set to be of 1100 fs^3 and 2000 fs^4 at the center frequency, respectively, the chirp of the pulse was optimally compensated for and a short optical pulse was generated. The measured FRAC trace is depicted in Fig. 3.13(b) (solid line), and the measured pulse spectrum is shown in the inset. The direct inverse Fourier-transform (IFT) of the compressed-pulse spectrum resulted in a pulse of 4.9 fs (FWHM) (circles). The good agreement between the measured FRAC trace and the IFT-constructed FRAC trace in the main peak of the pulse indicated the small residual phase errors existing in this region. The pulse was characterized using a second-harmonic generation frequency-resolved optical gating (SHG-FROG) apparatus [26] with a 10-μm thick BBO. The retrieved pulse and pulse spectrum are shown in Fig. 3.14. The pulse duration was evaluated to be 5.7 fs (FWHM). Compared with the measured spectrum, the retrieved spectrum was little bit narrow. This was due to the fact that the SHG crystal had a limited phase-matching bandwidth and resulted in the broadening of the pulse width.

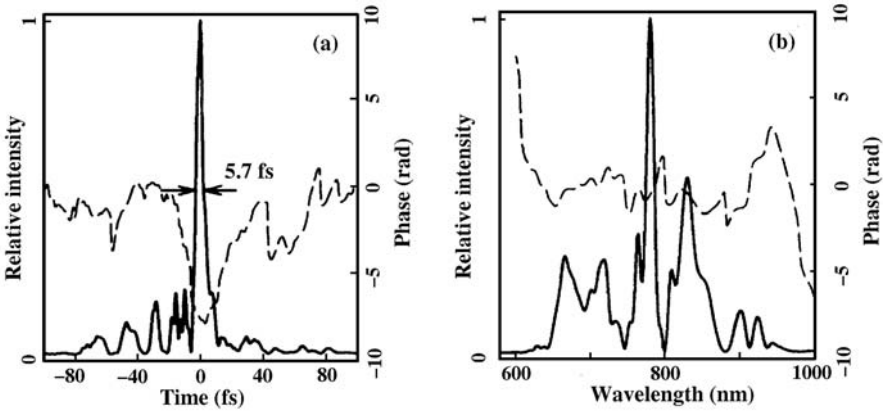

Fig. 3.14. Retrieved pulse intensities in (**a**) the time domain and (**b**) the frequency domain. *Dashed curve* indicates phases [15]

Only a Spatial Light Modulator Compensator

An ultrabroadband pulse generated from a gas-filled hollow waveguide was compressed using only a 4-f phase compensator to obtain a 5.0 fs pulse without using a pre-chirp compensator [16]. In this experiment, a spatial light modulator (SLM) with a large pixel number (648) was used. Initially, we investigated the group delay of optical components used in the experimental setup to estimate how much group delays must be compensated for by the SLM for cases with and without a prism-pair. Especially, we compared the required phase changes per pixel of the SLM for the pulse compression in both cases. We found that this value could be smaller when the prism-pair was not used if we chose the appropriate center wavelength of the Taylor expansion for determining the phase on the SLM. By not using the prism-pair, the optical throughput of the setup increased and the alignment of the setup became easier.

The experimental setup is shown in Fig. 3.15. The output beam of a Ti:sapphire laser-amplifier system (center wavelength ∼790 nm, pulse width 30 fs, repetition rate 1 kHz and pulse energy adjusted by the neutral density filter (ND) to be 140 μJ) was focused into a hollow fiber with 34-cm length and 0.1-mm inner diameter, which was positioned in a chamber filled with argon. The chamber had two 1-mm-thick sapphire windows. The output beam from the chamber was collimated by a spherical mirror and was directed to the 4-f system with the SLM. The 4-f system consisted of two spherical mirrors with a focal length of $f = 20$ cm and two silver reflective gratings (G1 and G2) with a ruling distance of $d = 1/150$ mm. The optical path lengths between the gratings to the spherical mirrors and those between the spherical mirrors to the SLM were all set to be f. The liquid crystal SLM (Citizen Co.) consists of 648, 97-μm-wide pixels with the 5-μm gap. The phase change

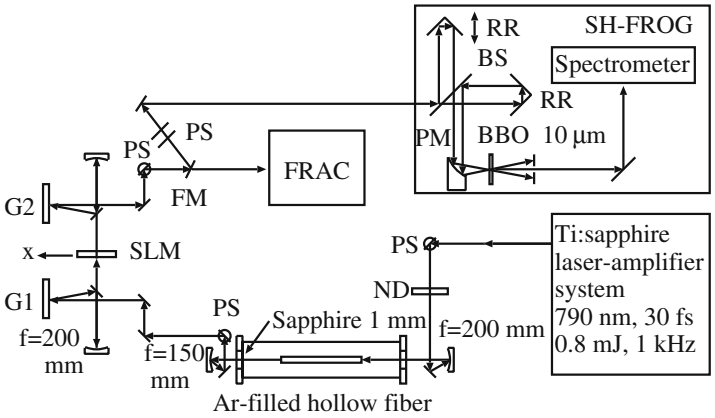

Fig. 3.15. Experimental setup for the generation of a 5.0-fs optical pulse. In this figure, PS: periscope, VND: variable neutral density filter, G1, G2: gratings, FM: flip mirror, RR: retroreflector, PM: parabolic mirror, and BS: beamsplitter [16]

dependence of the SLM on the wavelength and the gray scale was determined as described in the previous paragraph (see Figs. 3.10 and 3.11). Pulse energy after the fiber chamber was 22 μJ and the throughput of the 4-f system was 30%. In the setup, periscopes (PS) were used to change the height and/or the linear polarization direction of the beam and a flip mirror (FM) was used to change the beam direction for measurements of FRAC and SHG-FROG.

The SLM was used as a phase modulator and it could apply the phase variation of 2π for the light whose wavelength was less than about 1200 nm with the maximum resolution of 192. The applied phase $\phi_{\mathrm{SLM}}(x)$ by the SLM at the position x was given by the polynomial of the form:

$$\phi_{\mathrm{SLM}}(x) = \frac{\alpha}{2}(\omega(x)-\omega_0)^2 + \frac{\beta}{6}(\omega(x)-\omega_0)^3 + \frac{\gamma}{24}(\omega(x)-\omega_0)^4, \quad (3.27)$$

where ω_0 was the center angular frequency for the Taylor expansion and $\omega(x)$ was the angular frequency at the position x and was given by $\omega(x) = 2\pi c/(d\sin(\tan^{-1}(x/f) + \sin^{-1}(\lambda_c/d)))$ (c : the speed of light). $\lambda_c = 800\,\mathrm{nm}$ was the the wavelength at the central position of the SLM, $x = 0$. This λ_c did not have to be equal to the center wavelength for the Taylor expansion λ_0, where $\lambda_0 = 2\pi c/\omega_0$. α, β, and γ were the group delay dispersion (GDD), the third-order dispersion (TOD), and the fourth-order dispersion (FOD) at ω_0, respectively. The group delay $t_{d,\mathrm{SLM}}(x)$ applied by the SLM was given by

$$\begin{aligned} t_{d,\mathrm{SLM}}(x) &= \frac{\partial\phi_{\mathrm{SLM}}(\omega)}{\partial\omega} \\ &= \alpha(\omega(x)-\omega_0) + \frac{\beta}{2}(\omega(x)-\omega_0)^2 + \frac{\gamma}{6}(\omega(x)-\omega_0)^3. \quad (3.28) \end{aligned}$$

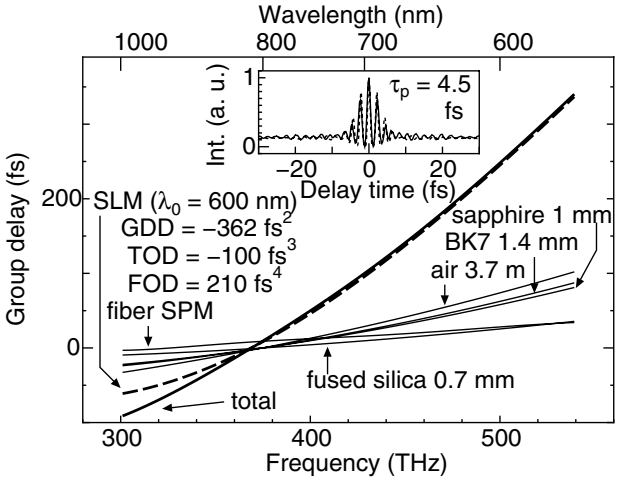

Fig. 3.16. Calculated group delay of each optical component (*solid lines*) at $\lambda_0 =$ 600 nm at an argon pressure of 2.0 atm. The total group delay (*thick solid line*) is compared with the negative of the experimentally-optimized group delay applied by the SLM (*dashed line*). Inset shows the experimental (*solid line*) and 4.5-fs fitted transform-limited (*dotted line*) FRAC traces at these parameters [16]

Parameters α, β and γ were initially estimated from the total group delay $t_d(\omega)$ of the optical components from the hollow fiber (including SPM) to the nonlinear crystal in the measuring apparatus. This $t_d(\omega)$ was fitted in the form of (3.28) and α, β, and γ were obtained. Then, the negative values of these fitted parameters were initially applied by the SLM to satisfy $t_{d,\mathrm{SLM}}(\omega) + t_d(\omega) \simeq$ constant in the whole frequency range. Theoretically, this condition should give the shortest pulses. However, in practice, it was necessary to adjust the phase applied by the SLM to obtain the shortest pulses because of the difference of group delays between the calculations and the experiments mainly due to the approximations used in calculations. The Taylor expansion used in (3.27) was found to be the natural way that allowed fine adjustment of the phase. Parameters α, β, and γ were fine-tuned using a computer to obtain the shortest pulse by the FRAC and later by the SHG-FROG apparatus. In Fig. 3.16, the group delay of the total, as well as each component in the optical path and its negative values applied by the SLM, are shown for which the shortest FRAC trace (inset: the 4.5-fs fitted transform-limited pulse) was obtained for conditions where λ_0 and the argon pressure were set to be 600 nm and 2.0 atm, respectively. As shown later, FROG results of 5.0-fs pulses were obtained under these conditions. Here, the effective group delay arising from propagation in the hollow fiber was obtained from numerical nonlinear propagation calculations [27] (See Chap. 1). For other optical components, it was calculated using the Sellmeier equations for the fused-silica [28] (beamsplitters of FRAC/FROG, 0.7 mm), BK7 [29]

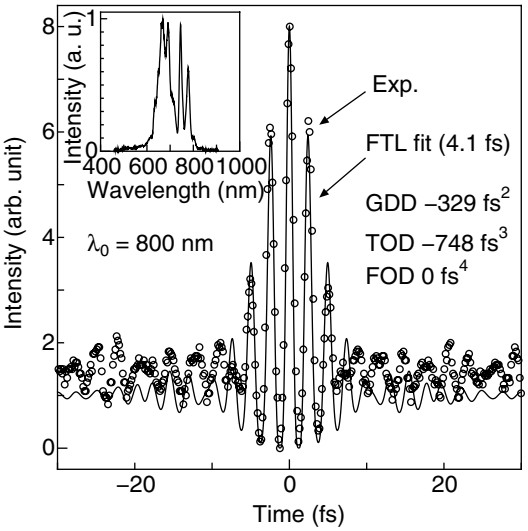

Fig. 3.17. Experimental (*circles*) and fitted transform-limited (FTL, *solid line*) FRAC traces obtained at $\lambda_0 = 800\,\text{nm}$ at an argon pressure of 2.8 atm. Inset shows the pulse spectrum [16]

(SLM substrates, 1.4 mm), sapphire [30] (a chamber window, 1 mm) and air [31] (3.7 m). As shown in Fig. 3.16, the agreement between the calculated group delay (thick solid line) and the negative of the group delay applied by the SLM (dashed line) when the parameters were optimized was reasonably good.

The value of λ_0 in (3.27) was initially set to be 800 nm with different values of α, β and γ from the ones in Fig. 3.16, and the FRAC trace as shown in Fig. 3.17, which was fitted well for the 4.1-fs transform-limited pulse, was obtained at argon pressure of 2.8 atm. However in this case, it was found that the measured pulse width by the FROG (∼6 fs) was longer than the transform-limited value. This underestimate of the pulse width may be understandable from the poor fit of the pedestals, the asymmetric temporal intensity profile [32] and the filter effect of the nonlinear crystal (See Sects. 4.1 and 4.2) in the autocorrelation trace, as well as the slightly different dispersion optics between the FRAC and the FROG apparatuses. This motivated us to search for better parameters for the SLM. Because of the finite pixel size, the phase applied by the SLM in (3.27) was step-wise, and as the difference of the phase between adjacent pixels (which we called $\Delta\phi(\lambda)$) became larger, phase compensation became more difficult because of the phase error introduced by the finiteness of the pixel width. For our experimental setup, the frequency-width for each pixel became larger as the wavelength became shorter because of the almost-linear relationship between the pixel number and the wavelength on the SLM. This made $|\Delta\phi(\lambda)|$ tend to become larger as the wavelength became

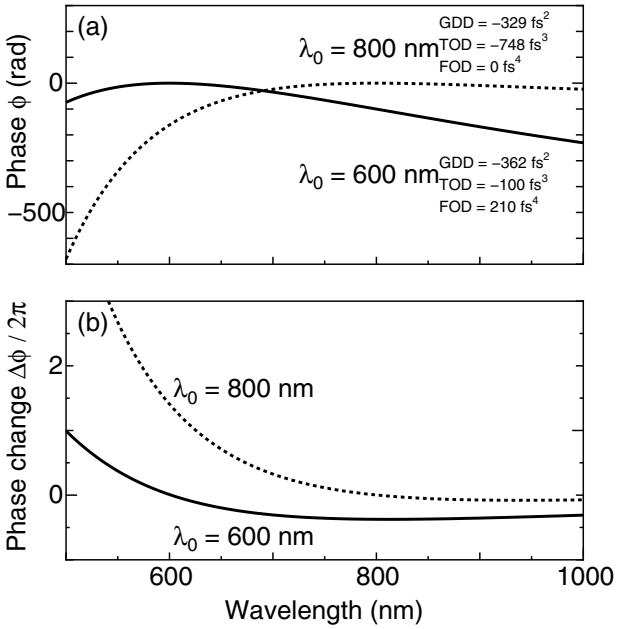

Fig. 3.18. (**a**) Applied phase $\phi(\lambda)$ and (**b**) phase change per pixel $\Delta\phi(\lambda)$ of the SLM for $\lambda_0 = 600\,\text{nm}$ (*solid curves*, parameters used in Fig. 3.16) and $\lambda_0 = 800\,\text{nm}$ (*dotted curves*, parameters used in Fig. 3.17) [16]

shorter than λ_0. In Fig. 3.18, the applied phase as well as the phase variation per pixel at SLM for $\lambda_0 = 600\,\text{nm}$ (Fig. 3.16) and $\lambda_0 = 800\,\text{nm}$ (Fig. 3.17) are shown. In both cases, the fitted group delays $t_{d,\text{SLM}}(\omega)$ were almost identical. However, the fitted phases were quite different as shown in this figure. We analyzed $|\Delta\phi(\lambda)|$ of the SLM, and found that for $\lambda_0 = 800\,\text{nm}$ it exceeded π for the wavelength below 672 nm and it was difficult to perform the phase compensation below this wavelength. This effect was pronounced since the generated spectrum had a peak at 670 nm. When $\lambda_0 = 600\,\text{nm}$, $|\Delta\phi(\lambda)|$ in the shorter wavelength range decreased considerably and it exceeded π only for the wavelength below 540 nm. This resulted in a significantly better phase compensation and pulses much closer to the transform-limit were obtained in the FROG measurements (See Sect. 3.2).

In Fig. 3.19, the results of pulse measurements using the SHG-FROG at $\lambda_0 = 600\,\text{nm}$ are shown. Owing to the slight difference of optics used in the FRAC and the FROG apparatuses, the SLM parameters were re-adjusted slightly for the FROG measurements. In the SHG-FROG apparatus (Fig. 3.16), the 0.5-mm thick broadband (400–1300 nm) dielectric beam splitter (BS) was used to separate the beam to the silver-coated retroreflector (RR) in the balanced configuration. The beam separation d_b at the parabolic mirror (PM) was 2 mm with the beam diameter w_m of 1 mm. It

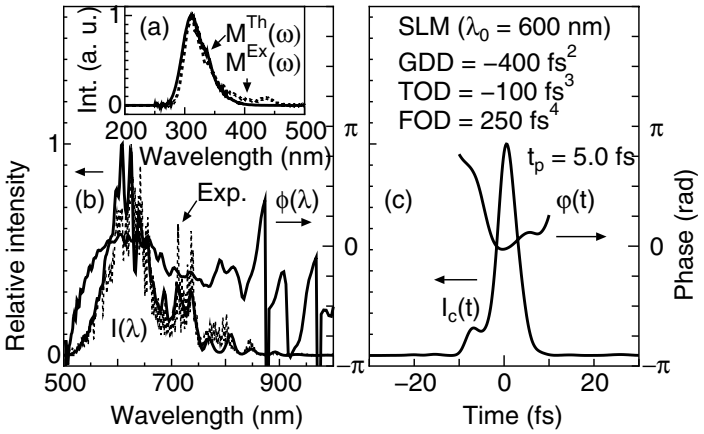

Fig. 3.19. Results of the marginal-corrected FROG measurements with SLM parameters are shown. (**a**) Marginal calculated from the experimental spectrum $M^{\mathrm{Th}}(\omega)$ (*solid curve*) and that obtained from the FROG trace $M^{\mathrm{Ex}}(\omega)$ (*dotted curve*). (**b**) Spectrum intensity $I(\lambda)$ and phase $\phi(\lambda)$. Experimental spectrum is shown by a *dotted curve*. (**c**) Temporal intensity $I_c(t)$ and phase $\varphi(t)$ [16]

gave the time smearing [33] $\tau_d = \sqrt{2\ln 2}\lambda d_b/(\pi c w_m) = 1.6\,\mathrm{fs}$ at the wavelength $\lambda = 650\,\mathrm{nm}$ on the assumption of the Gaussian space and time profiles. The 10-μm thick β-barium borate (BBO) crystal at the cutting angle of 40 degree was used in the type I geometry. Owing to the limited bandwidth of the crystal, the frequency marginal calculated from the FROG trace $M^{\mathrm{Ex}}(\omega)$ and that from the spectrum intensity autoconvolution $M^{\mathrm{Th}}(\omega)$ did not match as shown in Fig. 3.19(a). To correct for this effect, each value in the FROG trace was multiplied by a frequency-dependent factor such that the marginal calculated from the FROG trace became identical to that obtained from the spectrum [34]. After the marginal correction, the commercial FROG software was used to retrieve the pulse intensity and phase. In the measurements, the 1024-channel optical multichannel analyzer with the intensified CCD was used. The step number was 256 with a delay time of 1.34 fs. The time required for the measurement was about one minute and the stability of the pulses was excellent during this time period. Also we could reproduce the pulse width measured by FROG usually within 10% using the same parameters several hours after these were optimized. In Fig. 3.19(b)–(c), the spectrum and the temporal waveform of the pulse are shown. The FROG error was 0.0038. The measured and the calculated spectra agreed quite well because of the marginal correction. However, the temporal width was not changed by the marginal correction. The obtained pulse of 5.0-fs had 2.4 cycles at the center wavelength (633 nm) and its width was 14% longer than the transform-limited pulse width (4.4 fs for FROG measurement). If the geometrical smearing effect is taken into account, the pulse width was

estimated to be 4.7 fs. The residual phase was within $\pi/2$ in the wavelength range (550–800 nm) where the spectral intensity was significantly large.

Conventional Glass Fiber Experiment

Self-Phase Modulated Output Case

Ultrashort optical pulses in the 4–5 fs regime have been generated by external pulse compression [15,16,23–25,35,36] with an amplifier at the repetition rate of 1 kHz and directly from Ti:sapphire lasers at the repetition rate of 100 MHz [37,38]. For chirp compensations, combinations of prism pairs, grating pairs and chirped mirrors have been employed. However, such techniques have the disadvantages of interdependence among the group-delay dispersion (GDD), the third-order dispersion (TOD) and the higher-order dispersion, as well as bandwidth limitation and the inability to realize *in-situ* large phase adjustment without realignment. Therefore, accurate chirp compensation for the compression of few-optical-cycle pulses with ultrabroad spectra becomes increasingly difficult in the generation of shorter transform-limited pulses.

On the other hand, a pulse compression technique consisting of an Ar-gas-filled hollow fiber, a prism pair and a 4-f phase compensator with an SLM was demonstrated for the generation of sub-5 fs amplified pulses at a repetition rate of 1 kHz [15,16,21]. This technique has the ability to overcome the above-mentioned problems. Using this technique, we clarify quantitatively and experimentally a relationship between the chirped pulse and the applied TOD under the obtained optimum GDD in the time region less than 10 fs, and demonstrate the generation of 7.1-fs transform-limited pulses which are output from a silica fiber (2.5 mm length) at a 75-MHz repetition rate [39]. Single-mode silica optical fibers are attractive nonlinear media because of their low losses, small effective areas, low cost, commercial availability and the capacity of broadband spectra generation by low energy pulses at a high repetition rate. To demonstrate accurate compensation, it is particularly important to use high-repetition-rate pulses because their stability is higher than that of an amplified pulse output from a hollow fiber at a low repetition rate.

Experimental setup is shown in Fig. 3.20. The 12-fs, 10-nJ pulses with the center wavelength of 800 nm were generated from a mode-locked Ti:sapphire laser at the repetition rate of 75 MHz. The 12-fs pulses were coupled into a 2.5-mm silica fiber by a 36× reflective objective R1 which was made of gold mirrors and introduced no additional phase dispersion for the 12-fs pulses. The silica fiber was a polarization-preserving single-mode fused silica fiber with a core diameter of 2.7 μm. The coupling efficiency was measured to be 27%. The output from the 2.5-mm fiber was collimated by another objective R2 made of aluminum mirrors and its spectrum was measured by a spectrometer. In addition, the output pulse was characterized by an SHG-FROG apparatus. With an input pulse power of 120 kW, the fiber output spectrum

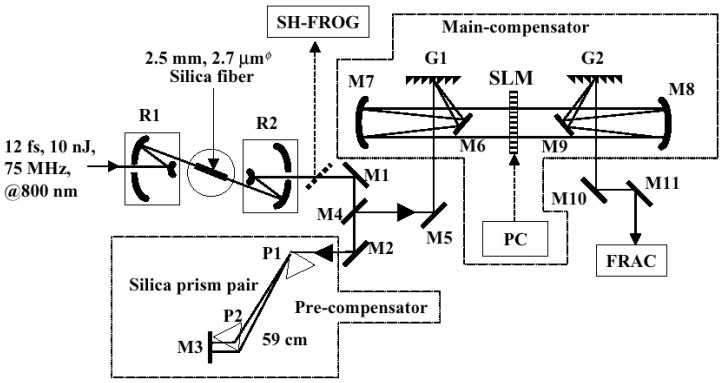

Fig. 3.20. Layout of the experimental setup. M1-6, M9-11, silver-coated plane mirrors; M7 and M8, silver-coated spherical mirrors, R = −400 mm; P1 and P2, Brewster-angle cut silica prisms; G1 and G2, gold-coated gratings, d=300 lines/mm; R1 and R2, reflective objectives (×36); SLM, spatial light modulator controlled by a computer (PC) [39]

was broadened due to the dispersive SPM effect. The chirped pulse was first precompensated by a pair of fused-silica Brewster prisms P1 and P2 with a separation length of 59 cm. The output pulse from the prism pair was coupled into a 4-f phase compensator [13, 15, 16, 21, 40] which consisted of a pair of 300 lines/mm gold-coated gratings G1 and G2 placed at the focal planes of a pair of 200-mm-focal-length concave-spherical silver mirrors M7 and M8. A programmable one-dimensional 256-pixel SLM with a total effective width of 27 mm and a height of 10 mm was set on the Fourier plane at the center of the two spherical mirrors between the gratings. In the SLM, each pixel had a width of 100 μm and an inter-pixel gap of 7 μm. The total transmission efficiency of the SLM phase compensator was about 20%. The chirp-compensated pulses from the 4-f system were measured by a fringe-resolved autocorrelator with a 25-μm-thick BBO crystal.

The spectral phase to be applied by the SLM, $\phi(\omega_j)$, is described by the following equation:

$$\phi(\omega_j) = \frac{1}{2}\phi''(\omega_j - \omega_0)^2 + \frac{1}{6}\phi^{(3)}(\omega_j - \omega_0)^3 + \dots , \tag{3.29}$$

where $j = 1, 2, \dots, 256$ (the pixel number), $\phi'' = \mathrm{d}^2\phi(\omega)/\mathrm{d}\omega^2|_{\omega_0}$ and $\phi^{(3)} = \mathrm{d}^3\phi(\omega)/\mathrm{d}\omega^3|_{\omega_0}$ at the center angular frequency $\omega_0 = \omega_{128}$ of the pulse spectrum (the corresponding wavelength $\lambda_0 = 800$ nm at the incidence angle $\theta_i = 0$) correspond to GDD and TOD, respectively, and $\omega_j - \omega_0$ represents the angular frequency difference between the jth pixel and the 128th pixel. The angular frequency ω_j is given by $\omega_j = 2\pi c/\lambda_j$, where c is the velocity of light in vacuum. The jth pixel wavelength λ_j is expressed with respect to the

Table 3.3. Evaluated dispersion for 800 nm from FROG measurements and various optical components, and applied GDD and TOD [39]

Optical components	GDD (fs^2) at 800 nm	TOD (fs^3) at 800 nm
Silica fiber output	342	187
Silica prism pair (59 cm)	−342	−479
SLM substrate (4.6 mm silica)	165	125
GDD, TOD applied by SLM	−150	220
Total	+15	+53

spatial position x_j as $\lambda_j = [d\{\sin(\tan^{-1}(x_j/f) + \sin(\lambda_c/d)) + \sin\theta_i\}]$, where $x_j = j\Delta x$ and Δx is the pixel width for the SLM. f denotes the focal length of the so-called 4-f configuration SLM compensator and $d = 1/300$ mm is a ruling distance of the grating.

To find the optimum distance between two prisms for precompensation and the optimum phase retardation to be applied by the SLM for main compensation, we measured the intensity and phase profiles of the output pulses from the silica fiber using the SHG-FROG apparatus. The pulse width of the temporal intensity profile was 92 fs and the change in temporal phase was nearly 100 radians. When the retrieved spectral phase $\phi(\omega)$ was extrapolated at the center angular frequency ω_0 using an equation similar to (3.29), the GDD and TOD values at $\lambda_0 = 800$ nm were determined to be $\phi'' = +342\,fs^2$ and $\phi^{(3)} = +187\,fs^3$, respectively. In order to precompensate for the obtained GDD of fiber output pulses, the prism distance was set at 59 cm to apply a negative GDD value of $-342\,fs^2$ at 800 nm (calculation from [8]) with the TOD value of $-479\,fs^3$. Similar calculations indicated that the GDD and TOD values at 800 nm for the fused-silica SLM substrates of a total thickness of 4.6 mm were $+165\,fs^2$ and $+125\,fs^3$, respectively. Based on these considerations (see Table 3.3), the GDD of $-150\,fs^2$ and the TOD of $+220\,fs^3$ at 800 nm were applied by the SLM in the 4-f configuration for main chirp compensation, as shown in Fig. 3.21, where the phase as a function of the pixel number was folded at each pixel exceeding $2\pi N$ radians ($N = 1, 2, 3, \ldots$). Regarding the GDD value, the optimum result was not obtained when the GDD of $-165\,fs^2$ was applied.

As a result of applying the phase shown in Fig. 3.21, to the SLM, the FRAC trace as shown in Fig. 3.22 (cross points) was obtained. This was compared with the FRAC trace of the 7.1-fs transform-limited pulse (the solid line) calculated from the measured spectrum ranging from 670 nm to 930 nm at the 4-f phase compensator output (the solid line of inset (a) in Fig. 3.22). The good agreement between the two FRAC traces suggested that 7.1-fs transform-limited pulses were generated. These were the shortest pulses generated with the combination of a silica fiber and the SLM compensator by non-amplified pulses.

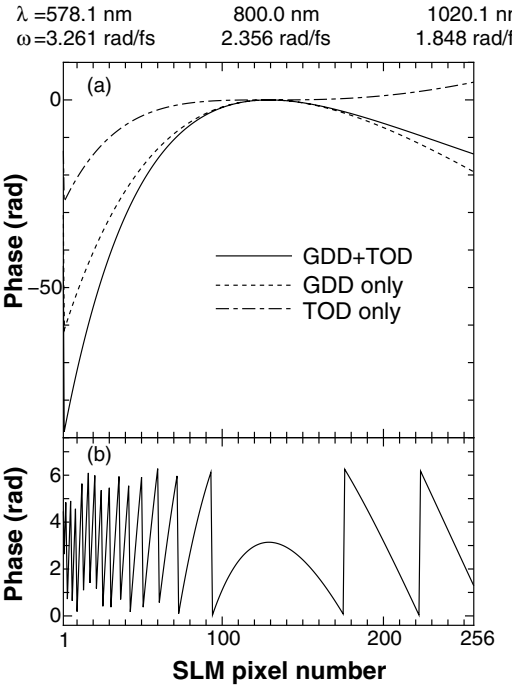

Fig. 3.21. (**a**) Applied phase distribution as a function of the SLM pixel number. (**b**) Corresponding folded phase distribution [39]

We investigated the TOD dependence of the FRAC trace while keeping the GDD ($-150\,\mathrm{fs}^2$) constant (Fig. 3.23). The FRAC traces were measured by changing only the TOD values and keeping the GDD value without any realignment of the FRAC apparatus (except for (a) where no phase pattern was applied by the SLM), using the computer-controlled SLM. When the applied GDD and TOD were both zero (Fig. 3.23(a)), the large substructure appeared in the FRAC trace, where the background in the far time region from the peak was low. However, when only the GDD was set at $-150\,\mathrm{fs}^2$ (Fig. 3.23(b)), the relative amplitude of the off-center features decreased. With increasing only the TOD from $+120$ to $+220\,\mathrm{fs}^3$, a good peak-to-background ratio of 8:1 was observed and the small wing corresponding to the transform-limited pulse profile (the inset (b) in Fig. 3.22) appeared. A further increase of the TOD from $+280$ to $+360\ \mathrm{fs}^3$ again yielded off-center features which slightly differed from earlier observations. These results suggest that even a small change in TOD ($+60\,\mathrm{fs}^3$ and $-100\,\mathrm{fs}^3$) greatly affects the temporal intensity profile of the pulse in the 7-fs regime.

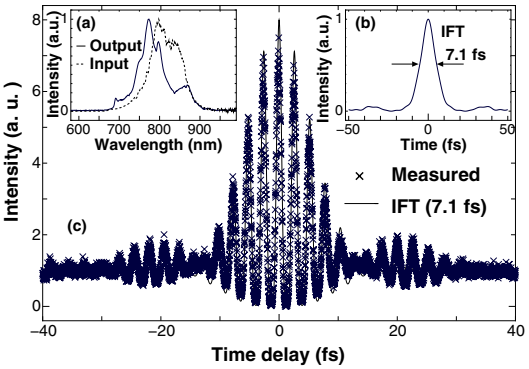

Fig. 3.22. (**a**) Measured pulse spectrum (*solid line*) from the 4-f phase compensator under optimum GDD and TOD values of $-150\,\mathrm{fs}^2$ and $+220\,\mathrm{fs}^3$, respectively. The dashed line shows the measured input spectrum of the fiber. (**b**) Inverse Fourier transformation (IFT) of the solid line of Fig. 3.22(**a**) with 7.1 fs FWHM. (**c**) The corresponding measured FRAC trace (*cross points*). The solid line is a fit from the above IFT [39]

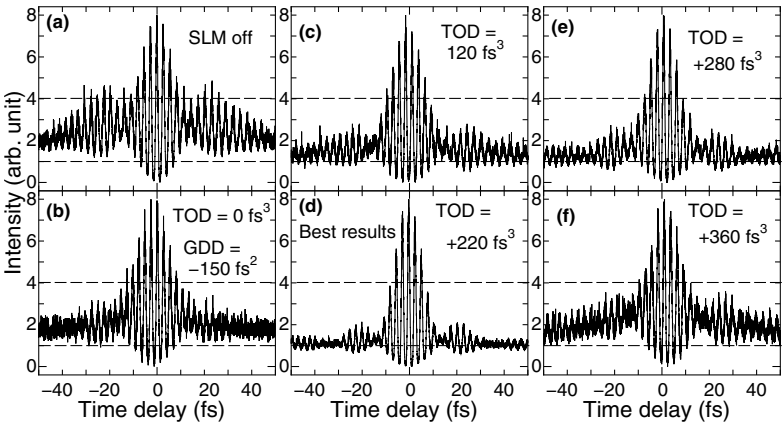

Fig. 3.23. Measured FRAC traces: (**a**) with no dispersion applied by the spatial light modulator; (**b**)–(**f**) as a function of different TOD values while keeping the GDD value constant at $-150\,\mathrm{fs}^2$ [39]

Induced Phase Modulated Output Case

As described in Chap. 2, the induced phase modulation (IPM) technique, where two different-color femtosecond pulses with a carrier phase locking are copropagated in a fiber, has the capability of more efficient broadband spectrum generation compared with that of the SPM technique. However, the spectral phase behavior is so complicated that it is difficult to compensate

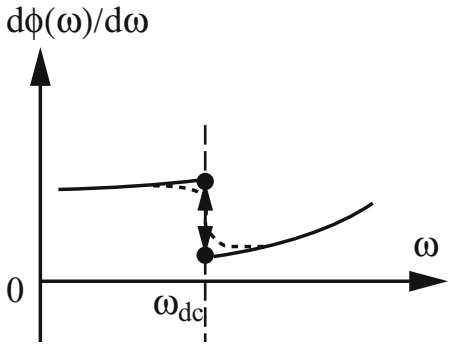

Fig. 3.24. Schematic drawing of the pulse group delay $\mathrm{d}\phi(\omega)/\mathrm{d}\omega$. Although in the sense, the spectral phase of the pulse $\phi(\omega)$ may be shown by the dashed line, it can be approximately expressed by a combination of two cubic spectral phase functions with respect to ω, as the solid line [41]

for chirp of IPM pulses by the conventional prism pair, the grating pair, chirped mirrors or their combination. Instead of those passive compensators, a preliminary experiment using a 4-f phase compensator with the SLM for IPM pulses was carried out [41] (see Sect. 5.2.1 for shorter pulse compression of few cycles by feedback compensation [42]).

The spectral-resolved autocorrelation experiment under prism phase-dispersion compensation, as pointed out in Sect. 2.2.2, suggested that the spectral phase $\phi(\omega)$ of IPM fiber output pulses has the effective discontinuity in group delay (GD) $\dot{\phi}$ and the effective discontinuity in group delay dispension (GDD) $\ddot{\phi}$ (Fig. 3.24). To confirm this funding, the following interesting experiment was performed. The experimental setup is shown in Fig. 3.25. The two input pulses into the fiber originated from the same light source. One pulse (the fundamental pulse) was generated by a Ti:sapphire regenerative amplifier at a 1-kHz repetition rate and had a duration of 80 fs, 12-nJ energy per pulse and a spectrum centered at 800 nm. The other pulse (the idler pulse), being centered at 1100 nm with an 80-fs duration and 48-nJ energy per pulse, was converted from the fundamental pulse by an optical parametric amplifier with locking of the carrier phase difference. The delay time of the fundamental pulse with respect to the idler pulse was adjusted for both pulses to meet at the fiber entrance. Both pulses were copropagated along the fiber. The output pulse from the fiber was directed to a pair of prisms with a slit for spectrally resolved measurements of autocorrelation traces, or to a SLM phase compensator. The distance between two fused-silica, 60-degree prisms with double paths was 610 mm. The 4-f phase compensator consisted of a pair of gratings (with grating constant $d = (1/150)$ mm), a pair of concave mirrors (focal length $f = 350$ mm) and a novel SLM. It has 648 pixels and an 8-bit resolution. The output pulse was characterized by a noncollinear autocorrelator with a 10-μm-thick BBO crystal.

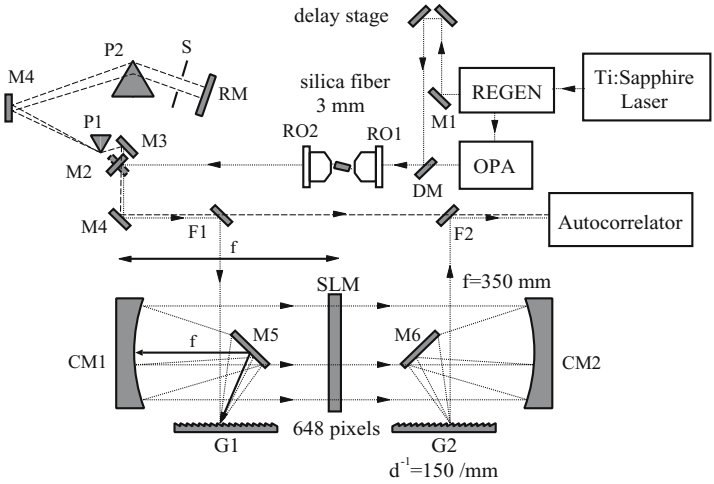

Fig. 3.25. Experimental setup for spectrally resolved autocorrelation (*dashed line*) and novel phase-dispersion compensation (*solid line*) of ultrabroadband femtosecond optical pulses generated by induced- and self-phase modulations. M1–M7: plane mirrors, DM: dichroic mirror (M2 is rotated by 90° when spectrally resolved measurements are performed), F1, F2: flip mirrors, RO1,RO2: reflective objectives, P1, P2: prisms, S: slit, RM: roof mirror, G1, G2: gratings, CM1, CM2: concave mirrors, SLM: spatial light-phase modulator [41]

The spectral broadening from 730 to 1250 nm due to dispersive IPM and SPM effects was observed (Fig. 3.26(a)). The corresponding autocorrelation trace of the fiber output was measured to be a 150-fs FWHM (Fig. 3.26(b)).

The chirp compensation implies, in general, that $\mathrm{d}[\phi(\omega)+\phi^{\mathrm{SLM}}(\omega)]/\mathrm{d}\omega = \text{const.}$, where $\phi(\omega)$ and $\phi^{\mathrm{SLM}}(\omega)$ are the spectral phase of pulses and the phase to be applied by a SLM, respectively. However, in the present case of the induced- and self-phase-modulated pulse, unlike the conventional case of the self-phase-modulated pulse, $\dot{\phi}(\omega) \equiv \mathrm{d}\phi(\omega)/\mathrm{d}\omega$ may include the effective group-delay discontinuity of $\dot{\phi}(\omega_{\mathrm{dc}}+0) - \dot{\phi}(\omega_{\mathrm{dc}}-0)$ at ω_{dc}, where

$$\dot{\phi}(\omega_{\mathrm{dc}}+0) \equiv \lim_{\omega\to\omega_{\mathrm{dc}}+0} \mathbf{d}\phi(\omega)/\mathbf{d}\omega, \tag{3.30}$$

$$\dot{\phi}(\omega_{\mathrm{dc}}-0) \equiv \lim_{\omega\to\omega_{\mathrm{dc}}-0} \mathbf{d}\phi(\omega)/\mathbf{d}\omega, \tag{3.31}$$

as shown by the solid line in Fig. 3.24. Therefore, for perfect compensation of the phase dispersion to generate the shortest pulse, the total group delay $t_{\mathrm{d}}^{\mathrm{SLM}}(\omega)$ to be applied by a SLM should be expressed by

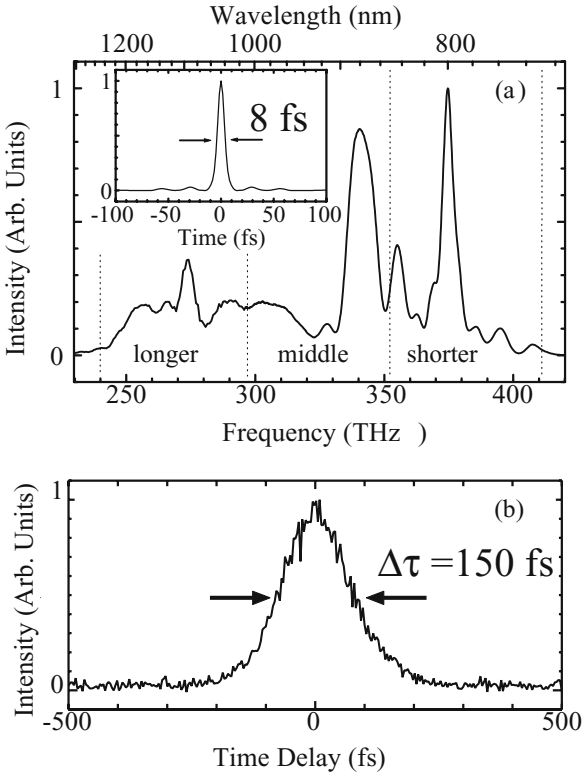

Fig. 3.26. **a** Spectrum of the output pulse from the fiber broadened by dispersive induced- and self-phase modulation. The corresponding calculated transform-limited pulse is shown in the inset. **b** The corresponding autocorrelation trace of the fiber output pulse without any compensation [41]

$$t_{\mathrm{d}}^{\mathrm{SLM}}(\omega) = \mathbf{d}\phi^{\mathrm{SLM}}(\omega)/\mathbf{d}\omega = \begin{cases} \ddot{\phi}_{(1)}(\omega_{01}) \times (\omega - \omega_{01}) + \dddot{\phi}_{(1)}(\omega_{01}) \times (\omega - \omega_{01})^2/2 & \omega < \omega_{\mathrm{dc}}, \\ t_{\mathrm{g}} + \ddot{\phi}_{(2)}(\omega_{02}) \times (\omega - \omega_{02}) + \dddot{\phi}_{(2)}(\omega_{02}) \times (\omega - \omega_{02})^2/2 & \omega \geq \omega_{\mathrm{dc}}, \end{cases} \tag{3.32}$$

where ω_{01} and ω_{02} are the center angular frequencies of the Taylor expansion corresponding to 1100 and 800 nm, respectively, and ω_{dc} is the angular frequency where the total group delay $t_{\mathrm{d}}^{\mathrm{SLM}}(\omega)$ is discontinuous. The value of ω_{dc} is determined to be 930 nm from the calculation describing IPM and SPM nonlinear propagation [11, 43, 44] (see Chap. 1). Parameters $\ddot{\phi}_{(i)}(\omega)$ and $\dddot{\phi}_{(i)}(\omega)$ $(i = 1, 2)$ are the GDD and the third-order dispersion (TOD) in the region of $\omega < \omega_{\mathrm{dc}}$ or $\omega \geq \omega_{\mathrm{dc}}$, respectively. The constant group delay t_{g} is

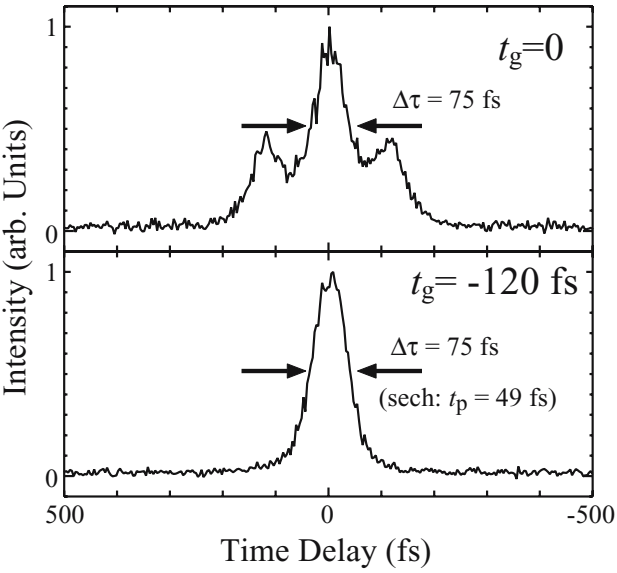

Fig. 3.27. Autocorrelation traces of pulses **a** with $\ddot{\phi}_{(1)}(\omega_{10}) = -500\,\mathrm{fs}^2$, $\dddot{\phi}_{(1)}(\omega_{10}) = -200\,\mathrm{fs}^3$, $\ddot{\phi}_{(2)}(\omega_{20}) = -700\,\mathrm{fs}^2$, $\dddot{\phi}_{(2)}(\omega_{20}) = -700\,\mathrm{fs}^3$ and t_g=0 fs (no frequency-independent group-delay adjustment), and **b** with the same parameters as in **a** except that $t_g = -120\,\mathrm{fs}$ (with the frequency-independent group-delay adjustment) [41]

determined so that the discontinuity $\dot{\phi}(\omega_{dc} + 0) - \phi'(\omega_{dc} - 0)$ of the group delay vanishes.

Two types of experiment using the SLM phase compensator were made. Figure 3.27(a) shows the autocorrelation trace in the case where $\ddot{\phi}_{(1)}(\omega_{01}) = -500\,\mathrm{fs}^2$, $\dddot{\phi}_{(1)}(\omega_{01}) = -200\,\mathrm{fs}^3$, $\ddot{\phi}_{(2)}(\omega_{02}) = -700\,\mathrm{fs}^2$ and $\dddot{\phi}_{(2)}(\omega_{02}) = -700\,\mathrm{fs}^3$ with $t_g = 0\,\mathrm{fs}$ were applied by the SLM. They were determined based on the fact that these values resulted in best chirp compensation when only the fundamental pulse or the idler pulse propagated in the fiber with only the SPM effect. The three-peak trace of Fig. 3.27(a), suggests the effective group-delay discontinuity. To cancel this frequency-independent group-delay effect, the value of t_g was applied to be $-120\,\mathrm{fs}$ together with the same $\ddot{\phi}_{(i)}(\omega_{0i})$ and $\dddot{\phi}_{(i)}(\omega_{0i})(i = 1, 2)$ values. A single-peak autocorrelation trace was obtained, as shown in Fig. 3.27(b). The correlation FWHM was 75 fs, which was the same as that of the main peak of Fig. 3.27(a), and the duration of the compensated pulse was evaluated to be 49 fs on the assumption of a sech^2 pulse shape. The corresponding duration of the transform-limited pulse is 8 fs, as shown in the inset of Fig. 3.26(a). The reason for this disagreement is considered to be as follows. In this experiment, the applied GDD and TOD dispersion parameters using the SLM were determined based on the

experimental results where only SPM occurred. That is, either the idler or the fundamental pulse propagated in a fiber. Moreover, fluctuation in pulse intensity and phase during a comparable long accumulation time to improve the signal to noise ratio for a low-intensity output from a fiber restricted the resolvable correlation FWHM to be ∼35 fs.

The optimum value of $t_g = -120$ fs was determined on the basis of the time difference between the main peak and the sub-peak in the autocorrelation trace of Fig. 3.27(a). This group delay is significantly different from the 48-fs propagation time difference of the idler pulse with respect to the fundamental pulse due to the group-velocity difference. Therefore, this result also suggests that the effective group-delay discontinuity originated from the dispersive IPM and SPM effects.

Thus, it should be noted that pulse compression using IPM with two phase-locked optical pulses requires not only conventional nonlinear-chirp compensation but also frequency-independent group-delay adjustment. Both compensations are simultaneously performed by a 4-f system with the SLM. The successful pulse compression will be described in Sect. 5.2.1.

3.3.2 Prism-Pair-Formed Compensator with SLM

Relation between Wavelength (or Angular-Frequency) and Spatial Position on SLM

Let us introduce the first experiment of the prism-pair-formed chirp compensator with the SLM [21]. The schematic of the prism-pair formed 4-f chirp compensator is shown in Fig. 3.28(a). It consists of a pair of highly dispersive TF5 (Pb-doped silica glass) prisms cut at Brewsters angle (60 deg.) at 780 nm, and a pair of concave spherical mirrors with a 200-mm focal length f. The programmable one-dimensional liquid crystal SLM with 128-pixel number is placed at the Fourier plane of the compensator where frequencies are spatially dispersed. The width of such pixel is 97 μm and the inter-pixel gap is 3 μm. Using Fig. 3.28(b) we can calculate the spatial distribution $x(\lambda)$ in the masking plane, where θ is an incident angle on the prism and $\phi_r(\lambda)$ is the refractive angle at the wavelength λ. The angle $\phi_r(\lambda)$ can be derived to be [45]:

$$\phi_r(\lambda) = \arcsin\Big[\sin(\theta)\cos(\pi-\alpha) + \sin(\pi-\alpha)\sqrt{n(\lambda)^2-(\sin(\theta))^2}\Big] \tag{3.33}$$

where α is the apex angle of the prism and $n(\lambda)$ represents the refractive index dispersion of the prism material. For the TF5 prism, the refractive index is 1.783 at 780 nm ($\alpha = 60°$, $\theta = 60°$). If the distance between the prism and the masking plane is set to f, and $\Omega_r = \phi_{r0} - \phi_r(\lambda)$ where ϕ_{r0}

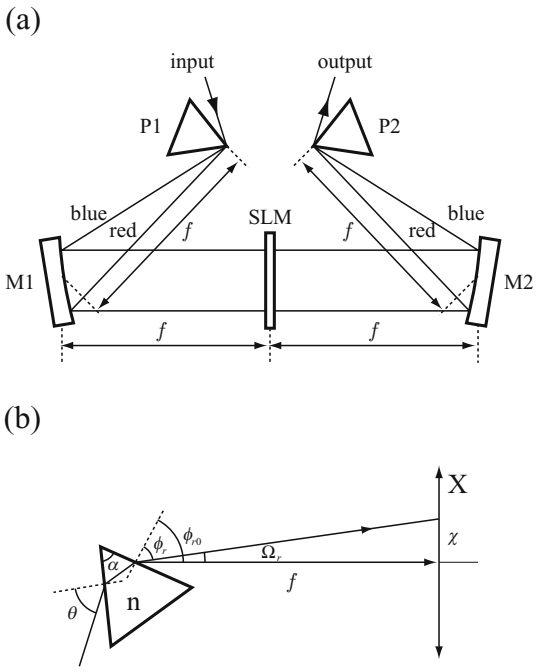

Fig. 3.28. (**a**) Schematic of a prism-pair formed 4-f chirp compensator. A pulse is spatially dispersed by a prism P1 and then collimated and focused by a spherical mirror M1 onto a liquid-crystal phase modulator which is located at the Fourier plane of a 4-f system. The output beam is recombined by a second mirror M2 and prism P2. (**b**) Geometry for calculating the spatial distribution of Brewster prism in the Fourier plane. θ represents the incident angle to the prism, $\phi_r(\lambda)$ is the refractive angle of the wavelength λ, and ϕ_{r0} is the refractive angle at the center wavelength λ_0 [21]

is the refractive angle at the center wavelength λ_0, the position $x(\lambda)$ at the wavelength λ in the masking plane is given by

$$x(\lambda) = f \tan \Omega_r \quad (= f \tan(\phi_{r0} - \phi_r(\lambda))) \tag{3.34}$$

which is shown in Fig. 3.29(a) and (b). We expand $x(\lambda)$ with respect to λ in a Taylor series as follows:

$$\begin{aligned} x(\lambda) = x_0 + x^{(1)}(\lambda_0) \times (\lambda - \lambda_0) + \frac{1}{2!} x^{(2)}(\lambda_0) \times (\lambda - \lambda_0)^2 \\ + \cdots + \frac{1}{n!} x^{(n)}(\lambda_0) \times (\lambda - \lambda_0)^n + \cdots \end{aligned} \tag{3.35}$$

where $x^{(n)}(\lambda_0) = \mathrm{d}^n x(\lambda)/\mathrm{d}\lambda^n|_{\lambda=\lambda_0}$ and x_0 is the position at the center wavelength. By letting the position x correspond to the pixel number of the SLM

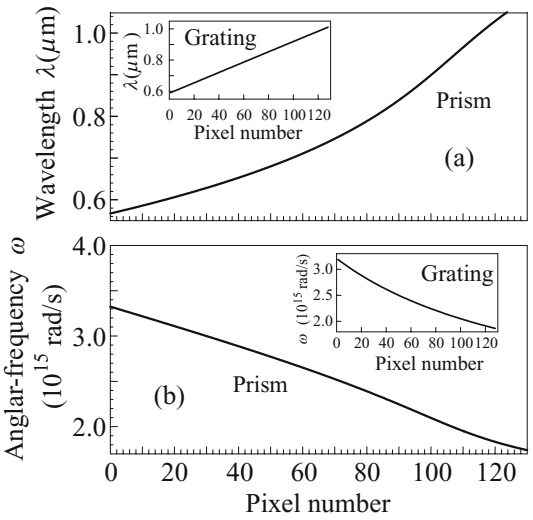

Fig. 3.29. (**a**) Spatial wavelength dispersion and (**b**) spatial angular-frequency dispersion at the Fourier plane of the TF5 prism-pair-formed chirp compensator. The spatial dispersion features of a grating partner are shown in the insets (here, $d = 1/300\,\text{mm}$, $f = 100\,\text{mm}$, and $\phi_r(\lambda_0) = 6.9\,\text{deg}$) [21]

we can approach the practical wavelength distribution or the angular frequency distribution (by a use of $\lambda = 2\pi c/\omega$) on the 128-pixel SLM and the acceptable range is from 570 to 1070 nm. Although the wavelength distribution is not linear, the angular-frequency distribution is almost linear over the range of $\Delta\omega = 1.5 \times 10^{15}$ rad/s corresponding to $\Delta\lambda = 500\,\text{nm}$. This result sharply contrasts with the case of the grating-pair formed compensator, which is shown in the insets of Fig. 3.29. It should be noted that this feature benefits programmable phase control of the SLM because the phase to be applied by the SLM is expanded in a Taylor series with respect to the angular frequency rather than the wavelength and the linear distribution means that a constant angular frequency difference $\Delta\omega$ exists between the adjacent pixels.

How to Phase-Control by Programmable SLM

At first, we have to calibrate the phase response of the SLM as a function of the voltage applied to liquid crystal pixels. One of the simple ways is to use a He-Ne laser interferometer [46, 47]. When an input pulse spectrum is very broad, calibrations for all wavelengths are needed. However, a uniformity of the phase shift in the range of 0-2π for all wavelengths is found. Accordingly, we can employ this feature and calibrate the SLM over the entire wavelength range. For phase control of chirped pulses, the phase $\phi_{\text{SLM}}(\omega_j)$ to be applied by the SLM is expressed as

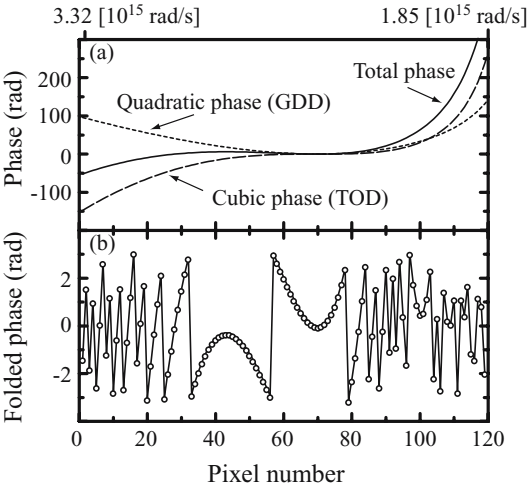

Fig. 3.30. (**a**) The phases applied on the SLM in the TF5 prism-formed chirp compensator when $\mathrm{d}^2\phi/\mathrm{d}\omega^2|_{\omega_0} = -330\,\mathrm{fs}^2$ and $\mathrm{d}^3\phi/\mathrm{d}\omega^3|_{\omega_0} = +2000\,\mathrm{fs}^3$ ($\lambda_0 = 760\,\mathrm{nm}$). (**b**) The folded phase within $[-\pi, \pi]$ [21]

$$\phi_{\mathrm{SLM}}(\omega_j) = \frac{1}{2!}\frac{\mathrm{d}^2\phi(\omega)}{\mathrm{d}\omega^2}\bigg|_{\omega=\omega_0} \times (\omega_j - \omega_0)^2 + \frac{1}{3!}\frac{\mathrm{d}^3\phi(\omega)}{\mathrm{d}\omega^3}\bigg|_{\omega=\omega_0} \times (\omega_j - \omega_0)^3 + \cdots \tag{3.36}$$

where $j = 1, 2, \cdots, 128$ (pixel number), $\ddot{\phi}(\omega_0) \equiv \mathrm{d}^2\phi(\omega)/\mathrm{d}\omega^2|_{\omega=\omega_0}$ and $\dddot{\phi}(\omega_0) \equiv \mathrm{d}^3\phi(\omega)/\mathrm{d}\omega^3|_{\omega=\omega_0}$ represent the group delay dispersion (GDD) and the third-order dispersion (TOD), respectively. In this experiment, the center angular frequency (corresponding to $\lambda_0 = 760\,\mathrm{nm}$) is set to $\omega_0 = \omega_{70}$, this $\omega_j - \omega_0$ means the angular-frequency difference between the jth pixel and the 70th pixel. If we can approximate a perfect linear angular-frequency distribution over the whole frequency range on the SLM, $\omega_j - \omega_0$ is $(j-70)\Delta\omega$ where $\Delta\omega$ is the angular-frequency difference between arbitrary adjacent pixels.

When we set $\ddot{\phi}(\omega_0) = -330\,\mathrm{fs}^2$ and $\dddot{\phi}(\omega_0) = +2000\,\mathrm{fs}^3$ at $\lambda_0 = 760\,\mathrm{nm}$, respectively, through programmably-controlled applied voltages, the phases on the SLM are evaluated to be as shown is Fig. 3.30(a). Since the components of the electric field spectrum of an ultrashort pulse are spectrally expanded on the SLM, chirp compensation by the programmable SLM is carried out in the frequency domain. The electric field in the frequency domain can be written as $E(\omega) = |E(\omega)|\exp(\mathrm{i}\phi(\omega)) \equiv |E(\omega)|\exp[\mathrm{i}(\Delta\phi(\omega) + 2m\pi)]$. Here, $\Delta\phi(\omega)$ is within $[-\pi, \pi]$ and $m = 0, \pm1, \pm2, \cdots$. As a result, we can fold a larger phase $\phi(\omega)$ into $\Delta\phi(\omega)\,\epsilon\,[-\pi, \pi]$, which is shown in Fig. 3.30(b). It should be noted that, in the case of chirp compensation, we do not need to adjust $\phi(\omega_0)$ (the

absolute phase) and $\dot{\phi}(\omega_0)$ (the group delay) unlike the phase compensation of the CW wave, and hence does not include those terms as given in Fig. 3.30.

SLM Chirp Compensation for Ultrabroadband Pulses

A typical experimental setup is shown in Fig. 3.31. The output pulses with a duration of 30 fs, a central wavelength of 780 nm, energy of 400 μJ at a repetition rate of 1 kHz were launched into an argon-filled glass hollow fiber with an inner diameter of 140 μm and a length of 60 cm. The fiber was placed in a 2.0-atom pressure chamber with 1-mm-thick sapphire windows. The output spectrum broadened from 500 to 1000 nm due to the dispersive SPM had pulse energy of 42 μJ with a pulse duration of 177 fs. The chirped pulses were collimated by a spherical mirror M1 with a focal length of 200 mm and then directed to a precompressor which consists of a pair of BK7 Brewster prisms. The compressor was designed to compensate for material dispersions of the TF5 prism pair and the SLM substrate glass. The GDD and TOD of TF5 glass, SLM substrate, BK7 glass and a pair BK7 prisms [48] at 780 nm are shown in Table 3.4, where the optical paths within the TF5 prisms and the BK7 prisms were assumed to be 4 and 24 mm (double passes), respectively. The BK7 prism pair with a separation of 65 cm provided a net GGD $= -80\,\mathrm{fs}^2$ and TOD $= -1645\,\mathrm{fs}^3$ when pulses passed through the precompressor and the SLM compensator (the SLM applied voltage is off). The output from the precompressor was coupled into the main chirp compensator with the SLM. In order to reduce the imaging distortion by astigmatic aberrations, two plane mirrors M7 and M8 were used to fold the beams. That is, the folding angles of the two spherical mirrors were kept as small as possible to alleviate aberration. Two TF5 prisms were placed at the focal planes of a pair of concave spherical mirrors of a 200-mm focal length to form a 4-f system. The output pulse duration was measured by a fringe-resolved autocorrelator

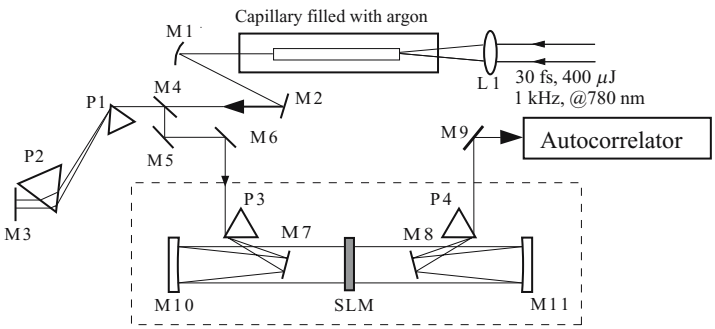

Fig. 3.31. Layout of experimental setup. M2-M9: Silver-coated plane mirrors; M1, M10, and M11: Al-coated spherical mirrors; R $= -400$ mm; L1: $f = 300$ mm; P1, P2 :Brewster-angle cut BK7 prisms; P3, P4: Brewster-angle cut TF5 prisms. SLM chirp compensator is shown within the dashed frame [21]

Table 3.4. The dispersion of the glass material, SLM substrate, and a prism pair at 780 nm [21]

	GVD (fs^2)	TOD (fs^3)
TF5 glass (4 mm)	+739	+257
SLM substrate (FS, 2 mm)	+75	+54
BK7 glass (24 mm)	+1116	+754
BK7 prism-pair (separation length of 65 cm, double passes)	−2010	−2710
Total dispersion	−80	−1645

with a 40-μm-thick BBO crystal to monitor the compensated pulse, as shown in Fig. 3.32. Since the net negative GDD from the precompressor is not sufficient for compensating for the linear part of the self-phase-modulated chirp, we first apply a negative GDD = $-330\,fs^2$ at 760 nm by the SLM. The correspondingly observed fringe-resolved autocorrelation (FRAC) trace is shown in Fig. 3.32(a). The incorrect ratio of the peak to the background hints that the nonlinear chirp is not compensated [49]. When the positive TOD of $+1000\,fs^3$ was added by the SLM, we observed that the FRAC becomes better and shorter (Fig. 3.32(b)). This means that the uncompensated pulses have the residual negative TOD, which is mainly due to the large negative TOD introduced by the precompressor and other optical elements (Table 3.4) but not due to the nonlinear chirp from the dispersive SPM. The shortest pulses were generated (Fig. 3.32(c)) when the applied TOD was $+2000\,fs^3$ (see Fig. 3.30(a)). From the fitting under the assumption of a $\mathrm{sech}^2(t)$ intensity profile, we obtain a pulse duration of 6 fs (FWHM). The result is close to the FRAC (Fig. 3.32(c)) of the 5.6-fs transform-limited pulses, which is calculated from the compensated spectrum from 600 to 1000 nm (Fig. 3.33). In order to compare the difference between the above-mentioned combined compensator and a conventional prism pair compensator, the output pulses for the precompensator were directly monitored by the autocorrelator. With more of the second BK 7 prism inserted (Fig. 3.31), shorter pulses were produced. However, the larger structures on the wings of the FRAC were observed, as shown in Fig. 3.34. This is attributed to some satellite pulses mainly originated from the larger uncompensated negative TOD of the BK7 prism pair. These unpleasant wing shapes of the FRAC can not be removed by only the prism-pair compensator due to its dispersion-interdependence feature. This fact suggests definitely that a programmable SLM compensator is significantly useful as an independent and accurate dispersion compensator.

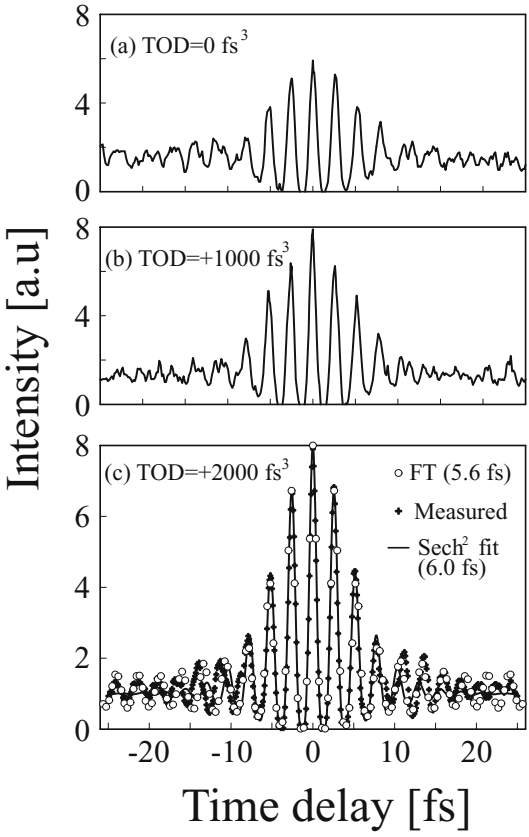

Fig. 3.32. The measured FRACs when applied phases of GDD $= -330\,\mathrm{fs}^2$ and: (**a**) TOD $= 0\,\mathrm{fs}^3$, (**b**) TOD $= +1000\,\mathrm{fs}^3$, and (**c**) TOD $= +2000\,\mathrm{fs}^3$. On curve (**c**), the fitting of a sech^2 gives a 6-fs pulse (FWHM) (*solid line*), and the calculation from the inverse Fourier transform of the measured pulse spectrum is 5.6 fs (FWHM) (*circles*) [21]

3.4 Conclusion

In this chapter, a variety of chirp compensation experiments using the liquid crystal SLM technique for the few-optical-cycle pulse generation as well as its principle and theoretical investigation for practical problems have been reviewed. It was clarified that the effect of the frequency-dependent time window, the gap effect between pixels of the SLM and the discreteness effect of the phase applied by the SLM do not seriously influence the chirp compensation of ultrabroadband pulses. Moreover, it was demonstrated experimentally that the programmable SLM technique of both types of prism-formed and grating-formed 4-f configurations with a pre-compensator is greatly useful for complete compensation for strongly chirped pulses with 600–1000 nm

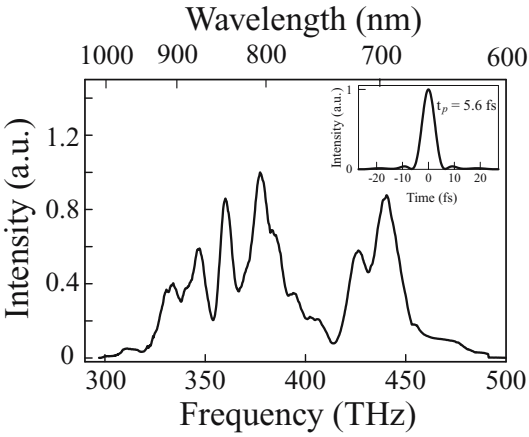

Fig. 3.33. The measured spectrum of the shortest compressed pulse. Note that the shorter wavelength is cut by the second BK7 prism in the precompressor. Inset: the intensity profile of the inverse Fourier transform of the measured spectrum [21]

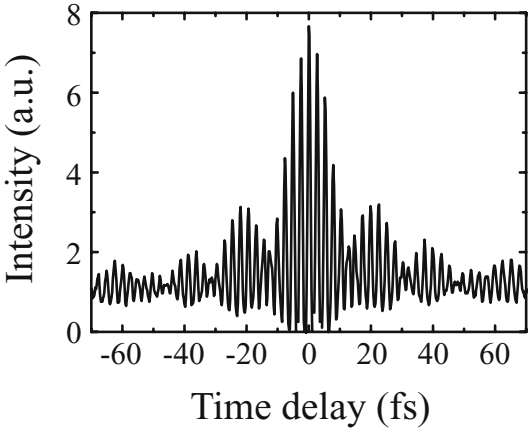

Fig. 3.34. Measured FRAC of the compressed pulse using a pair of BK7 prisms alone (see text). The large structures on the wings of FRAC attribute to some satellite pulses which mainly originate from the larger uncompensated negative TOD of the BK7 prism-pair [21]

spectral broadening. That is, 5–7 fs transform limited pulses were generated by applying independently different order phase dispersions $\phi^{(n)}(\omega)$. In addition, a use of the SLM with a large number of 648 pixels enabled us to completely compensate for the ultrabroadband pulses with a 500–1000 nm spectral broadening, without any pre-compensator, and to generate sub-5 fs pulses. These achievements suggest that the SLM technique has a capability of adaptive compensation for arbitrary spectral phase over the whole fre-

quency region exceeding one octave under the condition of in-situ adjustment without realignment of any optics.

Recently, alternative active compensation technique using a deformable mirror has been reported [14]. However, the deformable mirror technique of the smooth phase modulation has the following disadvantages compaired with the SLM technique: the low spatial and phase resolution, the cumbersome and imperfect phase calibration of membrane deflection, the small pixel number, high deflection losses, and the limitation of the maximum phase shift due to the deflection limit.

One of the subjects to be investigated in the near future for the SLM technique may be to develop the SLM that provides the deeper phase modulation ability, the larger pixel number and the smaller pixel and gap widths, to avoid the electric-field amplitude modulation at the 0–2π phase-modulation jump occurring on some pixels of the present SLM.

One of authors (M. Yamashita) thanks L. Xu and S. Nakamura for their experimental works of SLM chirp compensation.

References

1. J.-C. Diels, W. Rudolph: *Ultrashort Laser Pulse Phenomena* (Academic Press, San Diego, CA, 1996)
2. M. Yamashita: *Ultrafast Opto-Electronics* (ed. by T. Sueta and T. Kamiya, Baifukan, Tokyo, 1991) pp 15-54 in Japanese.
3. D.K. Barton: *Pulse Compression* (Raders vol.3, Artech House Inc., Dedham, MS, 1975)
4. E.B. Treacy: IEEE J. Quantum Electron. **5**, 454 (1969)
5. R.L. Fork, O.E. Martinez, J.P. Gordon: Opt. Lett. **9**, 150 (1984)
6. J. Kuhl, J. Heppner: IEEE J. Quantum Electron. **22**, 182 (1986)
7. M. Yamashita, M. Ishikawa, K. Torizuka, T. Sato: Opt. Lett. **11**, 504 (1986)
8. R.L. Fork, C.H. Brito Cruz, P.C. Becker, C.V. Shank: Opt. Lett. **12**, 483 (1987)
9. A. Stingl, M. Lenzner, C. Spielmann, F. Krausz, R. Szipőcs: Opt. Lett. **20**, 602 (1995)
10. J.D. Jung, F.X. Kärtner, N. Matuschek, D.H. Sutter, F. Morier-Genoud, G. Zhang, U. Keller, V. Scheuer, M. Tilsch, T. Tschudi: Opt. Lett. **22**, 1009 (1997)
11. M. Yamashita, H. Sone, R. Morita: Jpn. J. Appl. Phys. **35**, L1194 (1996)
12. A.M. Weiner, D.E. Leaird, J.S. Patel, J.R. Wullert: IEEE J. Quantum Electron. **28**, 908 (1992)
13. D. Yelin, D. Meshulach, Y. Silberberg: Opt. Lett. **22**, 1793 (1997)
14. E. Zeek, K. Maginnis, S. Backus, U. Russek, M. Murmane, G. Mourou, H. Kapteyn: Opt. Lett. **24**, 493 (1999)
15. L. Xu, L. Li, N. Nakagawa, R. Morita, M. Yamashita: IEEE Photonics Tech. Lett. **12**, 1540 (2000)
16. N. Karasawa, L. Li, A. Suguro, H. Shigekawa, R. Morita, M. Yamashita: J. Opt. Soc. Ame. B **18**, 1742 (2001)
17. K. Yamane, Z. Zhang, K. Oka, R. Morita, M. Yamashita, A. Suguro: Opt. Lett. **28**, 2258 (2003)

18. J.W. Goodman: *Introduction to Fourier Optics* (McGraw-Hill, San Francisco 1968) pp 77–100
19. F. Shimizu: Jpn. J. Appl. Phys. **26**, L53 (1987)
20. K. Ema, M. Kuwata-Gonokami, F. Shimizu: Appl. Phys. Lett. **59**, 2799 (1991)
21. L. Xu, N. Nakagawa, R. Morita, H. Shigekawa, M. Yamashita: IEEE J. Quantum Electron. **36**, 893 (2000)
22. K. Oka, T. Kato: Opt. Lett. **24**, 1475 (1999)
23. M. Nisoli, S. De Silvestri, O. Svelto, R. Szipőcs, C. Spielmann, S. Sartania, F. Krausz: Opt. Lett. **22**, 522 (1997)
24. Z. Cheng, G. Tempea, T. Brabec, K. Ferencz, C. Spielman, F. Krausz: In: *Ultrafast Phenomena XI*. Ed. by T. Elsaesser, J.G. Fujimoto, D.A. Wiersma, W. Zinth (Springer, Berlin 1998) p. 8
25. Z. Cheng, A. Fürbach, S. Sartania, M. Lenzner, C. Spielman, F. Krausz: Opt. Lett. **24**, 247 (1999)
26. R. Trebino, K.W. Delong, D.N. Fittinghoff, J. Sweetster, M.A. Krumbügel, B. Richman: Rev. Sci. Instrum. **68**, 3277 (1997)
27. N. Karasawa, R. Morita, H. Shigekawa, M.Yamashita: Opt. Lett. **25**, 183 (2000)
28. I.H. Malitson: J. Opt. Soc. Am. **55**, 1205 (1965)
29. Schott Glaswerke: *Schott Optical Glass Catalog*, (Schott Glaswerke, Mainz, Germany 1992)
30. I.H. Malitson: J. Opt. Soc. Am. **52**, 1377 (1962)
31. D.E. Gray (ed). : *American Institute of Physics Handbook*, 3rd edn (McGraw-Hill, New York 1972)
32. L. Gallmann, D.H. Sutter, N. Matuschek, G. Steinmeyer, U. Keller: Appl. Phys. B **70**, S67 (2000)
33. A. Baltuška, M.S. Pshenichnikov, D.A. Wiersma: Opt. Lett. **23**, 1474 (1998)
34. G. Taft, A. Rundquist, M.M. Murnane, I.P. Christov, H.C. Kapteyn, K.W. DeLong, D.N. Fittinghoff, M.A. Krumbügel, J.N. Sweetser, R. Trebino: IEEE J. Sel. Top. Quantum Electron. **2**, 575 (1996)
35. A. Baltuška, Z. Wei, M.S. Pshenichnikov, D.A. Wiersma: Opt. Lett. **22**, 102 (1997)
36. A. Shirakawa, I. Sakane, M. Takasaka, T. Kobayashi: Appl. Phys. Lett. **74**, 2268 (1999)
37. R.E.U. Morgner, F.X. Kärtner, S.H. Cho, Y. Chen, H.A. Haus, J.G. Fujimoto, E.P. Ippen, V. Scheuer, G. Angelow, T. Tschudi: Opt. Lett. **24**, 411 (1999)
38. D.H. Sutter, G. Steinmeyer, L. Gallmann, N. Matuschek, F. Morier-Genoud, U. Keller: Opt. Lett. **24**, 631 (1999)
39. S. Nakamura, L. Li, N. Karasawa, R. Morita, H. Shigekawa, M. Yamashita: Jpn. J. Appl. Phys. **41**, 1369 (2002)
40. A.M. Weiner: Rev. Sci. Instrum. **71**, 1929 (2000)
41. M. Shibata, M. Hirasawa, N. Nakagawa, R. Morita, A. Suguro, H. Shigekawa, M. Yamashita: Appl. Phys. B **74**, S291 (2002)
42. M. Yamashita, M. Hirasawa, N. Nakagawa, K. Yamamoto, K. Oka, R. Morita, A. Suguro: J. Opt. Soc. Am. B **21**, 458 (2004)
43. M. Yamashita, H. Sone, R. Morita, H. Shigekawa: IEEE J. Quantum Electron. **34**, 2145 (1998)
44. N. Karasawa, S. Nakamura, N. Nakagawa, M. Shibata, R. Morita, H. Shigekawa, M. Yamashita: IEEE J. Quantum Electron. **37**, 398 (2001)

45. F.A. Jenkins, E.H. White: *Fundamentals of Optics*, 3rd edn., (McGraw-Hill, New York, NY, 1957).
46. R.E.U. Morgner, F.X. Kärtner, S.H. Cho, Y. Chen, H.A. Haus, J.G. Fujimoto, E.P. Ippen: Opt. Lett. **24**, 511 (1999)
47. A. Efimov, C. Schaffer, D.H. Reitze: J. Opt. Soc. Am. B **12**, 1968 (1995)
48. M. Bass: *Handbook of Optics*, (McGraw-Hill, New York, NY, 1995)
49. J.C. Diels, J.J. Fontaine, I.C. McMichael, F. Sumoni: Appl. Opt. **24**, 1270 (1985)
50. D. Grischkowsky, A.C. Balant: Appl. Phys. Lett. **41**, 1 (1981)
51. M. Yamashita, K. Torizuka, T. Sato: Opt. Lett. **13**, 24 (1988)
52. M. Yamashita, K. Torizuka, T. Umemiya, J. Shimada: Appl. Phys. Lett. **58**, 2727 (1991)
53. R. Szipőcs, K. Ferencz, C. Spielmann, F. Krausz: Opt. Lett. **19** 201 (1994)
54. M. Nisoli, S. De Silvestry, O. Svelto: Appl. Phys. Lett. **68**, 2793 (1996)
55. A. Baltnska, Z. Wei, R. Szipőcs, M.S. Pshenichnikov, A. Wiersma: Appl. Phys. B **65**, 175 (1997)
56. R.E.U. Morgner, F.X. Kärtner, J.G. Fujimoto, E.P. Ippen, V. Scheuer, G. Angelow, T. Tschudi, M.J. Lederer, A. Boiko, B. Luther-Duvies: Opt. Lett. **26**, 373 (2001)
57. A. Baltuska, T. Fuji, T. Kobayashi: Opt. Lett. **27**, 306 (2002)
58. M. Adachi, M. Hirasawa, A. Suguro, N. Karasawa, S. Kobayashi, R. Morita, M. Yamashita: Jpn. J. Appl. Phys. **42**, L24 (2003)
59. M. Adachi, K. Yamane, R. Morita, M. Yamashita: IEEE Photonic. Tech. Lett. **16**, 1951 (2004)
60. K. Yamane, T. Kito, R. Morita, M. Yamashita: Tech. Digest of Conference on Lasers and Electro-Optics 2004 (CLEO'2004). Postdeadline Paper Book CPDC2 (Opt. Soc. Am., Washington DC, 2004)

4 Amplitude and Phase Characterization of Few-to-Mono Optical-Cycle Pulses

R. Morita, K. Yamane, and Z. Zhang

To characterize the amplitude and phase of optical pulses, many techniques have been developed. The progress in amplitude and phase characterization techniques of ultrashort optical pulses are summarized in Table 4.1. In this chapter, we describe the amplitude and phase characterization of few-optical-cycle pulses using various methods.

4.1 Introduction

We have several reasons for measuring ultrashort optical pulses. On the side of the laser scientists, we need to measure the pulse for better understanding of the lasers that emit such pulses to verify models of ultrashort pulse generation and to determine whether pulses can be made even shorter.

On the user side, determining the temporal resolution of an ultrashort optical pulse is important for designing an experiment. For example, we can use pulses of specific intensity and phase versus time to control chemical reactions as "coherent control", or, if we know the light in and light out, then we know the medium better.

Therefore we must measure the intensity and phase versus time or frequency to define a pulse. However, if we do not have a detector or modulator that is fast compared to the pulse width, we cannot measure the pulse intensity and phase with only linear measurements, such as a detector, interferometer, or a spectrometer. If we know the intensity autocorrelation of a pulse, there are still an infinite number of solutions for the spectral phase.

Many efforts have been made to retrieve the pulse field and phase by combining the spectrum and autocorrelation which has been called: temporal information via intensity (TIVI) [6]. It involves an iterative algorithm to find an intensity consistent with the autocorrelation. Then it involves another iterative algorithm to find the temporal and spectral phases consistent with the intensity and spectrum. Neither step has a unique solution.

If we use a collinear beam geometry, and allow the autocorrelator signal light to interfere in the SHG crystal from each individual beam, we will have so-called fringe-resolved autocorrelation (FRAC). The fringes are the result of the phase interference. It was claimed that FRAC, combined with the pulse interferogram (i.e., the spectrum), could yield the pulse intensity and

Table 4.1. Progress in amplitude and phase characterization techniques of ultrashort optical pulses

Year	Accomplishment	Researcher	References
1985	Fringe-resolved autocorrelation (FRAC)	Diels et al.	[1]
1989	Straightforward field retrieval from the measurement of a linear and second-order interferometric autocorrelation	Naganuma et al.	[2]
1993	Frequency resolved optical gating (FROG)	Kane, Trebino	[3]
1996	Temporal analysis, by dispersing a pair of light e-field (TADPOLE)	Fittinghoff et al.	[4]
1997	Sonogram	Wong, Walmsley	[5]
1998	Temporal information via intensity with the Gerchberg-Saxton algorithm (TIVI-GS)	Peatross, Rundquist	[6]
1999	Cross-correaltion FROG (X-FROG)	Linden, Kuhl, Giessen	[7]
1999	Spectral interferometry for direct electric field reconstruction (SPIDER)	Iaconis, Walmsely	[8]
1999	Phase and intensity from cross correaltion and spectrum only (PICASO)	Nicholson et al.	[9]
2001	Grating-eliminated no-nonsense observation of ultrafast incident laser light e-field (GRENOUILLE)	O'Shea et al.	[10]
2001	Homodyne optical technique for SPIDER (HOT SPIDER)	Dorrer, Londero, Walmsley	[11]
2001–2003	modified SPIDER and its improvement	Hirasawa, Yamane, Morita, Yamashita et al.	[12–14]
2001	variant of SPIDER	Zavelani-Rossi et al.	[15]

phase [2]. But the required iterative algorithm rarely converges. The fact is that the fringes yield little more information than the intensity autocorrelation and spectrum. Therefore, even nice FRAC traces have ambiguities. Two fatal limitations of FRAC are:

First, it is difficult to distinguish between different pulse shapes and, especially, different phases from FRAC. It is even harder to distinguish the traces when the pulses are shorter, when there are fewer fringes. Very different pulses have very similar interferometric autocorrelations [16]. Retrieving the

intensity from the FRAC is also difficult. We should not expect it to yield the full pulse intensity and phase.

Second, like the intensity autocorrelation, it must be curve-fit to an assumed pulse shape which should only be used for rough estimates. While in many cases the pulse shapes are not typically Gaussian, or sech^2, they may be asymmetrical and complicated.

In recent years, more precise techniques of phase measurement have been developed and demonstrated. The typical techniques include frequency resolved optical gating (FROG) [17] and spectral phase interferometery for direct electric filed reconstruction (SPIDER) [8]. Still, FRAC is still a good way of cross-checking of the retrieved intensity and phase, particularly when the pulse is shortened to few-cycle regime in which the fringe number clearly indicates the optical cycles. For this reason, FRAC is not replaceable. In practice, issues in FRAC to be solved are:

1. The conversion efficiency of the crystal must be kept low, or distortions due to "depletion" of input light fields will occur.
2. The amount of glass must be minimal in the beam before the crystal to minimize the group delay dispersion introduced into the pulse by the glass. This means that the pulses must be focused into the crystal by reflective optics, rather than lenses.
3. It is easy to introduce systematic errors. The only check point on the temporal measurement quality is that it should be maximal at $t = 0$ and symmetrical in delay.
4. The group-velocity mismatch must be negligible, otherwise the measurement will be distorted. In other words, the phase-matching bandwidth must be sufficient. Therefore very thin crystals ($<$100 μm, or $<$10 μm for monocycles) must be used. The crystal thickness for a Gaussian pulse can be estimated by

$$L = \frac{0.441 \times \lambda_0/\delta\lambda}{\mathrm{d}n(\lambda_0)/\mathrm{d}\lambda - \frac{1}{2}\mathrm{d}n_0(\lambda_0/2)/\mathrm{d}\lambda} \tag{4.1}$$

where $\delta\lambda$ is the required bandwidth of the fundamental wavelength. On the other hand, thin crystal reduces the efficiency and hence the sensitivity of the device on the same time.

The last issue is very important, because the pulse duration may be estimated to be shorter than that of its transform-limited duration on some conditions. In the next subsection, we will discuss the influence of the phase-matching bandwidth on the FRAC measurement.

4.2 Experimental and Theoretical Demonstration of Limitation in Fringe-Resolved Autocorrelation (FRAC) Measurements

Here, we investigate the influence of the frequency-dependent efficiency of the SH generation of few-cycle pulses to be measured by the FRAC method as the main origin. For ultrabroad-band optical pulses, we cannot consider that the SH electric field generated even in a thin nonlinear crystal is proportional to the square of the incident temporal electric field, because of the limitation of a phase matching bandwidth in the SH generation. We verify theoretically and experimentally such bandwidth limitation effects in FRAC measurement with type-I, 10-μm thick β-BaB_2O_4 (BBO) using two optical pulses of 5.3 and 3.6 fs. Furthermore, we demonstrate that the boundary pulse duration between the validity and the limitation of the FRAC method is in the sub-5-fs range.

4.2.1 Equations for FRAC Signals

FRAC signal is obtained by measuring the intensity of the SH wave generated from a pair of incident pulses with a relative delay time τ as a function of its τ by use of a "slow" detector. The ideal signal $S_{\mathrm{FRAC}}(\tau)$ is expressed by the following well-known form [1]:

$$S_{\mathrm{FRAC}}(\tau) = 2G(0) + 4G(\tau) + 4\mathrm{Re}\left[F_1(\tau)\right] + 2\mathrm{Re}\left[F_2(\tau)\right] \tag{4.2}$$

where

$$\begin{aligned} G(\tau) &= \int_{-\infty}^{\infty} \left|E^{(+)}(t)\right|^2 \left|E^{(+)}(t-\tau)\right|^2 \mathrm{d}t, \\ F_1(\tau) &= \int_{-\infty}^{\infty} \left(E^{(+)}(t)^2 + E^{(+)}(t-\tau)^2\right) E^{(+)*}(t) E^{(+)*}(t-\tau)\mathrm{d}t, \\ F_2(\tau) &= \int_{-\infty}^{\infty} E^{(+)}(t)^2 E^{(+)*}(t-\tau)^2 \mathrm{d}t, \end{aligned} \tag{4.3}$$

and the linearly polarized electric field $E^{(+)}(t)$ of the positive frequency ω component in a complex representation is expressed by the real electric field $E(t)$ including a carrier-wave term with a time-dependent phase $\varphi(t)$, as follows:

$$E^{(+)}(t) = \int_0^{\infty} \tilde{E}(\omega) \exp[-\mathrm{i}\omega t]\mathrm{d}\omega, \quad \tilde{E}(\omega) = \int_{-\infty}^{\infty} E(t) \exp[\mathrm{i}\omega t]\mathrm{d}t. \tag{4.4}$$

However, the SH generation is limited by a phase-matching bandwidth in a nonlinear crystal. Particularly, for few-optical-cycle pulses, the investigation of the bandwidth limitation effect is indispensable. Here, for the sake

of simplicity, let us consider the frequency-dependent efficiency of the SH generation from a thin nonlinear crystal in the frequency domain.

The SH electric field generated from a nonlinear crystal is derived by a nonlinear propagation equation [24]. The intensity $I_{\mathrm{SH}}(\Omega,\tau)$ of the SH electric field at an SH frequency Ω and a delay time τ with respect to a uniaxial negative nonlinear crystal such as BBO is given by,

$$\begin{aligned} I_{\mathrm{SH}}(\Omega,\tau) \propto \frac{\Omega}{n_{\mathrm{e}}(\Omega)}\Big|\int_{-\infty}^{\infty}\sqrt{\omega(\Omega-\omega)}\exp[\mathrm{i}V(\Omega,\omega)L]\mathrm{sinc}[V(\Omega,\omega)L] \\ \times(n_{\mathrm{e}}^2(\Omega)-1)(n_{\mathrm{o}}^2(\Omega-\omega)-1)(n_{\mathrm{o}}^2(\omega)-1) \\ \times\tilde{E}^{(+)}(\omega)\tilde{E}^{(+)}(\Omega-\omega)(1+\exp[\mathrm{i}\omega\tau])(1+\exp[\mathrm{i}(\Omega-\omega)\tau])\mathrm{d}\omega\Big|^2 \\ \equiv I_{\mathrm{SH,exact}}(\Omega,\tau), \end{aligned} \tag{4.5}$$

with a quantity concerning the type-I phase-matching condition

$$V(\omega,\Omega-\omega)=\frac{k_{\mathrm{o}}(\omega)+k_{\mathrm{o}}(\Omega-\omega)-k_{\mathrm{e}}(\Omega)}{2}, \tag{4.6}$$

where $n_{\mathrm{o}}(\omega)$ and $n_{\mathrm{e}}(\omega)$ are linear refractive indices for ordinary and extra-ordinary beams, respectively, $k_{\mathrm{o}}(\omega)$ and $k_{\mathrm{e}}(\omega)$ are wave numbers for ordinary and extra-ordinary beams, respectively, L is the crystal length, and $\tilde{E}^{(+)}(\omega)$ is the Fourier transform of the incident pulse electric field $E^{(+)}(t)$.

Under approximations $\sqrt{\omega\,(1-\omega/\Omega)}\simeq\sqrt{\Omega}/2$ and $V(\omega,\Omega-\omega)\simeq V(\Omega/2,\Omega/2)$ (we expanded $k_{\mathrm{o}}(\omega)$ and $k_{\mathrm{o}}(\Omega-\omega)$ into the Taylor series around $\Omega/2$ up to the 1st-order) in (4.5) [24], the intensity of the SH field can be conveniently decomposed to a product of a spectral filter function $R(\Omega)$ and an ideal SH intensity $I_{\mathrm{SH,ideal}}(\Omega,\tau)$ without taking account of the influence of the bandwidth limitation due to the SH wave conversion, as follows (the $I_{\mathrm{SH,exact}}(\Omega,\tau)$ of (4.5) is the equation without those approximation):

$$I_{\mathrm{SH,exact}}(\Omega,\tau)\simeq R(\Omega)I_{\mathrm{SH,ideal}}(\Omega,\tau)\equiv I_{\mathrm{SH,approx}}(\Omega,\tau), \tag{4.7}$$

where

$$R(\Omega)=\frac{\Omega^3}{4n_{\mathrm{e}}(\Omega)}\left[\left(n_{\mathrm{e}}^2(\omega)-1\right)\left(n_{\mathrm{o}}^2(\Omega/2)-1\right)^2\mathrm{sinc}[V(\Omega/2,\Omega/2)L]\right]^2 \tag{4.8}$$

$$\begin{aligned} &I_{\mathrm{SH,ideal}}(\Omega,\tau)= \\ &\left|\int_{-\infty}^{\infty}\tilde{E}^{(+)}(\omega)\tilde{E}^{(+)}(\Omega-\omega)(1+\exp[\mathrm{i}\omega\tau])(1+\exp[\mathrm{i}(\Omega-\omega)\tau])\mathrm{d}\omega\right|^2. \end{aligned} \tag{4.9}$$

Three different signals $S_{\mathrm{SH},\alpha}(\tau)$s are obtained by integrating $I_{\mathrm{SH},\alpha}(\Omega,\tau)$s over the whole spectral range ($\alpha=$ exact, approx and ideal):

$$S_{\mathrm{SH},\alpha}(\tau)=\int_{-\infty}^{\infty}I_{\mathrm{SH},\alpha}(\Omega,\tau)\,\mathrm{d}\Omega\quad(\alpha=\mathrm{exact,approx\ and\ ideal}). \tag{4.10}$$

In particular, it is easily confirmed that the FRAC signal $S_{\mathrm{SH,ideal}}$ is equivalent to (4.2).

Let us introduce the convenient value $\epsilon_{\alpha,\beta}$ for the evaluation of the difference between FRAC signals $S_{\mathrm{SH},\alpha}(\tau)$s,

RMS (root mean square) error $\epsilon_{\alpha,\beta}$

$$\epsilon_{\alpha,\beta} \equiv \sqrt{\int_{-\infty}^{\infty} \left(s_\alpha(\tau) - s_\beta(\tau)\right)^2 \mathrm{d}\tau} \quad (\alpha, \beta = \text{exact, approx and ideal}), \tag{4.11}$$

and the value $r_{\alpha,\beta}$ for the evaluation of the difference between full widths at half maximum (FWHMs) of their envelopes,

ratio of FWHMs of the envelope $r_{\alpha,\beta}$

$$r_{\alpha,\beta} \equiv \frac{\Delta t_\alpha}{\Delta t_\beta} \quad (\alpha, \beta = \text{exact, approx and ideal}), \tag{4.12}$$

where

$$s_\alpha(\tau) \equiv \frac{8 S_{\mathrm{SH},\alpha}(\tau)}{S_{\mathrm{SH},\alpha}(0)} \quad (\alpha = \text{exact, approx and ideal}) \tag{4.13}$$

and Δt_α is FWHM of the envelope of $s_\alpha(\tau)$. For Gaussian transform-limited (TL) pulses, we have the well-known value $\Delta t_{\mathrm{ideal}}/t_{\mathrm{p,in}}^{\mathrm{TL}} = 1.7$, where $t_{\mathrm{p,in}}^{\mathrm{TL}}$ is its pulse duration. The envelope function is calculated by absolute values of oscillating terms in $s_\alpha(\tau)$ (corresponding to $F_1(\tau)$ and $F_2(\tau)$ in (4.2)).

For example, in the case of α = ideal, the envelope function $S_{\mathrm{env}}(\tau)$ is exactly equivalent to the following equation in the temporal domain [1],

$$S_{\mathrm{env}}(\tau) = 2G(0) + 4G(\tau) + 4|F_1(\tau)| + 2|F_2(\tau)|. \tag{4.14}$$

4.2.2 Numerical Analysis: Deviation of Practical FRAC Signal from Ideal FRAC Signal

Figure 4.1 shows an example of the difference among three FRAC signals of $s_{\mathrm{ideal}}(\tau)$, $s_{\mathrm{exact}}(\tau)$ and $s_{\mathrm{approx}}(\tau)$, where $t_{\mathrm{p,in}}^{\mathrm{TL}}$ =4.01 fs, spectral FWHM $\Delta\nu_{\mathrm{in}} = 110$ THz, the center wavelength $\lambda_{\mathrm{c}} = 600$ nm, the angle between the incident pulse-train beam and the optic axis of 10-μm-thick BBO $\theta = 25°$ (hereafter we call the θ crystal angle). The dispersion and related values of n_{o} and n_{e} of type-I BBO were referred from [30]. This case indicates that the apparent pulse duration obtained from the FRAC signal $s_{\mathrm{exact}}(\tau)$, which exactly considers the bandwidth-limited SH-generation effect, is shorter than the correct pulse duration obtained from the FRAC signal $s_{\mathrm{ideal}}(\tau)$, which is not affected by its effect at all.

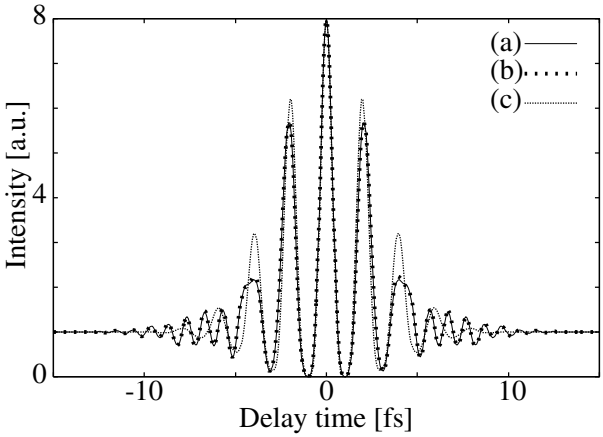

Fig. 4.1. Calculated FRAC traces for Gaussian TL pulses ($t_{\mathrm{p,in}}^{\mathrm{TL}} = 4.01\,\mathrm{fs}$, $\Delta\nu_{\mathrm{in}}$: 110 THz, center wavelength: 600 nm, θ=25°, $\epsilon_{\mathrm{exact,ideal}}/\epsilon_{\mathrm{max}} = 0.078$, $\epsilon_{\mathrm{exact,approx}}/\epsilon_{\mathrm{max}} = 0.0053$, $r_{\mathrm{exact,ideal}} = 0.88$) (a) with taking account of the bandwidth-limited SH-generation effect ($s_{\mathrm{exact}}(\tau)$) without filter approximation, (b) after filter approximation ($s_{\mathrm{approx}}(\tau)$) and (c) without the bandwidth limitation effect ($s_{\mathrm{ideal}}(\tau)$)

We investigated in detail the estimation values $\epsilon_{\alpha,\beta}$ and $r_{\alpha,\beta}$ as functions of temporal FWHM $t_{\mathrm{p,in}}^{\mathrm{TL}}$ of Gaussian TL pulses to be measured (the corresponding spectral FWHM $\Delta\nu_{\mathrm{in}}$) and the crystal angle θ for different pulse center wavelengths λ_{c}s (Figs. 4.2 and 4.3). In the following numerical calculations, we assumed that the nonlinear crystal for the SH generation is type-I 10-μm-thick BBO and limited the Gaussian spectrum to 400–2600 nm in consideration of the fact that transparency range of BBO is ∼ 200–2600 nm (we permitted the Gaussian pulses to have over-one-octave bandwidth). As a result, the following important findings were obtained (Figs. 4.2–4.5).

1. The relations $\epsilon_{\mathrm{exact,approx}} \ll \epsilon_{\mathrm{exact,ideal}}$ and $|r_{\mathrm{exact,approx}} - 1| \ll |r_{\mathrm{exact,ideal}} - 1|$ are satisfied over the whole $t_{\mathrm{p,in}}^{\mathrm{TL}} - \theta$ region ($441\,\mathrm{fs} \geq t_{\mathrm{p,in}} \geq 2.3\,\mathrm{fs}$; $10° \leq \theta \leq 45°$, $\lambda_{\mathrm{c}} = 600$, 700 and 800 nm: see Fig. 4.2), and any critical difference between $s_{\mathrm{exact}}(\tau)$ and $s_{\mathrm{approx}}(\tau)$ is not found (for example, see Fig. 4.1). Therefore, it is valid that we interpret results by using the filter function $R(\Omega)$.
2. Notice the angle θ_{opt} where the value of $\epsilon_{\mathrm{exact,ideal}}$ is minimum ($= \epsilon_{\mathrm{exact,ideal}}^{\mathrm{min}}$). For example, $\epsilon_{\mathrm{exact,ideal}}^{\mathrm{min}}/\epsilon_{\mathrm{max}} = 0.155$ at $\theta_{\mathrm{opt}} = 39.2°$, $t_{\mathrm{p,in}}^{\mathrm{TL}} = 5.0\,\mathrm{fs}$ $\Delta t_{\mathrm{ideal}} = 8.51\,\mathrm{fs}$ and $\Delta\nu_{\mathrm{in}} = 88\,\mathrm{THz}$) and $\lambda_{\mathrm{c}} = 600\,\mathrm{nm}$, where $\epsilon_{\mathrm{max}} = 7.083 \times 10^{-15}$ indicated the greatest value of all the calculated $\epsilon_{\alpha,\beta}$s. This corresponds to the result that $\Delta t_{\mathrm{exact}} = 8.99\,\mathrm{fs}$ is longer than $\Delta t_{\mathrm{ideal}} = 8.51\,\mathrm{fs}$. For $\lambda_{\mathrm{c}} = 600$, 700 and 800 nm, $\epsilon_{\mathrm{exact,ideal}}$s become the least ($= \epsilon_{\mathrm{exact,ideal}}^{\mathrm{min}}$) around $\theta_{\mathrm{opt}} = 39°$, 31° and 24° in the range of

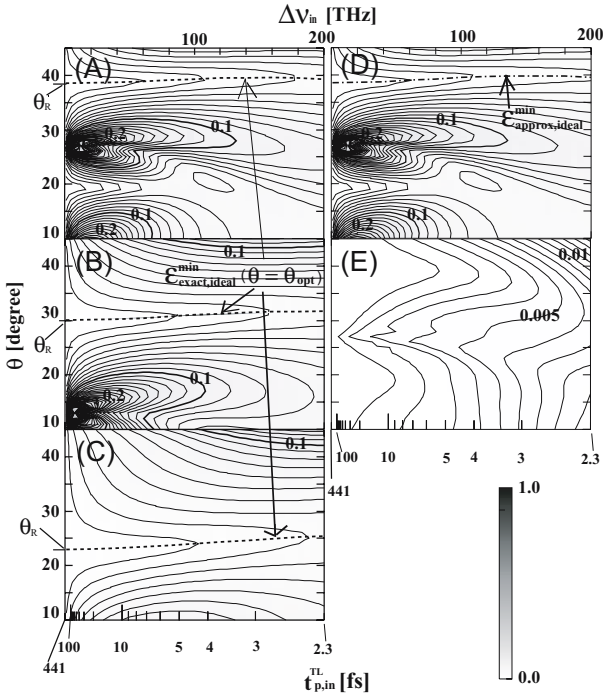

Fig. 4.2. Contour plots of $\epsilon_{\alpha,\beta}/\epsilon_{\max}$ ($\epsilon_{\max} = 7.083\times10^{-15}$) as functions of the input pulse duration $t^{\mathrm{TL}}_{\mathrm{p,in}}$ and the crystal angle θ. $\epsilon_{\mathrm{exact,ideal}}/\epsilon_{\max}$ at (A) $\lambda_{\mathrm{c}} = 600$, (B) 700 and (C) 800 nm. (D) $\epsilon_{\mathrm{approx,ideal}}/\epsilon_{\max}$ and (E) $\epsilon_{\mathrm{exact,approx}}/\epsilon_{\max}$ at $\lambda_{\mathrm{c}} =$ 600 nm

Table 4.2. θ_{pm}, θ_{R}, θ_{opt}, $\theta_{\max}$ for TL Gaussian pulses with $\lambda_{\mathrm{c}} = 600$, 700 and 800 nm (see the text for notations)

			For $t^{\mathrm{TL}}_{\mathrm{p,in}} = 5$ fs pulses		For $t^{\mathrm{TL}}_{\mathrm{p,in}} = 10$ fs pulses	
λ_{c} [nm]	θ_{pm} [deg.]	θ_{R} [deg.]	θ_{opt} [deg.]	$\theta_{\max}$ [deg.]	θ_{opt} [deg.]	$\theta_{\max}$ [deg.]
600	40.2	38.5	39.2	40.7	38.7	40.3
700	33.4	30	30.8	33.9	30.2	33.4
800	29	22.9	23.7	29.4	23.1	28.8

$t^{\mathrm{TL}}_{\mathrm{p,in}}$ of 2.3 – 441 fs, respectively (see dotted lines in Fig. 4.2). Each angle almost corresponds to the angle θ_{R} where the wavelength at the maximum value of $R(\Omega)$ equals to half of λ_{c} ($\theta_{\mathrm{R}} = 38.5°$, 30° and 22.9° for λ_{c} = 600, 700 and 800 nm, respectively (see Table. 4.2)). It should be noted that these optimal angles θ_{opt}s do not agree with phase-match angles θ_{pm} of the crystal ($\theta_{\mathrm{pm}} = 40.2°$, 33.4° and 29° for 600, 700 and 800 nm, respectively). In addition, their θ_{opt} values do not agree with the $\theta_{\max}$ angles where the strength of the FRAC signal becomes maximum (see Table 4.2).

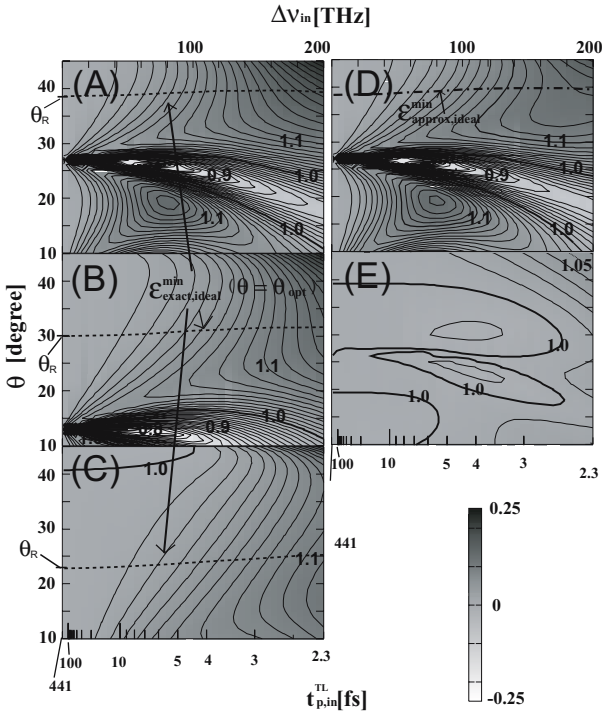

Fig. 4.3. Contour plots of $r_{\alpha,\beta}$ as functions of the input pulse duration $t_{\mathrm{p,in}}^{\mathrm{TL}}$ and the crystal angle θ. $r_{\mathrm{exact,ideal}}$ at (A) $\lambda_{\mathrm{c}} = 600$, (B) 700 and (C) 800 nm. (D) $r_{\mathrm{approx,ideal}}$ and (E) $r_{\mathrm{exact,approx}}$ at $\lambda_{\mathrm{c}} = 600\,\mathrm{nm}$

3. The longer λ_{c} is, the smaller $\epsilon_{\mathrm{exact,ideal}}$ is. It is because θ_{R} has the smaller value for pulses with the longer λ_{c}, and the bandwidth of $R(\Omega)$ with the smaller θ_{R} is the broader (see Fig. 4.4). That is, pulses with the longer center wavelength are less affected by the filter effect of the nonlinear crystal.
4. The duration ratio $r_{\mathrm{exact,ideal}}$ at the angle θ_{opt} where $\epsilon_{\mathrm{exact,ideal}}$ has the minimum value with respect to $t_{\mathrm{p,in}}^{\mathrm{TL}}$ is shown in Fig. 4.5. The ratio $r_{\mathrm{exact,ideal}}$ is always larger than 1 and increases with the decrease of $t_{\mathrm{p,in}}^{\mathrm{TL}}$. That is, the apparent pulse duration at $\theta \simeq \theta_{\mathrm{opt}}$ should be evaluated to be slightly longer than the correct one.
5. Except the $\theta \simeq \theta_{\mathrm{opt}}$ region, there is the region where $r_{\mathrm{exact,ideal}}$ is less than 1, that is, the apparent pulse duration should be shorter than the true one (For example, see $r_{\alpha,\beta} < 1$ region in Figs. 4.3(A) and (B)).

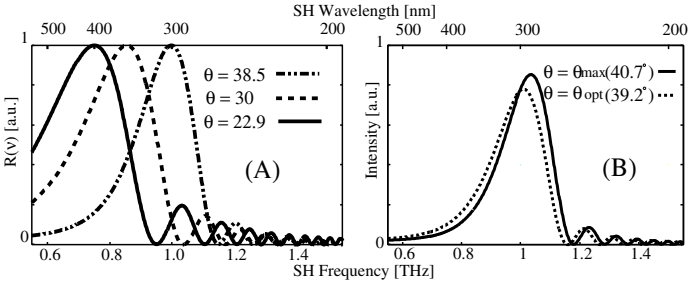

Fig. 4.4. Plots of the SH frequency-dependent filter function $R(\Omega)$ of (A) normalized ones and (B) non-normalized ones at various values of crystal angle θ

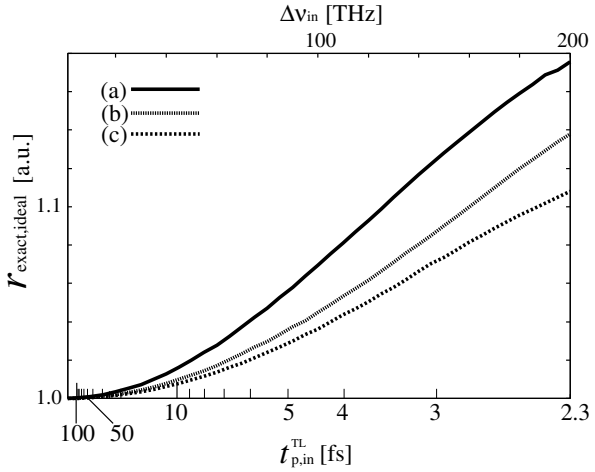

Fig. 4.5. Plots of $r_{\mathrm{exact,ideal}}$ at $\epsilon = \epsilon^{\mathrm{min}}_{\mathrm{exact,ideal}}$ for the input pulse duration $t^{\mathrm{TL}}_{\mathrm{p,in}}(\Delta\nu_{\mathrm{in}})$. Each plot for (a) λ_{c}: 600 nm, (b) λ_{c}: 700 nm and (c) λ_{c}: 800 nm

4.2.3 Experiments

We carried out few-cycle-pulse experiments for verification of the above-mentioned filter effect. Our experimental setup was almost the same as [14]. Optical pulses from a Ti:sapphire laser amplifier system (repetition rate: 1 kHz, center wavelength: 790 nm, pulse duration: < 30 fs, pulse energy: $\sim$200 μJ/pulse) were broadened by self-phase modulation (SPM) in an Ar-filled hollow fiber, and then guided into a feedback chirp compensation system [14] which consists of a modified-SPIDER (M-SPIDER) apparatus with a high sensitivity [13] and a 4-f phase compensator with a liquid crystal spatial light modulator [31]. The bandwidth of the spectrum was limited to 530–980 nm by use of a slit in the 4-f phase compensator, to avoid the background-light noise due to fundamental pulses in FRAC measurements. The chirp of the fiber output pulses was almost completely compensated for

by this feedback system, and then compensated pulses were independently measured by a FRAC apparatus with 10-μm-thick BBO (type I, θ=29°). In order to compare FRAC and M-SPIDER measurements precisely, we aligned those apparatuses to equalize optical path lengths to nonlinear crystals, and used beam splitters with the same properties (thickness: 0.5 mm, substrate: fused-silica, 20% reflection and 80% transmission for s-polarization from 400 to 1300 nm) for symmetric Michelson interferometers [29] in both apparatuses.

To clarify the practical limitation of the FRAC method, experiments for two cases (cases M-1 and M-2) were performed.

- Case M-1: 5.3-fs ($t_{\mathrm{p,in}}$), 2.2-cycle pulses with a center wavelength of 725.1 nm (λ_{c}) and a TL pulse duration of 4.42 fs ($t_{\mathrm{p,in}}^{\mathrm{TL}}$) (Fig. 4.7(A) and (B)). An Ar pressure of $p = 1.0$ atm.
- Case M-2: 3.6-fs ($t_{\mathrm{p,in}}$), 1.7-cycle pulses with a wavelength of 617.5 nm (λ_{c}) and a TL pulse duration of 3.5 fs ($t_{\mathrm{p,in}}^{\mathrm{TL}}$) (Fig. 4.8(A) and (B)). An Ar pressure of $p = 3$ atm.

The center wavelength λ_{c} was calculated by the following equation:

$$\frac{2\pi c}{\lambda_{\mathrm{c}}} = \frac{\int_{-\infty}^{\infty} \omega |\tilde{E}^{(+)}(\omega)|^2 \mathrm{d}\omega}{\int_{-\infty}^{\infty} |\tilde{E}^{(+)}(\omega)|^2 \mathrm{d}\omega}. \tag{4.15}$$

4.2.4 Comparison Between TL-Pulse FRAC Signals Based on Measured and Corresponding Gaussian Spectra

First of all, we calculated and compared FRAC traces of TL pulses using two measured spectral cases M-1 and M-2 and those using corresponding Gaussian spectral cases G-1 and G-2. We discussed them using the same pulse duration $t_{\mathrm{p,in}}^{\mathrm{TL}}$ and center wavelength λ_{c}.

It was confirmed that the θ_{opt} between cases M-i and G-i ($i = 1$ and 2) has almost the same values as well as the θ_{max} (see Table. 4.3) and $\theta_{\mathrm{opt}} \simeq \theta_{\mathrm{R}}$, but the $\epsilon_{\mathrm{exact,ideal}}^{\mathrm{min}}$ and the $r_{\mathrm{exact,ideal}}$ have different values between their cases.

Table 4.3. θ_{pm}, θ_{R}, θ_{opt} and θ_{max} for Gaussian spectrum (G-i) and measured spectrum (M-i) ($i = 1$: $t_{\mathrm{p,in}}^{\mathrm{TL}} = 4.42$ fs $\lambda_{\mathrm{c}} = 725.1$ nm, $i = 2$: $t_{\mathrm{p,in}}^{\mathrm{TL}} = 3.5$ fs $\lambda_{\mathrm{c}} = 617.5$ nm: see the text for notations). In all the cases except for the case of "PH" where spectral phases measured by M-SPIDER were also used, the θ_{opt} and θ_{max} values were calculated by use of their transform-limited pulses

	θ_{pm} [deg.]	θ_{R} [deg.]	θ_{opt} [deg.]	θ_{max} [deg.]	λ_{c} [nm]
M-1	32.2	28.1	29.7 (PH: 28.9)	33.3 (PH: 32.5)	725.1
G-1	32.2	28.1	29.1	32.8	725.1
M-2	38.8	36.9	36.8 (PH: 36.7)	39.4 (PH: 39.5)	617.5
G-2	38.8	36.9	37.9	39.7	617.5

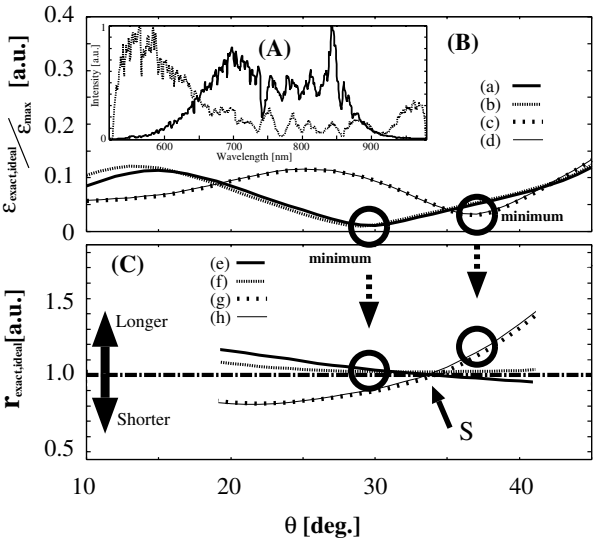

Fig. 4.6. (A) Measured spectra at the pressure $p = 1.0$ and 3.0 atm. (B) Dependence of $\epsilon_{\mathrm{exact,ideal}}$ on the crystal angle θ for (a) TL pulse at $p = 1$ atm, (b) retrieved one by M-SPIDER measurement at $p = 1$ atm, (c) TL pulse at $p = 3$ atm and (d) retrieved one by M-SPIDER measurement at $p = 3$ atm. (C) Dependence of $r_{\mathrm{exact,ideal}}$ on the crystal angle θ for (e) TL pulse at $p = 1$ atm, (f) retrieved one by M-SPIDER measurement at $p = 1$ atm, (g) TL pulse at $p = 3$ atm and (h) retrieved one by M-SPIDER measurement at $p = 3$ atm

However, for ~ 10 fs TL pulses the θ_{opt}, the $\epsilon^{\mathrm{min}}_{\mathrm{exact,ideal}}$ and the $r_{\mathrm{exact,ideal}}$ for measured and Gaussian spectral cases were not different. In addition, the filter effect of the nonlinear crystal hardly caused evaluation errors for ∼10-fs pulse durations.

Figures 4.6(B) and (C) show dependences of the normalized $\epsilon_{\mathrm{exact,ideal}}$ and the $r_{\mathrm{exact,ideal}}$ on the crystal angle θ for cases M-1 and M-2. Those figures suggest that the θ_{opt} values for cases M-1 and M-2 are 29.7° and 36.8°, where both measured apparent pulse durations become longer slightly than the correct pulse durations. Around $\theta = 34°$ (around S in Fig. 4.6(C)), the $r_{\mathrm{exact,ideal}}$ values are ∼1, although the $\epsilon_{\mathrm{exact,ideal}}$ values do not have the minimum values. However, we should not measure the FRAC trace around such region of $\theta \sim 34°$. This is because except at $\theta \sim \theta_{\mathrm{opt}}$, the FRAC signal is often distorted so remarkably that the spacing of the fringe differs, especially in its two wings, from that at $\theta \sim \theta_{\mathrm{opt}}$, although the apparent FRAC-envelope ratio $r_{\mathrm{exact,ideal}}$ becomes ∼1.

Moreover, we find that when pulse durations are measured around $\theta \simeq 40°$ for case M-1 and around $\theta \simeq 20°$ for case M-2, both apparent durations become shorter than the correct pulse durations, as previously reported [25–27, 31].

4.2.5 Experimental Comparison between Directly-Measured and Modified-SPIDER-Retrieved FRAC Signals

We compared measured FRAC traces with traces retrieved from modified SPIDER (M-SPIDER) measurements [13, 14] for cases M-1 and M-2. The experimental results are shown in Fig. 4.7(C) for M-1 and Fig. 4.8(C) for M-2. Curves (a), (b) and (c) of (A) in those Figs. 4.7 and 4.8 show the intensity spectrum ($\propto |\tilde{E}^{(+)}(\omega)|^2$), the spectral phase before chirp compensation and the spectral phase ($\phi(\omega)$) after compensation, respectively. Curves (a), (b) and (c) of (B) show the temporal intensity ($I(t)$), the temporal phase ($\varphi(t)$) and the TL pulse profile, respectively. Curves (i) of (C) show FRAC traces measured at the angle $\theta = 29°$ (close to the $\theta_{\rm opt}$ for case M-1: see Table. 4.3) of 10-μm thick BBO, and curves (h) and (i) of (C) show FRAC traces retrieved from $s_{\rm exact}(\tau)$ and $s_{\rm ideal}(\tau)$ in (4.13) using M-SPIDER results of $\phi(\omega)$ and $|\tilde{E}^{(+)}(\omega)|$, respectively.

In case M-1 ($t_{\rm p,in} = 5.3\,{\rm fs}$, 2.2 cycles, $t^{\rm TL}_{\rm p,in} = 4.42\,{\rm fs}$ and $\lambda_{\rm c} = 725.1\,{\rm nm}$), we could not find explicit differences among curves (g)–(i), as expected from calculated results of Figs. 4.6(B) and (C) (curves (b) and (f)). On the other hand, in case M-2 ($t_{\rm p,in} = 3.6\,{\rm fs}$, 1.7 cycles, $t^{\rm TL}_{\rm p,in} = 3.50\,{\rm fs}$ and $\lambda_{\rm c}$ =617.5 nm), the measured FRAC trace (curve (g)) agrees with the retrieved trace (curve (h)) with taking account of the spectral filter effect exactly, but there is the unignorable difference between curves (g) and (i) (the retrieved trace without the spectral filter effect), as expected from calculated results of Figs. 4.6(B)

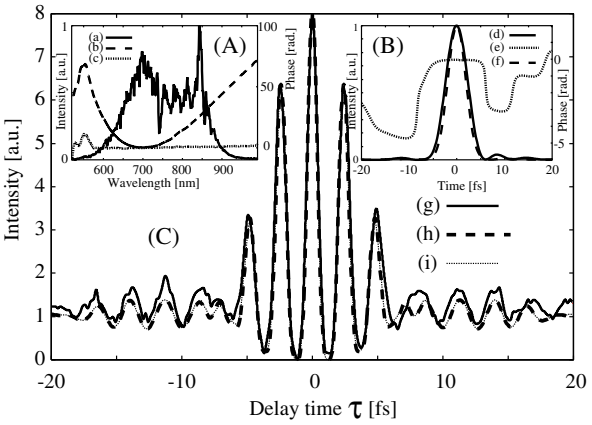

Fig. 4.7. Experimental results (Ar-gas pressure: 1 atm, fiber input: 150 μJ/pulse, fiber output: 16.5 μJ/pulse). (A) (a) Intensity spectrum and spectral phases (b) before and (c) after feedback chirp compensation. (B) (d) Temporal intensity (pulse duration: 5.3 fs, center wavelength: 725.1 nm) and (e) temporal phase after chirp compensation. (f) Temporal intensity of the Fourier transform-limited pulse (pulse duration: 4.42 fs). (C) (g) Measured FRAC trace and retrieved FRAC traces (h) with and (i) without taking account of the filter effect by the nonlinear crystal

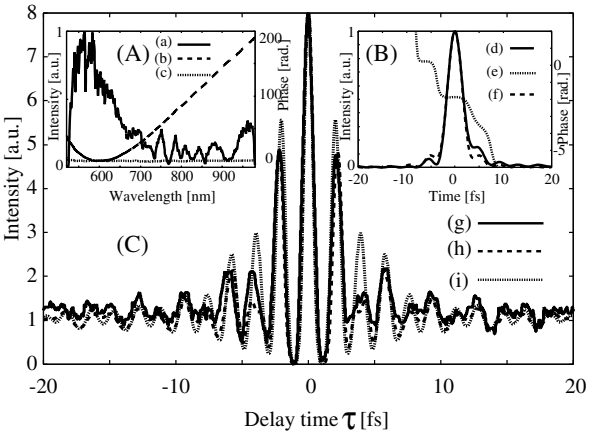

Fig. 4.8. Experimental results (Ar-gas pressure: 3 atm, fiber input: 140 μJ/pulse, fiber output: 18 μJ/pulse). (A) (a) Intensity spectrum and spectral phases (b) before and (c) after feedback chirp compensation. (B) (d) Temporal intensity (3.6 fs, center wavelength: 617.5 nm) and (e) temporal phase after chirp compensation. (f) Temporal intensity of the Fourier transform-limited pulse (3.50 fs). (C) (g) Measured FRAC trace and retrieved FRAC traces (h) with and (i) without taking into account of the filter effect by the nonlinear crystal

and (C) (curves (d) and (h)). Therefore, it was verified that the FRAC trace for sub-5 fs pulses was seriously distorted by the spectral filter effect due to the nonlinear crystal. In addition, in comparing curves (h) and (i) in Fig. 4.8(C), we found that $\Delta t_{\mathrm{exact}}$ is 11 % smaller than $\Delta t_{\mathrm{ideal}}$. That is to say, the apparent pulse duration may be evaluated to be 3.16 fs. This implies that the apparent pulse duration evaluated by the FRAC measurement is shorter than that of the TL pulse. This result agrees with not only the calculated result of Fig. 4.6 but also previously reported results [25–27, 31].

4.3 Frequency Resolved Optical Gating (FROG)

4.3.1 Principle

Principle

Frequency-resolved optical gating (FROG) is a developed technique that utilizes a phase retrieval algorithm to retrieve the amplitude and phase from a measured spectrogram of the pulse to be characterized [3, 17–24]. Experimentally, FROG data are obtained by taking the spectral intensity of the signal field, generated by a nonlinear autocorrelation signal of two replicas of the pulse to be measured with the time delay τ between them. Although third-order nonlinear optical processes have been used in FROG apparatus

to uniquely measure ultrashort optical pulses, in this section, we describe second-harmonic generation (SHG) FROG because of its higher sensitivity.

The real electric field of an optical pulse can be represented by

$$E(t) = 2\mathrm{Re}\left[\left|E^{(+)}(t)\right| \exp\{-\mathrm{i}[\omega_0 t - \varphi(t)]\}\right], \tag{4.16}$$

as in (5.12) and (5.20) in Sect. 5.3, where $\varphi(t)$ as the time-dependent phase, and ω_0 is the carrier frequency. In the frequency domain, as with the Fourier-transform, the field can be written by

$$\tilde{E}(\omega) = \int_{-\infty}^{\infty} \mathrm{d}t \ \mathrm{e}^{\mathrm{i}\omega t} E(t). \tag{4.17}$$

Here, we treat only the positive-frequency component $\tilde{E}^{(+)}(\omega)$ of $\tilde{E}(\omega)$ and neglect the negative-frequency component $\tilde{E}^{(-)}(\omega)$ of $\tilde{E}(\omega)$. The positive-frequency component of $\tilde{E}(\omega)$ is defined by

$$\begin{aligned} \tilde{E}^{(+)}(\omega) &= \int_{-\infty}^{\infty} \mathrm{d}t \ \mathrm{e}^{\mathrm{i}\omega t} E^{(+)}(t) \\ &= \left|\tilde{E}^{(+)}(\omega)\right| \exp[\mathrm{i}\phi(\omega)], \end{aligned} \tag{4.18}$$

and $\phi(\omega)$ is the spectral phase.

From the measurement of a spectrally resolved autocorrelation by plotting the signal spectral intensity versus delay instead of the signal energy versus delay, FROG yields a spectrogram of the pulse. Hence, FROG gives the full information in intensity and phase of the pulse in both the time and frequency domains. In SHG-FROG, the signal from an SHG autocorrelator is spectrally resolved. In the case of the ideal SHG, the signal field is

$$E_{\mathrm{sig}}(t, \tau) \propto E(t)E(t - \tau), \tag{4.19}$$

which yields the FROG trace

$$I_{\mathrm{FROG}}^{\mathrm{SHG}}(\omega, \tau) \propto \left| \int_{-\infty}^{\infty} \mathrm{d}t E(t)E(t - \tau) \exp(\mathrm{i}\omega t) \right|^2. \tag{4.20}$$

This experimentally measured FROG trace is then used as input to an algorithm. The FROG algorithm is based on the iterative-Fourier-transform algorithm and extracts the intensity and phase of the pulse from the FROG trace by finding the electric field that best reproduces the trace.

The SHG-FROG signal field $E_{\mathrm{sig}}(t, \tau)$ is

$$E_{\mathrm{sig}}(t, \tau) \propto E(t)E(t - \tau), \tag{4.21}$$

which yields the relation

$$E(t) \propto \int_{-\infty}^{\infty} \mathrm{d}\tau E_{\mathrm{sig}}(t, \tau). \tag{4.22}$$

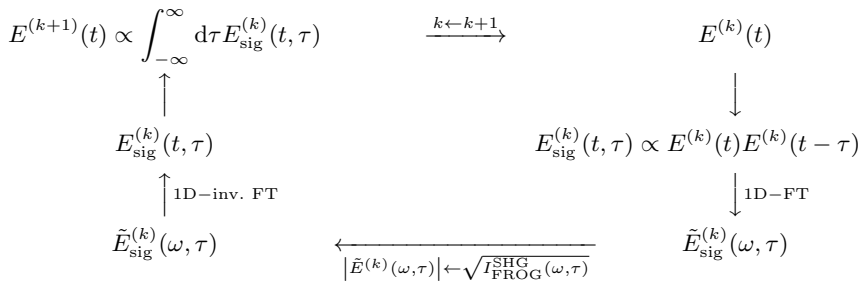

Fig. 4.9. Iterative-Fourier-transform algorithm for inverting a trace to obtain the intensity and phase of an ultrashort optical pulse. 1D-FT and 1D-inv. FT denote a one-dimensional Fourier transform with respect to t and a one-dimensional inverse Fourier transform with respect to ω, respectively

Thus an evaluation for $E_{\mathrm{sig}}(t,\tau)$ immediately gives an evaluation for $E(t)$ by means of (4.22).

The SHG-FROG algorithm is schematically shown in Fig. 4.9. It begins with a trial solution $E^{(1)}(t)$ for the optical field $E(t)$. In the kth iteration process (k =1, 2, 3, $\cdots$), using (4.21), the kth iteration $E_{\mathrm{sig}}^{(k)}(t,\tau)$ for $E_{\mathrm{sig}}(t,\tau)$ is generated as

$$E_{\mathrm{sig}}^{(k)}(t,\tau) \propto E^{(k)}(t)E^{(k)}(t-\tau). \tag{4.23}$$

Then, it is one-dimensional-Fourier-transformed with respect to t, into the (ω,τ) domain to obtain $\tilde{E}_{\mathrm{sig}}^{(k)}(\omega,\tau)$. Now, the magnitude of $\tilde{E}_{\mathrm{sig}}^{(k)}(\omega,\tau)$ is constrained to that of the experimentally measured FROG trace. This is performed by replacement of $\left|\tilde{E}_{\mathrm{sig}}^{(k)}(\omega,\tau)\right|$ with $\sqrt{I_{\mathrm{FROG}}^{\mathrm{SHG}}(\omega,\tau)}$ while the spectral phase is unchanged. Namely,

$$\tilde{E}_{\mathrm{sig}}^{(k)}(\omega,\tau) \longleftarrow \frac{\tilde{E}_{\mathrm{sig}}^{(k)}(\omega,\tau)}{\left|\tilde{E}_{\mathrm{sig}}^{(k)}(\omega,\tau)\right|}\sqrt{I_{\mathrm{FROG}}^{\mathrm{SHG}}(\omega,\tau)}, \tag{4.24}$$

where $\longleftarrow$ means the replacement of the left-hand term with the right-hand term. After the replacement in (4.24), $\tilde{E}_{\mathrm{sig}}^{(k)}(\omega,\tau)$ is one-dimensional inverse-Fourier-transformed with respect to ω, back into the (t,τ) domain to obtain $E_{\mathrm{sig}}^{(k)}(t,\tau)$. Then, from the kth iteration $E_{\mathrm{sig}}^{(k)}(t,\tau)$ for $E_{\mathrm{sig}}(t,\tau)$, the $(k+1)$th iteration $E^{(k+1)}(t)$ for $E(t)$ is found with the use of (4.22). That is,

$$E^{(k+1)}(t) \propto \int_{-\infty}^{\infty} \mathrm{d}\tau E_{\mathrm{sig}}^{(k)}(t,\tau). \tag{4.25}$$

Thus, from kth evaluation $E^{(k)}(t)$ for $E(t)$, a new evaluation $E^{(k+1)}(t)$ is constructed. In this manner, these processes are iterated. The FROG algorithm

measures convergence by calculationg the FROG error, $\epsilon^{(k)}$, defined as the root-mean-square difference between the measured FROG trace $I_{\mathrm{FROG}}^{\mathrm{SHG}}(\omega,\tau)$ and the FROG trace $I_{\mathrm{FROG,ret}}^{\mathrm{SHG},(k)}(\omega,\tau)$ of the retrieved field in the kth iteration:

$$\epsilon^{(k)} = \left\{ \frac{1}{N^2} \sum_{i=1}^{N} \sum_{j=1}^{N} \left[I_{\mathrm{FROG,ret}}^{\mathrm{SHG},(k)}(\omega_i,\tau_j) - I_{\mathrm{FROG}}^{\mathrm{SHG}}(\omega_i,\tau_j) \right]^2 \right\}^{1/2}, \quad (4.26)$$

where N is the number of sampling points of the FROG trace, and ω_i and τ_j are the ith frequency and jth delay in (ω,τ) domain, respectively. Satisfying convergence is assumed when $\epsilon^{(k)}$ is of the order of 10^{-3} to 10^{-4} for the experimentally measured data.

From a FROG trace with N^2 sampling points, an electric field sampled at N points, which has $2N$ degrees of freedom (N points of both amplitude and phase), is retrieved. Thus there is a redundancy in the FROG trace. Therefore, the optimum solution is searched for using the FROG algorithm mentioned above.

Ambiguity of Temporal Direction

Extensive numerical testing has proven the robustness of the algorithm in its ability to converge for test and experimental pulses. It is noted that, unlike FROG using third-order nonlinear processes, the SHG trace is symmetrical with respect to delay and hence has ambiguity in the direction of time. Electric fields $E(t)$ and $E(-t)$ give identical SHG-FROG traces and thus cannot be distinguished in a single SHG-FROG trace. Of course, the ambiguity in the direction of time can be simply eliminated by use of a second SHG-FROG trace after chirping the pulse, for example, with a thick piece of glass.

Frequency Marginal

Since FROG uses a nonlinear process, the spectral filtering effect due to nonuniformity of the conversion efficiency in the process results in the distortions in the signal spectral intensity, especially for the ultrabroadband pulses. However, the fact that the FROG trace contains redundant data enables us to perform checks on the consistency of the experimental data. These checks allow us to ensure that the entire pulse spectrum is converted to second-harmonic light. This is done by comparing the frequency marginal of the FROG trace with the independently-measured pulse spectral intensity. The frequency marginal is the integral of the FROG trace with respect to ω, as defined by

$$M_{\mathrm{FROG}}^{\mathrm{SHG}}(\omega) = \int_{-\infty}^{\infty} \mathrm{d}\tau I_{\mathrm{FROG}}^{\mathrm{SHG}}(\omega,\tau). \quad (4.27)$$

It should have a functional form identical to the autoconvolution of the pulse spectral intensity, which is proportional to $\left|\tilde{E}^{(+)}(\omega)\right|^2$:

$$M_{\mathrm{FROG}}^{\mathrm{SHG}}(\omega) \propto \left|\tilde{E}^{(+)}(\omega)\right|^2 * \left|\tilde{E}^{(+)}(\omega)\right|^2 = \int_{-\infty}^{\infty} \mathrm{d}\omega' \left|\tilde{E}^{(+)}(\omega-\omega')\right|^2 * \left|\tilde{E}^{(+)}(\omega')\right|^2, \tag{4.28}$$

where $*$ denotes convolution. Hence, one can easily check the consistency of the FROG data by simply measuring the spectral intensity of the pulse to be characterized. If the SHG-FROG frequency marginal does not agree with the autoconvolution of the pulse spectral intensity, one can be asserted that there is a systematic experimental error in the system, for example, a spectral filtering effect in the nonlinear crystal, a spectrometer or CCD camera response which depends on wavelength, wavelength or temporal calibration of the FROG data, spatial chirp, spatio-temporal distortions of the pulse at the focus and so forth.

There is also a delay marginal, which can be compared with the autocorrelation trace. However, it is less useful.

Time Smearing Effect

Another experimental problem, particularly for measurement of below 5 fs-optical pulses is smearing of the delay time owing to noncollinearity of the beams in the nonlinear crystal for SHG. When two pulses intersect each other at an angle in the horizontal plane, one pulse precedes the other on the right, and the other precedes the one on the left. When the delay time is assumed to be fixed at a single value at any one time, this effect smears out the temporal information in the FROG trace. In the presence of this time smearing, the FROG algorithm evaluates the resulting pulse duration $t_{\mathrm{p}}^{\mathrm{meas}}$ which is larger than the true pulse duration $t_{\mathrm{p}}^{\mathrm{true}}$. For a Gaussian intensity pulses with Gaussian spatial profile, $t_{\mathrm{p}}^{\mathrm{meas}}$ is expressed [23] by

$$(t_{\mathrm{p}}^{\mathrm{meas}})^2 = (t_{\mathrm{p}}^{\mathrm{true}})^2 + (\delta t)^2, \tag{4.29}$$

where

$$\delta t = \frac{\sqrt{2\ln 2}\, d_{\mathrm{b}} \lambda}{\pi c w}, \tag{4.30}$$

and d_{b} and w are the beam separation and beam diameter, respectively. c and λ are the speed and wavelength of the light in a vacuum, respectively. Here, the beam diameter is defined as the diameter of the $1/\mathrm{e}^2$-intensity contour and the pulse duration is defined as the full-width at half-maximum.

4.3.2 Apparatus and Characteristcs

Apparatus

The SHG-FROG apparatus that we used [31] was based on a multishot autocorrelator, as shown in Fig. 4.10. The input beam was split and recombined by a 0.5-mm-thick broadband (50±10% reflectivity for 400–900 nm) dielectric beam splitter (BS); each of the beams travels once through the beam splitter with both reflections occurring on the same air-coating interfaces. In the two arms of the autocorrelator, the silver-coated retroreflectors (RR) were used in a balanced configuration. One of the the arms was movable with a stepping motor which is controlled by a computer.

The pulses to be measured were focused in a nonlinear crystal β-barium borate (BBO) by an off-axial parabolic mirror (PM) with a focal length f of 50 mm. The BBO crystal with a thickness of 10 μm at a cutting angle of 40° was employed for second-harmonic generation in type-I geometry. To detect the FROG signals, a spectrometer with a 1024-channel, intensified CCD array was used. The step number was 256 and the delay-time step was 1.34 fs.

Ultrashort and Ultrabroadband Pulse Generation

Now we describe an example of the characterization results of the ultrashort or ultrabroadband optical pulses by FROG. The experimental setup for the ultrashort or ultra-broadband optical pulse generation that we used [31,32] is shown in Fig. 4.11. The output pulse of a Ti:sapphire laser-amplifier system centered at 790 nm with duration of 30 fs and repetition rate of 1 kHz was focused into a capillary fiber with 340-mm length and 0.1-mm inner diameter, which is located in a chamber filled with argon gas [31,33]. The pulse energy focused into the fiber was 140 μJ. The chamber had two 1-mm thick sapphire windows. The output pulse from the chamber was collimated by a spherical mirror and guided to a 4-f system with a spatial phase modulator (SLM). The 4-f system was composed of two spherical mirrors with a focal length $f =$

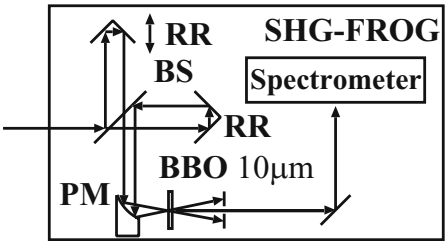

Fig. 4.10. Experimental setup of SHG-FROG BS: beam splitter, PM: parabolic mirror, RRs: retroreflectors, BBO: β-barium borate crystal with a thickness of 10 μm [31,32]

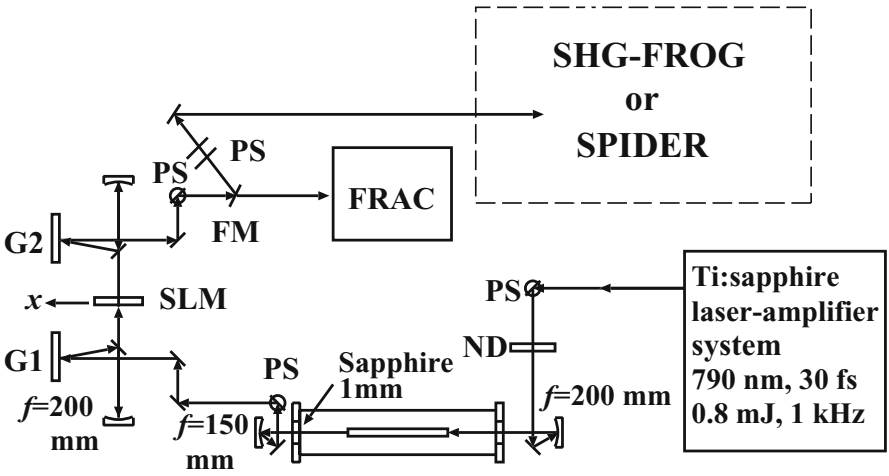

Fig. 4.11. Experimental setup for the generation of ultrashort optical pulses. of SHG-FROG. PSs: periscopes, ND: neutral-density filter, G1 and G2: reflective diffraction gratings, SLM: spatial phase modulator, FM: flip mirror [31, 32]

200 mm and two silver reflective gratings (G1 and G2) with a grating constant $d = 1/150$ mm. The optical path lengths from the gratings to the spherical mirrors and those from the spherical mirrors to the SLM were all adjusted to be $f = 200$ mm. The liquid-crystal SLM consisted of 648 pixels with width of 97 μm. The gap between adjacent pixels was 5 μm. The transmission of the SLM was more than 70% in 500–700 nm wavelength range, while it decreased in the longer wavelength range (e.g. 50% at 1000 nm). The pulse energy after passing the chamber was 22 μJ and the throughput of the 4-f system was 30%. In the setup we used periscopes (PSs) to change the height and/or the polarization direction of the beam, and a flip mirror (FM) to change the beam direction for measurements of FRAC and SHG-FROG. Here, in Fig. 4.11 as a pulse characterization apparatus, SHG-FROG (a part surrounded by a dashed line) as well as FRAC is used. In Sect. 4.4 or 4.5, it will be replaced with SPIDER or modified SPIDER.

The SLM was employed as a phase modulator which can impose a phase variation of 2π for light in the wavelength range less than 1400 nm with a resolution of 192 steps. The relationship between phase and digital input of 192 steps, being nonlinear, was measured and calibrated using the spectral interferometer [34, 35]. The phase $\phi^{\mathrm{SLM}}(\omega(x))$ applied by SLM at position x is given by

$$\phi^{\mathrm{SLM}}(\omega(x)) = \frac{C_2}{2}[\omega(x) - \omega_0]^2 + \frac{C_3}{6}[\omega(x) - \omega_0]^3 + \frac{C_4}{24}[\omega(x) - \omega_0]^4, \tag{4.31}$$

where ω_0 is the center angular frequency of the Taylor expansion, $\omega(x)$ is the angular frequency at position x and is given by

$$\omega(x) = 2\pi c \left[d\left\{\sin\theta_{\mathrm{in}} + \sin\left[\arctan\left(x/f\right) + \arcsin\left(\lambda_{\mathrm{c}}/d - \sin\theta_{\mathrm{in}}\right)\right]\right\}\right]^{-1}, \tag{4.32}$$

derived from the well-known diffraction formula of gratings [36]. Here, c is the velocity of light in a vacuum and λ_{c} is the wavelength at the central position of the SLM at $x = 0$. λ_{c} does not have to equal to the center wavelength for the Taylor expansion λ_0. θ_{in} is the incident angle of the beam to the grating. The parameters C_2, C_3 and C_4 are the group-delay dispersion (GDD), the third-order dispersion (TOD) and the fourth-order dispersion (FOD) at ω_0, respectively. Thus, the group delay $t_{\mathrm{d}}^{\mathrm{SLM}}(\omega(x))$ imposed by the SLM was

$$\begin{aligned} t_{\mathrm{d}}^{\mathrm{SLM}}(\omega(x)) &= \frac{\mathrm{d}}{\mathrm{d}\omega}\phi^{\mathrm{SLM}}(\omega(x)) \\ &= C_2[\omega(x) - \omega_0] + \frac{C_3}{2}[\omega(x) - \omega_0]^2 + \frac{C_4}{6}[\omega(x) - \omega_0]^3. \end{aligned} \tag{4.33}$$

The chirp compensation condition that gives Fourier-transform-limited (TL) pulses is when the residual group delay $t_{\mathrm{d}}^{\mathrm{res}}(\omega(x))$ at position x is independent of the frequency ω, that is,

$$t_{\mathrm{d}}^{\mathrm{res}}(\omega(x)) \equiv \frac{\mathrm{d}}{\mathrm{d}\omega}[\phi(\omega) + \phi^{\mathrm{SLM}}(\omega(x))] = \text{const.}, \tag{4.34}$$

where $\phi(\omega)$ is the spectral phase of the pulse to be compensated for.

Initially the expansion wavelength $\lambda_0 \equiv 2\pi c/\omega_0$ was set to be 800 nm with the values of $C_2 = -329\,\mathrm{fs}^2$, $C_3 = -748\,\mathrm{fs}^3$ and $C_4 = 0\,\mathrm{fs}^4$. In this case, the quasi-simultaneously measured FRAC trace at an argon pressure of 2.8 atm indicated that the duration of the pulse to be measured was 4.1 fs and in the zero-time delay region, this trace agreed well with that of the TL pulse obtained from the measured spectrum. In this case, we also characterized the optical pulses by SHG-FROG. However, the pulse duration measured by FROG was ∼6 fs, which is longer than that of the TL pulse or that measured by FRAC. This underestimate of the duration may be understandable from the poor agreement of the pedestal in the FRAC trace [37] and the asymmetric FROG-retrieved temporal intensity profile, as well as the slightly different dispersion optics in the FRAC and FROG apparatuses. Thus we were motivated to search for better parameters for the phase applied by the SLM.

The imperfection in nonlinear chirp compensation is due to the flat phase modulation in each pixel, which leads to a step-wise phase modulation in the whole wavelength region of interest. The phase $\phi^{\mathrm{SLM}}(\omega)$ applied by SLM, as expressed by (4.31), is a nonlinear function of ω, but the projection of wavelength components (as opposed to frequency) on the SLM (on the Fourier plane) is almost linear. Therefore, the error height of the phase step due to the discreteness at each pixel is higher in the short-wavelength region with respect to the center expansion wavelength λ_0 than in the long-wavelength region. That causes poorer chirp-compensation in the short-wavelength region than in the long-wavelength region. To avoid this imbalance of chirp compensation and to obtain a better chirp-compensation in the short-wavelength region, we perform the phase compensation by shifting the center expansion wavelength λ_0 to 600 nm. Parameters C_2, C_3 and C_4 were determined to be $-400\,\mathrm{fs}^2$, $-100\,\mathrm{fs}^3$ and $250\,\mathrm{fs}^4$, respectively, with fine tuning by a computer so that the FROG-retrieved result gave the shortest pulse.

Frequency Marginal Correction

The 10-μm-thick BBO crystal at a cutting angle of 40° was used in type-I geometry. Owing to the limited bandwidth of the crystal, the frequency marginal [23], $M^{\mathrm{Exp}}(\omega)$, calculated from the FROG trace did not match that from the spectrum intensity autoconvolution $M^{\mathrm{Theo}}(\omega)$, as seen in Fig. 4.12 (a). In order to correct this effect, we multiplied each value in the FROG trace by a frequency-dependent factor such that the marginal calculated from the FROG trace became identical to that obtained from the spectrum [23] After the correction of the marginals, the pulse intensity and phase were retrieved by use of commercial FROG software.

Evaluation of Time Smearing

The beam separation d_{b} at the parabolic mirror (PM) was 2 mm and the beam diameter w was 1 mm. The time smearing τ_{sm} [24, 38] was evaluated by use of (4.30) to be $\tau_{\mathrm{sm}} = \sqrt{2\ln 2}\lambda d_{\mathrm{b}}/(\pi c w) = 1.6\,\mathrm{fs}$ at the wavelength of $\lambda = 650\,\mathrm{nm}$ on the assumption of Gaussian spatial and temporal profiles.

Characterization Result

The time required for the measurement was ∼1 min, and the stability of the pulses was excellent during that time. We could usually reproduce the pulse duration measured by FROG within 10% by using the same parameters several hours after they had been optimized. In Fig. 4.12(b), the measured and retrieved spectra together with retrieved spectral phase are shown. In Fig. 4.12(c), the temporal intensity and phase profiles are shown. The FROG error was 0.0038. The measured and the calculated spectra agreed quite well

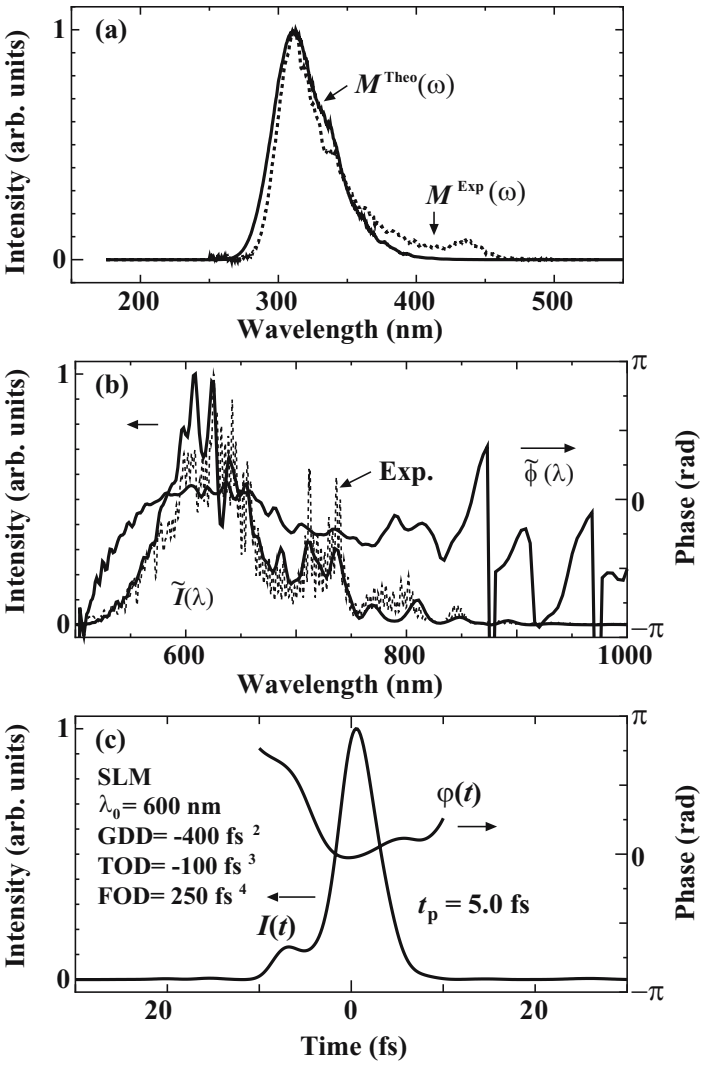

Fig. 4.12. Results of the corrected frequency marginal FROG measurement with SLM parameters. (a) Marginal calculated from the experimental spectrum $M^{\mathrm{Theo}}(\omega)$ (solid line) and that obtained from the FROG trace $M^{\mathrm{Exp}}(\omega)$ (dotted line). (b) Spectrum $\tilde{I}(\lambda)$ and spectral phase $\tilde{\phi}(\lambda)$. Experimental spectrum is depicted by the dotted line. (c) Temporal intensity $I(t)$ and phase profiles $\varphi(t)$ [31,32]

thanks to the correction of the marginals. However, the pulse duration was not changed by that correction. The duration obtained was 5.0 fs which corresponded to 2.4 cycles at the center wavelength of 633 nm. It was 14% longer than that of the TL pulse (4.4 fs). If the geometrical smearing effect is taken into account, the duration is evaluated to be 4.7 fs. As seen in comparison be-

tween the compression results for the expansion center wavelength $\lambda_0 = 800$ and 600 nm, an appropriate blue shift of λ_0 enabled us to perform better effective nonlinear-chirp compensation for ultra-broadband femtosecond optical pulses.

Characteristics

Let us now summarize the characteristics of SHG-FROG. Its disadvantages are

(d-1) the bandwidth limitation below an octave owing to second-harmonic generation,
(d-2) the complicated iteration algorithm for retrieving the spectral phase,
(d-3) the comparatively long acquisition time of spectrogram by moving an optical delay,
(d-4) the effect of time smearing due to noncollinear configuration;

its advantages are

(a-1) the high sensitivity using the second-order nonlinear interaction,
(a-2) the capability of self-consistency check or correction using the frequency marginal.

4.4 Spectral Interferometry for Direct Electric-Field Reconstruction (SPIDER)

4.4.1 Principle

The technique of SPIDER is a specific implementation of spectral shearing interferometry [8,39–43]. SPIDER utilizes nonlinear frequency mixing to generate a pair of identical but frequency-sheared replicas of the input pulse. The interference between this pair of pulses is recorded with a spectrometer as an interferogram. From this interferogram, the amplitude and phase of the input pulse can be directly (noniteratively) reconstructed.

The principle of SPIDER is schematically shown in Fig. 4.13. The pulse to be characterized is divided into two parts by a beam splitter. One forms a pair of replicas which are separated in time by a delay τ using, for example, two arms of a Michelson interferometer. The other passes through a dispersive medium to be linearly chirped. The two replicas with the time delay τ are frequency-mixed with the chirped pulse in a nonlinear crystal. Each pulse replica is frequency-mixed with a different time slice, and hence different spectral slice of the linearly chirped pulse. As a result, the upconverted pulses are frequency-sheared. The resulting interferogram is resolved with a spectrometer.

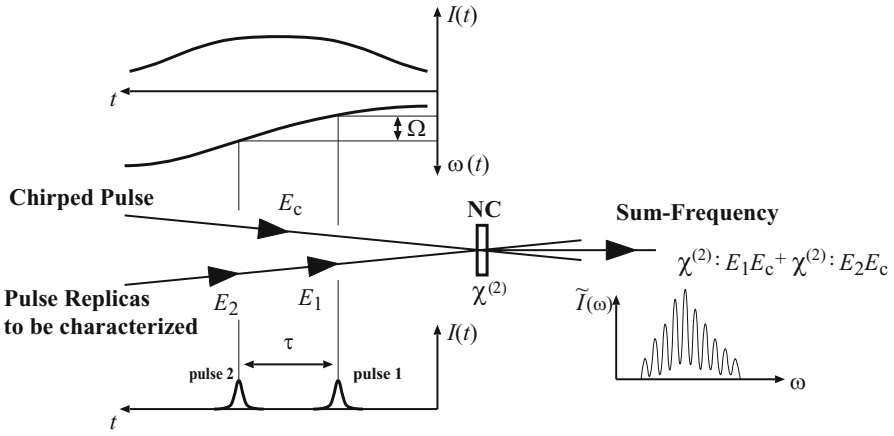

Fig. 4.13. Principle of SPIDER. NC represents a nonlinear crystal [32]

The measured interferogram $\tilde{S}(\omega)$ is given by

$$\tilde{S}(\omega) \propto \left|\tilde{E}^{(+)}(\omega)\right|^2 + \left|\tilde{E}^{(+)}(\omega-\Omega)\right|^2 + 2\left|\tilde{E}^{(+)}(\omega)\tilde{E}^{(+)}(\omega-\Omega)\right| \cos\left[\phi(\omega)-\phi(\omega-\Omega)+\omega\tau\right], \quad (4.35)$$

where $\tilde{E}^{(+)}(\omega)$ is the complex electric field defined by (4.18), and Ω and τ are the amount of the spectral shear and the delay time between the two replicas, respectively. $\tilde{S}(\omega)$ is a standard shearing interferogram which is composed of fringes nominally spaced in frequency at $\sim 2\pi/\tau$. For simplicity, we write the interferogram (4.35) as

$$\tilde{S}(\omega) \propto \tilde{S}^{(\mathrm{dc})}(\omega) + \tilde{S}^{(+\mathrm{ac})}(\omega)\exp(\mathrm{i}\omega\tau) + \tilde{S}^{(-\mathrm{ac})}(\omega)\exp(-\mathrm{i}\omega\tau), \quad (4.36)$$

where

$$\tilde{S}^{(\mathrm{dc})}(\omega) = \left|\tilde{E}^{(+)}(\omega)\right|^2 + \left|\tilde{E}^{(+)}(\omega-\Omega)\right|^2, \quad (4.37)$$

$$\tilde{S}^{(+\mathrm{ac})}(\omega) = \left|\tilde{E}^{(+)}(\omega)\tilde{E}^{(+)}(\omega-\Omega)\right| \exp\{\mathrm{i}\left[\phi(\omega)-\phi(\omega-\Omega)\right]\}, \quad (4.38)$$

$$\tilde{S}^{(-\mathrm{ac})}(\omega) = \left|\tilde{E}^{(+)}(\omega)\tilde{E}^{(+)}(\omega-\Omega)\right| \exp\{-\mathrm{i}\left[\phi(\omega)-\phi(\omega-\Omega)\right]\}. \quad (4.39)$$

The dc portion $\tilde{S}^{(\mathrm{dc})}(\omega)$ is the sum of the individual spectra of the pulse to be characterized and its frequency-sheared spectra and include no spectral phase information. The ac terms $\tilde{S}^{(+\mathrm{ac})}(\omega)$ and $\tilde{S}^{(-\mathrm{ac})}(\omega)$ are the interference terms which give the spectral phase in the form of the phase difference between spectral components separated by the shear Ω. These terms exhibit perturbation from the nominal fringe spacing.

There are three steps for retrieving the spectral phase from the interferogram as follows: (i) isolate one of the ac terms, and hence $\phi(\omega)-\phi(\omega-\Omega)+\omega\tau$, with a Fourier transform and filtering, (ii) remove linear phase term $\omega\tau$ by

subtracting a calibration phase, (iii) reconstruct the spectral phase $\phi(\omega)$ by concatenating or integrating the spectral phase difference.

In order to isolate the spectral phase difference $\phi(\omega)-\phi(\omega-\Omega)+\omega\tau$, the interferogram $\tilde{S}(\omega)$ is inverse Fourier transformed with respect to the spectrometer frequency, filtered, and Fourier transformed. The Fourier transform of $\tilde{S}^{(\mathrm{dc})}(\omega)$, $S(t)$ is

$$S(t) \propto \mathsf{F}^{-1}[\tilde{S}^{(\mathrm{dc})}(\omega)](t) + \mathsf{F}^{-1}[\tilde{S}^{(+\mathrm{ac})}(\omega)](t-\tau) + \mathsf{F}^{-1}[\tilde{S}^{(-\mathrm{ac})}(\omega)](t+\tau), \tag{4.40}$$

where the inverse Fourier transform operator F^{-1} for an arbitrary function $f(\omega)$, which yields a function of t, is defined by

$$\mathsf{F}^{-1}[f(\omega)](t) = \frac{1}{2\pi}\int_{-\infty}^{\infty} \mathrm{d}\omega \exp[-\mathrm{i}\omega t] f(\omega). \tag{4.41}$$

Equation (4.41) has components centered near $t=\pm\tau$ and $t=0$. The component at $t=0$ is the Fourier transform of the dc part of the spectrogram. The $t=\pm\tau$ components is the ac parts of the interferogram. If τ is sufficiently large, dc and ac parts are well separated and the dc and one of ac parts can be removed by filtering. Hence, only one ac part, which has the information of the spectral phase $\phi(\omega)-\phi(\omega-\Omega)+\omega\tau$, can be extracted.

In the second step of the phase reconstruction, the linear phase term $\omega\tau$ is removed from $\phi(\omega)-\phi(\omega-\Omega)+\omega\tau$. This is done by directly measuring the $\omega\tau$. The interferometer is calibrated by recording a spectrogram for the pair of replica pulses without giving the spectral shear. In this case, the inferred pulses are spectrally identical, thus only the phase contribution $\omega\tau$ is recorded. The linear phase term $\omega\tau$ obtained from calibration is subtracted from $\phi(\omega)-\phi(\omega-\Omega)+\omega\tau$, hence the phase difference $\phi(\omega)-\phi(\omega-\Omega)$ is extracted.

The third step is the reconstruction of the spectral phase $\phi(\omega)$ from the spectral difference defined by

$$\theta_{\mathrm{diff}}(\omega) \equiv \phi(\omega) - \phi(\omega-\Omega). \tag{4.42}$$

Usually $\theta_{\mathrm{diff}}(\omega)$ includes an unknown constant phase which gives a linear contribution to the reconstructed phase $\phi(\omega)$ and results in an unimportant temporal shift of the pulse. Thus the spectral phase at a certain frequency ω_0 can be set so that $\phi(\omega_0)=0$ and the spectral phase at $\cdots, \omega_0-2\Omega, \omega_0-\Omega, \omega_0, \omega_0+\Omega, \omega_0+2\Omega, \cdots$ are, respectively, expressed by

$$
\begin{aligned}
&\vdots \\
\phi(\omega_0 - 2\Omega) &= -\theta_{\mathrm{diff}}(\omega_0 - \Omega) - \theta_{\mathrm{diff}}(\omega_0), \\
\phi(\omega_0 - \Omega) &= -\theta_{\mathrm{diff}}(\omega_0), \\
\phi(\omega_0) &= 0, \\
\phi(\omega_0 + \Omega) &= \theta_{\mathrm{diff}}(\omega_0 + \Omega), \\
\phi(\omega_0 + 2\Omega) &= \theta_{\mathrm{diff}}(\omega_0 + \Omega) - \theta_{\mathrm{diff}}(\omega_0 + 2\Omega), \\
&\vdots
\end{aligned}
\tag{4.43}
$$

using concatenation. By adding up the phase differences, the spectral phase for frequencies separated by the spectral shear Ω is reconstructed.

If the magnitude of the spectral shear $|\Omega|$ is sufficiently small, the spectral phase can be reconstructed by integration of

$$
\phi(\omega) \simeq \frac{1}{\Omega} \int^{\omega} \mathrm{d}\omega' \theta_{\mathrm{diff}}(\omega'). \tag{4.44}
$$

The spectral step size of data is usually much smaller than the frequency shear. Hence, the concatenation method uses only a subset of the available data. In contrast to this, the integration method uses all of the data.

Parameters of Spectral Shear Ω and Delay Time τ

For a SPIDER apparatus, the spectral shear Ω and the delay time between the two replicas are key parameters. In principle, these are not independent because $\Omega \simeq \tau/|\phi''(\omega_\mathrm{c})|$ (ω_c: center frequency of the pulse). Moreover, both parameters are constrained individually as follows.

(i) The frequency shear Ω should be large so that the spectral phase difference is perceptible.
(ii) Inversely, Ω should be small so that the sampling step of the phase can be smaller than the Nyquist limit.
(iii) Because the spectral interferogram fringes are nominally spaced at $2\pi/\tau$, τ should be small so that the employed spectrometer can resolve the fringes.
(iv) On the other hand, τ should be large so that the ac terms can be separated from the dc term in the process of the phase difference extraction.

In addition, another parameter $\phi''(\omega_\mathrm{c})$ is also constrained: it should be large so that each of the pulse replicas can be upconverted with a quasi-cw slice of the chirped pulse.

4.4.2 Apparatus and Characteristics

Apparatus

Figure 4.14 shows the SPIDER apparatus that we made [44]. In this apparatus, specially-designed ultrabroadband beam splitters from 450 to 850 nm for the s-polarization in the Michelson-interferometric arm, a BBO crystal of 25 μm thickness, and a highly sensitive spectrometer attached by intensified-CCD with a high-wavelength resolution of 0.15 nm and the automatic and fast angle-control function of the two gratings with grating constants of 1/1200 and 1/150 mm were employed.

The pulse to be characterized was generated in an argon gas-filled hollow fiber and phase-compensated by a 4-f pulse shaper with an SLM in the similar manner to that used in Sect. 4.3. After the rotation to the s-polarization by the silver-coated periscope, the input pulse E to be characterized was divided into two equal-intensity beams by a specially-designed ultrabroadband dielectric beam splitter, BS1, ranging 450 to 850 nm. The beam splitter BS1 had 50±3% reflectivity for the input pulse spectrum from 480 to 835 nm with the single-stacking coating on a 0.5-mm-thick fused-silica glass. One beam was reflected by a silver-coated retroreflector for the adjustment of the time delay

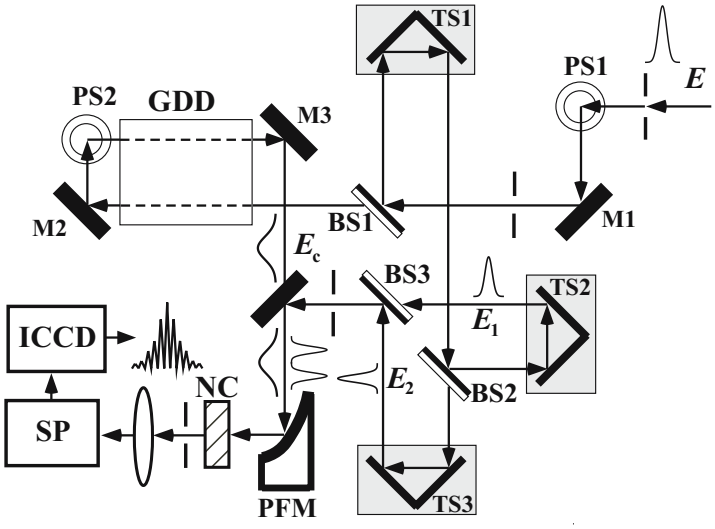

Fig. 4.14. SPIDER setup; BS1-BS3: specially-designed beam splitters (450–850 nm), GDD: TF5 glass block, TS1: translation stage for adjustment of temporal overlap of the short pulse pair with the stretched pulse, TS2 and TS3: translation stages for adjustment of delay time, PFM: aluminum 50-mm-focusing parabolic mirror, NC: nonlinear crystal (25 μm-thick type-II BBO), SP: spectrometer, ICCD: intensified charge-coupled device, PS1-2: periscopes, M1-3: mirrors [32, 44]

between the two beams and was sent to the Michelson-interferometric arm to make two-pulse replicas, E_1 and E_2, with the delay of τ.

The value of τ was selected to be 857 fs on the basis of the sampling theorem and the numerical simulation result of the optimum $\tau \simeq 2\pi N_\mathrm{s}/(N_\mathrm{t}\Delta\omega)$ [45]. Here N_s is the pixel number corresponding to the FWHM bandwidth $\Delta\omega/2\pi \simeq 133$ THz of the pulse spectrum and N_t is the pixel number per interference fringe of the SPIDER signal.

The interferometer with balanced reflectivity and dispersion used two 500-μm-thick dielectric beam splitters, BS2 and BS3, having the same reflection and transmission property as that of BS1. Another beam was transmitted twice through a 100-mm-thick TF5 dispersion glass, which is denoted by GDD and gives group-delay dispersion of 4.6×10^4 fs^2 at 665 nm. During the pass, we rotated this beam to the p-polarization by a periscope to produce the strongly-chirped pulse E_c for the sum-frequency generation with quasi-CW field. The two replica pulses, E_1 and E_2, were combined and nonlinearly mixed with the chirped pulse E_c by focusing on a 25-μm-thick type-II BBO crystal [43]. The calculation showed the 25-μm BBO generate the sum-frequency wave over the spectral range of 480 to 835 nm of the pulse E_1 or E_2. As a result, the SPIDER signal of the interferometric sum-frequency beam, $E_1E_\mathrm{c} + E_2E_\mathrm{c}$ was generated with a spectral shear of $\Omega/2\pi = 2.81$ THz, satisfying the sampling theorem [45]. After the removal of these pulses E_1, E_2 and E_c by a 0.5-mm slit, the spectral interferogram signal $E_1E_\mathrm{c} + E_2E_\mathrm{c}$ was focused on a multimode fiber-coupling spectrometer of 0.5 m by a 220-mm focal-length silica lens, and was detected by a 1024 × 256-pixel UV-enhanced intensified-CCD array which allowed rapid data acquisition. An incident slit of 150 μm and 1200 lines/mm grating resulted in the total wavelength resolution of 0.15 nm at 400 nm and the limited bandwidth of 37.5 nm. Thus the full bandwidth of the signal was automatically recorded by the synthesis of seven spectral parts of different center wavelengths at update time of $7 \times 2.5\,\mathrm{s} = 17.5\,\mathrm{s}$ with the calibration in wavelength and sensitivity, as shown in Fig. 4.15. This measurement time was much shorter than that of the FROG technique which is typically five minutes [31].

Characterization by SPIDER

We measured the two sum-frequency spectra of E_1E_c and E_2E_c in the main spectral region, as shown in Fig. 4.16(a), to determine the value of the spectral shear Ω in angular frequency, and the interferometric second-harmonic spectrum of $(E_1 + E_2)^2$ in the main spectral region, as shown in Fig. 4.16(b), by the 45° rotation of the BBO crystal in order to determine the value of the delay time τ. We confirmed the clear similarity between the former two spectra after smoothing. The visibility of the latter spectrum was sufficient to determine the accurate value of τ. The input spectrum of E was measured

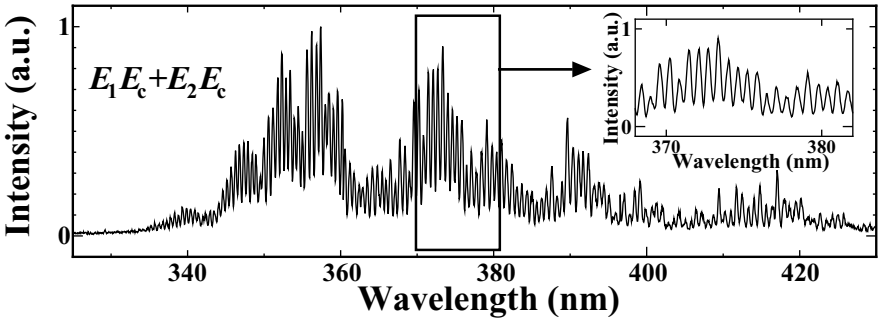

Fig. 4.15. SPIDER interferogram signal [32, 44]

by use of the 150 line/mm grating which was rapidly exchanged and automatically controlled the same detection system, as shown in Fig. 4.16(c). All the data recorded were analyzed by SPIDER software in which the dc and $-$ac parts after the inverse-Fourier-transform in the quasi-time τ' region shorter than $\tau' = 190$ fs $\simeq 2\pi/\Omega$ were eliminated and only the essential $+$ac part [8] was extracted.

The spectral phase $\phi(\omega)$ was reconstructed from the phase difference $\theta_{\text{diff}}(\omega)$ after removing the linear term $\omega\tau$. The reconstructed temporal intensity $I(t)$ and phase $\varphi(t)$ profiles and the corresponding spectrum $\tilde{I}(\lambda)$ and spectral phase $\tilde{\phi}(\lambda)$ as functions of wavelength λ are shown in Fig. 4.17(a) and (b), respectively. This result indicates that a 5.0 fs pulse was measured and that its group delay (derivative of spectral phase with respect to angular frequency) was almost constant in the whole spectral region. The corresponding TL pulse obtained from measured spectrum of E is also shown in the inset of Fig. 4.16. The $\tilde{I}(\lambda)$ reconstructed from the 256-point analysis for the horizontal axis agrees well with the measured spectrum of Fig. 4.16(c) after being smoothed to reduce the number of points from 1024 to 256. As an independent check of the accuracy of this result, the FRAC trace was simultaneously measured, as shown in Fig. 4.18, compared with that calculated from the SPIDER-reconstructed pulse. The agreement between them was good, indicating an FWHM of 5.0 fs. However, the pedestal parts were slightly different with each other. This may be due to the slight difference in dispersion optics between the SPIDER and FRAC apparatuses and the insensitivity to the low intensity of subpulses in the case of the FRAC measurement.

Characteristics

As the pulse duration becomes shorter and the spectral modulation becomes stronger, the pulse characterization by the SPIDER technique rapidly becomes more difficult because of the dispersion effect and the bandwidth limitation of the optics in the Michelson-interferometric arm, the weak sum-frequency interferometric signal resulting from the considerable decrease

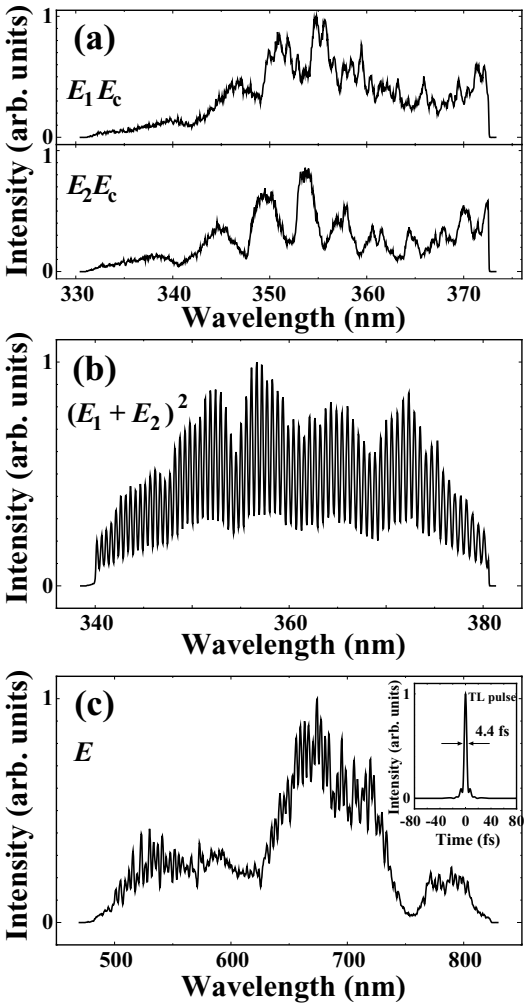

Fig. 4.16. (a) Two measured sum-frequency spectra, E_1E_c and E_2E_c. (b) Measured interferometric second-harmonic spectrum $(E_1 + E_2)^2$. (c) Measured spectrum of the input pulse E, and 4.4-fs Fourier-transform-limited pulse (inset) [32, 44]

in intensity of the strongly chirped reference beam, and the wavelength-resolution limitation of the broadband spectrometer.

In summary in this section, compared to FRAC or FROG, SPIDER has the following advantages;

(a-1) the elimination of the necessity for moving components (except gratings in the spectrometer for ultrabroadband pulse characterization),
(a-2) the non-iterative reconstruction algorithm,

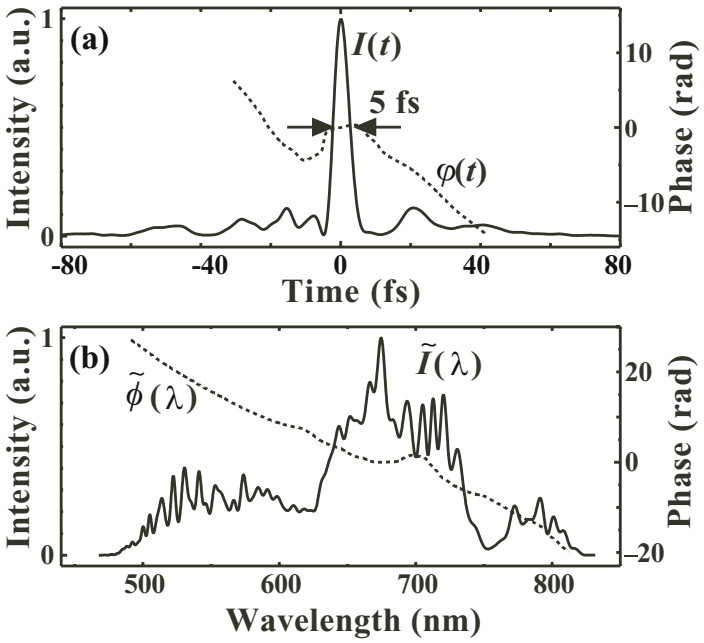

Fig. 4.17. (**a**) Retrieved pulse intensity (*solid line*) and phase (*dashed line*) in the time domain. (**b**) Retrieved spectrum (*solid line*) and spectral phase (*dashed line*) [32, 44]

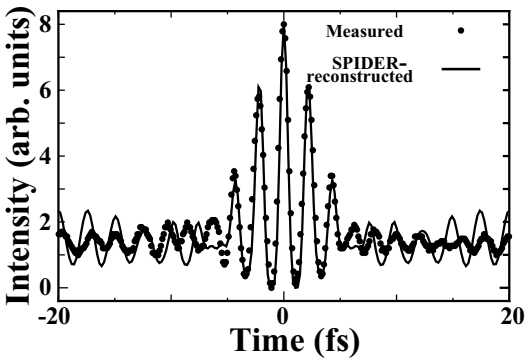

Fig. 4.18. Comparison of the measured FRAC trace (*dots*) with the SPIDER-reconstructed FRAC trace (*solid line*) [32, 44]

(a-3) the fast measurement time using a thicker nonlinear crystal, which gives the high intensity signal as a result of the type-II phase matching for the sum-frequency generation (SFG) between the spectrally ultra-broadband pulse field and the quasi-CW field,

(a-4) the lack of the time-smearing effect owing to use of the spectral interferometry, even in the noncollinear SFG configuration with the quasi-CW field,
(a-5) the measurement capability of monocycle-like pulses with ultrabroad spectra exceeding one-octave bandwidth, which is significant for the shorter pulse characterization.

The last advantage is due to the utilization of the sum-frequency light with the quasi-CW field as a signal, the insensitivity of the frequency dependences of the detection system and the phase mismatching spectrally-filtering effect of the nonlinear crystal owing to the measurement based on the spectral interferometry (SI)).

On the other hand, the disadvantage of SPIDER is

(d-1) the low sensitivity because most of the energy of the pulse to be characterized is used for the chirped pulse as a reference in the self-referencing configuration.

4.5 Modified SPIDER

4.5.1 Principle and Effect of Parameter Error

Principle

Although the SPIDER technique has some advantages mentioned in Sect. 4.4, it has a drawback of low sensitivity, particularly for the characterization of ultrashort and ultrabroadband pulses. This is due to a drastic decrease in peak intensity of the strongly-chirped self-reference pulse, which wastes most of the energy of the pulse to be characterized. In order to overcome such a drawback, a variant of the SPIDER [15] and a modified SPIDER[1] [12, 13] were developed independently. In the modified-SPIDER, instead of a chirped reference pulse split directly from the pulse to be characterized, a powerful external pulse which is coherent with the pulse to be characterized is employed as a highly-intensive chirped pulse. Thus, while the conventional SPIDER is one of the self-referencing spectral interferometries, the modified SPIDER is one of the cross-referencing spectral interferometries. The modified SPIDER is sometimes abbreviated as M-SPIDER or XSPIDER.

Effect of Parameter Error

For the modified SPIDER as well as the conventional SPIDER, the important parameters are the time delay τ between the two replicas of the pulse to be

[1] Although a modified-SPIDER technique was not described in reference [12], the experimental results using this technique were presented in the conference.

characterized and the spectral shear Ω after sum-frequency generation with the chirped pulse as a reference. The two replicas with the time delay τ are usually produced by two arms of a Michelson interferometer. The replicas are upconverted with the external reference chirped pulse, which passes through a dispersive medium, in a nonlinear crystal. The interferogram with a spectral shear Ω is measured by a spectrometer.

Here, we discuss the effect of the errors in the parameters Ω and τ on the characterization results by the modified-SPIDER. In the process of the phase reconstruction in the SPIDER, the derived phase difference $\theta_{\mathrm{SPIDER}}(\omega)$ containing a delay-dependent linear term $\omega\tau$ is expressed by

$$\theta_{\mathrm{SPIDER}}(\omega) = \phi(\omega) - \phi(\omega - \Omega) + \omega\tau. \tag{4.45}$$

This linear term $\omega\tau$ can be removed by measuring the delay time τ of the two replica pulse pair. If the time delay is measured to be $\tau + \delta\tau$, which includes an error of $\delta\tau$, the phase difference $\theta_{\mathrm{diff}}(\omega)$ defined (4.42) is evaluated as

$$\theta_{\mathrm{diff}}(\omega) = \phi(\omega) - \phi(\omega - \Omega) + \omega\delta\tau, \tag{4.46}$$

with an error of $\omega\delta\tau$. Hence, using (4.44) the evaluated spectral phase $\phi_{\mathrm{m}}(\omega)$ in the measurement is written by

$$\phi_{\mathrm{m}}(\omega) \simeq \phi_{\mathrm{t}}(\omega) + \frac{\delta\tau}{2\Omega}\omega^2, \tag{4.47}$$

where $\phi_{\mathrm{t}}(\omega)$ is the true spectral phase. Thus, the error $\delta\tau$ would introduce an additional second-order dispersion, which is a serious error for the phase compensation to compress pulses.

In contrast, if the spectral shear Ω is measured to be $\Omega + \delta\Omega$ with an error of $\delta\Omega$, the measured spectral phase $\phi_{\mathrm{m}}(\omega)$ is evaluated as

$$\phi_{\mathrm{m}}(\omega) \simeq \frac{\Omega}{\Omega + \delta\Omega}\phi_{\mathrm{t}}(\omega) \simeq \left(1 - \frac{\delta\Omega}{\Omega}\right)\phi_{\mathrm{t}}(\omega), \tag{4.48}$$

from (4.44). In this case, the error of $\delta\Omega$ results only in the factor error of the spectral phase, which is not so serious for the feedback chirp compensation described in the next subsection.

4.5.2 Apparatus and Characteristics

Appratus

Although the SPIDER technique has some advantages mentioned in Sect. 4.4, it has a drawback of low sensitivity, particularly for the characterization of ultrashort and ultrabroadband pulses. This is due to a drastic decrease in peak intensity of the strongly-chirped self-reference pulse, which wastes most of the energy of the pulse to be characterized. In order to overcome such a

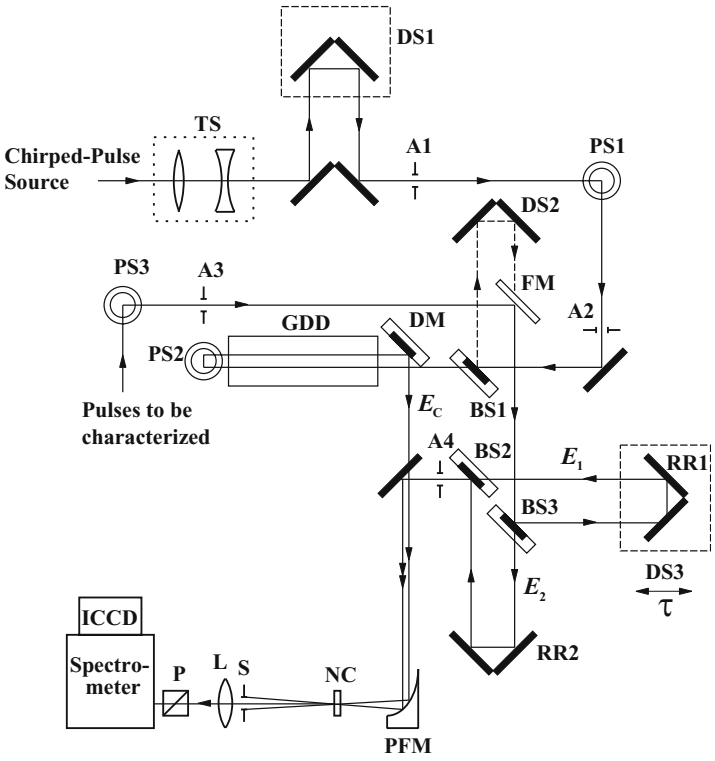

Fig. 4.19. Setup of the highly-sensitive modified-SPIDER apparatus. An external intense optical pulse is employed as a light source of a chirped pulse which is used for the sum-frequency generation with the pulse to be characterized. TS: telescope, DSi: delay stages, Ai: apertures, PSi: periscopes, BSi: beam splitters, GDD: TF5 glass, 100 mm long, group-delay dispersion medium, DM: dichroic mirror, FM: flipper mirror, RRi: retroreflectors, PFM: off-axial parabolic mirror, NC: nonlinear crystal, S: slit, L: lens, P: polarizer [13, 32]

drawback, a variant of the SPIDER [15] and a modified SPIDER [12,13] were developed independently. In the same manner, instead of a chirped reference pulse split directly from the pulse to be characterized, we employ a powerful fundamental external pulse directly from a Ti:sapphire laser amplifier as a highly-intensive chirped pulse. Thus, we demonstrated the experimental characterization of femtosecond weak pulses propagated through a single-mode, fused-silica fiber and evaluate the sensitivity and the signal-to-noise ratio of the modified-SPIDER apparatus compared with the conventional one.

Figure 4.19 illustrates the modified-SPIDER apparatus. It has two optical input parts; the one is for the pulse to be characterized, and the other is for the intense light source to generate the chirped pulse. All the employed mirrors, the periscopes PSi (i =1-3), the retroreflector RRi (i =1, 2) and the delay

stage (DSi (i =1-3)) were aluminum-coated, except for a flip mirror FM. The beam splitters BSi (i =1-3) are broadband dielectric multilayer mirrors. The pulse to be characterized was reflected by the silver-coated flip mirror FM and was input into a Michelson interferometer to make two-pulse replicas E_1 and E_2.

The mirror FM is used as a switch from the conventional-SPIDER mode to the modified-SPIDER mode. When the mirror FM is flipped out and a self-referencing interferometric technique is used, this apparatus becomes the conventional-SPIDER mode. By flipping out the mirror FM before measurements in the modified-SPIDER mode, the powerful external pulse (a dashed line) reflected by a fused-silica beam splitter BS1 (96% transmission with an anti-reflection coating) was sent to the Michelson-interferometer to produce two replicas. The interferometric second-harmonic spectrum of these two replicas was measured in order to determine the value of the delay time τ. In addition, this powerful, reflected pulse is conveniently used for an optical guide of the weak pulse to be characterized in the modified-SPIDER mode.

After the powerful, transmitted external pulse passed through a highly dispersive glass TF5 (100 mm in length), its linear polarization was changed to the p-polarization by a periscope PS2 and the pulse passed again through the dispersive glass (round-trip group-delay dispersion of $3.5\times10^4\,\mathrm{fs}^2$ at 800 nm). Thus, a strongly chirped pulse E_c with a 3.7-ps duration was generated. The chirped pulse (E_c) and two replicas (E_1 and E_2) were focused onto a BBO crystal NC (type II phase-matching; 50-μm in thickness) by an off-axial parabolic mirror PFM (50-mm focal length) to produce the SPIDER signal of the interferometric sum-frequency wave. After passing through a slit S, a focusing lens L and a polarizer P, the signal spectra were measured by a 1200-line/mm spectrometer with a 1024-pixel, intensified-CCD camera, where the spectral resolution is 0.2 nm. Because of the limited bandwidth of the spectrometer in the modified-SPIDER as well as in the conventional SPIDER, several spectral parts of different center wavelengths with the calibration in wavelength and sensitivity were synthesized at update time of ∼10 s to obtain SPIDER signals with the full bandwidth. This system enables us to easily compare the sensitivity between the modified-SPIDER technique and the conventional one under the same optical components without realignment.

Chracteristics

Figure 4.20 shows the SPIDER signal intensity as a function of energy of the input pulse to be characterized for modified (open circles) and conventional (open squares) techniques. The plotted relative intensity of the signal was evaluated from the intensity of the positive ac($+\tau$) component of the inverse Fourier transform of the observed interferometric SPIDER signal, which corresponds to the amplitude of the oscillating interferometric part. In the case of the modified-SPIDER technique, energy of input pulse (90 fs, 800 nm) was varied while energy of the 90-fs, 800-nm chirped reference pulse (1.2 μJ) was

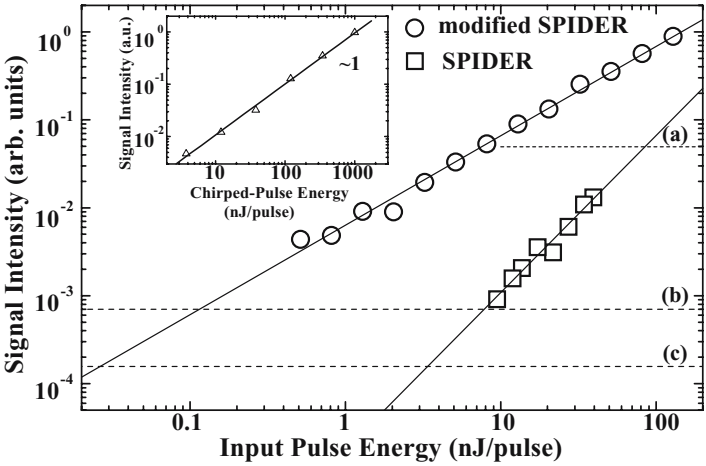

Fig. 4.20. SPIDER signal intensities of the conventional SPIDER and the modified SPIDER as a function of the pulse energy to be characterized. Inset shows the signal intensity as a function of chirped-pulse energy [13, 32]

maintained. In the case of the conventional technique, energy of the 90-fs, 800-nm input pulse had been varied before energy of the input pulse was split. Energy for the chirped reference pulse is 96 percents of incident energy at BS4. From Fig. 4.20 we find that the intensity for the modified-SPIDER mode indicates a linear function of input energy, while the intensity for the conventional mode indicates a quadratic dependence. This result suggests that the modified-SPIDER technique has a great advantage for the characterization of the weak intensity pulse. In Fig. 4.20 we also plot three broken lines (a), (b), and (c) that represent the experimental noise levels for (a) a single-shot case, (b) a 5000-pulse-accumulation case (corresponding to the five-second measurement time), and (c) a 100,000-pulse-accumulation measurement. The sensitivity of the modified-SPIDER technique is one hundred times higher than that of the conventional one. For a single-shot measurement, the modified one is ten times higher and has 1 nJ/THz-bandwidth. Moreover, in another experiment for output pulses from a tapered fiber (one of the microstructure fibers) spectrally ranging 350 to 450 THz, their amplitudes and phases were characterized with the sensitivity of 20 pJ/pulse by our modified SPIDER.

All the analyses of the electric-field reconstruction for pulses to be characterized were carried out using the measured $\Omega/2\pi = 3.87\,\mathrm{THz}$ and $\tau = 746\,\mathrm{fs}$ in the same manner as [44]. It was confirmed that the reconstructed temporal-intensity profile with the 90-fs duration agreed with the results of the independent measurement of the autocorrelation trace under the assumption of a sech^2 shape.

In addition to the high sensitivity, the modified-SPIDER technique has another advantage in signal-to-noise ratio, that is, a great reduction of background light. In both conventional- and modified-SPIDER techniques, the main origin of background light is due to the second harmonic generation at the nonlinear crystal and its scattering at surface. For the modified-SPIDER technique, unlike the conventional one, we can shift the frequency region of the SPIDER signal to the arbitrary frequency region to avoid the background by the independent choice of an appropriate chirped-pulse frequency ω_c.

Moreover, unlike the conventional self-reference SPIDER, particularly for ultrabroadband pulses, by an external reference, the wavelengths of upconverted replicas can be shifted to be longer, hence to avoid the bandwidth limitation of optics in the apparatus. It effectively results in broader measurable bandwidth for the pulses to be characterized [13].

The further merits of the modified SPIDER are the flexibility for pulses to be characterized, especially for strongly- and complicatedly-chirped pulses. The conventional SPIDER technique is poor in retrieving such pulses because the spectral shear Ω is not well-defined for those pulses. The strongly-chirped pulse has a wide temporal width, which dims the corresponding temporal frequency of the chirped reference pulse. To circumvent this situation, the spectrally-resolved, modified-SPIDER technique is promising. An independently-introduced chirped pulse of the pulse to be characterized greatly simplifies the characterization of the pulse in the entire spectral region.

Finally, we would like to point out a practical merit of the modified-SPIDER technique concerning the more accurate and easier determination of the delay time τ between two replicas, as we mentioned above. In the SPIDER algorithm, the accuracy of the group-delay dispersion of the retrieved pulse depends on that of the delay time. For a weak pulse, however, the accuracy of the delay time can hardly be guaranteed in the conventional SPIDER technique. In the modified-SPIDER technique, a high intensity, well-behaved pulse is available for the determination of the delay time instead of the fragile, weak one.

All the advantages of the modified-SPIDER technique, highly sensitive, high-signal-to-noise ratio, etc. will enable us the single-shot characterization of a weak pulse with an ultrabroadband.

Characterization by Sophisticated Modified-SPIDER

Here, we describe the pulse characterization of optical pulses with over-one-octave bandwidths and monocycle-like pulses using a further-improved or sophisticated modified-SPIDER [14]. For the details of the feedback phase compensation experiment, see Sect. 5.2.3. The improved M-SPIDER is shown in Fig. 4.21. The Ti:sapphire laser amplifier system as a light source, an Ar-filled hollow fiber and a 4-f phase compensator with an SLM are the same as in Sect. 5.2.3.

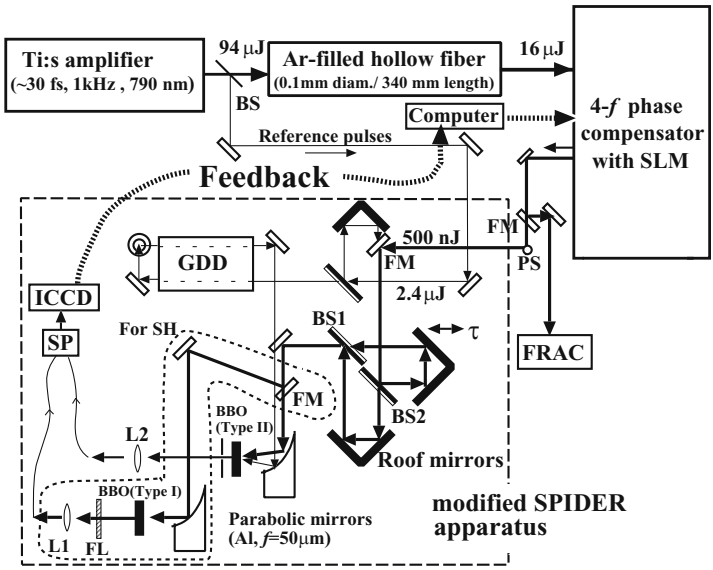

Fig. 4.21. Schematics of experimental setup. PS, Periscopes; L1, L2, focusing lenses (Fused silica, f = 50 mm); FM, flip mirrors; BS1, BS2, wedged beam splitters; FL, optical filter (cutoff: 500 nm)

The essential points for successful feedback are the accurate measurement and the accurate phase compensation, for which we exerted much effort. In order to accurately measure the phase $\phi(\omega)$, we analyzed the phase errors invoked by the inaccurately measured $\tau + \delta\tau$ and $\Omega + \Delta\Omega$. We found that the inaccurate $\tau + \delta\tau$ would introduce an additional second order dispersion $(\phi(\omega) + \delta\tau\omega^2/2\Omega)$, and the inaccurate $\Omega + \Delta\Omega$ would only result in an amplitude error of the phase $((1 - \Delta\Omega/\Omega)\phi(\omega))$, as described in the previous subsection 4.5.1. Therefore we mainly concentrated our effort on increasing the accuracy of τ.

In the SPIDER measurement, the derived phase difference $\theta_{\mathrm{SPIDER}}(\omega)$ contains a delay-dependent linear term $\omega\tau$ according to

$$\theta_{\mathrm{SPIDER}}(\omega) = \phi(\omega) - \phi(\omega - \Omega) + \omega\tau. \tag{4.49}$$

This linear term can be removed by the measurement of the delay of the two replica pulse pairs. However, as suggested by Iaconis and Walmsley [8], if there is system error in the arms of the Michelson interferometer, it would be best to measure the SPIDER signal for $\Omega = 0$ and subtract it as the background. This can be achieved by the measurement of the second-harmonic (SH) interferogram since the phase difference

$$\theta_{\mathrm{SH}}(\omega) = \omega\tau, \tag{4.50}$$

in the case of SH interferogram.

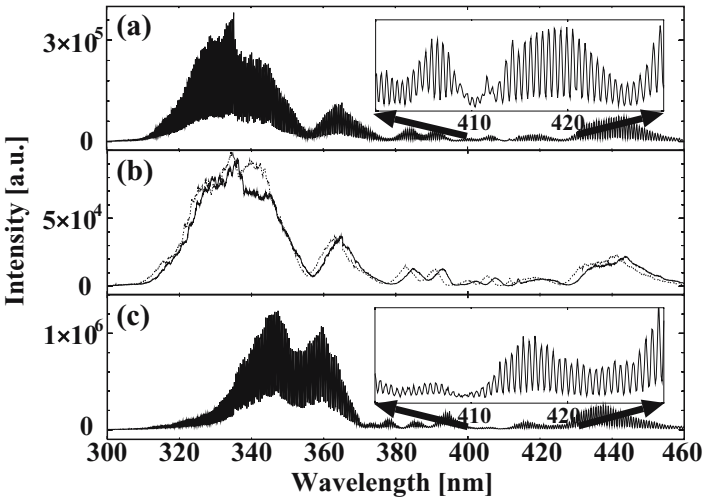

Fig. 4.22. Results of modified-SPIDER measurements. (**a**) modified-SPIDER signal, (**b**) replicas and (**c**) the second harmonic interferogram. The interference fringes are clearly resolved even in the weak signal regions [14, 32]

The crystal for the sum frequency generation in the SPIDER is cut for the type-II phase matching condition, which is insensitive to the bandwidth limitation, whereas the SHG is easily achievable with type I phase matching. Realignment of the crystal, the lens, the detector and the slit is required for the best signal intensity. This alignment does not correspond to the same conditions as measurement of the sum frequency waves of SPIDER. To avoid the perturbation of the SPIDER signal measurement and to obtain the reproducible signal, we built a separate optical path for the independent alignment and measurement of the SH interferogram, as shown in Fig. 4.21, This permitted highly reproducible measurements.

Next, we examined the error source in the previous system [13] and made some important modifications as described below.

First, we improved the beam splitters in the Michelson interferometer. We found that the SPIDER interferogram was spoiled by the interference between front and back surface reflections of the beam splitters. An antireflection coating on the backside should avoid this. However, it is difficult to make an antireflection coating for an over-one-octave bandwidth. Therefore, we replaced them with wedged beam splitters with the thickness of 0.5 mm and a wedged angle of 0.5° (20% reflection and 80% transmission for s-polarization from 400 to 1300 nm and fused silica substrates). Consequently, the back reflection interference is completely eliminated. Moreover, replacement of two retro-reflectors with two roof mirrors improved the spatial beam profiles of the replicas on BBO crystals and hence greatly increased the intensities of the two interferogram signals.

Second, we significantly increased the SH signal intensity. The intensity of the SH had been weak so far, and it had been difficult to measure over the same wavelength range as in the SPIDER measurement. The input pulse has a bandwidth from $\sim$ 470 to $\sim$ 1070 nm, corresponding to a SH signal from 235 to 535 nm. On the other hand, the SPIDER signal comes from $\sim$ 290 to $\sim$ 450 nm. The SH signal is too broad to cover the SPIDER wavelength range. Therefore, we initially reduced the pressure of Ar gas from 3.0 to 0.8 atm so that the spectral range of the intensified SH interferogram has approximately the same wavelength range as in the SPIDER (Fig. 4.22(c)). This enabled us to subtract the linear term $\omega\tau$ much more accurately than before.

In addition to these, we properly chose the blaze wavelength of the gratings in order to reduce the influence of the second-order diffraction on the output from the phase compensator.

On the basis of the above improvement, we conducted an M-SPIDER measurement. First, we measured the SH spectral phase interference (Fig. 4.22(c)) and then after a few minuites the SPIDER interferogram (Fig. 4.22(a)). Because the pulses have very broad bandwidths, it was necessary for us to obtain the signals by five rotations of grating in the spectrometer, which were automatically controlled (exposure time was 0.1 s and accumulated for 100 times). It should be noted that the SH and SPIDER interferograms were cleary resolved over the whole range from 300 to 460 nm, even in the weak signal regions. Moreover, we found that the replicas became similar over the whole range from 300 to 460 nm (Fig. 4.22(b)). This was due to the better spatial overlapping of the replicas with the reference beam by the replacement of the retro-reflectors with the roof-mirrors. Additionally, it should be emphasized here that, thanks to the cross-reference SPIDER configuration using a chirped reference pulse with a center wavelength of 792 nm, directly generated from the Ti:sapphire laser amplifier, this spectral range from 300 to 460 nm was away enough from the short-wavelength edge of the bandwith limit of the optical components, unlike in the configuration of the conventional self-reference SPIDER.

The solid curve in Fig. 4.23(a) is the measured spectrum intensity $\tilde{I}(\lambda)$ of the pulse output from the phase compensator in the SLM-off case; the dashed line in Fig. 4.23(a) represents the retrieved spectral phase $\phi(\lambda)$ from the improved M-SPIDER measurement. The corresponding temporal intensity $I(t)$ and phase $\varphi(t)$ profiles are depicted by the solid and dashed lines, respectively, in Fig. 4.23(b). The τ and $\Omega/2\pi$ confirmed in this experiment were 935 fs and 4.12 THz, respectively.

Conclusively, the improvements such as (i) building a separate optical path for the independent alignment and measurement of the SH interferogram, (ii) usage of the wedged beam splitters to eliminate back reflection, (iii) better beam overlapping in sum-frequency generation by replacing the retro-reflectors with the roof mirrors, (iv) measurement of the intensified SH interferogram by reducing the Ar-pressure, and (v) proper selection of the blazing wavelength of the gratings to reduce the influence of the second-order

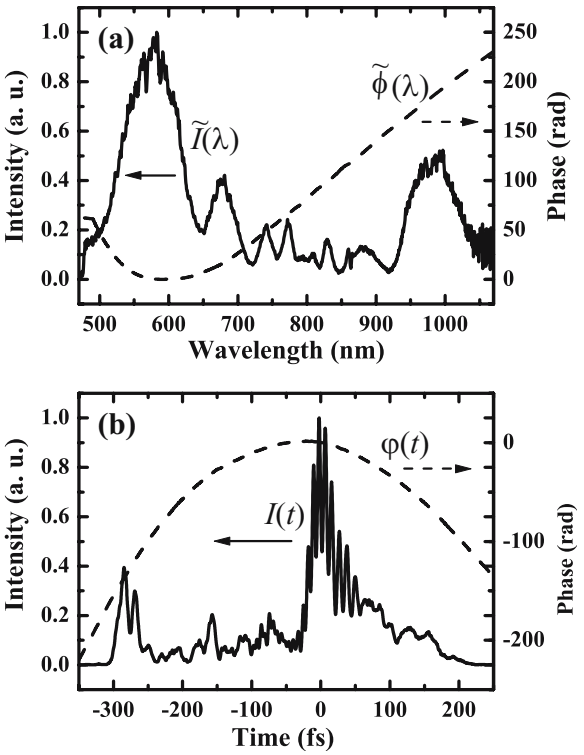

Fig. 4.23. Intensity spectrum $\tilde{I}(\lambda)$ ((**a**) *solid line*) in the SLM-off case, and the corresponding retrieved results of the spectral phase $\tilde{\phi}(\lambda)$ ((**a**) *dashed line*), the temporal intensity profile $I(t)$ ((**b**) *solid line*) and the temporal phase $\varphi(t)$ ((**b**) *dashed line*) from the sophisticated M-SPIDER measurement

diffraction on the output from the compensator, enabled us to characterize the optical pulses with over-one-octave bandwidths with better accuracy than before. Its better accuracy was supported by the fact that a 3.3-fs, 1.56 optical cycle pulse, close to the 2.8-fs transform-limits pulse was succcessfully generated after the feedback phase compensation on the basis of this sophisticated M-SPIDER measurement. The details of the feedback phase compensation are described in Sect. 5.2.3.

4.6 Comparison and Characteristics

We compare the pulse characterization techniques, FRAC, FROG, SPIDER, and modified SPIDER. Their characteristic features are summarized in Table 4.4. The details are in the following.

1. Bandwidth limitation: Using the interaction of second-harmonic generation, bandwidth of the pulses measured by FRAC and SHG-FROG is limited below an octave. In good contrast to this, SPIDER and modified-SPIDER using sum-frequency generation can characterize pulses with a bandwidth exceeding an octave.
2. Retrieve algorithm: For retrieve, FRAC needs the assumption of the pulse shape and phase or an iterative calculation using the information of the spectral intensity. The reconstruction algorithm of FROG is iterative and complicated. The reconstruction algorithm of SPIDER or modified-SPIDER is simple and not iterative.
3. Sensitivity: FRAC, SHG-FROG, SPIDER and modified SPIDER all use the second-order nonlinear interaction. However, in SPIDER, the sum-frequency light of a pulse to be characterized and a chirped reference pulse from it is employed. Hence, the decrease in intensity of this chirped pulse causes the lower sensitivity than in FRAC and SHG-FROG. Instead of the chirped reference pulse directly split from the pulse to be characterized, a highly-intensive chirped pulse as a reference pulse is introduced in modified SPIDER. Thus the sensitivity of modified SPIDER is high and controllable.
4. Data acquisition time: FRAC and FROG record the signal with the varying delay time. Hence they need longer data acquisition times. In general, FROG needs more sampling points than FRAC. Hence, the data acquisition time of FROG is longer than that of FRAC. On the other hand, because of spectral interferometry measurements the data acquisition times of SPIDER and modified-SPIDER are very short. This very short acquisition time is greatly significant for the characterization of below-two-cycle or monocycle pulses.

As noted in other remarks, FRAC tends to underestimate the pulse pedestal because of the squared signal in intensity and FROG is with the

Table 4.4. Comparison of pulse characterization techniques

	bandwidth	retrieve algorithm	sensitivity	acquisition time	other remarks
FRAC	below an octave	with assumption, or complicated (with spectrum)	high	comparatively short	underestimation tendency
(SHG-) FROG	below an octave	complicated	high	comparatively long	with time smearing, capability of self-check
SPIDER	over an octave	simple	comparatively low	very short	
modified SPIDER	over an octave	simple	high	very short	capability of shifting signal wavelength range

time smearing effect owing to noncollinear interaction. Regarding FROG technique, it has the capability of self-consistency check or correction using the frequency marginal, and in order to overcome its bandwidth limitation, the self-diffraction (SD) FROG or polarization-gate (PG) FROG using third-order nonlinear interaction can be used. They also have a characterization capability of pulses with the bandwidth over an octave. However, their sensitivities are low because of the third-order interaction.

Since, for more accurate characterization of below-two-cycle or monocycle optical pulses, single-shot measurement excluding the errors due to the pulse-to-pulse fluctuation is desirable. Modified-SPIDER possessing the advantages of high sensitivity and very short acquisition time is the most promising technique for the characterization of monocycle pulses without the errors due to pulse-to-pulse fluctuation.

4.7 Conclusion

Ultrabroadband optical pulses using the self-phase effect and the succeeding phase compensation by use of a 4-f pulse shaper with a SLM was performed to generate monocycle-like pulses. To characterize these pulses, we carried out the FRAC, FROG and SPIDER measurements and compared the results obtained from these measurements.

To characterize optical pulses more accurately by eliminating effects of intensity fluctuation and carrier-envelope phase drifting, the development of a single-shot pulse characterization technique is desirable. Except its low sensitivity, the SPIDER technique has some advantages over the other techniques in the following: (a) measurement capability of ultrabroadband pulses exceeding an octave, (b) simple non-iterative reconstruction algorithm and (c) short data acquisition time. The drawback of the SPIDER technique is due to the generation of the strongly-chirped reference pulse from the pulse to be characterized. In order to overcome such a drawback, the modified-SPIDER technique was used. Instead of a chirped reference pulse split directly from the pulse to be characterized, a powerful external pulse directly from a Ti:sapphire laser amplifier as a highly-intensive chirped pulse was employed. It was confirmed that the sensitivity of modified SPIDER is about a hundred times higher ($\sim$ 1 nJ/THz-bandwidth) than that of conventional SPIDER. This modified-SPIDER method is the most powerfull and useful for characterization of monocycle-like optical pulses. Further, by sophisticating this modified-SPIDER technique with improved hardware and retrieval process, the 3.3-fs, 1.56-optical pulse with an over-one-octave bandwidth was generated. To the best of our knowledge now, this is the shortest pulse in the visible-to-infrared region.

References

1. J.-C.M. Diels, J.J. Fontaine, I.C. McMichael, F. Simoni: Appl. Opt. **24**, 1270 (1985)
2. K. Naganuma, K. Mogi, H. Yamada: IEEE J. Quantum Electron. **25**, 1225 (1989)
3. D.J. Kane, R. Trebino: IEEE J. Quantum Electron. **29**, 571 (1993)
4. D.N. Fittinghoff, J.L. Bowie, J.N. Sweetser, R.T. Jennings, M.A. Krumbügel, K.W. Delong, R. Trebino: Opt. Lett. **21**, 884 (1996)
5. V. Wong, I.A. Walmsley: J. Opt. Soc. Am. **14**, 944 (1997)
6. J. Peatross, A. Rundquist: J. Opt. Soc. Am. B **15**, 216 (1998)
7. S. Linden, J. Kuhl, H. Giessen: Opt. Lett. **24**, 569 (1999)
8. C. Iaconis, I.A. Walmsley: IEEE J. Quantum Electron. **35**, 501 (1999)
9. J.W. Nicholson, J. Jasapara, W. Rudolph, F.G. Omenetto, A.J. Taylor: Opt. Lett. **24**, 1774 (1999)
10. P. O'Shea, M. Kimmel, X. Gu, R. Trebino: Opt. Lett. **26**, 932 (2001)
11. C. Dorrer, P. Londero, I.A. Walmsley: Opt. Lett. **26**, 1510 (2001)
12. M. Hirasawa, N. Nakagawa, M. Shibata, R. Morita, H. Shigekawa, M. Yamashita: *Technical Digest of Conference on Lasers and Electro-Optics* 270 (2001)
13. M. Hirasawa, N. Nakagawa, K. Yamamoto, R. Morita, H. Shigekawa, M. Yamashita: Appl. Phys. B **74**, S291 (2002)
14. K. Yamane, Z. Zhang, K. Oka, R. Morita, M. Yamashita, A. Suguro: Opt. Lett. **28**, 2258 (2003)
15. M. Zavelani-Rossi, G. Cerullo, S. De Silvestri, I. Gallmann, N. Matuschek, G. Steinmeyer, U. Keller, G. Angelow, V. Scheuer, T. Tschudi: Opt. Lett. **26**, 1155 (2001)
16. J.-H. Chung, A.M. Weiner: IEEE J. Selected Topics Quantum Electron. **7**, 656 (2001)
17. D.J. Kane, R. Trebino: Opt. Lett. **18**, 823 (1993)
18. R. Trebino, D.J. Kane: J. Opt. Soc. Am. B **10**, 1101 (1993)
19. K.W. Delong, R. Trebino, D.J. Kane: J. Opt. Soc. Am. B **11**, 1595 (1994)
20. K.W. Delong, R. Trebino, J. Hunter, W.E. White: J. Opt. Soc. Am. B **11**, 2206 (1994)
21. D.N. Fittinghoff, K.W. Delong, R. Trebino, C.L. Ladera: J. Opt. Soc. Am. B **12**, 1955 (1995)
22. K.W. Delong, D.N. Fittinghoff, R. Trebino: IEEE J. Quantum Electron. **32**, 1253 (1996)
23. G. Taft, A. Rudquist, M.M. Murnane, I.P. Christov, H.C. Kapteyn, K.W. Delong, D.N. Fittinghoff, M.A. Krumbügel, J.N. Sweetser, R. Trebino: IEEE J. Selected Topics Quantum Electron. **2**, 575 (1996)
24. A. Baltuška, M.S. Pshenichnikov, D.A. Wiersma: IEEE J. Quantum Electron. **35**, 459 (1999)
25. Z. Cheng, G. Tempea, T. Brabec, K. Ferencz, F. Krausz: *Ultrafast Phenomena XI* (Springer-Verlag, Berlin, 1998), p. 8
26. Z. Cheng, A. Fürbach, S. Sartania, M. Lenzner, C. Spielmann, F. Krausz: Opt. Lett. **24**, 247 (1999)
27. A. Shirakawa, I. Sakane, M. Takasaka and T. Kobayashi: Appl. Phys. Lett. **74**, 2268 (1999)

28. A.M. Weiner, IEEE J. Quantum Electron. **19**, 1276 (1983)
29. C. Spielmann, L. Xu, F. Krausz: Appl. Opt. **36**, 2523 (1997)
30. V.G. Dmitriev, G.G. Gurzadyan, D.N. Nikogosyan: *Handbook of Nonlinear Optical Crystals*, (Springer-Verlag, Berlin, 1991)
31. N. Karasawa, L. Li, A. Suguro, H. Shigekawa, R. Morita, M. Yamashita: J. Opt. Soc. Am. B **18**, 1742 (2001)
32. R. Morita, M. Hirasawa, N. Karasawa, S. Kusaka, N. Nakagawa, K. Yamane, L. Li, A. Suguro, M. Yamashita: Meas. Sci. Technol. **13**, 1710 (2002)
33. N. Karasawa, R. Morita, H. Shigekawa, M. Yamashita: Opt. Lett. **25**, 183 (2000)
34. Y. Ohtsuka, F. Nagaoka, K. Oka: Opt. Rev. **5**, 21 (1998)
35. K. Oka T. Kato: Opt. Lett. **24**, 1475 (1999)
36. See for example, M. Born, E. Wolf: *Principles of Optics* (Pergamon Press, Oxford 1980) p. 403
37. L. Gallmann, D.H. Sutter, N. Matuschek, G. Steinmeyer, U. Keller: Appl. Phys. B **70**, S67 (2000)
38. A. Baltuška, M.S. Pshenichnikov, D.A. Wiersma: Opt. Lett. **23**, 1474 (1998)
39. I.A. Walmsley and V. Wong: J. Opt. Soc. Am. B **13**, 2453 (1996)
40. C. Iaconis, V. Wong, I.A. Walmsley: IEEE J. Selected Topics Quantum Electron. **4**, 285 (1998)
41. C. Iaconis, I.A. Walmsley: Opt. Lett. **23**, 792 (1998)
42. C. Dorrer, I.A. Walmsley: J. Opt. Soc. Am. B **19**, 1019 (2002)
43. I. Gallman, D.H. Sutter, N. Matuschek, G. Steinmeiyer, U. Keller, C. Iaconis, I.A. Walmsley: Opt. Lett. **24**, 1314 (1999)
44. L. Li, S. Kusaka, N. Karasawa, R. Morita, H. Shigekawa, M. Yamashita: Jpn. J. Appl. Phys. **40**, L684 (2001)
45. M.E. Anderson, L.E.E. de Araujo, E.M. Kosik, I.A. Walmsley: Appl. Phys. B **70**, S85 (2000)

5 Feedback Field Control for Optical Pulse Generation in the Monocycle Region

M. Yamashita, K. Yamane, Z. Zhang, M. Adachi, and R. Morita

5.1 Basic Concept: Combination of Spectral Phase Compensation and Characterization

In Chap. 3, an active chirp compensation technique by 4-f configurations with a spatial light modulator (SLM) was introduced. The chirp compensation is made by the SLM according to presumptively calculated dispersion of the pulse using the cumbersome Taylor expansion. It is a typical open-loop phase control. With this technique, the pulse duration compressed to sub 5 fs [1]. For a more complicated phase, more precise pulse characterization technique should be employed. In Chap. 4, the spectral phase characterization techniques (SPIDER and M-SPIDER) were described, which provide an opportunity for closed-loop feedback compensation which will result in sub 3–4 fs generation in the monocycle region.

The open-loop phase compensation to few cycle regime experiments was based on calculations: the dispersion of the intra-cavity and extra-cavity elements including material dispersion of crystal and glasses, prism pairs, grating pairs, glass fibers, and hollow fibers, etc. Most effective material dispersions and/or nonlinear phase modulation could be calculated through Sellmeier equations and/or nonlinear pulse-propagation equations, respectively (see Chap. 1). However, though there are formulas for calculation of a prism pair and a grating pair, they are difficult to set for the desired dispersion in an experiment because of an inter-relation among different orders of dispersion. Furthermore, for example, the physical process in the microstructure optical fibers which were recently developed is very complicated. In the photonic crystal fiber, spectral broadening processes such as the soliton fission, non-soliton radiation, high harmonic generation [2], Raman scattering, four wave mixing [3], self-steepening, etc. [4] have been recognized. Those processes are difficult to describe by simple functions. Therefore, a closed-loop feedback becomes necessary.

The closed-loop phase control was proposed and demonstrated some years ago [5]. In the experiment, the optical pulse was deliberately distorted to $\sim$80 fs. The state of a liquid crystal phase modulator array in a 4-f configuration was adaptively controlled using a simulated annealing algorithm in order to maximize the average second harmonic signal measured after an external doubling crystal. The second harmonic was expected to be highest for

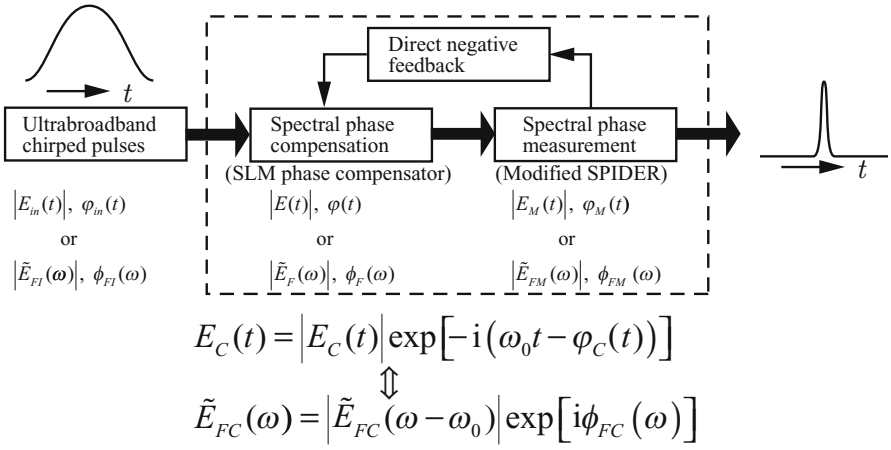

Fig. 5.1. Basic concept of an approach to direct feedback control of spectral phase without Taylor expansion for the optical pulse generation in the monocycle region

the shortest, most intense pulse. After 1000 iterations, the pulse was compressed to near transform limited 11 fs [5], and the pulse quality was greatly improved. The time required to run this experiment was roughly 15 minutes. In this kind of adaptive chirp compensation, neither the input pulse nor the output waveform need to be specified. One just needs to specify the target outcome and the adaptive learning algorithm. It can be particularly suitable to the case where the appropriate laser waveform is not known and the yield is the only matter concerned.

However, in the one-octave bandwidth and few-cycle pulse regime, the SHG intensity cannot be the unique target. As mentioned in Chap. 4, in the intensity autocorrelation and the FRAC measurement, the similar autocorrelation traces can have very different pulse shapes and phases. Likewise, the same SHG intensity cannot always define a minimized pulse. Up to date, the adaptive phase control has been applied to about < 200 nm bandwidth and the minimum pulse width achieved by adaptive phase control has been only in the >10 fs regime. Unless the pulse shape and phase are measured, the pulse cannot be fully determined.

As the spectral phase measurement techniques are developed and mature (see Chap. 4), the precise measurement and the prescribed phase control become possible without the need for the Taylor expansion method. Then, the adaptive control of the phase can be proceeded into the exact feedback and precision phase compensation, as shown in Fig. 5.1 [6]. If the measured phase is sufficiently accurate, the feedback immediately turns the pulse into the specified shape, without undergoing an iteration process. We demonstrated that the feedback technique led to the pulse be compressed to the sub 3–4 fs monocycle regime [7]. The spectral phase of the optical pulses was measured by M-SPIDER [7, 8] or SPIDER [9] techniques.

This chapter describes the feedback pulse compression that combines accurate spectral-phase characterization and compensation for ultrabroadband optical pulses with various types of complicated phase behaviors in the frequency region near or over the one octave. Among them, it should be noted that this precisely adaptive, sophisticated technique is shown to enable us to generate 2.8-fs transform-limited optical pulses in the monocycle region. This is the shortest optical pulse with a single clean temporal profile in the infrared-to-visible region to the best of our knowledge. Also, the time–frequency dynamic behavior of such monocycle-like pulses is clarified by an analysis using the Wigner distribution function.

5.2 Feedback Spectral-Phase Control Technique

5.2.1 Conventional Glass Fiber Experiment

Self-Phase Modulation

Experimental Setup and Feedback Procedure

The first demonstration using a computer-controlled feedback system that combines the active phase compensator with an SLM and the highly sensitive M-SPIDER apparatus was carried out for weak, self-phase-modulated pulses from a single-mode fused-silica fiber in 2002 [6]. The experimental setup is shown in Fig. 5.2. The 3-mm long glass fiber with a 2.7-μm core diameter was

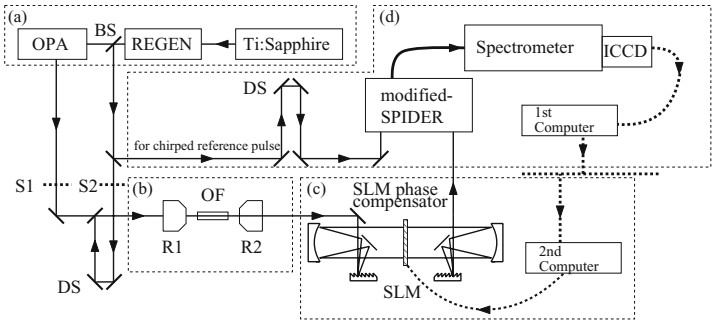

Fig. 5.2. Experimental set-up for adaptive compression for self-phase modulated pulses or self-phase modulated + induced phase modulated pulses based on direct feedback control of spectral phase. (**a**) Optical source for fiber input of 80-fs fundamental and signal pulses (Ti:sapphire, Ti:sapphire laser; REGEN, regenerative amplifier; OPA, optical parametric amplifier). S1, S2, shutter. DS, delay stage. (**b**) A fused-silica fiber (OF) for continuum generation using the SPM effect alone or the SPM + IPM effects (R1, R2, reflective objectives). (**c**) 4-f phase compensator with a feedback-controlled spatial light modular (SLM). (**d**) Quasi-real-time operative, modified SPIDER apparatus.

employed as a medium for spectral broadening due to the dispersive self-phase modulation (SPM) effect. For two color pulses, 800 nm (the fundamental) and 670 nm (the signal), similar pulse compression experiments were performed. The former and the latter had a duration of 80 fs and 41-nJ energy and a duration of 80 fs and 45 nJ energy, respectively. They were originated from a system consisting of a Ti-sapphire laser, a regenerative amplifier and an optical parametric amplifier at a 1-kHz repetition rate. To focus the input pulses into the fiber and to collimate the output from it, a pair of non-dispersive reflective objectives ($\times 36$) was used. They provided 20% fiber-output efficiency. The fiber output was directed to the feedback system for the spectral-phase compensation and measurement. The 4-f phase compensator was actively controlled by the programmable SLM, which was similar to that described in Sect. 3.3.1. The phase compensator consisted of a pair of gold (in)- and silver (out)- coated gratings (a 1/150-mm groove density), a pair of silver-coated plane mirrors, a pair of aluminum-coated concave mirrors (a 350-mm focal length) and a specially made 648-pixel SLM (a 97-μm pixel width and a 5-μm pixel gap). The throughput of the compensator including several guiding aluminum mirrors was 25%.

The output from the compensator was characterized by a M-SPIDER apparatus. The apparatus was almost the same as that introduced in Sect. 4.4. The powerful reference pulses E_c with strong chirp were directly generated by letting the split fundamental pulses (1.2 μJ energy, 800-nm center wavelength, 80-fs duration) from the regenerative amplifier pass through a highly dispersive glass (10-cm length TF-5 glass with a round-trip path: the group-delay dispersion of $3.6 \times 10^4\,\mathrm{fs}^2$ at 780 nm). The input pulses E to be characterized were converted to two replicas E_1, and E_2 with a delay time τ_d by means of a Michelson interferometer arm. Combined reference and two replica pulses were focused on a type II. β-BaB_2O_4 (BBO) crystal (a 50-μm thickness) by an aluminum parabolic mirror (a 50-mm focusing length) to produce a SPIDER signal $E_1E_c + E_2E_c$. The signal was focused on a multimode fiber-coupling spectrometer (a 1200 lines/mm grating with a 300 nm blaze wavelength) of 50 cm and was detected by an intensified CCD camera of 1024×256 channels. The total wavelength resolution was 0.05 nm at 400 nm and the limited bandwidth was 37.5 nm. All the SPIDER signals were measured under the condition of 25 s accumulation time corresponding to 25000 pulses. The time for the spectral phase reconstruction from measured data using the first computer was ~ 0.3 s. The operation of the SLM took ~ 0.8 s to modulate the spectral phase on all the pixels using the second computer where the reconstructed results were inputted. Totally, for one loop for the SPIDER measurement and feedback compensation, it took ~ 30 s.

The procedure of the feedback phase compensation was as follows: First (1), the interference signal of second-harmonic waves $(E_1 + E_2)^2$ of the replicas E_1, E_2, was measured by the blocking of the reference beam E_c and by the 45 degree rotation of the BBO crystal (Fig. 5.3 for the 800-nm input pulse) so that the delay time τ_d was obtained to be 960 fs. This value was

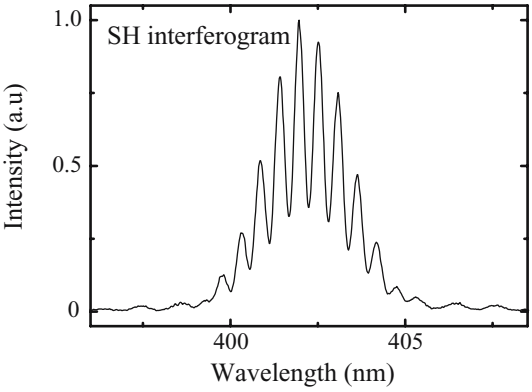

Fig. 5.3. Second-harmonic (SH) interferogram signal to determine the value of the delay time τ_{d} between two pulses

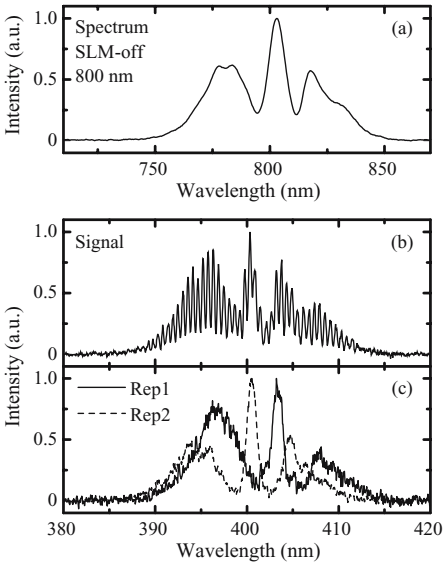

Fig. 5.4. In the SLM-off case, (**a**) 800-nm fiber-output spectrum, (**b**) SPIDER signal and (**c**) replica spectra

fixed for measurements of SPIDER signals in all the cases of the SLM-off (before compensation) and the SLM-on (after compensation). Next (2), the SPIDER signal in the SLM-off case was measured (Fig. 5.4(b) for the 800-nm input pulse), and then (3) the two sum-frequency signals between the replica and the reference, E_1E_{c} and E_2E_{c}, were measured (Fig. 5.4(c) for the 800-nm input pulse) to obtain the spectral shear $\Omega/2\pi = 5.23$ and 5.69 THz for the 800- and 670-nm input pulses, respectively. (4) After the spectral phase was reconstructed (solid line in Fig. 5.5(a) for the 800-nm input pulse)

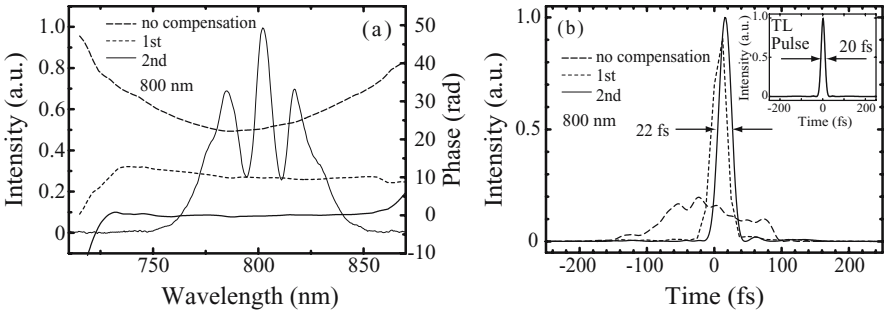

Fig. 5.5. The 800-nm SPM experiment. (**a**) Reconstructed spectral phase before (*dashed line*) and after first (*dotted line*) and second (*solid line*) feedbacks. A *thin solid line* is pulse spectrum after second feedback. (**b**) Corresponding reconstructed temporal intensity before (*dashed line*) and after first (*dotted line*) and second (*solid line*) feedbacks. Inset shows 19.8-fs Fourier transform-limited (TL) pulse

by the first computer and was used as feedback to the second computer, (5) the corresponding negative spectral phase was applied by the SLM controlled by means of the second computer. The closed loop of (5) $\rightarrow$ (2) in the SLM-on case $\rightarrow$ (4) $\rightarrow$ (5) was repeatedly performed several times for better phase compensation. Finally, the two sum-frequency signals, E_1E_c and E_2E_c, corresponding to the process (3), were again measured for confirmation of the above-obtained spectral shear. It should be noted that this negative feedback technique directly and quickly compensates for the spectral phase $\phi(\nu)$ over the whole frequency range without adjusting any order dispersion of $\phi(\nu)$ by the physical realignment of optical components and the usual method of the cumbersome Taylor expansion for $\phi(\nu)$ is not needed.

Results

As for the case of the 800-nm input pulse, the spectrum of the fiber output pulses was broadened from 730 to 870 nm, as shown in Fig. 5.4(a). The corresponding SPIDER signal and replicas in the SLM-Off case are shown in Fig. 5.4(b) and (c), repetitively. Their spectral profiles are similar to the fiber output spectrum, as expected in [10]. The spectral phase and temporal intensity profile reconstructed using these results are shown by dashed lines in Fig. 5.5(a) and (b), respectively. Those lines indicate that the phase varies asymmetrically over 25 radians and the pulses broadens also asymmetrically over 200 fs before compensation. In a similar manner, the reconstructed spectral phases and temporal intensity profiles after first (dotted lines) and second (solid lines) feedbacks are shown in Figs. 5.5(a) and (b), respectively. The corresponding SPIDER signal after the second feedback is shown in Fig. 5.6. Those solid lines (Fig. 5.5(a) and (b)) indicate that the spectral phase after the second feedback becomes flat over the whole spectral region and the temporal pulse becomes nearly transform-limited with a duration of 22 fs.

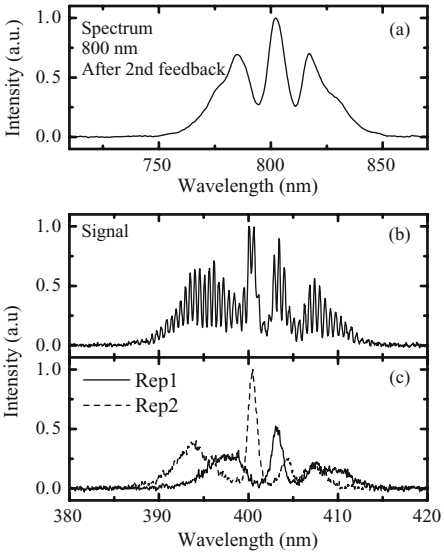

Fig. 5.6. The 800-nm SPM experiment. After second feedback, (**a**) the spectrum, (**b**) the SPIDER signal and (**c**) the replica spectra

The similar experiment for the case of the 670 nm input pulses was carried out. The corresponding SPIDER signal, the replicas, the reconstructed spectral phase and temporal intensity profile before and after the first, second and third feedbacks, and the SPIDER signal after the third feedback are also shown in Figs. 5.7–5.9. The result indicates that the fiber output pulse having a spectral broadening from 620 to 730 nm and a temporal broadening over 300 fs was compressed to 19 fs, which was close to the 16 fs transform-limited one.

These experiments suggest that the spectral-phase feedback technique is very powerful for quasi-real-time phase compensation. In addition, it is robust for pulse compression which avoids the effects of pulse fluctuation and the inevitable modulation of the spectral amplitude in the SLM phase modulation. Hence, it will become a greatly useful tool to obtain extremely short pulses, even for ones who are not familiar with ultrafast optical technologies.

Induced Phase Modulation

As described in Sect. 2.2, an induced phase modulation (IPM) technique based on nonlinear co-propagation of two different-color femtosecond pulses with a carrier-phase locking in a glass fiber enables us to broaden the spectral width more efficiently than that in a self-phase modulation technique. However, the spectral phase of the ultrabroadband pulse generated by the dispersive IPM effect is complicated greatly owing to the combined effect

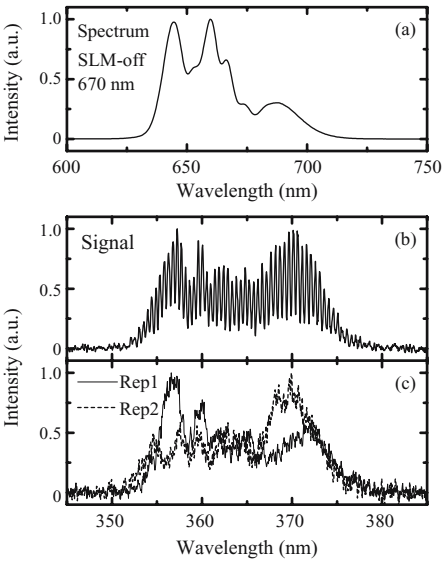

Fig. 5.7. In the SLM-off case, (**a**) 670-nm fiber output spectrum, (**b**) SPIDER signal and (**c**) replica spectra

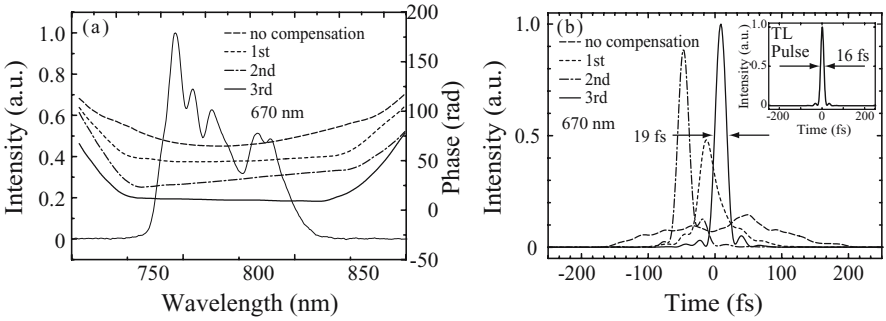

Fig. 5.8. The 670-nm SPM experiment. (**a**) Reconstructed spectral phases before (*dashed line*) and after first (*dotted line*), second (*dashed-dotted line*) and third (*solid line*) feedbacks. A *thin solid line* is pulse spectrum after third feedback. (**b**) Corresponding reconstructed temporal intensity before (*dashed line*) and after first (*dotted line*), second (*dashed-dotted line*) and third (*solid line*) feedbacks. Inset shows 16.1-fs Fourier transform-limited (TL) pulse

of the two-pulse interaction and high dispersion of the glass fiber. In addition, the peak power is relatively low. Therefore, it is difficult to precisely characterize and compensate for its spectral phase over the whole frequency range. In spite of these facts, compression of induced phase-modulated pulses has been demonstrated recently (2003) by the spectral-phase feedback technique [6, 11].

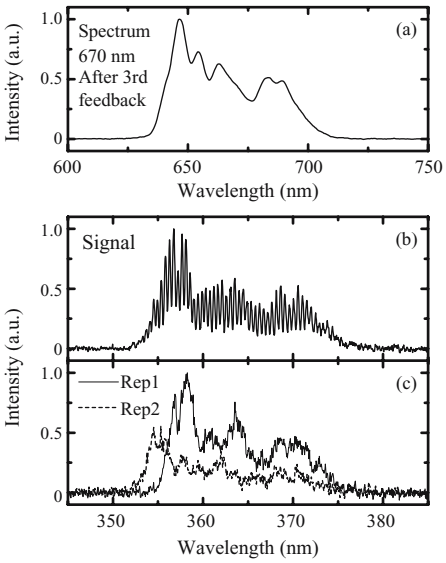

Fig. 5.9. The 670-nm SPM experiment. After third feedback, (**a**) the spectrum, (**b**) the SPIDER signal and (**c**) the replica spectra

Experiments

The experiment for IPM pulse compression was carried out using the almost same apparatuses (the femtosecond optical source, the 4-f phase compensator and the M-SPIDER apparatus including the feedback procedure for applying the phase shift: Fig. 5.2) as those for two SPM experiments described in the previous sub-section, except for the following points. Two color pulses with carrier-phase locking (800 nm, 80 fs, 64 nJ and 670 nm, 80 fs, 65 nJ for a center wavelength, a pulse duration and pulse energy, respectively) were co-propagated to a single-mode fused-silica fiber with a 4-mm length and a 2.7-μm core diameter. The delay time of the 800-nm fundamental pulse with respect to the 640-nm signal pulse was adjusted to overlap in the middle of the fiber and hence to yield the most efficient IPM effect. The typical fiber-output efficiency was 20%. The output pulse was spectrally broadened from 530 to 880 nm (Fig. 5.10(a) and was directed to a programmable-SLM phase compensator. As for the M-SPIDER measurements, the 1200 lines/mm grating in the spectrometer had to be rotated three times automatically because of the limited bandwidth of 37.5 nm at each grating angle. The full bandwidths of the SPIDER signal, the replicas and the second-harmonic (SH) interferogram were recorded automatically by the synthesis of three spectral parts of different center wavelengths at updated times of $3 \times 100\,\mathrm{s} = 300\,\mathrm{s}$. The delay time τ_d was determined to be 960 fs from the SH-interferogram measurement, and the spectral shear $\Omega/2\pi$ was determined to be 5.68 THz from the replica–spectra measurement.

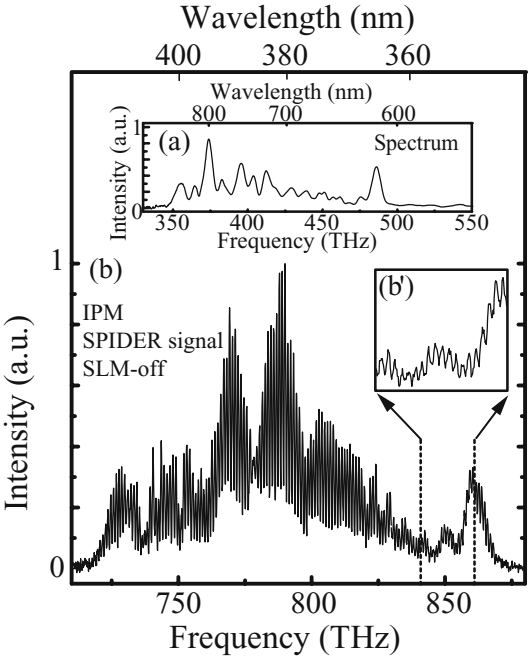

Fig. 5.10. (**a**) Pulse spectrum, and (**b**) (and (**b'**)) SPIDER signal in the SLM-off case

Results

The spectral phase reconstructed from the measured SPIDER signal (Fig. 5.10(b)) with the values of τ_{d} and $\Omega/2\pi$ is shown by a solid line in Fig. 5.11(a). It clarifies that the fiber output pulse has a significantly large and complicated phase variation over 150 rads as a function of the frequency. In addition, its group delay (a dashed line in Fig. 5.11(a)) as a function of the frequency varies over 600 fs and indicates an effective discontinuity ($\sim$ 50 fs jump) around 740 nm where the two input pulses spectrally overlap at the fiber output. This is mainly due to the delay time between the two pulses at the fiber input and their group-velocity mismatch as well as the IPM+SPM effects. This finding corresponds to the result found out through the spectrally-resolved autocorrelation study for near-infrared continuum generation (730 to 1250 nm) using the IPM effect (see Sects. 2.2 and 3.3) [12]. In general, such novel behavior of the spectral phase is not compensated for by conventional passive optics such as combinations of chirped mirrors, prism pairs and grating pairs. As for the reconstructed temporal behavior (Fig. 5.11(b)), the pulse broadens over 500 fs due to the dispersion and the group-delay jump, and the phase varies over 300 radians, both greatly asymmetrically and complicatedly.

Figures 5.12 and 5.13 show the spectral phase applied by the SLM at the third feedback time and its correspondingly measured SPIDER signal with

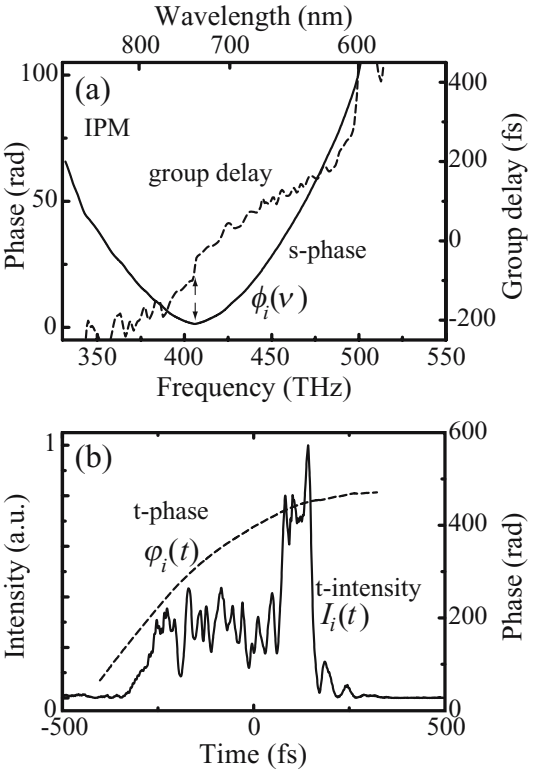

Fig. 5.11. (**a**) Reconstructed spectral phase (*solid line*) and spectral group delay (*dashed line*) in the SLM-off case. (**b**) Corresponding reconstructed temporal intensity (*solid line*) and temporal phase (*dashed line*)

the intensity spectrum, respectively. Also, Fig. 5.14 shows its correspondingly reconstructed results of the spectral phase $\phi(\nu)$ and temporal profiles $I(t)$, $\phi(t)$. The results suggest that even the novel complicated phase behavior is successfully compensated for over the nearly whole frequency range of $\Delta\nu \cong 110\,\mathrm{THz}$. That is, the multi-structured, asymmetric output pulse with a duration of about 500 fs from the fiber was compressed to 7.8 fs, which is close to the 4.4-fs transform-limited pulse. This is the first demonstration of the optical pulse compression for the white continuum generated by the IPM effect. It seems that the small variation of about one radian in the spectral phase after compensation (Fig. 5.14(a)) is caused by the intensity fluctuations of the fundamental and signal fiber-input pulses. The difference between the compressed and transform-limited pulses may be mainly due to the imperfect compensation of the rapidly-varying spectral phase at the low and high frequency edges (Fig. 5.11(a)). These occur because the applied phase shift per one pixel at the edges exceeds π radians (Fig. 5.12). These

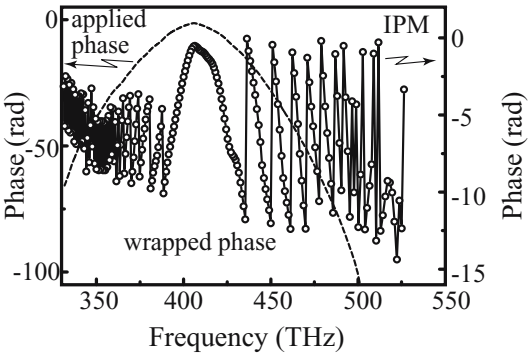

Fig. 5.12. Spectral phase applied by SLM after three-time feedback operation (*dashed line*) and its folded phase (*solid line*)

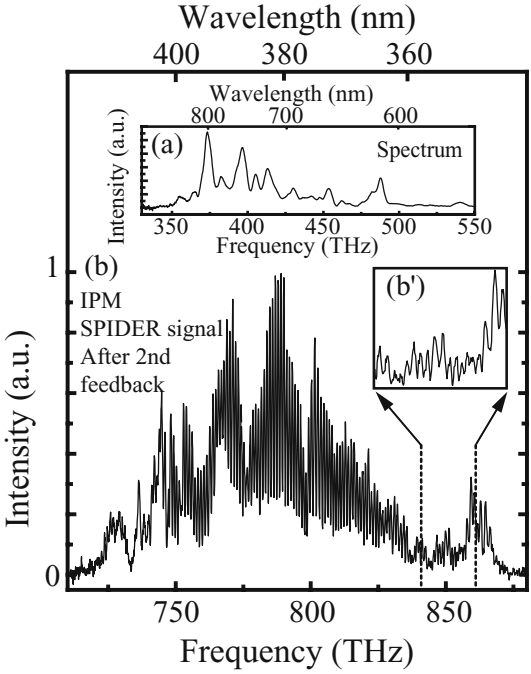

Fig. 5.13. (**a**) Pulse spectrum, and (**b**) (and (**b**)') SPIDER signal in the SLM-on case

problems will be solved by a suitable selection of components of an SLM phase compensator such as longer focal-length concave mirrors and larger $1/d$ gratings.

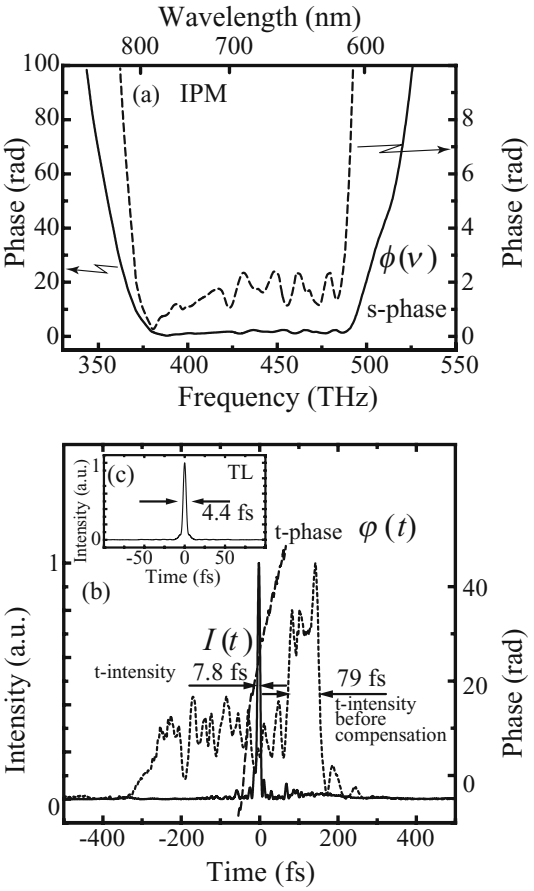

Fig. 5.14. (**a**) Reconstructed spectral phase (*solid line*) and its enlarged one (*dashed line*) in the SLM-on case. (**b**) Corresponding reconstructed temporal intensity (*solid line*) and temporal phase (*dashed line*). *A dotted line* shows temporal intensity of fiber output pulse before compensation. (**c**) Calculated transform-limited (TL) pulse profile

Discussion

Let us discuss the influence of the pulse intensity fluctuation and the group-delay time change Δt_g of the input signal pulse (with respect to the input fundamental pulse) on the compressed pulse during one feedback loop. For this purpose, two additional experiments were carried out. One is measurements for the long term stability of the averaged pulse intensity using a photo-diode with an oscilloscope. The result showed that the pulse intensity fluctuation of the fiber output was $\pm 2.5\%$. Another is measurements (faster than one second) for the difference between the fiber-output intensity spec-

trum under the 100-Hz oscillatory change in group-delay time ($\Delta t_{\mathrm{g}} = \pm 3.5\,\mathrm{fs}$) of the input signal pulse (its central angular frequency $\omega_{\mathrm{s},0}$) using a piezo-transducer attached mirror and that under no change in group-delay time. The result showed that only the spectral structure around 740 nm appearing in the latter case (no change in group-delay time) was relatively smoothed in the former case (change in group-delay time) and changed in intensity (several percent) of its spectral region. This central region corresponds to the overlapping region of the spectrally broadband signal and fundamental pulses. Those findings suggest that even the group delay change exceeding $2\pi(= \Delta t_{\mathrm{g}} \times \omega_{\mathrm{s},0})$ causes only the several-percent intensity change in the central region of the spectrum.

On the basis of these results, the computer simulation was carried out to clarify the practical influence of the fluctuations of the pulse intensity and group delay on the compressed pulse. That is, the spectral phase and intensity of the fiber output as well as the phase compensated pulse were calculated using two equations which describe IPM and SPM effects during nonlinear pulse propagation (see Sect. 2.2 and [13, 14]) with experimental parameters. The calculation is based on the model that the spectral phases obtained after the intensity fluctuation $\Delta I/I$ and/or the group delay change Δt_{g} are compensated for by the use of the spectral phases obtained before these fluctuations. As a result, the group-delay change yielded a small change in only the fine structure in the central overlapping region of the output intensity spectrum, which corresponds to the experimental result. Moreover, the simultaneous fluctuations of the intensity ($\Delta I/I = 2.5\%$) and the group delay ($\Delta t_{\mathrm{g}} = \pm 3.5\,\mathrm{fs}$) caused only a slight increase of the sub-pulse intensity and a less-than 1% broadening of the main pulse duration for the compressed pulse. These fluctuations also indicated that the increase of the ratio of the sub-pulse energy to the whole pulse energy was at most less than 4%.

The influence of the carrier-envelope phase fluctuation was also investigated numerically. This influence was much less than that of the intensity and group-delay fluctuations. The reason is as follows: first, nonlinear phenomena of the IPM occur due to the pulse intensity but not the phase-sensitive electric field of the pulse; secondly, since both the present durations (80 fs) of the input signal pulse and the input fundamental pulse having huge optical cycles are remarkably long compared to the time shift due to the carrier-envelope phase fluctuation, the ultrabroad spectra of the intensity $I(\omega)$ and the group delay $t_{\mathrm{g}}(\omega)$ at the fiber output are greatly insensitive unlike the case of the few-optical-cycle pulse.

Finally, let us consider the influence of the independent group-delay change $\Delta t_{\mathrm{g,r}}$ in the reference chirped pulse on the M-SPIDER signal. When the reference pulse has a group-delay change of $\Delta t_{\mathrm{g,r}}$, the response function $N_{\mathrm{e}}^{p}(t;\Omega)$ of the temporally-linear phase modulation in [10] becomes $\exp[-\mathrm{i}\Omega(t + \Delta t_{\mathrm{g,r}})]$. This yields only a constant shift for the spectral-phase pre-difference $\theta'_{\mathrm{SPI}}(\omega)$ [10] according to $\theta'_{\mathrm{SPI}}(\omega) = \phi(\omega) - \phi(\omega - \Omega) + \tau_{\mathrm{d}}\omega + \Omega \times \Delta t_{\mathrm{g,r}}$. That is, the group delay change does not affect the reconstructed spec-

tral phase except for a small constant shift of $\Omega \times \Delta t_{\mathrm{g,r}} \cong 10^{-3}$ rad) and hence the reconstructed profile of the temporal intensity. This issue was also confirmed by the excellent agreement between the M-SPIDER measurement (for a few hundreds seconds) and the independent autocorrelation measurement for sub-7-fs pulses in another recent experiment [15] which will be introduced in Sect. 5.2.2.

5.2.2 Unconventional Glass Fiber Experiment

Photonic Crystal Fiber

It was reported that ultrabroad-spectrum pulses were generated using a photonic crystal fiber (PCF) in 2000 [16,17] (see Sect. 2.4). The efficient generation was demonstrated by using low peak power pulses produced directly from a femtosecond laser oscillator at 100 MHz repetition rate. It is based on the use of unusual dispersion properties of a PCF. Furthermore, recently (2003), pulse compression using a PCF was attempted by a passive chirp compensator consisting of the combination of a prism pair and a chirped mirror [18]. It was investigated on the basis of the conventional measurement of only the group-delay dispersion (GDD) of the fiber output (a 700–810 nm spectral broadening) by a spectral gating method with the sum frequency generation. The compressed pulse duration was estimated to be 25 fs by the measurement of a fringe-resolved autocorrelation (FRAC) trace with relatively large wings under the assumption of a pulse shape. This imperfect pulse compression far from the 18-fs transform limited pulse is due to the following problems :

- the bandwidth limitation and the inter-relation between the GDD and third-order phase dispersion of the employed chirp compensator.
- insufficient information on the complicated spectral phase $\phi(\omega)$ of the output from the PCF where several nonlinear phenomena occur simultaneously such as self-phase modulation, parametric four-wave mixing, stimulated Raman scattering, soliton formation and self-steepening, as well as the unusual dispersion profile [3].
- non-exact measurement of the temporal intensity profile of the compressed pulse.
- the relatively low peak power of the output pulse from the PCF, which is due to the ultrabroadening of its spectrum and the limitation of the fiber-input power available directly from a Ti:sapphire laser.

In this subsection, let us show that the direct feedback technique of the spectral phase without the Taylor expansion enables us to perfectly compress much broader-band pulses from the PCF and to solve the above-mentioned problems [15].

The main experimental setup (Fig. 5.15) consists of a 12-fs Ti:sapphire laser, a 3-mm long PCF, a computer-controlled feedback system that combines a 4-f chirp compensator with a spatial light modulator (SLM) and a

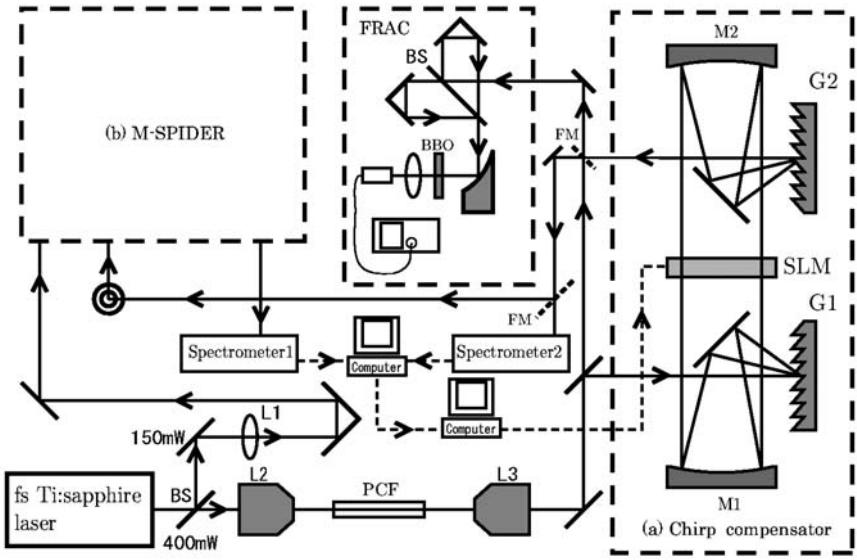

Fig. 5.15. Experimental setup for adaptive photonic-crystal fiber pulse compression. (**a**) 4-f chirp compensator with a feedback-controlled spatial light modulator (SLM); G1, G2, gratings; M1, M2, concave mirrors. (**b**) Quasi-real-time operative, modified SPIDER; BS, beam splitter; FM, flipper mirror. L1, collimating lens (f=1000 mm); L2, L3, objective lenses (×20) [15]

modified spectral-phase interferometer for direct electric-field reconstruction (M-SPIDER) apparatus, and a fringe-resolved autocorrelator. The employed feedback system is basically the same as the recently-developed one [7] (see Sect. 5.2.3).

The pulse beam from a mode-locked Ti:sapphire laser (12 fs pulse duration, 600 mW average power, 75 MHz repetition rate and 800 nm center wavelength with a spectrum from 670 to 920 nm) was split with a 1:3 beam splitter. The lower intensity pulse (150 mW) was passed through a focusing lens (100 cm focal length) for collimation and then directed into the M-SPIDER apparatus as an intensified chirped reference pulse. The higher intensity pulse (450 mW) was coupled into the PCF (2.6 μm core diameter, 3 mm length, 900 nm zero dispersion wavelength) by a reflective objective (× 36, Au coated), and the output pulse was recollimated by another reflective objective (×36, Al coated) to avoid the dispersion and astigmatism effects of conventional glass lenses. The effective coupling and transmission efficiency was 20%. The PCF output spectrum was measured by a 50-cm spectrometer. The self-phase modulated output pulse (60 mW) with complicated, large nonlinear chirp was directed into the 4-f chirp compensator which consists of a pair of gold-coating gratings (300 lines/mm groove density), a pair of silver-coating mirrors, a pair of silver-coating concave mirrors

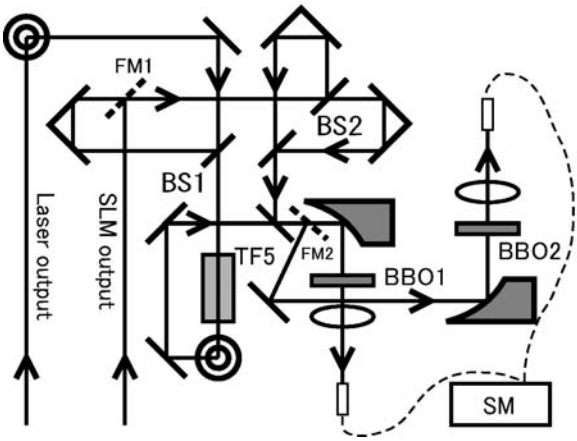

Fig. 5.16. Optical configuration for highly sensitive and reproducible M-SPIDER. When flipped mirrors FM1 is off and FM2 is on, the SH interferogram is measured using a 25-μm thick BBO crystal (BBO2: type I). BS1, BS2; ultrabroadband beam splitters. TF5; highly dispersive glass. BBO1; 50-μm thick BBO crystal (type II). SM; multi-mode-fiber attached spectrometer [15]

(200 mm focal length) and an SLM (648 pixels, 97 μm pixel width, 5 μm pixel gap, 66.1 mm total length, 85% transmission at 800 nm).

The pulse (15 mW) which passed the 4-f chirp compensator, was directed into the M-SPIDER apparatus for characterization (Fig. 5.16). The input pulse was divided into two beams with a 1:4 beam splitter, and the delay τ between the two pulses was controlled by a Michelson interferometer arm. The reference pulse, which was earlier split from the laser oscillator output, was used to provide a strongly chirped pulse by round-trip transmission through TF5 glass (2×10 cm length). The duration of the chirped reference pulse was 20 ps. These three pulses were combined and focused onto a β-barium borate (BBO) crystal (type II, 50 μm thickness) by an aluminum parabolic mirror (50 mm focal length) to produce the sum-frequency wave of them. The SPIDER signal was detected by a 50-cm spectrometer (1200 lines/mm groove density, 800 nm blaze wavelength) with an intensified CCD camera of 1024×256 channels. The total wavelength resolution was less than 0.05 nm at 400 nm. Since the limited bandwidth at a fixed angle of the grating was 37.5 nm at 400 nm, the grating was automatically rotated three times (center wavelengths of 380, 410 and 440 nm) to detect the SPIDER signal with the ultrabroadband spectrum (370–445 nm). Then, it took $3 \times 10\,\mathrm{s} = 30\,\mathrm{s}$ to get one signal.

The delay time was evaluated from the measurement of the second-harmonic (SH) interferogram (Fig. 5.17(e)) of the intensified pulses split directly from the oscillator (Fig. 5.16) instead of the conventional measurement of the SH interferogram of the replicas, because the former interfero-

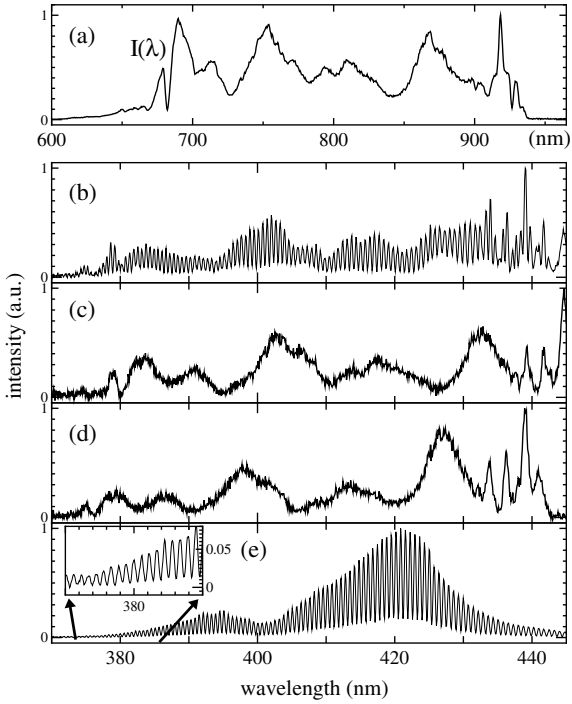

Fig. 5.17. In the SLM-off case, (**a**) PCF output spectrum, (**b**) SPIDER signal, (**c**) and (**d**) replica spectra. (**e**) SH interferogram [15]

gram has a much better signal-to-noise ratio than that of the latter interferogram and the former spectral range (370–455 nm) is almost the same as that (370–445 nm) of the SPIDER signal. In addition, the another SH arm for the independently-adjustable measurement of the SH interferogram was added with a flipped mirror, a parabolic mirror, a 25-μm thick BBO (type I), a filter and a fused-silica lens. To accurately reconstruct the spectral phase over the whole spectral range, we employed the following subtraction method [7, 10] which permits us to avoid the nonlinear wavelength error appearing in measurements in the greatly broad spectral range with the high wavelength resolution, but not employed the delay time of the constant value (approximately $\tau \cong 850$ fs). The phase difference $\theta_{\mathrm{SPI}}(\omega)$ obtained from the SPIDER signal [10] contains a delay-dependent linear term $\tau\omega$ (which must be removed for the spectral phase reconstruction) according to $\theta_{\mathrm{SPI}}(\omega) = \phi(\omega) - \phi(\omega - \Omega) + \tau\omega$. On the other hand, the corresponding phase difference $\theta_{\mathrm{SH}}(\omega)$ obtained from the SH interferogram contains only the delay term $\tau\omega$ according to $\theta_{\mathrm{SH}}(\omega) = \tau\omega$. Therefore, if there is a system error concerning the determination of the delay time, it is best to subtract

$\theta_{\mathrm{SH}}(\omega)$ from $\theta_{\mathrm{SPI}}(\omega)$ over the whole spectral range as a background to correctly remove the term $\tau\omega$ [7, 10].

The procedure for feedback chirp compensation is as follows.

1. Measure the SH interferogram.
2. Measure the SPIDER signal and the replica pair spectra in the SLM-off case.
3. Reconstruct the spectral phase in the SLM-off case.
4. Apply the corresponding negative spectral phase by the SLM to compensate for the chirp.
5. Return to step (2) in the SLM-on case.

After two further iterations in the SLM-on case, (2)→(3)→(4)→(2), the pulse compression was accomplished. The PCF output spectrum with 60 mW average power broadened from 600 to 965 nm, as shown in Fig. 5.17(a). The SPIDER signal and replica spectra of the PCF output before feedback (SLM-off case) are shown in Fig. 5.17(b),(c) and (d). The replica spectral structures are similar to the PCF output one, implying that the thickness of the BBO crystal does not affect the SPIDER signal. Moreover, the intensity of the SPIDER interferogram is strong enough to characterize the spectral phase of the PCF output pulse over the whole spectral region.

The value of the spectral shear $\Omega/2\pi$ was measured to be 8.24 THz. The reconstructed spectral phase is shown by a dashed-dotted line in Fig. 5.18(a). It indicates the complicated behavior in the 720 to 920 nm wavelength region and the variation over 30 rads. A dotted line and a solid line in Fig. 5.18(a) show the spectral phases after first and second feedbacks, respectively. The compensated spectral phase after second feedback was converged within 1.3 rad throughout the pulse spectral region. The spectral phase applied by SLM at the second feedback time is shown in Fig. 5.18(b). In actuality, the applied phase change was wrapped between 0 to 4π due to limitations of the modulation depth of the SLM.

The corresponding reconstructed temporal intensity and phase profiles are shown in Fig. 5.19. The temporal intensity profile of the PCF output broadens asymmetrically over 150 fs and the phase varies complicatedly over 30 rads. After first and second feedback compensations its pulse width was reduced to 7.1 fs (Fig. 5.19(b)) and 6.6 fs (Fig. 5.19(c)), respectively. This compressed pulse almost corresponds to the 6.3 fs transform-limited one. To the best of our knowledge, this is the first complete pulse compression of the PCF output in the two-cycle region.

The compressed pulse after second feedback was also measured independently by the FRAC method, as shown by a solid line in Fig. 5.20. The employed fringe-resolved autocorrelator has a flipped mirror, a thin polarizer to select the p-polarization, a 25-μm thick BBO (type I) and a filter to cut the fundamental pulse. The FRAC trace calculated from the reconstructed spectral phase and measured spectral intensity is shown by a dotted

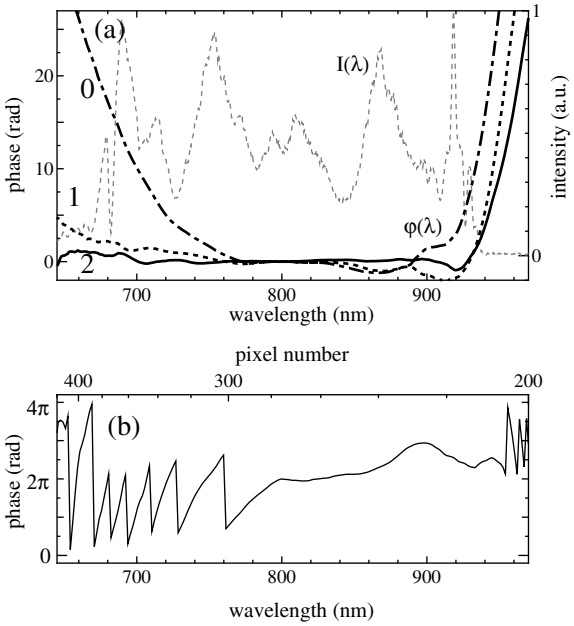

Fig. 5.18. (**a**) *Dashed-dotted*, *dotted* and *solid lines* are reconstructed spectral phases before and after first and second feedbacks, respectively. A *thin dashed line* is SLM-output spectrum after second feedback. (**b**) Wrapped spectral phase applied by SLM at the second feedback time [15]

line in Fig. 5.20. The agreement between the measured and calculated (using M-SPIDER data) FRAC traces is excellent. This result suggests that the spectral-phase feedback technique without using any Taylor expansion method for $\phi(\omega)$ is significantly reliable and powerful even for complicated nonlinear-chirp compensation. Moreover, this simple technique can be applied for chirp compensation of any unknown or fluctuated spectral phase $\phi(\omega)$ in the quasi-real time mode. This means that it has the potential to be a greatly useful tool to generate extremely short pulses, even for those who are not familiar with ultrafast optical technologies.

More recently (in 2004) we have generated shorter pulses with a duration of 5.8 fs (2.3 cycles) using a different PCF (853 nm ZDW, 2.6 μm core diameter, 2 mm length) [43].

Tapered Fiber

The generation of ultra-broad spectrum by a tapered fused-silica fiber (TF) is well known [19]. However, pulse compression using a tapered fiber has not yet been achieved. One of the reasons is the fact that the behavior of the spectral phase of the fiber output is so complicated that the output

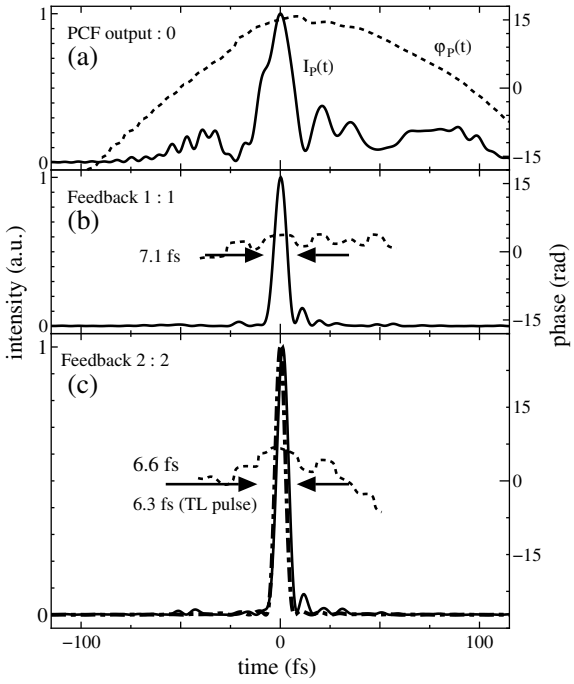

Fig. 5.19. Reconstructed temporal intensity profiles (*solid lines*) and phases (*dotted lines*) for (**a**) before and after (**b**) first and (**c**) second feedbacks. A *dashed-dotted line* in (**c**) is the 6.3-fs transform limited pulse

chirp is not compensated for by conventional passive compensators, such as chirped mirrors, prism pairs, grating pairs or their combinations. Another reason stems from the difficulty to characterize the spectral phase due to the relatively low peak power.

Here, let us describe the first experimental demonstration of spectral phase characterization of TF output and its pulse compression [20]. For this purpose, the experimental system similar to the one described in the previous subsection was used (but the first tentative system [8, 20]). That is, a modified spectral phase interferometer for direct electric-field reconstruction (M-SPIDER) apparatus [8, 21] was employed for characterization of the spectral phase. It was demonstrated that this technique has a high sensitivity comparable with the conventional fringe-resolved autocorrelator [8]. The feedback system consisted of the M-SPIDER apparatus and an active chirp compensator with a programmable spatial light modulator (SLM) [1, 22].

The 74-mm-long TF with a waist diameter of 2 µm and a waist length of 32.5 mm was manufactured from a standard telecommunication fiber (Fujikura OST-8251) with a core diameter of 9 µm and a clad diameter of 125 µm by means of heating and stretching in a flame. The zero-dispersion wavelength

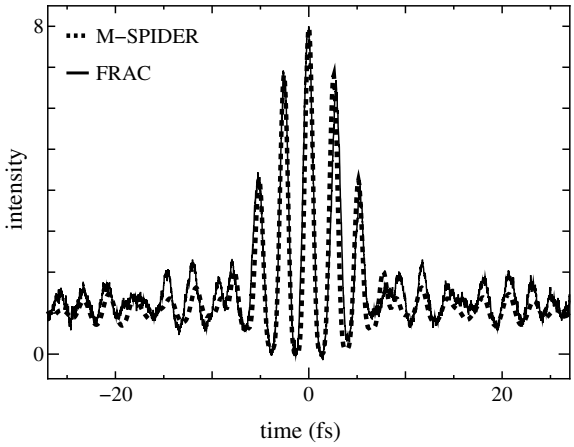

Fig. 5.20. FRAC traces of direct measurement (solid line) and calculation from M-SPIDER data (dotted line) [15]

(ZDW) of our TF was evaluated to be 710 nm from the result calculated in a similar manner to that in [19] (The nonlinear refractive index is the same as that of a conventional fused-silica fiber). The slightly up-chirped pulse beam from a mode-locked Ti:sapphire laser (185 fs pulse duration, 300 mW average power, a normalized linear-chirp coefficient of 0.16, a 100 MHz repetition rate and a 785 nm center wavelength with a spectral width of 30 nm) after passing through a focusing lens (100 cm focusing length) for collimation was split into two beams with an intensity ratio of 2 : 1. The lower-intensity beam with a p-linear polarization was coupled into the TF by an objective lens ($\times$20) and the same linear polarized output was collimated by another objective lens ($\times$20). The effective coupling and transmission efficiency was 33%. The higher-intensity beam was sent to the M-SPIDER apparatus as chirped reference pulses E_c to observe weak SPIDER signals. The fiber output spectrum was measured using a calibrated spectrometer. It was confirmed that when the full power (295 mW average power) from the laser was directly propagated along the fiber, the output spectrum was broadened from 425 to 955 nm and had a significantly modulated structure. This suggested that the output has a complicated spectral phase.

After the output pulse with strong chirp was collimated and passed through an aperture, it was directed to the programmable chirp compensator by aluminum-coated mirrors. The 4-f chirp compensator consisted of a pair of gold-(in) and silver (out)-coated gratings ($d = 1/150$ mm), a pair of plane mirrors with silver coating, a pair of concave mirrors with aluminum coating (f = 350 mm), and a specially made large-pixel-number SLM (648 pixels, 97 μm pixel width, 5 μm pixel gap, 66.1 mm total size and 85% trans-

mission at 800 nm). The throughput of the compensator including several guiding mirrors was 25% [8, 11, 20].

The pulse after passing through the compensator, as well as the fiber input pulse, was characterized using the highly sensitive M-SPIDER apparatus equipped with a 30 cm spectrometer (a grating of 1200 lines/mm, a blaze wavelength of 300 nm) having an intensified CCD camera of 1024×256 channels. The total wavelength resolution was 0.05 nm at 400 nm. The 100-mW-average-power pulse that split directly from the laser oscillator provided an intense reference pulse beam E_c with strong chirp after double-passing through a dispersive TF5 glass of 10 cm length (the group-delay dispersion of $\ddot{\phi} = 3.7{\times}10^4\,\mathrm{fs}^2$ at 785 nm, the pulse duration of 3.5 ps). The weak input pulse E with 2 mW average power after a 2 mm entrance aperture of the M-SPIDER apparatus was converted to two replicas E_1 and E_2 with a delay time by means of a Michelson interferometer arm. Combined reference and replica pulses were focused on a type II β-BaB_2O_4 (BBO) crystal with 50 μm thickness by an aluminum parabolic mirror (50 mm focusing length) to produce a SPIDER signal $E_1\ E_c + E_2\ E_c$.

First (1), the interference signal $(E_1 + E_2)^2$ of second-harmonic waves of the replica was measured by blocking of the reference beam E_c and by the 45 degree rotation of the BBO crystal so that the delay time τ_d was obtained to be 533.8 fs. This value was fixed for all the measurements of SPIDER signals before and after chirp compensation as well as that for the fiber input pulse. Next (2), the SPIDER signal was measured under the condition of 100 s accumulation time, and then (3) the two sum-frequency signals between the replica and the reference, $E_1\ E_c$ and $E_2\ E_c$, were measured under the same accumulation condition to obtain spectral shear $\Omega/2\pi$. The values of the spectral shear were 2.45, 2.38 and 2.49 THz for the cases of the SLM-off (before the feedback operation), the SLM-on (after the feedback operation) and the fiber input, respectively. The slight difference among these values may be due to a highly nonlinear chirp of the reference pulse. A theoretical relationship of $\Omega/2\pi = \tau_d/\ddot{\phi}$, which is derived in the ideal case of the linear-chirp pulse, is predicted to have a constant value of 2.30 THz. It was confirmed that this slight difference hardly affects the reconstruction results of the spectral phase and the temporal intensity profile. (4) After the spectral phase was reconstructed by the first computer and was used as feedback to the second computer, (5) the corresponding negative phase dispersion was applied by the SLM controlled by means of the second computer to compensate for the chirp. This laser system for pulse compression operated stably for more than 1 h.

Figure 5.21(a) shows the fiber output spectrum with 20 mW average power, which broadened from 658 to 889 nm for the 60 mW input average power. The spectrum has split into two peaks at 760 and 818 nm with a separation of 28 THz. This spectral splitting is due to the effect of intrapulse parametric four-wave mixing ($\omega_p + \omega_p \rightarrow \omega_s + \omega_{as}$) occurring around the zero-dispersion wavelength (ZDW) with phase matching, which was already

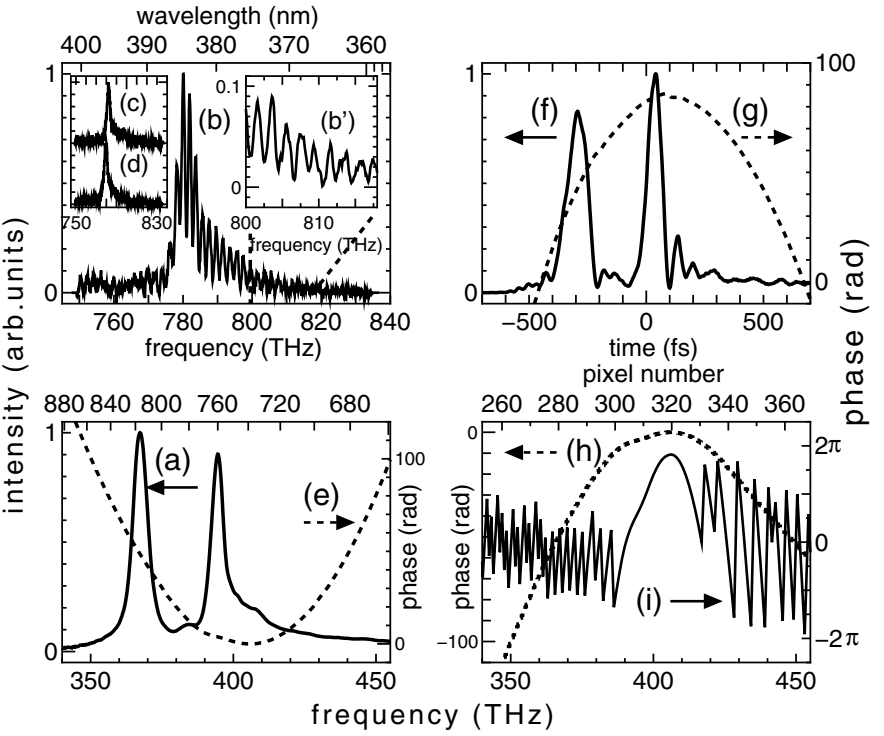

Fig. 5.21. Modified SPIDER measurement in SLM-off case and imparted spectral phase. (**a**) Pulse spectrum (*solid line*). (**b**) and (**b'**) SPIDER signal. (**c**),(**d**) replica spectra. (**e**),(**f**) and (**g**) are reconstructed spectral phase (*dashed line*), temporal intensity (*solid line*) and temporal phase (*dashed line*), respectively. (**h**) and (**i**) are spectral phase imparted by SLM after feedback operation (*dashed line*) and its folded phase (*solid line*), respectively [20]

reported for a photonic crystal fiber [3, 19, 23]. Figure 5.21(b)–(d) shows the SPIDER signal and the two replica spectra of sum-frequency waves. This result for 2-mW-average-power pulses implies that the present M-SPIDER apparatus has a sensitivity as high as 20 pJ/pulse (80 THz bandwidth), which is the most highly sensitive apparatus ever developed by the SPIDER technique to our knowledge. That is, the M-SPIDER technique has a higher sensitivity than the recently proposed homodyne optical technique for SPIDER [24]. The reconstructed spectral phase and the reconstructed temporal intensity and phase profiles are shown in Fig. 5.21(e)–(g). Since the frequency range of the measured SPIDER signal and replica spectra was limited due to a fixed grating angle of the ICCD spectrometer and feedback operation, the spectral phase at the high ($> 435\,\mathrm{THz}$ $(= \omega_\mathrm{H}/2\pi)$) and low ($< 362\,\mathrm{THz}$ $(= \omega_\mathrm{L}/2\pi)$) frequency wings was obtained by an extrapolation method on the basis of quadratic frequency dependences at $\omega_\mathrm{H}(\ddot{\phi}_\mathrm{H} = 2.08 \times 10^3\,\mathrm{fs}^2)$ and

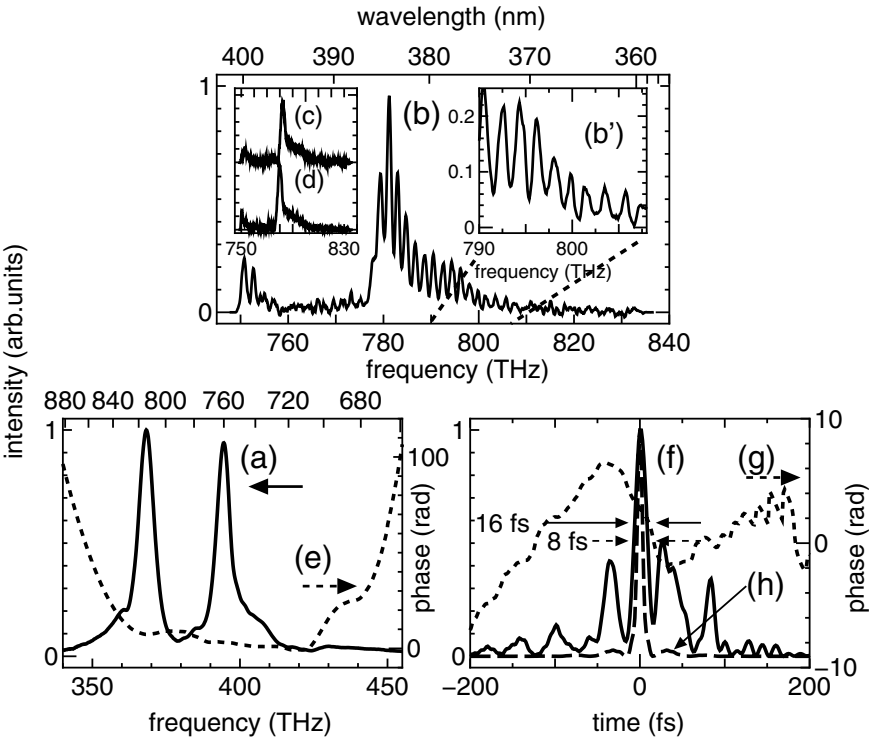

Fig. 5.22. Modified SPIDER measurement in SLM-on case. (**a**) Pulse spectrum (solid line). (**b**) and (**b'**) SPIDER signal. (**c**),(**d**) replica spectra. (**e**),(**f**) and (**g**) are reconstructed spectral phase (*dashed line*), temporal intensity (*solid line*) and temporal phase (*dashed line*), respectively. (**h**) Calculated transform-limited pulse profile (*long-dashed line*) [20]

$\omega_{\mathrm{L}}(\ddot{\phi}_{\mathrm{L}} = 1.36 \times 10^3\,\mathrm{fs}^2)$. From Fig. 5.21(e), we see that the spectral phase deviates from the sum of quadratic and cubic frequency functions, especially at around 395 THz (760 nm). The temporal pulse profile splits into two peaks with a time separation of 330 fs. This large separation of two pulse peaks causes the deviation from the similarity of the replica spectra (Fig. 5.21(c)–(d); correspondingly the envelope spectrum of the SPIDER signal Fig. 5.21(b)) to the original pulse spectrum (Fig. 5.21(a)). The temporal phase suggests a complicated, nonlinear up-chirp.

Figure 5.21(h) shows the phase dispersion applied by the SLM after the feedback operation [8], which corresponds to the negative value of the spectral phase in the SLM-off case (Fig. 5.21(e)). The SPIDER signal measured in the case of the SLM-on, the replica spectra, the reconstructed spectra phase and the reconstructed temporal intensity and phase profiles as well as the pulse spectrum and its transform-limited pulse are shown in Fig. 5.22. The spectral

phases at the high ($> 450\,\mathrm{THz}$ ($= \omega_{\mathrm{H}'}/2\pi$); $\ddot{\phi}_{\mathrm{H}'} = 1.613 \times 10^4\,\mathrm{fs}^2$) and low ($< 362\,\mathrm{THz}$ ($= \omega_{\mathrm{L}'}/2\pi$); $\ddot{\phi}_{\mathrm{L}'} = 5.58 \times 10^3\,\mathrm{fs}^2$) frequency wings were obtained by a similar extrapolation method to the SLM-off case. The temporal intensity profile (Fig. 5.22(f)) indicates that the 185 fs fiber-input pulse was compressed to 16 fs with subpulses. This compressed pulse profile fairly corresponds to the 8 fs transform-limited one with subpulses. The 36 fs time separation between the main pulse and one of the subpulses agrees with the inverse of the 28 THz frequency difference between the two spectral peaks (Fig. 5.22(a)), suggesting that the subpulses are due to the beat effect between their spectral components. The slight difference between the compressed and transform-limited pulse profiles may be due to the imperfect compensation of the rapidly varying spectral phase at the low and high frequency edges (Fig. 5.21(e)). This occurs because the applied phase shift per one pixel at the edges exceeds π radians (Fig. 5.21(i)). This problem will be solved by a suitable selection of components of a 4-f phase compensator such as longer focal-length concave mirrors, larger $1/d$ gratings and so on.

In 2004, we have succeeded in shorter pulse compression to 8.4 fs for TF input pulses with a duration of 12 fs and an average power of 200 mW at a 75 MHz repetition rate [43].

5.2.3 Gas-Filled Hollow Fiber Experiment

Few-Optical-Cycle Pulse Generation

The key technologies to realize monocycle pulses are the generation of over-one-octave ultrabroadband pulses, their phase and amplitude characterization and precise phase compensation. The generation of sub-5.0 fs optical pulses was achieved in recent years by several groups [1, 23, 25]. In 2002, 4 fs pulse compression in noncollinear optical parametric amplifiers (NOPAs) with a bandwidth from 480 to 750 nm was reported [25,26]. However, further compression using the NOPA technique is limited by the insufficient spectrum bandwidth and the difficulty in ultrabroadband phase matching and compensation of the high-order spatial chirp. In addition, the filtering effect of a nonlinear crystal in the employed second-harmonic generation frequency-resolved optical gating (SHG-FROG) measurement results in a severe bandwidth limitation. In this subsection, the experimental generation of sub-3-fs optical pulses in the monocycle region will be introduced.

High pressure noble gas-filled hollow fiber is an attractive way of producing ultrabroadband spectrum with intense laser pulses, with its advantages of high transmission, long interaction length, and perfect spatial mode (see Sect. 4.3.1). The noble gases offer the following important advantages: (i) high threshold intensity for multiphoton ionization; (ii) pure electronic third order nonlinearity for not extraordinarily high pressures; (iii) nonlinearity controlled by changing the gas pressures. In the argon-filled hollow fiber, the nonlinear refractive index is $n_2/p = 9.8 \times 10^{-24}\,\mathrm{m}^2/\mathrm{W\,atm}$ [27],

and the group velocity dispersion is $k'' \approx 40\,\mathrm{fs}^2/\mathrm{m}$ [28]. The light propagates in hollow fibers through grazing incidence reflection along the inner dielectric surface of the fiber. For the hollow fiber, the lowest loss mode is EH_{11} hybrid mode, whose intensity cross section profile is given by a zero order Bessel function $I(r) = I_0 J_0^2(2.405r/a)$, where I_0 is the peak incident intensity, a is the bore radius of the fiber. The real and the imaginary parts of the propagation are given by [29]

$$\beta = \frac{2\pi}{\lambda}\left[1 - \frac{1}{2}\left(\frac{2.405\lambda}{2\pi a}\right)^2\right] \tag{5.1}$$

$$\frac{\alpha}{2} = \left(\frac{2.405\lambda}{2\pi a}\right)^2 \frac{\lambda^2}{2a^3}\frac{\nu^2+1}{\sqrt{\nu^2-1}} \tag{5.2}$$

where λ is the laser central wavelength in the gas medium and ν is the ratio between the refractive indices of the external (fused silica) and the inner (gas) media. The parameters that govern the bandwidth generated by self-phase modulation (SPM) are: the fiber radius, the fiber length, the gas pressure and the input pulse. The optimum fiber length L_{opt} is defined by [28]

$$L_{\mathrm{opt}} \approx 1.4\sqrt{L_{\mathrm{D}} L_{\mathrm{NL}}} \tag{5.3}$$

where L_{D} and L_{NL} are the *dispersion length* and *the nonlinear length*, respectively [28]. For Ar gas at a pressure of 3.3 atm, the group velocity dispersion is about $40\,\mathrm{fs}^2/\mathrm{m}$. For the incident pulse energy of 200 μJ, pulse width of 30 fs, the wavelength of 800 nm, and the fiber bore diameter of 100 μm, $L_{\mathrm{D}} = 22.5\,\mathrm{m}$, $L_{\mathrm{NL}} = 0.21 \times 10^{-2}\,\mathrm{m}$, we have L_{opt}=30.2 cm. The actual length was selected to be 34 cm.

For a Gaussian pulse, the maximum broadened bandwidth, either the low or high frequency side, is given by [28]

$$\delta\omega_{\max} = 0.86\gamma P_0 z_{\mathrm{eff}}/\tau_{\mathrm{p}} \tag{5.4}$$

where $z_{\mathrm{eff}} = [1 - \exp(-\alpha l)]/\alpha$, P_0 the pulse peak power, τ_{p} the half width of the pulse (at $1/e$ peak intensity), l the fiber length. The nonlinear coefficient γ is defined as $\gamma = n_2\omega_0/cA_{\mathrm{eff}}$, A_{eff} is the effective mode area. For argon gas and the fiber diameter of 100 μm, A_{eff}=$3.41\times10^{-5}\,\mathrm{cm}^2$, at the pressure of 3 atm, and the peak power of 6.7 GW, the maximum bandwidth $\delta\omega_{\max} \approx 2.95 \times 10^{15}$ rad/s, and $\delta\nu_{\max} \approx 470$ THz. This is slightly larger than the measured 510 THz for the whole range. The overestimated bandwidth may be attributed to the uncertainty of the quoted n_2 value [27].

Although the spectral phase interferometry for direct electric-field reconstruction (SPIDER) technique [10] has the potential of characterizing the spectral phase which extends to over one octave, it has a low sensitivity when measuring such ultrabroadband (low spectral density) signals. We developed a modified SPIDER (M-SPIDER) technique, which greatly improved its sensitivity [8,30] (see Sects. 4.3 and 4.4).

On the other hand, it is difficult to compress broadband optical pulses with an over-one-octave bandwidth by use of conventional passive chirp compensators such as prism and/or grating combinations, chirped mirrors, because of their bandwidth limitation and high-order dispersion. 4-f phase compensators with spatial light modulators have been shown to be flexible and broadband phase compensators. The modulators include the liquid crystal array (SLM) [1, 5, 22, 31, 32], acousto-optic modulator (AOM) [33], and deformable mirror (DM) [34]. All spatial-light-modulator phase-compensators apply spatio-temporal distortions in the pulse, which are proportional to the magnitude of the shaping.

Liquid crystal SLM is a superior candidate for a programmable phase compensator of over-one-octave pulses. It has a transmission spectrum from 300 nm to 1500 nm. But it has dead spaces (see Sect. 3.2).

Acousto-optic modulators (AOMs) [33] have a very high number of effective "pixels" − the number of sound waves that fit across the aperture of the crystal. However, the efficiency of AOM is less than other methods since it relies on the diffracted light. In addition, AOMs have dispersion too large to be used as compensators for ultrabroadband chirped pulses.

Deformable mirror [34] is a phase-only modulator. It has large pixels without dead spaces, and is efficient, but it has the disadvantages of cumbersome, imperfect phase calibration of the membrane deflection, low spatial and phase resolutions and high deflection losses. There has been no sub-10-fs pulse reported from the phase compensator with deformable mirrors [35, 36] (except for the combination with the other compensators in [26]) and AOMs [33].

We demonstrated that an SLM phase compensator enables us to compress pulses to sub 5–6-fs by inputting individual orders of dispersion into the SLM [1, 31, 32] (see Sect. 3.3). It was expected that more precise phase compensation by direct phase feedback technique (Sect. 5.1) leads to better results. By the novel technique, we demonstrated a preliminary 4.0-fs optical compression of output pulses from Ar-filled hollow fiber, as shown below [37].

The experimental setup is shown in Fig. 5.23. The output beam from a Ti:sapphire laser amplifier system (pulse duration of <30 fs, center wavelength at 790 nm, repetition rate of 1 kHz) was divided into two beams. One beam with pulse energy of 230 μJ was coupled into a hollow fiber with 34-cm length and 100-μm bore diameter, which was positioned in a chamber filled with argon gas. The chamber had two 1-mm-thick fused-silica windows. The other beam with pulse energy of 22 μJ was sent into the M-SPIDER as the external reference beam.

After passing through the hollow fiber, the pulses (11.2 μJ energy) were injected into an active phase compensator containing a specifically designed liquid crystal SLM (number of pixels 648, pixel width 97 μm, gray-scale resolution 192), two aluminum coated gratings (blazing wavelength of 500 nm, groove density of 150 lines/mm), and two concave mirrors (focal length of 350 mm). The output pulse (0.6 μJ energy, 470 to 1050 nm spectral broadening (Fig. 5.25)) from the phase compensator was injected into the M-

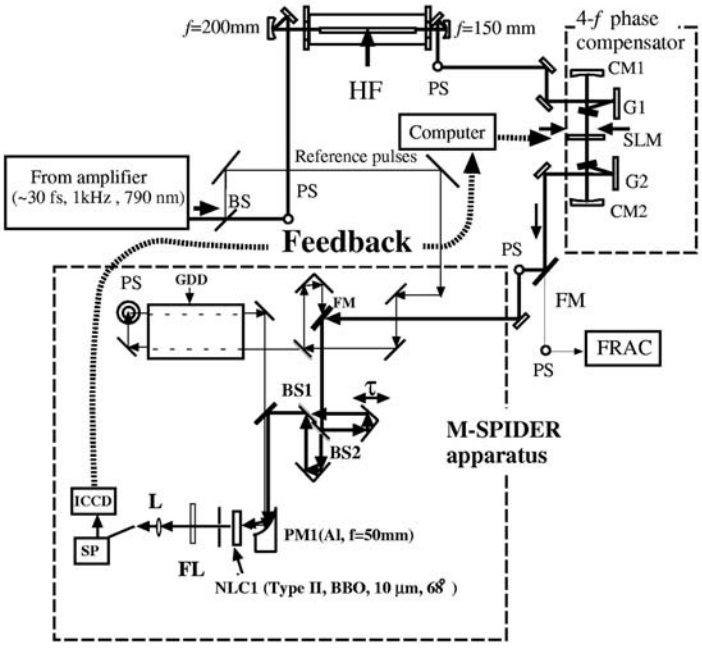

Fig. 5.23. System layout of direct feedback phase compensation for the 4-fs pulse generation. GDD: 10-cm-long TF5 dispersive glass, L: focusing lens ($f = 5\,\mathrm{cm}$, fused silica), FL: high pass filter, HF: hollow fiber ($l = 340\,\mathrm{mm}$, $2a = 100\,\mathrm{mm}$) PM1: parabolic mirror, BS1,BS2: 0.5-mm-thick beamsplitters, CM1,CM2: concave mirrors ($f = 350\,\mathrm{mm}$), G1,G2: reflective gratings (blazing wavelength $\lambda_\mathrm{b} = 500\,\mathrm{nm}$, 150 lines/mm), BS: beamsplitter, PS: periscopes, FM: flip mirrors, FRAC: fringe-resolved autocorrelator, SLM: liquid crystal spatial light modulator [37]

SPIDER. In the M-SPIDER, the two replicas with a delay time τ were produced by a Michelson interferometer. The replicas were up-converted with the external reference chirped pulse, which passed through a 10-cm-long TF5 glass twice, by a 10-μm-thick barium borate crystal (BBO; Type II, 68°). The interferogram with a spectral shear $\Omega/2\pi$ was measured by a spectrometer (1200 lines/mm) with an intensified charge coupled device (ICCD; 1024×256 pixels). The experimental results are shown in Fig. 5.24. The spectral shear $\Omega/2\pi$ was 2.63 THz, and the delay time τ was estimated at 887.2 fs by measurements of the interference between replicas not-upconverted by chirped pulses. The negative of the spectral phase measured by M-SPIDER apparatus was applied by the liquid crystal SLM, After feedback phase compensation, the reconstructed spectral phase was almost flattened (Fig. 5.25). We found that the duration of compressed pulses is 4.0 fs (Fig. 5.26). We couldn't obtain further pulse shortening, although the duration of its Fourier transform-limited pulse was evaluated to be 2.5 fs.

System Improvement for Optical Pulse Generation in Monocycle Regime

Since the light source was stable and the 4-f phase compensator had the ability to compensate for chirp, the limitation in the previous subsection was mainly attributed to measurement errors. Therefore, we clarified the problems in our measurement apparatus thoroughly, and then demonstrated the 1.56 optical-cycle, 3.3-fs [1] pulse generation [7] using a significantly improved M-SPIDER apparatus. In this subsection, we will mainly focus on the description of this experiment.

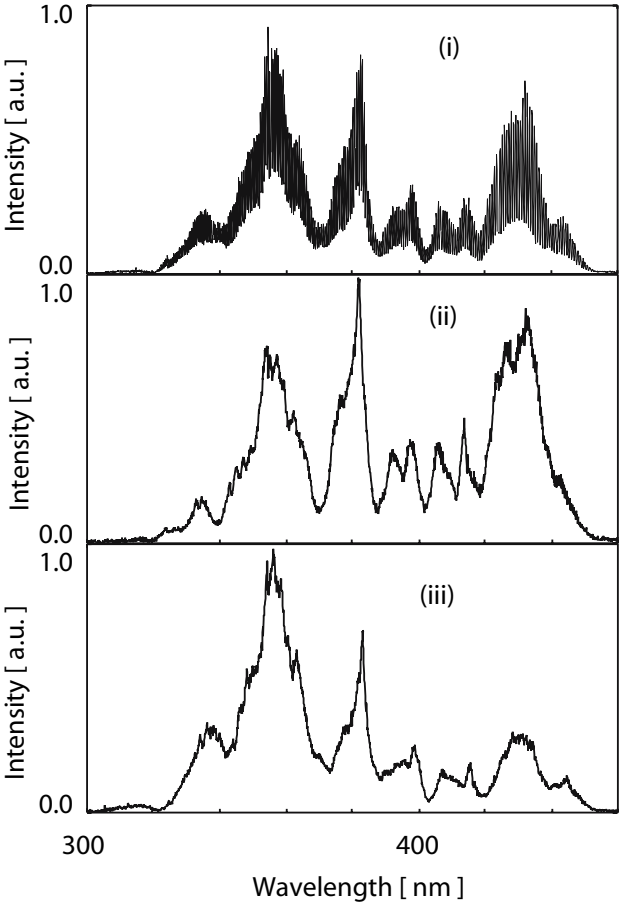

Fig. 5.24. Measured signals. (**i**) SPIDER signal and (**ii**), (**iii**) replicas before feedback compensation [37]

[1] The pulse duration "3.4 fs" described in [7] was corrected to be "3.3 fs" as a result of fine recalibration of measurement instruments.

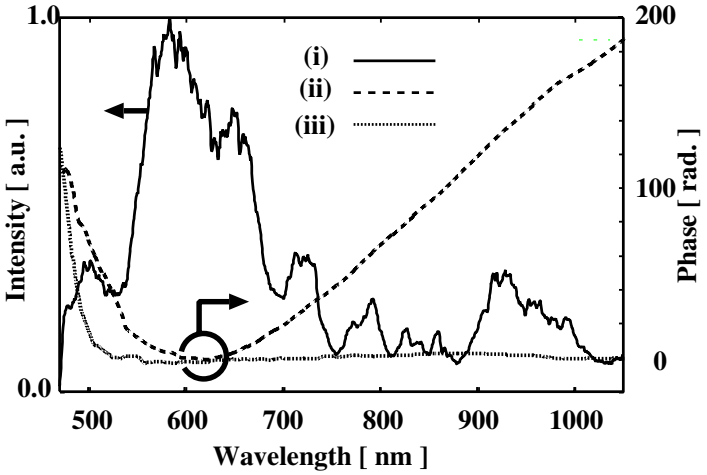

Fig. 5.25. Measured intensity spectrum and reconstructed spectral phases (**i**) Intensity spectrum and spectral phases (**ii**) before and (**iii**) after feedbacks [37]

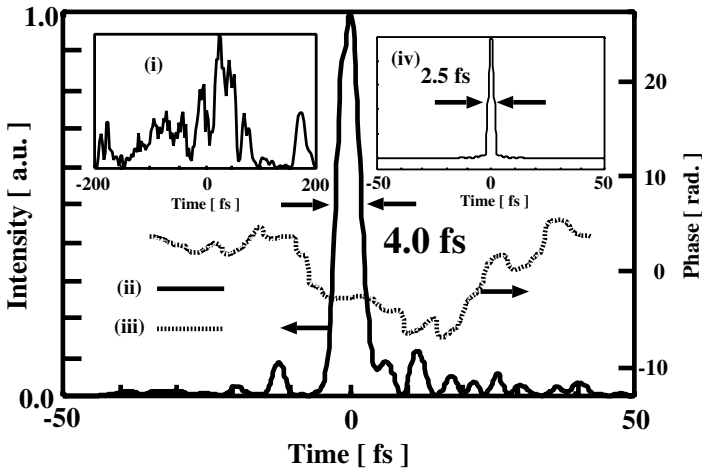

Fig. 5.26. Reconstructed pulse intensity and phase. Temporal intensities (**i**) before and (**ii**) after feedbacks. (**iii**) Temporal phase after feedback. (**iv**) Fourier transform-limited pulse intensity [37]

The essential needs for successful feedback are accurate measurement and accurate phase compensation. We examined the error source in the previous system [8, 30, 37] and made some important modifications (Fig. 5.27).

In SPIDER measurement, the phase difference contains a delay-dependent linear term τ according to $\theta(\omega) = \phi(\omega + \Omega) - \phi(\omega) + \omega\tau$ [10]. The term $\omega\tau$ can be removed by measuring the delay of the two replica pulse pair. Let us

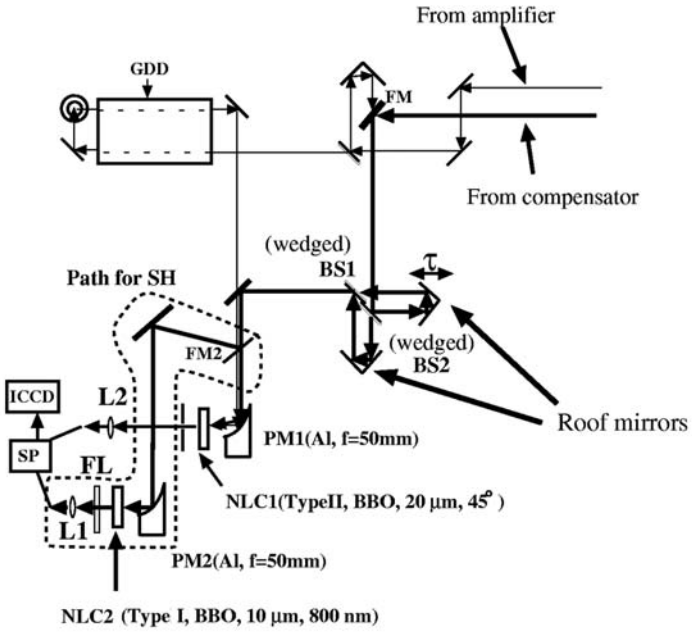

Fig. 5.27. Improved M-SPIDER. BS1,BS2: 0.5-mm-thick wedged beamsplitters (fused silica, 0.5°), L1,L2: focusing lenses (fused silica, $f = 5\,\mathrm{cm}$) [7]

suppose that the delay time and the spectral shear have errors like $\tau + \delta\tau$, and $\Omega + \Delta\Omega$, due to inaccurate measurements. We find that the influence of these two parameters is different as shown below. For example, if τ is not accurately determined, the resulting error in $\theta(\omega)$ will appear to be term of $\omega\delta\tau$:

$$\theta(\omega) = \phi(\omega + \Omega) - \phi(\omega) + \omega\tau - \omega(\tau + \delta\tau) \approx \Omega\frac{\mathrm{d}\phi(\omega)}{\mathrm{d}\omega} - \omega\delta\tau \tag{5.5}$$

The resulted phase by integration of $\theta(\omega)$ will be:

$$\phi(\omega) = \frac{1}{\Omega}\int \theta(\omega)\mathrm{d}\omega + \frac{\delta\tau}{2\Omega}\omega^2 \tag{5.6}$$

Clearly there is a quadratic phase error in the retrieved phase $\phi(\omega)$. In contrast, the error $\Delta\Omega$ will only result in an amplitude error of the measured phase $\phi_\mathrm{m}(\omega)$

$$\phi_\mathrm{m}(\omega) = \frac{1}{\Omega + \Delta\Omega}\int \theta(\omega)\mathrm{d}\omega = \frac{\Omega}{\Omega + \Delta\Omega}\phi_0(\omega) \tag{5.7}$$

where $\phi_0(\omega) = (\Omega)^{-1}\int \theta(\omega)\mathrm{d}\omega$ is supposed to be the correct phase. Since the former additive error $(\delta\tau/2\Omega)\omega^2$ is serious compared with the latter multi-

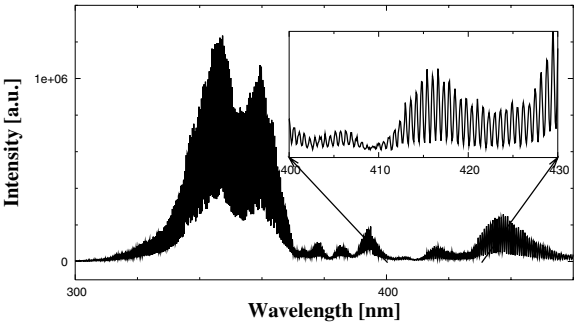

Fig. 5.28. Second-harmonic (SH) interferogram [7]

plicative error $(-\Delta\Omega/\Omega)\phi_0(\omega)$, we mainly concentrate our effort on increasing the accuracy of τ.

As suggested by Walmsley [10], if there is a system error in the Michelson interferometer, it will be best to measure the SPIDER signal for $\Omega = 0$ and to subtract it as a background. This can be achieved by measuring the second harmonic (SH) interferogram between replicas since $\theta_{\mathrm{SH}}(\omega) = \omega\tau$.

However, as the nonlinear crystal for the sum frequency generation in the SPIDER was cut for the type II phase matching condition and not for type I phase matching for the second harmonic generation (SHG) of the pulse pair. To obtain the intense SH interferogram, the crystal has to be rotated for type I phase matching. This also requires a fine realignment of the lens, the detector and the slit, for the best signal intensity. This alignment will turn the system conditions away from that for measuring the sum frequency waves of SPIDER. To avoid the perturbation of the SPIDER measurement and to get a reproducible signal, we built a separate optical path for the independent alignment and measurement of the SH interferogram (Fig. 5.28). This enabled highly reproducible measurements. The following improvements are also very important:

1. We improved the beam splitters in the Michelson interferometer. We found that the SPIDER interferogram was superimposed by the interference between front and back surface reflections of the beam splitters. An anti-reflection coating on the backside should avoid this, however, it is difficult to make an anti-reflection coating for over-one-octave bandwidth. Therefore, we replaced them with wedged beam splitters with a thickness of 0.5 mm, and a wedged angle of 0.5° (20% reflection and 80% transmission for s-polarization from 400 to 1300 nm: fused silica substrate). Consequently, the back reflection interference is completely eliminated.
2. We recalibrated the spectrometer. We calibrated the spectrometer using a mercury lamp (less than 0.05 nm in the whole spectral range of 300 to 460 nm) at a sufficiently high accuracy. However, we found that the

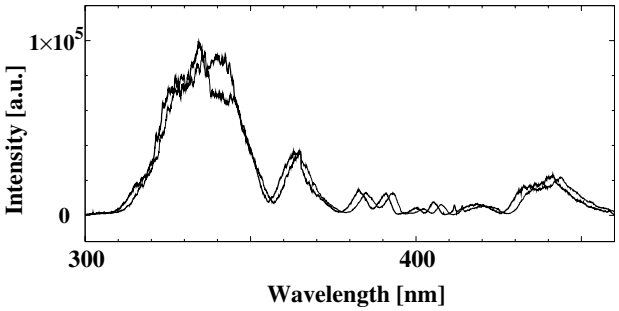

Fig. 5.29. Sum-frequency-wave spectra of replicas [7]

calibrated wavelength contains a nonlinear error that produces a very small but not negligible distortion in measured spectral interference fringe spacing. This error may cause an error of the delay time τ in the order of a few femtoseconds that results in a group-delay dispersion error of several tens of fs^2. This error makes subtracting the $\omega\tau$ from the measured phase difference more crucial, rather than just determining the delay time τ through the measured fringe period.

3. We significantly increased the SH signal intensity. The intensity of the SH interferogram was very weak and it was difficult to measure over the same wavelength range as in the SPIDER measurement. The input pulse has a bandwidth from ∼470 to ∼1100 nm, corresponding to a SH signal from ∼235 to ∼550 nm. On the other hand, the SPIDER signal comes from 300 to 460 nm. The SH signal is too broad to cover the SPIDER wavelength range. Therefore, we initially reduced the pressure of Ar gas from 3.0 to 0.8 atm so that the spectral range of the intensified SH interferogram is roughly the same wavelength range as in the SPIDER (Figs. 5.28, 5.30 and 5.31).
4. Phase compensation with multiple feedbacks is very much required, especially in the case where the spectral shear Ω for each frequency component cannot be regarded as a constant. This could happen when the input pulse has a broader temporal width than the necessary ten percent of the reference pulse width [10]. The first feedback could make the input pulse narrow down such that the spectral shear Ω can be taken as a constant. Then the second feedback with this Ω can remove the residual errors. In general, n-multiple feedbacks rapidly decrease insufficiency of phase compensation, which is due to any errors $\Delta\Omega$ of the spectral shear, according to

$$\phi^n(\omega) = \left|\frac{\Delta\Omega}{\Omega + \Delta\Omega}\right|^n \phi^0(\omega) \tag{5.8}$$

where $\phi^0(\omega)$ and $\phi^n(\omega)$ are the phases before and after n-times feedback compensation, respectively.

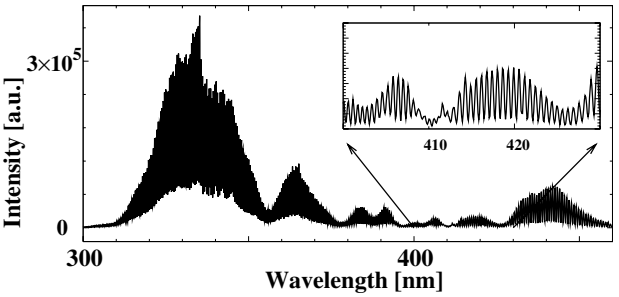

Fig. 5.30. SPIDER interferogram before feedback [7]

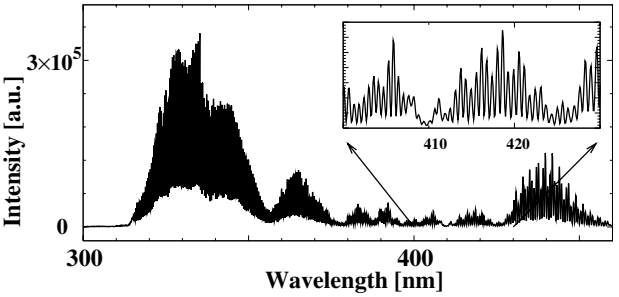

Fig. 5.31. SPIDER interferogram after 2nd feedback [7]

The following improvements had already been done in the experiments in the previous subsection, but they are worth pointing out:

1. Since the pulse has an over-one-octave bandwidth, the first order diffraction of the gratings can overlap with the second order on the SLM. In the 4-f system, the second order diffraction can be modulated unexpectedly by the SLM and reduces the accuracy of phase compensation. It was found that the proper choice of a blazing wavelength could reduce the influence of the second order diffraction on the output from the compensator. For a spectrum of $\sim$470 – $\sim$1060 nm bandwidth, if the blazing wavelength is chosen to be 500 nm, the intensity of the second order diffraction can be reduced to only a few percent of the first order.
2. The use of the longer focal length (from f=200 mm in [1] to f=350 mm) of two concave mirrors reduced the loaded bandwidth of each pixel (from $\Delta\lambda$=3.0 to 1.9 nm) and hence the load of phase compensation per pixel.

Based on the above improvements, we conducted a further pulse compression experiment. The experimental setup except pulse energy (fiber input: 94 μJ, fiber output: 16 μJ, compensator output: 0.5 μJ, chirped reference pulse: 2.4 μJ) was almost the same as in the previous subsection. Because

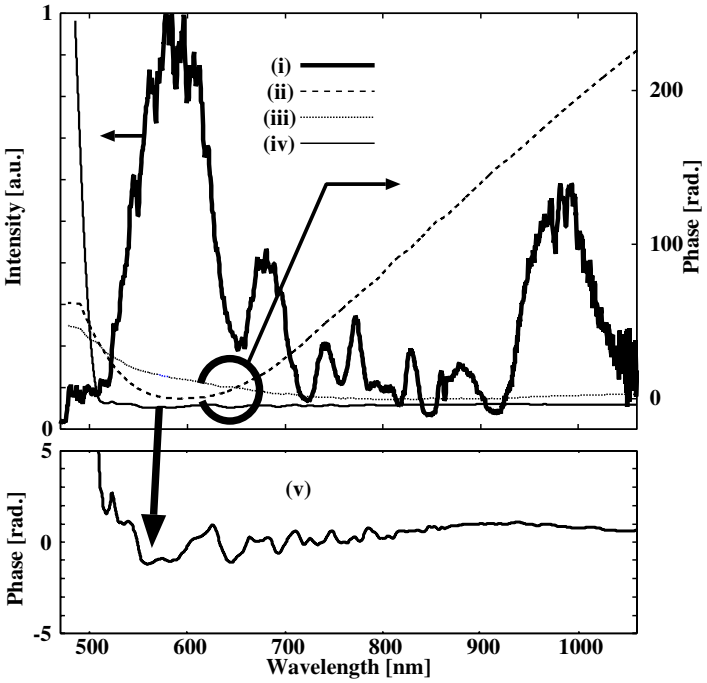

Fig. 5.32. Measured intensity spectrum and reconstructed spectral phase with respect to wavelength. (**i**) Intensity spectrum and spectral phases (**ii**) before feedback, (**iii**) after 1st feedback and (**iv**) after 2nd feedback. (**v**) detail of (**ii**) [7]

the pulse had very broad bandwidths, it was necessary to take the signals by five rotations of the grating in the spectrometer, which was automatically controlled by a computer. The exposure time was 0.1 s×100 for each rotation. The ICCD was synchronously gated for increasing the signal-to-noise ratio.

First, we measured the SH interferogram (Fig. 5.28) and then the SPIDER signal (Fig. 5.30). The SH interferogram was used as $\omega\tau$ for subtracting from the SPIDER signal.

For determining the value of the spectral shear $\Omega/2\pi$ and checking the validity of the SPIDER interferogram, we measured the spectrum of each replica pulse. We found that both replica spectra became very similar to the envelopes of the SPIDER signals over the whole spectral range from 300 to 460 nm (Figs. 5.29–5.31) and the pulse intensity spectrum (Fig. 5.32(i)), which ensures the quality of SPIDER fringes. Figure 5.32(ii)–(v) is the retrieved spectral phase for before and after feedback compensation, with $\omega\tau$ subtracted. After two times feedback compensation, the spectral phase was almost flat (curve (iv) in Fig. 5.32 and the enlarged section is curve (v)), demonstrating the power of this feedback technique for extremely short pulse

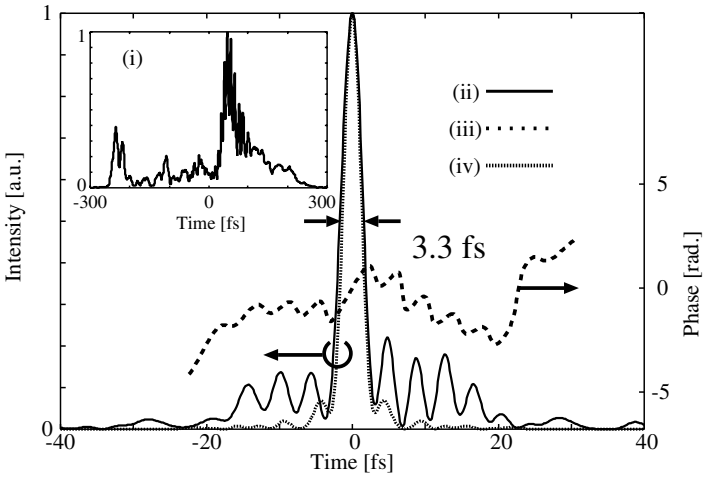

Fig. 5.33. Reconstructed pulse intensity profiles and phase. Temporal intensity profiles (**i**) before and (**ii**) after 2nd feedback. (**iii**) Temporal phase after 2nd feedback. (**iv**) Fourier transform-limited pulse intensity profile [7]

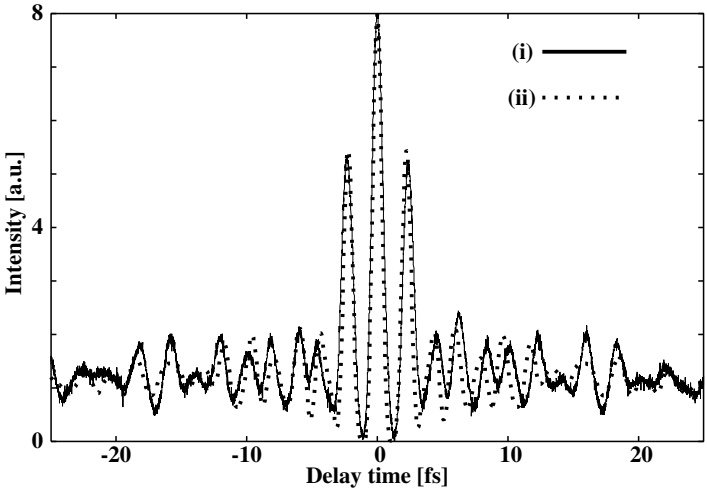

Fig. 5.34. FRAC traces ((**i**) Measured FRAC trace and (**ii**) a trace retrieved from SPIDER measurement)

compression. The parameters τ and $\Omega/2\pi$ were confirmed to be 935 fs and 4.12 THz, respectively.

Figure 5.32(i) is the measured spectrum (475 to 1060 nm spectral broadening) of the pulse output from the phase compensator. The retrieved temporal intensity and phase of compensated pulses are shown in Figs. 5.33(ii) and (iii) (and Fig. 5.33(i), before compensation). We found that side-lobes

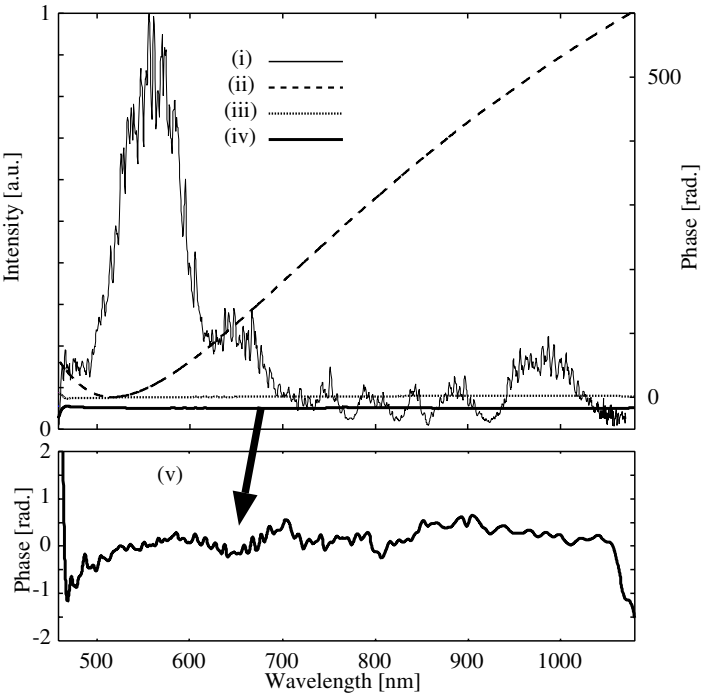

Fig. 5.35. Measured intensity spectrum and reconstructed spectral phases. (**i**) Intensity spectrum. Spectral phases (**ii**) before, after (**iii**) 1st feedback and (**iv**) 2nd feedback. (**v**) detail of (**iv**)

were almost eliminated and the pulse duration was 3.3 fs, close to the 2.8 fs transform-limited pulse with small side-lobes (Fig. 5.33(iv)). This pulse duration corresponds to 1.6 cycles, for the central wavelength of 636.3 nm. This pulse compression was also confirmed by an independent measurement of fringe-resolved autocorrelation (FRAC) traces under the bandwidth limitation (480–960 nm) by a slit on the SLM, although the small additional phase ($-20\,\mathrm{fs}^2$ for the group-delay dispersion and $-20\,\mathrm{fs}^3$ for the third-order dispersion at 800 nm) was applied for optimization of FRAC measurement (which was necessary for the difference between dispersion of optical components in the SPIDER apparatus and that in the FRAC one (Fig. 5.34)).

Furthermore, we have recently succeeded to generate clean 2.8-fs, 1.5-optical-cycle pulses nearly without side-lobes (Fig. 5.36(ii)) [42]. This has been enabled by paying close attention to the following important points: First, self-phase modulated pulses with a shorter and broader spectrum (460 to 1060 nm: Fig. 5.35(i)) have been used as pulses to be feedback-compensated. Second, the spectral phase function applied by the SLM has been optimized by adding linear terms (a constant phase ϕ and a frequence-independent group delay $\dot{\phi}(\omega_0)$) to reduce the phase-modulation load pixel

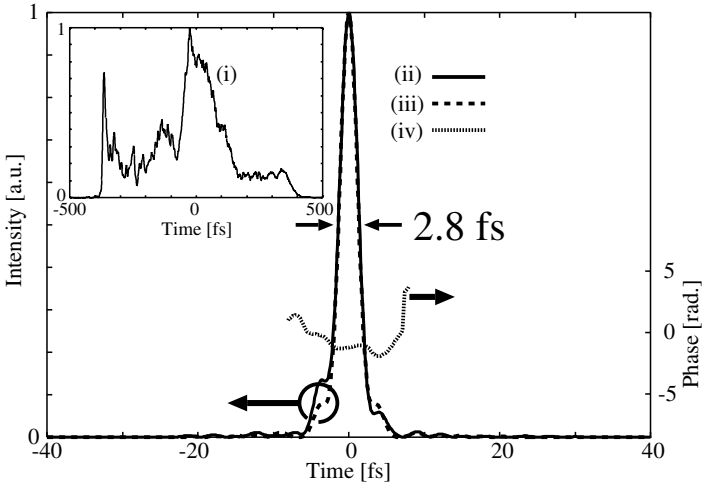

Fig. 5.36. Reconstructed pulse intensity profiles and phase. Temporal intensity profiles (**i**) before and (**ii**) after 2nd feedback (2.83 fs). (**iii**) Fourier transform-limited pulse intensity profile (2.75 fs). (**iv**) Temporal phase after 2nd feedback

of the SLM (such a modification does not influence the intensity time profile at all). As a result, the structured spectral-amplitude modulation that sometimes occurs due to the 0-2π applied-phase jump in the shortest-wavelength region (see Sects. 3.2 and 3.3), which disturbs the ability to get the robust SPIDER signal in its wavelength region and hence makes it difficult to get the reliable spectral phase of pulses, has been avoided completely. Third, the exact alignment of the 4-f phase compensator has been done by a unique procedure. That is, the 2nd-order wave (of the original input-pulse 1st-order wave deflected by the input grating G1) deflected by the output grating G2 has interfered and overlapped angular-spatially with the 3rd-order wave (of the original 2nd-order wave deflected by G1) deflected by G2 at the spatially displaced position of the compensator output by moving slightly both the distances of G2 and G1. Consequently, both the positions of the input G1 and output G2 gratings have been adjusted to make the 4-f configuration precisely dispersion-free.

As shown in Fig. 5.35, the chirp of pulses has been almost completely compensated for with only a slight fluctuation of the spectral phase over the entire frequency range (Fig. 5.35(v)). The temporal intensity profile has been very close to that of its Fourier-transform-limited pulse (2.75 fs) (Fig. 5.36(iii)).

5.3 Characterization of Monocycle-Like Optical Pulses Based on Wigner Distribution Function

Standard Fourier analysis manifests only the information in the time and frequency domain. In good contrast to this, time-frequency distribution functions enable us to intuitively interpret the characteristics of the pulse since they can simultaneously describe the temporal and spectral behavior of optical pulses by showing time-resolved spectral structure or frequency-resolved temporal structure. The Wigner distribution function (WDF) [38] is one of these time-frequency distribution functions, and has a simple form. Thus, it has been applied for the analysis of ultrashort pulses [39,40]. Here, characterization of monocycle-like pulses with over-one-octave bandwidths is discussed on the basis of WDFs.

Time-Frequency Wigner Distribution Function for Electric Field

The real electric field $E(t)$ can be decomposed into its complex electric field $E^{(+)}(t)$ and $E^{(-)}(t)$ using the following relations:

$$\tilde{E}(\omega) = \int_{-\infty}^{\infty} \mathrm{d}t \ \mathrm{e}^{\mathrm{i}\omega t} E(t), \tag{5.9}$$

$$E^{(+)}(t) = \frac{1}{2\pi} \int_{0}^{\infty} \mathrm{d}\omega \ \mathrm{e}^{-\mathrm{i}\omega t} \tilde{E}(\omega), \tag{5.10}$$

$$E^{(-)}(t) = \frac{1}{2\pi} \int_{-\infty}^{0} \mathrm{d}\omega \ \mathrm{e}^{-\mathrm{i}\omega t} \tilde{E}(\omega), \tag{5.11}$$

$$E(t) = E^{(+)}(t) + E^{(-)}(t) = 2\mathrm{Re}[E^{(+)}(t)]. \tag{5.12}$$

Here, $E^{(+)}(t)$ and $E^{(-)}(t)$ are complex-conjugate with each other. This temporal representation is related to a frequency representation by a Fourier transform,

$$\tilde{E}^{(+)}(\omega) = \int_{-\infty}^{\infty} \mathrm{d}t \ \mathrm{e}^{\mathrm{i}\omega t} E^{(+)}(t), \tag{5.13}$$

and vice versa (Inverse Fourier transform),

$$E^{(+)}(t) = \frac{1}{2\pi} \int_{-\infty}^{\infty} \mathrm{d}\omega \mathrm{e}^{-\mathrm{i}\omega t} \tilde{E}^{(+)}(\omega). \tag{5.14}$$

The Wigner distribution function for the complex electric field $E^{(+)}(t)$ in the time domain is defined by

$$W(t,\omega) = \int_{-\infty}^{\infty} \mathrm{d}t' \ \mathrm{e}^{\mathrm{i}\omega t'} E^{(+)}(t + t'/2) E^{(+)*}(t - t'/2). \tag{5.15}$$

An equivalent definition is possible using the electric field $\tilde{E}^{(+)}(\omega)$ in the frequency domain, and is written by

$$W(t,\omega) = \frac{1}{2\pi} \int_{-\infty}^{\infty} \mathrm{d}\omega' \mathrm{e}^{-\mathrm{i}\omega' t} \tilde{E}^{(+)}(\omega + \omega'/2) \tilde{E}^{(+)*}(\omega - \omega'/2). \tag{5.16}$$

Equations (5.15) and (5.16) indicate that the Wigner distribution function is a two-dimensional distribution function in the time-frequency domain. Hence it takes into account both temporal and spectral properties of optical pulses.

Integrals of the Wigner distribution function over t and ω give intensity functions as follows:

$$\frac{1}{2\pi} \int_{-\infty}^{\infty} \mathrm{d}\omega W(t,\omega) = \left| E^{(+)}(t) \right|^2, \tag{5.17}$$

$$\int_{-\infty}^{\infty} \mathrm{d}t W(t,\omega) = \left| \tilde{E}^{(+)}(\omega) \right|^2, \tag{5.18}$$

$$\frac{1}{2\pi} \int_{-\infty}^{\infty} \mathrm{d}\omega \int_{-\infty}^{\infty} \mathrm{d}t W(t,\omega) = \mathcal{E}_{\mathrm{pulse}} / 2\epsilon_0 c, \tag{5.19}$$

where $\mathcal{E}_{\mathrm{pulse}}$ is the pulse energy and ϵ_0, c are permittivity and velocity of light in a vacuum, respectively. That is, the integrations with respect to ω, t, and both ω and t represent the temporal intensity profile, the spectral intensity, and the pulse energy (divided by $2\epsilon_0 c$), respectively.

For an electric field for an arbitrary pulse with the carrier frequency ω_0 of

$$E^{(+)}(t) = \left| E^{(+)}(t) \right| \exp\{-\mathrm{i}[\omega_0 t - \varphi(t)]\}, \tag{5.20}$$

in the time domain, which corresponds to

$$\tilde{E}^{(+)}(\omega) = \left| \tilde{E}^{(+)}(\omega) \right| \exp[\mathrm{i}\phi(\omega)] \tag{5.21}$$

in the frequency domain, the frequency averaged at time t is given by

$$\begin{aligned} \langle \omega \rangle_t &= \frac{1}{2\pi} \int_{-\infty}^{\infty} \mathrm{d}\omega \ \omega W(t,\omega) \Bigg/ \frac{1}{2\pi} \int_{-\infty}^{\infty} \mathrm{d}\omega W(t,\omega) \\ &= \omega_0 - \frac{\mathrm{d}}{\mathrm{d}t} \varphi(t) \\ &\equiv \omega(t), \end{aligned} \tag{5.22}$$

where $\omega(t)$ is the instantaneous frequency.

Similarly, the time averaged at frequency ω is given by

$$\langle t\rangle_\omega = \int_{-\infty}^{\infty} \mathrm{d}t\ tW(t,\omega) \Big/ \int_{-\infty}^{\infty} \mathrm{d}t\ W(t,\omega)$$
$$= \frac{\mathrm{d}}{\mathrm{d}\omega}\phi(\omega). \tag{5.23}$$

This is the frequency-dependent group delay (GD). Thus, Wigner representation directly expresses how the instantaneous frequency changes with the time evolution and how the group delay varies with the frequency.

Time-Frequency Analysis of Monocycle-Like Optical Pulses Using WDFs

We already demonstrated the generation of ultrabroadband optical pulses (300–1000 nm) utilizing induced-phase modulation (IPM) as well as self-phase modulation (SPM) in an argon-filled hollow fiber [41] (see Sect. 2.3), chirp compensation of ultrabroadband optical pulses by only a spatial light modulator (SLM) [1] (see Sect. 3.3) and 3.3 fs, 1.56 optical-cycle pulse generation with an over-one-octave bandwidth [7] (see Sect. 5.2). In the present section, we analyze temporal and spectral properties of monocycle-like optical pulses with over-one-octave bandwidth using WDFs, especially focusing attention on the deviations from their Fourier transform-limited (TL) pulses. All the monocycle-like pulses analyzed in this section were generated using the system described in detail in Sect. 5.2. That is, the adaptive compression system for 30-fs, 780-nm amplified pulses at a 1-kHz repetition rate consisted of an Ar-filled hollow fiber, a feedback spectral-phase compensator with an SLM and a spectral phase characterizer based on M-SPIDER [8].

We define the normalized Wigner distribution function by

$$W^{\mathrm{norm}}(t,\omega) = W(t,\omega) \Big/ \frac{1}{2\pi}\int_{-\infty}^{\infty}\mathrm{d}\omega\int_{-\infty}^{\infty}\mathrm{d}t\, W(t,\omega). \tag{5.24}$$

The integral with respect to t and ω satisfies

$$\frac{1}{2\pi}\int_{-\infty}^{\infty}\mathrm{d}\omega\int_{-\infty}^{\infty}\mathrm{d}t\, W^{\mathrm{norm}}(t,\omega) = 1. \tag{5.25}$$

Thus, $W^{\mathrm{norm}}(t,\omega)\mathrm{d}t\mathrm{d}\omega/2\pi$ represents 'the intensity probability' in the time-frequency domain $[t, t+\mathrm{d}t]\times[\omega,\omega+\mathrm{d}\omega]/2\pi$.

Figures 5.37–5.39 show typical results of phase compensation to obtain monocycle-like optical pulses with over-one-octave bandwidths. Here, for comparison, Wigner distribution functions $W^{\mathrm{norm}}(t,\omega)$ and $W_{\mathrm{TL}}^{\mathrm{norm}}(t,\omega)$ of a pulse and its corresponding TL pulse, respectively, are normalized by $\mathcal{E}_{\mathrm{pulse}}/2\epsilon_0 c$ as expressed by (5.24), where $\mathcal{E}_{\mathrm{pulse}}$ is their total pulse energy. Hence the difference $W_{\mathrm{diff}}^{\mathrm{norm}}(t,\omega)\equiv W^{\mathrm{norm}}(t,\omega) - W_{\mathrm{TL}}^{\mathrm{norm}}(t,\omega)$ denotes the

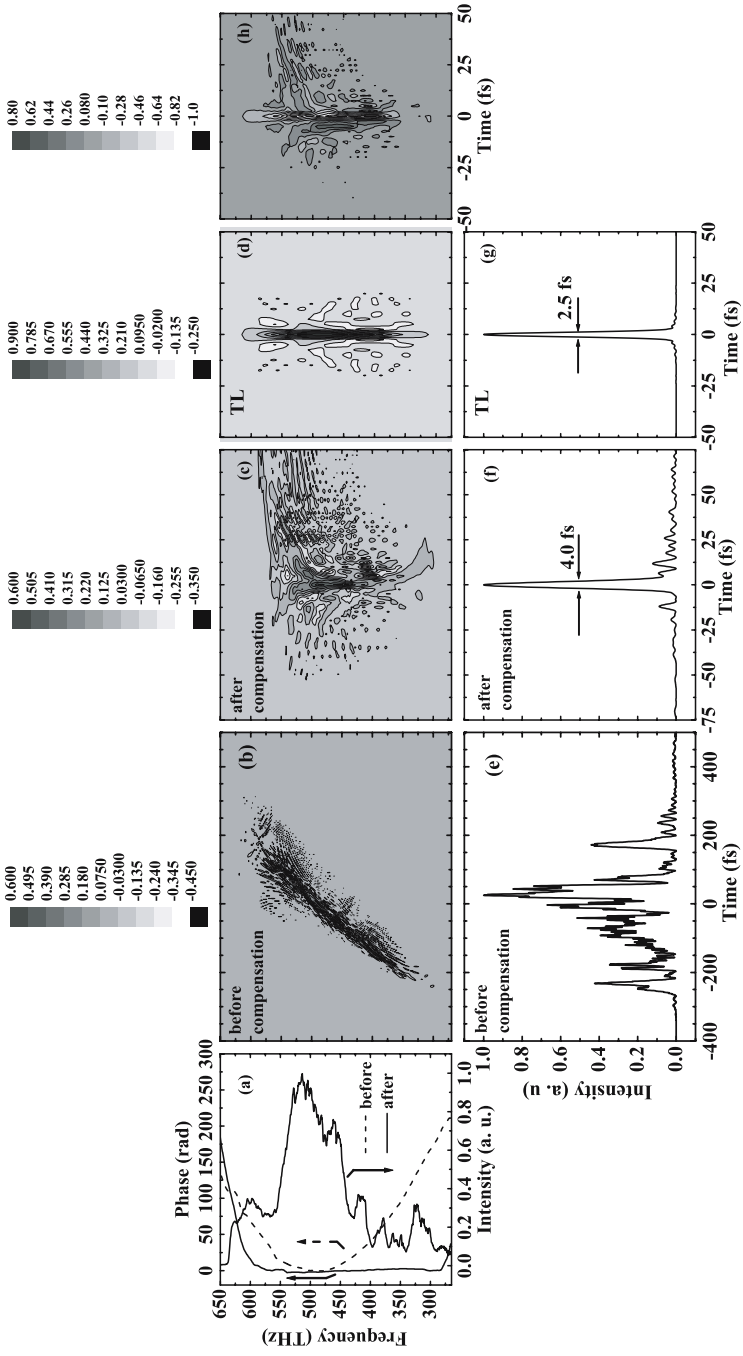
(a)
(b)
(c)
(d)
(e)
(f)
(g)
(h)
before
compensation
after
compensation
TL
Phase (rad)
Intensity (a. u.)
Frequency (THz)
Intensity (a. u)
Time (fs)
4.0 fs
2.5 fs
0.600
0.495
0.390
0.285
0.180
0.0750
-0.0300
-0.135
-0.240
-0.345
-0.450
0.600
0.505
0.410
0.315
0.220
0.125
0.0300
-0.0650
-0.160
-0.255
-0.350
0.900
0.785
0.670
0.555
0.440
0.325
0.210
0.0950
-0.0200
-0.135
-0.250
0.80
0.62
0.44
0.26
0.080
-0.10
-0.28
-0.46
-0.64
-0.82
-1.0

Fig. 5.37.

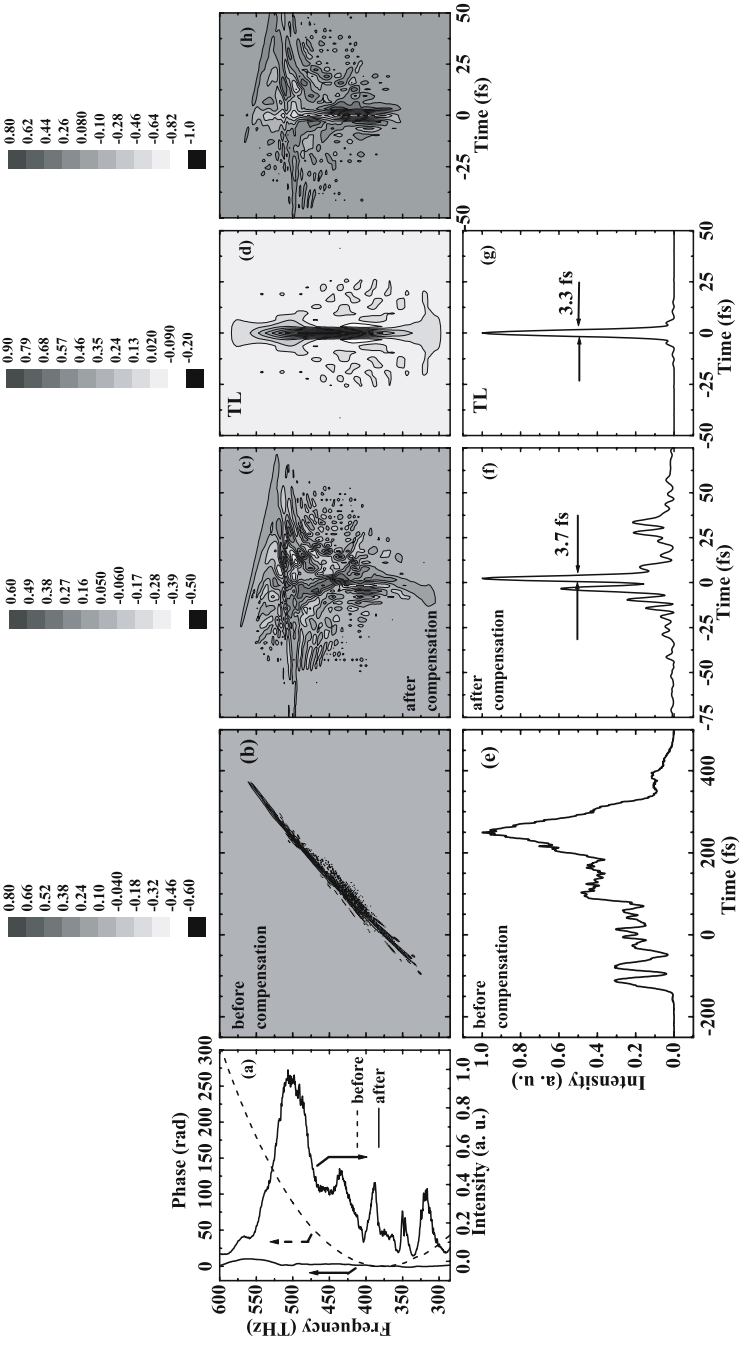
(a)
(b)
(c)
(d)
(e)
(f)
(g)
(h)
before
after
before compensation
after compensation
TL
3.7 fs
3.3 fs
Phase (rad)
Intensity (a. u.)
Frequency (THz)
Intensity (a. u.)
Time (fs)

Fig. 5.38.

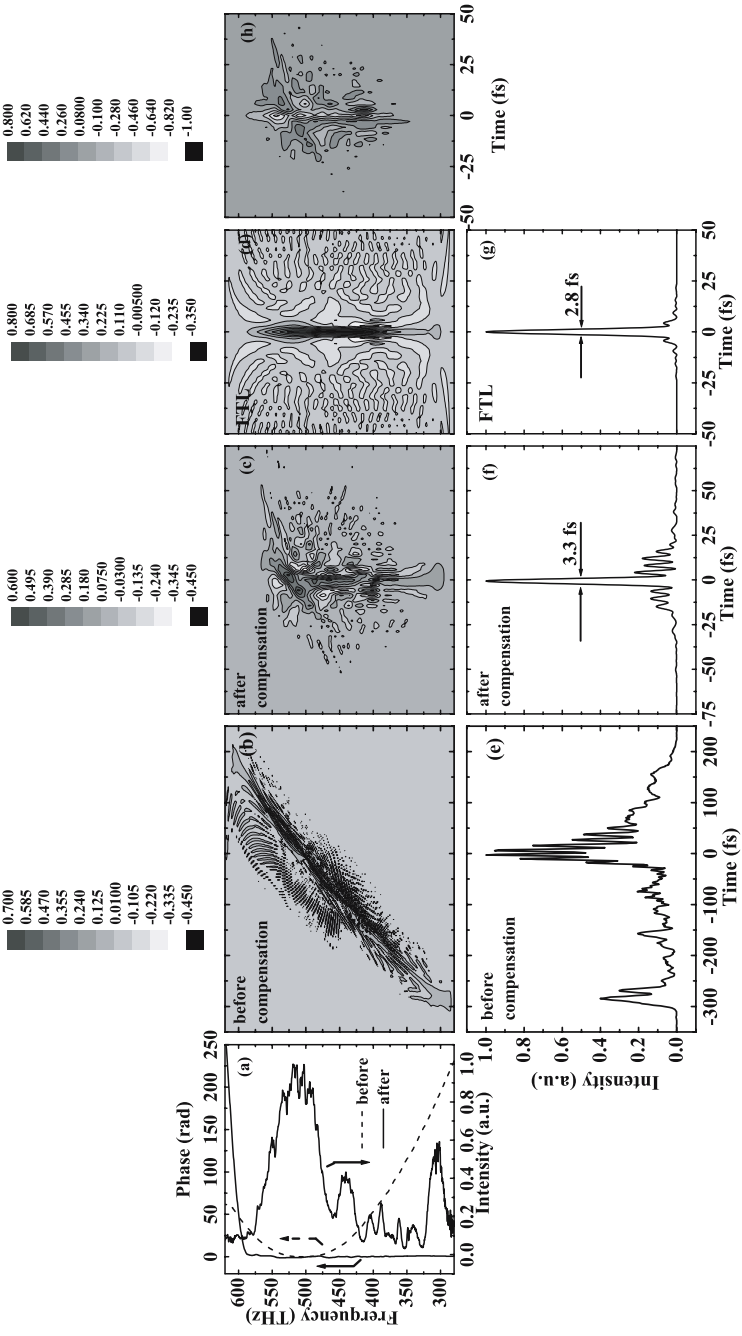
Phase (rad)
Intensity (a.u.)
Frequency (THz)
(a)
before
after
(b)
before
compensation
(c)
after
compensation
(d)
FTL
(e)
before
compensation
(f)
after
compensation
3.3 fs
(g)
FTL
2.8 fs
(h)
Time (fs)
Intensity (a.u.)

Fig. 5.39.

Fig. 5.37. (**a**) Spectral intensity (∼275 to ∼630 THz) and spectral phase of a 4.0 fs-compressed pulse, (**b**) corresponding normalized WDF before phase compensation, (**c**) corresponding normalized WDF $W^{\mathrm{norm}}(t,\omega)$ after phase compensation, (**d**) normalized WDF $W_{\mathrm{TL}}^{\mathrm{norm}}(t,\omega)$ for the corresponding TL pulse. Corresponding temporal profiles (**e**) before (∼–330 to ∼210 fs) and (**f**) after phase compensation, and (**g**) temporal profile for the corresponding TL pulse. (**h**) $W_{\mathrm{diff}}^{\mathrm{norm}}(t,\omega) \equiv W^{\mathrm{norm}}(t,\omega) - W_{\mathrm{TL}}^{\mathrm{norm}}(t,\omega)$

Fig. 5.38. (**a**) Spectral intensity (∼285 to ∼600 THz) of a 3.7 fs-compressed pulse, (**b**) corresponding normalized WDF before phase compensation, (**c**) corresponding normalized WDF $W^{\mathrm{norm}}(t,\omega)$ after phase compensation, (**d**) normalized WDF $W_{\mathrm{TL}}^{\mathrm{norm}}(t,\omega)$ for the corresponding TL pulse. Corresponding temporal profiles (**e**) before (∼–140 to ∼ 450 fs) and (**f**) after phase compensation, and (**g**) temporal profile for the corresponding TL pulse. (**h**) $W_{\mathrm{diff}}^{\mathrm{norm}}(t,\omega) \equiv W^{\mathrm{norm}}(t,\omega) - W_{\mathrm{TL}}^{\mathrm{norm}}(t,\omega)$

Fig. 5.39. (**a**) Spectral intensity (∼280 to ∼620 THz) and spectral phase of a 3.3 fs-compressed pulse, (**b**) corresponding normalized WDF before phase compensation, (**c**) corresponding normalized WDF $W^{\mathrm{norm}}(t,\omega)$ after phase compensation, (**d**) normalized WDF $W_{\mathrm{TL}}^{\mathrm{norm}}(t,\omega)$ for the corresponding TL pulse. Corresponding temporal profiles (**e**) before (∼–300 to ∼220 fs) and (**f**) after phase compensation, and (**g**) temporal profile for the corresponding TL pulse. (**h**) $W_{\mathrm{diff}}^{\mathrm{norm}}(t,\omega) \equiv W^{\mathrm{norm}}(t,\omega) - W_{\mathrm{TL}}^{\mathrm{norm}}(t,\omega)$

WDF deviation after phase compensation from the TL pulse and can be compared with those of other pulses. Figure 5.37 shows a result of phase compensation for a 4.0 fs-compressed pulse with an over-one-octave bandwidth (from ∼275 to ∼630 THz). Figure 5.37(a) shows the spectral intensity of the pulses with spectral phases before and after phase compensation. The normalized Wigner distribution functions are depicted in Fig. 5.37(b), (c) and (d) for the pulse before phase compensation, the pulse after phase compensation and the TL pulse, respectively. The corresponding temporal profile are shown in Fig. 5.37(e), (f) and (g), respectively. The $W_{\mathrm{diff}}^{\mathrm{norm}}(t,\omega)$ is shown in Fig. 5.37(h). For the case before compensation, it is found from the nearly linearly inclined WDF ranging from ∼275 to ∼630 THz and ∼–330 to ∼210 fs, or the almost quadratic spectral phase that the pulse has group-delay dispersion with a significantly large linear-chirp coefficient of ∼0.68 THz/fs. Corresponding to the complicated structure of the temporal profile, the WDF also is very complicated. After phase compensation to make the spectral phase almost flat in the range of ∼300 to 540 THz, by the 4-f system with the SLM based on the modified SPIDER measurement, a 4.0 fs pulse was obtained. The normalized Wigner distribution function $W^{\mathrm{norm}}(t,\omega)$ or $W_{\mathrm{diff}}^{\mathrm{norm}}(t,\omega)$ is greatly asymmetric and indicates that slight third- or higher-order dispersion, which is seen from a trail of the local maxima (from ∼500 to ∼570 THz and ∼5 to ∼60 fs) in $W^{\mathrm{norm}}(t,\omega)$ or $W_{\mathrm{diff}}^{\mathrm{norm}}(t,\omega)$, remains. This gives a long tail in the temporal pulse profile, particularly in the positive temporal region (∼5 to ∼60 fs). Moreover, the large value in $|W_{\mathrm{diff}}^{\mathrm{norm}}(t,\omega)|$ around t =0 corre-

sponds to the deviation of the pulse duration from that of the TL pulse with a duration of 2.5 fs.

Figure 5.38 indicates a different result of phase compensation for a 3.7 fs-compressed pulse with an over-one-octave bandwidth (from ∼285 to ∼600 THz). Figure 5.38(a) shows the spectral intensity of the pulses with spectral phases before and after phase compensation. The normalized Wigner distribution functions are depicted in Fig. 5.38(b), (c) and (d) for the pulse before phase compensation, the pulse after phase compensation and the TL pulse, respectively. The corresponding temporal profiles are shown in Fig. 5.38(e), (f) and (g), respectively. The $W_{\mathrm{diff}}^{\mathrm{norm}}(t,\omega)$ is shown in Fig. 5.38(h). For the case before compensation, it is found from the nearly linearly inclined WDF ranging from ∼285 to ∼600 THz and ∼–140 to ∼ 450 fs or the almost quadratic spectral phase that the pulse has group-delay dispersion with a significantly large linear-chirp coefficient of ∼0.47 THz/fs. After phase compensation to make the spectral phase comparatively flat in the range of ∼300 to 520 THz, by the 4-f system with the SLM based on the modified SPIDER measurement, a 3.7 fs pulse was obtained. The normalized WDF $W^{\mathrm{norm}}(t,\omega)$ or $W_{\mathrm{diff}}^{\mathrm{norm}}(t,\omega)$ is greatly asymmetric and quite complicated. It also indicates that partial second-, third- and higher-order dispersions, which are found from a trail of the local maxima (from ∼510 to ∼520 THz and ∼5 to ∼35 fs, ∼470 to ∼510 THz and ∼5 to ∼35 fs, and ∼460 to ∼510 THz and ∼–20 to ∼–5 fs) in $W^{\mathrm{norm}}(t,\omega)$ or $W_{\mathrm{diff}}^{\mathrm{norm}}(t,\omega)$, are left in the whole temporal range. This results in subpulses in ∼–20 to ∼30 fs range.

Figure 5.39 shows another different result of phase compensation for a 3.3 fs-compressed pulse with an over-one-octave bandwidth (from ∼280 to ∼620 THz). Figure 5.39(a) shows the spectral intensity of the pulses with spectral phases before and after phase compensation. The normalized WDFs are depicted in Fig. 5.39(b), (c) and (d) for the pulse before phase compensation, the pulse after phase compensation and the TL pulse, respectively. The corresponding temporal profiles are shown in Fig. 5.39(e), (f) and (g), respectively. The $W_{\mathrm{diff}}^{\mathrm{norm}}(t,\omega)$ is shown in Fig. 5.39(h). For the case before compensation, it is found from the nearly linearly inclined WDF ranging from ∼280 to ∼620 THz and ∼–300 to ∼220 fs or the almost quadratic spectral phase that the pulse has group-delay dispersion with a significantly large linear-chirp coefficient of ∼0.65 THz/fs. In good contrast to results for 4.0 fs- and 3.7 fs-compressed pulses, for a 3.3 fs-compressed pulse, $W^{\mathrm{norm}}(t,\omega)$ or $W_{\mathrm{diff}}^{\mathrm{norm}}(t,\omega)$ is comparatively symmetric and $|W_{\mathrm{diff}}^{\mathrm{norm}}(t,\omega)|$ has the small value in the whole temporal and frequency range. Whereas the values of $W_{\mathrm{diff}}^{\mathrm{norm}}(t,\omega)$ for the 4.0 and 3.7 fs-compressed pulses range from –1 to 0.8, the 3.3 fs-compressed pulse, in good contrast, ranges only from –0.7 to 0.6. This means the phase compensation for the 3.3 fs-compressed pulse was much better performed. It is found that the second-order dispersion around ∼480 to ∼550 THz and ∼–20 to ∼20 fs region is slightly left. This gives the small pedestal in the ∼–20 to ∼20 fs region of the temporal profile.

Conclusively, the normalized difference $W_{\mathrm{diff}}^{\mathrm{norm}}(t,\omega)$ sensitively, intuitively and usefully gives more detailed time-frequency information than other representations, especially for monocycle-like pulses which are almost ultimately close to the corresponding TL pulses. Even for pulses which are ultimately close to the TL pulse and have very small temporal pedestals, from WDFs we can see the fine time-frequency structures that are attributed to the temporal pedestals. On the basis of the fine time-frequency structures in WDFs, we can perform phase compensation using the SLM by concentrating on only the corresponding frequency regions to remove the pedestals and compress the pulses more. With the incorporation of this WDF analysis into the feedback phase compensation process, this technique is useful in the stage where the temporal pulse profiles, after several steps of feedback phase compensation over the whole frequency range, hardly change.

5.4 Conclusion

An advanced photonic system was created by combining a programmable SLM technique for spectral phase control (Chap. 3) and highly sensitive M-SPIDER for spectral phase characterization (Chap. 4), both of which have capabilities of quasi-real-time operation and a one-octave exceeding bandwidth in the near infrared to visible, near-ultraviolet region. The sophisticated system enables us to adaptively compensate for various kinds of complicated spectral phases $\phi(\omega)$ over the frequency range of the more-than three-hundred THz bandwidth. That is, this direct feedback technique without using the conventional Taylor expansion method for the spectral phase $\phi(\omega)$ was successfully applied for different chirped pulses from the glass fiber SPM output, the glass fiber IPM output, the photonic crystal fiber SPM output, the tapered fiber SPM output and the hollow fiber SPM output, whose spectral phases were unknown. Consequently, all the compensated pulses indicated the nearly transform-limited ones within the pulse durations from 2.8 to 20 fs (corresponding to 460–1060 nm to 740–860 nm spectral broadening) at the few feedback operations. It should be noted that the 2.8-fs, 1.5-cycle pulses generated by compensation for the hollow fiber output are the shortest optical pulses with a single clean profile in the near-infrared to the visible wavelength region to the best of our knowledge

For such extremely short and broadband pulses in the mono-cycle region, the Wigner function analysis quantitatively provided the detailed information on the time-frequency dynamic behavior.

This computer-controlled ultrabroadband phase compensator, which is an adaptive apparatus of the next generation, has significant potential for wide availability, automatic adjustability, high accuracy and robust operation. That is, the spectral phase feedback controller will become a greatly convenient tool even for those who are unfamiliar with the optics field. Moreover, the present technique can be extended to an automatic generator of

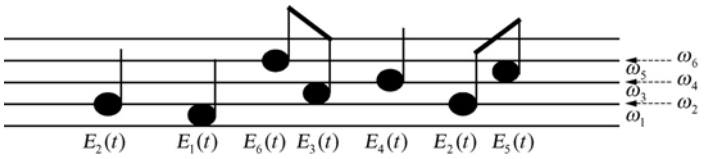

$$E(t) = \left|E(t)\right| \exp\left[-\mathrm{i}\left(\omega_0 t - \varphi(t)\right)\right]$$
$$\Updownarrow$$
$$\tilde{E}_F(\omega) = \left|\tilde{E}_F(\omega - \omega_0)\right| \exp\left[\mathrm{i}\phi(\omega)\right]$$

Fig. 5.40. Intuitive concept of optical-wave musical instrument and/or optical function generator. That is arbitrary time-sequential, automatic manipulator of optical electric-field wavepackets

high-power monocycle pulses by use of IPM output from a hollow fiber [41], and an arbitrary time-sequential, automatic manipulator of optical electric-field wavepackets such as an optical function generator. Thus, an optical-wave musical instrument (Fig. 5.40) similar to an ordinary acoustic-wave musical instrument will open new fields in quantum state control technology, information technology, ultrafast coherent engineering technology for biomolecular dynamics as well as nanometer phenomena and so on.

One of the authors (M. Yamashita) thanks M. Hirasawa for his experimental works concerning conventional glass fibers.

References

1. N. Karasawa, L. Li, A. Suguro, H. Shigekawa, R. Morita, M. Yamashita: J. Opt. Soc. Am. B **18**, 1742 (2001)
2. J. Herrmann, U. Griebner, N. Zhavoronkov, A. Husakou, D. Nickel, J.C. Knight, W.J. Wadsworth, P.S.J. Russell, G. Korn: Phys. Rev. Lett. **61**, 33 (2001)
3. X. Fang, N. Karasawa, R. Morita, R.S. Windeler, M. Yamashita: IEEE Photonics. Technol. Lett. **15**, 233 (2003)
4. N. Karasawa, S. Nakamura, N. Nakagawa, M. Shibata, R. Morita, H. Shigekawa, M. Yamashita: IEEE J. Quantum Electron. **37**, 398 (2001)
5. D. Yelin, D. Meshulach, Y. Silberberg: Opt. Lett. **22**, 1793 (1997)
6. M. Hirasawa, N. Nakagawa, K. Yamamoto, A. Hashimoto, R. Morita, A. Suguro, H. Shigekawa, M. Yamashita: *Tech. Digest of Conference on Lasers and Electro-Optics 2002 (CLEO 2002)*, (Opt. Soc. Ame., Washington DC, 2002) p. 356
7. K. Yamane, Z. Zhang, K. Oka, R. Morita, M. Yamashita, A. Suguro: Opt. Lett. **28**, 2258 (2003)

8. M. Hirasawa, N. Nakagawa, K. Yamamoto, R. Morita, H. Shigekawa, M. Yamashita: Appl. Phys. B **74**, S225 (2002)
9. D. Schenkel, J. Biegert, U. Keller, C. Vozzi, N. Nisoli, G. Sansone, S. Stagira, S.De Silvestri, O. Svelto: Opt. Lett. **28**, 1987 (2003)
10. C. Iaconis, I.A. Walmsley: IEEE J. Quantum Electron. **35**, 501 (1999)
11. M. Yamashita, M. Hirasawa, N. Nakagawa, K. Yamamoto, K. Oka, R. Morita, A. Suguro: J. Opt. Soc. Am. B **21**, 458 (2004)
12. M. Shibata, M. Hirasawa, N. Nakagawa, R. Morita, A. Suguro, H. Shigekawa, M. Yamashita: Appl. Phys. B. **74**, S291 (2002)
13. M. Yamashita, H. Sone, R. Morita: Jpn. J. Appl. Phys. **35**, L1194 (1996)
14. M. Yamashita, H. Sone, R. Morita, H. Shigekawa: IEEE J. Quantum Electron. **34**, 2145 (1998)
15. M. Adachi, K. Yamane, R. Morita, M. Yamashita: IEEE Photonic. Tech. Lett. **16**, 1951 (2004)
16. J.K. Ranka, R.S. Windeler, A.J. Stentz: Opt. Lett. **25**, 25 (2000)
17. A. Bjarklev, J. Broeng, A.S. Bjarklev: *Photonic Crystal Fibers* (Kluwer Academic Publishers, Dordrecht, 2003)
18. S. Lakó, J. Seres, P. Apai, J. Balázs, R.S. Windeler, R. Szipőcs: Appl. Phys. B **76**, 267 (2003)
19. T.A. Birks, W.J. Wadsworth, P.S.J. Russell: Opt. Lett. **25**, 1415 (2000)
20. M. Adachi, M. Hirasawa, A. Suguro, N. Karasawa, S. Kobayashi, R. Morita, M. Yamashita: Jpn. J. Appl. Phys. **42**, L24 (2003)
21. M. Zavelani-Rossi, G. Cerullo, S. Silvestri, L. Gallmann, N. Matuschek, G. Steinmeyer, U. Keller, G. Angelow, V. Scheuer, T. Tschudi: Opt. Lett. **26**, 1155 (2001)
22. A.M. Weiner, D.E. Leaird, J.S. Patel, J.R. Wullert: Opt. Lett. **15**, 326 (1990)
23. S. Coen, A.H.L. Chau, R. Leonhardt, J.D. Harvey, J.C. Knight, W.J. Wadsworth, P.S.J. Russell: Opt. Lett. **26**, 1356 (2001)
24. C. Dorrer, P. Londero, I.A. Walmsley: Opt. Lett. **26**, 1510 (2001)
25. A. Baltuška, T. Fuji, T. Kobayashi: Appl. Phys. B **75**, 427 (2002)
26. A. Baltuška, T. Fuji, T. Kobayashi: Opt. Lett. **27**, 306 (2002)
27. M. Nisoli, S. De Silvestri, O. Svelto: Appl. Phys. Lett. **68**, 2793 (1996)
28. G.P. Agrawal: *Nonlinear Fiber Optics*, 2nd edn (Academic Press, San Diego, 1995) pp. 91–93
29. E.A.J. Marcatili, R.A. Schmeltzer: Bell Syst. Tech. J. **43**, 1783 (1964)
30. R. Morita, M. Hirasawa, N. Karasawa, S. Kusaka, N. Nakagawa, K. Yamane, L. Li, A. Suguro, M. Yamashita: Meas. Sci. Technol. **13**, 1710 (2002)
31. L. Xu, N. Nakagawa, R. Morita, H. Shigekawa, M. Yamashita: IEEE J. Quantum Electron. **36**, 893 (2000)
32. L. Xu, L. Li, N. Nakagawa, R. Morita, H. Shigekawa, M. Yamashita: IEEE Photonics Tech. Lett. **12**, 1540 (2000)
33. M.A. Dugan, J.X. Tull, W.W. Warren: J. Opt. Soc. Am. B **14**, 2348 (1997)
34. G. Vdovin, S. Middelhoek, P.M. Sarro: Opt. Eng. **36**, 1382 (1997)
35. P. Baum, S. Lochbrunner, L. Gallmann, G. Steinmeyer, U. Keller, E. Riedle: Appl. Phys. B **74**, S219 (2002)
36. E. Zeek, K. Maginnis, S. Backus, U. Russek, M. Murnane, G. Mourou, H. Kapteyn, G. Vdovin: Opt. Lett. **24**, 493 (1999)
37. K. Yamane, Z. Zhang, A. Suguro, R. Morita, M. Yamashita: *Tech. Digest of Conference on Lasers and Electro-Optics 2003 (CLEO 2003)* (Opt. Soc. Ame., Washington DC, 2003)

38. E. Wigner: Phys. Rev. **40**, 749 (1932)
39. S. Yeremenko, A. Baltuška, M.S. Pshenichnikov, D.A. Wiersma: Appl. Phys. B **70**, S109 (2000)
40. K.-H. Hong, J.-H. Kim, Y.H. Kang, C.H. Nam: Appl. Phys. B **74**, S231 (2002)
41. N. Karasawa, R. Morita, H. Shigekawa, M. Yamashita: Opt. Lett. **25**, 183 (2000)
42. K. Yamane, T. Kito, R. Morita, M. Yamashita: Tech. Digest of Conference on Lasers and Electro-Optics 2004 (CLEO 2004). Postdeadline Paper Book CPDC2 (Opt. Soc. Ame., Washinghton DC. 2004)
43. M. Adachi, K. Yamane, R. Morita, M. Yamashita: *Ultrafast Phenomena XIV* (Springer-Verlag, Berlin, 2004) in press

6 Field Manipulation of Ultrabroadband Optical Pulses

R. Morita and Y. Toda

6.1 Principle and Theory

To obtain a terahertz-rate pulse train using a pulse shaping technique, periodic spectral phase modulation is used [1–3]. Here, the typical periodic spectral phase modulation of the binary code periodic phase modulation and trigonometric-function phase modulation are described.

The real electric field $E(t)$ can be decomposed into its complex electric field $E^{(+)}(t)$ and $E^{(-)}(t)$ using the following relations:

$$\tilde{E}(\omega) = \int_{-\infty}^{\infty} \mathrm{d}t \ \mathrm{e}^{\mathrm{i}\omega t} E(t), \tag{6.1}$$

$$E^{(+)}(t) = \frac{1}{2\pi} \int_{0}^{\infty} \mathrm{d}\omega \ \mathrm{e}^{-\mathrm{i}\omega t} \tilde{E}(\omega), \tag{6.2}$$

$$E^{(-)}(t) = \frac{1}{2\pi} \int_{-\infty}^{0} \mathrm{d}\omega \ \mathrm{e}^{-\mathrm{i}\omega t} \tilde{E}(\omega), \tag{6.3}$$

$$E(t) = E^{(+)}(t) + E^{(-)}(t) = 2\mathrm{Re}[E^{(+)}(t)]. \tag{6.4}$$

Here, $E^{(+)}(t)$ and $E^{(-)}(t)$ are complex-conjugate with each other. This temporal representation is related to a frequency representation by a Fourier transform,

$$\tilde{E}^{(+)}(\omega) = \int_{-\infty}^{\infty} \mathrm{d}t \ \mathrm{e}^{\mathrm{i}\omega t} E^{(+)}(t), \tag{6.5}$$

and vice versa (Inverse Fourier transform),

$$E^{(+)}(t) = \frac{1}{2\pi} \int_{-\infty}^{\infty} \mathrm{d}\omega \mathrm{e}^{-\mathrm{i}\omega t} \tilde{E}^{(+)}(\omega). \tag{6.6}$$

For the spectral phase modulation function $\tilde{m}(\omega)$, the spectral amplitude of the complex electric field $\tilde{E}_{\mathrm{m}}^{(+)}(\omega)$ after spectral phase modulation is expressed as

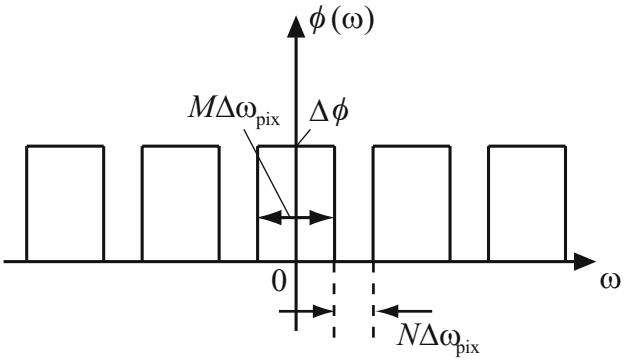

Fig. 6.1. Phase for modulation of binary-code periodic modulation. A frequency period of the modulation is composed of M pixels for modulation and N pixels for non-modulation

$$\tilde{E}_{\mathrm{m}}^{(+)}(\omega) = \tilde{m}(\omega)\tilde{E}^{(+)}(\omega). \tag{6.7}$$

Hence, the complex electric field $E_{\mathrm{m}}^{(+)}(t)$ in the time domain corresponding to $\tilde{E}^{(+)}(\omega)$ is given by

$$E_{\mathrm{m}}^{(+)}(t) = m(t) * E^{(+)}(t) \equiv \int_{-\infty}^{\infty} \mathrm{d}t' m(t-t') E_{\mathrm{m}}^{(+)}(t'), \tag{6.8}$$

where $m(t)$ is the inverse Fourier transform of $\tilde{m}(\omega)$ and the symbol $*$ denotes the convolution integral. Therefore, the real electric field $E_{\mathrm{m}}(t)$ after spectral phase modulation is yielded by

$$E_{\mathrm{m}}(t) = 2\mathrm{Re}[E_{\mathrm{m}}^{(+)}(t)] = 2\mathrm{Re}[m(t) * E^{(+)}(t)]. \tag{6.9}$$

Binary-Code Periodic Phase Modulation

Let us now consider the spectral phase modulation by periodic binary codes as follows:

$$\tilde{m}(\omega) = \exp[\mathrm{i}\phi(\omega)], \tag{6.10}$$

$$R(\omega) = \begin{cases} 1, & (|\omega| \le M\Delta\omega_{\mathrm{pix}}/2), \\ 0, & (|\omega| > M\Delta\omega_{\mathrm{pix}}/2), \end{cases} \tag{6.11}$$

$$\phi(\omega) = \Delta\phi \sum_{n=-\infty}^{\infty} R(\omega - n(M+N)\Delta\omega_{\mathrm{pix}}), \tag{6.12}$$

where the non-negative integers M and N represent the number of modulated and unmodulated pixels of the SLM, and $\Delta\phi$ is the magnitude of the binary modulation, as described in Fig. 6.1. The parameter $\Delta\omega_{\mathrm{pix}}$ is the loaded bandwidth for each pixel of the SLM. In a strict sense, $\Delta\omega_{\mathrm{pix}}$ is not

constant, but $\Delta\omega_{\rm pix}$ is assumed to be constant here for simplicity. Thus $\tilde{m}(\omega)$ can be written by

$$\tilde{m}(\omega) = 1 + [\exp(\mathrm{i}\Delta\phi) - 1] \sum_{n=-\infty}^{\infty} R(\omega - n(M+N)\Delta\omega_{\rm pix}). \tag{6.13}$$

Using the period of the spectral phase modulation defined by

$$\Omega = (M+N)\Delta\omega_{\rm pix}, \tag{6.14}$$

the inverse Fourier transform of $R(\omega - n(M+N)\Delta\omega_{\rm pix}) = R(\omega - n\Omega)$ is

$$\begin{aligned} &\mathsf{F}^{-1}[R(\omega - n(M+N)\Delta\omega_{\rm pix})] = \mathsf{F}^{-1}[R(\omega - n\Omega)] \\ &= \frac{1}{2\pi}\int_{-\infty}^{\infty} \mathrm{d}\omega R(\omega - n\Omega) = \frac{1}{2\pi}\exp(-\mathrm{i}n\Omega)\int_{-\infty}^{\infty}\mathrm{d}\omega R(\omega) \\ &= \frac{M\Delta\omega_{\rm pix}}{2\pi}\exp(-\mathrm{i}n\Omega)\mathrm{sinc}\left(\frac{M\Delta\omega_{\rm pix}}{2}t\right), \end{aligned} \tag{6.15}$$

where the sinc-function is defined by

$$\mathrm{sinc}x = \frac{\sin x}{x}. \tag{6.16}$$

By using the Fourier series of the Dirac delta-function $\delta(x)$ for the region of $x \in [-\pi, \pi]$, the formula

$$\sum_{n=1}^{\infty}\cos nx = \pi\delta(x) - \frac{1}{2} \tag{6.17}$$

is derived and it can be expanded to the region of $x \in (-\infty, \infty)$, owing to its periodicity of 2π, as

$$\sum_{n=1}^{\infty}\cos nx = \pi\sum_{n=-\infty}^{\infty}\delta(x - 2n\pi) - \frac{1}{2}. \tag{6.18}$$

Thus, the summation $\sum_{n=-\infty}^{\infty}\exp(-\mathrm{i}n\Omega t)$ for the region $t \in (-\infty, \infty)$ can be written in the form of the Dirac delta-function as

$$\sum_{n=-\infty}^{\infty}\exp(-\mathrm{i}n\Omega t) = 1 + 2\sum_{n=1}^{\infty}\cos(n\Omega t) = \frac{2\pi}{\Omega}\sum_{n=-\infty}^{\infty}\delta\left(t - \frac{2n\pi}{\Omega}\right). \tag{6.19}$$

Thus, from (6.13)–(6.15) and (6.19), the inverse Fourier transform of $\tilde{m}(\omega)$ is yielded by

$$
\begin{aligned}
&m(t) = \mathsf{F}^{-1}[\tilde{m}(\omega)] \\
&= \delta(t) + \frac{M}{M+N}\left[\exp(\mathrm{i}\Delta\phi) - 1\right] \mathrm{sinc}\left(\frac{M\Delta\omega_{\mathrm{pix}}}{2}t\right) \sum_{n=-\infty}^{\infty} \delta\left(t - \frac{2n\pi}{\Omega}\right).
\end{aligned}
\tag{6.20}
$$

Hence, from (6.8), the complex electric field $E_{\mathrm{m}}^{(+)}(t)$ after spectral phase modulation is given by

$$
\begin{aligned}
&E_{\mathrm{m}}^{(+)}(t) \\
&= E^{(+)}(t) + \frac{M}{M+N}\left[\exp(\mathrm{i}\Delta\phi) - 1\right] \sum_{n=-\infty}^{\infty} \mathrm{sinc}\left(\frac{n\pi M}{M+N}\right) E^{(+)}\left(t - \frac{2n\pi}{\Omega}\right).
\end{aligned}
\tag{6.21}
$$

Thus, it is seen that, when the pulse duration of the complex electric field t_{p} is much less than $T \equiv 2\pi/\Omega = 2\pi/(M+N)\Delta\omega_{\mathrm{pix}}$, a pulse train with the repetition rate of T is obtained. The highest repetition rate is limited to the total pixel number of SLM or the pulse duration of the shaped pulses. In contrast, the lowest repetition rate is determined by the time window of the 4-f pulse shaper system as described in Chap. 3. In addition, the intensity of the nth pulse at $t = nT$ is modulated by the factor of $\mathrm{sinc}^2(nM\Omega T/2(M+N))$. The durations of the constituent pulses are the same as that of the input pulse. Hence when a Fourier-transform-limited pulse is used as an input, the pulse train composed of the Fourier-transform-limited pulses is generated.

Here, it is assumed that the loaded bandwidth $\Delta\omega_{\mathrm{pix}}$ in frequency for each pixel of the SLM is constant. Strictly speaking, from the theory of pulse shaping for ultrabroadband pulses, whereas the loaded bandwidth $\Delta\lambda_{\mathrm{pix}}$ in wavelength for each pixel of the SLM is constant, the loaded bandwidth $\Delta\omega_{\mathrm{pix}}$ in frequency is a non-constant function of ω. This should be taken into account in the case of pulse shaping for ultrabroadband pulses.

Trigonometric-Function Phase Modulation

Here, we consider the trigonometric-function spectral phase modulation and define the spectral phase modulation function as

$$
\tilde{m}(\omega) \equiv \exp[\mathrm{i}\phi(\omega)] = \exp(\mathrm{i}A\cos\omega T), \tag{6.22}
$$

as shown in Fig. 6.2. Using the formula of the Bessel function $J_n(z)$

$$
\exp(\mathrm{i}z\sin\theta) = \sum_{n=-\infty}^{\infty} J_n(z)\exp(\mathrm{i}n\theta), \tag{6.23}
$$

$\tilde{m}(\omega)$ is written by

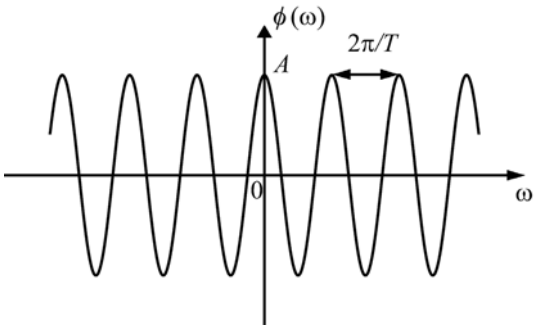

Fig. 6.2. Phase for modulation of trigonometric-function modulation of $\phi(\omega) = A\cos(\omega T)$

$$\tilde{m}(\omega) = \sum_{n=-\infty}^{\infty} J_n(A) \exp\left[\mathrm{i}n\left(\omega T + \frac{\pi}{2}\right)\right]. \tag{6.24}$$

Hence the inverse Fourier transform of $\tilde{m}(\omega)$ is

$$m(t) = \mathsf{F}^{-1}[\tilde{m}(\omega)] = \sum_{n=-\infty}^{\infty} J_n(A) \exp\left(\mathrm{i}\frac{n\pi}{2}\right) \delta(t - nT). \tag{6.25}$$

Therefore, from (6.8), the complex electric field $E_{\mathrm{m}}^{(+)}(r)$ in the time domain after the spectral phase modulation is given by

$$E_{\mathrm{m}}^{(+)}(t) = \sum_{n=-\infty}^{\infty} J_n(A) \exp\left(\mathrm{i}\frac{n\pi}{2}\right) E^{(+)}(t - nT). \tag{6.26}$$

When the pulse duration of the complex electric field t_{p} is much less than T, the pulse train with the repetition rate of T^{-1} is obtained and the intensity of the nth pulse at $t = nT$ is modulated by the factor of $[J_n(A)]^2$. The durations of the constituent pulses are the same as that of the input pulse. Hence when a Fourier-transform-limited pulse is used as an input, the pulse train composed of the Fourier-transform-limited pulses is generated. Of course, the spectral phase modulation by SLM is discretized because of its finite pixel size. However, the loaded bandwidth for each pixel is usually much less than the whole bandwidth of the pulse to be shaped. Thus, (6.26) well explains the experimental results using the SLM. By adjusting the parameter T, pulse trains with a desired repetition rate are obtained. In practice, the highest repetition rate of the shaped pulse train is limited to be in the order of a tenth of the bandwidth of the pulse to be shaped, and the lowest repetition rate is roughly determined by twice loaded bandwidth in frequency for each pixel of the SLM or the time window.

6.2 Two-Color Beam Generation with Tunable THz-Pulse Trains

In this section, simultaneous coherent multicolor pulse shaping using a two-dimensional spatial light amplitude- and phase-modulator is demonstrated. Our experimental setup for simultaneous coherent multicolor pulse shaping is shown in Fig. 6.3. The light source that we used was a multi-pass 1-kHz Ti:sapphire amplifier, which can produce pulses having a duration of 30 fs centered at 780 nm and energy up to 1 mJ. A pulse of energy of 160 μJ was focused by a 200-mm-focal spherical lens L into an argon-filled glass capillary fiber with an inner diameter of 140 μm and a length of 600 mm. The fiber was located in a high-pressure chamber with 1-mm-thick uncoated sapphire windows. In the same manner as our previous reports [12–14], owing to self-phase modulation at the gas pressure of 2.0 bar, an almost continuum pulse broadened from 600 to 850 nm was produced as shown in Fig. 6.4. After propagating in the fiber, the beam was collimated by a spherical mirror SM with a focal length of 200 mm. The output mode was circular (fundamental mode) and pulse energy is around 38 μJ corresponding to 13% coupling efficiency. This somewhat lower efficiency attributed to losses of non-AR-coated sapphire windows and bending and surface-roughness of the capillary fiber. The output pulse was measured to be longer than ∼ 200 fs full width at half-maximum (FWHM) with strong chirp (the prism compensator surrounded

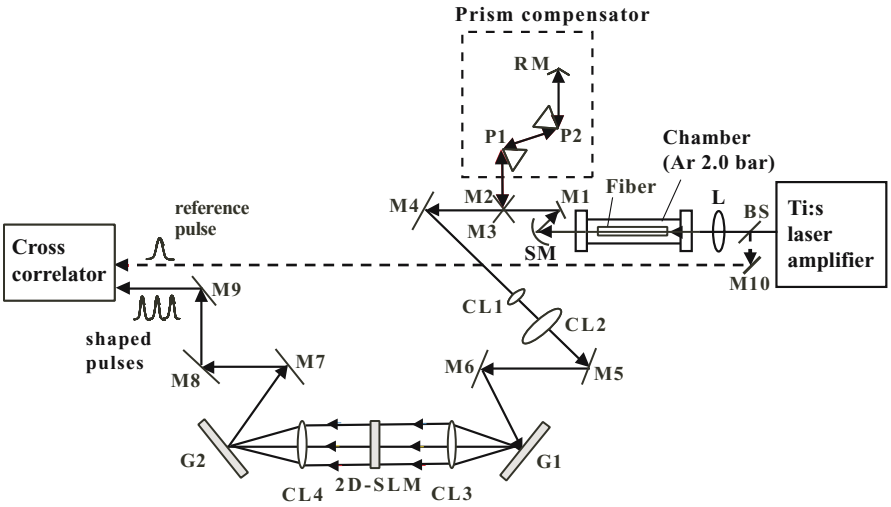

Fig. 6.3. Experimental setup for simultaneous coherent multicolor pulse shaping. L: spherical lens; SM: spherical mirror; M1-M10: plane mirrors; BS: beam splitter; G1, G2: gratings; CL1: concave cylindrical lens; CL2-4: convex cylindrical lenses; 2D-SLM: two-dimensional spatial light phase modulator with a spatial filter; P1, P2: prisms; RM: roof mirror

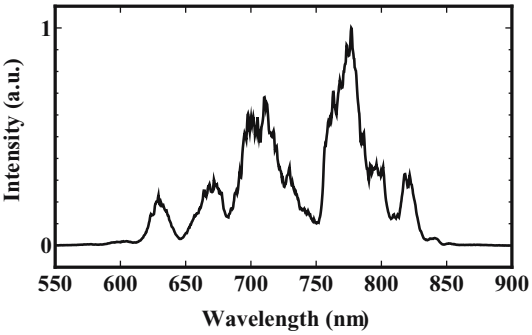

Fig. 6.4. Broadened spectrum by self-phase modulation in an Ar-gas filled fiber before amplitude and phase modulation for two-color beam generation with tunable THz-pulse trains

by the dashed line in Fig. 6.3, which was set later for three-color simultaneous pulse shaping, was not used for two-color simultaneous pulse shaping). This spectrally-broadened laser beam was spread in the vertical direction and collimated by a cylindrical lens pair CL1 and CL2 with the focal lengths of -20 and 70 mm. The vertically-spread beam was guided into the 4-f system consisting of two diffraction gratings G1 and G2 with a grating constant $d = 1/600$ mm, cylindrical lenses CL3 and CL4 with a focal length $f = 150$ mm and a two-dimensional (2D) spatial light phase modulator (SLM) with 648 $\times$ 4 pixels. The pixel size of the SLM was 2 mm $\times$ 97 μm and the inter-pixel gap is 5 μm. The 2D SLM was accompanied with a spatial filter in order to modulate amplitudes or select the spectral components, independently in the vertical direction. After the selection of spectral components, by making phase modulation using 2D SLM, pulses whose center wavelengths were different from one another in the vertical direction were shaped independently and simultaneously. After simultaneous multicolor pulse shaping, vertically-independent pulses were characterized by the intensity cross-correlator with a pre-shaped pulse directly split from the laser amplifier by a beam splitter BS (transmission 99: reflection 1), using a 100 μm-thick $\beta-$barium borate crystal.

A typical example of simultaneously shaped two-color pulse trains using 648 $\times$ 4 pixels of the SLM is shown in Fig. 6.5. Figure 6.5(a) and (c) indicate the intensity cross-correlation trace and the spectrum of a vertically-independent shaped pulse in the upper two horizontal lines of the SLM, respectively. Figure 6.5(b) and (d) indicates the intensity cross-correlation trace and the spectrum of a vertically-independent shaped pulse in the lower two horizontal lines of the SLM, respectively. The patterns of phase modulations, being typical periodic binary code patterns, were (111000) for the upper and (10) for the lower lines. Here, 0 and 1 represent to 0- and 1.1π-phase modulation for each frequency component, respectively. The pulse intervals of the

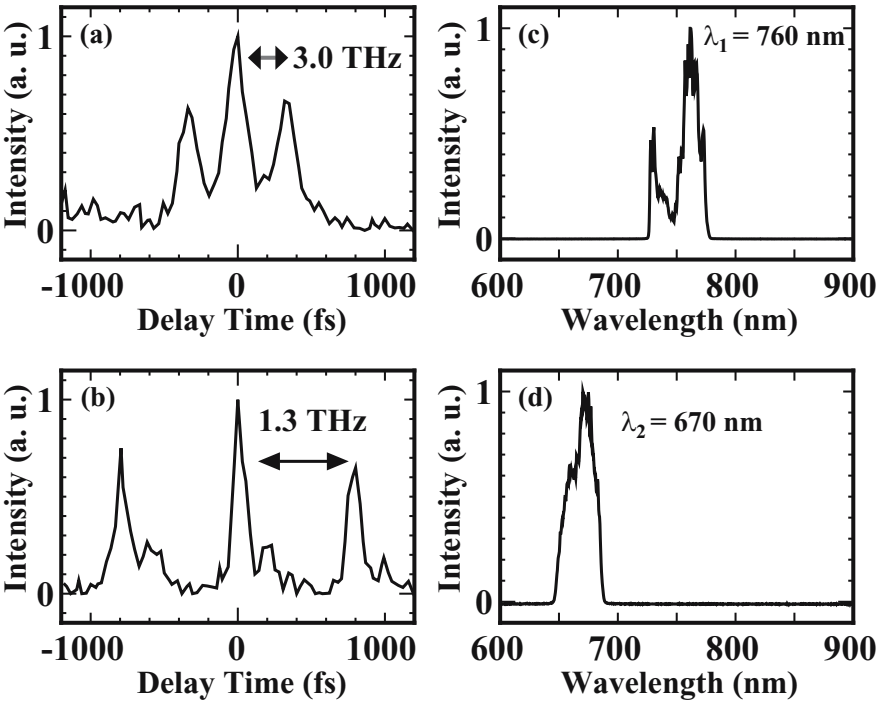

Fig. 6.5. (**a**) Intensity cross-correlation trace and (**c**) spectrum of a simultaneous coherent multicolor shaped pulse with a center wavelength $\lambda_1 = 760\,\mathrm{nm}$ in the upper side of the SLM. (**b**) Intensity cross-correlation trace and (**d**) spectrum of a simultaneous coherent multicolor shaped pulse with a center wavelength $\lambda_2 = 670$ nm in the lower side of the SLM

shaped pulse trains are 330 fs for the upper and 800 fs for the lower side. They correspond to repetition rates of 3.0 and 1.3 THz (100 and $42\,\mathrm{cm}^{-1}$), respectively. The center wavelengths after passing through the spatial filter were $\lambda_1 = 760\,\mathrm{nm}$ ($\omega_1/2\pi = 13160\,\mathrm{cm}^{-1}$) for the upper and $\lambda_2 = 670\,\mathrm{nm}$ ($\omega_2/2\pi = 14930\,\mathrm{cm}^{-1}$) for the lower side. This corresponds to a frequency difference of $|\omega_1 - \omega_2|/2\pi = 1770\,\mathrm{cm}^{-1}$. The loaded bandwidth $\Delta\lambda$ in wavelength for each pixel of the SLM was evaluated to be 1.0 nm. Thus theoretically expected repetition rates for shaped pulses are 3.0 and 1.3 THz, respectively, for the upper and lower sides. They well agree with those obtained experimentally.

The time window for the wavelength λ component of the normal incident beam to the grating for our 4-f system with an input beam diameter ω_0 of 10 mm was evaluated to be over 10 ps from (3.23). However, since the n-th shaped pulse intensity was modulated by a factor of $[\sin(1.1n\rho\pi)/(1.1n\rho\pi)]^2$ and became low at the large $|n|$, only the temporal range from ~ -1 to ~ 1 ps are shown in Fig. 6.5. Here, $\rho = M/(M+N)$ where M and N are numbers of modulated and nonmodulated pixels, respectively, in a periodical phase-

modulation pattern. The pulse at time $t = 0$ is labeled as $n = 0$, and the pulse for $t > 0$ and $t < 0$ are labeled as $n = 1, 2, 3 \ldots$ and $n = -1, -2, -3, \ldots$, respectively. The obtained repetition rates were limited by the duration of constituent pulses that equals to the duration of the pre-shaped pulses. The asymmetry of the shaped-constituent pulses was considered to be due to that of the pre-shaped pulses. The strong chirp of the pre-shaped pulse and the spectral slicing by the spatial filter resulted in the somewhat weak cross correlation signals.

Although the SLM was not used for chirp compensation here, we can additionally modulate the phase using the SLM for chirp compensation as well as for pulse shaping. Using our experimental setup with the $d = 1/600$ mm grating pair, the $f = 150$ mm lens pair and the 66 mm-wide SLM, we can perform a pulse shaping of up to 392 THz-bandwidth (455–1125 nm) coherent optical pulses which are generated through self- and induced-phase modulation. Our simultaneous coherent multicolor pulse shaping technique has an advantage that the repetition rate and the center frequency can be almost arbitrarily controlled. In addition, our technique has two remarkable features unlike a technique using a 1D SLM as follows; the simultaneously shaped multicolor beams are spatially separated and the frequency components of shaped pulses can be overlapped partially or perfectly. This technique becomes a powerful tool for a quantum interference experiment for example, where shaped optical pulses are needed to be partially-spectrally overlapped with each other having different instantaneous frequency evolutions and different propagation direction.

6.3 Three-Color Beam Generation with Tunable THz-Pulse Trains

To increase the power of the multicolor simultaneously-shaped pulses, the system was improved by adding the prism compensator (surrounded by dashed lines in Fig. 6.3). The pair of prisms used were made of quartz. The apex angle was 67°. The separation of the prisms was set to be 600 mm. Thus, through simultaneous three-color shaping, three-color generation with tunable THz-pulse train was demonstrated. The primary part of the experimental setup for the simultaneous three-color shaping is depicted in Fig. 6.6(a).

A pulse of the energy of 210 μJ was focused by a 200-mm-focal spherical lens into an argon-filled glass capillary fiber with an inner diameter of 140 μm and a length of 600 mm. The pressure of the argon gas was 2.0 bar. The pulse was spectrally broadened 500 to 900 nm thanks to the self-phase modulation effect, as shown in Fig. 6.7. The output pulse from the fiber was spread in the vertical direction and collimated by a cylindrical lens pair CL1 and CL2 with the focal lengths of −20 and 70 mm. The vertically-spread beam was guided into the 4-f system consisting of two diffraction gratings G1 and G2 with a grating constant $d = 1/600$ mm, cylindrical lenses CL3 and CL4 with a

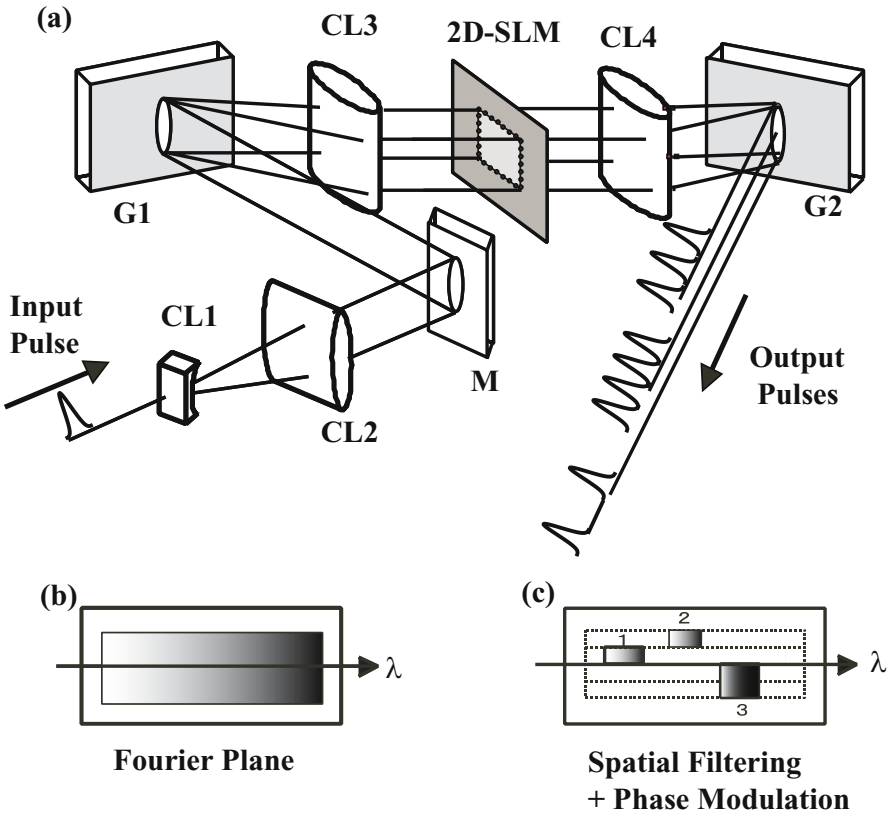

Fig. 6.6. (**a**) Primary part of the simultaneous three-color shaping setup. M: plane mirrors (corresponds to M5 and M6 in Fig. 6.3); G1, G2: gratings; CL1: concave cylindrical lens; CL2-4: convex cylindrical lenses; 2D-SLM: two-dimensional spatial light phase modulator with a spatial filter. (**b**) The Fourier plane projected on the SLM. (**c**) Individual and simultaneous spatial filtering and phase modulation on the SLM

focal length f =150 mm and a 2D SLM with 648 × 4 pixels. The pixel size of the SLM was 2 mm × 97 μm and the inter-pixel gap was 5 μm. The 2D SLM was accompanied with a spatial filter in order to modulate amplitudes or select the spectral components independently in the vertical direction. After the selection of spectral components, by making phase modulation using 2D SLM, pulses whose center wavelengths were different from one another in the vertical direction were shaped independently and simultaneously. In the case of the simultaneous three-color pulse shaping, on the Fourier plane projected on the SLM (Fig. 6.6(b)), the spectral slicing was done by the spatial filter as follows. The first and second horizontal lines were used for the middle and the shorter wavelength region, respectively. The third and fourth lines were

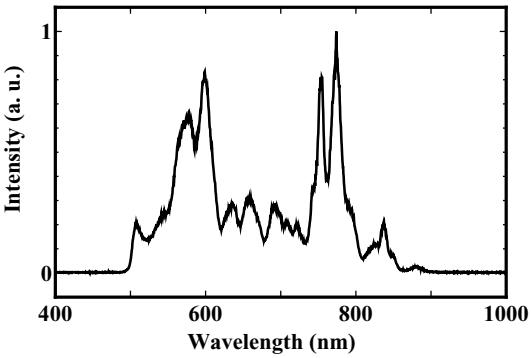

Fig. 6.7. Broadened spectrum by self-phase modulation in an Ar-gas filled fiber before amplitude and phase modulation for three-color beam generation with tunable THz-pulse trains

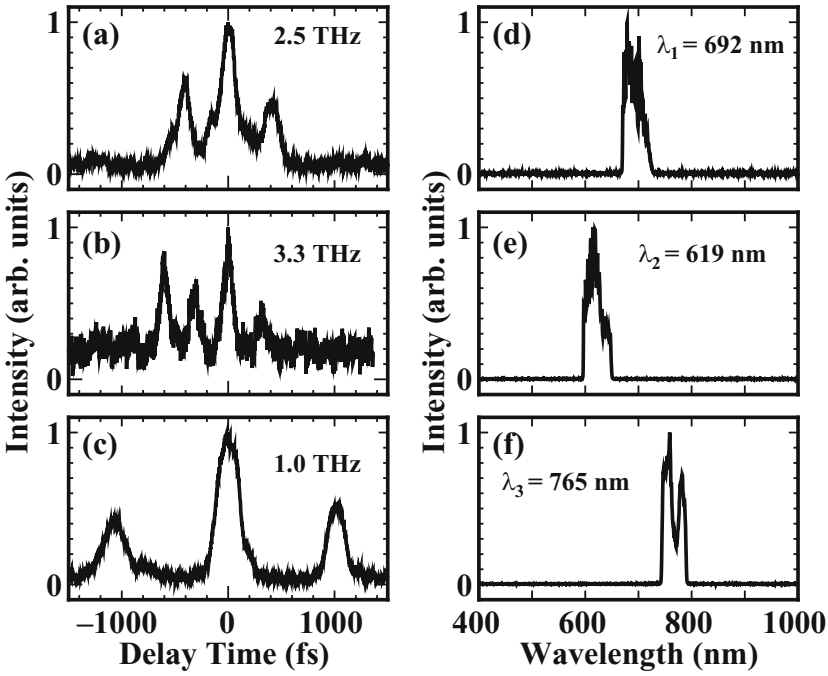

Fig. 6.8. (**a**) Intensity cross-correlation trace and (**d**) spectrum of a simultaneous coherent multicolor shaped pulse with a center wavelength $\lambda_1 = 692\,\text{nm}$ passing the first horizontal line on the SLM. (**b**) Intensity cross-correlation trace and (**e**) spectrum of a simultaneous coherent multicolor shaped pulse with a center wavelength $\lambda_2 = 619\,\text{nm}$ passing the second horizontal line on the SLM. (**c**) Intensity cross-correlation trace and (**f**) spectrum of a simultaneous coherent multicolor shaped pulse with a center wavelength $\lambda_3 = 765\,\text{nm}$ passing the third and fourth horizontal lines on the SLM

used for longer wavelength region to compensate for the weakness in the cross correlation signal in the longer wavelength region, as depicted an Fig. 6.6(c).

A typical example of simultaneously shaped three-color pulse trains using 648×4 pixels of the SLM is shown in Fig. 6.8. The intensity cross-correlation trace and the spectrum of a vertically-independent shaped pulse using the first horizontal line of the SLM are depicted in Fig. 6.8(a) and (d), respecticely. The pattern of the phase modulations was a periodic binary pattern of (1100). Here, 0 and 1 represent to 0- and 1.1π-phase modulation for each frequency component, respectively. The pulse interval of the shaped pulse train was 400 fs corresponding to the repetition rate of 2.5 THz. The center frequency λ_1 was 692 nm ($\omega_1/2\pi = 14450\,\mathrm{cm}^{-1}$).

Figure 6.8(b) and (e) shows the intensity cross-correlation trace and the spectrum of a vertically-independent shaped pulse using the second horizontal line of the SLM, respectively. The pattern of the phase modulations was a periodic binary pattern of (1110). The pulse interval of the shaped pulse train was 300 fs corresponding to the repetition rate of 3.3 THz. The center frequency λ_2 was 619 nm ($\omega_2/2\pi = 16160\,\mathrm{cm}^{-1}$). The intensity cross-correlation trace and the spectrum of a vertically-independent shaped pulse using the third and fourth horizontal lines of the SLM are indicated in Figs. 6.8(c) and (f), respectively. The pattern of the phase modulations was a periodic binary pattern of (10). The pulse interval of the shaped pulse train was 1000 fs corresponding to the repetition rate of 1.0 THz. The center frequency λ_3 was 765 nm ($\omega_1/2\pi = 13070\,\mathrm{cm}^{-1}$). From the loaded bandwidth $\Delta\lambda$ in wavelength of 1.0 nm for each pixel of the SLM, theoretically expected repetition rates for shaped pulses are 2.5, 3.1 and 1.0 THz, respectively, for the upper, middle and lower sides. Their agreement with those obtained experimentally was excellent. Fig. 6.8 shows only in the range of ~ -1 to ~ 1 ps owing to the same reason as the one mentioned in the case of the two-color experiment. The frequency differences in this case were $|\omega_1 - \omega_2|/2\pi = 1710\,\mathrm{cm}^{-1}$, $|\omega_2 - \omega_3|/2\pi = 3090\,\mathrm{cm}^{-1}$, and $|\omega_3 - \omega_1|/2\pi = 1380\,\mathrm{cm}^{-1}$.

The present maximum repetition rates are limited by the same reason as the one in the case of the two-color experiment. However, when we additionaly modulate the phase using the SLM for chirp compensation as described in Chap. 3, as well as for pulse shaping, these limitations will be solved. Then, using our experimental setup with the $d = 1/600$ mm grating pair, the $f = 150$ mm leans pair, the 66 mm-wide SLM and the center wavelength $\lambda_0 = 790$ nm, from (3.15), we shall be able to perform a pulse shaping of up to 430 THz-over-octave-spanning-bandwidth (430–1150 nm) coherent optical pulses which are generated through self- and induced-phase modulations [14]. In addition, we shall be able to generate up to ~ 200 THz-repetition rate pulse trains with up to four different center wavelengths and bandwidths.

6.4 Application for Vibrational Motion Control of Molecules

6.4.1 Principle and Theory

The recent development of ultrafast technology has enabled us to generate optical pulses whose duration is shorter than the molecular vibration or rotation period. Typical values of the vibrational or rotational period corresponding to the Stokes shift in many Raman scattering media are of the order of $10^{-13} - 10^{-14}$ s. This means that with the use of laser pulses whose duration is ∼10–100 fs, many Raman modes can be excited in a time-resolved stimulated Raman scattering (SRS) experiment simultaneously [4–6], but not selectively. On the other hand, selective excitation of a specific Raman mode or quantum control of molecular motion with a high time resolution has been carried out using femtosecond shaped optical pulse sequences (consisting of N-pulse trains) whose repetition rate are equal to their vibrational or rotational frequency [7, 8]. In addition, an analysis of this selective excitation with the N-pulse train has been done only under the assumption that each constituent pulse is a δ-function in time [9, 10]. However, a more realistic analysis of the selective excitation with the N-pulse train consisting of pulses with a finite duration is essential for proper analysis of experimental results.

In this section, it is shown that the practical analysis of selective excitation of molecular vibration or rotation using an N-pulse train with finite pulse duration leads to a low selectivity or efficiency due to the envelope spectral modulation arising from the finite pulse duration [11]. In order to overcome this problem we propose an ultrafast vibrationally-synchronized pumping technique with frequency-difference resonance where not only the pulse repetition rate (T^{-1}) but also the center frequency difference ($(\omega_1 - \omega_2)/2\pi$) between carrier phase-locked two-color femtosecond-pulse-train beams are tuned to the corresponding resonance frequency ($\omega_{\mathrm{R,int}}/2\pi$) of a specific vibrational or rotational mode. With this detailed analysis that accounts for the finite pulse duration, it is demonstrated that this novel technique allows efficient selective excitation.

Principle

Here we propose a vibrationally-synchronized pumping technique with frequency-difference resonance for efficient selective molecular vibrational or rotational excitation that can be applied up to the high-frequency region. The basic concept of the vibrationally-synchronized pumping technique with frequency-difference resonance is that both the center frequency difference and the repetition rates of two-color N-pulse train beams can be simultaneously tuned to the resonance of a specific molecular vibrational or rotational frequency of interest. For example, this vibrationally-synchronized pumping technique with frequency-difference resonance can be implemented as shown

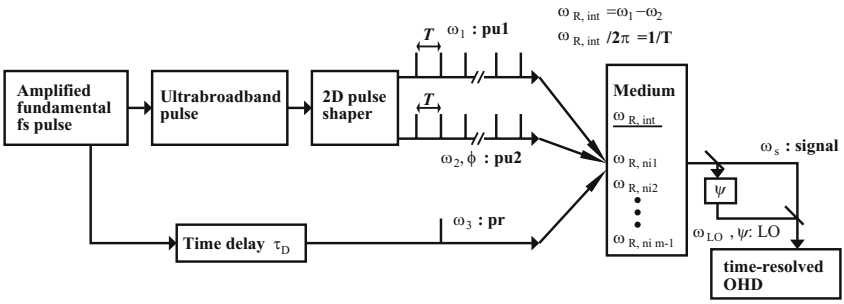

Fig. 6.9. Schematic diagram of the vibrationally-synchronized pumping technique with frequency-difference resonance [11]

in Fig. 6.9. After the amplified femtosecond optical pulses are spectrally-broadened by self- or induced-phase modulation [12–14], they are guided into a two-dimensional (2D) pulse shaper consisting of a $4f$-system in which a 2D spatial light amplitude- and phase-modulator are located in the Fourier plane. By use of this 2D-pulse shaper, simultaneous two-color pulse shaping is carried out with an arbitrary center frequency (wavelength) selection (ω_1 and ω_2) and with arbitrary control of the pulse intervals T (pulse repetition rates: T^{-1}). Thus we generate two-color shaped N-pulse train beams whose center frequencies are ω_1 and ω_2, with the same repetition rates T^{-1} as the pump beams (pump1 and pump2) which are focused into the medium under study. When we adjust the center frequency difference of these beams $\omega_1 - \omega_2$ to a specific molecular vibrational or rotational frequency of interest $\omega_{\mathrm{R,int}}$ and the pulse repetition rates T^{-1} to $\omega_{\mathrm{R,int}}/2\pi$, we can achieve vibrationally-synchronized pumping excitation with frequency-difference resonance. In this vibrationally-synchronized pumping technique with frequency-difference resonance, the *pulse-repetition-rate synchronization with vibration* leads to selective excitation and the *center-frequency difference resonance* brings Raman-signal enhancement of the selective excitation. That is, the $\omega_{\mathrm{R,int}}$-vibrational or rotational mode is selectively excited with a relatively high signal intensity. When the probe pulse having time delay τ_{D} between the pump1 and pump2 is also focused into the medium, we can observe behavior characteristic of temporally stimulated Raman scattering of a selected Raman mode. A local oscillator pulse LO, derived from a portion of the signal before detection, is used for optical heterodyne detection (OHD). We term ϕ the relative phase of the pump2 with respect to the pump1 or probe and ψ the phase of the local oscillator with respect to the probe. The phase difference between the pump1 and the probe is arbitrary. When one adjusts ϕ and ψ to the appropriate values, the real and imaginary parts of the Raman response can be obtained.

Theory

Proposal

In order to clarify the advantage of selective excitation using two-color pulse trains, we first describe the analysis of selective excitation by a N-pulse train with finite duration including the two-color pump case as well as the one-color pump case here. Consider a thin medium interacting with an external electric field:

$$E(\boldsymbol{r},t) = E_{\mathrm{pu}}(\boldsymbol{r},t) + E_{\mathrm{pr}}(\boldsymbol{r},t), \tag{6.27}$$

$$E_{\mathrm{pu}}(\boldsymbol{r},t) = \frac{1}{2}\bar{E}_{\mathrm{pu1}}(t)\exp[\mathrm{i}(\boldsymbol{k_1}\cdot\boldsymbol{r}-\omega_1 t)] + \frac{1}{2}\bar{E}_{\mathrm{pu2}}(t)\exp[\mathrm{i}(\boldsymbol{k_2}\cdot\boldsymbol{r}-\omega_2 t-\phi)] + \mathrm{c.c.}, \tag{6.28}$$

$$E_{\mathrm{pr}}(\boldsymbol{r},t) = \frac{1}{2}\bar{E}_{\mathrm{pr}}(t-\tau_{\mathrm{D}})\exp[\mathrm{i}(\boldsymbol{k_3}\cdot\boldsymbol{r}-\omega_3 t)] + \mathrm{c.c.}, \tag{6.29}$$

$$E_{\mathrm{LO}}(\boldsymbol{r},t) = \frac{1}{2}\bar{E}_{\mathrm{LO}}(t-\tau_{\mathrm{D}})\exp[\mathrm{i}(\boldsymbol{k_s}\cdot\boldsymbol{r}-\omega_{\mathrm{LO}}t-\psi)] + \mathrm{c.c.} \tag{6.30}$$

Here, $\bar{E}_{\mathrm{pu1}}(t), \bar{E}_{\mathrm{pu2}}(t), \bar{E}_{\mathrm{pr}}(t)$ and $\bar{E}_{\mathrm{LO}}$ denote the temporal envelopes of pump1, pump2, probe and local oscillator pulses with different center frequencies ω_j ($j = 1, 2, 3$ or LO), respectively. The probe pulse is delayed by the time interval τ_{D} with respect to pump1 and pump2.

Pump1 and pump2 interfere in the medium, creating a transient grating with a wavevector $\boldsymbol{k_1} - \boldsymbol{k_2}$. The probe beam then is Bragg-diffracted by this grating, resulting in the scattered beam in the $\boldsymbol{k_s} = \boldsymbol{k_1} - \boldsymbol{k_2} + \boldsymbol{k_3}$ direction. The center frequency of the scattered signal is $\omega_{\mathrm{s}} = \omega_1 - \omega_2 + \omega_3$. An experimental setup of the box-CARS geometry for coherent Raman scattering is one of the cases of this configuration. In addition to these three pulses, a fourth pulse that can be used as a local oscillator for optical heterodyne detection is included here [16–18].

We here focus on Raman processes, with off-resonant electronic-state excitation such that

$$\omega_{\mathrm{eg}} \pm \omega_1 \gg 1/t_{\mathrm{p},1}, \qquad \omega_{\mathrm{eg}} \pm \omega_2 \gg 1/t_{\mathrm{p},2}, \qquad \omega_{\mathrm{eg}} \pm \omega_3 \gg 1/t_{\mathrm{p},3}, \tag{6.31}$$

where $\hbar\omega_{\mathrm{eg}}$ is the energy difference between the electronic excited and ground states, and $t_{\mathrm{p},i} (i = 1, 2, 3)$ is the pulse duration of pump1, pump2 and the probe pulses, respectively. In this case, the optical-heterodyne-detected coherent Raman scattering signal in the $\boldsymbol{k_s}$-direction is given by

$$S_{\mathrm{hetero}}(\boldsymbol{k_s},\tau_{\mathrm{D}}) \propto -2\omega_{\mathrm{s}}\mathrm{Im}\Big\{\int_{-\infty}^{\infty}\mathrm{d}t\left|\bar{E}_{\mathrm{pr}}(t-\tau_{\mathrm{D}})\right|^2 \times \int_0^{\infty}\mathrm{d}\tau\bar{E}_{\mathrm{pu1}}(t-\tau)\bar{E}^*_{\mathrm{pu2}}(t-\tau)\exp[\mathrm{i}(\omega_1-\omega_2)\tau]\sum_j r_j(\tau)\exp[\mathrm{i}(\phi+\psi)]\Big\}, \tag{6.32}$$

integrated over all times t, on the assumption that $E_{\mathrm{LO}}(t) \propto \exp[\mathrm{i}(\boldsymbol{k}_{\mathbf{s}} \cdot \boldsymbol{r} - \omega_{\mathrm{s}} t)] +$ c.c. $r_j(t)$ is the Raman response function of the medium exhibiting the jth vibrational mode ($j = 1, \cdots, m$), expressed by

$$r_j(t) = A_j \exp(-\gamma_j t/2) \sin(\bar{\omega}_{\mathrm{R},j} t), \tag{6.33}$$

$$\bar{\omega}_{\mathrm{R},j} = \sqrt{\omega_{\mathrm{R},j}^2 - (\gamma_j/2)^2}, \tag{6.34}$$

where A_j, γ_j and $\omega_{\mathrm{R},j}$ are the relative strength, the damping rate and the natural vibrational frequency of the jth mode, respectively. In accordance with the philosophy of selective excitation, m modes are classified into a mode of interest ($\omega_{\mathrm{R,int}}$) and $m-1$ modes of no particular interest ($\omega_{\mathrm{R,ni}\ 1}$, $\cdots$, $\omega_{\mathrm{R,ni}\ m-1}$), hereafter. We do not include the electronic response function here.

The Fourier transform of a function $f(t)$ is defined by

$$\mathsf{F}\{f(t)\} = \int_{-\infty}^{\infty} \mathrm{d}t\ \mathrm{e}^{\mathrm{i}\omega t} f(t). \tag{6.35}$$

Hence, the optical-heterodyne-detected coherent Raman Scattering signal is expressed by

$$S_{\mathrm{hetero}}(\boldsymbol{k}_{\mathbf{s}}, \tau_{\mathrm{D}}) \propto -2\omega_{\mathrm{s}} \mathrm{Im}\Bigg[\int_{-\infty}^{\infty} \mathrm{d}t \left| \bar{E}_{\mathrm{pr}}(t - \tau_{\mathrm{D}}) \right|^2 \int_{-\infty}^{\infty} \frac{\mathrm{d}\omega}{2\pi} \mathrm{e}^{-\mathrm{i}\omega t}$$
$$\times \mathsf{F}\Big\{ \bar{E}_{\mathrm{pu1}}(t) \bar{E}^*_{\mathrm{pu2}}(t) \Big\} \mathsf{F}\Big\{ \exp[\mathrm{i}(\omega_1 - \omega_2)t] u(t) \sum_j r_j(t) \Big\} \exp[\mathrm{i}(\phi + \psi)] \Bigg], \tag{6.36}$$

from (6.32). Here, $u(t)$ is the unit step function, represented by

$$u(t) = \begin{cases} 0 \text{ if } t < 0\,, \\ 1 \text{ if } t \geq 0\,. \end{cases} \tag{6.37}$$

Mode Selection

The coherent Raman scattering signal produced by the vibrationally-synchronized pumping technique with frequency-difference resonance is analyzed by describing the profiles of the pump pulses, using a shaped-pulse train in the form

$$\bar{E}_{\mathrm{pu1}}(t) = \bar{E}_{\mathrm{pu2}}(t) = \sum_{n=1}^{N} F([t + (n-1)T]/T_0)/\sqrt{W}, \tag{6.38}$$

$$W = \int_{-\infty}^{\infty} \mathrm{d}t \left| \sum_{n=1}^{N} F([t + (n-1)T]/T_0) \right|^2, \tag{6.39}$$

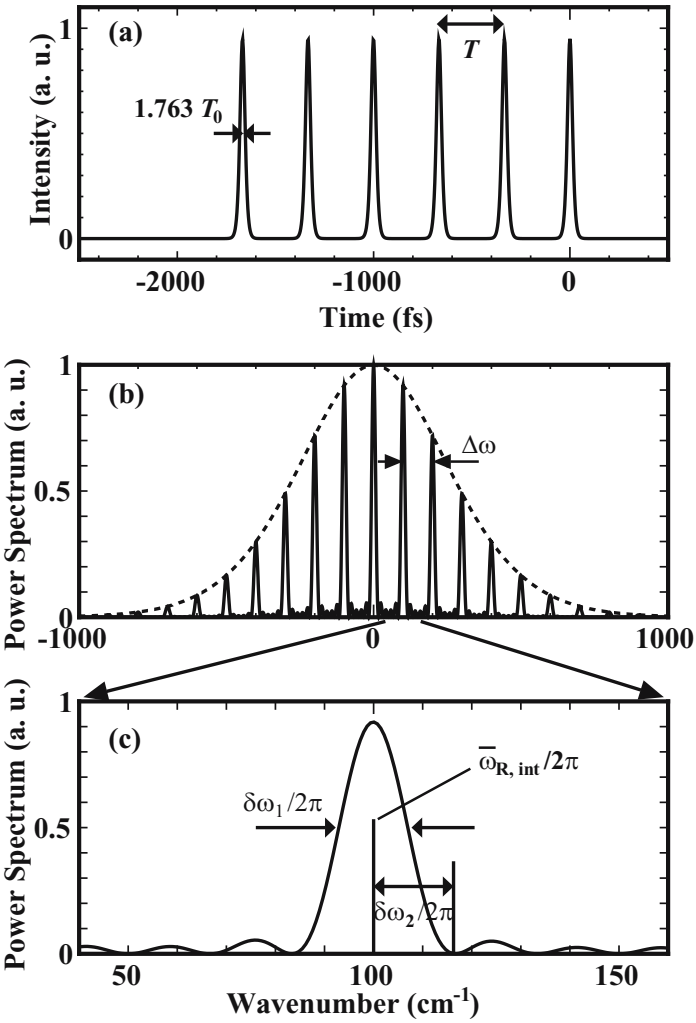

Fig. 6.10. (**a**) An example of an N-pulse train ($F(t/T_0) = \mathrm{sech}(t/T_0)$, $t_p = 1.763T_0 = 30\,\mathrm{fs}$, $N = 6$ and $T = 333.56\,\mathrm{fs}$). (**b**) Its spectra is represented by the solid line. The dashed line corresponds to a spectra of a $t_\mathrm{p} = 30\,\mathrm{fs}$-single pulse. The wavenumber $0\,\mathrm{cm}^{-1}$ corresponds to the center wavelength. (**c**) The spectral peak around $T^{-1} = 100\,\mathrm{cm}^{-1}$ is magnified. The full width at half maximum $\delta\omega_1$ of the peak approximately equals $\delta\omega_2$, which is the difference between the peak and the first adjacent zero point [11]

where $F(t/T_0)$ denotes the profile of each constituent pulse composing an N-pulse train with the constituent-pulse duration parameter T_0, and T is the time interval between pulses, as shown by Fig. 6.10(a). Considering practical

cases for selective excitation using pulse trains, the electric field is normalized by $\sqrt{W}$ under the condition that the total pulse energy is constant. In the case where $T_0 < T$,

$$\begin{aligned}\bar{E}_{\mathrm{pu1}}(t)\bar{E}^*_{\mathrm{pu2}}(t) \simeq \Bigg\{ & \sum_{n=1}^{N} \left| F([t+(n-1)T]/T_0) \right|^2 \\ & + \sum_{n=1}^{N-1} F([t+(n-1)T]/t_0) F^*([t+nT]/t_0) \\ & + \sum_{n=2}^{N} F([t+(n-1)T]/t_0) F^*([t+(n-2)T]/t_0) \Bigg\} / W. \end{aligned} \tag{6.40}$$

When $T_0 \ll T$, the second and the third terms in (6.40) can be neglected. Thus, the Fourier transform of the first term in (6.40) is

$$\mathsf{F}\left\{ \bar{E}_{\mathrm{pu1}}(t)\bar{E}^*_{\mathrm{pu2}}(t) \right\} \simeq \frac{1}{W} \frac{\sin(N\omega T/2)}{\sin(\omega T/2)} \mathrm{e}^{-\mathrm{i}(N-1)\omega T/2} \mathsf{F}\left\{ \left| F\big(t/T_0\big) \right|^2 \right\}. \tag{6.41}$$

The spectrum of (6.41) is almost discretized with the frequency spacing $\Delta\omega = 2\pi/T$, determined by the time interval T of the N-pulse train. This discretization enables us to excite coherent phonons selectively, that is, to excite only a specific vibrational mode. This is in stark contrast to the single-pulse (non-pulse-train; $N = 1$) case where many Raman modes are excited simultaneously. This selective excitation can be explained through (6.36): among the Raman modes represented by $r_j(t)$, only a specific vibrational mode $\bar{\omega}_{\mathrm{R,int}}$ is filtered by the spectrum

$$\mathsf{F}\left\{ \bar{E}_{\mathrm{pu1}}(t)\bar{E}^*_{\mathrm{pu2}}(t) \right\},$$

when $m\Delta\omega = \bar{\omega}_{\mathrm{R,int}}$ (m: integer) in (6.34).

Fundamental Analysis

In the case where pump1 and pump2 have the same pulse-train envelopes and $T_0 \ll T$, as shown in Fig. 6.10(a), the factor

$$\mathsf{F}\left\{ \bar{E}_{\mathrm{pu1}}(t)\bar{E}^*_{\mathrm{pu2}}(t) \right\}$$

in (6.36) has the form

$$\sin(N\omega T/2)\mathrm{e}^{-\mathrm{i}(N-1)\omega T/2} \mathsf{F}\left\{ \left| F\big(t/T_0\big) \right|^2 \right\} / W \sin(\omega T/2).$$

From this, it should be noted that, because of the finite pulse duration, the spectrum of an N-pulse train is modulated by a factor

$$\mathsf{F}\left\{\left|F\left(t/T_0\right)\right|^2\right\}.$$

This corresponds to the spectrum of the constituent pulse, unlike in the delta-function pulse train case. The conventional analysis using an infinitesimal duration is impractical because it could excite a mode strongly in an arbitrarily high vibrational frequency region. As an example, in our analysis here, we consider $F(t/T_0)$ as a hyperbolic secant function. Then

$$C(\omega) \equiv \mathsf{F}\left\{\left|F\left(t/T_0\right)\right|^2\right\} = \mathsf{F}\left\{\operatorname{sech}^2\left(t/T_0\right)\right\} = \pi\omega T_0^2 \operatorname{cosech}\left(\pi\omega T_0/2\right), \tag{6.42}$$

as shown in Fig. 6.10(b). Since spectral filtering for selective excitation at $\omega_{\mathrm{R,int}}$ is done by the peak of $\omega = \omega_{\mathrm{R,int}} = 2\pi/T$, the stimulated Raman signal for N-pulse train beams with a finite duration is reduced by a factor of $C(\omega_{\mathrm{R,int}})/C(\omega = 0)$ compared to that for delta-function N-pulse train beams. For the example described in Sect. 6.4 ($\omega_{\mathrm{R,int}}/2\pi = 448.2\,\mathrm{cm}^{-1}$ and $T_0 = 30/1.763 = 17.0\,\mathrm{fs}$), the analysis using the N-pulse train with an infinitesimal duration overestimates the power spectrum of the coherent Raman scattering signal excited selectively at $\omega_{\mathrm{R,int}}/2\pi = 448.2\,\mathrm{cm}^{-1}$ by about a factor of five compared to our analysis using the N-pulse train with finite duration. Thus the analysis using the N-pulse train with a finite duration is essential for an accurate interpretation of the experimental results.

Optimum Number of an *N*-Pulse Train

For a practical consideration of the selective excitation using an N-pulse train with finite duration, the condition that the total energy of the N-pulse train is constant should be considered. Stimulated Raman scattering is a third-order nonlinear process governed by the pulse peak intensities. Thus, under the constant total-energy condition, it is important to derive the formula that determines the minimum pulse number for efficient selective excitation in both cases of one- and two-color N-pulse train beams. Figure 6.10(c) shows the magnification of the first positive-frequency (or negative-frequency) sub-spectrum of $\mathsf{F}\left\{\bar{E}_{\mathrm{pu1}}(t)\bar{E}^*_{\mathrm{pu2}}(t)\right\}$ at $\omega = \pm 2\pi/T$, which is used for conventional selective excitation. From (6.41), the shape of this sub-spectrum is expressed mainly through the factor $\sin(N\omega T/2)/W\sin(\omega T/2)$. Adjacent spectral zero points are at $\omega = 2\pi(1 \pm 1/N)/T$. Approximating the shape around the first positive-frequency sub-spectrum to that of an isosceles triangle, we can evaluate the full width at half maximum (FWHM; $\delta\omega_1$) of the first positive-frequency (or negative-frequency) sub-spectrum to be $2\pi/NT$, which is equal

to half of the base width $\delta\omega_2$ of the triangle. Considering that only the Raman spectral component almost within the FWHM of the first positive-frequency (or negative-frequency) sub-spectrum can be excited effectively, we find that the condition for efficient selective excitation is that the FWHM should be smaller than the minimum interval $(\Delta\omega_{\mathrm{R}})_{\min}$ of the intervals between the Raman line $\omega_{\mathrm{R,int}}$ of interest and the lines $\omega_{\mathrm{R,ni\,j}}$ $(j = 1, \cdots, m-1)$ of no interest. That is,

$$N \gtrsim \frac{2\pi}{(\Delta\omega_{\mathrm{R}})_{\min} T}. \tag{6.43}$$

This is the criterion for the optimum pulse number N for efficient selective excitation using an N-pulse train. It should be noted that the optimum pulse number does not depend on the shape of each pulse that constitutes the N-pulse train, because the width of the first positive-frequency (or negative-frequency) sub-spectrum is determined by the factor $\sin(N\omega T/2)/W\sin(\omega T/2)$.

Efficient Selective Excitation

As mentioned above, the spectral modulation of $\mathsf{F}\{\bar{E}_{\mathrm{pu1}}(t)\bar{E}^*_{\mathrm{pu2}}(t)\}$ in (6.36) leads to a low selective-excitation efficiency of a specific Raman mode in the high frequency region in the case of $\omega_1 - \omega_2 = 0$. In order to avoid this low selective-excitation efficiency, due to the factor $\mathsf{F}\{\bar{E}_{\mathrm{pu1}}(t)\bar{E}^*_{\mathrm{pu2}}(t)\}$, we take notice of another factor of

$$\mathsf{F}\Big\{ \exp[\mathrm{i}(\omega_1 - \omega_2)t]u(t) \sum_j r_j(t) \Big\}$$

in (6.36). While the spectral modulation due to $\mathsf{F}\{\bar{E}_{\mathrm{pu1}}(t)\bar{E}^*_{\mathrm{pu2}}(t)\}$ decreases the spectral amplitude at $\omega = \omega_{\mathrm{R,int}}$, especially in the high frequency region, the spectral amplitude at $\omega = 0$ is not modulated even in the finite duration case. Moreover, shifting the Raman spectrum is possible with a factor $\exp[\mathrm{i}(\omega_1 - \omega_2)t]$ in

$$\mathsf{F}\Big\{ \exp[\mathrm{i}(\omega_1 - \omega_2)t]u(t) \sum_j r_j(t) \Big\}$$

by varying the $\omega_1 - \omega_2$ value. When we adjust $\omega_1 - \omega_2 = \omega_{\mathrm{R,int}}$, we can shift the Raman spectrum by $\pm\omega_{\mathrm{R,int}}$, thus we can use the un-modulated spectral component at $\omega = 0$ of the N-pulse train for selective Raman-mode excitation. That is, to greatly improve on the low efficiency of selective excitation in the high frequency region, we employ the vibrationally-synchronized pumping technique with frequency-difference resonance. We use two-color N-pulse train beams with a frequency difference of $\omega_1 - \omega_2$ which corresponds to the Raman frequency $\omega_{\mathrm{R,int}}$ and for which the pulse interval T satisfies

$\omega_{\mathrm{R,int}} = 2\pi/T$. These two-color N-pulse train beams, as well as one-color N-pulse train beams, can selectively excite the specific Raman mode of $\omega_{\mathrm{R,int}}$. Moreover, when adjusting the center frequencies of the two-color beams that satisfy $\omega_1 - \omega_2 = \omega_{\mathrm{R,int}}$, we can shift the spectrum of the Raman response effectively to make them resonant with the central spectral peak of the N-pump-pulse trains. Thus, we can perform efficient selective excitation even in the high frequency region, with complicated Raman lines, using two-color N-pulse train beams.

As an example, we investigate the efficient selective excitation of tetrachloroethylene that has Raman modes at 236.6, 346.5, 448.2 and 511.9 cm^{-1} in the high frequency region [15], as shown in Fig. 6.11(a). Here, we consider the selective excitation of the 448.2 cm^{-1} Raman line. The pulse interval T for selective excitation at 448.2 cm^{-1} is 74.4 fs, and the minimum frequency interval $(\Delta\omega)_{\min}/2\pi$ is 63.7 cm^{-1}. To avoid a decrease in power of each constituent pulse for selective excitation under the condition that the total energy of the N-pulse train is constant, N should be at least 7 to satisfy the inequality (6.43).

The power spectrum of (6.41) in the case where $\bar{E}_{\mathrm{pu1}}(t) = \bar{E}_{\mathrm{pu2}}(t)$, $\omega_1 = -\omega_2$, $F(t/T_0) = \mathrm{sech}(t/T_0)$, $N = 7$, $T = 74.4$ fs and every pulse duration $t_{\mathrm{p}} = 2T_0 \ln(1+\sqrt{2}) = 30$ fs ($T_0 = 17.0$ fs) for selective excitation at 448.2 cm^{-1} is shown in Fig. 6.11(b). The height of the first peak at the positive or negative frequency ($\omega/2\pi = \pm 448.2\,\mathrm{cm}^{-1}$) is much lower than that of the peak at the center of $\omega = 0\,\mathrm{cm}^{-1}$.

As a measure of the selectivity and efficiency of excitation, we define a factor η_{S}, such that

$$\eta_{\mathrm{S}} = \left| \frac{\tilde{S}_{\mathrm{hetero}}(\boldsymbol{k}_{\mathrm{s}}, \omega_{\mathrm{R,int}})}{\tilde{S}_{\mathrm{hetero}}(\boldsymbol{k}_{\mathrm{s}}, \omega_{\mathrm{R,ni}}^{\max})} \right|^2 . \tag{6.44}$$

The ratio of the power spectrum $|\tilde{S}_{\mathrm{hetero}}(\boldsymbol{k}_{\mathrm{s}}, \omega_{\mathrm{R,int}})|^2$ of the stimulated Raman scattering signal $\tilde{S}_{\mathrm{hetero}}(\boldsymbol{k}_{\mathrm{s}}, \omega)$ at the specific frequency of interest $\omega_{\mathrm{R,int}}$ to $|\tilde{S}_{\mathrm{hetero}}(\boldsymbol{k}_{\mathrm{s}}, \omega_{\mathrm{R,ni}}^{\max})|^2$ at another Raman frequency $\omega_{\mathrm{R,ni}}^{\max}$ that maximizes the spectral intensity among the Raman frequencies $\omega_{\mathrm{R,ni,j}}$ ($j = 1, \cdots, m-1$; $\tilde{S}_{\mathrm{hetero}}(\boldsymbol{k}_{\mathrm{s}}, \omega)$ is the Fourier transform of $S_{\mathrm{hetero}}(\boldsymbol{k}_{\mathrm{s}}, \tau_{\mathrm{D}})$). In Sect. 6.4, the efficient selective excitation by the vibrationally-synchronized pumping technique with frequency-difference resonance will be discussed together with the η_{S} values. Figure 6.12 shows the calculated coherent Raman scattering signals as a function of delay time in the optical heterodyne detection scheme for four cases ((A) $N = 1, \omega_1 - \omega_2$, (B) $N = 7, \omega_1 = \omega_2$, (C) $N = 1, (\omega_1 - \omega_2)/2\pi = 448.2\,\mathrm{cm}^{-1}$ and (D) $N = 7, (\omega_1 - \omega_2)/2\pi = 448.2\,\mathrm{cm}^{-1}$), on the assumption that the damping rates γ of all Raman modes in (6.33) are all 20 cm^{-1}. To obtain maximum signal intensities in the optically-heterodyne detection scheme, we set the $\phi+\psi$ values to $\pi/2$ and 0 for the $\omega_1 - \omega_2 = 0$ and 448.2 cm^{-1} cases, respectively. In the $N = 1$ (Fig. 6.12(A) and (C)) cases, it

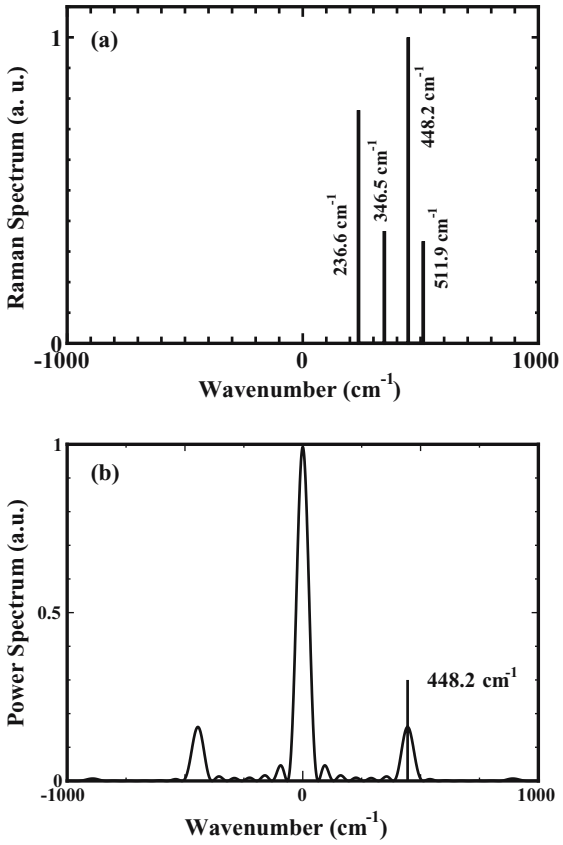

Fig. 6.11. (**a**) Raman spectra of tetrachloroethylene. (**b**) The spectra of an $N = 7$ pulse train for selective excitation at $448.2\,\mathrm{cm}^{-1}$ mode. The wavenumber $0\,\mathrm{cm}^{-1}$ corresponds to the center wavelength [11]

is found that the signals exhibit combined oscillation of more than one frequency. In the $N = 7$ and $\omega_1 - \omega_2 = 0$ case (Fig. 6.12(B)), it is seen that the signal oscillates with a specific frequency at $\omega_{\mathrm{R,int}}$ but the signal oscillating at $\omega_{\mathrm{R,int}}$ is weak. In the $N = 7$ and $(\omega_1 - \omega_2)/2\pi = 448.2\,\mathrm{cm}^{-1}$ (Fig. 6.12(D)), it is seen that the signal is dominated by a non-oscillating component. This non-oscillating part corresponds to the selectively-excited mode of interest owing to the frequency shift of $(\omega_1 - \omega_2)/2\pi = 448.2\,\mathrm{cm}^{-1}$. By considering the integral of the non-oscillating part with respect to the time delay, the selectively-excited Raman signal at $\omega_{\mathrm{R,int}} = 448.2\text{-cm}^{-1}$ mode is found to be comparatively large. (See the inset of Fig. 6.12(D).) To further clarify the selectivity of the excitation, the corresponding power spectra are shown in Fig. 6.13. Signal intensities when $\omega_1 - \omega_2 = 0$ (Fig. 6.13 (A) and (B)) are low owing to the spectrum modulation factor $\mathsf{F}\{|F(t/T_0)|^2\}$ in (6.36). On

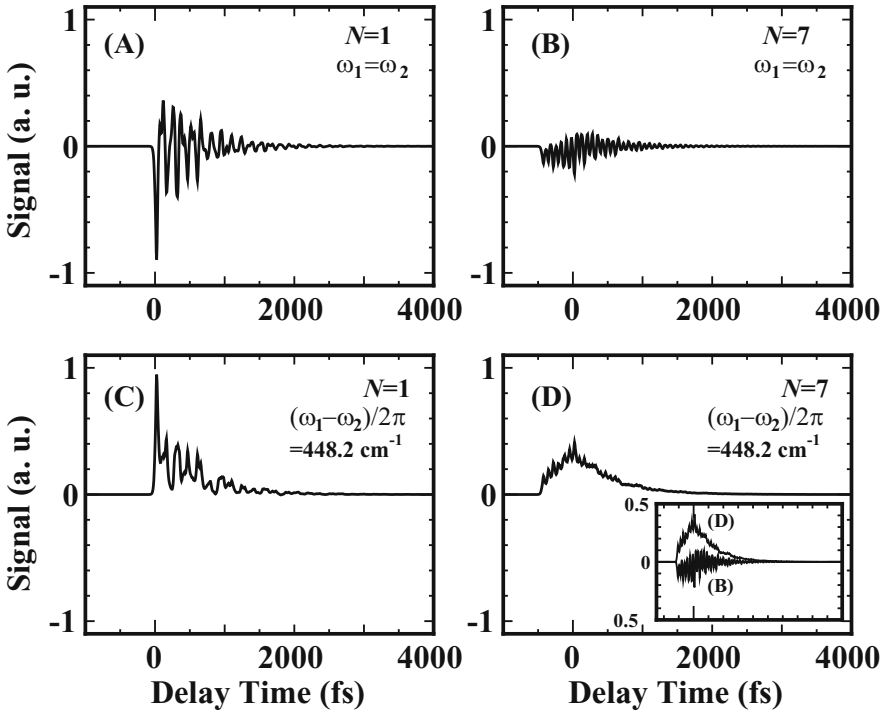

Fig. 6.12. Temporal profiles of heterodyne-detected coherent Raman scattering signals with pump pulses of (**A**) $\omega_1 - \omega_2 = 0$ and $N = 1$, (**B**) $\omega_1 - \omega_2 = 0$ and $N = 7$, (**C**) $(\omega_1 - \omega_2)/2\pi = 448.2\,\mathrm{cm}^{-1}$ and $N = 1$, and (**D**) $(\omega_1 - \omega_2)/2\pi = 448.2\,\mathrm{cm}^{-1}$ and $N = 7$. The comparison of the signals in the (B) and (D) cases is shown in the inset [11]

the other hand, signal intensities when $(\omega_1 - \omega_2)/2\pi = 448.2\,\mathrm{cm}^{-1}$ (Fig. 6.13 (C) and (D)) are much more enhanced than those when $\omega_1 - \omega_2 = 0$. For Fig. 6.13(C) and (D), the horizontal axis represents wavenumber corresponding to $[\omega - (\omega_1 - \omega_2)]/2\pi$. Thus, the peak at $0\,\mathrm{cm}^{-1}$ corresponds to the vibrational mode of $448.2\,\mathrm{cm}^{-1}$. That is, by adjusting $(\omega_1 - \omega_2)/2\pi$ to the mode frequency $\omega_{\mathrm{R,int}}/2\pi$ of interest, we can effectively shift the Raman mode frequencies by $-(\omega_1 - \omega_2)/2\pi$ so that the only the signal intensity of interest is strengthened. As a result we can achieve much more efficient excitation at $\omega = 0\,\mathrm{cm}^{-1}$. In addition, the $N = 7$ pulse train enables the further selective excitation of only the $448.2\,\mathrm{cm}^{-1}$ mode (Fig. 6.13 (D)), while the $N = 1$ pulse excites all the Raman modes simultaneously (Fig. 6.13 (C)). The quantitative comparison of the selection factor η_{S} defined by (6.44) makes it clear that the η_{S} values are 0.285, 7.35, 12.2 and 199 for Fig. 6.13(A), (B), (C) and (D), respectively. Thus, it is found that, even in the high frequency region, efficient selective excitation can be made with two-color synchronized shaped-

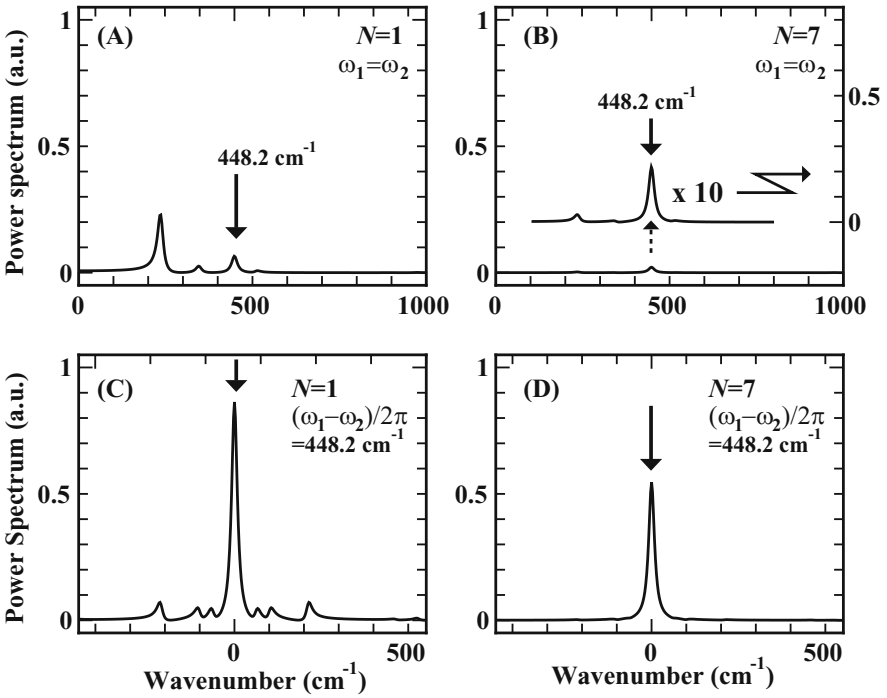

Fig. 6.13. Power spectra of heterodyne-detected coherent Raman scattering signals with pump pulses of (**A**) $\omega_1 - \omega_2 = 0$ and $N = 1$, (**B**) $\omega_1 - \omega_2 = 0$ and $N = 7$, (**C**) $(\omega_1 - \omega_2)/2\pi = 448.2\,\mathrm{cm}^{-1}$ and $N = 1$, and (**D**) $(\omega_1 - \omega_2)/2\pi = 448.2\,\mathrm{cm}^{-1}$ and $N = 7$. The selectivity is determined by η_S, which is defined by (6.44). This is evaluated to be (A) 0.285, (B) 7.35, (C) 12.2 and (D) 199 [11]

N-pulse train beams whose frequency difference is adjusted to the phonon mode frequency of interest (Fig. 6.13(D)). The calculated results show that this vibrationally-synchronized pumping technique with frequency-difference resonance (Fig. 6.13(D)) has the advantage of exhibiting an enhancement factor about twenty-times larger in the power spectrum of Raman signal for selective excitation than the conventional one-color pulse shaping technique (Fig. 6.13(B)).

6.4.2 Experiment

Two-pulse excitations with different polarization combinations have been demonstrated for selective excitation of molecular vibrations in CCl_4 liquid. Selective enhancements as well as suppressions of the two asymmetric vibration motions were achieved by changing the separation time of the two-pump pulses. In addition, the anti-correlated selective excitations were observed in the opposite configuration of polarization between the two-pump pulses.

The results can be understood in terms of classical oscillator model using impulsive stimulated Raman scattering.

Selective control of molecular motions using a femtosecond pulse laser is a promising technique for controlling photochemical reactions in the time domain [19]. So far, various experimental techniques have advanced this field dramatically. Optical pulse shaping has made it possible to produce complex excitation light fields for manipulating the specific motions and interactions in the target molecules [20]. In this technique, pulse shaping can be optimized by learning the algorithm [21–27]. By means of coherent anti-stokes Raman scattering (CARS), multiple color excitations enable us to control the vibration motions both in the time and frequency domains [28–30]. In addition, recent progress of pulse shaping techniques allows for multi-dimensional coherent control, such as excitations for vibration motions with higher-order [31], generation of multimode vibration modes [32], and spatio-temporal controls [33]. On the other hand, since the polarization in excitation and detection is sensitive to the symmetry of vibration motions, polarization-selective measurements in the time domain is used to prepare fine selectivity for controlling the molecular motions [18, 34–43]. In addition to the vibration motions, polarized measurements have also provided information about nonlinear optical responses of electron motions in molecules [44–50].

In this subsection, we introduce the experimental results of a simple two-pump-pulse excited Raman spectroscopy. Raman signals in the time domain were observed by the optical heterodyne detected (OHD) Raman induced Kerr effect spectroscopy (OHD-RIKES(OKE)). Although OHD-RIKES provides only anisotropic elements of molecular motions, we can compare the selectivities in the different excitation conditions because of its linear response with respect to the molecular motions. Experimental section describes the vibration motions of CCl_4 and our experimental set-up. In results and discussion, we compare the experimental results of time-resolved Raman with steady state Raman. We also discuss the selective excitations by two-pump pulse excitations. The experimental results indicate the enhancements and suppressions of each vibration motion according to the separation time between the two pump pulses and the combinations of polarizations.

Experimental Section

The sample used in this study is carbon tetrachloride (CCl_4) in liquid form. This is an excellent sample for demonstrating the molecular dynamics because of its simple vibrational motions. ν_1 (A_1) at $460\,cm^{-1}$ the symmetric stretch is a Raman active, ν_2 (E) at $214\,cm^{-1}$ the Cl-C-Cl bend is Raman active, ν_3 (T_2) at $793\,cm^{-1}$ the asymmetric stretch is both IR and Raman active, and ν_4 (T_2) at $314\,cm^{-1}$ another bend mode is both IR and Raman active.

Figure 6.14 shows a schematic illustration of our experimental set-up. The time-resolved analysis of molecular vibration motions was achieved by OHD-RIKES. The light source is a mode-locked Ti:sapphire laser (center wave-

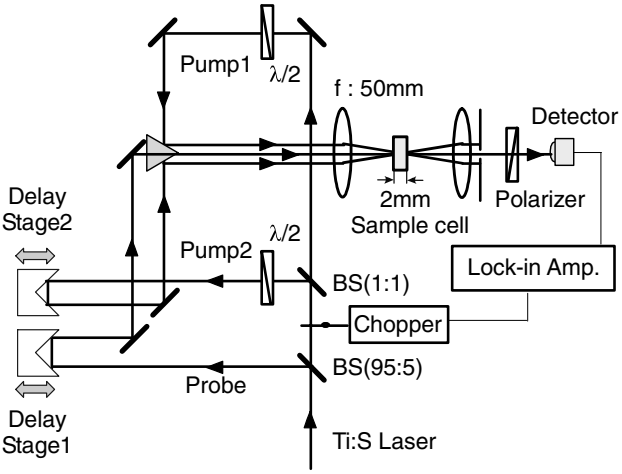

Fig. 6.14. Experimental set-up for two-pump pulse excitations. The time separations of probe and two-pump pulses are achieved by the delay stage 1 and 2, respectively

length ∼ 800nm, pulse width ∼10–30 fs, repetition rate 76 MHz). The output from the laser is split by a partially reflected thin glass plate (reflectivity 5%) to provide the pump and probe pulses. For the two-pulse excitations, the pump is again divided into two beams by another half-beam splitter. The polarized pump pulses and probe pulse are focused by a plano-convex lens (f = 50 mm) onto the same point inside the 1 mm-thick fused glass cell. It is important to note that the difference of the spot size of the incoming three pulses leads to the relative phase shift of the signals. In order to increase the spatial overlap of the incoming fields at the focal point, the three beams are positioned at the triangular geometry in front of the lens. The polarizations between pulses are controlled by two half-wave plates for optimizing the signals. The polarization of the transmitted probe is selected by a Grand–Thompson prism. In order to reduce the contributions of the stray light, the probe pulse goes through the spatial filter. The pump(s) are chopped and induced polarization changes of the probe are detected at the chopping frequency by a lock-in amplifier.

Results and Discussions

OHD-RIKES of CCl_4

The OHD-RIKES (OKE) is a widely used time-resolved technique and the details of the measurements and their theoretical treatments are described in detail elsewhere [35–37, 44–50]. Briefly, we give an overview of the characteristics of OHD-RIKES spectra by comparison with the steady state Raman.

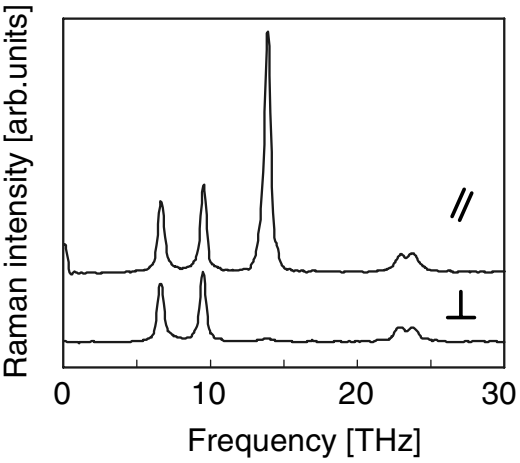

Fig. 6.15. Raman spectra of CCl_4 in different polarization configurations

We consider the interactions between the light and molecular vibrations. Because the vibration motions change the polarizability of molecule, the incident light is scattered with the shift of its polarization together with the shift of its energy. This is the so-called Raman process. The depolarization of the scattered light $\rho = I_\perp / I_\parallel$, calculated by the intensities from perpendicular ($I_\perp$) and parallel ($I_\parallel$) polarization light, is connected with the symmetry of Raman active vibration mode. For totally symmetric vibrations ρ takes a value smaller than 3/4 and the value of 1 for asymmetric ones.

Figure 6.15 shows typical Raman spectra of CCl_4 liquid, recorded in 90 degree geometry with different polarization configurations. The excitation laser is a continuous-wave (CW) Ti:Sapphire laser operating at 800ṅm. Dispersion and detection of the scattered light was achieved by a 1-m long double monochromator with a charge-coupled device (CCD) camera. The Raman peak around 14 THz shows small depolarization ratio, thus indicating the totally symmetric stretch mode of CCl_4. In contrast, lower two modes, both of which are attributed to the asymmetric bend mode, show 3/4 depolarization. Another depolarized signal around 24 THz is the asymmetric stretch mode. The relative intensities of the lower two modes are estimated to be I_{ν_2}:I_{ν_4} = 1:1.3.

Based on the results of the steady state Raman, we discuss the results of time-resolved measurements of CCl_4. Figure 6.16 shows a typical OHD-RIKES signal as a function of delay time between pump and probe pulses. Here we used only one-pump pulse excitation. The data consists of a large signal at zero time delay and oscillatory damped signals with longer decay time. The instantaneous change agrees with the autocorrelation of the laser, which is attributable to the non-resonantly excited electron response of the sample. After the instantaneous electron response, the signal is dominated by

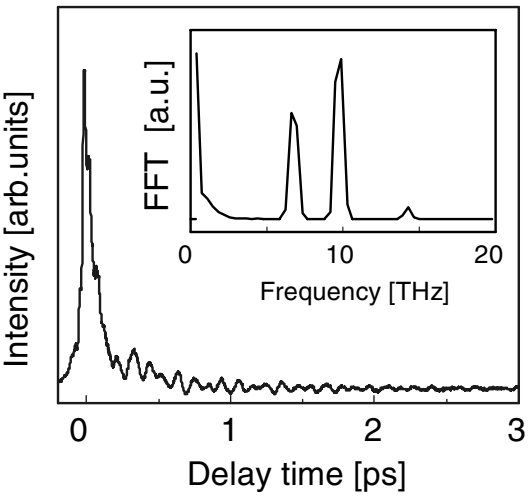

Fig. 6.16. OHD-RIKES data in the one-pulse excitation. The data involve two oscillation modes, which can clearly be seen in FFT power spectrum in the inset

the mixing of oscillations superimposed on the small signal with slow decay. The inset of Fig. 6.16(b) shows the Fourier transformed power spectrum of the data, in which we can directly compare with the steady state Raman in Fig. 6.15. In the figure, the frequencies of two intense peaks are identical with the asymmetric modes in the Raman, indicating the fact that the OHD-RIKES signal only reflects the asymmetric motions of a molecule. In the higher frequency, another tiny feature can be seen at 15 THz and may be attributed to the symmetric mode from the contribution of the ISRS signal. In the lower frequency, the signal shows a less structured band, which has been attributed to the intermolecular response of CCl_4 [35–37, 49].

The relative intensity ratio of the two intense peaks is I_{ν_2}:I_{ν_4} = 1:1.4, which is also identical with the steady state Raman discussed above. Because OHD gives a signal over the local oscillator field, the detected intensity has linear correspondence to the molecular response while the normal OKE reflects the second power of the pump field. Thus we can directly investigate the molecular motions in the Fourier transformed OHD-RIKES spectrum.

Selective Enhancement and Suppression by Using Three-Pulse Excitation

According to the Heisenberg uncertainty principle, a transform-limited pulse shorter than the vibration period has a bandwidth larger than the vibration frequencies. Therefore impulsive stimulated Raman scattering (ISRS) can be generated if the vibration motion is Raman active [51]. This stimulated Raman process yields a driving force for the coherent molecular vibration [52]. In the simple oscillator model, the dynamic equation of a molecular motion is described by

$$\frac{\mathrm{d}^2Q}{\mathrm{d}t^2} + 2\gamma\frac{\mathrm{d}Q}{\mathrm{d}t} + \omega_0^2 Q = \frac{1}{2}N\left(\frac{\mathrm{d}\alpha}{\mathrm{d}Q}\right)_0 E^2, \tag{6.45}$$

where Q is the displacement of molecule from the equilibrium, ω_0 is a fundamental frequency of a molecular vibration, γ is the decay rate, and N is the number density of molecules. The $(\mathrm{d}\alpha/\mathrm{d}Q)_0$ is the polarizability change of a molecule induced by ISRS. When the pulse width is short compared to the oscillation period of the molecular vibration and *gamma* is smaller than *omega*, the time dependence of the molecular motion is given by $Q \propto \exp(-\gamma t)\sin(\omega t)$, indicating the damped oscillation. When we introduce the second pulse soon after the first pulse excitation, the second pulse produces the driving force again through the ISRS process. The molecular motion in the time domain is thus expressed by

$$Q \propto \exp\left(-\frac{t}{\Gamma}\right)\sin(\omega t) + \exp\left(-\frac{t-\Delta t}{\Gamma}\right)\sin(\omega(t-\Delta t)), \tag{6.46}$$

where $\Gamma = 1/\gamma$, $\omega = (\omega_0^2 - \gamma^2)^{1/2}$, and Δt indicates the separation time between the two pulses. From the expression, one can easily understand that the total oscillation amplitude is enhanced when $\omega\Delta t = \pi$, which indicates the selective excitation, in which only the vibration with the frequency of two-pump pulses is enhanced, whereas the vibrations with other frequencies are suppressed. On the other hand, the total oscillation amplitude is canceled when $\omega\Delta t = \pi/2$, indicating the selective suppression of the vibration motion.

In Fig. 6.17, several OHD-OKE signals of CCl_4 taken with the two-pulse excitation are plotted as a function of the delay time for various separation times with different polarization geometries. Since the time widths of incident pulses are as large as 80 fs in this one-pulse excitation, the relative intensities $I_{\nu_2} : I_{\nu_4}$ are estimated to be 4:1 from Fourier analysis. At $\Delta t = \pi/\nu_2$, the ν_2 mode is dominant after the second pulse excitation, while at $\Delta t = \pi/(2\nu_2)$, the ν_2 mode is almost canceled and the ν_4 mode becomes dominant. In contrast, the ν_2 mode is enhanced again at $\Delta t = \pi/(2\nu_2)$ but with the crossed polarization geometry in which the polarization of the second pump pulse is set perpendicular to that of first pump. Since the RIKES signal reflects the anisotropic change of nonlinear susceptibility depending on the pump field, the two pump pulses with crossed polarization results in an oscillation with opposite sign in each excitation. The time evolution of the molecular motion in the double pulse excitation with crossed polarization is thus given by

$$Q \propto \exp\left(-\frac{t}{\Gamma}\right)\sin(\omega t) - \exp\left(-\frac{t-\Delta t}{\Gamma}\right)\sin(\omega(t-\Delta t)), \tag{6.47}$$

where the total oscillation is suppressed when $\omega\Delta t = \pi$ while $\omega\Delta t = \pi/2$ enhances the oscillation.

The selective excitation (suppression) in each vibrational motion is confirmed in Fourier analysis of the data. Figure 6.18 shows a series of FFT

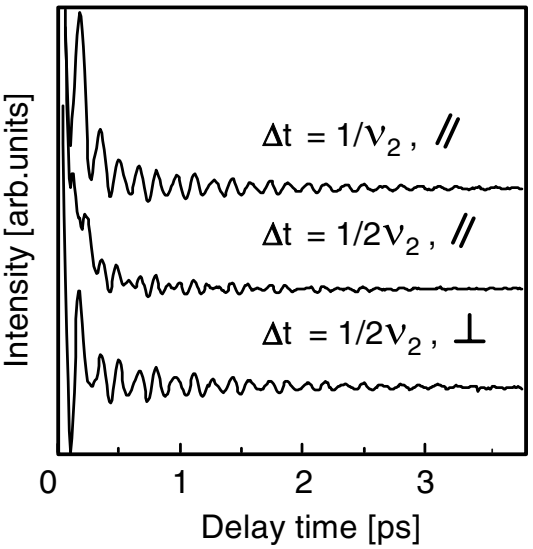

Fig. 6.17. OHD-RIKES data with different time separations and polarization configurations between two-pump pulses

power spectra for double pulse excitations with various separation times as well as different polarization configurations. The data clearly demonstrate the mode-selective amplifications and cancellations. Furthermore, inversely correlated spectra can be observed between parallel and crossed polarization excitation. While the imperfection of selective control remains in the data, which is mainly due to the incompleteness of the spatial overlap of the three incoming field, the anti-correlation spectra in each polarization combination suggests the feasibility of coherent control of the vibration motion using the polarization changes of the excited pulses.

6.5 Future Direction

In this chapter, the field manipulation of ultrabroadband optical pulses, that is the principle and theory of the generation of the pulse train using a 4-f pulse shaper, experiments of two- and three-color beam generation with tunable THz pulse trains, and application for vibrational motion control of molecules was described. Finally, the future direction of the field manipulation of ultra-broadband optical pulses is mentioned here.

1. Repetition rate of shaped pulses: The highest repetition rate of the shaped pulses is determined by the bandwidth of the input pulse. The broader the bandwidth of the input pulse, the higher the repetition rate of the shaped pulse. For example, when a monocycle-like pulse with a duration

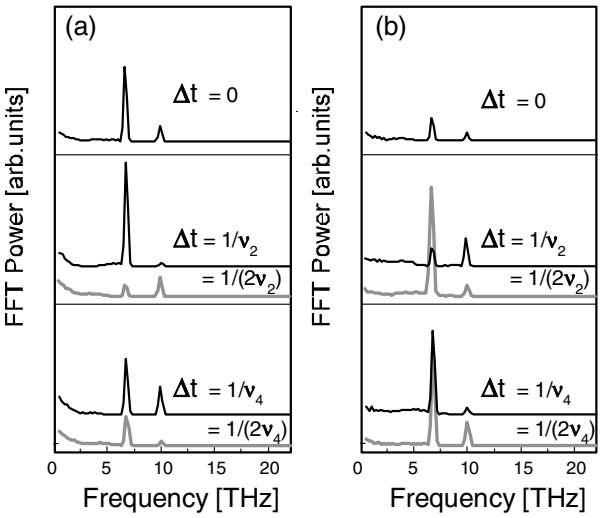

Fig. 6.18. FFT power spectra with different separation times between two-pump pulses. (**a**) parallel polarization between two-pump pulses and (**b**) crossed polarizations

of ∼3 fs and a bandwidth of ∼300 THz is used as an input, the highest repetition rate can be several tens of THz. Of course, when the spectral slicing is done in shaping, the highest repetition rate of the multicolor shaped pulses are reduced.

2. Shaping temporal range: The temporal range controlled in pulse shaping is limited to the time window $T_{\mathrm{w}}(\omega_{\mathrm{high}})$ of the highest frequency component of the input pulse. The time window $T_{\mathrm{w}}(\omega)$ is proportional to w_0/d, where w_0 is the radius of the input beam and d is the grating constant of the 4-f pulse shaper. Hence, when the wide temporal range is necessary, by adjusting the beam radius w_0 and the grating constant d, the shaping temporal range can be broadened.
3. Frequency tunability: The broader the pulse bandwidth is, the broader the tunable range of the simultaneously shaped multicolor pulses.
4. Polarization shaping: By adding two more SLMs on the Fourier plane in a 4-f pulse shaper, polarization shaping as well as simultaneous multicolor shaping can be done.
5. Simultaneous performing of pulse compression and shaping: The 4-f pulse shaper can be used for both pulse shaping and pulse compression. Hence, by simultaneously applying the phases for compression and shaping on the SLM, the pulse shaping of the monocycle-like pulse or the multicolor pulse shaping whose constituent pulses are the Fourier-transform-limited pulses can be performed even from the chirped pulse.

Conclusively, our simultaneous coherent multicolor pulse shaping technique has an advantage that the repetition rate and the center frequency can be almost arbitrarily controlled. In addition, our technique has two remarkable features unlike a technique using a 1D SLM, that is, the simultaneously shaped multicolor beams are spatially separated and the frequency components of shaped pulses can be overlapped partially or perfectly. Such multicolor shaped-pulse trains will enable us to apply to not only the selective and efficient excitation of a specific Raman mode even in the high vibration frequency region, but also the multi-selective coherent wave-packet control with multicolor tailored pulse sequences. For example, the experiment of the interference of the electronically-excited wave packets using the simultaneously shaped multicolor pulses with the partially overlapped spectra will be promising. Further, this simultaneous multicolor shaping technique is applicable to the source of the basic experiment of the coherent optical communication with multicolor high-repetition-rate pulses.

References

1. A.M. Weiner, J.P. Heritage, E.M. Kirschner: J. Opt. Soc. Am. B **5**, 1563 (1988)
2. A.M. Weiner, D.E. Leaird: Opt. Lett. **15**, 51 (1990)
3. A.M. Weiner, S. Oudin, D.E. Leaird, D.H. Reitze: J. Opt. Soc. Am. A **10**, 1112 (1993)
4. Y.X. Yan, E.B. Gamble, K. Nelson: J. Chem. Phys. **83**, 5391 (1985)
5. J. Herrman, A. Nazarkin: Opt. Lett. **19**, 2065 (1994)
6. E.M. Belenov, A.V. Nazarkin, I.P. Prokopovich: JETP Lett. **55**, 218 (1992)
7. A.M. Weiner, D.E. Leaird, G.P. Widerrechet, K.A. Nelson: Science **247**, 1317 (1990)
8. A.M. Weiner, D.E. Leaird, G.P. Widerrechet, K.A. Nelson: J. Opt. Soc. Am. B **8**, 1264 (1991)
9. Y.J. Yan, S. Mukamel: J. Chem. Phys. **94**, 997 (1991)
10. S. Mukamel: *Principles of Nonlinear Optical Spectroscopy* (Oxford University Press, 1995), Chap. 14.
11. R. Morita, M. Yamashita, A. Suguro, H. Shigekawa: Opt. Commun. **197**, 73 (2001)
12. L. Xu, N. Karasawa, N. Nakagawa, R. Morita, H. Shigekawa, M. Yamashita: Opt. Commun. **162**, 256 (1999)
13. N. Karasawa, R. Morita, L. Xu, H. Shigekawa, M. Yamashita: J. Opt. Soc. Am. B **16**, 662 (1999)
14. N. Karasawa, R. Morita, H. Shigekawa, M. Yamashita: Opt. Lett. **25**, 183 (2000)
15. See for example, G. Herzberg: *Molecular Spectra and Molecular Structure* (Krieger, 1991) p. 639.
16. P. Vöhringer, N.F. Scherer: J. Phys. Chem. **99**, 2684 (1995)
17. Y.J. Chang, P. Cong, J.D. Simon: J. Phys. Chem. **99**, 7857 (1995)
18. S. Matsuo, T. Tahara: Chem. Phys. Lett. **264**, 636 (1997)
19. I. Prigogine, S.A. Rice: *Advances in Chemical Physics: Chemical Reactions and Their Control on the Femtosecond Time Scale* (John Wiley & Sons Inc,1997)

20. A.M. Weiner, D.E. Leaird, G.P. Wiederrecht, K.A. Nelson: Science **247**, 1317 (1990)
21. D.J. Tannor, S.A. Rice: J. Chem. Phys. **83**, 5013 (1985)
22. D.J. Tannor, R. Kosloff, S.A. Rice: J. Chem. Phys. **85**, 5805 (1986)
23. R.S. Judson, H. Rabitz: Phys. Rev. Lett. **68**, 1500 (1992)
24. H. Rabitz, R. deVivie Riedle, M. Motzkus, K.-L. Kompa: Science **288**, 824 (2000)
25. W.S. Warren, H. Rabitz, M. Dahleh: Science **259**, 1581 (1993)
26. A. Assion, T. Baumert, M. Bergt, T. Brixner, B. Kiefer, V. Seyfried, M. Strehle, G. Gerber: Science **282**, 919 (1998)
27. D. Meshulach, Y. Silberberg: Nature **396**, 239 (1998)
28. M. Schmitt, G. Knopp, A. Materny, W. Kiefer: J. Phys. Chem. A **102**, 4059 (1998)
29. A. Vierheilig, T. Chen, P. Waltner, W. Kiefer, A. Materny, A.H. Zewail: Chem. Phys. Lett. **312**, 349 (1999)
30. D. Oron, N. Dudovich, Y. Silberberg: Phys. Rev. Lett. **90**, 213902 (2003)
31. A. Tokmakoff, M.J. Lang, D.S. Larsen, G.R. Fleming, V. Chernyak, S. Mukamel: Phys. Rev. Lett. **79**, 2702 (1997)
32. R.A. Bartels, T.C. Weinacht, S.R. Leone, H.C. Kapteyn, M.M. Murnane: Phys. Rev. Lett. **88**, 033001 (2002)
33. T. Feurer, J.C. Vaughan, K.A. Nelson: Science, **299**, 374 (2003)
34. F.W. Deeg, M.D. Fayer: J. Chem. Phys. **91**, 2269 (1989)
35. A. Tokmakoff: J. Chem. Phys. **105**, 1 (1996)
36. M. Khalil, O. Golonzka, N. Demirdolven, C.J. Fecko, A. Tokmakoff: Chem. Phys. Lett. **321**, 231 (2000)
37. J.D. Eaves, C.J. Fecko, A.L. Stevens, P. Peng, A. Tokmakoff: Chem. Phys. Lett. **376**, 20 (2003)
38. Y.J. Chang, E.W. Castner: J. Chem. Phys. **99**, 7289 (1993)
39. Y.J. Chang, E.W. Castner: J. Phys. Chem. **100**, 3330 (1996)
40. H.P. Deuel, P. Cong, J.D. Simon: J. Phys. Chem. **98**, 12600 (1994)
41. K. Tominaga, K. Yoshihara: Phys. Rev. Lett. **76**, 987 (1996)
42. T.H. Joo, M.A. Dugan, A.C. Albrecht: Chem. Phys. Lett. **177**, 4 (1991)
43. L.J. Kaufman, D.A. Blank, G.R. Fleming: J. Chem. Phys. **114**, 2312 (2001)
44. W.T. Lotshaw, D. Mcmorrow, N. Thantu, J.S.Melinger, R. Kitchenham: J. Raman Spec. **26**, 571 (1995)
45. D. McMorrow, W.T. Lotshaw, G.A. Kenney-Wallace: IEEE J. Quantum Electron. **QE-24**, 443 (1988)
46. C.J. Fecko, J.D. Eaves, A. Tokmakoff: J. Chem. Phys. **117**, 1139 (2002)
47. M. Khalil, N. Demirdoven, O. Golonzka, C.J. Fecko, A. Tokmakoff: J. Phys. Chem. A, **104**, 5711 (2000)
48. M. Khalil, N. Demirdoven, O. Golonzka, C.J. Fecko, A. Tokmakoff: Chem. Phys. Lett. **321**, 231 (2000)
49. T. Hattori, A. Terasaki, T. Kobayashi, T. Wada, A. Yamada, H. Sasabe: J. Chem. Phys. **95**, 937 (1991)
50. K. Kamada, M. Ueda, T. Sakaguchi, K. Ohta, T. Fukumi: Chem. Phys. Lett. **249**, 329 (1996)
51. Y.X. Yan, E.B. Gamble, K.A. Nelson: J. Chem. Phys. **83**, 5391 (1985)
52. Y.R. Shen, N. Bloembergen: Phys. Rev. **137**, 1787 (1965)

7 Fundamental of Laser-Assisted Scanning Tunneling Microscopy (STM)

O. Takeuchi and H. Shigekawa

7.1 Introduction

In the previous chapters, we have discussed how we can make the temporal width of the currently shortest laser pulse even shorter. For the purpose, three key techniques are developed. Firstly, an ultrabroadband laser pulse was generated by using the self-phase modulation and/or induced phase modulation effect in a fiber and its phase and amplitude properties were theoretically studied. Secondly, a new measurement technique that can experimentally determine the spectral phase and amplitude of an ultrabroadband laser pulse with moderate power is developed as the modified SPIDER. Thirdly, active chirp compensation system for ultrabroadband optical pulses is developed with a computer-feedback-controlled spatial light modulator. With these techniques, a laser pulse with less than two optical cycles has been generated.

Such extremely short laser pulses, by themselves, improve the temporal resolution of ultrafast optical measurements that use the pulse as their light source. This is because, in general, the temporal resolution of such measurements is, by virtue of the pump-probe technique, only limited by the pulse width of their light source. Thus, shortening the laser pulse benefits all the ultrafast optical measurements.

In the rest of this book, we will concentrate our discussion on improving the spatial resolution of conventional optical measurements. It is not to be argued that the optical measurement techniques have their unique advantages over other measurement techniques. They are generally nondestructive, enable high energy resolution and are not interfered with by other signals. Above all, the picosecond/femtosecond time resolution that must be necessary for future device development can be only realized by the optical pump-probe measurements using ultrashort laser pulses. On the other hand, the spatial resolution of optical measurement is, in general, not very high. One can resolve features in 0.1 mm dimension with his/her eyes. An optical microscope will resolve sub-micron objects. As is well known, the resolution of an optical microscope is limited in the dimension of the wavelength. The development of scanning nearfield optical microscopy (SNOM) overcame this limitation with detecting non-propagating electromagnetic waves. The resolution of state-of-the-art SNOMs reaches several tens of nanometers. This is, however, not

sufficient for the research of future nanodevices such as self-organized nanostructures and molecular devices. In order to have even better resolution, we have been developing a very new technique, laser-assisted scanning tunneling microscopy (STM), the systematic exposition of which is the main theme of the second part of this book.

In this chapter, after reviewing the fundamentals of STM techniques, the possible setup to realize the laser-assisted STM and their difficulties will be discussed. Next, in Chap. 8, our effort to realize a noble characterization technique of nano band structure in nanoscale semiconductor structures is presented, which is based on the modulation of the laser assisted scanning tunneling spectroscopy. Chapters 9 and 10 will be devoted to the introduction of our effort for the development of femtosecond–angstrom technologies. Femtosecond time resolution of the ultrashort pulse laser and ångstrom spatial resolution of STM technologies will be successfully combined there.

7.2 Potentialities of Laser Combined STM

In order to demonstrate the high potential of laser-assisted STMs for basic research of next generation nanodevices, let us present our recent study of optical control of single molecule, briefly, which is investigated by combination of laser excitation and STM observation. Indeed, the understanding and control of molecular functions at a single-molecule level is extremely important in nanoscale science and technology. When performing SPM experiments under photoillumination, structural change due to optical control of a single molecule could be directly observed.

The study shown here is regarding the control and direct observation of the cis-trans photoisomerization of Azobenzen [1]. The Azo molecule is a typical photoactive isomer and has been widely studied because of its simple structure and reversible cis-trans isomerization under photoillumination. Irradiation with ultraviolet (UV) (∼350 nm) and blue (Vis) (∼440 nm) lights induces isomerization to metastable "cis" and stable "trans" conformations, respectively, as shown in Fig. 7.1. Schematic of the potential barrier is shown in Fig. 7.2 [2]. The absorption characteristic is easily controllable by the addition of polar groups on the Azo molecule. From these characteristics, the Azo molecule is promising for not only photoswitching and storage materials, but also photoactive biomaterials that, for example, control DNA hybridization.

The sample was prepared as following. Figure 7.3 shows the schematic structures of [4-(Phenyldiazenyl)phenyl]-*N*-(2-sulfanylethyl)carboxyamide (Azo) and *n*-dodecanethiol (C_{12}). C_{12} self-assembled monolayer (SAM) films were formed by dipping the Au(111) substrate into a toluene solution with C_{12} molecules. After rinsing to remove the physisorbed molecules, the C_{12}/Au system was immersed in a toluene solution containing Azo molecules, resulting in the formation of C_{12} SAM including isolated Azo molecules. Figure 7.4 shows a typical STM image of the Azo-embedded C_{12} film. Bright protrusions

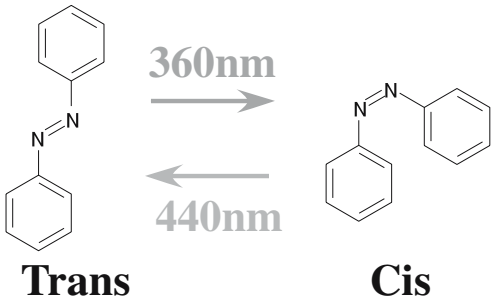

Fig. 7.1. Cis-trans photoisomerization of Azo-molecule

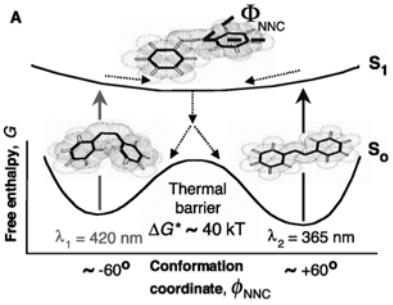

Fig. 7.2. Schematic of potential barrier in the photoisomerization of Azo-molecule

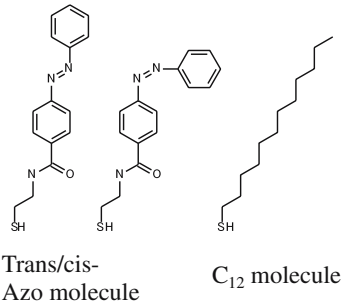

Fig. 7.3. Molecular structures of [4-(Phenyldiazenyl)phenyl]-*N*-(2-sulfanylethyl)carboxyamide (Azo) and *n*-dodecanethiol (C_{12})

correspond to the Azo molecules. A schematic of the isolated Azo molecular structure is shown in Fig. 7.5.

As is shown in the schematic of the experimental setup, Fig. 7.6, photoisomerization of the isolated Azo molecules was controlled by illumination with ultraviolet (UV) (325 nm) and visible (Vis) (440 nm) lights using a He-Cd laser during STM measurements. All STM images were obtained in N_2 atmosphere at room temperature using a Pt/Ir tip.

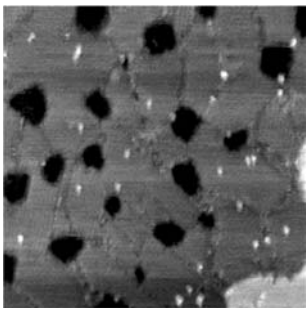

Fig. 7.4. STM topograph of Azo-embedded C_{12} film

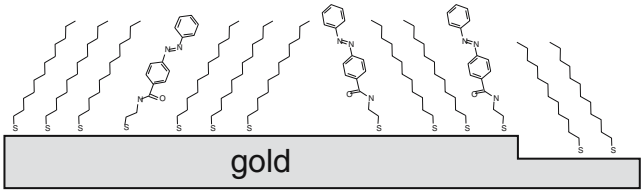

Fig. 7.5. Schematic of Azo-embedded C_{12} film

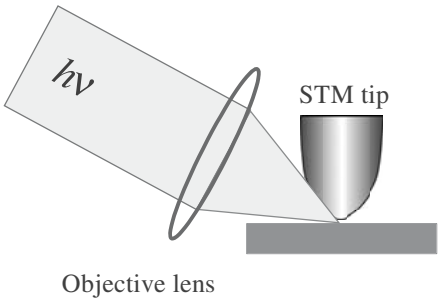

Fig. 7.6. Experimental setup of laser-assisted STM

Figure 7.7 shows a typical example of a series of STM images representing the cis-trans change in isolated Azo molecules induced by alternating UV and Vis photoillumination. The Azo molecules show cis and trans structures, as expected, under UV and Vis photoillumination, respectively.

High potential of the laser-assisted STM for the local structural analysis of materials is clear. Furthermore, in addition to the nanoscale observation of the light induced physical properties, lasers have been combined with STM to realize the selective and swift fabrication and structuring of the target materials in nanoscale range.

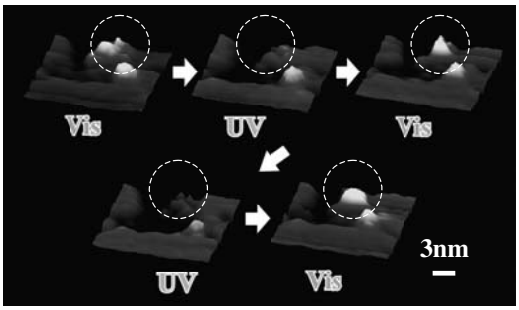

Fig. 7.7. Series of STM images showing the Azo molecule switching embedded in C_{12} film

7.3 Fundamental of Scanning Probe Microscopy

Scanning tunneling microscopy (STM) was developed in 1982 by Binnig and Rohrer [3], and is well known as a microscopy that can truly image *atoms*, as was demonstrated in their first paper to image the Si(111)-7×7 surface structure with atomic resolution. With further development of this technique, it has been providing the atom-resolved images of all kinds of conductive materials, such as metal surfaces, semiconductor surfaces and molecules adsorbed on conductive materials. Since only the scanning probe technique can give us information about the locally modulated structures, the high potential of this technique for the development of future nanoscience and technology is certain. Here we review the fundamental issues of the STM technique.

7.3.1 How to Visualize the Nanoscopic World

STM is one of the variations of so-called scanning probe microscopy (SPM). Today, various kinds of SPM have been developed and most of them provide nanometer to sub-ångstrom resolutions. In principle, an SPM measurement uses some nanoprobe that can acquire a particular local physical property of the sample. The physical property measured differs from one SPM to another, but one point is common for all SPMs; the sensitivity of the nanoprobes only ranges from sub-ångstrom to a hundred nanometers. Thus, when the nanoprobe is scanned over a region of the sample surface with an adequate precision, one can map the physical property on the sample surface. As shown in Fig. 7.8, the set of measured values is often visualized with some color (or gray) scale, as a function of the position of the nanoprobe on the sample surface, and it is shown as the *image* of the sample surface observed by the SPM.

As can be seen, the images obtained in such methods are not directly related to the corrugation of the sample surface. It is always a map of the physical property. However, since the sensitivity of the nanoprobes only reaches a

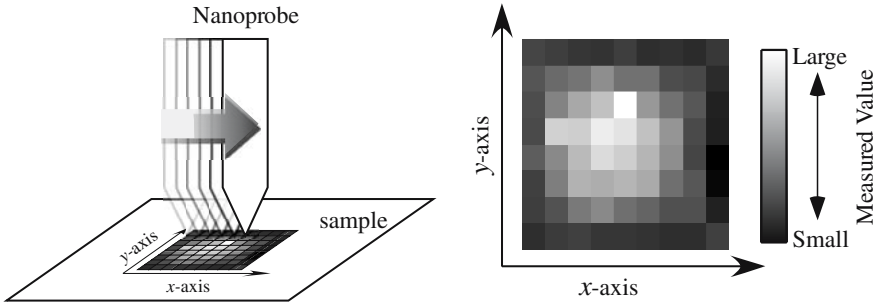

Fig. 7.8. Schematic of SPM imaging

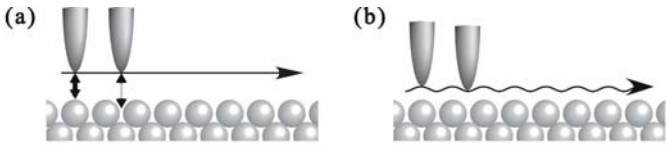

Fig. 7.9. Two different working modes in SPM imaging: (**a**) Constant height mode and (**b**) constant value mode

very short distance, the measured value diminishes rapidly when the probe is further from the sample. So, when scanning the probe in parallel to the averaged slope of the sample surface, we observe larger signals when the probe is on bumps of the sample surface and smaller signals above dips. The situation is illustrated in Fig. 7.9(a). As a result, the obtained images more or less represent the corrugation of the sample surface unless a very inhomogeneous sample is measured because, without inhomogeniety, the probe-sample distance dominates the contrast in the measured images. Of course, any inhomogeneity of the sample also affects the images. Interpretation of SPM results on such samples should be done carefully.

There is another, and often better, way of obtaining sample corrugation by SPM: plotting the isovalue surface of the physical property over the sample surface. In these measurements, the probe-sample distance is controlled by a feedback circuit to maintain the measured value of the sample property equal to some reference value continuously during the scan. Then, the trajectory of the probe motion is recorded as the isovalue trace along the scan line as illustrated in Fig. 7.9(b). The probe displacement perpendicular to the surface is plotted in a color scale as a function of the lateral position of the probe. This method also assumes the measured signal mainly depends on the probe-sample distance. Indeed, this assumption is often valid and, in such cases, the tip–sample distance is kept constant during the scan and the obtained images allow us to know the exact morphology of the sample surface with precise height information. The measurement method shown in Fig. 7.9(a) is often called as "constant height" mode and that in Fig. 7.9(b) as "constant value"

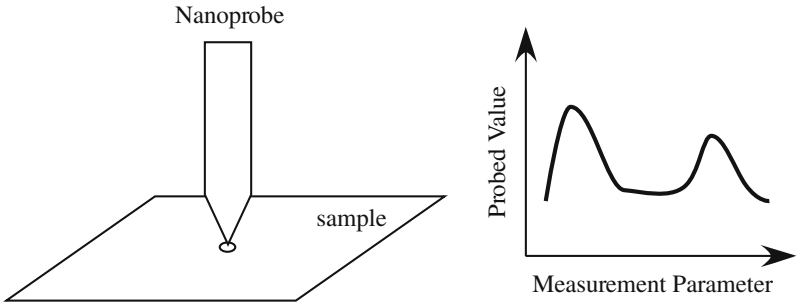

Fig. 7.10. Schematic of scanning probe spectroscopy (SPS)

mode. The "constant value" mode is better for most applications because it provides the actual surface morphology while avoiding crashing the probe into the sample surface with large corrugations.

Besides its imaging ability, the spectroscopic measurement is also very useful in SPM technology. This time, the measurement is simple. The SPM probe is fixed at a specific point on the surface with a specific separation between the probe and the surface as shown in Fig. 7.10. Then the sample property is probed while some measurement parameter is swept over a range of values; the parameter can be the bias voltage between probe and sample, the tip-sample distance, the direction or magnitude of magnetic field, the intensity of the optical excitation, etc. In any case, the sample property at well defined sampling point can be detected by the nanoprobe as a function of the parameter.

In both imaging and spectroscopy using SPM, the excellent spatial resolution down to subatomic level is the most prominent attribute compared to that of other experimental methods. Then, what determines the spatial resolution in these measurements? Two factors, how rapidly the sensitivity of the probe diminishes with the probe-sample distance and how precisely the relative position of probe and sample can be controlled, dominate the resolution. The former is obvious. If the probe sensitivity extends a long distance, such as several microns, no atomic resolution can be expected. The radius of the probe apex together with the physical principle, with which we pick up the signal, determines the range of sensitivity. The latter is also easy to understand. If the tip position fluctuates during measurement, the image will become diffuse. However, fluctuation of the probe position does not only result in a lesser spatial resolution. Since the probe signal is very sensitive to the tip-sample distance, fluctuation of tip position perpendicular to the sample surface also causes intolerable amplitude of noise in the detected signal. In the worst case, too much fluctuation will crash the tip apex into the sample surface. Thus, good SPM instruments are carefully designed to insulate the microscope from the external vibrations both from the floor and from the acoustic environment, and to avoid thermal fluctuation of the tip-

sample distance by allocating multiple materials to compensate the thermal expansion.

7.3.2 Tunnel Current as a Probe Signal

In a conventional STM experiment, a well sharpened metal tip is used as the nanoprobe. A finite bias voltage is applied between this metal tip and the sample surface. Then the tip and surface are brought close to contact. The tunnel current flowing between the tip and the sample is measured as the probe signal. Typical measurement conditions are tunnel current I_t of 1 nA at sample bias voltage V_s of 50 mV for a metallic sample and $I_t = 1$ nA at $V_s = 1.5$ V for a semiconductive sample. As described below, the amount of tunnel current represents "the amount of the spatial and energetic overlap between the electron states of the STM tip and that of the sample" and "to which energy level the electron states are filled by electrons (local Fermi level)". Thus, STM provides both the morphology of the sample surface and its electric properties.

The tunnel effect is defined in a textbook as a phenomenon where an electron in a low energy state penetrates an energy barrier that is higher than the energy of the electron and appears on the other side of the barrier. In a STM setup, the electron at first exists either in the STM tip or in the sample, depending on the polarity of the bias voltage. The energy of the electron is smaller than the vacuum level at least by the work function of the tip/sample material. Thus, the gap between the tip and the sample surface, the tunnel junction, that is sometimes filled with some gas or liquid, works as the energy barrier. And the other side is again the sample or the tip. The situation can be illustrated in a schematic like Fig. 7.11.

The lateral axis denotes the spatial distance measured perpendicular to the sample surface and the vertical axis denotes energy level for electrons. The three regions are, from left to right, the metallic tip, the tunnel gap and the sample. In the regions in the tip and the sample, there are plenty of energy states for electrons, which form the band structures. The electron states are occupied by electrons up to the Fermi levels and those above the Fermi levels are empty. The Fermi levels of the tip and the sample are shifted by the amount of eV_s, with the elementary charge e and the sample bias voltage V_s. In this schematic, both the tip and the sample are metallic.

In the most cases, the electron tunnels through energy barriers elastically. In other words, the electron does not gain or lose its energy during the tunnel process. Thus, only when the electron state is filled on one side and is empty on the other side at a same energy level, the electron in the filled state can tunnel into the empty state with a finite probability. At zero temperature, this condition stands only in the case when the energy state is between energy levels between the two Fermi levels, as is shown in Fig. 7.11. At a finite temperature, however, the amount of filled/empty states can be obtained by multiplying Fermi functions to the density of state. Thus, in a simple model

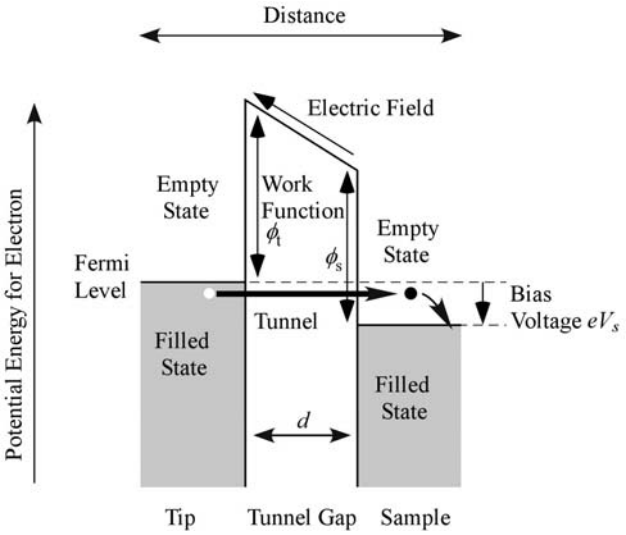

Fig. 7.11. Energy diagram of STM measurement

with WKB approximation, the total tunnel current I_t can be expected as the next rather inaccurate but useful form:

$$\begin{aligned} I_t \propto & \int_{-\infty}^{\infty} f(E)\psi_t(E)\{1-f(E+eV_s)\}\psi_s(E+eV_s)T(E,eV_s,d)dE \\ & -\int_{-\infty}^{\infty}\{1-f(E)\}\psi_t(E)f(E+eV_s)\psi_s(E+eV_s)T(E,eV_s,d)dE \end{aligned} \tag{7.1}$$

$$= \int_{-\infty}^{\infty}\{f(E)-f(E+eV_s)\}\psi_t(E)\psi_s(E+eV_s)T(E,eV_s,d)dE, \tag{7.2}$$

with the Fermi function f, the charge of an electron $-e$, the electronic state density of tip ψ_t and the sample ψ_s, the tunnel transmission coefficient T and the tip–sample distance d. Note that the filled state density in the tip is represented by multiplying Fermi function to the density of state as $f(E)\psi_t(E)$ and the empty state density in the sample is represented as $\{1-f(E-eV_s)\}\psi_s(E)$. Thus, the first term in (7.1) denotes the current flowing from the sample to the tip (i.e., electrons tunneling from the tip to the sample), while the second term denotes the current flowing in the opposite direction. The transmission coefficient T will be a function of the effective energy barrier height $(\phi_t+\phi_s+eV_s)/2-E$ and the barrier width d:

$$\begin{aligned} T(E,eV_s,d) &= T(\{\phi_t+\phi_s+eV_s\}/2-E,d) \\ &= \exp\left(-2d\sqrt{2m_e}/\hbar\sqrt{\{\phi_t+\phi_s+eV_s\}/2-E}\right) \end{aligned} \tag{7.3}$$

with the work functions of the tip, ϕ_t and the sample, ϕ_s, Planck's constant over 2π, $\hbar$ and mass of the electron m_e. This equation tells us that the

tunnel coefficient decreases drastically when the barrier height or barrier width (tip–sample distance) increases. With assigning typical parameters for STM conditions, it shows that the tunnel current is reduced by a factor of ten when increasing the tip-sample distance by only a few angstroms. The strong dependence of tunnel current on the tip–sample distance gives the excellent spatial resolution of STM.

In a more precise description, the transmission coefficient T is no longer independent of individual electron states. Bardeen described the tunnel current as:

$$I_t = \frac{2\pi e}{\hbar} \sum_{\mu\nu} \{f(E_\mu) - f(E_\nu + eV)\} |M_{\mu\nu}|^2 \delta(E_\mu - E_\nu) \tag{7.4}$$

$$M_{\mu\nu} \equiv \frac{\hbar^2}{2m} \int_{S_0} d\mathbf{S} \cdot (\psi_\mu^* \nabla \psi_\nu - \psi_\nu \nabla \psi_\mu^*) \tag{7.5}$$

with the eigen functions of the tip ψ_μ and the sample ψ_ν calculated without counting the interaction between them, element of the transition matrix $\mathrm{M}_{\mu\nu}$ arbitrary surface that divides the tip and the surface $\mathbf{S_0}$ and the delta function δ. Here we know the tunnel coefficient is indeed determined by the spatial overlap of tip and sample electron states at the same energy level. The exponential decay of the tunnel coefficient in (7.3) comes from the exponential decay of local density of states on the outside of tip and sample materials.

7.3.3 Scanning Tunneling Spectroscopy

As we learned in the previous section, the tunnel current depends on the spatial and energetic overlaps of local density of states (LDOS) exuding out from tip and sample surfaces, together with the charge distribution in these electron states. Experimentally, the former depends on the tip–sample distance, local corrugation and LDOS distribution on the sample surface and effective bias voltage and the latter depends on the local Fermi level. In other words, STM can detect all these properties of sample surfaces at subangstrom spatial resolution. There have been a lot of studies using STM, which studied various phenomena that occurs on conductive surfaces, such as thin film growth, molecular adsorption, chemical reaction, electron standing wave, charge density wave, thermodynamics of vortex at the surface of high-T_c superconductors.

In addition to using STM for imaging, we can also do spectroscopy with an STM instrument. The method is called scanning tunneling spectroscopy (STS). From (7.2), spectroscopic data can be obtained as

$$\begin{aligned}(\mathrm{d}I/\mathrm{d}V) \propto\ & e\rho_t(0) \cdot \rho_s(eV) \cdot T(eV, eV, z) \\ & + \int_0^{eV} \rho_t(E - eV) \cdot \rho_s(E) \cdot \frac{\partial T(E, eV, z)}{\partial V} \mathrm{d}E\end{aligned} \tag{7.6}$$

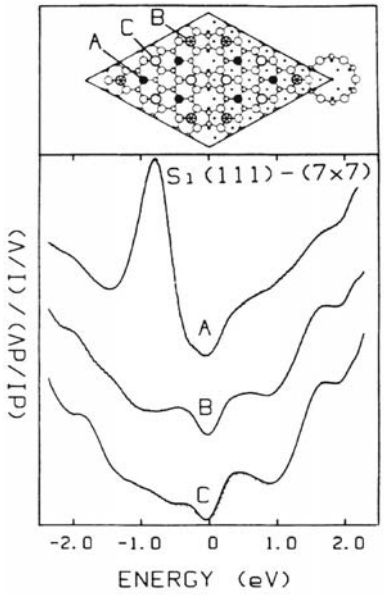

Fig. 7.12. STS curves measured on different adatoms on Si(111)-7×7 clean surface

Very often, the normalized $(dI/dV)/(I/V)$ form is used to reduce the effect of the tunnel coefficient T and the second term to extract the factor $\rho_t(0) \cdot \rho_s(eV)$. A noteworthy point is that although only filled or empty state is studied by conventional spectroscopic techniques, both of the filled and empty states near the Fermi level can be analyzed by STS.

Figure 7.12 shows an example of STS measurement of a Si(111)-7×7 clean surface [4]. Three spectra corresponds to the probe position at (A) rest atom, (B) corner adatom and (C) center adatom. These spectra are clearly distinguishable reflecting the different electronic environment of each Si atom.

7.3.4 Characteristic of the STM Measurement System

Tip Control: Circuit Response and Thermal Noise

In principle, what an STM instrument does is to move the STM tip over the sample surface and to detect the tunnel current. Thus, the STM measurement requires two fundamental techniques: 1) precise control of the relative positioning between the STM tip and the sample surface and 2) noiseless detection of tunnel current that ranges from subpicoamperes to a hundred nanoamperes.

Regarding to the latter issue, STM electronics should also supply the bias voltage and power for the preamplifier in a stable manner. This is, today, not a difficult task. To have suitable balance between the time constant for the

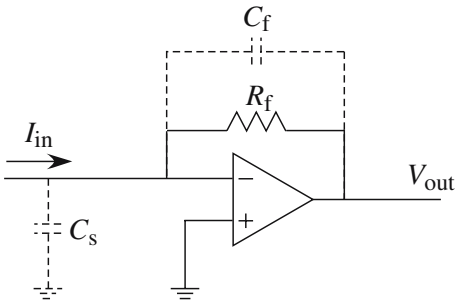

Fig. 7.13. Circuit diagram of an STM current-voltage converter

detection and the noise level of the signal is considered more important. This section is devoted to a brief overview of this point.

STM preamplifier generally has an I/V converter circuit with an operational amplifier (OP amp.), as is shown in Fig. 7.13, in its first stage. This circuit ideally has a relation of $V_{\text{out}} = -I_{\text{in}}R_f$ between the input current I_{in} and the output voltage V_{out}, where R_f is the feedback resistance. However, in the actual circuits, its transfer function depends on the signal frequency due to the fact that the characteristic of the OP amp. is not ideal for the high frequency region. In the case of STM operation, the characteristic of the preamplifier influences the closed loop gain of the feedback system for the z-piezo. Therefore, the preamplifier gain in the high frequency region is designed to decrease like a first order low pass filter with a certain time constant t_c. In order to realize this condition, a bypass condenser C_f is located in parallel to R_f as shown in Fig. 7.13 to keep the phase characteristic at high frequency region behaving properly. In addition, since the input impedance of the OP amp. is finite in the high frequency region, the stray capacitance C_s at the tunnel gap and signal-line also influences the response of the circuit. The time constant of the actual circuit with a properly adjusted frequency characteristic is generally given by

$$t_c \sim 10\mu\text{s} \cdot R_f/100G\Omega. \tag{7.7}$$

Therefore, in order to realize the fast response of the preamplifier, multiple stage amplification is adopted. For instance, a two stage amplifier with the first amplification of $\times 10^5$–10^6 and the second amplification of $\times 10$–100 realizes the total amplification of $\times 10^7$–10^8 with much shorter response time compared to a single stage preamplifier.

Furthermore, when four stages of $\times 100$ amplification elements are combined, the frequency response beyond 1 GHz range is expected for a total amplification of $\times 10^8$. This type of amplification is, however, not realistic because of the disadvantage of its high noise level. In principle, the lowest thermal noise level produced at a resistance R at temperature T is theoretically given as

$$\Delta V = \sqrt{4kTRB}, \tag{7.8}$$

with the Boltzman constant k and the bandwidth of the amplifier B. In a current–voltage converter circuit, this noise level governs the lowest noise level of the V_{out} signal. Since ΔV is proportional to $R^{1/2}$ and the magnification of the amplifier is proportional to R, the noise level converted into the input current scale is proportional to $R^{-1/2}$. Hence, a $\times 100$ amplifier has 10^3 times larger noise level than a $\times 10^8$ amplifier.

In consideration of the trade-off between the circuit response and noise level, $\times 10^6$–10^8 amplifications are used for the first stage, which results in the cut-off frequency of 1 MHz–10 kHz (1 µs–100 µs). Apparently, STM is not a fast measurement technique by itself.

Stability of the Tip Position: Thermal Drift and Acoustic Noise

The three dimensional STM tip positions are controlled by the piezo elements. A scan area of 200 nm–2 µm (x, y directions) is covered by applying $\pm 100 \sim 200$ V to the piezo device. The change in the piezo length is usually 1–10 nm/V. The motion in the z-direction, perpendicular to the sample surface, is controlled by the piezo elements with less ratio in order to have more precise control. When the tip position is moved a large distance, such as $\sim$1 µm, hysteresis of the piezo element may influence the positioning, however, for the range of several tens of nm, accurate control of the tip position can be realized assuming proportional dependence between tip position and the applied voltage.

The controllability of the tip position described above is in the short time scale. Namely, to keep the tip position at the same point longer than several tens of seconds is a different issue. Due to the thermal drift and creep of piezo elements, change in the relative position between the STM tip and sample surface in the scale of nano and angstrom range is inevitable. This problem is reduced for the low temperature system ($T < 100$ K), as is well known.

Fluctuation in the tip–sample distance is also an important factor for the analysis of the local structures. In addition to the feedback condition, acoustic noises from the floor or air influence the stability of the tip sample distance. In order to get rid of the effects, STM is generally set on a certain vibration isolation system, and has a hood against acoustic noise from the air.

The influence of the vibration isolator is represented by the two-spring oscillator model as shown in Fig. 7.14. Although the STM head is generally designed to be rigid, it is impossible to form a resonance-free structure and it must have some mechanical resonances. Usually, the lowest resonance frequency f_1 exists at several kilohertz. Thus, without a vibration isolator, the transfer function from floor vibration to tip–sample distance, $T_1(f)$ is 1 at $f > f_1$, has a peak at $f = f_1$ and decreases rapidly at $f < f_1$, as shown in Fig. 7.15(a). On the other hand, the resonant frequency of the vibration

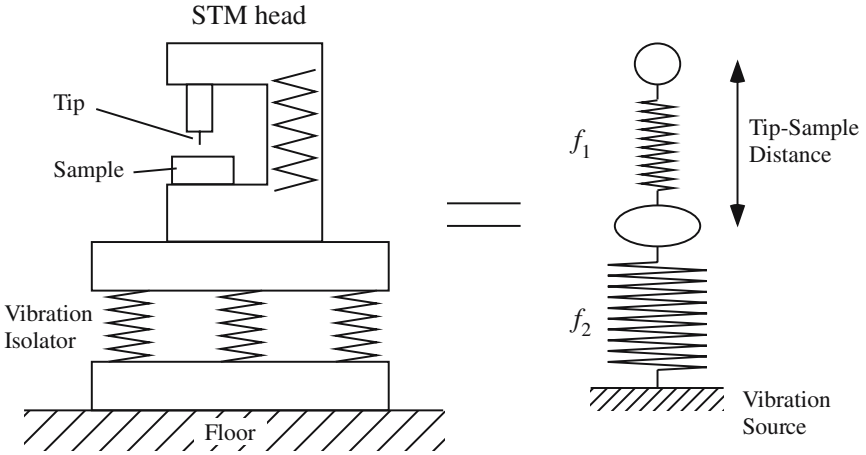

Fig. 7.14. Double spring model for vibration analysis of an SPM

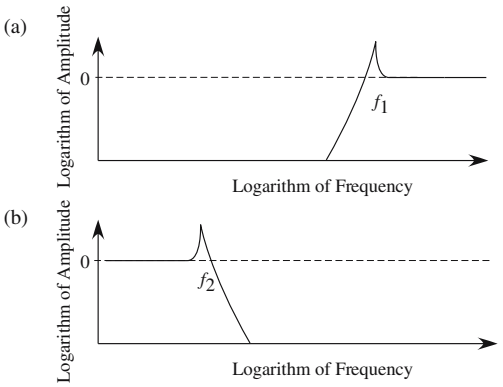

Fig. 7.15. Transfer functions of vibration (**a**) of vibration isolator and (**b**) of STM head

isolator f_2 is generally designed as low as possible. The transmission function from the floor to the top of the vibration isolator, $T_2(f)$ is 1 at $f < f_2$, has a peak at $f = f_2$ and decreases rapidly at $f > f_2$, as shown in Fig. 7.15(b). Thus, when the two resonant frequencies f_1 and f_2 are far apart, the composite transfer function from the floor to the tip–sample distance that is obtained by multiplying T_1 and T_2, can be largely suppressed in particular at the frequency $f_2 < f < f_1$. In particular, in the case of STM for a vacuum, since the structure of the STM head becomes complicated in order to enable in-vacuum exchange of the tip and the sample, its resonant frequency becomes low. Thus, reduction of the resonant frequency of the vibration isolator is very important. The resonant frequency of a nicely designed vibration isolator is about 1–5 Hz.

For the development of the laser-assisted STM, however, the lowering of the isolator resonant frequency brings another problem; aiming. When the sample surface is illuminated to study the photo-induced effect, the light spot is focused to just below the tip position in order to get rid of the thermal effect. Even in the case of the UHV-type STM, it is possible to focus the light spot down to $\sim$10 μm by using the combination of the lenses and laser light source. In such cases, if the STM head is on the very soft vibration isolator, the spot position is easily influenced by the oscillation of the isolator. In order to avoid the problem, the total system of STM and light source should be set on the same vibration isolator. By this procedure, the light spot size can be reduced to $\sim$100 μm, unless very strong light intensity is needed.

7.4 Previous STM Studies in Various Fields

In this section, we review some examples of STM studies from various nanoscience fields, for the purpose of understanding the wide applicability of the STM technique.

Figure 7.16(a) shows an STM image of a low dimensional organic conductor, $\beta-(\text{BEDT-TTF})_2\text{PF}_6$ [5–7]. Two kinds of molecular rows were observed along c-axis, as indicated by C and A in Fig. 7.16(a). These rows should be, however, identical if the bulk structure is simply terminated by the surface. This suggests that the surface is reconstructed. Reconstruction of the surface structure from the ideal bulk terminated structure is generally observed for inorganic crystals. The surface reconstruction of an organic crystal was confirmed for the first time. Furthermore, the reconstruction of the molecular shape was also confirmed by the same experiment. Figure 7.16(b) shows the spatial distribution of density of states for the molecular structure

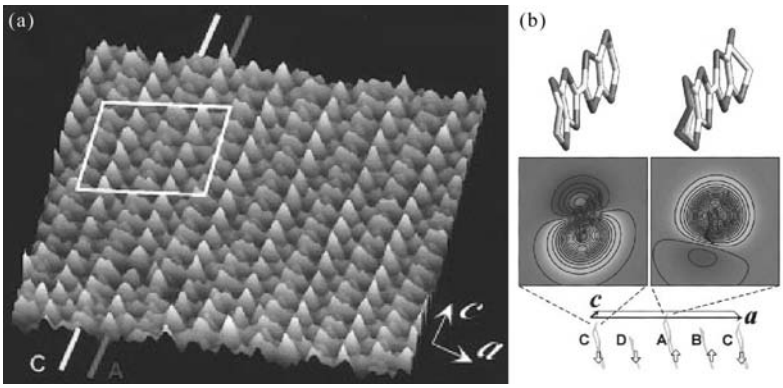

Fig. 7.16. (**a**) Surface structure of $\beta-(\text{BEDT-TTF})_2\text{PF}_6$ observed by STM, (**b**) theoretically predicted density of states for two different molecular conformations

with two different conformations. These results reproduce the experimentally-obtained two molecular features on this surface. Although self-assembled monolayer (SAM) has been attracting researchers' interest as a technique of self-organization, this result strongly indicates the importance of the interactions between molecular elements in order to realize the desired macroscopic functions. The detailed analysis of intra molecular structures is not so easy by the conventional methods. When modulation is caused by the local structures such as defects or surface steps, its analysis becomes almost impossible except through the STM technique.

By combining low temperature experimental techniques with SPM, physical properties in materials such as electronic structures inducing Kondo effect, super conductivity and low dimensional characteristics of materials, have been analyzed with atomic spatial resolution in deeper levels [6]. Figure 7.17 shows an example of STM study on the charge density wave (CDW) observed on the surface of $\beta-(\text{BEDT-TTF})_2\text{PF}_6$ [6]. Instead of the 2 kF CDW state along the c axis which appears in the bulk state, 3, 4 and 5 fold CDWs were observed on the surface as some of them are shown in Fig. 7.17. Instability of the charge density wave in organic material surfaces had been a controversy for a long time. The STM study suggested the answer to the question. In the bulk state, there is a considerable charge transfer between BEDT-TTF molecule and PF_6 molecule. Since the topmost molecules at the surface do not have the other molecule on the vacuum side, however, the charge transfer is incomplete for these molecules. Hence, the Fermi surface of the surface layer becomes different from that of the bulk state as shown in Fig. 7.18, resulting in the appearance of the different and unstable CDWs on the surface. Since such CDW states are unstable and observed locally at the molecular defects and steps, it had been difficult to analyze the structures without SPM techniques.

Recently, the local band structural modulation of a carbon nanotube (CN) peapod was successfully demonstrated by using STM [8]. This modulation is also a very locally modulated structure induced by the C_{60} introduced inside the CN.

As an example of the study of adsorbates, Fig. 7.19 shows a typical STM image of Kr atoms adsorbed on Si(111)-7×7 surfaces obtained at 6 K [9, 10]. With the analysis of spatial distribution of the Kr atoms, existence of a long-range interaction between Kr atoms was suggested. The adsorption of the first adatom modulates the substrate property slightly and the adsorption of the next adatom is affected by the modulation, which results in the correlation between Kr adsorption sites. If the adsorbates' distribution were periodic, the surface structure could be analyzed by diffraction methods. When the structure lacks long range periodicity, like the present case, SPM is the only available method to analyze such surfaces.

The very initial nuclear formations and stability of the local surface structures such as structures in phase transitions, and adsorbate growth on semiconductor or metal substrate surfaces widely attract attention from both

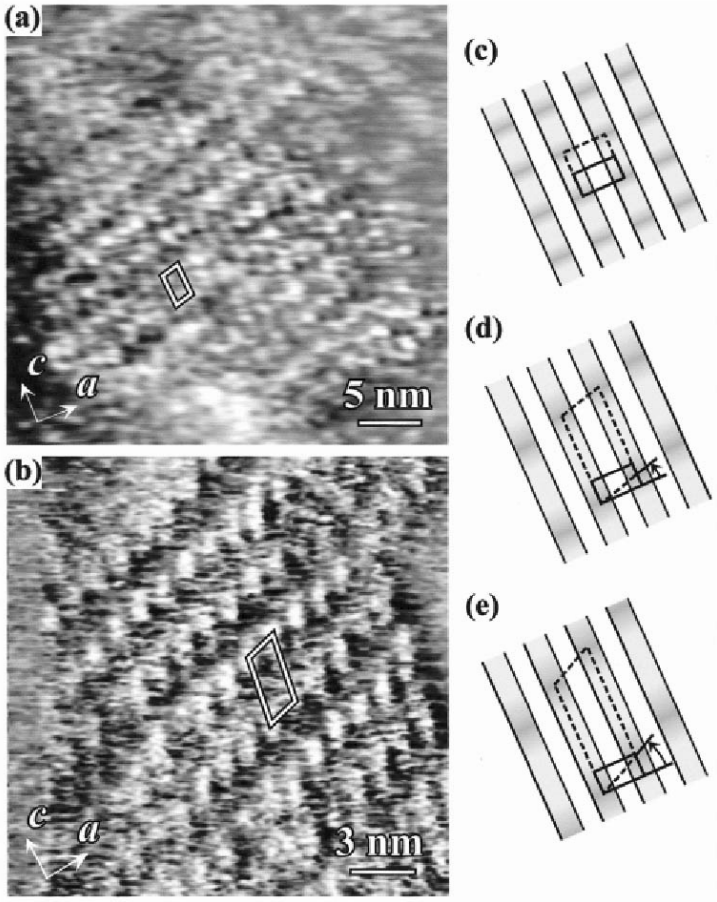

Fig. 7.17. STM images of two different CDW phases observed on $\beta-$(BEDT-TTF)$_2$PF$_6$ surface at 285 K and their schematic moldels of (**c**) bulk CDW state, (**d**) that observed in (**a**), that observed in (**b**). The black rectangles indicate the unit cells of surface structure while the dotted rectangles indicate the unit cells of CDW

fundamental and practical points of view [11–15]. And these local structures can also be analyzed by the technique of SPM.

As an example, Fig. 7.20 shows a schematic for the analysis of the flip-flop motion of an Si(100) dimer structure. Since this material is an essential element for present and future industrial nanodevices, understanding of its surface property is indispensable. On the Si(100) surface, neighboring two Si atoms form a dimer structure, and the dimer plays an extremely important role in determining the characteristic properties of the surface [16]. A dimer has two metastable conformational positions and flip-flop between them at

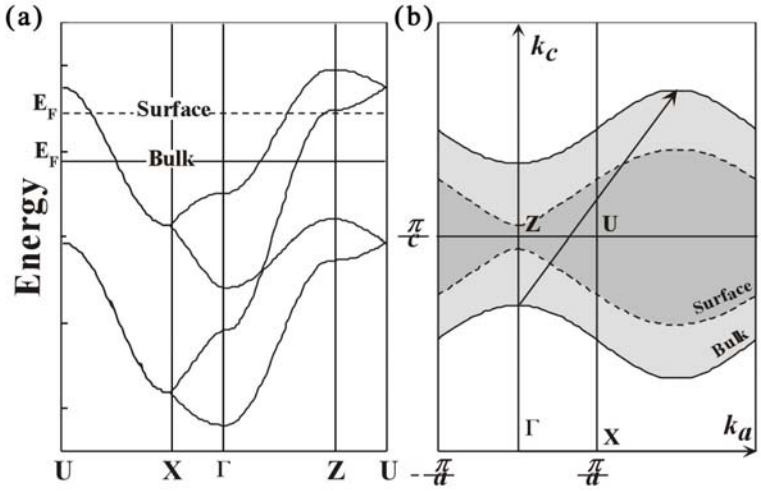

Fig. 7.18. (**a**) Band filling of the surface and bulk states of $\beta-(\text{BEDT-TTF})_2\text{PF}_6$ and (**b**) their Fermi surfaces

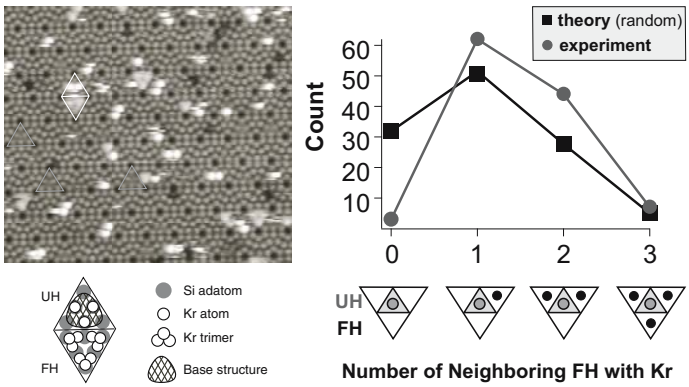

Fig. 7.19. STM observation on Kr/Si(111)-7 × 7 surface: STM topograph (upper left), structural model (lower left) and the analysis of the adsorbate distribution (right)

a certain frequency depending on the local electronic and elastic conditions surrounding it. Therefore, analyzing the flip-flop motion at a single dimer level gives us very important information which can not be obtained by the conventional techniques. In the study, the flip-flop frequency was analyzed by hovering the STM tip above the one of the two Si atoms in a dimer and measuring the change in the tunneling current as a function of the time, as Fig. 7.21. The flip-flop motion causes the change in the height of the Si atom under the STM tip, which results the change of the tip-atom separation so

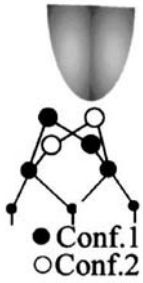

Fig. 7.20. Schematic of hovering STM experiment [17]

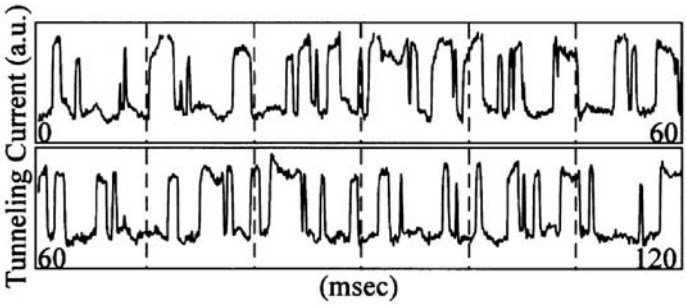

Fig. 7.21. Flip-flop motion of silicon dimer on Si(001) at 70 K observed in STM tunnel current signal [17]

as the change in the tunnel current. From the statistical analysis of the flip-flop frequency, the very local potential for the motion of a single dimer, in the order of 10–100 meV, can be obtained, which can be related to the local electronic and elastic structures [17].

In addition, by applying the higher voltage between the STM tip and sample, the dimer flip-flop motion can be induced in the local area on the surface. STM observation of the surface following the modification also gives us the information about the surface dynamics in a visual form [18, 19]. This technique can be applied also for the analysis of the conformational change of a single molecule [1].

As will be explained later in this book, local spectroscopy is also possible by STM. From the results of spectroscopic analysis of Xe adsorbates on Cu(111) surface, modulation of the band structure of the substrate due to charge transfer with the adsorbed layer was clearly shown [20, 21], even though the rare gas atoms are generally very inert due to their closed shell electronic structures.

Recently, single molecular observation is performed by several techniques, but in order to understand and realize the functional materials at a single molecular level, detailed study of the intramolecular structure is important

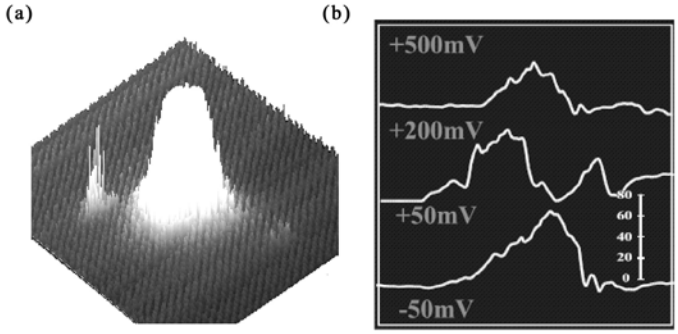

Fig. 7.22. (**a**) An STM image of Si nanoparticle on HOPG and (**b**) its cross sections at different bias voltages

even for the single molecular case. Figure 7.22 shows an STM image of a Si nanoparticle, and its cross sections at different bias voltages. Since an Si nanoparticle is emissive, it is expected to be a future nanoscale optical element.

The figure clarifies that an Si nanoparticle is not homogeneous and has internal structure in its local density of electron state. Furthermore, the cross sections at different bias voltages have different structures as shown in Fig. 7.22(b). As is well known, since STM images at different voltages reflect the local density of electronic states at the different energy levels, the observed results indicate that there exist different distributions of local electronic structures. This example clearly shows the high potential of STM for the analysis of intrananostructure/intramolecular property of nanodevices.

In the case of more complex materials such as functional polymers, understanding of the molecular function on the basis of the molecular structures becomes more difficult despite its importance.

For example, π-conjugated polymers have been developed as advanced materials for photonic or electronic applications. If the π-conjugated polymer chain can be controlled in the higher order structure, novel functions at the molecular level will become available due to the characteristic π-electron system. Many studies confirming the fact that a π-conjugated polymer has a helical structure have already been completed. Most of these studies have provided us with data on molecular aggregates or data on the average of many molecules. Although we now understand that the main chain of the polymer takes the form of a helix, does one chain have both right- and left-handed helices? What is the ratio of the right-handed helices to the left-handed ones? What about the regions where the helix is reversed and how does it dynamically change? The answers already provided to all these fundamental questions have been based only on conjecture. Therefore, it is necessary to establish a technique that can determine the structure at the single-molecule level in order to achieve the above-mentioned objective.

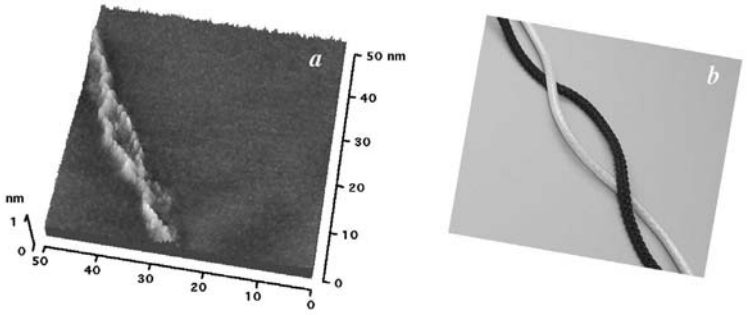

Fig. 7.23. STM image of [(-)-poly(MtOCAPA)] and its schematic model

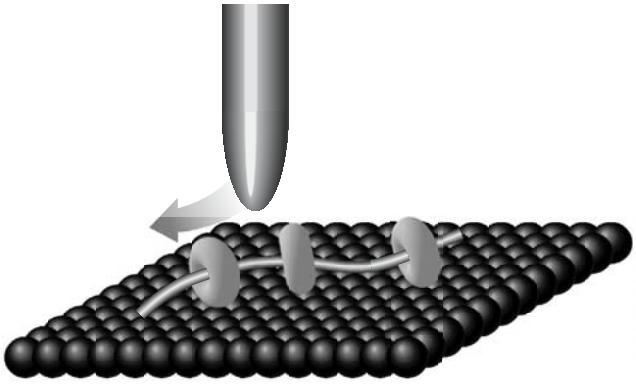

Fig. 7.24. STM manipulation of *molecular necklace*

Figure 7.23 shows an STM image of a π-conjugated polymer, an optically active polyphenylacetylene bearing menthoxycarbonylamino groups [(-)-poly(MtOCAPA)]. A hierarchical structure such as the presence of a quaternary structure was clearly observed with the fact that the main chain of the (-)-poly(MtOCAPA) was flexible in spite of the π-conjugated system.

We have seen the potential of STM to visualize nanoscale materials with atomic resolution, but there is another extremely noteworthy point, i.e., a technique for an atomic and molecular manipulation by STM. Since Eigler's pioneering research, STM and related techniques have been recognized as the most powerful tools for the manipulation of atoms and molecules on the surfaces. The possibility of developing a molecular counting device was demonstrated by repositioning C_{60} molecules along the steps of a Cu metal surface [22]. Here, the selected α-cyclodextrin (CyD) molecule(s) in the molecular necklace, with the structure of polyrotaxane, was reversibly shuttled using a STM [23] as schematically shown in Fig. 7.24.

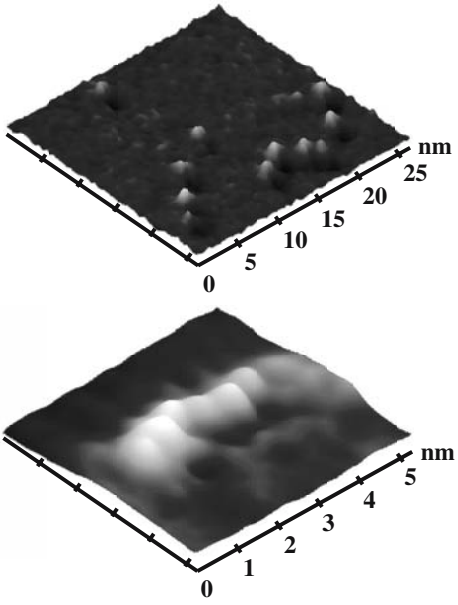

Fig. 7.25. STM observation of *molecular necklace*

In previous manipulation of atoms and molecules using a STM, strictly controlled conditions (ultrahigh vacuum (UHV), low-temperature (e.g., liquid He temperature), and/or specifically structured substrates) were required. However, the present manipulation of α-CyDs is expected to be stable in air at room temperature, mainly due to the characteristic structure of the polyrotaxane.

Figure 7.25 shows a typical STM image of the molecular necklace on a MoS_2 substrate. As schematically shown in Fig. 7.24, the main chain consisting of a poly(ethyleneglycol) (PEG) molecule runs along the surface of the substrate, and the α-CyDs lie with their longitudinal axis parallel to the surface. The rotaxane structure of the molecular necklace is clearly visualized on an atomic scale.

Then, one of the α-CyDs in the molecular necklace was mechanically pushed by the STM tip along the main chain of PEG, as has been performed previously to manipulate atoms/molecules on the substrate surfaces. An example of the shuttling is shown in Fig. 7.26. The images were acquired before and after each manipulation, respectively. The target α-CyD molecule (designated by the arrow in Fig. 7.26) was moved by the tip-sweep from right to left and vice versa. Since the PEG chain is railed diagonal in these images, the target α-CyD stably moved in the direction along the chain.

As will be explained in detail later, molecular structure and even chemical reactions can be manipulated by STM using the inelastic tunneling processes.

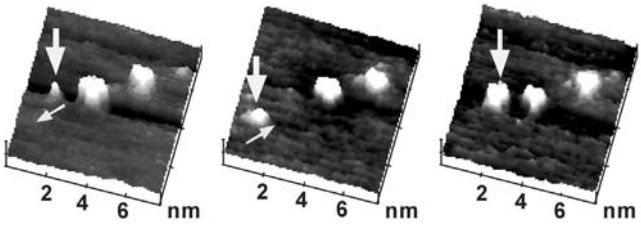

Fig. 7.26. Manipulation of a CyD molecule in a molecular necklace

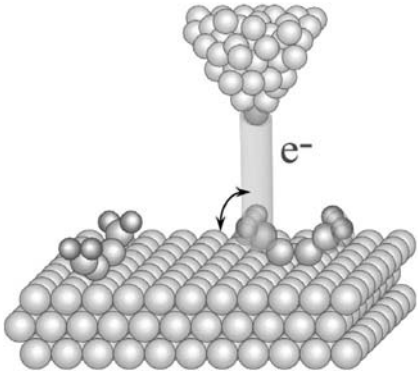

Fig. 7.27. Excitation of molecular vibration by inelastic tunnel effect

The excitation effect of a selected vibrational mode can be investigated by the process with atomic resolution as schematically shown in Fig. 7.27. A selective excitation of a specific vibrational mode may be realized and analyzed by combining the excitation of the molecule with THz pulse trains and the analysis with STM.

As has been shown, locally modulated inhomogeneous structures can be investigated only by the technique of STM. In fact, STM has been playing important roles in the scientific and technological development until now. Therefore, for the future development of nano-scale based functionalities of materials, exploring and constructing the world by STM is undoubtedly one of the most important and promising key technologies.

7.5 Development of Laser-Assisted STM

7.5.1 Performance of Optical Measurements

Here, we consider the performance of conventional optical measurements in comparison with STM. The simplest optical measurement is looking at objects by eyes. We can resolve 0.1 mm separation and distinguish slight differences in color, i.e., wave length of reflected/transmitted light. With using

optical microscopy, the spatial resolution can be improved down to sub micrometers. This resolution is good for looking at cells but never for looking atoms or molecules. The ideal resolution is limited by numerical aperture (NA) and the wavelength. We can look at individual molecules by an optical microscope with dispersing molecules very dilutely. Then, molecules are well separated from each other so that we can distinguish the emission from each molecule. However, the spatial resolution can not be improved down to nanometer scale because of the long wavelength of the light, $\sim$100 nm. This spatial resolution is far from the spatial resolution of STM.

On the other hand, the resolution of optical measurements in energy scale or in time scale can be excellent. The energy resolution of a monochromator or laser source can be much better than the thermal energy. That means an experiment using them does not broaden the spectrum, unlike STS, where the electron distribution is diffused by thermal energy. In addition, we can choose the wavelength from a very wide region: IR for molecular vibration spectroscopy, UV-Vis for electron excitation, gamma ray for nuclear excitation.

As seen in the previous chapters, the time resolution of pump-probe methods using ultrashort pulsed lasers reaches a few femtoseconds. This is much better than the time resolution of STM. The time resolution of STM current detection is usually limited to $\sim$10 μs. If we make it better, we lose signal-to-noise ratio. The femtosecond time resolution allows us to see the ultrafast decay of photo-excited carriers in materials and the accompanying excitation of coherent phonons, quantum interference effects and so on.

7.5.2 Combination of STM with Optical Methods

Both STM and optical measurement methods have their own advantages and drawbacks. Our purpose is developing better measurement techniques by combining these two techniques. We will combine their advantages and supplement their drawbacks with each other. Namely, we make use of the spatial resolution of STM and the energy/time resolution of optical measurements. It will realize optical spectroscopy at atomic/molecular resolution and ultrafast experiment in femtosecond time scale at atomic/molecular resolution. But how should we combine them?

There might be two contrasting approaches. One is exciting samples with optical methods and detecting the signal with tunnel current. The other is exciting samples with tunnel current and detecting the signal with optical methods. Although the latter might sounds strange, such techniques have already been suggested [31]. It is called light-STMs. The principle is as follows. The tunnel electrons have generally higher energy than the Fermi level of destination materials. Thus, these electrons will lose energy in some form. There are cases where the energy decay accompanies light emission and can be detected by spectrometers. The spatial resolution of the measurement is characterized by the length for which the injected carriers diffuse before they

decay and the spectrometer can measure the energy of the emission precisely. Local band structures of materials are investigated by such methods [31]. However, time resolution might be difficult to achieve with this setup.

We adopted the other method; we excite our sample by irradiation and detect the signal with STM. When detecting the signal with STM, ångstrom spatial resolution of the measurement is guaranteed. By saying it, we do not insist that we will always acquire as small futures as ångstrom scale in our images because the physical phenomena caused by the irradiation do not necessarily have ångstrom spatial variation. What we insist here is that when the physical property has spatial variation at the angstrom scale, we will be able to see it with light-excited STMs. We can tune the wavelength of irradiation to have spectroscopic resolution and use pulse lasers to have time resolution as shown in Chaps. 9 and 10.

7.5.3 How to Combine the Two Techniques?

Various Ways of Combining STM with Optical Methods

Even after we decided to excite samples with light and look at the result with STM, we still have many options of measurement setup. Here, we will discuss systematics of possible setups of light-excited STM measurements. We classify measurement methods by (1) when the sample is excited by light and when it is observed by STM, (2) what kind of change in the sample is detected by STM and (3) how such change is caused by the irradiation. This discussion clarifies the existence of a variety of ways of combining STM with optical excitation and their great possibilities.

Temporal Order of Excitation and Observation

We can choose one of these:

1. To compare the STM signals before and after light illumination.
2. To compare the STM signals with and without light illumination.
3. To compare the STM signals with different parameters of light illumination.

The first one is simple. We observe the sample with STM in dark condition, illuminate sample with some light source, turn off the light and observe it again with STM. Although the measurement is very simple, in changing the condition of illumination, we can still obtain spectroscopic, time-resolved and atom-resolved characteristics of the sample. Technically speaking, since the STM observation and light illumination are independently done in this method, there is not much to be discussed. However, it is still not too easy because illumination of the sample causes a slight increase of the system temperature, resulting in the variation of relative tip–sample position. Thus, one can very easily lose the imaging frame. It is generally difficult to compare

images of the same area before and after illumination. In order to overcome this difficulty, one possible solution is to make use of statistical methods. If the change of the sample caused by the illumination is homogeneous, it is meaningful to compare statistical values of different image frames. A statistical approach also solves the problem of the inability to repeat experiments. Since this type of experiment often causes irreversible change in the measured system, one needs to re-prepare the sample each time. In fact, in such cases, surveying large areas with the statistical method is almost the only way to check the reproducibility and the accuracy of the obtained result. An example will be presented in Chap. 9.

The second and third ones observe the change in STM signal with varying intensity or some other property of light illumination. Although these methods have potential to provide all benefits of the spectroscopic, time-resolved and spatial resolutions in nondestructive way, in this case one has to consider the interference of the STM observation with light irradiation. In particular, when intense illumination is applied to the system, we can never modulate the intensity of illumination. Because a large change in the amount of heat brought by the illumination to the STM tip causes large amplitude of elongation/shrinking of STM tip, this results in a crash of tip apex into the sample surface. This point is discussed in detail in Sect. 7.5.4. When the modulation is applied some other property of illumination, the existence of illumination does not affect STM observation too much.

What Change in the Sample Property Is Detected by STM?

As we learned above, an STM observation detects spatial/energetic overlap of electron states of tip and of sample, and their local Fermi levels. Thus, if irradiation of the sample affects the STM signal, at least one of the following changes should occur in the sample:

A) change in the amount of spatial overlap between tip and sample electron states
B) change in the amount of energetic overlap between tip and sample electron states
C) change in the charge distribution in the electron states

The first one, spatial overlap of electron states, can be affected by the change in the tip–sample distance by irradiation, although which is almost always better to be avoided. It can be also effected by the change in the shape of specimen due to rebonding of atomic structure or deformation of molecular shape, and the change in the distribution of electronic states due to charge transfer caused by photo excitation. The last issue might also cause the change in the distribution of the electronic states against the energy scale. Energetic overlap of the electron state is also affected, in addition, by the change in the effective bias voltage due to the penetration of the electric field between tip and sample into the subsurface region of the sample. The electric

field of the light wave also causes a modulation of bias voltage at very high frequency. Since the frequency of the modulation is too high, the modulation in the tunnel current synchronized to the light wave can not be detected by STM. However, nonlinearity of I/V characteristics of the tunnel junction partially rectifies the high frequency modulation of bias voltage and results in a small direct current component in tunnel current as shown following. Here, the bias voltage as a function of time is assumed to be $V_s = V_s^0 + \Delta V_s \sin(\omega t)$. Then the tunnel current will be as follows.

$$I_t(V_s) = I_t(V_s^0) + \Delta V_s \frac{\partial I_t}{\partial V_s} \sin(\omega t) + \frac{1}{2} \Delta V_s^2 \frac{\partial^2 I_t}{\partial V_s^2} \sin^2(\omega t) + O(\Delta V_s^3) \quad (7.9)$$

The time-averaged signal is not affected by the second term in the right hand side but depends on the third term.

$$\overline{I_t(V_s)} \sim I_t(V_s^0) + \frac{1}{4} \frac{\partial^2 I_t}{\partial V_s^2} \Delta V_s^2 \quad (7.10)$$

Thus, the averaged signal also contains a small but finite component that is proportional to the amplitude of bias modulation.

Change of the charge distribution in the electron states can be caused by the photoinduced electron transfer in a molecule or the diffusion/drift of photoexcited carriers in semiconductor materials. Change of the charge distribution affects the effective density of state at the initial and final state of tunneling transition.

How Does the Light Excitation Modulate the Sample Property?

The interaction between photons and the sample material, and sometimes also tip material, is dependent on the wavelength and the physical properties of the exact system. Physical properties by photostimulation, such as band structural modulation, excitation of electrons in single and collective modes, molecular vibrations, have been studied by various techniques. In particular, ultrafast reactions have been studied by optical pump-probe techniques. Figure 7.28 and 7.29 show examples of band structural modulation of GaAs and phonon dynamics of highly oriented pyrolytic graphite (HOPG). In the former case, following the carrier excitation by the pump probe, relaxations in the conduction band and from the conduction to the valence band result in the observed change in the probe pulse reflectivity [24]. In the latter case, an observed change in the reflectivity reflects the phonon relaxation processes caused by the excited electron-phonon interactions [25]. These changes in the materials are supposed to influence the tunnel current and produce the signal of the light-combined STM measurement as will be described in the following sections. In addition, manipulation of the material structures by light-combined STM will be shown in Chap. 9.

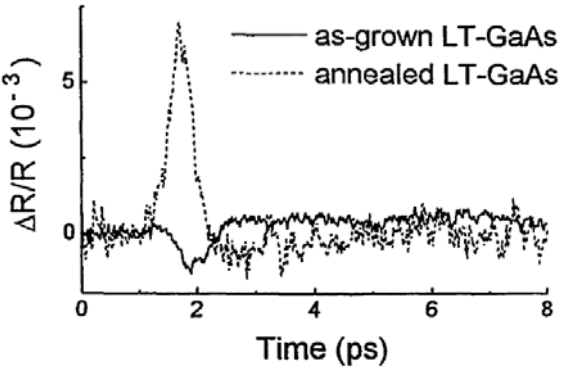

Fig. 7.28. Pump-probe reflectivity measurement on low temperature grown GaAs sample using 805 nm laser pulses [24]

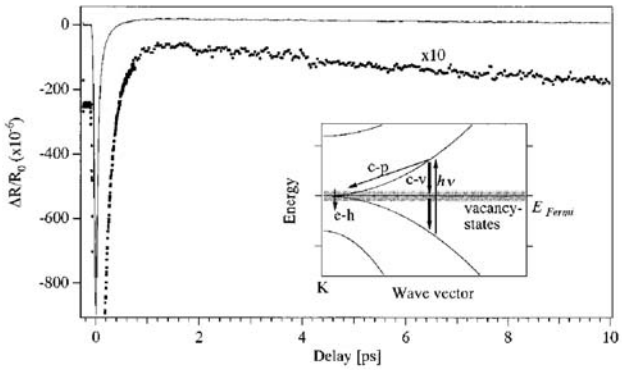

Fig. 7.29. Pump-probe reflectivity measurement on HOPG using 800 nm laser pulses [25]

7.5.4 Specific Issues in Combining Light Irradiation and STM

Thermal Expansion/Shrinking of STM Tip

There are several barriers to be overcome for the development of the light-combined STM. The most critical one is caused by the thermal expansion of tip and sample due to photo illumination of the tunnel gap. Since the tunneling current is sensitive to the tip–sample distance, this effect strongly influences the STM/STS measurement.

When an optical chopper is used for the lock in detection, or a strong light source is needed, change in the light intensity due to chopping or fluctuation of the strong light source causes the apparent thermal expansion effect. However, the thermal expansion effect is reduced when the photoillumination is stably performed and the thermal equilibrium condition is achieved. Let us

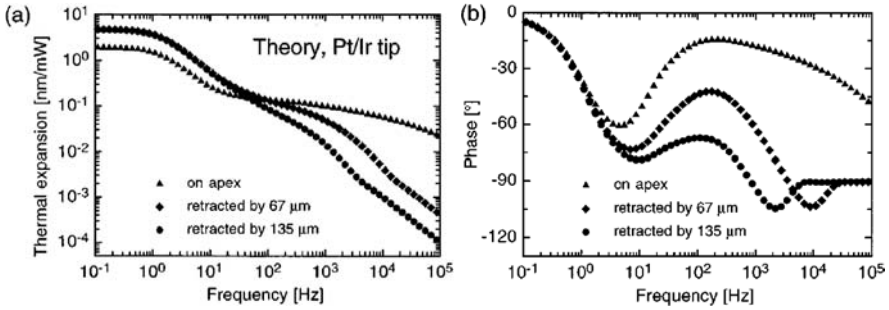

Fig. 7.30. Frequency dependence of thermal expansion/shrinking of STM tip by chopped laser illumination

consider the case of the modulation of an optical chopper. The STM tip is lengthened and shortened when the photoillumination is on and off, respectively. Therefore, although the actual change is a little bit more complicated, if the on/off frequency is fast enough, the tip length is considered to be kept at the thermal equilibrium value.

Figure 7.30 shows the frequency dependence of the thermal expansion effect [26]. An experiment was performed for a W tip of 0.25 mm diameter and Au sample combination with the photo illumination of a 17 µm-spot-light. As shown in the figure, the amount of thermal expansion decreases with the chopping frequency, however, it strongly depends on the tip shape. And when the photoillumination is focused on the tip apex, the thermal expansion is not reduced even at the frequency of 100 kHz.

Photoelectron Emission by Multi-photon Absorption

When photoelectrons are emitted from the sample surfaces, these electrons influence the tunneling current measurements. In particular, in the case of short pulse lasers, since the signal is supposed to be extremely weak and each pulse has a strong intensity, multiphoton absorption must have a strong effect on the STM measurement. In fact, this effect was confirmed by measuring the signal intensity as a function of the tip–sample distance [27]. As expected, an STM signal was observed even for the tip–sample distance of 20 µm. This effect is strong for the UHV-STM, however that decreases with surrounding pressure, and can be neglected for the case of the experiment in air.

Shadowing Effect by Tip

In general, photoillumination is performed with a certain angle to the tip-sample gap. On the other hand, the STM tip is sharpened by such processes as chemical etching. However, it has a certain curvature. Figure 7.31 shows

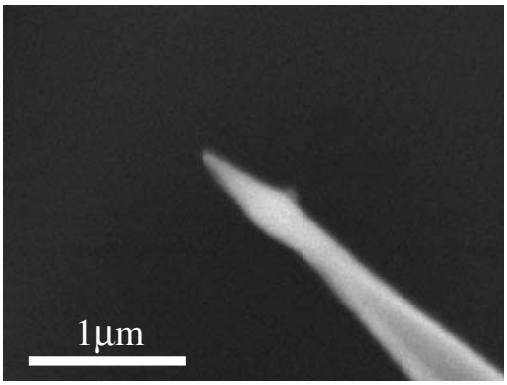

Fig. 7.31. SEM observation of chemically-etched tungsten STM tip

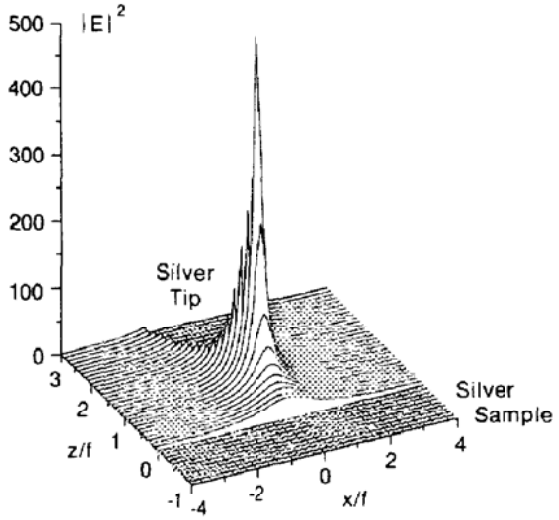

Fig. 7.32. Field enhancement effect under the STM tip

an example of an STM tip chemically etched with NaOH solution observed by scanning electron microscopy (SEM).

Does shadowing by the STM tip influence the photoillumination of the sample surface just below the tip? Generally, the curvature of the tip apex can be reduced down to less than 100 nm, and the light wavelength is longer then 100 nm even when UV light is used. When infrared light is used, the wave length becomes $\sim$1 μm. Therefore, the dominant effect of the tip is not shadowing but scattering. The tunnel gap can be illuminated even when the STM tip exists.

Field Enhancement Effect

When the STM tunnel gap is illuminated by laser under a certain condition, the local electric field is strongly enhanced due to the effect of tip–sample shape characteristic. This is called the field enhancement effect. For example, $\times 500$ amplification of the field enhancement was observed with the condition of the plasmon resonance on the tip surface [28–30].

This field enhancement effect becomes prominent with the following conditions: 1) polarization is parallel to the incident plane (p-polarization), 2) small tip–sample distance, 3) small tip apex curvature, 4) at plasma resonant frequency. This effect can cause $\times 1000$ magnification for specific conditions, and theoretical analysis has been performed actively [28–30]. Since the STM signal is expected to be enhanced together with the enhancement of the electric field of illumination, the field enhancement effect is preferable for the light-combined STM measurement. The field enhancement effect is also caused by the corrugation of metalic sample surfaces as the nanoscale Ag particles are utilized in an enhanced Raman spectroscopy. Thus, combination of sharp STM tip with a metalic substrate with appropriate corrugation will be ideal for enhancement of electric field at tunnel junction.

References

1. S. Yasuda, T. Nakamura, M. Matsumoto, H. Shigekawa: J. Am. Chem. Soc. **125**, 16430 (2003)
2. T. Hugel, N.B. Holland, A. Cattani, L. Moroder, M. Seitz, H.E. Gaub: Science **296**, 1103 (2002)
3. G. Binnig, H. Rohrer, Ch. Gerber, E. Weibel: Phys. Rev. Lett., **50**, 120 (1983)
4. R. Wolkow, P. Avouris: Phys. Rev. Lett. **60**, 1049 (1988)
5. M. Ishida, O. Takeuchi, T. Mori, H. Shigekawa: Phys. Rev. B **64**, 153405 (2001)
6. M. Ishida, T. Mori, H. Shigekawa Phys. Rev. Lett. **83**, 596 (1999)
7. M. Ishida, O. Takeuchi, T. Mori, H. Shigekawa, Jpn. J. Appl. Phys. **39**, 3823 (2000)
8. J. Lee, H. Kim, S.-J. Kahng, G. Kim, Y.-W. Son, J. Ihm, H. Kato, Z. W. Wang, T. Okazaki, H. Shinohara, Y. Kuk: Nature **415**, 1005 (2002)
9. Y.J. Li, O. Takeuchi, D.N. Futaba, H. Oigawa, K. Miyake, H. Shigekawa, Y. Kuk: Phys. Rev. B **68**, 033301 (2003)
10. O. Takeuchi, H. Shigekawa: Jpn. J. Appl. Phys. **42**, 4890 (2003)
11. K. Miyake, K. Hata and H. Shigekawa: Phys. Rev. B **55**, 5360 (1997)
12. K. Miyake, T. Kaiko, K. Hata, R. Morita, M. Yamashita, H. Shigekawa: J. Vac. Sci. Technol. A **17**, 1596 (1999)
13. K. Miyake, H. Oigawa, K. Hata, R. Morita, M. Yamashita, H. Shigekawa: Surf. Sci. **429**, 260 (1999)
14. W.L. Ling, O. Takeuchi, D.F. Ogletree, Z.Q. Qiu, M. Salmeron: Surf. Sci. **450**, 227 (2000)
15. O. Takeuchi, M. kageshima, H. Sakama, A. Kawazu: Jpn. J. Appl. Phys. **40**, 4414 (2001)

16. K. Hata, S. Yoshida, H. Shigekawa, Phys. Rev. Lett. **89**, 286104 (2002)
17. K. Hata, Y. Saino, H. Shigekawa, Phys. Rev. Lett. **86**, 3084 (2001)
18. K. Hata, M. Ishida, K. Miyake, H. Shigekawa, Appl. Phys. Lett. **73**, 40 (1998)
19. S. Yoshida, O. Takeuchi, K. Hata, R. Morita, M. Yamashita, H. Shigekawa, Jpn. J. Appl. Phys. **41**, 5017 (2002)
20. J. Y. Park, U. D. Ham, S.-J. Kahng, Y. Kuk, K. Miyake, K. Hata, H. Shigekawa Phys. Rev. B **62**, R16341 (2000)
21. K. Shinohara, S. Yasuda, G. Kato, M. Fujita, H. Sghiekawa J. Am. Chem. Soc. **123**, 3619 (2001)
22. M.T. Cuberes, R.R. Schlittler, J.K. Gimzewski, Appl. Phys. Lett. **69**, 3016 (1996)
23. H. Shigekawa, K. Miyake, J. Sumaoka, A. Harada, M. Komiyama J. Am. Chem. Soc. **122**, 5411 (2000)
24. J-S. Yu, S. Horng, C-C. Chi, Jpn. J. Appl. Phys. **37**, 554 (1998)
25. K. Ishioka, M. Hase, M. Kitajima, K. Ushida: Appl. Phys. Lett. **78**, 3965 (2001)
26. S. Grafstro m, P. Schuller, J. Kowalski, R. Neumann: J. Appl. Phys. **83**, 3453 (1998)
27. J. Jersch, F. Demming, I. Fedotov, K. Dickmann, Appl. Phys. A **68**, 637 (1999)
28. W. Denk and D.W. Pohl: J. Vac. Sci. Technol. B **9** 510 (1991)
29. F. Demming, J. Jersch, K. Dickmann, P.I. Gechev: Appl. Phys. B **66**, 593 (1998)
30. P.I. Geshev, F. Demming, J. Jersch, K. Dickmann: Thin Solid Films **369**, 156 (2000)
31. J.K. Gimzewski, C. Joachim, R.R. Schlitter, V. Langlais, H. Tang, I. Johannsenn: Science **281**, 531 (1998)

8 Spatially-Resolved Surface Photovoltage Measurement

O. Takeuchi and H. Shigekawa

8.1 Background

As the dimension of semiconductor devices shrinks down to nanometer scales, control of the dopant and defect profiles in the device material is getting more and more important. In addition, the surface effect and/or quantum effect, which have not appeared in larger devices, show considerable influences on the electric properties of the entire devices. Consequently, there have been urgent needs for the noble evaluating techniques that can investigate the precise band structure including localized energy levels within nanoscale semiconductor devices. In addition, such techniques might be also applicable to the basic research of the future organic/inorganic molecular devices, which has completely new physical mechanisms for realizing its noble functions.

When the scale of specimen was much larger, photo-assisted spectroscopy provided valuable information for the electronic structures in materials. For example, photoelectron spectroscopy (UPS, XPS) revealed the filled state density of the surface states and the surface photovoltage (SPV) measurement gave the information of the subsurface band structures. However, now the device size is already as small as a few tens of nanometers. These conventional optical methods are no longer applicable. The spatial resolution of these methods is generally limited to the dimension of their wavelengths, which are larger than 100 nm. At this moment, the best candidate for investigating the electric structure within such nanostructures is scanning probe microscopy (SPM) technology. Hence, many researchers have been devoting efforts for developing noble characterization techniques of local band structures using SPM instruments: such as scanning tunneling spectroscopy (STS), SPV measurement, Kelvin force microscopy (KFM), barrier height (BH) measurement and standing wave measurements using SPM.

Among these SPM techniques, local SPV measurement using STM is superior in one sense that it can provide not only the static but the dynamic properties of band structures. It inherits all advantages from the conventional macroscopic SPV measurement and also posesses the spatial resolution of STM. In general, it measures the difference in the amount of surface band bending on dark and illuminated conditions. As is known, in the one dimensional model for a homogeneous semiconductor material, the surface band bending is caused by the pinning of Fermi level at the surface by the mid-gap

surface states and/or by the characteristic carrier recombination/generation rate at the surface. On real device surfaces, band bending is also caused by the inhomogeneity of the materials. The amount of bending reflects the composition of semiconductor materials, the densities of dopant/defect states and the generation rate of photo carriers.

Historically, SPV measurement in macroscopic dimension originated in the early 1950s [1] and, up to now, the method has been fairly established [2]. It provides important electric properties of semiconductor materials, such as the polarity and magnitude of surface band bending, the recombination rate of photocarriers, surface conductivity, dopant/defect density and localized quantum levels. Hence, combining the conventional photo-assisted technique, SPV measurement with SPM technology to acquire spatially resolved SPV (SR-SPV) simultaneously with an atomic topograph of sample surface by STM will lead to a greater understanding of the electric functions of future nanodevices on the basis of their atomic structures. In this chapter, we introduce our recent achievement in the study of SPV measurement technique by STM.

8.2 Surface Photovoltage (SPV)

In order to explain the basic concept of SPV, the band structure in the surface region of a one dimensional n-type semiconductor is illustrated for dark and illuminated conditions in Fig. 8.1(a) and (b). In this schematic, the lateral axis indicates the position perpendicular to the surface and the vertical axis indicates the potential energy for the electrons. The semi-infinite sample extends from the surface at the right end of the figure towards the left hand side. Generally, the band structure in the dark condition bends in the surface region. In many cases, the bending is governed by the pinning of the Fermi level by the mid-gap surface states at the surface. Some other

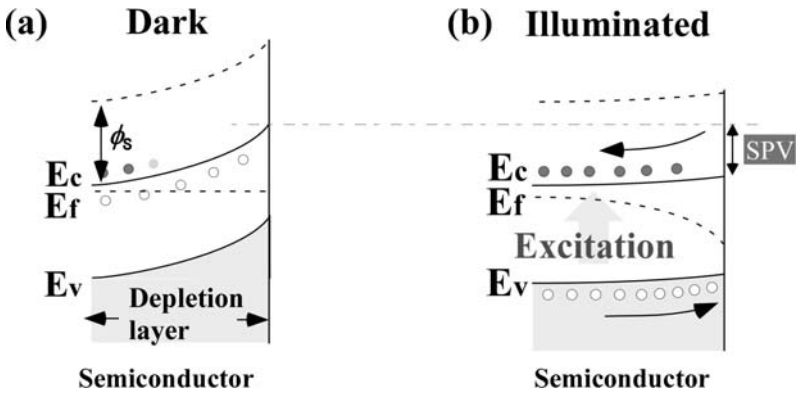

Fig. 8.1. Surface photovoltage effect

factors can also affect the band bending, such as the difference in the generation/recombination rate of thermal carriers at the surface in comparison to the bulk. The bent band structure indicates the existence of the depletion layer and the built-in electric field there. In the figure, the white circles indicate the ionized donor states and the filled circles indicate the electron as the major carriers. In the bulk region, the density of the donor states and that of the carrier electrons are equal so that the net charge density is zero. However, in the depletion layer, the net charge density is almost equal to the donor density. Thus with a condition of fully ionized dopant levels, which is often realized at room temperature, the amount (height) of the band bending eV_{bb} and the depth of the depletion layer d has a relationship as

$$d = \sqrt{2\epsilon\epsilon_0 V_{bb}/eN_A}, \tag{8.1}$$

with the dopant concentration in the bulk N_A, relative dielectric constant ϵ, vacuum dielectric constant $\epsilon_0 = 8.85 \times 10^{-12}\mathrm{F/m}$ and elementary charge $e = -1.6 \times 10^{-19}\mathrm{C}$. Thus, small dopant concentration results in a thick depletion layer and large dopant concentration results in a thin depletion layer. Typical values of d range from 10 to more than 100 nm. In the thermal equilibrium, this electric field compensates the difference in the chemical potential of the electrons so that the net flux of the carriers is zero everywhere in the material. Namely, the Fermi level is constant all through the semiconductor material.

When the sample is illuminated by a super-bandgap light, as illustrated in Fig. 8.1(b), the photo-excited carriers are generated in the surface region. Although the light intensity diminishes from the surface into the bulk due to the absorption, often the decay length of the light intensity as a function of the depth in the semiconductor is larger than the thickness of the depletion layer. In such cases, the light intensity is almost constant through the depletion layer. Generated carriers drift due to the electric field of the band bending and cause the charge separation. When the sample is n-type, electrons drift into the bulk and holes drift towards the surface. As a result, the positive charge builds up at the surface, which results in the reduction of the electric field of the bandbending. Since, when the band bending is reduced, the drift of the photoexcited carriers is also reduced, the charge build-up eventually saturates and the system reaches a steady state. Do not mistake this steady state with the thermal equilibrium. The word of "steady" just denotes that the amount of the band bending is temporally constant. In this situation, the Fermi level can not be defined in the illuminated area and the quasi-Fermi levels independently defined for electrons and for holes take different values to each other. When the intensity of illumination is sufficiently large, the band bending is almost flattened and further increases of light intensity do not change the band structure. As can be seen, the relaxation of the band bending causes the shift of the potential energy of the surface from its equilibrium position. This shift is defined as SPV. Hence, SPV is generally smaller than or equal to the amount of original band bending. It is notable that, with sufficient illumination, SPV is equal to the amount of the

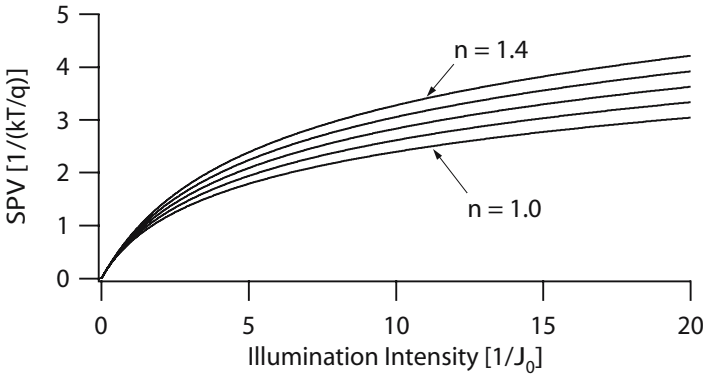

Fig. 8.2. Surface photovoltage as a function of illumination intensity with changing nonideality factor n from 1.0 to 1.4

original band bending. With moderate intensity of illumination, SPV is not determined only by the original band bending but also reflects dynamic properties of the samples: such as carrier generation/recombination rates, carrier mobilities, density of localized states and so on.

We can describe the above situation with the analogy to a metal semiconductor interface (Schottky contact), treating the surface states as a very thin metal layer. In the steady state, there must not exist a net charge transfer, which is realized only when the drift current due to the photo-excited minority carriers arriving at the surface $J_{\rm pc}$ is exactly compensated by the thermionic emission current of the majority carriers across the depletion region $J_{\rm th}$ [3]. Generally, with not too large illumination intensity, $J_{\rm pc}$ is proportional to the illumination intensity P and the depth of the depletion layer d. $J_{\rm th}$ is given with the nonideality factor $n \geq 1$ that allows for deviations from pure thermionic emission as

$$J_{\rm th} = J_0 \exp(eV_{\rm SPV}/nkT)[1 - \exp(-eV_{\rm SPV}/kT)], \tag{8.2}$$

with $J_0 = A^*T^2 \exp(-e\phi_h/kT)$. Here, A^* denotes the effective Richardson constant and ϕ_h the Schottky barrier height. For Si, $A^* \sim 30\,{\rm Acm^2K^2}$ for holes and $A^* \sim 100\,{\rm Acm^2K^2}$ for electrons [3]. Assuming $J_{\rm th}$ is equal to $J_{\rm pc}$, we obtain the amount of the SPV as in Fig. 8.2. If $n = 1$, the result can be written in a simple form as

$$V_{\rm SPV} = (kT/e)\ln(J_{\rm pc}/J_0 + 1). \tag{8.3}$$

If $n \neq 1$, SPV in the small and large signal limits,

$$\begin{aligned} V_{\rm SPV} &= (kT/e)(J_{\rm pc}/J_0) \qquad J_{\rm pc} \ll J_0 \\ V_{\rm SPV} &= (nkT/e)\ln(J_{\rm pc}/J_0) \qquad J_{\rm pc} \gg J_0 \end{aligned} \tag{8.4}$$

Note that these equations does not saturate but continuously increase with increasing J_{pc}. However, in reality, J_{pc} itself saturates for high illumination intensity P because of the reduction of the depth of the depletion layer d.

The model we discussed above is the simplest one. In reality, there might be some other factors to be considered, such as the defect concentration, external fields and inhomogenuity of sample properties. To extract such properties from the SPV signal, more precise theoretical analysis is required.

8.3 Macroscopic Measurement of SPV

In macroscopic measurements, SPV is often measured by the Kelvin probe method or the metal-insulator-semiconductor (MIS) approach. The former method originally measures the difference between the work functions of a sample and a metal probe. Since the surface dipole is usually insensitive to the illumination, the change in the surface bandbending causes the same amount of change in the work function. Thus, the SPV can be measured by comparing the work functions of the sample with and without illumination. To measure the work function, a metal plate electrode is faced against the semiconductor surface and the gap distance between the two surfaces is periodically modulated. When the two surfaces are short-circuited, even though their Fermi levels are in equilibrium, there exists a finite electric field between them. This is due to the difference between their work functions, which causes the difference of the vacuum levels at their surfaces. This is called as contact potential difference (CPD). Since the CPD is inherent for the combination of the two surfaces, the gap modulation causes the modulation of the electric field between them. Consequently, the displacement current flows from the capacitor consisting of the metal plate and the sample surface. When a bias voltage is applied to the sample, the electric field is changed and so is the displacement current. Only when the bias voltage compensates for the CPD is the displacement current nullified. Thus, measuring the bias voltage where the displacement current becomes zero, one can measure the CPD between the sample and the probe. One can perform the CPD measurement both in the dark and illuminated conditions and obtain the SPV from the difference of the CPD in the two cases.

On the other hand, the metal-insulator-semiconductor approach measures the photo voltage directly. Imagine a metal plate electrode is placed close to the sample suface but without contact. At first, the two electrodes are short-circuited to have equilibrium in dark conditions, where their Fermi levels becomes equal to each other. When the sample is illuminated after open-circuiting them, the surface potential changes by the amount of SPV. This change can be measured as the photo-induced voltage change between the two electrodes.

8.4 Photovoltage and Photocurrent Measurement by STM

With using a smaller probe electrode, the spatial resolution of the SPV measurement can be improved. In particullar, the MIS method combined with STM has a potential of probing the SPV and the surface morphology at an atomic resolution. Thus, since the pioneering work by Hamers and Markert [5], much research has been done for measuring spatially resolved SPV by using STM.

The experimental methods developed so far can be classified into two categories, namely, those for measuring intrinsic (zero bias) SPV [5–8] and those for measuring SPV under finite bias voltages [9–12]. In both cases, the measurement setup is very similar to the macroscopic MIS approach, except for the following two points; there exists finite tunnel current flowing between the sample and the metal probe, and the shape of the probe is not a plate but a needle, i.e., the STM tip. Although these two points make the interpretation of the obtained signal more difficult compared to the conventional MIS approach, the one dimensional MIS model is still useful for the first order approximation. Figure 8.3 shows the schematic of the measurement of the intrinsic SPV using STM. In the dark condition, it is obvious that the tunnel current is zero when the bias voltage is zero, i.e., the Fermi levels of the sample and of the tip coincide each other. In the illuminated condition, on the other hand, the photovoltage, i.e., the amount of bending of the quasi-Fermi level in the surface region, works as an additional bias voltage. Thus, the same amount of bias voltage with opposite polarity is required to nullify the tunnel current, in order to align the Fermi level of the sample surface and that of the probe. Consequently, when using the STM probe as the voltmeter under the illuminated condition, atomic scale SPV variation can be obtained. By simply extending this argument, the STS curve under an illuminated condition will have a same shape of that in the dark condition but

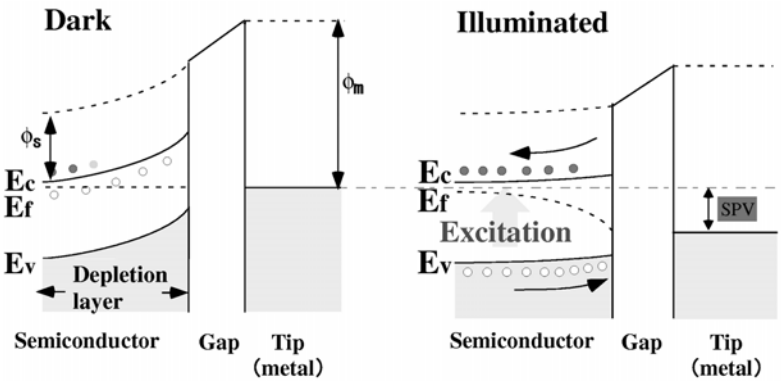

Fig. 8.3. Intrinsic surface photovoltage measurement using STM

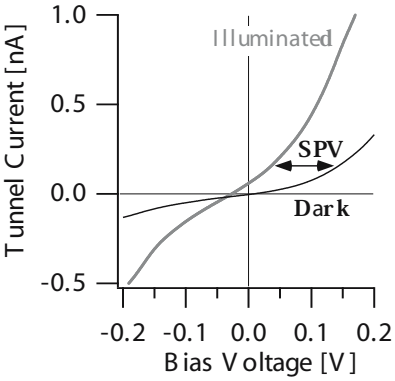

Fig. 8.4. Lateral shift of IV curves under dark/illuminated conditions

just shifted in the lateral direction by the amount of the SPV. However, in reality, since the SPV is generally bias voltage dependent, the two STS curves are not just shifted in the lateral direction but have different shapes as shown in Fig. 8.4. Measuring the lateral shift of IV curves under dark/illuminated conditions for each bias voltage, one can obtain the bias voltage dependence of the spatially-resolved SPV.

As seen in the above, the simplest SPV measurement by using STM can be performed by obtaining the two STS curves under illuminated and dark conditions. However, this is not an easy task for two main reasons. One is that when the sample and the tip are illuminated, a finite amount of heat is brought by the light to the measurement system. In particular, warming up of STM tip easily causes the extention of the tip length, resulting in the unfavorable decrease of the tunnel gap distance. Thus, if you obtain an IV curve in the dark condition and then illuminate the sample to obtain an illuminated IV curve, the tip–sample distance is no longer as same as that under the dark condition. The other issue is the measurement time to obtain an SPM image of spatially resolved SPV. Usually, the measurement of an IV curve takes 0.1–1.0 s. If IV curves are measured for every pixel of a high resolution image, the number of IV curves required to construct an image becomes several ten thousands. It would take hours to obtain a single image. Thus, the reduction of measurement time is important. To overcome these issues, a variety of technical methods to measure SPV with using STM have been proposed.

Before summarizing such methods, let us give a short consideration for the accuracy of an SPV measurement with STM. Since we measure the lateral shift of two IV curves, the accuracy of the obtained value ΔV_{SPV} is given by the noise level on the tunnel current signal ΔI_t divided by the slope of the IV curve at the interested point, i.e., differentiated tunnel conductance $\mathrm{d}I/\mathrm{d}V$.

$$\Delta V_{\mathrm{SPV}} = \Delta I_t/(\mathrm{d}I/\mathrm{d}V) \tag{8.5}$$

Thus, when the intrinsic SPV is measured, the disappearance of the differential tunnel conductance $\mathrm{d}I/\mathrm{d}V$ at the low bias voltage region enhances the small noise and possible offset in tunnel current detection, resulting in a large noise/artifact in the obtained intrinsic SPV signal. Thus, SPV measurement is now often performed under finite bias voltages. In such cases, however, the local band structure beneath the STM probe can be affected by the strong electric field and high current density required for the tunnel current detection of STM. Hence, the measurement conditions must be carefully taken into consideration in interpreting the obtained results.

In order to obtain the intrinsic SPV value, we do not have to measure the dark tunnel current but we can just seek the zero crossover of the tunnel current under illuminated conditions. In the simplest method, this can be done by acquiring IV curves. However, it takes a long time and the measurement accuracy is limited because of the small $\mathrm{d}I_t/\mathrm{d}V$ around the zero effective bias voltage. Hamers and Markert designed a special electronics to measure the intrinsic SPV for the first SPV measurement using STM. At each measurement point, the z-feedback for the normal STM operation is opened and, instead, bias voltage feedback that seeks zero tunnel current is applied. With this method, the settled point of the bias voltage gives the SPV value directly. Compared to obtaining whole IV curves, a method that can take a longer time to find the exact zero, this method is expected to give better accuracy with less time. However, it was still slow because of the small error signal level for the bias voltage feedback, due to very small $\mathrm{d}I_t/\mathrm{d}V$, and suffered from the artifact from a very small tunnel current offset and/or remaining tunnel current after a finite period of the bias voltage feedback. Actually, the spatially resolved SPV image they reported turned out to have originated from the measurement artifact. Hagen et al. improved the Hamers' method by using the z-feedback to keep the differentiated tunnel conductance $\mathrm{d}I_t/\mathrm{d}V$ to be constant during imaging instead of the tunnel current I_t [8]. With this method, the two feedback circuits, one for the bias voltage to cancel I_t and one for the z piezo to keep $\mathrm{d}I_t/\mathrm{d}V$ constant can be enabled simultaneously. Thus, they could avoid the switching time of the two feedback circuits and greatly reduce the total imaging time. In addition, the tip–sample distance for the current nulling operation in their method is, in general, much smaller than that of Hamers' method, which was realized much higher accuracy. With any experimental method, however, a sample that has no surface state density at the Fermi level can not be investigated by the measurement of the intrinsic SPV with STM, because when the differentiated tunnel conductance is truly zero at the Fermi level, the zero crossover of the IV curve is undeterminable. In such cases, we must think of measuring the SPV under finite bias voltage, where the differentiated tunnel conductance is not zero.

Along with the strategy described above, obtaining the SPV value at finite bias voltage is more complicated than obtaining the intrinsic SPV, because, now, we must at least know the dark and illuminated tunnel current for the two different bias voltages. There have been two methods introduced in order

to do this task. One is called the double-modulation method, introduced by Cahill and Hamers. They chopped the photo illumination with a frequency f_1 and, simultaneously, modulated the bias voltage with a sinusoidal wave at a frequency f_2 ($\neq f_1$). These frequencies are higher than the cut-off frequency of the z-feedback loop that keeps the tip–sample separation constant during the imaging or sweep of bias voltage, i.e., the z-feedback tries to keep the averaged tunnel current to be the reference value. The resultant tunnel current contained two oscillating components; one is the square-wave component at f_1 due to the SPV effect and one is the sinusoidal component at f_2 due to the bias modulation. When using two lock-in amps, these two components are separated and the oscillation amplitudes ΔI_1 and ΔI_2 are measured, independently. Since the photo-induced change of the tunnel current is not only dependent on SPV but also dependent on the differential tunnel conductance $\mathrm{d}I_t/\mathrm{d}V$, i.e., $\Delta I_1 = \mathrm{d}I_t/\mathrm{d}V \cdot V_{\mathrm{SPV}}$, SPV can not be obtained only from ΔI_1. However, from the ΔI_2 and the amplitude of the bias modulation ΔV, we can obtain an approximated value for $\mathrm{d}I_t/\mathrm{d}V$ by dividing ΔI_2 by ΔV. When assigning this experimentally obtained differentiated tunnel conductance, we can obtain the SPV value by

$$V_{\mathrm{SPV}} = (\Delta V/\Delta I_2) \cdot \Delta I_1. \tag{8.6}$$

Strictly speaking, this equation is valid only when the dark and illuminated IV curves are linear and their slopes are exactly the same. Although these conditions are not met in reality, when the photo-induced current is small, this method works pretty well.

McEllistrem et al. improved this double modulation method by synchronizing the two modulations [10,11]. They applied additional bias voltage only when the illumination was on. In the SPV measurement, they adjusted the polarity and amplitude of this additional bias voltage component so that the photo-induced change in the tunnel current was compensated. Remember that we are assuming SPV works as an additional component for the effective bias voltage at the tunnel gap. Thus, the tunnel current under the illumination can be written as $I_t(V_0 + V_{\mathrm{SPV}})$, where $I_t(V_0)$ represents the tunnel current under the dark condition. They introduced an additional bias component of ΔV and adjusted the polarity and amplitude so that $I_t(V_0) = I_t(V_0 + V_{\mathrm{SPV}} + \Delta V)$. Since $I_t(V)$ is monotone increasing function, when this condition is established we can assume the $-\Delta V$ is equal to V_{SPV}. Actually, even when the proper ΔV is applied, the tunnel current contains sharp spikes when the illumination and the bias voltage are switched. This is due to the slow response of the tunnel current preamplifier and the displacement current from the capacitance existing between the tip and the sample. Thus, the feedback for the additional bias component was temporally gated so that the transient current was filtered out. The z-feedback to keep the tip–sample distance constant was also temporally gated so that it was only active during the middle part of the dark period. The SPV value obtained by this method is not an approximated value unlike the old double modulation

method. The control of the tip–sample distance is also improved because the former method could only keep the averaged tunnel current between dark and illuminated condition to be constant, which means that the tip–sample distance was dependent on the amount of photo induced current even for the same bias voltage. Also, these double modulation methods are suitable for imaging because they require less time for measuring the SPV value for each point. These two double modulation methods are also capable of doing spectroscopy. Namely, we can fix the lateral position of the STM tip at a specific point of the sample surface and sweep the bias voltage while measuring SPV as a function of bias voltage. An important aspect of these two methods is that, even when the bias voltage is swept, the tip–sample distance is adjusted so that the (averaged) tunnel current is kept constant, unlike the basic approach where the illuminated and dark IV curves are independently measured.

Instead of measuring the dark and illuminated IV characteristics, Kuk et al. pointed out that comparison between the positions of peaks in the two $(\mathrm{d}I/\mathrm{d}V)/(I/V)$ spectra for dark and illuminated conditions gives amount of SPV, when the dependence of SPV on the bias voltage is rather small. The $(\mathrm{d}I/\mathrm{d}V)/(I/V)$ spectra obtained in the STS measurement corresponds to the local density of electron states (LDOS). Thus, when the surface potential is shifted by the SPV effect, the peak positions in the spectrum also shift by the same amount. In this experiment, there is no need to have the tip–sample distance be constant for measuring both illuminated and dark spectra; the measurement is not very complicated. However, the measurement of the spectrum for each measurement point takes a long time and it has limited resolution in the bias voltage dependence of the SPV value.

By applying these methods, SPV measurements on several systems have been reported. As pointed out above, however, the obtained SPV are found to be generally affected by bias voltage and the tip–sample distance, reflecting the strong electric field and current density under the STM tip. Indeed, some of the previous studies reported apparently conflicting results for the dependence of SR-SPV on the experimental conditions.

First, Cahill et al. described the SPV dependence on the tip–sample distance by using the concept of charging effect [9]. The tunnel current flowing during the measurement was thought to determine the amount of space charge under the STM probe mainly under the dark condition and to govern the deviation of SPV from the intrinsic value. Accordingly, until now, most SPV measurements have been performed under constant tunnel current conditions using the double modulation method. However, McEllistrem et al. reported that SPV was strongly dependent on bias voltage even with a constant tunnel current, when the surface had a lower density of states at the Fermi level, while SPV for metallic surfaces was not affected by bias voltage [10]. It was suggested that, since the less metallic surface state does not screen the electric field from the STM probe, the penetration of the electric field into the subsurface region affected the surface potential under dark

conditions. On the other hand, Sommerhalter et al. insisted that both tunnel current and bias voltage affect surface potential when the surface has a negligible surface state density [13]. In particular, they suggested that it is not the surface potential under a dark condition, but rather that under an illuminated condition that is strongly affected by the tip–sample distance.

For the realization of local band structure characterization, suitable experimental conditions for SR-SPV measurement and a procedure for the analysis of the obtained results must be established. In order to clarify the disagreements among the results of previous studies, exhaustive studies of the SPV dependence on experimental conditions will be required. In this chapter, we introduce a simple experimental method, light-modulated scanning tunneling spectroscopy (LM-STS), as a powerful method for such studies.

8.5 Light-Modulated Scanning Tunneling Spectroscopy

LM-STS has three advantages compared to the previous SPV measurement techniques. First, it gives the SPV dependence on experimental conditions complementary to those obtained in previous methods. Namely, it measures the SPV dependence on bias voltage under the condition of a constant tip–sample distance, in contrast to previous methods in which the condition of constant tunnel current is maintained. Secondly, it provides not only SR-SPV but also the complete illuminated and dark I-V curves simultaneously, providing a deeper insight into the sample properties. Thirdly, it can be performed using unmodified, commercially available STM electronics, making itself easily accessible to researchers.

Typical LM-STS measurement is performed as follows [15]. Mechanically chopped illumination is provided from 45 degrees off-normal to the surface and focused onto a spot of $\sim$0.05 mm diameter at the tunnel junction as illustrated in Fig. 8.5. The problematic thermal expansion/shrinkage of the STM tip (electrochemically etched tungsten wire, ϕ0.25 mm) is negligible with a chopping frequency higher than 40 Hz and an illumination power less than 1 mW (HeCd laser, 325 nm and 441 nm) in this condition. STM topographs can be stably obtained under these conditions, although small modulation is observed due to the intermittent SPV effect. In order to obtain an SPV spectrum, the scanning is stopped and a conventional STS measurement is performed under the chopped illumination. Part of a typical result for an n-type Si(111)-7$\times$7 sample (30 Ωcm) is shown in Fig. 8.6(a). The I-V curve (thick solid) oscillates widely between the two virtual I-V curves (thin dotted), corresponding to the dark and illuminated conditions. The SPV spectrum is acquired by plotting the lateral separation between these two virtual curves against the bias voltage under the dark condition, as shown in Figs. 8.6(b) and 8.6(c).

More specifically, an I-V curve consisting of two thousand points is obtained in 1–2 seconds with a chopping frequency of $\sim$40 Hz. The tunnel cur-

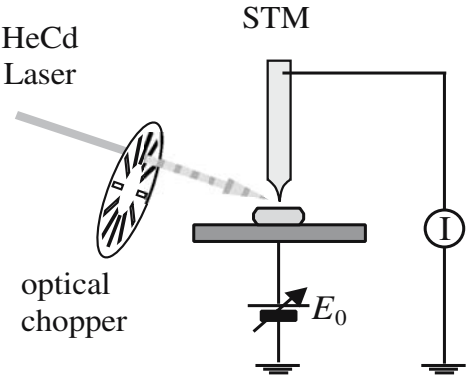

Fig. 8.5. Schematic of LM-STS setup

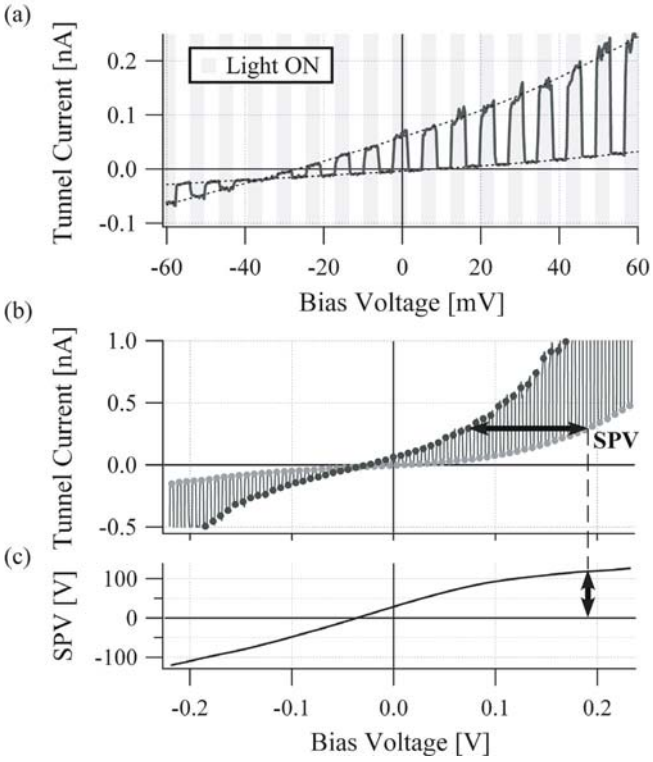

Fig. 8.6. Example of SPV Spectrum

rent for 30–80% of each illuminated/dark period was averaged to extract the illuminated/dark current at the corresponding bias voltage, which are shown by the black/gray circles, respectively, in Fig. 8.6(b). The gate time is introduced to eliminate the artifacts due to the finite transient time of illumination during which the laser power changes from 0% to 100% and vice versa, from the displacement current as a result of capacitance change of the tunnel junction, and from the recovery time of the MIS junction [16]. Finally, the illuminated/dark I-V curves for calculating SPV, which are shown by the thin dotted lines in Fig. 8.6(a), are obtained by interpolating the measured points using the smoothing spline function. In the present case, the precision of the tunnel current detection is limited by a few percent of relative error due to mechanical vibration and a few picoamperes of absolute error due to broadband noise in the signal. These errors in the tunnel current, together with the magnitude of $\mathrm{d}I/\mathrm{d}V$, determine the accuracy of measured SPV. When the tip–sample distance is longer, $\mathrm{d}I/\mathrm{d}V$ in the low-bias-voltage regime becomes too small. Accordingly, SPV could be measured only for the high-bias-voltage regime in such cases.

8.6 Point Spectroscopy

The left-hand column of Fig. 8.7 shows SPV spectra for a p-type Si(001)-2×1 surface (0.03 Ωcm) with various tip–sample distances [15]. The distances were determined by the servo action of conventional STM electronics under chopped illumination. The bias voltage was changed from (a) 0.3 V (b) 0.4 V (c) 0.5 V (d) 0.6 V with a fixed current reference of 1.0 nA. Twenty-five spectra were measured at random points on the surface under each servo condition. The dotted lines represent individual SPV spectra and the solid black ones represent the averaged ones. It can be seen that, even under a same servo condition, the SR-SPV spectra scatter widely. This is not because of the spatially varying SPV but mainly because of the uncertainty in determining the tip–sample distance. In our procedure, the tip–sample distance fluctuates due to the servo action under the periodic illumination, because the servo action tries to compensates the periodic SPV effect. Thus, when the servo is deactivated for an STS measurement asynchronously to the chopping, the tip–sample distance has finite variation. To visualize the amount of the variation, the dotted spectra are colored by the tunnel current at a bias voltage of −0.5 V. The gray scale of black to white corresponds to 70–150% of the tunnel current compared with the averaged value. In the right-hand column of Fig. 8.7, the SR-SPV at zero bias voltage (intrinsic SR-SPV) is summarized in histograms.

In the remainder of this section, we discuss the above results. Figure 8.6 clearly shows that SR-SPV can be strongly dependent on bias voltage even for a surface with a metallic surface state, such as the Si(111)-7×7 surface. Namely, the SPV value increased linearly as a function of the sample bias voltage in the low-voltage regime ($|V_s| < 0.1$ V) but showed saturation in

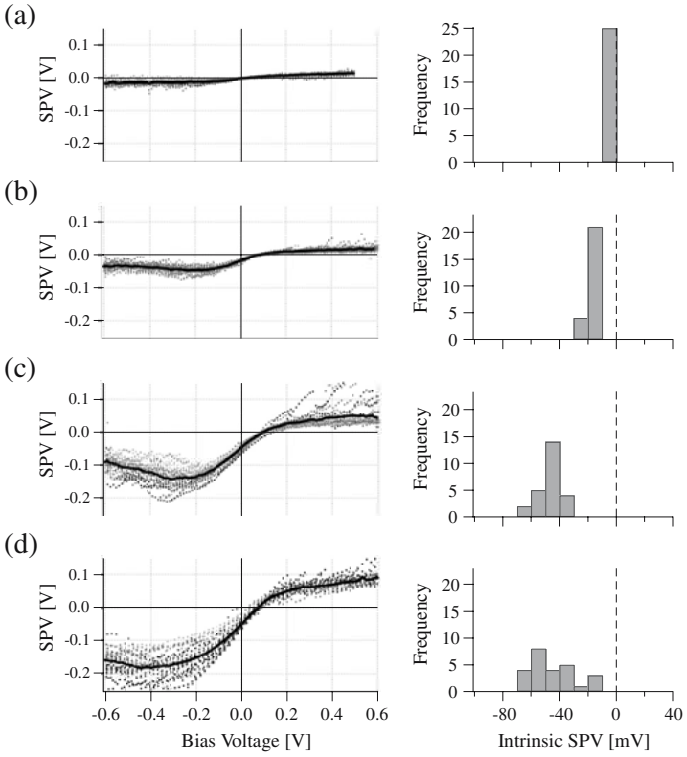

Fig. 8.7. SPV spectra of p-type Si(001)-2×1 surface (0.03 Ωcm)

the high-voltage regimes ($V_s < -0.1\,\mathrm{V}$ and $0.1\,\mathrm{V} < V_s$). The linear segments in these three regimes, with different slopes, were also confirmed in SR-SPV spectra for a nonmetallic Si(001)-2×1 surface, as shown in Fig. 8.7. These spectra cannot be simply explained in terms of the charging effect because the tunnel current changes more in the high-bias-voltage regimes than in the low-bias-voltage regime. Instead, penetration of the electric field due to the bias voltage into the subsurface region under dark condition and the amount of accumulated carriers under illuminated condition should be considered. Sommerhalter et al. reported that the surface band bending of the nonmetallic p-type WS_2 surface under STM measurement can be qualitatively represented by a simple one-dimensional MIS junction model [13]. The three regimes observed in the SPV spectra for p-type Si(001) surface can be explained in accordance with their result as follows. In the high-positive-voltage regime ($0.1\,\mathrm{V} < V_s$), sufficient accumulation of majority carrier occurs under dark conditions. Hence, the little band bending under the dark condition results in a small SPV. At a negative bias voltage, depletion of majority carrier occurs and the amount of surface band bending is proportional to bias voltage under the dark condition. Thus, in the low-bias-voltage regime

($|V_s| < 0.1\,\mathrm{V}$), the band bending is fully relaxed by illumination, resulting in the linear dependence of SPV on bias voltage. At high negative bias voltages ($V_s < -0.1\,\mathrm{V}$), however, the amount of band-bending relaxation saturates because of the limited back-diffusion of minority carrier.

In addition to bias voltage dependence, the SPV dependence on the tip–sample distance can also be explained by the same model. In Fig. 8.7, a small tip–sample distance resulted in a small SPV. In addition, the same tendency was obtained in the comparison of the dotted spectra in a same plot; the one with a larger current showed a smaller SPV. When the tip–sample distance is small, the photogenerated carriers tunnel efficiently into the STM tip and the accumulation of carriers at the surface region is insufficient, preventing the complete relaxation of band bending.

Furthermore, the SR-SPV at zero bias voltage was also dependent on the tip–sample distance, as shown in the right-hand column of Fig. 8.7. This is rather surprising, since there is no tunnel current between the tip and the sample in this situation. We conjecture that the very high tunnel transmission coefficient between the tip and the sample pins the surface potential, preventing the band-bending relaxation. In some of the previous studies on the SPV at zero bias voltage, shortening of the tip–sample distance was attempted in order to increase the measurement accuracy [8,12]. The presented result revealed the fundamental limitation of such an approach to measure the precise SPV at zero bias voltage.

8.7 Nanoscale Spatial Variation of SPV

In the previous section, the sample surface was homogeneous. Thus, the LM-STS spectrum did not have spatial variation. Here, we apply the LM-STS technique to an inhomogeneous surface to confirm and to make use of the spatial resolution of this technique. We prepare an unsaturated silver monolayer on Si(001) surface [15, 17].

The interface of Ag/Si(001) has been studied intensively as a prototype of metal/semiconductor interfaces. This is because its interface shows an abrupt transition from semiconductor to metal, almost within one atomic layer. Its well-defined interface is supposed to be ideal for the detailed study of a metal/semiconductor interface, unlike the rather diffuse interface of Au/Si(001) system. According to previous studies [18–25], silver films grow in Stranski-Krastanov mode on Si(001) substrate. The initial monolayer of silver has been reported to have several different structures depending on the growth and/or anneal temperature. Among them, a 2×3 structure is the most stable structure. Figure 8.8 shows an STM image of this structure. As can be seen, the 2×3 structure lacks mirror symmetry in the direction of $\times2$ translation symmetry. The structure grows as characteristic two-dimensional islands with a diamond shape on Si(001) terraces. It is reported that the 2×3 structure contains 0.4–0.6 ML of silver atoms and 0.5 ML of Si atoms in it,

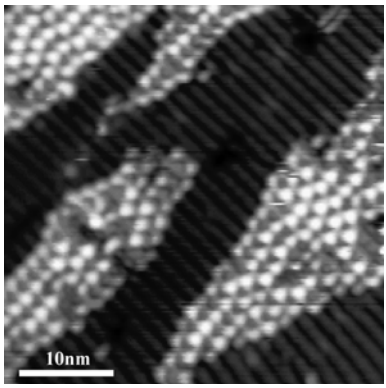

Fig. 8.8. STM topograph of Ag/Si(100)-2×3

i.e., the island is not made of pure silver. It is two dimensional alloy of silver and Si.

For the LM-STS experiment, partially covered Ag/Si(100)-2×3 structure is prepared by depositing ∼0.2 ML of silver onto clean Si(100) substrate (n-type ∼0.005 Ωcm) at room temperature. Then the sample is annealed at 700 K for 1 min. STM observation was done at 80 K with a chemically-etched tungsten tip. Illumination was done by a HeCd laser beam with an intensity of 2 mW focused into a 0.1 mm diameter spot. Chopping frequency was 80 Hz.

Figure 8.9(a) shows an STM topograph of the 2×3 structure grown from the lower edge of SB steps. Since the image is scanned at negative bias voltage, the 2×3 islands are not as apparent as in Fig. 8.8. To help the reader's eye, the islands are outlined by the black dotted lines. During the acquisition of Fig. 8.9(a), the STM tip is stopped at 27×27 grid points and LM-STS measurement is done at each point. The SPV values at bias voltage of 2.4 V were extracted from the 729 spectra and displayed by the contour lines superimposed onto the topograph. The SPV values for the area between the grid points are calculated by linear interpolation of neighboring grid points. As is clearly seen, the SPV value is affected by the existence of the two dimensional silver island. The resulting spatial variation of SPV has the characteristic dimension of several nanometers. It is suggested that this length scale is determined by the screening length of the electric field at the sample surface.

Since the whole LM-STS spectrum is measured at every grid point, SPV mappings for different bias voltages are also available from a single set of acquired data. To see the spatial variation and bias voltage dependence of SPV value in detail, the line profile of SPV mapping for the region indicated by the white hatch in Fig. 8.9(a) is plotted in Fig. 8.9(c). In general, a larger bias voltage gave a smaller SPV value, unlike what was observed in previous section. The area covered by the island gave a larger SPV. The characteristic length scale of the spatial variation is 5–10 nm. The SPV value does not show an abrupt change at the edge of the islands or Si step edges. This is reasonably

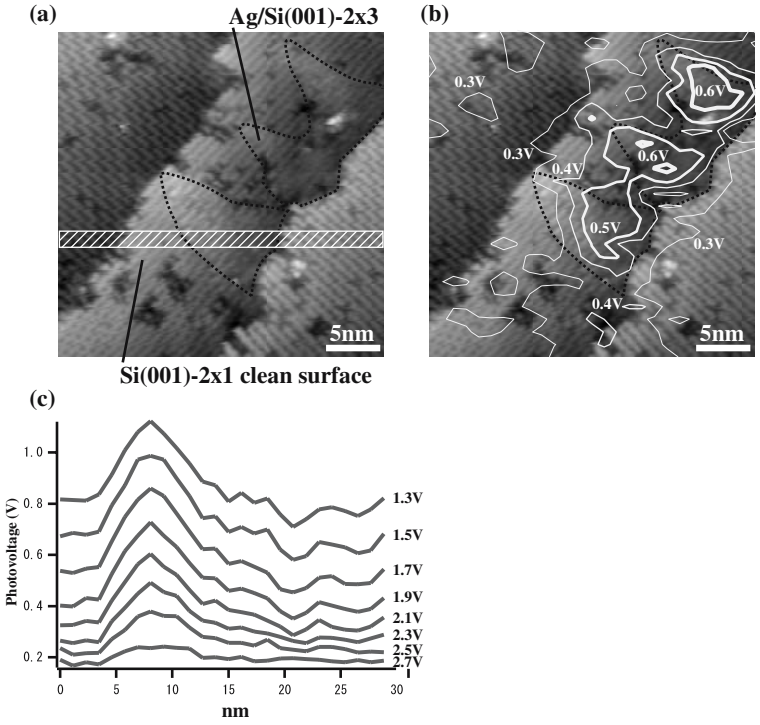

Fig. 8.9. (**a**) STM topograph of Ag/Si(100)-2×3 observed with a sample bias voltage of -2.0 V. (**b**) SPV for a sample voltage of 2.4 V is indicated by the contour lines. (**c**) SPV values for variety of sample bias voltages measured in the hached area in (**a**) are projected to the horizontal axis and plotted

expected because the spatial variation of band bending should be governed by the screening length of the electric field in the surface region. The continuity of SPV value suggests that the LM-STS technique is not affected very much by the local corrugation of the sample morphology nor local density of states.

Why and how much the SPV value increases with the existence of the silver island is still under discussion. If the island is truly metallic, the existence of a metallic layer should suppress the SPV effect. The 2×3 structure is, however, not very metallic. It is alloy of silver and Si. The existence of the 2×3 island varies the work function, local density of states, surface conductance and carrier recombination/generation rate. At this time which effect dominates the SPV variation remains to be studied.

8.8 Conclusion

LM-STS was proposed as an easily accessible and very powerful method for investigating SR-SPV under various experimental conditions. Unlike previous

methods, it can obtain not only the SR-SPV spectrum but also the entire illuminated/dark IV characteristics with a constant tip–sample distance, without the need for specially-designed STM electronics. The spatial variation of SPV with a length scale of a few nanometers was successfully observed while a STM topograph with atomic resolution was simultaneously obtained.

References

1. L. Kronik, Y. Shapira: Surf. Sci. Rep. **37**, 1 (1999)
2. L. Kronik, Y. Shapira: Surf. Interface Anal. **31**, 954 (2001)
3. E.H. Rhoderick, R.H. Williams: Metal-Semiconductor Contacts (Clarendon, Oxford, 1988)
4. S. Grafström: J. Appl. Phys. **91**, 1717 (2002)
5. R.J. Hamers, K. Markert: J. Vac. Sci. Technol. A **8**, 3524 (1990)
6. Y. Kuk, R.S. Becker, P.J. Silverman, G.P. Kochanski: Phys. Rev. Lett. **65**, 456 (1990)
7. Y. Kuk, R.S. Becker, P.J. Silverman, G.P. Kochanski: J. Vac. Sci. Technol. B **9**, 545 (1991)
8. T. Hagen, S. Grafstr om, J. Kowalski, R. Neumann: Appl. Phys. A **66**, S973 (1998)
9. D.G. Cahill, R.J. Hamers: J. Vac. Sci. Technol. B **9**, 564 (1991)
10. M. McEllistrem, G. Haase, D. Chen, R. J. Hamers: Phys. Rev. Lett. **70**, 2471 (1993)
11. D. Gorelik, S. Aloni, G. Haase: Surf. Sci. **432**, 265 (1999)
12. D. Gorelik, S. Aloni, J. Eitle, D. Meyler, G. Haase: J. Chem. Phys. **108**, 9877 (1998)
13. C. Sommerhalter, T.W. Matthes, J. Boneberg, P. Leiderer, M.C. Lux-Steiner: J. Vac. Sci. Technol. B **15**, 1876 (1997)
14. L. Kronik, Y. Shapira: Surf. Interface Anal. **31**, 954 (2001)
15. O. Takeuchi, M. Aoyama, R. Oshima, Y. Okada, H. Oigawa, N. Sano, R. Morita, M. Yamashita, H. Shigekawa: Appl. Phys. Lett., **85**, 3268 (2004)
16. Maeda, M. Uota, Y. Mera: Mater. Sci. Eng. B **42**, 127 (1996)
17. S. Yoshida, T. Kimura, O. Takeuchi, K. Hata, H. Oigawa, T. Nagamura, H. Sakama, H. Shigekawa: Phys. Rev. B. (2004) in press.
18. X.F. Lin, K.J. Wan, J. Nogami: Phys. Rev. B **47**, 13491 (1993)
19. X.F. Lin, K.J. Wan, J. Nogami: Phys. Rev. B **49**, 7385 (1993)
20. D. Winau, H. Itoh, A.K. Schmid, T. Ichinokawa: Surf. Sci. **303**, 139 (1994)
21. S.M. Shivaprasad, T. Abukawa, H.W. Yeom, M. Nakamura, S. Suzuki, S. Sato, K. Sakamoto, T. Sakamoto, S. Kono: Surf. Sci. **344**, L1245 (1995)
22. D. Winau, H. Itoh, A.K. Schmid, T. Ichinokawa: J. Vac. Sci. Technol. B **12**, 2082 (1994)
23. S. Folsch, D. Winau, G. Meyer, K.H. Rieder, M. Horn-von Hoegen, T. Schmidt, M. Henzler: Appl. Phys. Lett. **67**, 2185 (1995)
24. N. Doraiswamy, G. Jayaram, L.D. Marks: Phys. Rev. B **51**, 10167 (1994)
25. T. Michely, M.C. Reuter, M. Copel, R.M. Tromp: Phys. Rev. Lett. **73**, 2095 (1994)

9 Atomic-Level Surface Phenomena Controlled by Femtosecond Optical Pulses

D.N. Futaba

9.1 Introduction

Bonding at surfaces holds fundamental importance in our understanding and manipulation of chemistry and materials. For example, femtosecond (fs) laser-induced breaking or forming chemical bonds can provide crucial insight into these surface-related processes. Not only is it a great challenge in the pursuit of detailed experimental investigations of chemical reactions, the advent of new experimental technologies allows for a multitude of new possibilities by combining the strengths of separate techniques and tremendously impacting chemical physics. For this purpose, a considerable amount of research has already been done on the study of the interaction between light and solid-state surfaces [1–3] in particular, on semiconducting surfaces, for both the fundamental understanding and the technological importance to solid-state devices. Structural changes have been observed as a result of this interaction using lasers, and electronic processes have been shown to play important roles when the laser intensity was below the melting threshold [4–6]. Charge transfer and rearrangement are also thought to be key in making and breaking surface chemical bonds. In addition, the coupling of photoexcited electrons to the nuclear motion of the surface species and the time scale involved in bond dissociation and formation are two important issues. However, such optically-induced dynamic surface phenomena have not been well studied experimentally at the atomic scale [7].

In ultrafast laser technology, temporal resolution down to the femtosecond has been achieved. Moreover, not only are the dynamics of chemical reactions now observable, reactions can now be controlled. Short pulse lasers have been used to control reaction branching ratios of an organometallic molecule through the coherent control of independent chemical reaction channels [8]. Furthermore, microscopic techniques, particularly proximal probe microscopes, have reached the ultimate in spatial resolution in attaining sub-atomic lateral resolution. However, the complexity of the research drives us to use the combination of these two techniques in ultimately obtaining true experimental investigation of surface reactions.

We wish to address such questions as: What role does the surface structure, such as surface dislocations, surface contaminants, and atomic coordination, play in the reaction of interest? Beyond the fact that a structural

change occurred on the surface, we hope to gain a microscopic understanding of the process. Without question, energy transfer is a key issue, but the nature of the surface bonding, i.e., surface geometry, is critically involved in how that energy is transfered to a particular location, such as an adsorbate.

The advent of the scanning tunneling microscope (STM) [9] brought the reality of imaging the surface microscopically more closely than previously achieved. Based on the principle of quantum mechanical tunneling from a conducting or semiconducting sample to a sharpened metal tip, the STM generated a contour map of the surface local density of states near at the Fermi energy of the surface with atomic resolution [10]. This instrument is ideal for locally probing surface morphology due to changes of the surface layer. In this chapter we discuss the use of scanning tunneling microscopy (STM) to locally probe surface structure induced by femtosecond optical pulses. To this point, very little research has been done using an STM as a final states probe, which limits our detailed microscopic understanding of fs-induced reactions at surfaces.

The goals, therefore, of using an STM as a final-states probe for fs laser excitation is to gather sub-nanometer resolved imaging of the reacted surface and to not only investigate what has microscopically occurred on the surface but where it occurred as well. While the ultimate goal in combining ultrafast laser technology and STM is to obtain the dynamics of laser-mediated surface reactions with the ultimate lateral specificity, this is outside the realm of this chapter. In contrast to laser-assisted STM [11, 12] or time-resolved STM [7, 13–15], final states probing avoids the many problems associated with irradiation of the tunneling junction, such as thermal effects [16–18] and light-induced nanomodifications [19–22].

9.2 Femtosecond Pulse Pair Controlled Phenomena at Surfaces

Because a large portion of physics occurs at solid-state surfaces, it is natural to study the electronic interaction between the surface and the adsorbed species. Adsorption to solid-state surfaces results in a significant change in the electronic structure as well as the local environment of the adsorbed species from that found in the gas state. Depending on the coverage, the proximity of neighboring adsorbates can be particularly high compared to that in the gas state, which holds particular significance on the probability of intermolecular reactions. In addition, the adsorbate falls within binding site potential wells, which determine preferential bonding geometries and plays an important role in energy and electron transfer. Moreover, adsorption to such surfaces as late transition metals can act to lower reaction barriers and perhaps make otherwise inaccessible reaction channels possible. Perhaps most importantly with regards to this chapter, surfaces can provide an additional

channel where photon energy can be absorbed and redirected, which may not be possible in the gas phase [23, 24].

When directed onto a surface, it is understood that laser pulses, with durations much shorter than the electron–phonon coupling time and the electron diffusion time in the substrate, create a high density of energetic electrons within a cold atomic lattice. This results in a highly nonequilibrium state in the substrate that can lead to very different chemical reactions and phase transitions on the surface from those induced by other excitation sources.

For metal substrates with a single monolayer of adsorbates, the adsorbate layer can adsorb only a small fraction of the incident laser energy while the remainder is either reflected or absorbed by the substrate. Thus, the excitation of the substrate is inevitable. In short, assuming that the photoexcited electrons in the substrate thermalize instantaneously, the two coupled subsystems, e.g., the electrons and the phonons, are in internal equilibrium [25, 26]. These two systems are coupled through electron–phonon interactions [27]. Because all the energy is initially deposited into the electrons and the electron heat capacity is about two orders of magnitude smaller than the phonon heat capacity, the temperature associated with the electrons peaks for a couple of picoseconds while the phonon temperature remains much colder. After 10 ps the electrons and phonons come to thermal equilibrium, and after about 100 ps, the surface cools through electron diffusion into the bulk.

A variety of interesting surface phenomena have been already been observed using fs lasers on surfaces. To mention a few, fs-induced surface melting and surface disorder have been observed on silicon and GaAs [28–30]. Intriguing surface restructuring has been done with fs excitation of a CO overlayer on Pt(111) [31] as well as the creation of silicon microspikes [32]. In addition, numerous groups have reported on the desorption of adsorbed molecular species, such as NO from Pd(111) [33], CO from Cu(111) [34], benzene multilayers and O_2 from Pt(111) [35, 36]. However, the study of femtosecond induced reactions of molecular adsorbates have been highly limited perhaps due to the complexity of the energy coupling or the lack of fundamental understanding involving bond scission and formation. Despite these obstacles, the oxidation of carbon monoxide has been observed on a Pt and Ru in a number of experiments [25, 37, 38] as well as the dissociation of O_2 on Pd(111) [39]. While not technically an adsorbate–substrate system, the preferential characteristics of silicon adatom desorption from the Si(111)-7 $\times$ 7 surface have been studied with time-of-flight mass spectrometry and STM using nanosecond and fs single pulses [4–6].

While these probes can provide much useful information, only STM is capable of providing microscopic information at the sub-nanometer scale. Because the adsorption site and geometry can play a significant role in the energy transfer from the orbital hybridization with the surface, a more local investigation regarding the local environment is essential in order for a more complete understanding of surface chemistry at the molecular level. STM can

provide a microscopic look at the surface electronic structure, revealing such things as bonding sites, defects and local order/disorder.

The use of STM with femtosecond laser-induced chemistry has been very limited perhaps due to the technological obstacles or limited spectroscopic capability. While final states imaging elucidates little regarding the dynamics of the reaction, it does not suffer from other unwanted drawbacks resulting from in-situ irradiation, such as thermal bending and expansion of the STM probe [16–18].

9.2.1 Experiment: Site-Selective Silicon Adatom Desorption Using Femtosecond Laser Pulse Pairs and STM

To investigate the possible adatom desorption selectivity through pulse pair excitation, we performed an experimental study of silicon adatom desorption from the Si(111)-7×7 surface. We used fs laser pulse pairs with 80-fs pulse duration, 800-nm center wavelength, 300-mW average power and a 100-MHz repetition rate. After excitation, we observed microscopic changes induced to the surface with STM and directly recorded the desorption characteristics at each delay setting for each of the four adatom binding sites. The study revealed a preferential dependence between the delay time and the adatom sites within a 66.6–1000 fs delay range. In addition, we observed a dependence on the polarization of the incident pulse pairs. The experimental findings of this section demonstrate that the femtosecond delay time in optical pulse pair excitation plays a role in the site-selective desorption of Si adatoms below melting point irradiation. These findings can provide a basis for a new selective fabrication technique for nanometer-scale devices as well as physical and chemical insight into ultrafast dynamic processes at surfaces with atomic scale resolution.

The Si(111)-7×7 surface, whose structure consists of distortions from the ideal bonding tetrahedral sp^3 bonding geometry, relies heavily on electron-lattice interaction for structural stability [40]. This reconstructed silicon surface presents four distinct adatom sites, which differ both electronically and dynamically [41, 42] and it is thought they could serve as sites to excite localized vibrations.

This experiment was performed at room temperature using a fs laser-STM system as illustrated in Fig. 9.1. The STM was a commercially purchased low-temperature ultrahigh vacuum instrument by UNISOKU Co., Ltd., Japan, and was operated at a base pressure of 8.0×10^{-11} Torr. Si(111) samples were cut from an n-type, As-doped ($r = 0.001$–$0.005\,\Omega$/cm) Si(111) wafer and degassed under ultrahigh vacuum conditions at 600° for 10 hours. The samples were subsequently flash-heated at 1150° for 10 seconds in order to form the 7×7 reconstruction. During flash-heating, the pressure never exceeded 1.5×10^{-10} Torr. Linearly polarized pulses from a mode-locked Ti:sapphire laser (100-MHz repetition rate, 80-fs pulse width, 300-mW average power,

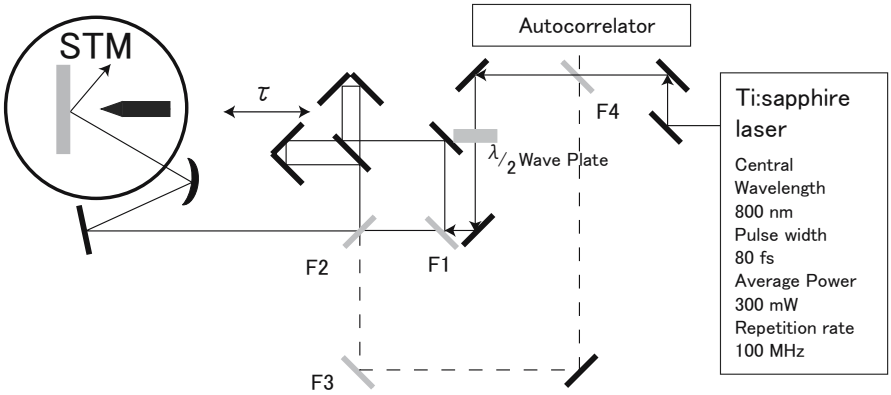

Fig. 9.1. Pulses from a mode-locked Ti:sapphire laser (100-MHz repetition rate, 80-fs pulse width, 300-mW average power, and 800-nm central wavelength) are directed into the STM vacuum chamber after being diverted through Michelson-type interferometric delay. Flip mirrors (F1–F4) allow for pulse characterization during the experiment

and 800-nm central wavelength) were directed into a Michelson-type interferometric delay and were then focused to a 300-mm diameter spot on the sample surface by a silver concave mirror (focal length of 300 mm). The air to vacuum transition presented a unique problem in that we were forced to pass the pulses through a medium other than air. The choice of viewports is fairly limited, but for our pulse width, we found that a borosilicate glass demonstrated both high transmission as well as negligible dispersion qualities when tested. The p-polarized (parallel to the reflection plane) laser pulses were incident to the surface at approximately 45°. During laser irradiation, the tip was withdrawn out of the path of the laser to avoid the possibility of desorbing any adsorbed species that may have resided on the tip. Although tips were routinely annealed before insertion into the STM, gradual adsorption of residual gases is unavoidable. The pulse pair delays ranged from 66.6 to 1000 fs (15.0 to 1.0 THz) with an irradiation time of 60 minutes. The adatom removal yield was found roughly to be on the order of 5 vacancies per 20 unit cells.

After verifying sample cleanliness by STM, we characterized the number of pre-existing adatom vacancies by examining several thousand unit cells. Subsequently we irradiated the surface. The surface was once again examined by STM. Similar to the initial states imaging, the final states images were taken in both polarities in order to rule out the possibility that apparent vacancies, which appear as dark spots, were due to adsorbed gases, which can appear as vacancies in one polarity and not the other [43, 44]. An example of such a case is marked with a circle in Fig. 9.2. Accordingly, by using this as a rule, we are confident that the dark spots are adatom vacancies. The desorption yield was determined by counting the number of vacancies for images

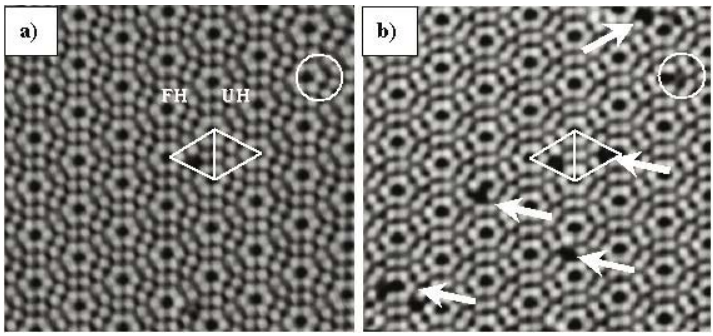

Fig. 9.2. (**a**) An STM image of the 7×7 surface before irradiation. $I = 0.2\,\text{nA}$; Bias $= 1.5\,\text{V}$. Both polarities were taken for each location to identify adsorbed gases; (**b**) An STM image after one hour of irradiation of two pulses. $I = 0.2\,\text{nA}$; Bias $= 1.5\,\text{V}$. The circle indicates an adsorbed gas as identified from the negative bias image

both before and after irradiation, and this procedure was repeated several times for each delay setting to confirm reproducibility. All STM observations were done using PtIr tips and were taken in constant-current mode 0.20 nA, 1.5 V).

Initial attempts at desorption using 800 nm (1.55 eV) light yielded no measurable desorption yield because it was thought that the 1.55 eV photons were insufficiently energetic to induce the 2.0 or 2.5 eV surface band transition believed to be a principle contributor to the desorption process [4–6]. However, using 800 nm pulse pairs showed desorption of adatoms from both center and corner sites, with fluences 100,000 times lower than previously reported. While not as dramatic as with higher fluences, the increase in the number of vacancies per unit area between the pre-exposed surface and irradiated surface is quite distinct.

STM images of sampled regions before and after laser irradiation of 4-mJ/cm^2 fluence revealed that the number of vacancies increases after laser exposure (Fig. 9.2). We repeated the experiment for a variety of delay and found that as we decreased the delay (increased the pulse pair frequency), we observed that the total desorption yield tended to increase. As shown in Fig. 9.3(a), this trend is clearly apparent except for the unexplained anomaly at 25 fs (12 THz). In addition, the profile of the total desorption yield suggested that significant desorption occurred only below 333 fs (above 3 THz).

We then examined the images further and compared the relative amount of desorption from center sites to corner sites at each delay setting. We found that the center-to-corner ratio ranged in value from as low as 0.876 to as high as 22.7 for each delay setting (Fig. 9.3(b)). This revealed a desorption preference which varied with the excitation delay time. In addition, it showed one delay setting (8 THz) to have a particularly high selectivity for center

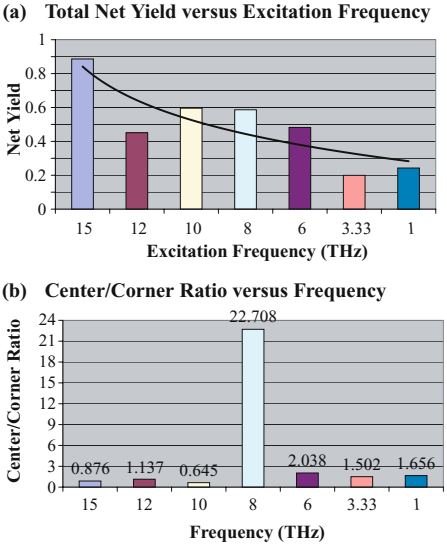

Fig. 9.3. (**a**): Total net yield as a function of excitation frequency. The trend indicates a general increase with higher frequencies (shorter delays); (**b**) The center to corner adatom ratio for each of the same excitation frequencies showing the preferential desorption between binding sites changes despite showing differences in total yield

sites. It seems that this result corresponds to the fact that the faulted-half (FH)-center adatoms have the most prominent peak at 8 THz for the surface phonon spectrum (one of the vibrational frequencies of localized phonons at adatom sites), while the FH-corner adatoms have no peaks at this frequency. This discovery prompted us to further investigate the adatom site-dependence on the desorption yield.

As summarized in Fig. 9.4, a detailed investigation of the desorption yields for each binding site revealed subtle trends for each frequency setting and for each adatom site. This breakdown of data is presented with the binding sites arranged in increasing binding energy site (i.e., FH-center, unfaulted-half (UH)-center, FH-corner, and UH-corner) [45] to make any related trends more easily identifiable. The most obvious trends are the individual desorption profile for each binding site and the desorption profile at each excitation delay setting. Generally, FH-center sites showed the greatest level of desorption. This seems to correlate with the fact that the FH-center sites have the lowest binding energy among the four adatom sites. Throughout the excitation frequency spectrum, save the 1–3 THz (to be discussed later) and the 12 THz setting, the efficiency for the FH-center sites was roughly unvarying. The UH-center sites, however, showed a slightly varying behavior, being strongly efficient at 8 THz and considerably less efficient at 10, 12, and 15 THz. Similarly distinct peaks existed at 10 and 15 THz for the FH-corner

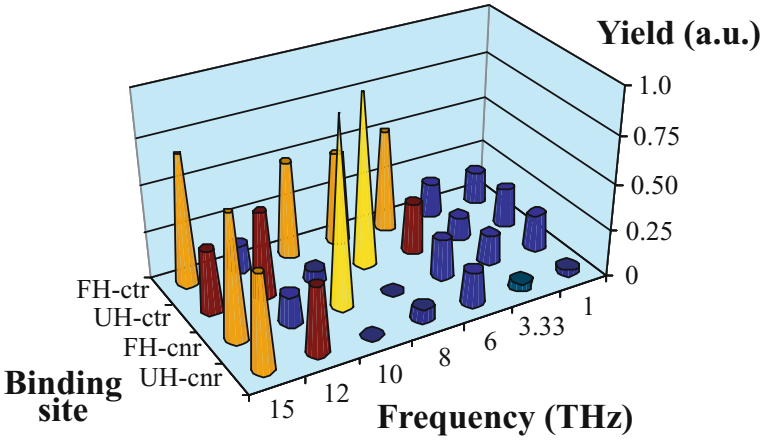

Fig. 9.4. Desorption yield as a function of binding site and excitation frequency with a pulse pair (1/delay time)

sites. The UH-corner sites exhibited maxima in the desorption yield at 12 and 15 THz.

Examining the profiles for each excitation setting, we observed that at lower frequencies, such as 1–3 THz, not only was there an insignificant level of desorption, there appeared to be no prominent site-preferred vacancies (Fig. 9.4). With higher frequencies, 6–12 THz, not only did the desorption efficiency increase, but also site-preferences emerged. At 6 THz, the desorption levels at all sites increased with a prominent peak for the FH-center sites. At 8 THz, highly selective profiles appeared with negligible desorption at two higher binding-energy sites (FH-corner and UH-corner) and distinct peaks at the two lower ones (FH-center and UH-center). At 10 THz and 12 THz, in contrast to prior trends where we observed preferences between center and corner sites, we observed a preference between subunits. At 10 THz, there was a marked preference to the FH-center and FH-corner sites desorption, while at 12 THz this tendency was reversed. Finally, at 15 THz, the desorption at all sites showed increased yields while showing no clear preferential behavior.

9.2.2 Interpretation

We believe that the process governing desorption is a two-step excitation. The first pulse excites an electron in a surface bonding state to an intermediate state with a lifetime τ, which is characteristic to the local electronic properties of the binding site. Additionally, as deduced from Fig. 9.4, this lifetime is

shorter than 333 fs. Using a single 1.55 eV photon, with the intensity below the melting threshold, the probability for removing an adatom is virtually zero. However, if a second pulse interacts with the medium within the lifetime of the excited surface bonding state, its energy can add to the first. In such a case, local phonons around the adatom, whose electron contributes to the substrate bonding, are further excited, which gives rise to the possibility of bond breakage. This two-photon process must therefore depend on the delay time. Further, we believe that differences in the desorption preferences stem from differences in the local dynamic properties surrounding each adatom site [42]. To be complete, detailed energy-band-structure calculations are needed to locate the precise energy levels involved.

A polarization dependent study comparing the experimental results of s-polarized and the previously mentioned p-polarized fs-pulses showed differences in delay-time dependent yield and binding site preferences (Figs. 9.5 and 9.6). Total yield with p-polarization demonstrated a definite monotonic trend with the excitation frequency while the yield from s-polarization is negligible and appears independent of the excitation frequency (Fig. 9.5). Moreover, while the calculated center-to-corner adatom ratio for excitation with p-polarization showed a definite preference at 8 THz, the s-polarization showed negligible levels and the fluctuation in the values were due mostly to the low yield. These results strongly suggested that surface heating associated with fs-laser irradiation is not the dominant desorption mechanism particularly at short delay times. Furthermore, it also suggests a dipole-like interaction between the adatom sites (including the dangling bonds) and the electric field of the laser. Consequently, this gives rise to localized phonons modes oriented along the surface normal direction [42].

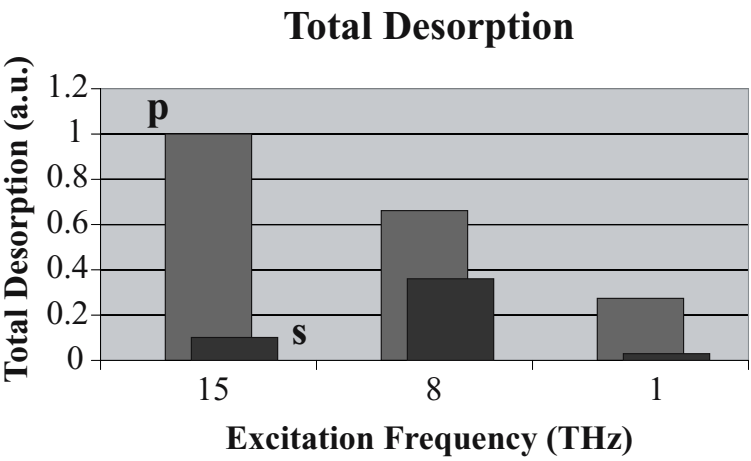

Fig. 9.5. Comparison of the total desorption between p- and s-polarization for several excitation frequencies

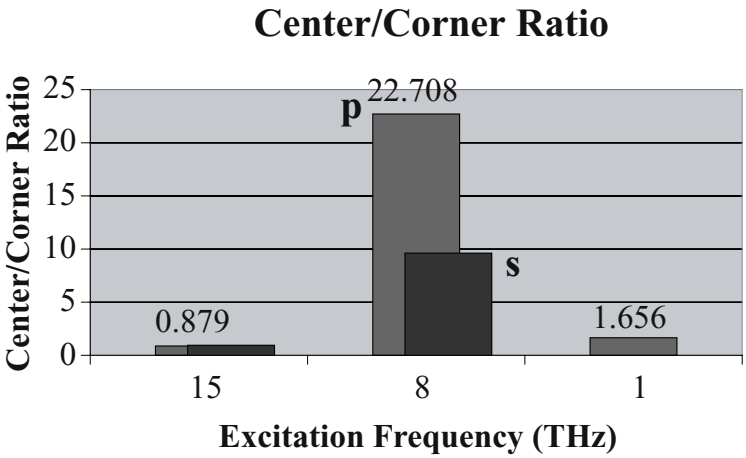

Fig. 9.6. Comparison of the center-to-corner adatom ratio between s- and p-polarizations for several excitation frequencies

In summary, the desorption characteristics of silicon adatoms from the Si(111)-7×7 surface were investigated using fs laser pulse pair excitation and direct observation with STM. A delay-time dependence on the overall desorption yield and desorption character was observed. With shortened delay time (increased excitation frequency), the total desorption yield increased. In addition, preferences among adatom binding sites were observed as a function of the delay time.

Inspired by these results for silicon adatom desorption, we have now set out to induce chemical reactions on a late transition metal surface. The two experiments we are exploring are the fs laser induced reactions of adsorbed organic hydrocarbons on Pt(111) using the fs laser as an excitation source. The first is the dehydrogenation of p-xylene adsorbed on the platinum surface and the second is the polymerization of styrene to polystyrene. The ultrashort laser pulses, which are well-below damage thresholds, are incident on the surface and used to promote a chemical reaction. We then compare it to the known product formation using different excitation sources, such as thermal desorption spectroscopy [49, 50]. For p-xylene, partial dehydrogenation occurred at 350 K from the methyl groups and aromatic CH bond breakage did not occur until about 550 K. At 300 K, of ethylbenzene have been observed to immediately dissociate to styrene upon adsorption to the Pt(111) surface. It has been observed that at heating to 400 K with a background pressure of ethylbenzene or styrene, the styrene polymerizes to polystyrene. Therefore, we wish to characterize the reaction changing various excitation laser parameters, such as polarization, pulse pairs, etc., investigate the role the surface states play in these reactions, and ultimately gain an empirical understanding for selecting the reaction pathway. Both molecules have a dis-

tinct molecular shape that is discernable in STM images. Additionally, it is expected that the p-xylene molecule will reorient itself to a tilt from the surface if the initial dehydrogenation occurs from the same methyl group.

9.3 Future Directions

The use of STM as a final states probe for femtosecond-induced surface phenomena is very much in its infancy. As such, there are numerous directions for improvement. First, the current availability of highly stable and low-noise commercial ultrahigh vacuum, air, and liquid microscopes allow for more complex experiments, such as at low temperature to reduce unwanted thermal effects, or in a liquid environment for an increased background density of adsorbates. Second, the feedback between excitation and reaction is extremely slow. Depending on the stability of the system, this could be on the order of hours, which leads to the next point. Third, *in situ* laser irradiation seems most desirable because of the simplicity in observing the same region before and after reaction. However, in order to avoid detrimental tip effects, such as thermal expansion [16–18] and contamination from tip residue, a highly clean tip is required. Such techniques have been developed to routinely prepare highly sharpened and highly cleaned tips [46], but there also exists the problem of choosing a proper experimental system where no reaction occurs before changing some character of the excitation source, such as delay time, polarity, or phase. Fourth, numerous recent advances in ultrafast laser technology give rise to a number of new excitation sources, such as shaped optical pulses through spatial light modulation of fs laser pulses [47]. Such technology has already been used for such purposes as laser cooling of molecular internal degrees of freedom [48]. In that experiment, the phase of the radiation was found to be the active control parameter, which promotes the transfer energy into certain vibrational levels and not others. By using such techniques, the radiation can be tailored such that energy is directed to avoid an undesired molecular vibration and thus drive the molecule along a different reaction path.

To conclude, as with reaction processes, the support of theoretical modeling is crucial in fully understanding the interaction between the surface and adsorbed species as well as the energy transfer between the two. Such theoretical support is also essential in choosing appropriate systems for study.

References

1. M. Vol Allmen: *Laser-Beam Interaction with Materials* (Springer-Verlag, Berlin, 1987)
2. P.J. Kelly: *Special issue on Laser-Induced Material Modifications*, Opt. Eng. **28** (1989)

3. H.-L. Dai, W. Ho (eds.): *Laser Spectroscopy and Photochemistry on Metal Surfaces*, Part II (World Scientific, Singapore, 1995)
4. K. Ishikawa, J. Kanasaki, Y. Nakai, N. Itoh: Surf. Sci. Lett. **349**, L153 (1996)
5. K. Ishikawa, J. Kanasaki, K. Tanimura, Y. Nakai: Solid State Commun. **48**, 913 (1996)
6. J. Kanasaki, T. Ishida, K. Ishida, K. Tanimura: Phys. Rev. Lett. **80**, 4080 (1998)
7. O. Takeuchi, R. Morita, M. Yamashita, H. Shigekawa: Jpn. J. Appl. Phys. **41**, 4994 (2002)
8. A. Assion, T. Baumert, M. Bergt, T. Brixner, B. Kiefer, V. Seyfried, M. Strehle, G. Gerber: Science, **282**, 919 (1998)
9. G. Binnig, H. Rohrer: Helv. Phys. Acta **55**, 726 (1982)
10. J. Tersoff, D.R. Hamann: Phys. Rev. Lett. **50**, 1998 (1983)
11. V. Gerstner, A. Knoll, W. Pfeiffer, A. Thon, G. Gerber: J. Appl. Phys. **88**, 4851 (2000)
12. S. Grafsröm: J. Appl. Phys. **91**, 1717 (2002)
13. S. Weiss, D.F. Ogletree, D. Botkin, M. Salmeron, D.S. Chemla: Appl. Phys. Lett. **63**, 2567 (1993)
14. M.R. Freeman, A.Y. Elezzabi, G.M. Steeves, G. Nunes, Jr.: Surf. Sci. **386** 290 (1997)
15. N.N. Khusnatdinov, T.J. Nagle, G. Nunes, Jr.: Appl. Phys. Lett. **77** 4434 (2000)
16. S. Grafsröm, P. Schuller, J. Kowalski: J. Appl. Phys. **83**, 3453 (1998)
17. R. Huber, M. Koch, J. Feldmann: Appl. Phys. Lett. **73**, 2521 (1998)
18. J. Jersch, F. Demming, I. Fedotov, K. Dickman: Appl. Phys. A **68**, 627 (1999)
19. C.-Y. Liu, A.J. Bard: Chem. Phys. Lett. **174**, 162 (1990)
20. A.A. Gorbunov, W. Pompe: Phys. Status Solidi A **145**, 333 (1994)
21. V.A. Ukraintsev, J.T. Yates, Jr.: J. Appl. Phys. **80**, 2561 (1996)
22. Z. Dohna Llek, I. Lyubinetsky, J.T. Yates, Jr.: J. Vac. Sci. Technol. A **15**, 1488 (1997)
23. T.J. Chuang: Surf. Sci. Rep. **3**, 1 (1983)
24. W. Ho: Comments Cond. Mat. Phys. **13**, 293, (1988)
25. F.J. Kao, D.G. Busch, D.G.D. Costa, W. Ho: Phys. Rev. Lett. **70**, 4098 (1993)
26. F. Buddle, T.F. Heinz, M.M.T. Loy, J.A. Misewich, F. de Rougemont, H. Zacharias: Phys. Rev. Lett. **66**, 3024 (1991)
27. S.I. Anisimov, B.L. Kapeliovich, T.L. Perelman: Sov. Phys. Jetp **39**, 375 (1974)
28. M.C. Downer, R.L. Fork, C.V. Shank: J. Opt. Soc. Am., B **2**, 595 (1985)
29. S.V. Govorkov, I.L. Shumay, W. Rudolph, T. Schroeder: Opt. Lett. **16**, 1013 (1991)
30. P. Saeta, J.-K. Wang, Y. Siegal, N. Bloembergen, E. Mazur: Phys. Rev. Lett. **67**, 1023 (1991)
31. F. Fournier, W. Zheng, S. Carrez, H. Dubost, B. Bourguignon: Surf. Sci. **528**, 177 (2003)
32. M.Y. Shen, C.H. Crouch, J.E. Carey, R. Younkin, E. Mazur, M. Sheehy, C.M. Friend: Appl. Phys. Lett. **82**, 1716 (2003)
33. J.A. Prybyla, T.F. Heinz, J.A. Misewich, M.M.T. Loy, J.H. Glownia: Phys. Rev. Lett. **64**, 1537 (1990)
34. J.A. Prybyla, H.W.K. Tom, G.D. Aumiller: Phys. Rev. Lett. **68**, 503 (1992)
35. H. Arnolds, C.E.M. Rehbein, G. Roberts, R.J. Levis, D.A. King: Chem. Phys. Lett. **314**, 389 (1999)

36. F.J. Kao, D.G. Busch, D. Cohen, D.G.D. Costa, W. Ho: Phys. Rev. Lett. **71**, 2094 (1993)
37. S. Deliwala, R.J. Finlay, J.R. Goldman, T.H. Her, W.D. Mieher, E. Mazur: Chem. Phys. Lett. **242**, 617 (1995)
38. C. Hess, S. Funk, M. Bonn, D.N. Denzler, M. Wolf, G. Ertl: Appl. Phys. A **71**, 477 (2000)
39. T.F. Heinz, J.A. Misewich, U. Höfer, A. Kalamarides, S. Nakabayashi, P. Weigand, M. Wolf: Proc. SPIC **2125**, 276 (1994)
40. K. Takayanagi, Y. Tanishiro, M. Takahashi, S. Takahashi: J. Vac. Sci. Technol. A **3**, 1502 (1985)
41. W. Daum, H. Ibach, J.E. Muller: Phys. Rev. Lett. **59**, 1593 (1987)
42. J. Kim, M.-L. Yeh, F.S. Khan, J.W. Williams: Phys. Rev. B, **52**, 14709 (1995)
43. I.-W. Lyo, P. Avouris, B. Schubert, R. Hoffman: J. Phys. Chem. **94**, 4400 (1990)
44. J.J. Boland: Surf. Sci. **244**, 1 (1991)
45. Y.F. Zhao, H.W. Yang, J.N. Gao, Z.Q. Xue, S.J. Pang: Surf. Sci. Lett. **406**, L614 (1998)
46. O. Albrektsen, H.W.M. Salemink, K.A. Mørch, A.R. Thölen: J. Vac. Sci. Technol. B **12**, 3187 (1994)
47. A.M. Weiner: Prog. Quant. Electr. **19**, 161 (1995)
48. A. Bartana, R. Kosloff: J. Chem. Phys. **99**, 196 (1993)
49. D.E. Wilk, C.D. Stanners, Y.R. Shen, G.A. Somorjai: Surf. Sci. **280**, 298 (1993)
50. W. Ranke, W. Weiss: Surf. Sci. **465**, 317 (2000)

10 Femtosecond-Time-Resolved Scanning Tunneling Microscopy

O. Takeuchi and H. Shigekawa

10.1 Femtosecond-Ångstrom Technology

As discussed in Chap. 7, scanning tunneling microscopy (STM) has realized atomic scale spatial resolution using the sensitivity of a tunneling current on as small a change in the tip-sample distance as 0.1 ångstrom. The spatial resolution of STM in parallel to the sample surface reaches 1 ångstrom and that perpendicular to the sample surface reaches 0.1 ångstrom. On the other hand, the time resolution of ultrafast experiments using ultrashort laser pulses is being improved continuously. Since the time resolution is determined by the pulse width of the lasers, the shorter the pulses we generate, the better time resolution we can obtain. As described in this book, noble quantum optics can provide laser pulses consisting of only few cycles of electric field oscillation. Time resolution realized by such lasers can be in the order of several femtoseconds. Until recently, these spatial resolution and time resolution were, however, independently developed and had not been realized simultaneously in one experiment. In this chapter, the recent achievement in combining these two techniques to develop a measurement system that possesses both ångstrom spatial resolution and femtosecond time resolution is introduced, namely, the pioneering of a new research field of *femtosecond-ångstrom technology*. The technology will assist the trend of future device development, which is getting smaller and smaller, and faster and faster. The time-resolved-atom-resolved microscopy will be absolutely imperative to investigate the ultrafast dynamics of carriers in nanoscale semiconductor devices and the charge transfer in future molecular devices.

In fact, the atomic resolution and femtosecond resolution had never been compatible. The time resolution of conventional STM is limited by the bandwidth of the current–voltage converter of STM, which is about 10 kHz–1 MHz, which corresponds to the time scale of 1–100 μs. Improvement in the circuit diagram can make it better [1–3] but it is still in the order of 0.1 μs. In fact, the femtosecond time resolution will never be realized by means of an electric method. The switching time of any transistor takes about a few picoseconds. The dispersion of a metallic wire is too high in the terahertz range, so that a femtosecond electric pulse will easily lose its shape when traveling a very short length. We definitely need an optical method to achieve femtosecond time resolution. On the other hand, the spatial resolution of an optical mi-

croscope can not be much better than the wavelength of the light being used, because the resolution is given by the product of the wavelength and the numeric aperture (NA) of the optics. Generally, the NA can not be as small as 1/100 or 1/1000. We can still observe the emission from a single molecule with such optics with a spatial resolution of sub micrometers if the molecules are sparsely scattered on a substrate. However, this does not mean the improvement of the spatial resolution. The best spatial resolution in optical observation is, at this moment, realized by the detection of a nearfield electromagnetic wave. The method is called scanning nearfield optical microscopy (SNOM) or nearfield optical scanning microscopy (NSOM). Since nearfield waves decay exponentially in the length scale of a few tens of nanometers, noble SNOM setup can achieve 10–20 nm spatial resolution. At the same time, since SNOM is a purely optical technique, a variety of the conventional ultrafast techniques may also be applicable to SNOM measurement [4,5], although the chirp compensation for the long fiber optical path, which is commonly used in SNOM setup, might be a critical experimental problem. The spatial resolution of SNOM, however, will not be as good as that of STM. The decay length of a nearfield electromagnetic wave is much longer than that of the electron wave function. Therefore, sub-molecular resolution will not be achieved by the SNOM techniques.

In order to pioneer the ångstrom-femtosecond technology, a combination of STM with ultrashort pulsed laser is the most promising method to observe ultrafast transient processes ($\sim$ several femtoseconds) that occurs in ångstrom region.

10.2 Previous Studies in This Field

Since the development of STM in 1980 [6], many researchers have been making efforts to accomplish the difficult task [7–12] of pioneering ångstrom-femtosecond technology. The ultimate goal is to analyze and control the electronic and/or structural dynamics of materials with atomic resolution on a femtosecond time scale. There have been two major concepts proposed for achieving this goal.

One is to introduce an ultrafast photoconductive gate into the current detection line of STM as shown in Fig. 10.1. Weiss et al. called this type of microscope a photoconductively gated STM and presented that it generates a time-resolved current signal in the order of 1 ps [7]. They used two laser beams, namely, one to excite the samples, which also had photoconductive gate in their demonstrative experiment so that the tunnel current was sensitively modulated by the illumination, and the other to switch the photoconductive gate in the current detection line. In each beam, a train of laser pulses with the exactly same repetition rate $\sim$100 MHz impinges the sample and the gate, respectively. Without the photoconductive gate, since the repetition rate of laser pulses is much higher than the bandwidth of the

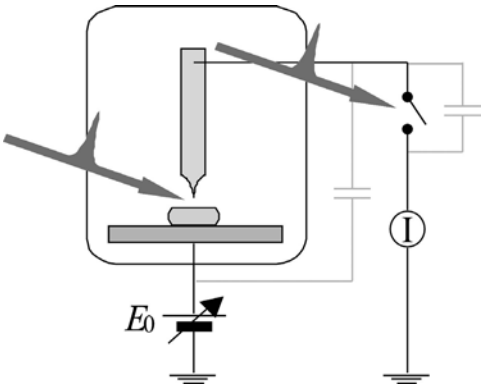

Fig. 10.1. Schematic of photoconductively gated STM

tunnel current detector, the periodic tunnel current modulation by each laser pulses exciting the sample can not be detected. What will be observed is the change in the averaged tunnel current. However, with the photoconductive gate in the current detection line, the system will detect the transient current value just at the moment when the gate is in the on-state. In reality, the signal sampled by the gate is also time-averaged by the slow current detector. Thus, although the signal level will become very low, a signal proportional to the transient tunnel current can be measured. When the current value is recorded as a function of the delay time between the excitation and gating, the transient tunnel current will be reproduced in real time scale.

The basic concept described above is the same as the optical pump-probe experiments. Thus, if this were indeed the case, the system would be a time-resolved STM. However, Groeneveld and van Kempen pointed out that the detected signal should have been primarily due, instead of tunneling current, to the displacement current generated by the coupling of two stray capacitances, one at the tunneling junction and the other at the photoconductive gate [13]. When the signal arises from the displacement current, the lateral resolution of measurement is given by the geometric dimension that defines the capacitance at the junction and is much worse than that of STM; it is typically about 1 μm. Up to now, several attempts have been made to improve this type of STM [8,9]. Junction mixing STM has exhibited 1 ps time resolution with 1 nm spatial resolution. However, this spatial resolution originates from the nanoscale variation of the tunnel-current-voltage dependence of the sample while the ultrafast phenomenon itself does not have an atomic-scale structure. It is of rather limited application. Moreover, the time resolution of this type of STM, in principle, cannot overcome the response time of the photoconductive gate, which is typically about 1 ps.

The other approach relies on the direct excitation of the tunneling junction by a sequence of laser pulses and the detection of the induced tunneling current as a function of interpulse spacing. Hamers and Cahill, in their pi-

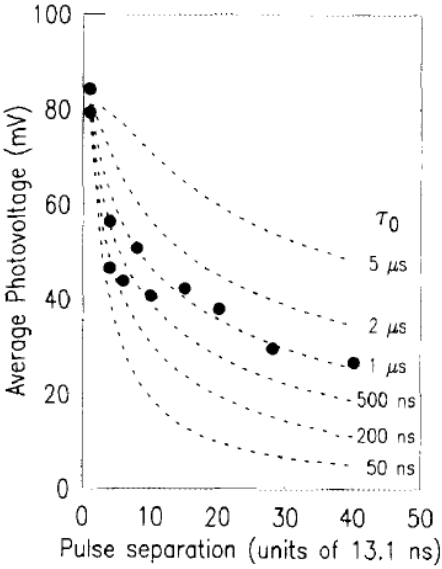

Fig. 10.2. Photovoltage values for various repetition rates of pulse laser illumination measured on Si(111)-7×7 surface [10]

oneering work, determined the carrier relaxation time at the Si(111)-7×7 surface with about 10 ns time resolution and 1 μm spatial resolution by this approach [10]. They positioned their STM tip above their sample with tip–sample separation of ∼100 nm. Thus, to be accurate, their experiment was indeed not a STM experiment. But, it addresses other important issues in time resolved STM. They illuminated the sample surface just below their tip, with a chopped illumination consisting of a train of laser pulses with the repetition rate of 80 MHz. Since the surface potential is modulated by illumination due to surface photovoltage (SPV) effect, the STM tip detects the displacement current when the illumination turns on to off and vice-versa, due to the charge/discharge process of stray capacitance at the tip–sample separation. They measured this displacement current by a lock-in amplifier, which is proportional to the magnitude of SPV. Then, they changed the repetition rate of laser pulses with eliminating one of every two, two of every three, $n-1$ of every n pulses from the original pulse train. By elimination, the repetition period becomes $n \times \Delta t$, where n is a natural number and Δt is the repetition period of the original pulse train. Figure 10.2 plots the signal level as a function of the repetition period. From this plot, they concluded that the carrier lifetime in their sample is about 1 μs because of the following argument. When the interpulse period is longer than the carrier lifetime, the surface bandbending of the sample is always fully relaxed. However, as the interpulse period becomes shorter than the lifetime, the surface bandbending

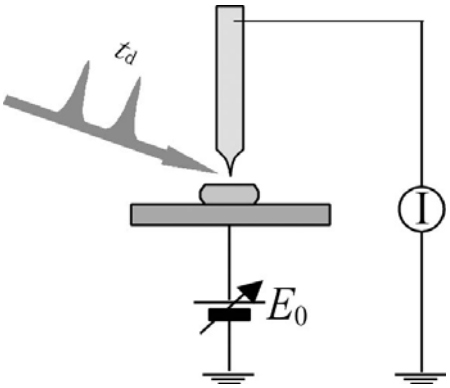

Fig. 10.3. Schematic of pulse-pair excited STM

remains until the next pulse injects new photo carriers. Thus, the amount of bandbending depends on the interpulse period of the laser pulses. Therefore, change in the signal as a function of the repetition time gives us information about the band relaxation mechanism. A method similar to this will have a time resolution as good as the repetition rate of the laser pulse train.

In order to obtain a time resolution better than the repetition rate, pulse-pair-excited STM is proposed, where the illumination is composed of a sequence of pulse pairs and the tunneling current is measured as a function of the delay time between the two laser pulses in a pulse pair as shown in Fig 10.3. The signal from this kind of setup is dependent on individual physical systems; thus the interpretation of the obtained signal will be complicated compared to more straightforward approaches such as photoconductively gated STM, but it will be free from the drawback of slow response of the electronic circuit. In addition, the time resolution is determined by the time delay between the two pulses, instead of the repetition rate of the original laser. Thus, the resolution can be improved without any limitation by shortening the laser pulse width. Consequently, in principle, pulse-pair-excited STM has the potential of achieving femtosecond and angstrom resolution. We have chosen this type of measurement setup.

10.3 Fundamentals of the Pulse-Pair-Excited STM

In the pulse-pair-excited STM experiment, we expect the tunnel current changes as a function of the delay time between the pulse pair. Here, let us discuss in which situation the dependency of tunnel current on the delay time appears.

We start with reminding the general conditions. The tunnel gap of an STM is illuminated by laser pulses. We, of course, expect the tunnel current to be changed by the pulse illumination. There are a variety of physical origins

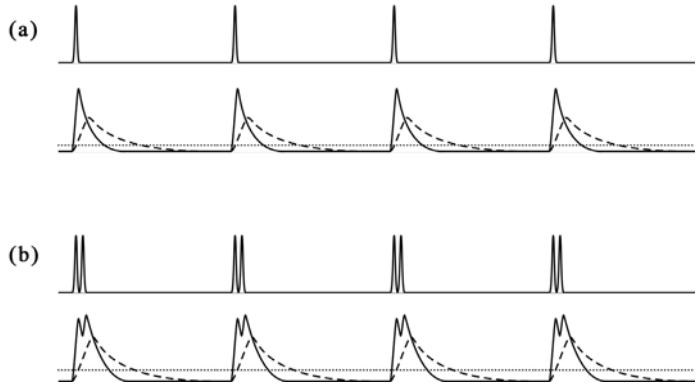

Fig. 10.4. Time evolution of laser intensity (*upper*) and tunnel current response (*lower*) for (**a**) pulse and (**b**) pulse-pair illumination

causing such changes in tunnel current, such as photocarrier excitation and excitation of plasmon/polariton. Here, however, we are not concerned with the specific origin of the change in the tunnel current. We just assume the tunnel current is affected by the illumination. Since our STM preamplifier has relatively narrow bandwidth, the photo-induced change in the tunnel current can not be accurately observed. The situation is illustrated in Fig. 10.4(a). The true change in tunnel current (solid line) will be deformed as a broken line. Moreover, when the response of the preamplifier is much slower, slower than the repetition rate of laser pulses, what we observe will be the averaged tunnel current (dotted line). We will no longer distinguish each laser pulse in the tunnel current signal. When we use the pulsed lasers with ∼100 MHz repetetion rate, this condition indeed stands.

The situation is same for the pulse-pair-excited STM. This time, pulse pairs with a delay time of 10 fs–100 ps impinge the tunnel gap at the repetetion rate of the original laser source, as illustrated in Fig. 10.4(b). An STM preamplifier can never resolve the two paired pulses in the tunnel current signal. What we can observe will be, again, the deformed or averaged tunnel current signal as shown by the broken and dotted lines.

What happens when we change the delay time between the paired two pulses in this situation? Look at Fig. 10.5. When the delay time is longer than the lifetime of the excited state of the sample, as shown in Fig. 10.5(a), the sample excited by the first pulse relaxes before the second pulse impinges it. Thus, the total tunnel current deviation caused by the two pulses will be exactly twice of that by one pulse. However, when the delay time is reduced as shown in Fig. 10.5(b)–(d), the second pulse impinges an excited sample. Hence, the current deviation caused by the second pulse (shadowed area) might be different from that caused by the first pulse. The figure illustrates the case where the current deviation becomes smaller when the pulse impinges an excited sample. In reality, it might become larger, depending on the specific

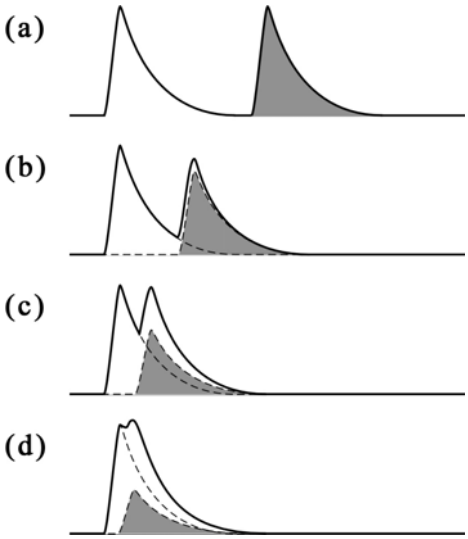

Fig. 10.5. Delay time dependence of current deviation due to the second pulse

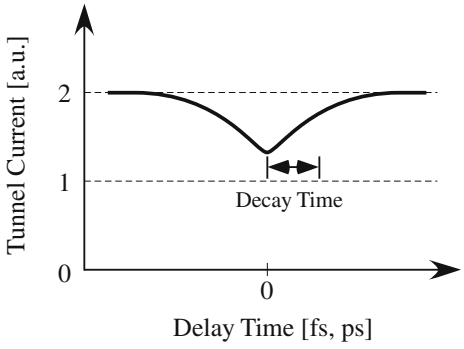

Fig. 10.6. Delay time dependence of the averaged current

physical system. The important point is that, when this type of dependency exists, we can observe the decay of the excited sample just by measuring the integrated or averaged tunnel current without knowing the exact shape of tunnel current change, in other words, with a narrow bandwidth preamplifier. By plotting the averaged tunnel current against the delay time, we will obtain a result like Fig. 10.6. The vertical axis has a zero point at the tunnel current without laser illumination and the signal is normalized by the tunnel current deviation when only one of the two pulses impinges the tunnel gap. When the two pulses have the same intensity, the plot will be symmetric against zero delay time, $t_d = 0$. When the delay time is close to zero, the signal will decay on both the $t_d < 0$ and $t_d > 0$ sides. The life time of the excited state of the sample can be obtained from this region.

It is not surprising that such a relationship between the averaged tunnel current and the delay time exists. As described above, when the delay time is long enough, the photoinduced tunnel current component caused by a pulse pair will be exactly equal to twice that caused by a single pulse. On the other hand, when the delay time is zero, the photoinduced tunnel current is generated by a single pulse twice as intense as the original pulse. Thus, the tunnel currents for these two cases are equal only when the photoinduced tunnel current has perfectly linear dependency on the excited laser intensity. Conversely, however, any nonlinearity in the relationship will result in the difference between the two cases. Thus, when the delay time is swept, we will obtain a time-resolved tunnel current signal by the pulse-pair-excited STM.

In summary, in the pulse-pair-excited STM, the first laser pulse works as the pump pulse to excite and modulate the sample surface and the tunnel current deviation caused by the second laser pulse will be measured as the probe signal. The method will really combine the ultimate temporal resolution of the optical pump probe approach and the ultimate spatial resolution of scanning tunnel microscopy. It is a very promising way to explore the new field of femtosecond-ångstrom technology.

10.4 Design of the Measurement System

The setup of the pulse-pair-excited STM is illustrated in Fig. 10.7 [15]. In the prototype system, a Ti:Sapphire oscillator with 80 MHz repetition rate is used as the laser source. Its center wavelength is 800 nm and the width of the spectrum was ∼30 nm. When combined with a chirp compensation circuit with a prism pair, laser pulses with a pulse width of 25 fs and averaged power of 200 mW can be obtained. When replacing this laser source with the monocycle optics with a fiber and a spatial light modulator that was described in the previous chapters, the temporal resolution of the system could be further improved. However, there might be a trade off between the pulse width and the power/stability of the laser source.

The repetition rate of the laser source should be carefully chosen. For example, when we use a regenerative amplifier to have much higher peak intensity of laser pulses, the repetition rate decreases and that may cause the thermal expansion/shrinkage of STM tip, synchronized with the laser repetition rate. Use of a laser system with a repetition rate less than 100 kHz is not realistic when we need to use high intensity excitation. It should also be considered that the very high peak intensity obtained by a regenerative amplifier might cause multiple photon excitation of sample/tip electrons, resulting in photoelectron emission from these materials. This considerably affects the measurement of tunnel current. When the tip–sample distance is short, a laser intensity as small as 0.5 MW/cm^2 can cause electron emission in vacuum conditions [16]. When a laser beam with a repetition rate of 1 kHz and a pulse width of 100 fs is focused in 1 mm diameter, only an averaged

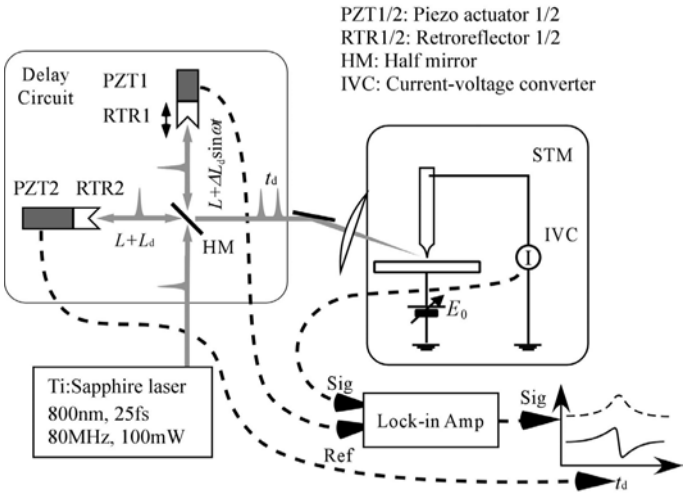

Fig. 10.7. Schematic of our shaken-pulse-pair-excited STM system

power of 1 μW corresponds to the threshold peak intensity of 0.5 MW/cm^2. Although the threshold must be largely increased when the experiment is done in the air, a regenerative amplifier may not be used in the time-resolved STM experiment.

Another issue in choosing the repetition rate of the laser illumination is the signal level of the time-resolved component of the tunnel current. Assume that the tunnel current increases with laser illumination by 1 nA and decays in 10 ps and the pulses impinge every 10 ns which corresponds to the repetition rate of the laser pulses, i.e., 100 MHz. Then, the change in the averaged tunnel current will be 1 pA. The time resolved component of the tunnel current change is a part of this 1 pA. If the component was 10% of it, we can expect a 0.1 pA signal. This is a reasonable signal level to detect with a noble measurement system. On the other hand, when we simply substitute 1 kHz for the repetition rate, the signal level decreases five orders of magnitude. Such a small signal is no more detectable. Thus, it should be determined which of the increase of peak intensity and the decrease of repetition rate dominates the signal level.

Each laser pulse emitted by the laser source is split into two pulses by the beam splitter in the delay circuit. The two pulses made by the delay circuit are output onto the identical beam path so that the pump pulses and the probe pulses can be easily focused into the very same spot. The end mirror of one of the two arms in the delay line can be translated by a piezo device in the range of ±2 cm as fast as 20 Hz.

The STM head is a commercial desktop STM system working in the air, which is placed on the same optical bench to which the whole optical setup is fixed. To isolate vibration and air flow, an rubber isolator is inserted

between the STM head and optical bench, and a hood with a small hole covers the whole STM head. The laser beam illuminates the sample surface from a direction ∼45 degrees from normal through the hole on the hood. The distance between the sample and the objective lens was about 100 mm. It can not be shortened very much because of the physical dimension of instruments. In order to obtain a small numerical aperture (NA), the laser beam is widened by the diverging lens up to a diameter of 10 mm and finally focused by the objective lens. With these optics, the spot size of a few tens of micrometer is obtained. The maximum average power of the laser is ∼20 mW for both pump and probe beams. This power corresponds to the peak power of ∼1 GW/cm^2.

10.5 Shaker Method

Now, we discuss how to detect time-resolved tunnel current signals as small as a few tens of femto-ampere from the noisy tunnel current signals. It is common to use a lock-in amplifier to reduce the broadband noise in the signal and to have a good signal-to-noise (S/N) ratio.

For example, the conventional pure-optical pump-probe experiments often modulate the intensity of the pump laser beam by using an optical chopper and use a lock-in amplifier to detect the variation of the probe signal synchronized to the pump intensity modulation. Such methods increase the S/N ratio several orders of magnitude. When we combine the pump-probe technique with STM, the modulation of pump laser intensity causes a critical problem. Imagine an optical chopper to be inserted into one of the two arms of the delay line and the tunnel current is lock-in detected at the modulation frequency. Then, the obtained signal will be the difference in the tunnel current between the two conditions of one pulse excitation and of two pulses excitation. Since the difference becomes very large even if the tunnel current has no nonlinear dependence on the laser intensity, in order to detect a relatively small component of the time-resolved tunnel current, one will need unrealistic dynamic range for the lock-in detection. Moreover, chopping the laser illumination causes the thermal expansion/shrinking problem of the STM tip. In particular, when the lock-in detection is done synchronized to the chopping frequency, it is impossible to avoid the thermal problem even with the increase of the chopping frequency, because the chopping frequency cannot exceed the bandwidth of the STM preamplifier, which is commonly as narrow as 100 kHz.

In order to overcome these problems, a noble technique, double lock-in technique, was proposed, where the pump and probe beams are chopped with similar but different frequencies f_1 and f_2, and the tunnel current is detected by a lock-in amplifier at the difference frequency $|f_1 - f_2|$ [12]. The detected signal is proportional to the difference between the tunnel current under the condition where the two pulses impinge independently and that under the condition where the two pulses impinge as a pulse pair. In other

words, the signal is proportional to the nonlinear component of the tunnel current against the laser illumination. With this technique the dynamic range of the detection can be improved. Moreover, since the lock-in detection is not performed at the chopping frequencies f_1 and f_2 but at the difference frequency $|f_1 - f_2|$, the chopping frequency can be increased to reduce the thermal expansion/shrinking problem of the STM tip, without the limitation of preamplifier bandwidth [12]. In the previous study, although the nonlinear component of the tunnel current was acquired, the time resolved signal was not distinguished. Since this method also modulates the laser intensity, thermal expansion and shrinking of the STM tip cannot be avoided. Measurement with high intensity of the exciting laser, which generally gives larger nonlinearity in the tunneling current, can not be performed in this setup.

The new setup we proposed is fundamentally not affected by the thermal problem. In this method, instead of the laser intensity, the delay time of the pulse pair is periodically modulated and the tunnel current is lock-in detected at the modulation frequency. We call this shaken-pulse-pair-excited STM (SPPX-STM). When the delay time of the two pulses t_d is modulated with a small value Δt_d around the center position t_d^0 at frequency ω, the tunnel current can be represented as

$$I_t(t_d^0 + \Delta t_d \sin \omega t) = I_t(t_d^0) + \Delta t_d \sin \omega t \frac{\mathrm{d}I_t}{\mathrm{d}t_d} + O(\Delta t_d^2). \tag{10.1}$$

With the use of a lock-in amplifier, the coefficient of the term $\sin \omega t$, $\mathrm{d}I_t/\mathrm{d}t_d$, can be obtained. In this system, when the tunneling current is independent of the delay time, the output is zero. There is no background at all. Thus, the signal-to-background ratio is maximized. The fluctuation of laser intensity can be reduced by lock-in detection. Finally, since the laser intensity is not modulated, thermal expansion and shrinking of the STM tip does not occur.

10.6 Performance of the System

In order to confirm the validity of delay-time-modulated method, the performance of the system was examined using a surface photovoltage effect. A nondoped n-GaAs(001) was used as the sample (carrier density $\sim 1 \times 10^{15}\,\mathrm{cm}^{-3}$). Figure 10.8 shows the I-V curves obtained with and without laser illumination (set point $V_s = -2.5\,\mathrm{V}$, $I_s = 0.10\,\mathrm{nA}$). Because of the low doping level, when a positive sample bias voltage is applied, the wide depletion layer formed at the tunneling gap prevents the tunneling current under a dark condition. With illumination, however, the photoinduced carriers decrease the depletion layer, allowing the tunneling current to flow. The tunnel current increases with the intensity of the excitation laser. Since the sample is nondoped, small changes in the photoillumination intensity at the tunnel junction can be sensitively detected as changes in the tunnel current. According to the independence of

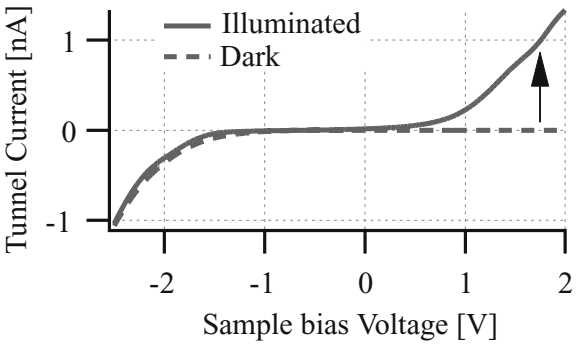

Fig. 10.8. I-V curves obtained for n-type GaAs(100) with and without laser illumination

the current difference between illuminated and dark conditions on the frequency of switching, the displacement current component is determined to be negligible. In addition, the absence of the photoinduced tunnel current difference for negative sample bias voltages indicates the thermal expansion effect of the tip is also negligible under our experimental condition. Thus, almost all of the current change at positive sample bias voltage is attributed to a change of the tunneling current.

Figure 10.9 shows an experiment for evaluating the temporal resolution of our system. The tunneling current was recorded during sweeping of the temporal delay of the paired laser pulses with a static tip–sample separation. When the delay time is small compared to the pulse width and the two pulses are temporarily overlapped, sweeping the delay time causes the oscillation of the total laser intensity at the periodicity of the carrier wave owing to the interference between the two pulses. The oscillation decreases as the portion of the overlap decreases, and when the two laser pulses are separated, the oscillation vanishes. The oscillation of illumination intensity at the tunneling junction can be detected as an oscillation in tunneling current as shown in Fig. 10.9. The wavelength of the laser pulse is centered at 800 nm, and the pulse width is 25 fs. As is shown in Fig. 10.9(a), the tunneling current oscillates at 2.6 fs, which corresponds to the periodicity expected from the wavelength of 800 nm.

Similar measurement was performed by Gerstner et al. [12]. However, in their case, thermal expansion of the STM tip was used for the analysis. In the present case, by using a nondoped n-GaAs(001) as the sample, the laser intensity could be kept low so that the thermal expansion effect could be avoided. As a result, not the total power of the illumination impinging on the STM tip, but rather the laser intensity exactly at the tunneling junction, could be obtained.

Now let us see the performance of the newly developed shaker method. Figure 10.9(b) shows the lock-in amplifier signal (time constant = 30 ms)

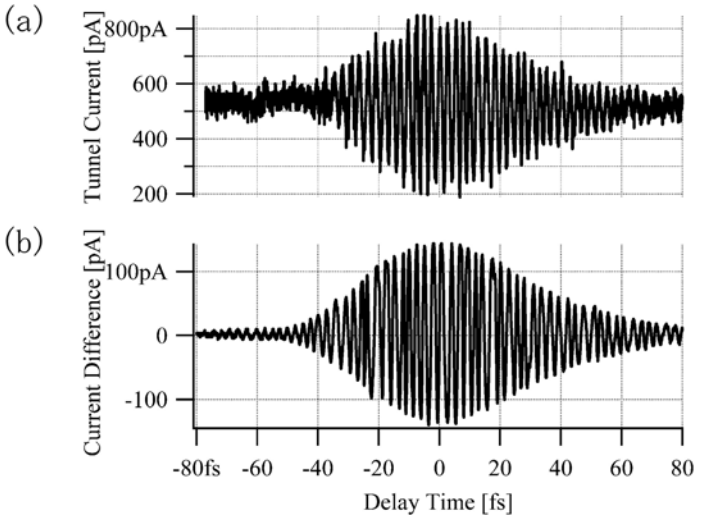

Fig. 10.9. Results of the temporal resolution of our system; (**a**) delay-time-dependent tunneling current, (**b**) SPPX-STM signal

plotted versus delay time, where the delay time was modulated by 0.5 fs around the center value at 400 Hz. The derivative of the graph in Fig. 10.9(a) was successfully obtained with a lower noise level, indicating the expected performance of our time-resolved STM. Its temporal resolution is limited by the pulse width, in the range of femtoseconds. In the actual experiment, one has to maintain a delay time longer than the pulse width to avoid the interference effect shown here.

10.6.1 Discussion of the Interference Effect

Here, we notice a critical problem. The delay time modulation method is superior to other methods in that it does not modulate the illumination intensity in order to avoid the thermal expansion/shrinking problem of the STM tip and to realize a stable measurement even under a high intensity excitation. As is discussed above, however, the constant excitation intensity is not preserved when the delay time becomes close to zero. When the delay time is as small as the pulse width, the interference between the two pulses causes an oscillation of the average power. This might cause the crash of the STM tip apex into the sample surface. Even if the crash can be avoided, it will considerably affect the tunnel current. The interference can be diminished by having the polarizations of the pump or probe pulse perpendicular. As pointed out previously [12], however, this technique does not fully get rid of the problem. Since the scattering effect is very strong near the STM tip apex, the polarization of pump and probe pulses is not perfectly preserved.

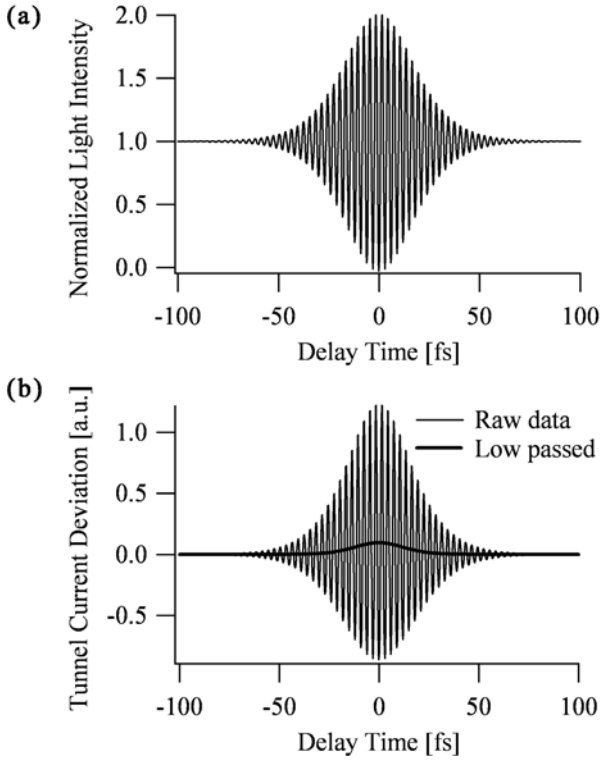

Fig. 10.10. (**a**) Simulated interference intensity signal of 25 fs wide sech pulses. (**b**) Expected tunnel current response

How does the interference affect the measurement? In the ideal case, the averaged laser power oscillates from zero to twice the original power as shown in Fig. 10.10(a). Although this oscillation will also result in an oscillation in the tunnel current signal, if the tunnel current has a linear dependency on the laser intensity, the averaged current signal shows no effect from this oscillation and the measurement does not suffer from interference. In reality, however, the relationship between tunnel current and laser intensity is highly nonlinear. As illustrated in Fig. 10.10(b), the averaged tunnel current is also affected by the interference. In the figure, the thin solid line shows the actual tunnel current signal and the thick one shows the low-passed signal. In particular, the component caused by the thermal expansion of the tip is effective because of the strong nonlinearlity depending on the tip–sample distance. Similarly, when the sample is a semiconductor, and a large photovoltage effect is expected, there is a large influence on the measurement because of the fact that the tunneling current has a nonlinear dependence on the bias voltage.

On the other hand, for the time-resolved STM with the delay time modulation method, the amplitude of the modulation is larger than the pulse width. Otherwise, the signal in the tunneling current becomes too small for detection. Therefore, with rough approximation, the change in the tunneling current due to the interference can be considered as a delta function compared to the amplitude of the delay time modulation. Then the observed change in the tunneling current can be represented as

$$I_t(t_d^0 + \Delta t_d \sin \omega t) = I_t(t_d^0) + \Delta t_d \frac{\mathrm{d}I_t}{\mathrm{d}t_d} \sin \omega t + I_t^0 \delta(t_d^0 + \Delta t_d \sin \omega t) \quad (10.2)$$

here, since $\int \delta(f(x))\mathrm{d}x = \sum_{f(x_n)=0} |1/f'(x_n)|$, the output of the lock-in signal when $-\Delta t_d < t_d^0 < \Delta t_d$ is represented as

$$\begin{aligned} S(t_d^0) =& \frac{\omega}{2\pi} \int I_t(t_d^0 + \Delta t_d \sin \omega t) \cdot \sin \omega t \mathrm{d}t \\ =& \frac{1}{2} t_d \frac{\mathrm{d}I_t}{\mathrm{d}t_0} + \frac{4\pi}{\Delta t_d} I_t^0 \frac{t_d^0/\Delta t_d}{\sqrt{1-(t_d^0/\Delta t_d)^2}}. \end{aligned} \quad (10.3)$$

The value obtained for $\mathrm{d}I_t/\mathrm{d}t_d = 0$ and $\Delta t_d = 1\,\mathrm{ps}$ is shown as a dotted lined in Fig. 10.10(a). In this equation, the value diverges when $t_d^0 \sim \Delta t_d$, which does not happen, however, for a finite pulse width. The theoretical result, obtained for a pulse width of 25 fs, is shown by the solid line. The integration of those curves results in half ellipses with a lateral width of $2\Delta t_d$, as shown in Fig. 10.10(b).

As is known by the equation, the interference effect is proportional and inversely proportional to I_t^0 and Δt_d, respectively. Furthermore, when the change in I_t^0 is due to the thermal expansion of the STM tip, the amplitude of the signal is also inversely proportional to $\omega \Delta t_d$. Consequently, the interference signal rapidly decreases with the increase of Δt_d and ω.

10.7 Time-Resolved STM Experiment on GaNAs

10.7.1 Sample Preparation

The first experiment using the SPPX-STM was performed on a GaNAs sample [15]. GaNAs has been investigated as a good candidate for the laser emitting material that can be used in future fast information transfers with the 1.3 μm/1.55 μm band of quartz fiber, similar to the other III-V-N compound semiconductors such as GaInNAs. These materials are superior in the several points to the conventional III-V compound semiconductors, such as GaInAsP and AlGaInAs. Namely, they can form mixed crystals epitaxially grown on the low-cost Si or GaAs substrates. The emitting wavelength can be widely tuned by controlling the composition of nitrogen. They operate much

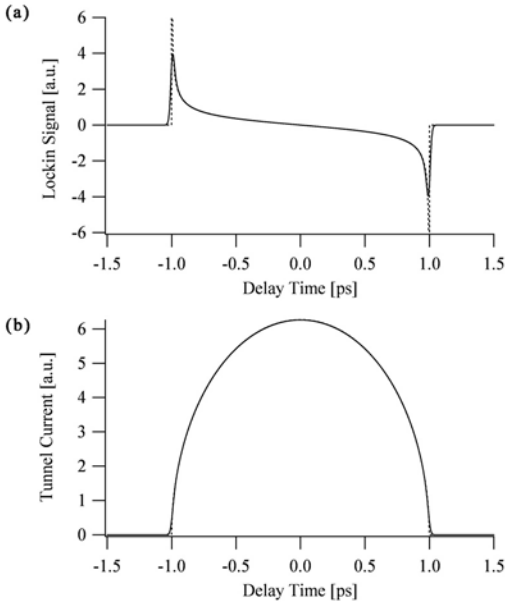

Fig. 10.11. (**a**) Interference signal in the derivative curve for ideally short laser pulse (*dotted*) and for that of 25 fs width (*solid*). (**b**) Integrated signals

more stably at high working temperatures. Besides usage in semiconductor lasers, the III-V-N compound semiconductor is also known as an excellent material to make high efficiency solar cells. However, in order to make use of these valuable properties in realistic device applications, the introducing process of nitrogen should be further investigated. Currently, the introduction of nitrogen often accompanies a considerable amount of defects, which act as non-emitting recombination sites of carriers. Basic research for increasing the crystal quality is intensively being performed.

In such studies, atomic hydrogen exposure during the crystal growth is being given attention. Until recently, hydrogen exposure was generally thought to affect the growth of compound semiconductors negatively. It was reported to passivate the acceptors in p-type semiconductors, to decrease the indium composition in InGaN crystals and to reduce the crystal quality of GaInNAs. However, recent studies suggest that it is not molecular hydrogen but atomic hydrogen that can improve eptaxial growth of compound semiconductors [17–19].

$GaN_{\alpha}As_{1-\alpha}$ (α =0.36%) crystal was used as a specimen, which was grown at low temperature (480°C) with hydrogen exposure (0.3 SCCM) and successively annealed (500–650°C) for reduction of crystal defects.

10.7.2 Analysis by the Optical Pump-Probe Technique

For a better understanding of the sample properties, let us first see the results obtained by the conventional optical pump-probe reflectivity measurement. A schematic of the system setup is shown in Fig. 10.12. Light source is a Ti:Sapphire laser (800 nm wave length, 25 fs pulse width, 80 MHz, <300 mW). The intensity of the pump pulses was adjusted to ∼5 mW. The pump pulses were chopped by an optical chopper. The intensities of the probe pulses before and after reflected by the sample surface are measured by the photodiode-1 (PD1) and photodiode-2 (PD2). Finally, the difference of these signals is detected by the lock-in amplifier synchronously to the chopping frequency. The polarities of the pump and probe pulses were set to be orthogonal, and only the probe signal was selectively detected by using a polarizer in front of each photodiode. The obtained signal was divided by the PD2 value to give the relative change in the sample reflectivity, ΔR/R, caused by the excitation by the pump pulse.

Figure 10.13 shows a typical result obtained for the sample grown at 480°C and annealed at 500–650°C, both in atomic hydrogen environment.

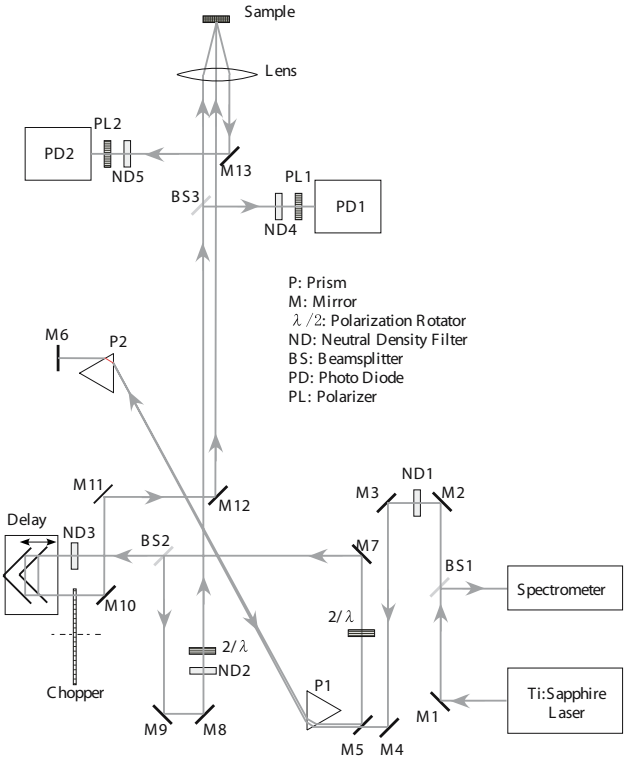

Fig. 10.12. Experimental setup for optical pump-probe reflectance measurement

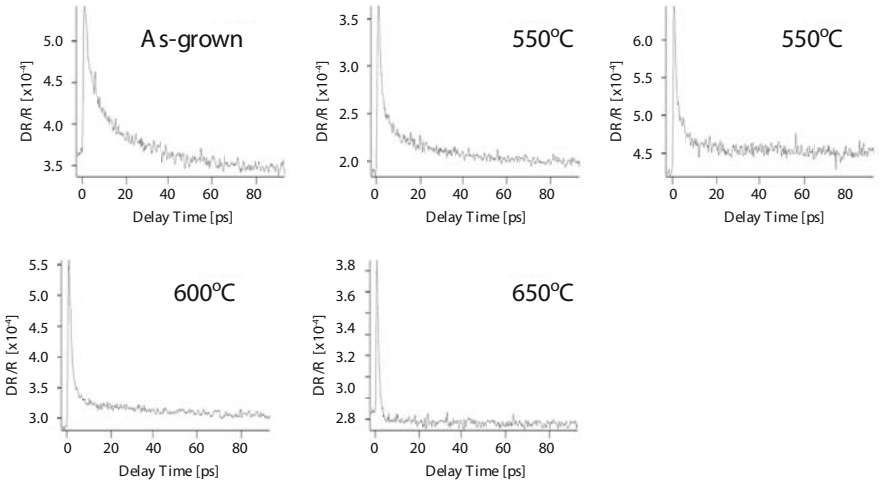

Fig. 10.13. Optical pump-probe reflectivity measurement for $GaN_\alpha As_{1-\alpha}$ ($\alpha = 0.36\%$) sample grown at 470°C and annealed at 500–650°C

ΔR/R signal is plotted as a function of the delay time. As can be seen, two exponential components of a few picoseconds and a few tens of picoseconds decay times were obtained. From the exponential fitting, it was revealed that the shorter decay time is reduced from 2.3 ps for as-grown to 0.71 ps for 650°C by annealing and the amplitude of the slow component of ∼22 ps decay time decreases by annealing.

10.7.3 Results Obtained by the SPPX-STM

Results obtained by the SPPX-STM measurement [15] are discussed in this section. Typical experimental conditions are as follows; Ti:Sapphire excitation laser of 300 mW, central wavelength: 800 nm, bandwidth: 30 nm, pulse width: 25 fs, pulse repetition rate: 80 MHz, delay line: 150 ps, delay line modulation frequency: 20 Hz. Defocusing the laser beam with a concave lens increases the NA of the objective lens to ∼20. The incident angle of the laser pulses is 40–50 degrees from the surface normal, and the pump and probe pulses are *s*-polarized. The light intensity at the tip–sample gap is ∼10 mW. The first step of the STM preamplifier is $\times 10^9$, namely 1 nA/V multiplication with low noise. Weak feedback to the STM *z*-piezo is applied with the cut-off frequency less than 0.2 Hz, and the STM set point is adjusted to 100 pA for sample bias voltage −2 V. The delay time is modulated at ∼20 Hz, and the central value of the modulation is swept linearly with ∼200 sec periodicity. The time constant of the lock-in amplifier is 100 ms and slope of the decay is −24 dB/oct.

Figure 10.14 shows a typical result obtained for the GaNAs sample grown at 480°C and annealed at 600°C in atomic hydrogen environment. The STM

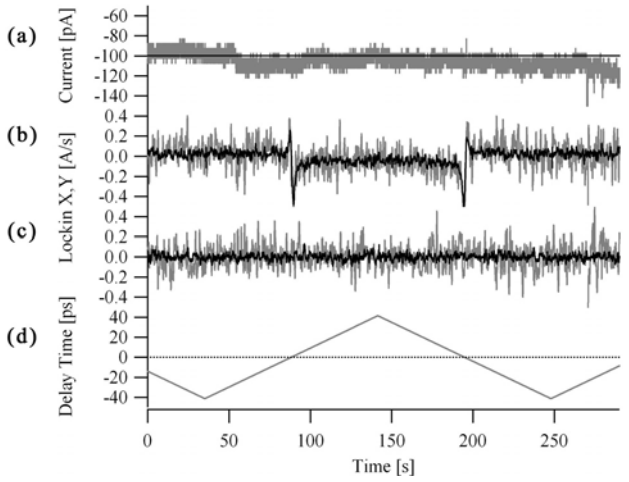

Fig. 10.14. (**a**) Tunnel current, (**b**) in-phase current oscillation amplitude, (**c**) out-of-phase current oscillation amplitude, (**d**) delay time sweep during FTS-STM measurement

measurement was performed in air. Tunnel current, in-phase and out-of-phase lockin signals and delay time are measured as a function of the time and plotted by the gray lines for the first 1.5 scans of delay time. Although high and low frequency noises are included, the peak-to-peak amplitude of the tunnel current deviation is less than ±10% of the reference value (100 pA). In actual measurement, 10–100 sweeps of delay time were performed and the result was averaged in order to reduce the broadband noise. The black lines in the figure represent the results obtained by 32 scans average. As is well known, the noise level decreases with the inverse of the root mean square of the number of scans. Since the thermal drift of tip–sample position affects the experiment, high stability of the tip position must be achieved to analyze the local structure with large amount of averaging.

Figure 10.15(a) shows the obtained signal as a function of the delay time. The up scan and down scan represent the data obtained with increasing and decreasing the delay time, respectively. Generally, there is a slight shift between the two signals due to the lock-in time constant.

Since the measured signal is the derivative, it must be numerically integrated to obtain the delay-time-dependent tunneling current as shown in Fig. 10.15(b). Since the integral constant can not be obtained by the experiment, the absolute value of the tunnel current is undetermined. Here, the value at the left end of the graph is taken to be zero for plotting the data. In general, graphs have a peak or a dip at the zero delay time. The vertical axis represents the amount of change in the tunneling current. Namely, in the case of GaNAs, the tunneling current increased by a few percent when the delay

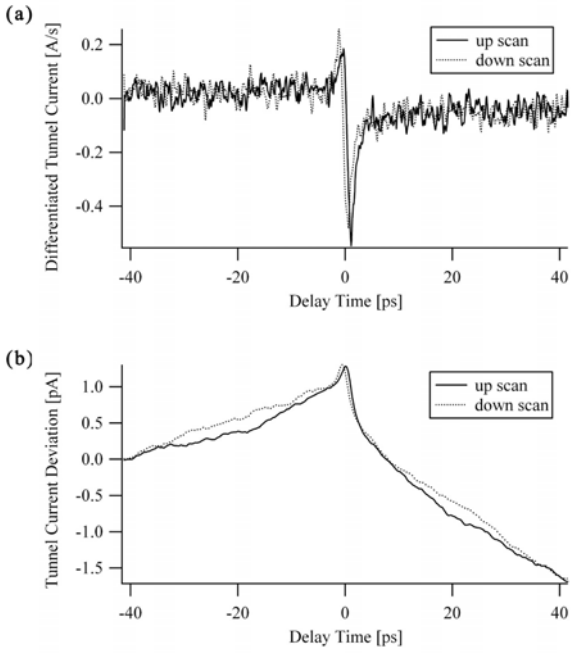

Fig. 10.15. (**a**) Raw and (**b**) integrated signal of FTS-STM from a GaNAs sample

time is reduced to zero. Since sample bias is negative, the tunnel current is measured from the tip to the sample in this experiment. According to the plot, there are two exponential components with a fast (<2 ps) and a slow (∼50 ps) decay time. The plot is asymmetric for positive and negative delay time, due to the difference of the light intensities of the pump and probe pulses (1:2 in this case). When the delay time is negative, the stronger pulse impinges the sample first.

10.7.4 Localized Sensitivity of Time-Resolved Tunnel Current Signal

There may be doubts if this signal is really a tunnel current or not. Namely, various problems have been reported for the laser combined STM measurement until now, such as displacement current due to the stray capacitance of the tunneling gap and photo electrons produced by multiple photon absorption. In particular, there has been a similar result reported by Pfeiffer et al. [20]. They found a delay-time-dependent current signal in their pulse-pair-excited STM experiment with Tantalum and GaAs(110) as samples in UHV. They, however, concluded that their signal was due to the electron emission from the surfaces, which was caused by the multiple photon absorption. In

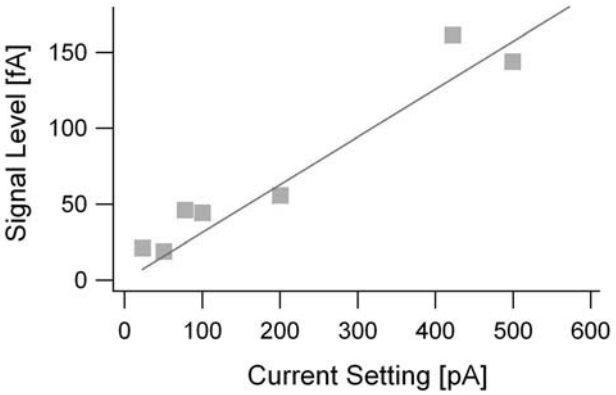

Fig. 10.16. Dependence of FTS-STM signal intensity on tip–sample distance

such cases, spatial resolution is reduced because of the fact that a large area is included in the processes. And the superior space resolution of STM cannot be used. In order to clarify this point, it is important to check if the probe signal is truly spatially localized or not.

Figure 10.16 shows the change in the time-resolved signal as a function of the averaged tunnel current which is related to the tip–sample distance. As is shown in Fig. 10.16, there is a clear linear relationship, and this indicates the signal is really obtained from the area just below the STM tip similar to the ordinary STM measurement.

10.7.5 Relative Intensity of Pump and Probe Pulses

The plots in Fig. 10.15 have peaks at zero delay time and decays towards both left and right sides. However, the plots are not symmetric against left-to-right-flipping. This asymmetry is considered in detail here.

As mentioned above, this asymmetry comes from the light intensity difference between pump and probe pulses. Figure 10.17(a) shows the results obtained by changing the intensity ratio between the intensities of the two pulses from 1 to 4, with one of two being kept constant [21]. When the ratio is 1:1, there remains only a little asymmetry, probably due to the slight misalignment of the tip apex and the spot positions. When the intensities are different, negative delay time represent that the more intense pulse hits the sample first and the weaker one comes later. As shown in Fig. 10.17, the combination of the weak pump and strong probe pulses ($t_d > 0$) shows a strong time dependence and that of the strong pump and weak probe ($t_d < 0$) shows a weak time dependence. In particular, when the ratio becomes $4 : 0.5$, almost no time dependence could be observed when $t_d < 0$.

As seen in Fig. 10.17, in spite of the change in the amplitude, the decay times of the spectra are all similar. To verify this point more clearly, let us

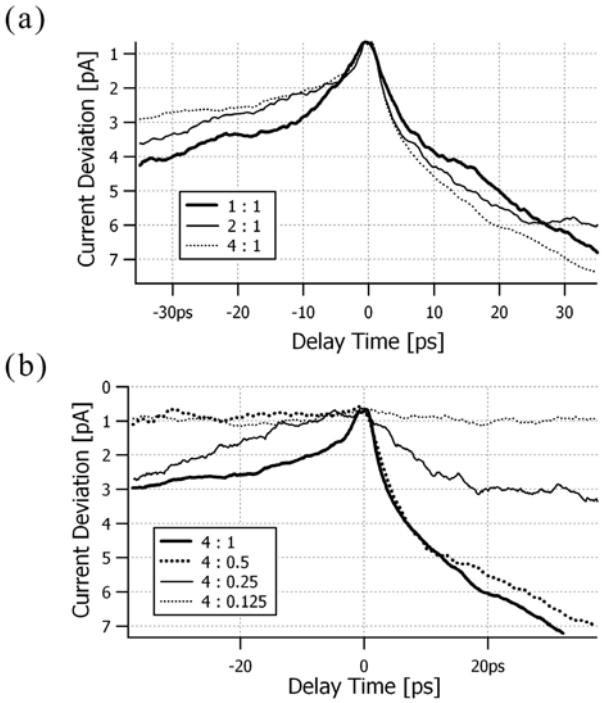

Fig. 10.17. Change in the spectrum shape when the relative intensity of pump and probe pulses are changed

compare the temporal evolution of each spectrum in the $t_d < 0$ and $t_d > 0$ regions. The solid lines in Fig. 10.18(a) to (c) show the tunnel current dependence on the decay time, $I_t(t_d)$, obtained for the intensity ratios of 1:1, 2:1 and 4:1 as seen in Fig. 10.17. The dotted lines are obtained by multiplying (negative delay time region) and dividing (positive delay time region) the inverted signals against zero decay time, $I_t(-t_d)$, by the specific factors. As can be seen in each plot, the factors of 1.6, 2.0, 2.9 give the best fit, which reproduces the original curves very well. This result indicates that the curves for $t_d < 0$ and $t_d > 0$ have similar temporal evolution against the various values of the intensity ratios, besides the prefactors determined by the pulse intensities.

When the intensity of one pulse is increased, as shown in Fig. 10.17(a), the signals increase and decrease for $t_d > 0$ and $t_d < 0$, respectively. Understanding of the phenomena is left for future analysis.

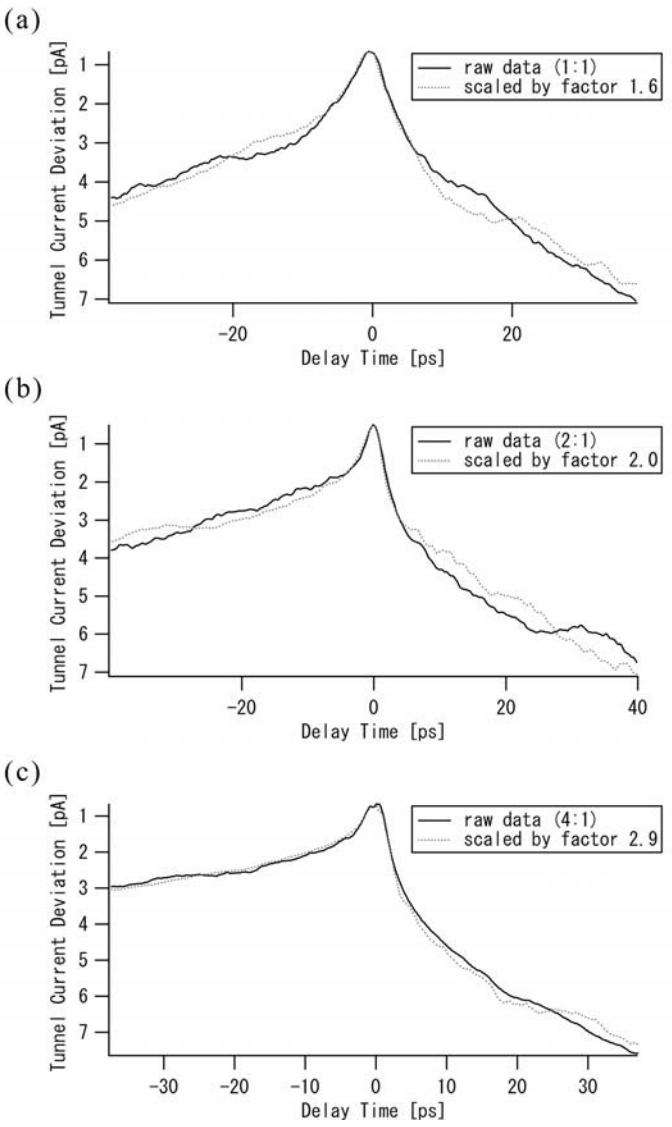

Fig. 10.18. Comparison between the spectrum shapes for negative and positive delay time. The negative/positive delay time region of dotted curve is divided/multiplied by the scale factor

10.7.6 Accurate Fitting Procedure of Time-Resolved Current Signal

Figure 10.19 shows the schematic for the fitting components of the observed graph. As has been seen, the time-dependent STM signal has two exponential components with two different decay constants. And the base lines for the positive and negative delay time region should have the same value, which was approximately represented by a step function as shown in Fig. 10.19. This difference of the base line indicates the existence of a long time scale physical process in the system.

Now, let us discuss the method for accurate analysis of the time constant of the fast response system. Experimental results strongly depend, for example, on the pulse width, parameters of the delay time modulation, and the lock-in time constant. So how do these elements influence the experimental results?

In this case, the pulse width is 25 fs and is small enough compared to the decay time constants of ∼0.5 ps and ∼50 ps so that its influence is not so large. Figure 10.20 shows the autocorrelation of pulse intensity. The difference between the tunnel current signal with and without consideration of the pulse width is shown in Fig. 10.21. As expected, a slight influence appears on the shape of the function around the zero point of the delay time as shown in the magnified graph in the inset.

Next, let us see the relation between the delay time modulation and the lock-in detection. As shown in Fig. 10.22, the delay time was swept between −40 ps and +40 ps at ∼200 s periodicity with ±0.7 ps modulation. When the tunneling current has a delay time dependence as shown in Fig. 10.21, the change in the tunneling current with the sweep will have a structure as shown in Fig. 10.23. In actual measurement, since the slow change of tunneling current is compensated by the weak feedback applied to the z-motion of the piezo, only the high frequency component osscillating at the modulation frequency, whose amplitude is proportional to the derivative of the tunneling current as a function of the delay time sweep appears as a signal. Since

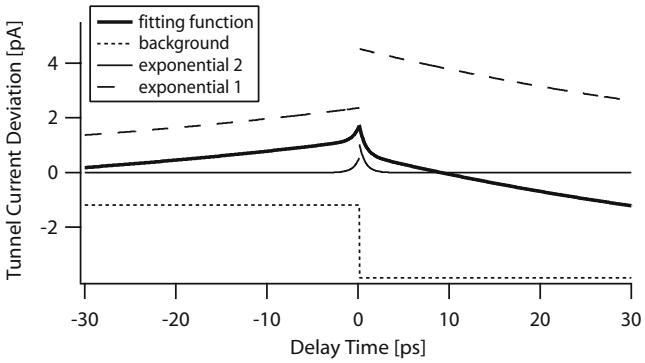

Fig. 10.19. Fitting function for time resolved tunnel current spectrum

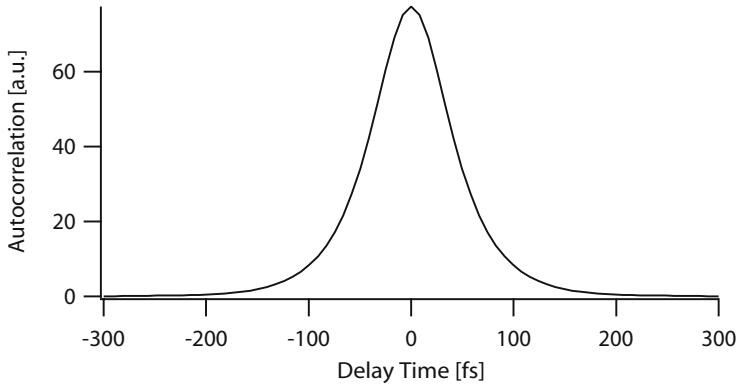

Fig. 10.20. Autocorrelation of pulse intensity

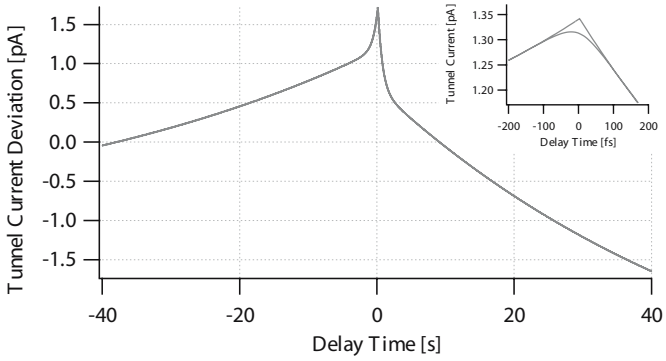

Fig. 10.21. Time-resolved signal with and without consideration of the pulse width

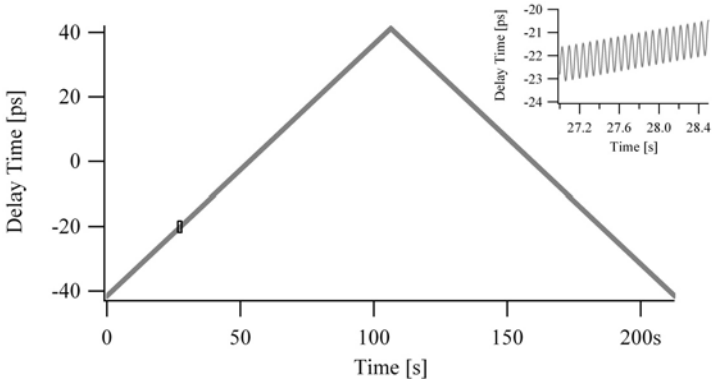

Fig. 10.22. Delay time as a function of time

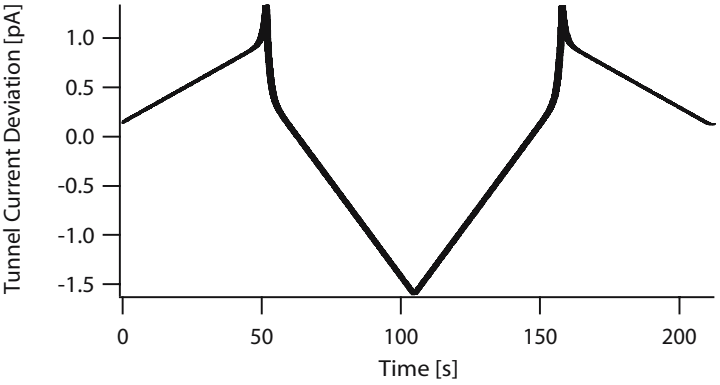

Fig. 10.23. Tunnel current as a function of time

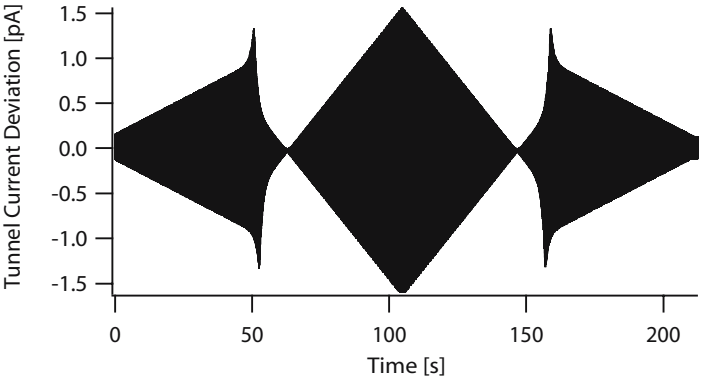

Fig. 10.24. Internal signal in the lock-in amplifier generated by multiplying the tunnel current signal by the sinusoidal modulation signal

the amount of the feedback is about 1% of the tunneling current (typically 100 pA), the influence of the feedback on the measurement can be neglected.

In the lock-in amplifier, the signal shown in Fig. 10.23 is multiplied by a sine wave with the modulation frequency of the same phase, which results in the signal shown in Fig. 10.24. The modulation frequency is too fast to be resolved in the plot. The graph looks as if it is being painted out. This signal appears as the output of the lock-in amplifier after passing through a low pass filter.

A low pass filter is characterized by the time constant t_c and the decay slope in the higher frequency region. For example, the first order low pass filter has slope of -6 dB/oct and the second, third and fourth order filters have -12 dB/oct, -18 dB/oct and -24 dB/oct, respectively. The transmission function of the nth order low pass filter is represented as

$$T_n(s) = 1/(1 + st_c)^n \tag{10.4}$$

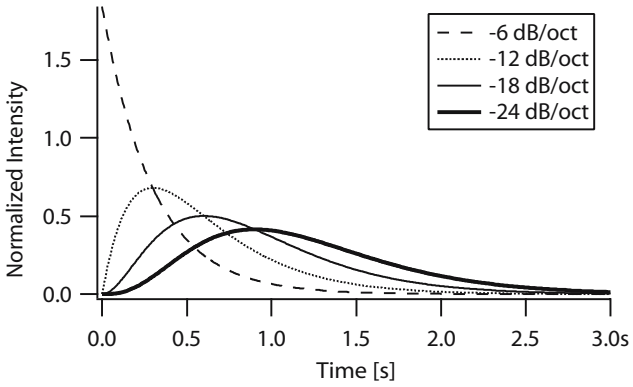

Fig. 10.25. Impulse response of the nth low pass filter

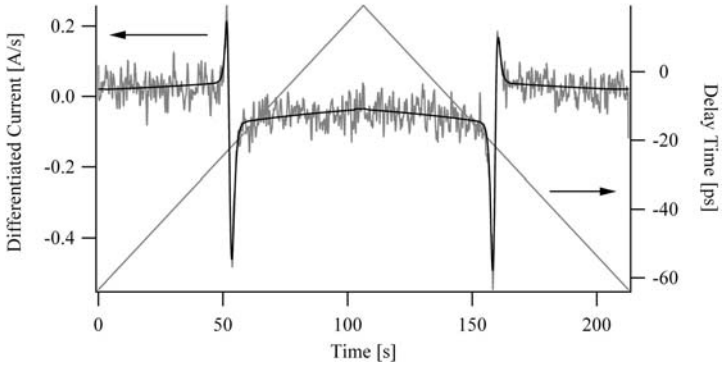

Fig. 10.26. The output of lockin amplifier

And the impulse response of the transmission function becomes

$$I(t) = Ct^{n-1} \exp(-t/t_c). \tag{10.5}$$

As examples, the impulse responses of the filters for the time constant of 100 ms are represented as those in Fig.10.25.

The output of the lock-in amplifier can be obtained by convoluting the impulse response of the low pass filter to the input signal after multiplying by a sine wave. The calculated result is represented by the black line in Fig. 10.26. The detailed shape is influenced by the time constant, and the appearance of asymmetry explains the experimental results well.

Then, optimal fitting of the experimental result by adjusting the fitting parameters will give us the set of accurate parameters to explain the relaxation system of the sample. All the graphs shown in the figures are those obtained by this procedure.

In comparison of the numerically integrated result with that obtained by the fitting process, the shape of the former becomes dull, for the large delay

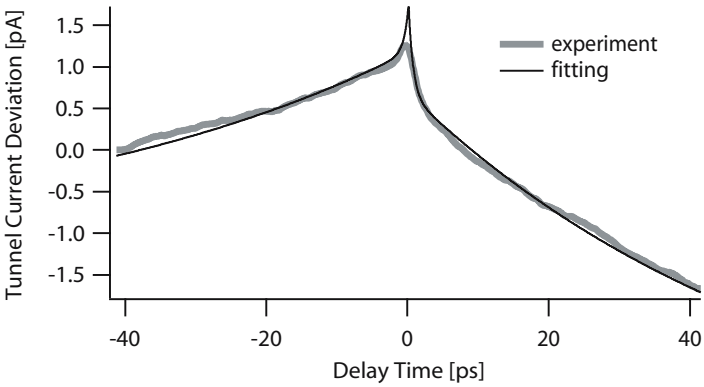

Fig. 10.27. Experimental data and the best fit

time region. This is due to the fact that the original derivative values are obtained by the average of the intensity, which changes over the delay time modulation.

As has been shown, much more accurate values can be obtained by the proposed fitting procedure. Indeed, lifetimes as short as the amplitude of delay time modulation can be derived accurately by the procedure. The obtained parameters are summarized in Table 10.1.

Although these were two exponential components found in the spectra in both experiments, when comparing this result to that of the optical pump-probe reflectivity measurement, the time constants did not coincide. The time constants obtained for the reflectivity measurement were 1.2 ps and 30 ps for a sample annealed at 600°C. Both the lifetimes are longer by a factor of two for the reflectivity measurement. We believe this disagreement is not due to any accidental error. It probably indicates that what we observed by time-resolved STM is not a same physical property of a sample as the measured in the reflectivity measurement.

Table 10.1. Parameters extracted from FT-STM data for GaNAs

Amplitude of the fast decay component	0.55 ± 0.014 pA
Lifetime of the fast decay component	0.653 ± 0.025 ps
Amplitude of the slow decay component	2.36 ± 0.15 pA
Lifetime of the slow decay component	55.1 ± 5.0 ps
Shift of the base line at $t_d = 0$	2.66 ± 0.15 pA

10.8 Conclusion

A noble method, shaken-pulse-pair-excited time-resolved STM was developed to integrate the ultimate time resolution of the optical pump-probe method

with the ultimate spatial resolution of STM technology. When modulating the delay time instead of laser intensity, the method operates stably under the extraordinarily high power excitation of the tunnel gap. When applied to a low temperature grown GaNAs sample, it successfully detected a time-resolved tunnel current signal in subpicosecond transient time. According to the comparison of the time-resolved STM result with that of the conventional optical pump-probe reflectivity measurement, it is suggested that the physical property that is detected by the new method is not the same as what can be obtained by the conventional method.

References

1. F. Demming, K. Dickmann, J. Jersch: Rev. Sci. Inst. **69**, 2406 (1998)
2. J. Jersch, F. Demming, I. Fedotov, K. Dickmann: Rev. Sci. Inst. **70**, 3173 (1999)
3. J. Jersch, F. Demming, I. Fedotov, K. Dickmann: Rev. Sci. Inst. **70**, 4579 (1999)
4. T. Tokizaki, K. Sugiyama, T. Onuki, T. Tani: J. Microscopy **194**, 321 (1999)
5. H. Kawashima, M. Furuki, T. Tani: J. Microscopy **194**, 516 (1999)
6. G. Binnig, H. Rohrer, C. Gerber, E. Weibel: Phys. Rev. Lett. **50**, 120 (1983)
7. S. Weiss, D. Botkin, D.F. Ogletree, M. Salmeron, D.S. Chemla: Phys. Stat. Sol. (b) **188**, 343 (1995)
8. M.R. Freeman, A.Y. Elezzabi, G.M. Steeves, G. Nunes, Jr.: Surf. Sci. **386**, 290 (1997)
9. N.N. Khusnatdinov, T.J. Nagle, G. Nunes, Jr.: Appl. Phys. Lett. **77**, 4434 (2000)
10. R.J. Hamers, D.G. Cahill: J. Vac. Sci. Technol.B **9**, 514 (1991)
11. M.J. Feldstein, P. Vohringer, W. Wang, N.F. Scherer: J. Phys. Chem. **100**, 4739 (1996)
12. V. Gerstner, A. Knoll, W. Pteiffer, A. Thon, G. Gerber: J. Appl. Phys. **88**, 4851 (2000)
13. R.H.M. Groeneveld, H. van Kempen: Appl. Phys. Lett. **69**, 2294 (1996)
14. B.S. Shwartzentruber: Phys. Rev. Lett. **76**, 459 (1996)
15. O. Takeuchi, M. Aoyama, R. Oshima, Y. Okada, H. Oigawa, N. Sano, R. Morita, M. Yamashita, H. Shigekawa: Appl. Phys. Lett. **85**, 3268 (2004)
16. J. Jersch, F. Demming, I. Fedotov, K. Dickmann: App. Phys. A **68**, 637 (1999)
17. Y. Okada, S. Seki, T. Takeda, M. Kawabe: J. Crystal Growth, **237-239**, 1515 (2002)
18. Y. Suzuki, T. Kikuchi, M. Kawabe, Y. Okada: J. Appl. Phys. **86**, 5858 (1999)
19. Y. Okada, S. Ohta, H. Shimomura, A. Kawabata, M. Kawabe: Jpn. J. Appl. Phys. **32**, L1556 (1993)
20. W. Pfeiffer, F. Sattler, S. Vogler, G. Gerber, J-Y. Grand, R. Möller: Appl. Phys. B **64**, 265 (1997)
21. O. Takeuchi, M. Aoyama, R. Oshima, Y. Okada, H. Oigawa, H. Shigekawa: to be published

11 Outlook

M. Yamashita, H. Shigekawa, and R. Morita

We, the editors, would like to briefly point out near-future subjects and directions in few-to-mono cycle photonics (Fig. 11.1) and optical STM. Some details have been already described in the last sections of several chapters.

In few-to-mono cycle photonics, first of all, the complete characterization of the electric field $E(t)$ in few-to-mono cycle pulses should be investigated. For example, when a temporal intensity profile of a sub-two cycle pulse is extremely asymmetric with multi-structures, sub-pulses and side-lobes, its temporal electric field seriously depends on ambiguous quantities of the center angular-frequency ω_0, the group delay $t_{\mathrm{g},0} = \mathrm{d}\phi(\omega)/\mathrm{d}\omega|_{\omega=\omega_0}$ and the constant phase $\phi(\omega_0)$. The generation of completely transform-limited, clean mono-cycle pulses by the improvement of the feedback technique and the application of IPM technique is also an urgent subject. In addition, a study of the coherent synthesis of ultrabroad, high spectral-amplitudes of electric fields with different center wavelengths will play a important role in the near-future development of this field. Moreover, the independent or simultaneous temporal control of different optical parameters in electric fields such as the amplitude $\tilde{E}(t)$, the polarization $\boldsymbol{e}(t)$, the deflection $\boldsymbol{k}(t)$ and the phase $\varphi(t)$ will offer new aspects to the quantum-state control application as well as the information technology application. The extension of this various-parameters control to the four dimensions $(t, \boldsymbol{r})$ might lead to interesting phenomena. Furthermore, one might expect a study on high-field mono-cycle wavepackets to be useful for the development of efficient attosecond x-ray generation and the compact x-ray laser.

On the other hand, the theoretical extension to the nonlinear interaction between optical wavepackets and media including multi-resonant systems without the rotational-wave approximation will be desirable. For example, the extension to the complicated dispersion medium for the super-luminal control, the four dimensional $(t, \mathbf{r})$ extension for the spatiotemporal soliton and the interaction with time-sequential manipulated fields in phase and amplitude for selective biomolecular quantum-state controls will be required.

As is well known, progress in nanoscience and nanotechnology has lowered the barrier height between different fields, and has been realizing the fusion of interdisciplinary research fields day by day. In the last half of this book, we introduced our effort for the development of a new extreme technology that has both capabilities of the ultimate temporal resolution of the ultrashort

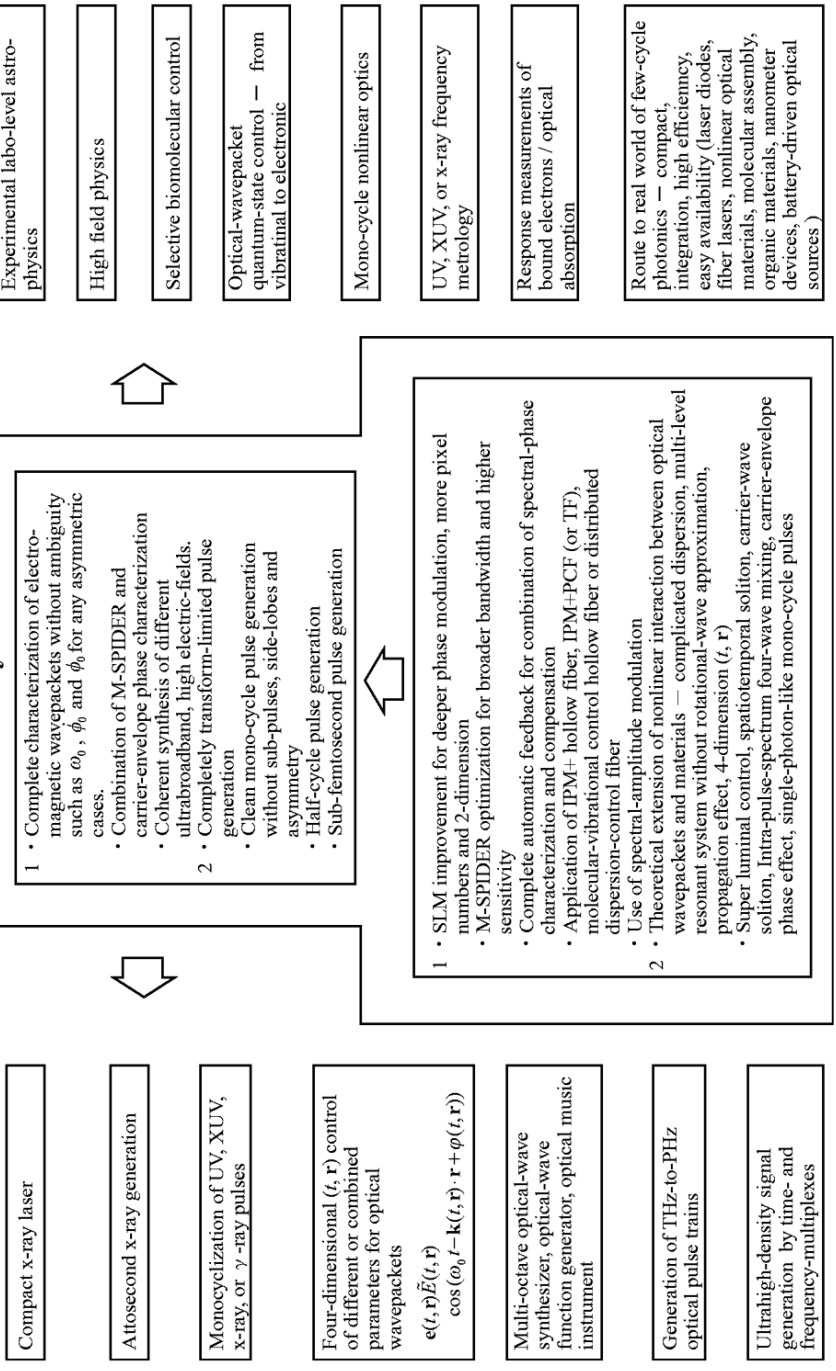

Fig. 11.1. Future directions in "Few-to-Mono Cycle Photonics"

laser pulse technology and of the ultimate spatial resolution of the scanning tunneling microscopic technology. The new technology enables us not only to analyze optically induced electronic and elastic responses of the local structure in a single element, but also to control and manipulate material elements with highly selective and swift performances. Since the interaction between material elements and light plays extremely important roles in the physical properties of material functions, the new technology is expected to be more essential for the nanoscale structures where quantum processes become more effective.

A summary concerning the variety of scanning probe microscopy (SPM) and related techniques (Table 11.1) just presents the future directions that will be realized by the fusion between STM and laser technologies. SPMs are roughly summarized into four categories depending on the type of probes, namely, tunneling current (electrons), photons, atomic or molecular forces and the others. In each category, they are further divided according to the detailed type of external fields, variable parameters or modulations. Although they are all based on positional control methods of the STM tip, physics observed by each technique depends on the type of the probe or the parameters adopted for each. For example, in the case of scanning tunneling spectroscopy (STS), the tunneling current is measured as a function of the bias voltage. And generally, the differentiated signal can be compared with the local density of states (LDOS) of the sample material. On the other hand, when the tunneling current is differentiated as related to the tip-sample distance, the local barrier height for the tunneling process, and the decay constant of the electron wave function can be acquired (BH-STM). Atomic force microscopy (AFM) and related techniques pick up the information of the interaction between the sharp tip on the cantilever and the sample surface just below the tip. In this case, since the interactive force is used as a feedback control instead of tunneling current, low conductive materials can be probed. The tunneling current can be measured simultaneously.

If we measure the force under a laser modulation, we can pick up the dynamics of the system that, for example, influences the interaction between two single molecules. Analysis of the spin-related phenomena (SP-STM, ESR-STM : Table 11.1) must play an important role for the understanding of the nanoscale magnetic characteristic of materials and for the development of fields such as spintronics. In the case of P-STM and SNOM (Table 11.1), the photon is already combined, which technique is expected to give us complementary information. Development in a time scale may bring further possibilities. Recently, carbon nanotube tips have been developed for use as a probe of a more clearly definite local structures under more stable conditions. Besides that, a more applicable probe technique, using multiple tips, has been realized. Combinations of these techniques with our system must open further possibilities.

Table 11.1. Variety of scanning probe microscopy [1–5]

name	probe	modulation, parameter, external field
STM: scanning tunneling microscopy	I_t tunnal current	V:bias voltage
STS: scanning tunneling spectroscopy	$(\mathrm{d}I_t/\mathrm{d}V)/(I_t/V)$:LDOS	
IETS: inelastic tunneling spectroscopy		
BH-STM: barrier height STM	$((\mathrm{d}I_t/\mathrm{d}z)$:LDOS)	gap distance
KPM: Kelvin probe microscopy		
BEEM: ballistic electron emisson microscopy	photon	
ESTM: electrochemical STM	EC current	
STP: scanning tunneling potensiometry		
SP-STM: spin polarized STM	electron-spin	magnetic field
ESR-STM: electron spin resonance STM	electron-spin	
O-STM: optical STM		photon
PM-STM: photomodulated STM		time
FS-STM: femtosecond time resolved STM	electron-spin	
P-STM: photon STM	photon	tunnel electron
SNOM: scanning nearfield optical microscopy		photon
AFM: atmomic force microscopy	force	gap distance
c-AFM: contact AFM		
T-AFM: tapping AFM		
nc-AFM: noncontact AFM		
D-AFM: dynamic AFM		
LFM: lateral force microscopy		friction
CFM: chemical force microscopy		molecule
DFS: dynamic force spectroscopy		loading rate
SCM: scanning capacitance microscopy		V: bias voltage
SMM: scanning maxwell stress microscopy		
EFM: electrostatic force microscopy		
MFM: magnetic force microscopy		magnetic field
TAM: tunneling acoustic microscopy	phonon	phonon
SThP: scanning thermal profiler	heat	temperature
SHM: scanning hall-probe microscopy	hall voltage	magnetic field

References

1. T. Sakurai, T. Watanabe: *Advances in Scanning Probe Microscopy*, (Springer, Berlin, 1999)
2. R. Wisendanger: *Scanning Probe Microscopy* (Springer, Berlin, 1998)

3. S. Morita, R. Wiesendanger, E. Meyer: *Noncontact Atomic Force Microscopy* (Springer, Berlin, 2003)
4. R. Wiesendanger: *Scanning Probe Microscopy and Spectroscopy* (Cambridge University Press, Cambridge, 1994)
5. S. Grafström: J. Appl. Phys. **91**, 1717 (2002)

Index